HAL
open science

Paleomagnetism and petrogenesis of Paleoproterozoic units from the Uatumã event in the northern Amazonian Craton

Paul Yves Jean Antonio

To cite this version:

Paul Yves Jean Antonio. Paleomagnetism and petrogenesis of Paleoproterozoic units from the Uatumã event in the northern Amazonian Craton. Paleontology. Université Paul Sabatier - Toulouse III, 2017. English. NNT : 2017TOU30042 . tel-01531494v2

HAL Id: tel-01531494

https://theses.hal.science/tel-01531494v2

Submitted on 8 Jun 2018

HAL is a multi-disciplinary open access archive for the deposit and dissemination of scientific research documents, whether they are published or not. The documents may come from teaching and research institutions in France or abroad, or from public or private research centers.

L'archive ouverte pluridisciplinaire **HAL**, est destinée au dépôt et à la diffusion de documents scientifiques de niveau recherche, publiés ou non, émanant des établissements d'enseignement et de recherche français ou étrangers, des laboratoires publics ou privés.

Université Fédérale
Toulouse Midi-Pyrénées

THÈSE

En vue de l'obtention du

DOCTORAT DE L'UNIVERSITÉ DE TOULOUSE

Délivré par :

Université Toulouse 3 Paul Sabatier (UT3 Paul Sabatier)

Cotutelle internationale avec l'Université de São Paulo (IAG-USP)

Présentée et soutenue par :
Paul Yves Jean Antonio
le jeudi 16 février 2017 à São Paulo (Brésil)

Titre :

Paléomagnétisme et pétrogenèse des unités paléoprotérozoïques de l'évènement Uatumã au nord du craton amazonien.

École doctorale et discipline ou spécialité**:**
ED SDU2E : Sciences de la Terre et des Planètes Solides

Unité de recherche :
Géosciences et Environnement Toulouse(GET)

Directeur/trice(s) de Thèse :

Prof. Anne Nédélec
Prof. Manoel Souza D'Agrella-Filho

Jury :

Anne Nédélec	Professeur émérite	Directrice de thèse
Manoel Souza D'Agrella-Filho	Maître de conférences	Directeur de thèse
Hervé Théveniau	Directeur de recherche	Rapporteur
Augusto Ernesto Rapalini	Maître de conférences	Rapporteur
Jean Luc Bouchez	Professeur émérite	Président du jury
Wilson Teixeira	Professeur d'Université	Examinateur

UNIVERSIDADE DE SÃO PAULO
INSTITUTO DE ASTRONOMIA, GEOFÍSICA E CIÊNCIAS ATMOSFÉRICAS
DEPARTAMENTO DE GEOFÍSICA

Paleomagnetismo e petrogênese de unidades Paleoproterozóicas do evento Uatumã no norte do Craton Amazônico

Paul Yves Jean Antonio

Orientadores: Prof. Dr Manoel Souza D'Agrella Filho

Prof. Dr Anne Nédélec

São Paulo

Fevereiro de 2017

Paul Yves Jean Antonio

Paleomagnetism and petrogenesis of Paleoproterozoic units from the Uatumã event in the northern Amazonian Craton.

PhD thesis presented to the Instituto de Astronomia Geofísica e Ciências Atmosféricas da Universidade de São Paulo (IAG-USP) to obtain a PhD. In Geophysics.

Supervisors: Prof. Dr Manoel Souza D'Agrella Filho

Prof. Dr Anne Nédélec

São Paulo

February, 2017

AGRADECIMENTOS - REMERCIEMENTS

Eu gostaria de agradecer prioritariamente meus orientadores da tese pela orientação e a confiança que me depositaram para terminar este trabalho. Ao Prof. Manoel Souza D'Agrella Filho que me orientou desde os trabalhos de campo até a redação da tese. Foi ele (e seus braços) quem me deu força para amostrar a Provincia Carajás. Je tenais aussi remercier le Prof. Anne Nédélec grâce à qui j'ai pu réaliser ce projet de recherche entre le Brésil et la France. Elle a toujours été présente dans ces 4 années de thèse pour prendre du temps afin de répondre à toutes mes questions. Gostaria de agradecer também o Prof. Ricardo I.F Trindade (meu terceiro Professor). Ele estava sempre lá para me ajudar, durante minha adaptação na vida brasileira, uma "casa", minhas questões científicas e ainda mais... Agradeço vocês por estes quatro anos de tese que me ensinaram muito, cientificamente e humanamente (embora meu português não seja ainda muito bom).

Também gostaria de agradecer todas as pessoas do laboratorio do IAG. Os (as) secretários (as) que perderam muito tempo com meus documentos (Marcel, Ana, Teca,....). Os técnicos e amigos do laboratorio que estavam sempre presentes quando nada funcionava e também, para beber uma cervejinha (Dani, Plinio, Giovanni). Também, a todos os estudantes do laboratorio que ficam as noites trabalhando para a ciencia (a lista é longa...). Agradeço especialmente Franklin Bispo dos Santos que sempre me ajudou a responder as minhas perguntas (quase meu quarto professor) e por todas as discussões sobre vários assuntos.

Agradeço todos os Professores que me ajudaram durante os campos na Amazônia - o Prof. Davis Carvalho, o Profa. Marcia Barros, o Prof. Elming, o Prof. Roberto Dall'Agnol - e também os estudantes, Mayara Fraeda, Fernando Fernandes Da Silva, Bhrenno Marangoanha, Jão, Mariana... Também, à todas as pessoas do laboratorio de Ouro Preto (Prof. C. Lana e a Ana) que me ajudaram datar meus zircões e aos estudantes Carmen, Capucine, Léo..., por me ajudarem a descobrir esta cidade maravilhosa. Agradeço também à minha Carmen (meu amor que me ajudou até o final).

Agradeço a todos os amigos que não são do IAG e que encontrei em São Paulo com quem eu descobri a vida brasileira (Jean Seb, Guigui, Nanahide, André, Vagner, Joelson, Ricardo, Pedro Sangafé e o O' doborogodo, e o CEPE USP...). Agredeço também todas as pessoas com quem eu descobri o canionismo no Brasil.

De temps à autres j'étais au laboratoire du GET à Toulouse donc je remercie encore toutes les personnes du laboratoire qui m'ont beaucoup aidé. Je remercie bien sûr Philippe et Sophie du service microsonde, Thierry du service MEB, Jo et Manu en salle blanche, et Stéphanie du TIMS.

Je remercie notamment tous les thésards et post-docs que j'ai côtoyés de près et de loin en passant par le père Boutin, Adrien, Thomas, Léandre, Damien, Arno, Bryan, Florent, Baptiste, Mathieu, Jing, Laetitia, Nicolas ; Sofia… et bien sûr Caro avec qui je partage cette fin de thèse et nos petits soucis sud-américains.

Je dédicace bien sûr cette thèse à mes parents, ma grand-mère, ma famille, et mes amis qui m'ont toujours soutenu et supporté dans les moments difficiles ainsi qu'à mon papi qui est parti trop tôt et qui n'aura jamais pu voir la fin...

Finally, I would like to thank the members of my dissertation committee - not only for their time and extreme patience, but for their intellectual contributions to improve the manuscript.

Agradeço à Universidade Federal do Pará (UFPA) pelo suporte logístico nas viagens de campo e à **FAPESP** pelo suporte financeiro, através da bolsa de Doutorado (*2012/20335-4*), da bolsa BEPE (*2013/23036-0*) e dos projetos de pesquisa (*2011/50887-6*, *2016/13689-5*) que financiaram todo o meu trabalho.

"I think that this rather astonishing, even fascinating, idea (of TPW) deserves the serious attention of anyone who concerns himself with the theory of the earth's development."

A. Einstein (Hapgood, 1958)

Resumo

Um grande magmatismo intraplaca cobriu várias áreas (1.500.000 km^2) do Cráton Amazônico há 1880 Ma, o qual define uma grande província ígnea (SLIP) chamada coletivamente de "evento Uatumã". O objetivo deste trabalho é estudar o paleomagnetismo e a petrologia dessas rochas para definir o contexto espaço-temporal do evento Uatumã e a posição do cráton Amazônico dentro do Supercontinente Columbia. Duas áreas de estudo foram escolhidas para a amostragem, localizadas no sudoeste do cráton Amazônico (Pará): (1) A região de Tucumã, onde 16 diques félsicos, 7 diques máficos, um dique de gabro e 3 sítios da granodioritos do embasamento Arqueano foram coletadas. (2) A região de São Felix do Xingu, onde 7 sitios de lavas riolíticas, 2 sitios de ignimbritos, um dique felsico e um de brechas vulcânicas da Formação Santa Rosa foram amostrados. Seis sitios da Formação Sobreiro (rochas vulcanoclásticas andesíticas) e um dique felsico da Suite Velho Guilherme foram também coletados. O estudo petrológico em amostras dos diques felsicos de Tucumã (1880.9 ± 6.7 Ma U-Pb zrn) mostra que eles representam um sistema de siques associado à Formação vulcânica Santa Rosa. A magnetização remanente dos diques felsicos é portada por magnetita PSD e hematita. A hematita é sin- a pós-magmática e a mineralogia magnética pode ser usada para quantificar esta alteração hidrothermal. Desmagnetizações AF, térmica, LTD + AF e LTD + térmica mostram uma componente característica com direção noroeste e inclinação positiva (Componente A) para amostras de 16 sítios, cuja direção média é Dm= 330.5, Im= 27.9 (N= 16, α95= 11.4, R= 14.7, k= 11.47). O pólo paleomagnético calculado com a média dos PGVs está localizado em 52.9°S, 76.4°E (A_{95}= 10.4°, K= 13.52). Entretanto, esta componente parece ser decorrente de uma remagnetização, provavelmente ocorrida durante o final do Neoproterozoico. Outra componente (chamada de Componente B) foi também isolada para estas rochas, a qual foi associada a uma remagnetização regional ocorrida durante a formação da Província Magmática do Atlântico Central (PMAC). Ainda, uma Terceira componente (C), representada por direções sudoeste e inclinações positivas baixas foi isolada para amostras de alguns sítios. Esta componente foi interpretada como sendo relacionada ao evento magmático da Suíte Intrusiva Velho Guilherme com idade de ~1860 Ma. Os melhores resultados, entretanto, foram obtidos para a região de São Felix do Xingu. Dois novos polos paleomagnéticos, considerados de origem primária, foram encontrados para o Craton Amazônico: O polo SF1 (319.7°E; 24.7°S; N= 10; A_{95}= 16.9°) foi obtido para rochas félsicas e andesíticas, as quais foram datadas em 1877.4 ± 4.3 Ma (U-Pb zrn, LA-ICP-MS), sendo que sua origem primária é embasada em um teste de contato cozido inverso. A investigação petrográfica mostra que o portador magnético desta componente é atribuído à hematita, formada por processos hidrotermais tardi- a pós-magmáticos. O polo SF2 (220.1°E;

31.1°S; N= 15; A_{95}= 9.7°) foi determinado para a componente de magnetização revelada para o dique da Suíte Velho Guilherme, Esta componente é também encontrada como componente secundária em amostras das formações Santa Rosa e Sobreiro, além de algumas amostras de sítios coletados na região de Tucumã (Componente C). Uma idade de 1853.7 ± 6.2 Ma (U-Pb zrn, LA-ICP-MS) foi atribuída à componente SF2 e sua origem primária é confirmada pelo teste de contato cozido positivo realizado para este dique. Os polos SF1 e SF2 são bem discrepantes, embora a diferença de idade destes polos seja de apenas 25 Ma. Resultados similares têm sido obtidos para polos de mesma idade de outros blocos cratônicos (India, Superior (Laurentia), Slave (Laurentia), Kalahari, Baltica e Sibéria), os quais podem ser explicados por um evento de deriva polar verdadeira (DPV) ocorrido nesta época, em decorrência de uma reorganização do Manto. Esta época (1880 Ma) é marcada por uma alta atividade do Manto, a qual culminou com a formação do Supercontinente Columbia, por volta de 1850 – 1800 Ma. A formação de superplumas e o isolamento térmico causado pela consequente formação do Columbia podem ter sido causas de perturbações de densidades que alteraram o tensor inercial da Terra e, consequentemente, um evento de DPV pode ter deslocado os continente e as superplumas para a região do equador. Estas condições podem estar ligadas a uma inteira reorganização mantélica que seguiu um período de pouca atividade magmática, ocorrido entre 2400 e 2200 Ma.

Palavras chaves : Cráton Amazônico, Paleomagnetismo, Columbia, Deriva polar verdadeira, Uatumã.

Abstract

An anorogenic magmatism covered a large part (1.500.000 km^2) of the Amazonian craton at *ca*. 1880 Ma and defined a Silicic Large Igneous Province (SLIP) called the Uatumã event. The aim of this work is to study the paleomagnetism and petrology of these rocks to define the space-time framework of the Uatumã event and to try to elucidate the Amazonian craton evolution during the Columbia supercontinent amalgamation. Two regions were selected in the southwestern Amazonian craton (Pará) for sampling: (1) The Tucumã area where 16 felsic dikes, 7 mafic dikes, a gabbroic dike and 3 sites of the Archean basement were collected, and (2) the São Felix do Xingu area where, 7 sites of rhyolitic lava flows, 2 sites of ignimbrites, a felsic dike and a volcanic breccia belonging to the Santa Rosa Formation were sampled, and also 6 sites of the Sobreiro Formation (volcanoclastic rocks, andesitic) and one felsic dike of the Velho Guilherme Suite were collected. Petrology of the felsic dikes of Tucumã (1880.9 ± 6.7 Ma U-Pb zrn) showed that they represent the dike swarm associated with the Santa Rosa volcanic Formation. The remanent magnetization of the felsic dikes is carried by PSD magnetite and hematite. This hematite is syn- to post magmatic derived from hydrothermal fluids. Magnetic mineralogy can be used as a proxy to quantify the hydrothermal alteration. AF, thermal, LTD + AF and LTD + thermal demagnetizations show a northwest direction with a positive inclination (component A), whose site mean directions gives a paleomagnetic pole located at 52.9°S, 76.4°E, A_{95}= 10.4 °, K= 13.52). However, this component seems to represent a remagnetization, probably occurred at Neoproterozoic times. Another magnetic component (named component B) was also isolated for these rocks, and it was associated to a Mesozoic regional remagnetization related to the Central Atlantic Magmatic Province (CAMP). Yet, a third southwestern direction with low positive inclination (component C) was also isolated for some sites. This component was interpreted to be related with the ca. 1760 Ma Velho Guilherme magmatic intrusion. The best paleomagnetic results were obtained in the São Felix do Xingu area. Two new primary paleomagnetic poles have been determined: (i) SF1 pole (319.7°E, 24.7°S, N= 10; A_{95}= 16.9 °) was obtained for andesites and rhyolites dated to 1877.4 ± 4.3 Ma (U-Pb zrn, LA-ICPMS), and its primary origin is confirmed by an inverse baked contact test (> 1853 Ma). Petrography shows that the magnetic mineralogy of this component is hematite formed by hydrothermal fluids syn- to post magmatic. (Ii) SF2 pole (220.1°E, 31.1°N, N= 15 ° A_{95}= 9.7 °) was determined by the remanent magnetization of the felsic dike of the Velho Guilherme Suite but also as secondary magnetizations in samples of the Santa Rosa and Sobreiro Formations. An age of 1853.7 ± 6.2 Ma (U-Pb zrn, LA-ICPMS) is calculated for the felsic dike carrying SF2, whose primary

origin is confirmed by a positive baked contact test. The SF1 and SF2 poles have a significant difference in angular distance, for a time interval of only ~25 Ma.

Similar coeval paleomagnetic discrepancies were observed for other cratons (India, Superior (Laurentia), Slave (Laurentia), Kalahari, Baltica and Siberia), which can be explained by a True Polar Wander (TPW) event at *ca*. 1880 – 1860 Ma. This period is marked by a high mantle activity, which results in the amalgamation of the Columbia supercontinent, formed at *ca*. 1850 – 1800 Ma. Amalgamation of supercontinent may cause the formation of superplume and thermal insulation which can disturb mass distribution in mantle and alter the inertial gravity tensor of the Earth. A True Polar Wander (TPW) event may thus have taken place, which will move the cratons and the superplumes towards the equator. These conditions may be related to a reorganization of the whole mantle following a global magmatic quiescence between 2400 and 2200 Ma.

Keywords: Amazonian craton, Paleomagnetism, Columbia, True polar wander, Uatumã.

Résumé

Un volumineux magmatisme anorogénique a recouvert une large partie (1.500.000 km^2) du craton Amazonien à 1880 Ma et définit une province magmatique felsique qu'on appelle l'événement Uatumã. L'objectif de ce travail est d'étudier le paléomagnétisme ainsi que la pétrologie de ces roches afin de préciser le cadre spatio-temporel de cet événement et de définir la place du craton Amazonien au sein du Supercontinent Columbia. Deux régions d'études localisées dans le sud-ouest du craton Amazonien (Pará) ont permis de collecter les échantillons nécessaires : (1) la région de Tucumã où 16 filons felsiques, 7 filons mafiques, un filon gabbroïque et 3 sites du socle archéen ont été collectés. (2) la région de São Felix do Xingu où on a échantillonné 7 sites de laves rhyolitiques, 2 sites d'ignimbrites, un filon felsique et un site de brèches volcaniques qui appartiennent à la formation Santa Rosa. 6 sites de la formation Sobreiro (roches volcanoclastiques andésitiques) ainsi qu'un filon felsique de la suite Velho Guilherme ont aussi été collectés. Un des résultats majeurs de la pétrologie des filons felsiques de Tucumã (1880.9 ± 6.7 Ma U-Pb sur zircon) a été de montrer qu'ils représentent le système filonien associé à la formation volcanique Santa Rosa. L'aimantation rémanente des filons felsiques est portée par la magnétite et l'hématite. Cette hématite est syn- à post-magmatique et sa formation, à partir des fluides hydrothermaux, peut être quantifiée grâce certaines propriétés magnétiques. Les désaimantations (en champ alternatif, thermiques) montrent une composante A caractéristique de direction nord-ouest avec une inclinaison positive dont la moyenne par site donne un pôle paléomagnétique localisé à 52.9°S, 76.4°E (A_{95}= 10.4°, K= 13.52). Une réaimantation régionale mésozoïque en relation avec les filons de la CAMP (Central Atlantic Magmatic Province) est observée dans cette région. Les meilleurs résultats paléomagnétiques ont été obtenus dans la région de São Felix de Xingu. Deux nouveaux pôles paléomagnétiques primaires, ont été déterminés: (i) Le pôle SF1 (319.7°E, 24.7°S, N= 10; A_{95}= 16.9°) est obtenu pour des andésites et des rhyolites datés à 1877.4 ± 4.3 Ma (U-Pb zrn, LA-ICPMS), son origine primaire est confirmée par un test de contact inverse (> 1853 Ma). La pétrographie montre que la minéralogie magnétique de cette composante est l'hématite formée par des fluides hydrothermaux syn- à post-magmatiques. (ii) Le pole SF2 (220.1°E, 31.1°N, N= 15; A_{95}= 9.7°) est déterminé par l'aimantation rémanente du filon felsique de la Suite Velho Guilherme, mais aussi par l'aimantation secondaire dans les échantillons de la formation Santa Rosa et Sobreiro. Un âge de 1853.7 ± 6.2 Ma (U-Pb zrn, LA-ICPMS) est calculé pour le filon felsique portant SF2, dont l'origine primaire est confirmée par un test de contact positif. Les pôles SF1 et SF2 sont très différents, malgré une différence d'âge de seulement ~25 Ma. Des résultats paléomagnétiques similaires ont été obtenus pour les pôles de même âge dans d'autres cratons (Inde, Supérieur (Laurentia), Slave (Laurentia), Kalahari,

Baltica et Sibérie), et peuvent être expliqués par un événement de Vrai Dérive Polaire (VDP). Cette époque (~1880 Ma) est marquée par une forte activité du manteau, qui aboutit à la formation du Supercontinent Columbia, autour de 1850 – 1800 Ma. La formation de superpanaches est une conséquence possible de l'assemblage du supercontinent et de l'effet d'isolation thermique du manteau qui en résulte, ou bien lui est concomitante. Les superpanaches peuvent provoquer des perturbations de densité modifiant le tenseur inertiel de gravité de la Terre. Un rapide événement de Vrai Dérive Polaire (VDP) peut ainsi avoir eu lieu, ce qui va déplacer rapidement les continents et les superpanaches vers l'équateur. Ces événements peuvent être liés à une réorganisation du manteau dans son ensemble à la suite d'une période de faible activité magmatique entre 2400 et 2200 Ma.

Mots clés : Craton Amazonien, Paléomagnétisme, Columbia, Vrai dérive polaire, Uatumã.

Summary

Resumo 6
Abstract 8
Résumé 10
Summary 12
Introduction générale 15
Introduction 18
Chapter.1: Paleoproterozoic Era and the Columbia supercontinent 21
1.1 Paleoproterozoic geodynamics 21
1.1.1 Earth's Atmosphere, Hydrosphere, and Biosphere 22
1.1.2 Cooling of the mantle and crustal evolution 25
1.1.3 Stabilization of cratons 30
1.2 Definition and evolution of supercontinents 38
1.3 Evidence for a Paleoproterozoic supercontinent 42
1.4. Models for the Columbia supercontinent 54
Chapter 2: Position of the Amazonian craton in Columbia: 65
The paleomagnetic problem 65
2.1 The Amazonian craton 65
2.2 Paleomagnetic database for the Amazonian craton – implications to the paleocontinent Columbia 68
2.3 Paleomagnetic problem and birth of this study 70
2.4 Paper "Amazonian Craton paleomagnetism and paleocontinents" (co-author) 71
Chapter. 3: The Carajás Province, Sampling 97
3.1 Target of the study: The Uatumã LIP, a Paleoproterozoic SLIP 97
3.2 The Carajás Province 99
3.3 Sampling and geological setting 105
3.3.1 Tucumã area 105
3.3.2 São Felix do Xingu area 108
Chapter. 4: Methodology 113
4.1 Paleomagnetism 113
4.1.1 Paleomagnetic sampling 113
4.1.2 Anisotropy of magnetic susceptibility (AMS) 115
4.1.3 The remanent magnetization 116
4.1.4 Demagnetization techniques 119
4.1.4.1 Alternating Field (AF) demagnetization 119
4.1.4.2 Thermal demagnetization 120

4.1.4.3 LTD demagnetization 121
4.1.5 Magnetic mineralogy 122
4.1.6 Analysis of components 125
4.1.7 Field tests and paleomagnetic stability 129
4.1.7.1 Reversals test 129
4.1.7.2 Baked contact test....129
4.1.7.3 Regional consistency 130
4.1.8 Paleomagnetic pole....131
4.1.9 Paleogeographic reconstruction in the Precambrian....133
4.1.9.1 GAD through Precambrian? 133
4.1.9.2 Paleolatitude reconstruction 135
4.1.9.3 Comparison between two cratons 136
4.1.9.4 True Polar Wander (TPW) reconstruction....138
4.2 Geochronology....143
4.2.1 U-Th-Pb system 143
4.2.2 SHRIMP analysis 145
4.2.3 LA-ICPMS analysis 146
4.3 Geochronological and paleomagnetic systems....147
Chapter. 5: Petrology and magnetic mineralogy of the Tucumã dike swarms; overview of the dike swarm of the Uatumã event 151
5.1 Lithology....151
5.1.1 Field observations 151
5.1.2 Microgranitic dikes 153
5.1.2.1 Petrography 153
5.1.2.4 Sequence of crystallization....158
5.2 Mineral chemistry of microgranites 159
5.3 Geochronology....161
5.4 Magnetic properties....161
5.4.1 Magnetic Mineralogy 161
5.4.1.1 Hysteresis curves....161
5.4.1.2 Isothermal remanent magnetization (IRM) curves 163
5.4.1.3 Kruiver’s analysis 165
5.4.1.4 Day plot....166
5.4.1.5 Thermomagnetic curves....167
5.4.2 Summary for the magnetic mineralogy 168
5.5 Whole rock geochemistry 171
5.5.1 Major and trace elements geochemistry....171
5.5.2 Relation between petrology and magnetism....174

5.6 Paper of da Silva et al. (2016) (co-author) 175
Chapter. 6: AMS and paleomagnetic data for the Tucumã dike swarms 196
6.1 Magnetic Mineralogy 196
6.2 Anisotropy of magnetic susceptibility (AMS) 197
6.3 Paleomagnetic results 202
6.3.1 Magnetic components 202
6.3.2 Mean directions and paleomagnetic poles 204
6.4 Baked contact tests 207
6.5 Reliability of Tucumã poles 210
Chapter. 7: Turmoil before the boring billion: Paleomagnetism of the 1880 – 1860 Ma Uatumã event in the Amazonian craton 214
Abstract 214
7.1 Introduction 215
7.2 Geological setting and lithology 216
7.3 Sampling and analytical methods 220
7.3.1 Paleomagnetism 220
7.3.2 Geochronology 223
7.4 U-Pb Geochronology 224
7.5 Paleomagnetic results 227
7.6 Baked contact test 231
7.7 Magnetic mineralogy 233
7.8 Oxide textural analysis 235
7.9 Discussion 237
7.9.1 U-Pb geochronology 237
7.9.2 Confidence of the paleomagnetic poles 237
7.9.3 Paleomagnetic discrepancies between 1.9 – 1.8 Ga 240
7.9.4 True polar wander and paleogeography at 1880 – 1860 Ma 244
7.9.5 Geological turmoil during the amalgamation of the Supercontinent Columbia 251
7.10 Conclusions 253
Acknowledgements 253
Conclusions (English) 254
Conclusions (French) 258
List of Figures 262
List of Tables 271
REFERENCES 273
SUPPLEMENTARY MATERIAL 302

Introduction générale

Le paléomagnétisme est considéré comme l'unique méthode quantitative pour analyser le mouvement horizontal des masses continentales au cours des temps géologiques. Il est même la première preuve irréfutable que les masses continentales se sont déplacées à la surface de la Terre donnant naissance à la théorie de la tectonique des plaques (Creer et al., 1954; Runcorn, 1965). Il a été longtemps admis que continents actuels ont évolué à partir d'un continent unique, ou supercontinent, la Pangée qui s'est formée autour de 280 Ma. Les planchers océaniques d'âge > 200 Ma ayant disparu, il est difficile de reconstruire la position des paléo-continents par l'étude des anomalies magnétiques océaniques. Le paléomagnétisme est ainsi la méthode principale permettant de retracer l'évolution des continents dans le passé. Pour établir les reconstructions les plus précises possibles on associe le paléomagnétisme à l'alignement des ceintures orogéniques, la géochronologie, les «code-barres» des Provinces Magmatiques Géantes (PMG), et la paléontologie. Les études paléomagnétiques suggèrent que la tectonique des plaques a entraîné la formation de plusieurs supercontinents antérieurs à la Pangée. Ces supercontinents paraissent se former de manière cyclique au cours du temps. Le supercontinent le plus célèbre avant la Pangée est la Rodinia, qui s'est formée autour de 1000 Ma et a persisté pendant une bonne partie du Néoproterozoique. Le supercontinent Columbia précède la Rodinia avec un âge probable d'assemblage fini-paléoprotérozoïque. L'existence de supercontinents archéens est encore très débattue voire hypothétique en raison de données paléomagnétiques insuffisantes. La valse des continents pré-Pangée reste encore méconnue du grand public et les paléomagnéticiens du monde entier ont fourni un travail titanesque ces 30 dernières années afin de préciser la position des masses continentales les unes par rapport aux autres dans le passé. Néanmoins, certains continents ont été largement étudiés alors que d'autres manquent encore de données paléomagnétiques. C'est notamment le cas du craton Amazonien qui, malgré sa taille, possède une base de données paléomagnétiques relativement faible contrairement aux cratons du bouclier canadien ou du bouclier baltique. La faible quantité de données est principalement due à la couverture végétale abondante (la forêt Amazonienne) et l'accès restreint aux affleurements (réseau routier peu dense, limité à la saison sèche).

Les travaux préliminaires sur le paléomagnétisme guyanais ont été menés dans les années 80 par l'équipe du Professeur T. C. Onstott (Princeton University) (Onstott, 1981a; Onstott et al., 1984; Onstott, 1981b). De nouvelles données paléomagnétiques ont été obtenues à partir des années 2000 par deux équipes différentes, (1) le groupe de paléomagnéticiens du BRGM (Bureau de Recherches Géologiques et Minières), et (2) le groupe de l'IAG-USP (Instituto de Astronomia e Geofisica, Université de São Paulo, Brésil).

Ces derniers résultats ont notamment permis de replacer le craton Amazonien durant son évolution au Paléoprotérozoïque (2500 – 1600 Ma) et de reconstruire la première courbe de dérive apparente des pôles (CDAP) pour ce continent (Nomade et al., 2003; Théveniaut et al., 2006). De nouvelles données paléomagnétiques montrent que le craton Amazonien et le craton Ouest-africain forment un seul continent vers ~2000 – 1960 Ma (Bispo-Santos et al., 2014a; Nomade et al., 2003). La place de ce bloc continental au sein du Supercontinent Columbia (~1800 Ma) est précisée par deux nouveaux pôles paléomagnétiques datés à ~1790 Ma (Bispo-Santos et al., 2008; Bispo-Santos et al., 2014b). Etant donné que ces deux nouveaux pôles paléomagnétiques de même âge sont différents, la position du craton Amazonien et sa relation avec les autres cratons au sein du Supercontinent Columbia reste problématique. Par ailleurs, la longévité du Supercontinent Columbia jusqu'à ~1400 Ma a pu être récemment testée grâce à de nouveaux travaux paléomagnétiques dans le sud du craton Amazonien (Bispo-Santos et al., 2012; D'Agrella-Filho et al., 2012; D'Agrella-Filho et al., 2016).

Cette thèse s'inscrit à la suite des études paléomagnétiques réalisées sur le craton Amazonien par le Groupe de l'IAG-USP ces dernières années. Ce travail de thèse est aussi dans la continuité d'une collaboration de longue durée entre le laboratoire de l'IAG-USP (Brésil) et le laboratoire GET (Géosciences et Environnement Toulouse, France), avec les travaux de Jean Luc Bouchez, Ricardo Trindade, Anne Nédélec, Eric Font, Lucieth Vieira et Elder Yokohama. Cette étude s'attache à poursuivre les études paléomagnétiques sur le craton Amazonien, notamment dans l'intervalle 1960 – 1790 Ma afin de préciser sa position au sein du Supercontinent Columbia. Cette période est marquée par un important magmatisme anorogénique qui aurait recouvert une vaste zone du nord du craton Amazonien et est désigné comme l'événement Uatumã. L'ampleur de cet événement et le volume de magma associé en fait un des plus grands événements magmatiques au cours des temps géologiques (Ernst, 2014). Ma thèse est un travail pluridisciplinaire qui associe le paléomagnétisme à la pétrologie pour caractériser les roches étudiées. Les roches magmatiques associées à l'événement Uatumã (~1880 Ma) affleurent très bien au nord du Mato Grosso ainsi que dans la Province de Carajás au sud de l'état du Pará. L'échantillonnage a été réalisé lors de quatre missions de terrain entre 2012 et 2015. Le développement scientifique de ce mémoire sera organisé en trois grandes parties.

(1) La première partie est consacrée à la description de la Géodynamique au Paléoprotérozoïque. En effet, il faut bien prendre conscience que le principe d'actualisme ne peut pas être toujours appliqué il y a ~1880 Ma lorsque l'on évoque la tectonique des plaques ainsi que les phénomènes géologiques associés (volcanisme, tectonique, déformation, sédimentologie,…). La Terre est un objet planétaire dynamique qui a évolué depuis sa formation il y a ~4543 Ma et notamment à cause de

son refroidissement séculaire. Il est donc indispensable, lorsque l'on étudie des unités paléoprotérozoïques, de se faire une idée précise sur la Géodynamique Précambrienne. Je détaille aussi dans ce chapitre tous les modèles associés au Supercontinent Columbia, l'objet de notre étude. Je pose la problématique de ce travail à l'aide d'une révision des données paléomagnétiques pour le craton Amazonien aboutissant à la publication d'un article dans la revue *Brazilian Journal of Geology* (D'Agrella-Filho et al., 2016) dont je suis co-auteur.

(2) La deuxième partie du manuscrit se consacre à l'échantillonnage et à la méthodologie adoptée pour répondre à la problématique. La description des unités échantillonnées, les observations de terrain détaillées et illustrées ainsi que les coordonnées GPS des sites de l'étude sont présentés dans le chapitre 3. La partie méthodologie du chapitre 4 décrit toutes les méthodes utilisées pendant ces quatre ans de travaux et se décline en deux parties avec le paléomagnétisme et la géochronologie.

(3) La troisième partie décrit les principaux résultats obtenus à la suite de cette étude. Une première étape a été la caractérisation des roches de l'essaim de filons de Tucumã dans la Province de Carajás (chapitre 5). L'échantillonnage, la pétrographie et la détermination géochimique ont été réalisées avec l'aide de l'équipe du Professeur D. C Oliveira de Belém, Universidade Federal do Pará (Brésil). La géochimie des filons de Tucumã a été publiée dans la revue *Journal of South American Earth Sciences* (da Silva et al., 2016) (article dont je suis co-auteur). Les résultats paléomagnétiques associés à ces filons de Tucumã sont décrits dans le chapitre 6. Le chapitre 7 propose les principaux résultats paléomagnétiques obtenus dans la région de São Felix do Xingu sous la forme d'un article soumis à *Gondwana Research* (Antonio et al., submitted). Ces résultats ont notamment permis de mettre en évidence un événement de vraie dérive polaire (VDP) à 1880 Ma.

Introduction

Paleomagnetism is considered as the only quantitative method to analyze the horizontal movement of landmasses through geological time. It is even the first irrefutable proof that the continental masses have moved over the Earth's surface giving rise to the plate tectonics theory (Creer et al., 1954; Runcorn, 1965). It has been admitted for a long time that these continental masses have evolved from a single continent called Pangea, supposed to have been formed around 280 Ma. Because the past oceanic margins as well as the magnetic anomalies no longer existed, the position of the continents before the Pangea formation is difficult to be established. Therefore, paleomagnetism is the main available approach to precisely chart the continental motion before 280 Ma. However, to make those reconstructions more accurate, paleomagnetism may be coupled to other tools as geochronology, the LIP - "barcodes", the geometry of orogenic belts and the paleontology. Progressively, paleomagnetic studies have shown that continents moved before Pangea and that plate tectonics led to the formation of several "single continents" or supercontinents. The repeated formation of these supercontinents is called the supercontinental cycle. Before Pangea, the most famous supercontinent is Rodinia. It was assembled around 1000 Ma during the Neoproterozoic. However, another clustering of landmasses before Rodinia is believed to have occurred between 2000 and 1800 Ma. This supercontinent is called Columbia. The existence of an Archean supercontinent (before 2500 Ma) is still debated and remains hypothetical. This is mostly explained by the scarcity of available paleomagnetic data and the difficulty to obtain high quality paleomagnetic poles for Archean rocks. The paleogeography of continents before Pangea is not yet well-known even with the colossal effort of all paleomagnetic groups in the last three decades. Moreover, paleomagnetic data are not equally distributed. Indeed, some continents have been largely studied, while for others paleomagnetic data are scarce. This is the case for the Amazonian craton. Despite its large surface, only few data are available. This paleomagnetic dataset scarcity is mainly explained by the lush vegetal cover (Amazonian forest) and the difficulty to reach outcrops (by boat limited to the riversides, a complex access by road, and possible only during the dry season).

Preliminary paleomagnetic work on the Guyana Shield was carried out in the 1980s by the group of Professor T. C. Onstott (Princeton University) (Onstott, 1981a; Onstott et al., 1984; Onstott, 1981b). New paleomagnetic data of good-quality have been obtained during the 2000s by two different groups: (1) the BRGM group (Bureau de Recherches Géologiques et Minières, France); and (2) the IAG-USP group (Instituto de Astronomia, Geofisica e Ciências Atmosféricas, University of São Paulo, Brazil). These results have important tectonic implications for the Amazonian craton evolution during the Paleoproterozoic (2500 – 1600 Ma)

and permitted to trace the first apparent polar wander path (APWP) for this cratonic unit (Nomade et al., 2003; Théveniaut et al., 2006). Recent paleomagnetic data show that the Amazonian craton and the West African craton formed a single-continent at ~2000 – 1960 Ma (Bispo-Santos et al., 2014a; Nomade et al., 2003). Position of this continental block within Columbia supercontinent (~1800 Ma) was tested by two new paleomagnetic poles dated at *ca*. 1790 Ma (Bispo-Santos et al., 2008; Bispo-Santos et al., 2014b). Given that these two coeval paleomagnetic poles are different, the position of the Amazonian craton and its relationship with the other cratons within the Columbia supercontinent is not yet well-defined and many models exists. The longevity of this supercontinent up to ~1400 Ma could be recently tested thanks to new paleomagnetic work in the southwestern of the Amazonian craton (Bispo-Santos et al., 2012; D'Agrella-Filho et al., 2012; D'Agrella-Filho et al., 2016).

This thesis is a continuation of a long-term collaboration between the laboratory of the IAG-USP (Brazil) and the laboratory of GET (Geosciences and Environment Toulouse, France), with the work of Jean Luc Bouchez, Ricardo Trindade, Anne Nédélec, Eric Font, Lucieth Vieira and Elder Yokohama. This study intends to give continuity on these paleomagnetic works, particularly in the interval 1960 – 1790 Ma trying to clarify the Amazonian craton paleogeography in the agglutination of the Columbia supercontinent. This period is marked by a voluminous anorogenic magmatism that covered a large area of the northern Amazonian craton, which was designated as the Uatumã event. The magnitude of this event and the associated volume of magma make it one of the greatest magmatic events in geological time (Ernst, 2014).

This is a pluridisciplinary work that combines paleomagnetism, geochronology and petrology to characterize the studied rocks. The magmatic rocks associated with this event (~1880 Ma) are very well-exposed in the northern of Mato Grosso State and in the Carajás Province, in the southern Pará state. Sampling was carried out during four field missions between 2012 and 2015. The scientific development of this thesis will be organized in three main parts.

(1) The first part is devoted to the description of Paleoproterozoic Geodynamics. Indeed, it must be realized that the principle of actualism cannot be applied at ~1880 Ma when one evokes the plate tectonics as well as the associated geological processes (volcanism, tectonics, deformation, sedimentology ...). Earth is a dynamic planetary object that has evolved since its formation at *ca*. 4543 Ma and especially because of its secular cooling. It is therefore essential when studying Paleoproterozoic units to get a precise idea of Precambrian Geodynamics. I also detail in this part all the models associated with the Columbia supercontinent, the subject of our study. I pose the

problem of this work using a revision of the paleomagnetic data for the Amazonian craton leading to the publication of a paper in the *Brazilian Journal of Geology* (D'Agrella-Filho et al., 2016) (co-author).

(2) The second part of the manuscript is devoted to the description of sampling and the adopted methodology. Description of the sampled units, detailed and illustrated field observations and GPS coordinates of the study sites are presented in Chapter 3. Chapter 4 (Methodology) describes all the methods used during these four years of work with paleomagnetism and geochronology.

(3) The third part describes the main results obtained in this study. Chapter 5 describes the characterization of the rocks from the Tucumã dike swarms in the Province of Carajás. Sampling, petrography and geochemical determination were carried out with the team of Professor D. C Oliveira of Belém, Universidade Federal do Pará (Brazil). The geochemistry of Tucumã dikes was published in the *Journal of South American Earth Sciences* (da Silva et al., 2016) (co-author). Paleomagnetic results associated to the Tucumã dike swarms are presented in Chapter 6. Chapter 7 presents the main paleomagnetic results for the São Felix do Xingu area under the submitted form to *Gondwana Research* (Antonio et al., submitted). New robust paleomagnetic poles are presented which provides a test for a possible True Polar Wander event at *ca*. 1880 Ma.

Chapter.1: Paleoproterozoic Era and the Columbia supercontinent

1.1 Paleoproterozoic geodynamics

Precambrian geodynamics presents a challenge and a fundamental barrier in our understanding of how the Earth evolved through time (Gerya, 2014). The Paleoproterozoic Era extends between 2500 and 1600 Ma and corresponds to ~20 % of the Earth's History. This period was characterized by changes on Earth during the Archean – Proterozoic transition at *ca.* 2500 Ma. These changes are listed in Table 1.1 and occured gradually at the end of the Archean over 1 Ga and were not sudden as believed previously (Condie, 2016).

Cooling of the mantle	Stabilization of craton	Atmosphere/Hydrosphere/Biosphere
• Decrease in frequency of komatiites • Decrease in komatiite MgO content • Decrease in Ni/Fe in BIFs (banded iron formation) • Increase in Nb/Yb and similar element ratios in non-arc basalts	• Changes in incompatible element ratios in TTGs and continental crust • Peak in orogenic gold reserves at 2.7 Ga • Production of thick lithosphere at 2.7 Ga • Increase in $\delta^{18}O$ in granitoid zircons • Increase in Nb/Th and εNd(T) in non-arc oceanic basalts	• The 2350 Ma Great Oxidation Event (GOE). • The 2300 – 2100 Ma Lomagundi-Jatuli Event. • The 2050 Ma Shunga Event. • First eukaryote life. • Decrease in frequency of BIFs (banded iron formations)

Table 1.1: Summary of the events in the Late Archean – Early Paleoproterozoic (See (Condie, 2015) for an exhaustive review).

1.1.1 Earth's Atmosphere, Hydrosphere, and Biosphere

The Paleoproterozoic atmosphere was certainly different from today. Indeed, at *ca.* 2350 Ma the oxygen level increased sharply during an event well-known as the Great Oxidation Event (GOE). Oxygen then becomes free in the atmosphere for the first time on Earth and could be present at the surface of the ocean (but deep ocean stayed anoxic) (Figure 1.1.A) (Holland, 2006). The first presence of oxygen in the atmosphere is marked by the appearance and deposition of redbeds (oxidized fluvial deposits), an increase of evaporate sulfates, and manganese deposits. Presence of atmospheric O_2 is also marked by the disappearance of major deposits of uraninite-pyrite and banded iron formations (BIFs). The end of the BIF's deposition at ~1880 Ma would suggest the oxidation of the deep oceans (Holland, 1984), whereas an alternative model would suggest the development of sulphidic deep oceans (H_2S), the "Canfield Ocean" (Canfield, 1998) (Figure 1.1.C). BIFs *"sensu lato"* are divided into two groups with different textures, the BIFs "*sensu stricto"* are dominant in the Archean whereas GIFs (Granular iron formations) is much common in Paleoproterozoic after GOE, which would suggest different environment and depositional process (Bekker et al., 2010). During the Proterozoic, most studies consider the presence of two O_2 concentration upsurges without intermediate variations, the first at *ca.* 2350 Ma (GOE event) and a second at *ca.* 850 Ma during the Neoproterozoic (Bao et al., 2008; Lyons et al., 2014). Increase of oxygen in the atmosphere has important implications on the sulfur isotope fractionation. We have indications that the sulfur cycle during Archean times was different before the GOE, characterized by a mass-independent signal. We can explain this behavior with low concentration of O_2 in the atmosphere coupled with photochemical reactions on SO_2 (Farquhar et al., 2000). After ~2450 Ma the signal was greatly dominated by mass-dependent fractionations (Figure 1.1.B) (Johnston, 2011).

After the Archean – Proterozoic transition, the sedimentary rocks on all continents have recorded the largest positive carbonate carbon isotope excursions with $\delta^{13}C$ values between + 5 and + 16 ‰ (Figure 1.1.B). This excursion is referred to the Lomagundi-Jatuli Event which lasted from 2300 Ma up to 2100 Ma (Martin et al., 2013). Its role and association with the Great Oxidation Event are not well understood and require more consideration. Mechanisms to explain a positive excursion of $\delta^{13}C$ imply increase in organic carbon burial rates (changes in chemistry of ocean or methanogenesis) or more acidic weathering conditions with increase in biological productivity (Schrag et al., 2013). Following the Lomagundi-Jatuli Event, the Shunga Event at *ca.* 2050 Ma occurred relatively close in time. We can observe this event in the Onega Basin (Fennoscandia) or in the Francevillian Group (Gabon). This event records the largest burial in carbon which form huge volume of sediments rich in carbon (giant petrified oil field)

(Melezhik et al., 2009). Asael et al. (2013) associate this event with a severe decrease in oceanic oxygenation.

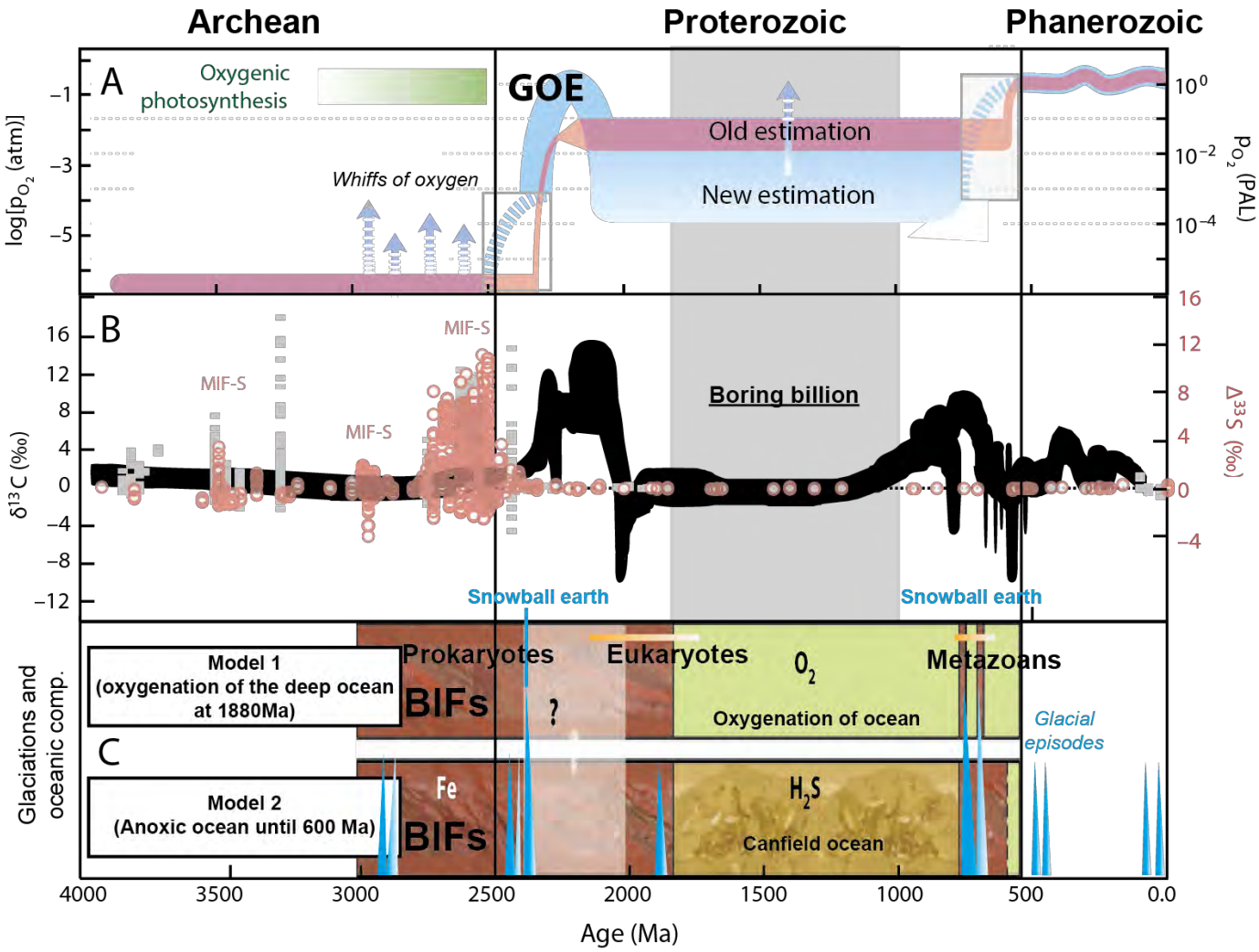

Figure 1.1: A: Evolution of Earth's atmospheric oxygen content through time according Lyons et al. (2014). Two models are illustrated: the red curve show two sharp steps for the rise of the oxygen and the blue curve is the emerging model with more fluctuation. Blue arrows are possible rise of O_2 in the atmosphere. B: Summary of carbon (black) and sulphur (red and grey) isotope data in Earth History (Lyons et al., 2014). C: Two models for the oxygenation of the ocean with the model 1 of Holland (2006) and the model 2 of Canfield (1998) with anoxie until 540 Ma. Glaciations and possible snowball earth are represented. Eukaryotes and metazoans apparitions are indicated.

Fluctuations in the Precambrian paleoclimate is marked by the presence of paleoclimatic indicators. Laterites and bauxites are geological markers for hot/humid climates. Eolian sandstones and evaporites are indicators for arid climate but not always for hot or warm weathers. Redbeds are rather indicators for semi-arid to arid climate. Diamictites, tillites, glacial pavement, striated rocks, and dropstones are good indicators for widespread cold climates. Major glaciations could have occurred at ca. 2400 – 2200 Ma, the so-called Huronian glaciations. The low-latitude position for the Superior craton (Laurentia) at that time suggests an episode of snowball earth and/or high obliquity (Evans et al., 1997) (Figure 1.1.C).

Glaciation also occurred at *ca.* 1800 Ma in NW Australia, as denoted by the glaciogenic King Leopold Sandstones (Kimberley Basin), and paleomagnetic data suggest this glaciation also occurred at low latitudes (Williams, 2005). Some authors proposed that the observed oxygen rise occurred as a consequence of the deglaciation of the two snowball earth episodes, at ~2200 Ma and ~750 Ma (Harada et al., 2015; Kirschvink et al., 2000; Kopp et al., 2005).The absence of BIFs, glaciations and isotopic fluctuations in the period between 1850 Ma and 850 Ma has been referred to as the "Boring billion" or the "Barren billion" period (Young, 2013) (Figure 1.1).

Precambrian times were a crucial period for the diversity of life and in addition of fossils record (rare or absent for these ages) we can use the geochemistry to reconstruct the history of life (Knoll et al., 2016). Recently, Jackson (2015) used the manganese – iron (Mn/Fe) ratio - as proxy of the oxidation-reduction potential (Eh) in non-detrital marine sediments (cherts, dolomite,...) at the time of deposition to quantify biological evolution and observe variations with time (Figure 1.2). Fe oxides precipitate more easily than Mn. So a high Mn/Fe suggests an oxidizing setting during the deposition of the sediment (for a constant pH). High values at *ca.* 3416 Ma (localized oxidation by cyanobacteria) is supported by a prokaryote life in Archean times with production of stromatolites. Early fossil record is registered from the Apex chert basalt at *ca.* 3460 Ma in Australia (Brasier et al., 2015). The ratio decreases until a minimum between 2500 – 1880Ma (Supposed age for the Gunflint Fm. - Superior craton). Major change at *ca.* 1880 Ma would reflect the accumulation of O2 in the atmosphere, which coincides with the evolution of first eukaryotic photoautotrophs (algae) and eukaryotic primary consumers fossils. Fossils record is very well preserved in the 1880 Ma Gunflint chert (Brasier et al., 2015). The increase of Mn/Fe ratio between 1880 – 800 Ma suggests gradual evolution in natural process (eukaryotes evolution and O_2 concentration) until the last upsurge in O_2 in atmosphere during the Neoproterozoic (800 – 680 Ma). This gradual evolution changes the general view that oxygen levels in Mesoproterozoic is low and without significant fluctuations. Besides, Mukherjee and Large (2016) have also reported a possible oxygenation event around ~1400 Ma. Oxygenation of the atmosphere and hydrosphere could have boosted the evolution of eukaryote and the rise of metazoans (Margulis et al., 1976).

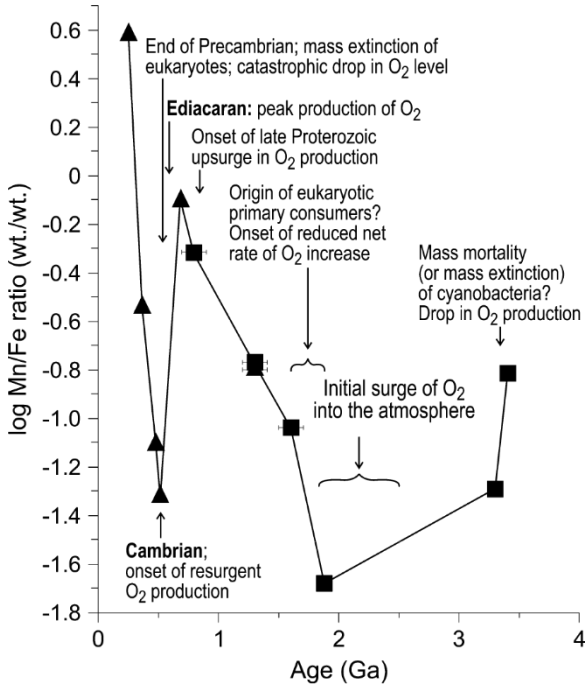

Figure 1.2: Diagram of Jackson (2015) showing variation in the Mn/Fe ratio (proxy for the oxide-reduction) in non-detrital sedimentary rocks (chert dolomite) through time.

1.1.2 Cooling of the mantle and crustal evolution

All changes described above seem to be tied directly or indirectly to the cooling of Earth's mantle. This reflects also in a gradual change in the Earth tectonics.

⇨ **Thermal model for the mantle evolution through time**

The thermal History of the Earth is controlled in first approximation by a balance between internal heating by radioactive elements (^{232}Th (44%), ^{238}U (39%), ^{40}K (15%) ^{235}U (2%)) in the mantle (H), and the surface heat loss by mantle convection (Q), following the formula (Christensen, 1985):

$$C\frac{dT_i}{dT} = H_{(t)} - Q_{(t)}$$

Where C is the heat capacity of the whole Earth, T_i is the average mantle temperature, and (t) is the time.

We can approximate the evolution of the internal temperature, T_i, using the notion of mantle potential temperature, $\mathbf{T_p}$, which is the temperature expected at the surface after correcting for adiabatic cooling (See Korenaga (2013) for a review). With the knowledge of half-lives of relative abundance of radioactive elements we can estimate the past values $H_{(t)}$. $Q_{(t)}$ is more problematic because different scenarios are possible following the modalities of the

convection. Usually the mantle heat flux is considered as a function of T_p, noted as Q (T_p). The Urey ratio (Ur), can describe the heat balance and is defined as (Korenaga, 2008):

$$Ur = \frac{Internal\ heat\ production}{Surface\ heat\ flux} = \frac{H}{Q}$$

Estimation for the present value for the convective Urey ratio, $Ur_{(0)}$, is 0.23 ± 0.15 (Korenaga, 2008). With a ratio of ~0.3 (< 1), it is logical to assume that Earth cools over time and that the mantle was warmer in the Archean and Paleoproterozoic. But by extrapolating this ratio in the past, we reach too high and unrealistic temperatures for the mantle at times before 2000 Ma, this would be the so-called "thermal catastrophe" (Christensen, 1985) (Figure 1.3.A). To avoid this problem, researchers have assumed a higher Urey ratio as 0.7 – 0.8 (Figure 1.3.A) (Davies, 2009; McGovern and Schubert, 1989) but these values are not compatible with the budget of decay of radioactive elements (Ur ~0.3) which is constrained by the chemical composition of the Earth.

We have very little evidence on the mantle temperature in the past. Herzberg et al. (2010) have calculated the mantle potential temperature T_p using non-arc basalts of Archean and Proterozoic ages. They found a maximum temperature of 1500 – 1600°C at *ca.* 2500 – 3000 Ma (1350°C is the estimation today – see Figure 1.3.B) to form these primary magmas. Non arc-basalts are therefore indicative of a warmer ambient mantle. Besides, higher T_p of komatiites (1600 – 1780°C) is consistent with plume model conditions. Petrological estimations are consistent with low Urey ratio of ~0.34 and supports an onset of plate tectonic between 2 and 3 Ga (Figure 1.3.B). Shirey and Richardson (2011) propose that lithospheric subduction in the sense of modern plate tectonics appeared at *ca.* 3 Ga after the nature of mineral inclusions in Archean diamonds.

In the Korenaga's model, the onset of plate tectonics at *ca.* 1 Ga would imply a too cold mantle to produce the non-arc basalts and seems unlikely. So the onset of plate tectonics was likely gradual in the early Earth (> 2500 Ma). Moreover geodynamic modeling suggests that Earth may have begun as a hot stagnant-lid and evolved through an episodic transitional state into plate tectonics over 1 – 3 Ga (O'Neill et al., 2016) (Figure 1.3.B).

More realistic models use non-classical behavior for mantle convection with (1) difference in the rheology of the lower mantle (Solomatov, 2001), (2) dehydration stiffening upon mantle melting in the upper mantle (Korenaga, 2006), (3) the gradual hydration of the whole mantle (Korenaga, 2011). To evaluate the effect of water we can consider an open-system evolution where the net water content in the mantle can vary over time, or a close system evolution where this content is constant (Figure 1.3.C).

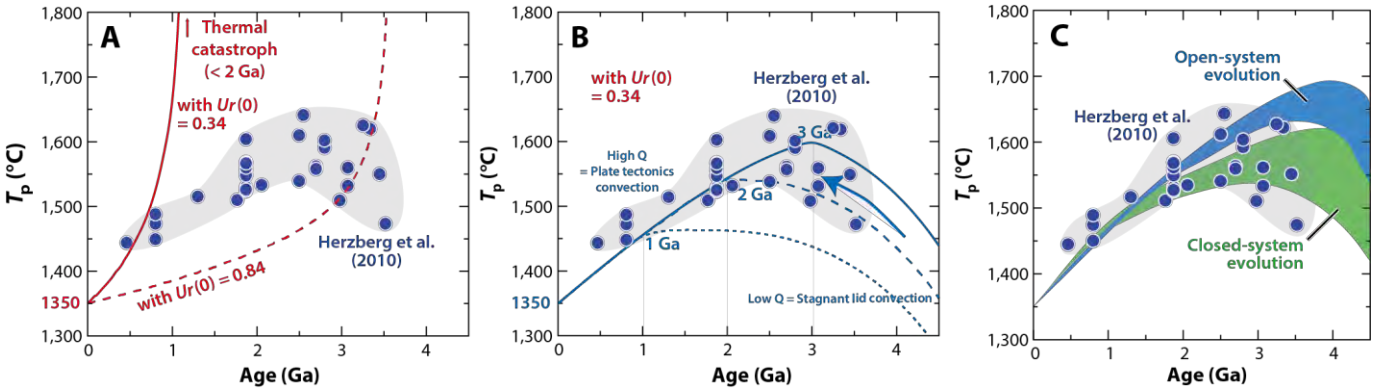

Figure 1.3: Thermal evolution modeling modified from Korenaga (2013). (A) Evolution of mantle heat production (H in red) with low present-day Urey ratio (0.34) and Ur (0.84) related to the potential mantle temperature, T_p. (B) Evolution of mantle heat flux (Q in blue) during the transition between a stagnant lid convection toward a plate tectonics convection (simulation at 3 Ga, 2 Ga and 1 Ga) with the relation to the potential mantle temperature, T_p. (C) Thermal evolution modeling with the effect of water in plate tectonics in open-system or close-system. Solid circles denote petrological estimates on past potential temperature (Herzberg et al., 2010).

The Archean mantle is thus hotter but also drier than today. The first implication is to produce a thicker oceanic crust (~30 – 35 km) that contrasts with the current oceanic crust thickness of 7 km. This thicker dehydrated lithosphere implies a lower difference of relative viscosity with the asthenosphere than today. Subduction is the main process for the hydration of the mantle. A drier mantle than today could imply more voluminous oceans and the immersion of continents during the Archean (Korenaga, 2011). Indeed, the bulk silicate Earth (BSE) contains approximately one ocean of water within the crust and the mantle. A drier asthenosphere has a lower viscosity in comparison to the lithosphere. Finally, a hotter mantle implies a thicker lithosphere which slows down the plate tectonics because the process of subduction is more difficult. Mantle hydration facilitates the establishment of plate tectonics throughout Earth's history (Korenaga, 2013).

⇨ Geological evidence for the decrease in mantle temperature

Komatiites are olivine spinifex-textured ultramafic rocks (> 18 wt.% MgO, 40 – 45 wt.% SiO_2, < 1 wt.% TiO_2, low incompatible trace element concentrations) (Nisbet and Arndt, 1982). They result from melting under extreme conditions of the mantle (> 1600 °C). There is an intense debate if the komatiites are derived from a dry and hot mantle with the partial melting of super-hot Archean plumes (Berry et al., 2008) or derived from the melting under hydrous conditions of the mantle at lower temperature in the context of subduction (Parman and Grove, 2005). Recently, Sobolev et al. (2016) showed that the low oxygen fugacity is inconsistent with a subduction setting and confirm a plume origin for komatiites with a hydrous reservoir in the deep mantle. The gradual decrease in frequency for the komatiites at the end of the Archean (Isley and Abbott, 1999) is considered as a decrease of the mantle temperature through time

(Figure 1.4.A). We can note that the last pulse for Precambrian komatiites is at *ca.* ~1880 Ma. In the Late Cretaceous (~90 Ma) ultramafic and mafic lavas of the Gorgona Island (Colombia) are identified as komatiites (Gansser et al., 1979) and is a geological peculiarity witnessing the existence of a Cretaceous superplume.

Figure 1.4.B represent the average (red squares) in MgO content for komatiites (purple dots) from a given greenstone belt (Condie et al., 2016). The decrease in the average MgO content at the end of the Archean (after 2500 Ma) could reflect a decrease in mantle temperature as viewed previously in the model of Korenaga (2013).

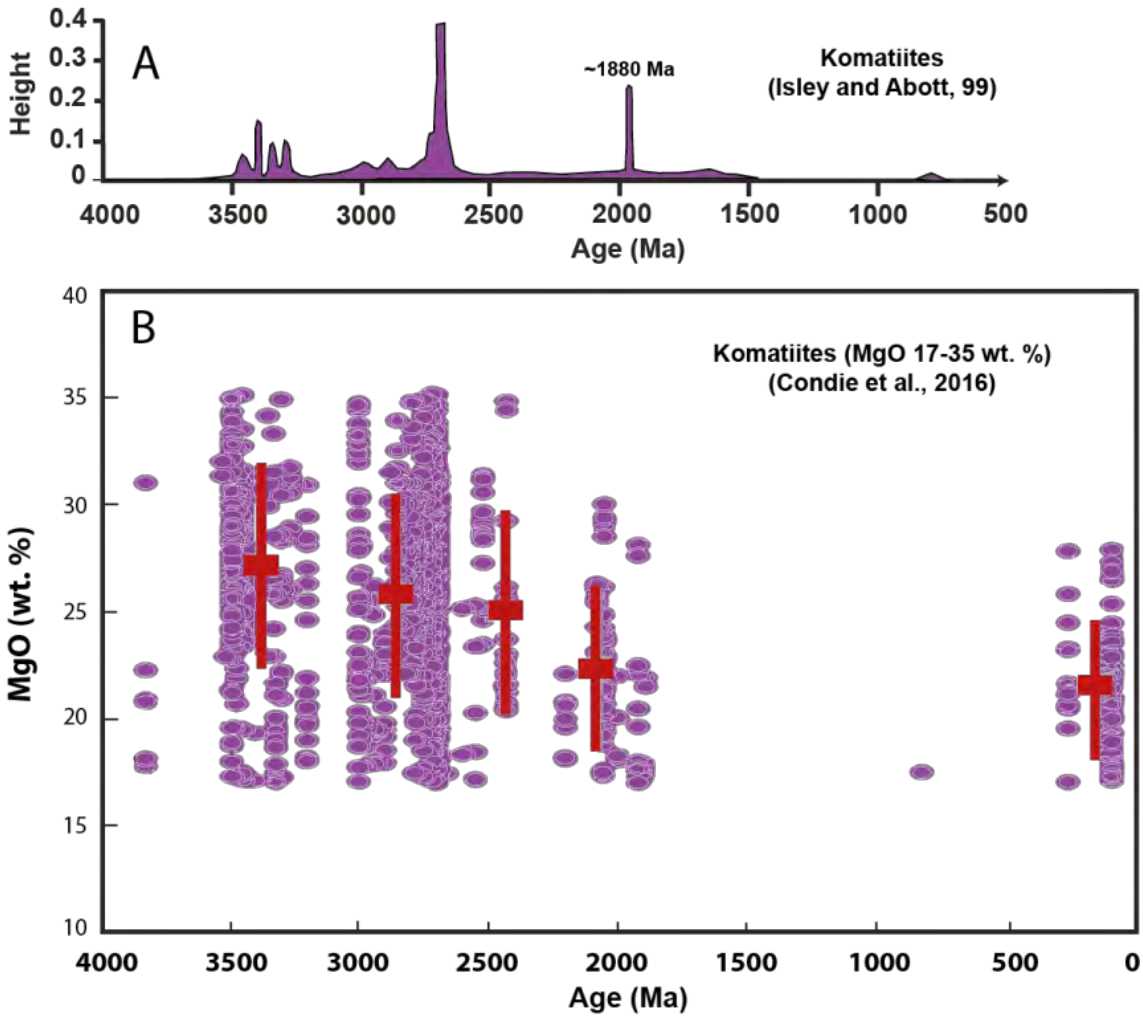

Figure 1.4: Komatiites through time. A: Time series of occurrences of komatiites modified after Isley and Abbott (1999). B: Secular variation in MgO in komatiites (Condie et al., 2016). In purple – MgO content; In red – aveage MgO content with respective error bars.

The decrease in Ni/Fe ratio in BIFs (banded irons formations) is also associated to the reduction of komatiites frequency (Figure 1.5). Because komatiites frequency decreases, the Ni content into the ocean is reduced and the decrease of the Ni/Fe ratio in BIFs can be associated with a global decrease in mantle temperature (Konhauser et al., 2009).

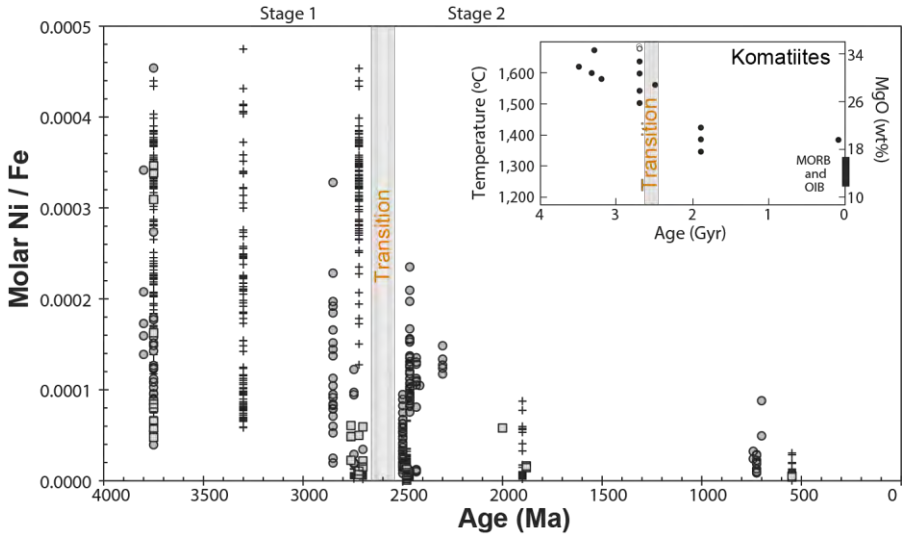

Figure 1.5: Ni/Fe mole ratios for iron banded formation (BIF) through time after Konhauser et al., (2009). Inset: Evolution of the temperature is deduced by calculation of the MgO content of komatiite liquids (T°C = 1000 + 20MgO).

Increase in incompatible element ratios such as Nb/Yb (Figure 1.6) in non-arc oceanic greenstone (basalts) is visible after 2500 Ma, which also implies a decrease in the degree of partial melting, and so a decrease in mantle temperature (Condie and O'Neill, 2010).

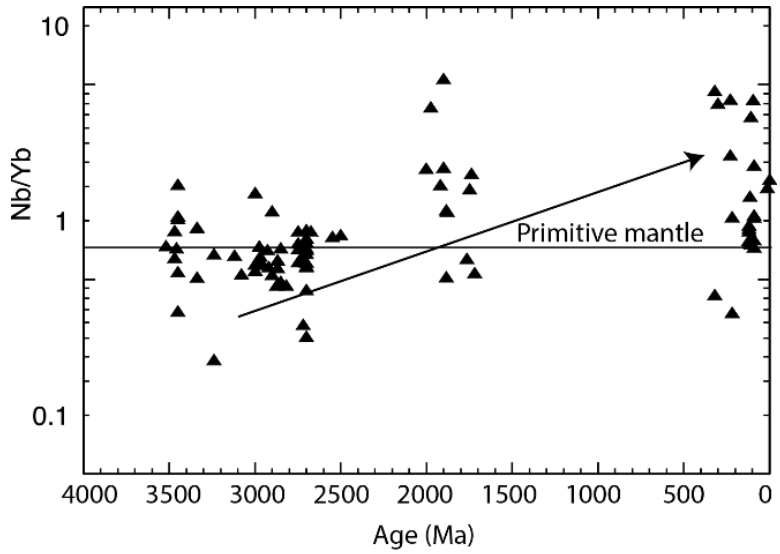

Figure 1.6: Nb/Yb through time in non-arc oceanic basalts modified from Condie and O'Neill (2010).

1.1.3 Stabilization of cratons

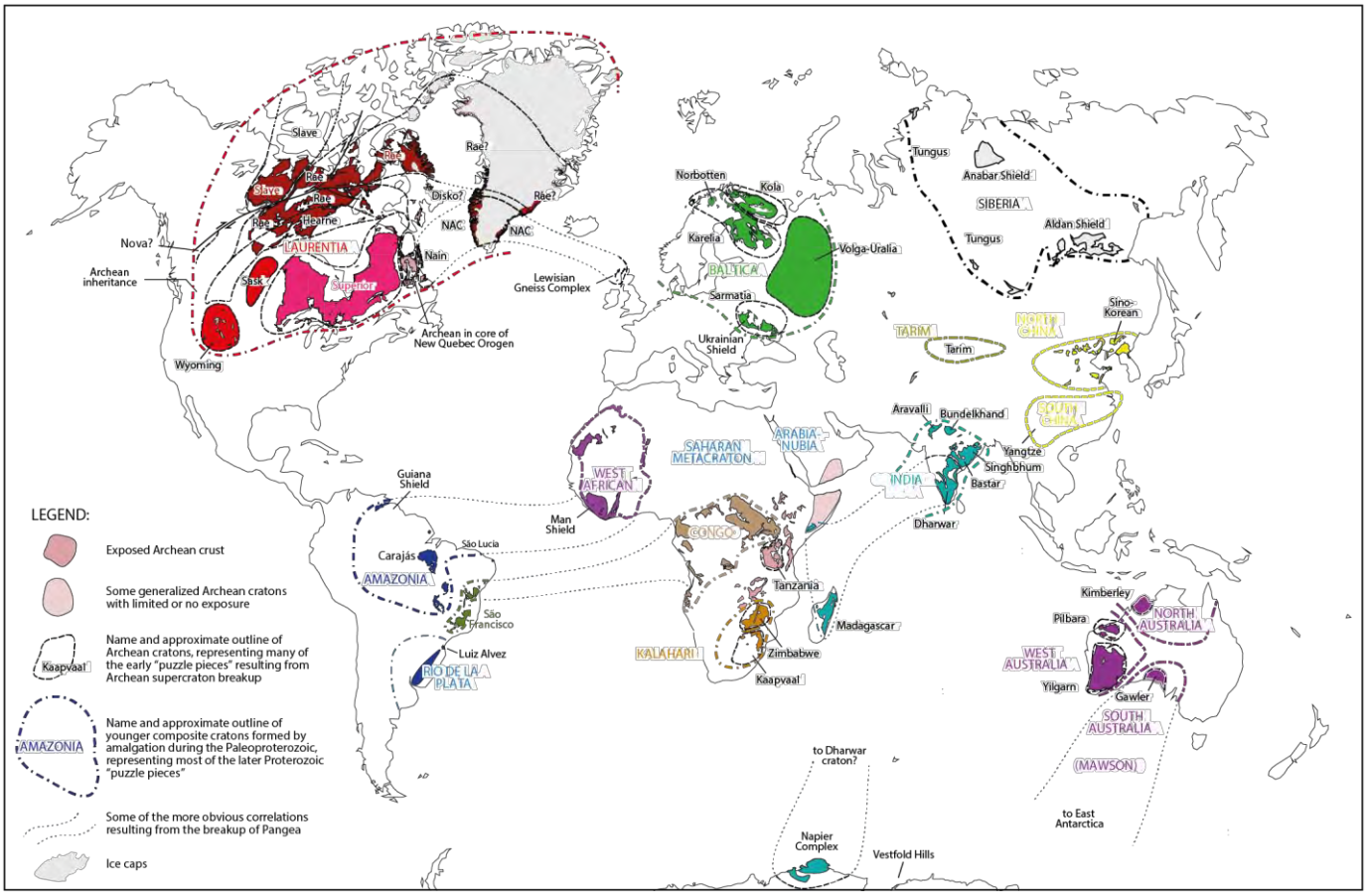

Figure 1.7: Localization of the different cratons in the world, modified from Ernst et al. (2013a).

The Precambrian rocks exposed on the Earth's surface are found primarily on the cratons (Figure 1.7). The cratons (or "shields") are stable areas of continental crust with a thick continental lithospheric mantle, named SCLM ("Subcontinental lithospheric mantle") with a thickness of 250 km. The SCLM is a peridotitic mantle root highly melt-depleted, and cold. A low density for this keel allows to the cratonic lithosphere to be significantly buoyant relative to the asthenosphere. The formation of the SCLM is a matter of debate in the literature but it is accepted that the cratonic roots are formed before 2500 Ma and would be remained "cold and stable" until today. We can know the age of the SCLM by investigating the Re-Os isotopic system of mantle xenoliths in kimberlites. Os is compatible in relation with Re, so Os is retained in the Re-poor residue and Re is evacuated in the melt. Re-Os depletion ages from mantle xenoliths suggests that the thick SCLM was formed before 2500 Ma with a peak at *ca.* 2700 Ma (Carlson, 2005). Many studies on mantle xenoliths show that the SCLM can be refertilized by episodic events. The North China Craton (NCC) is one of the most typical example because the SCLM was almost destroyed during the Paleozoic (Gao et al., 2002). Recently, Liu et al. (2016b) showed that the Rae craton was formed at *ca.* 2700 Ma (Laurentia – North America),

and suffered an episodic refertilization during the Paleoproterozoic 1770 – 1700 Ma Kivalliq-Nueltin event which can explain the layered structure for the SCLM.

The models proposed for the SCLM formation can be included in 4 categories (Figure 1.8): (1) high-degree melting of a plume head (> 1650°C) (Lee, 2006), (2) slabs stacking, (3) subduction zone, and (4) continental collision. Formation by plume was reviewed by Arndt et al. (2009) who propose a compositional stratification in a very hot plume (~1700 °C) with the Fo-rich olivine (forsterite) ± orthopyroxene in the upper parts of the melting zone. The partial melting is possible in the range of pressures up to 7 GPa. Denser (more fertile) material with Fe-rich olivine ± garnet is ejected of the system by gravitational redistribution.

Formation through accretion of different slabs of oceanic lithosphere (slabs stacking) is consistent with shallow conditions for the partial melting (~4 GPa) and lateral accretion would imply a greater amount of eclogite.

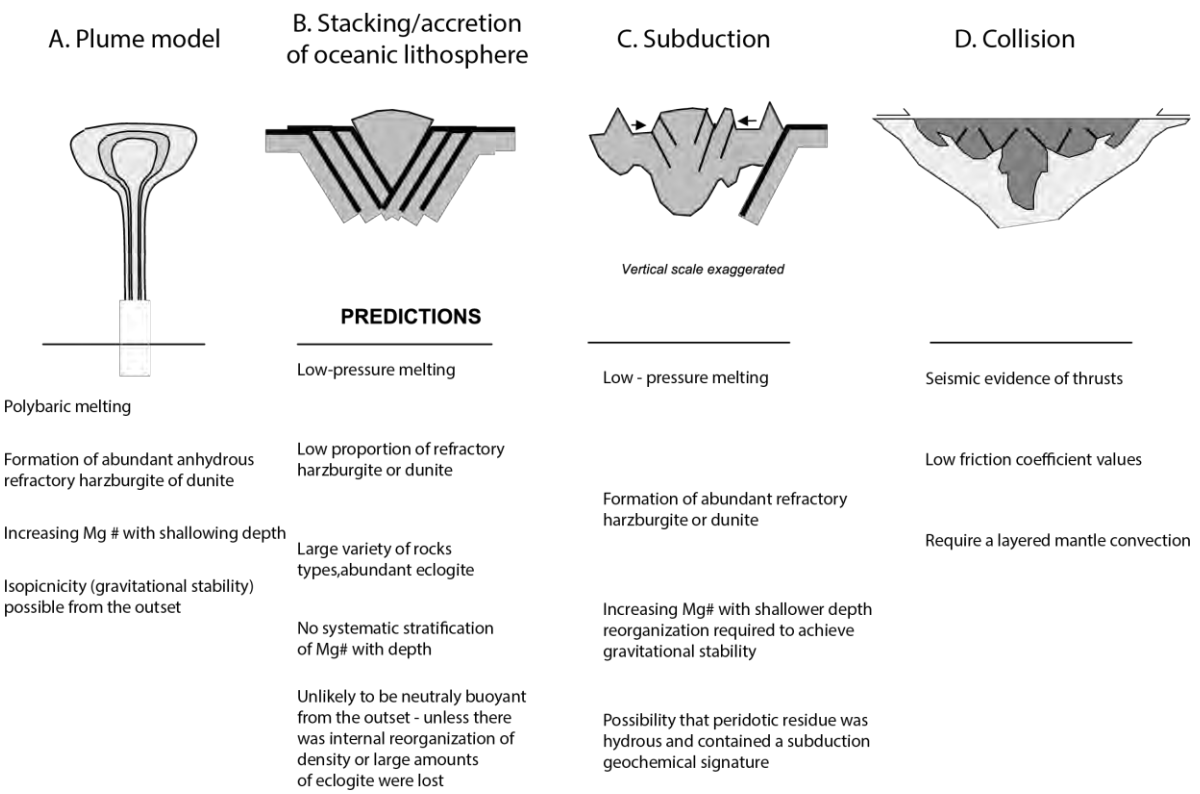

Figure 1.8: Models for the formation of the subcontinental lithospheric mantle (SCLM) adapted from Lee (2006).

Another model suggest the formation of the SCLM in the mantle wedge above a subduction zone (Simon et al., 2007). Transformation of fertile peridotite in more refractory harzburgite or dunite is induced by partial melting with fluids related to the subduction. The thickening of 200 km is induced by deformation during the accretion. In this model redistribution of lithologies is

needed to produce a gravitationally stable configuration with the ejection of the large quantity of eclogite. The problem of this model is the efficiency of the partial melting to produce the necessary material.

The last model implies the “continental” collision. Cooper et al. (2006) conducted numerical simulations and they show the possibility to form the cratonic lithosphere by thrust stacking over conductive downwelling. Gray and Pysklywec (2010) have studied the thickening of the lithosphere depending on the composition of the crust and the degree of radioactive (heat production). They show three modes to deform the lithosphere, which are imbrication (weak crust and low radioactive), underplating (lower crust strong) and pure-shear thickening (high temperature by radiogenic heat production).

Among these four models, the plume model (Arndt et al., 2009) and the collision model seem to have the fewest number of problems.

⇨ Continental growth and evolution of the continental crust

Formation and thickening of the cratons early in the Earth’s History are crucial parameters to know how the continental growth evolved. *Continental growth* is the net grain in mass continental crust per unit time (balance production/recycling).

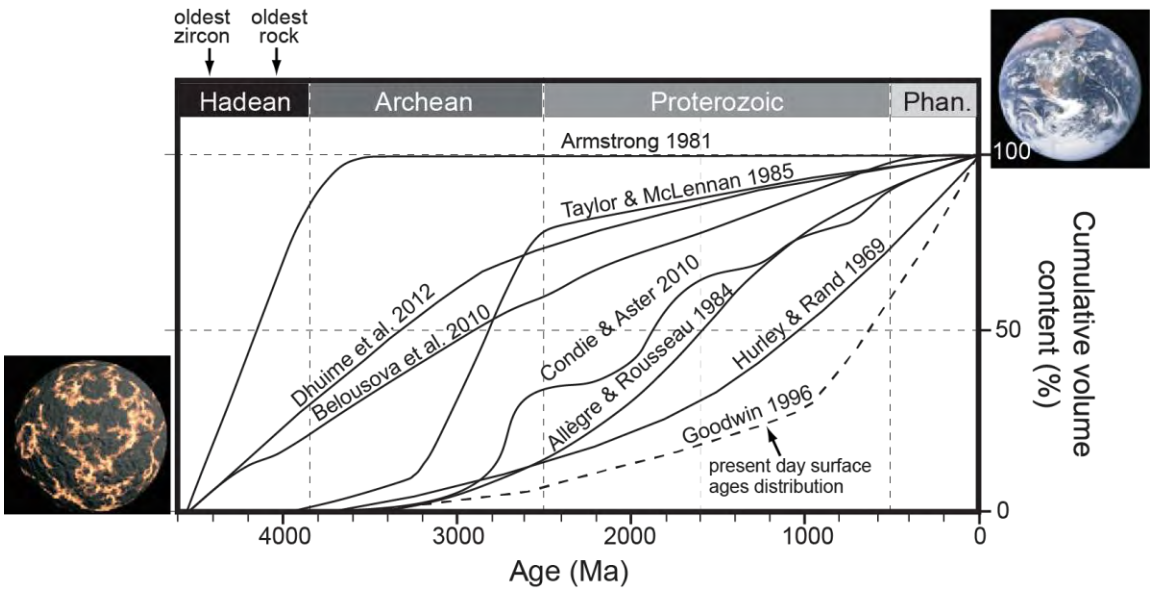

Figure 1.9: Crustal growth models for the continental crust, adapted from Cawood et al. (2013).

Models of growth of the continental crust are based on age and radiogenic isotopic data on rocks and minerals. Different methods imply a range of models on the rate of growth of the continental crust (Figure 1.9). Since the formation of the Earth, most models indicate that the continental crust has increased in volume and area with time (Allègre and Rousseau, 1984;

Armstrong and Harmon, 1981; Armstrong, 1991; Belousova et al., 2010; Dhuime et al., 2012; Fyfe, 1978; Hurley et al., 1962; Hurley and Rand, 1969; Taylor and McLennan, 1985; Veizer et al., 1979, 1985). Armstrong and Harmon (1981); Armstrong (1991) proposed an early burst of continental growth during the Hadean, followed by steady-state or decreasing thereafter. This suggests a process for recycling the crust with time to maintain a constant volume. Most models in Figure1.9 favor continuous growths, and more recently an episodic growth with pulses was also proposed (Condie and Aster, 2010). Dhuime et al. (2012) proposed two stages to explain the continental growth: a rapid production of ~65% of the current volume prior to 3000 Ma, followed by a slower production due to the recycling process on Earth (plate tectonics with subduction zones).

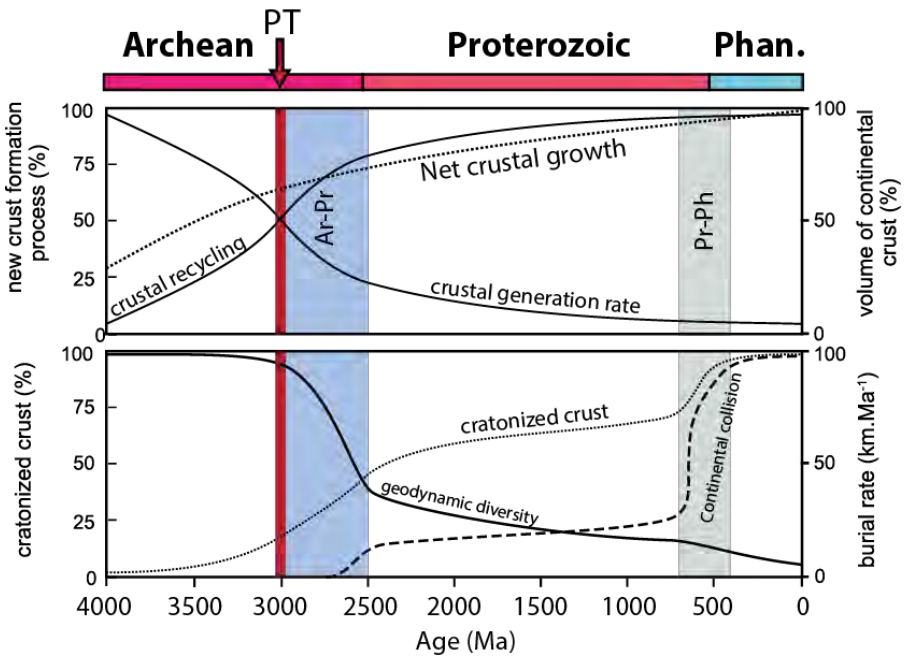

Figure 1.10: Evolution for crustal processes modified from Nicoli et al. (2016). The Archean – Proterozoic transition shows the first evidence for continental collisions in convergent settings wth the onset of plate tectonics. Ar-Pr = Archean – Proterozoic transition. Pr-Ph = Proterozoic – Phanerozoic transition. PT = Onset for the plate tectonics in this model.

Recently, Nicoli et al. (2016) proposed a new model that attempts to take into account the thermal evolution over time (Figure 1.10). Brown (2006) compiled a database for the metamorphic conditions through time. During the Archean granulite-ultrahigh temperature metamorphism (G-UHTM) predominated in contrast with modern gradients with high pressure – ultrahigh pressure metamorphism (HPM-UHPM). Nicoli et al. (2016) used these data to constrain an apparent metamorphic gradient and calculate a burial rate (km.Ma^{-1}) for each craton since 4000 Ma. Burial rates correspond to the crustal shortening and give an indication on the velocity for recycling and tectonic regime. Before 3000 Ma a large range of burial rates associated with a large variety of geodynamic mechanisms (vertical/sagduction and different horizontal displacements) were proposed. After *ca.* 3000 Ma, recycling became dominant on

Earth in convergent settings and the geodynamic diversity decreased until the modern duality subduction-collision. The Proterozoic is a period with long-lived accretionary orogens (100 – 700 Ma) with a good potential for the recycling and reworking of the continental crust. In this period a large amount of examples for mixed orogens, hot orogens and ultra-hot orogens can be observed (Chardon et al., 2009). The transition Archean – Proterozoic (Ar-Pr) is consistent with the onset of continental collision (CC) but modern collision would start predominantly on Earth at the Proterozoic – Phanerozoic (Pr-Ph) transition.

The evolution of the continental crust through time is characterized by major changes in composition. The crust evolved from a highly mafic bulk composition before 3000 Ma to a more felsic bulk composition (Tang et al., 2016). Archean crust is represented by mafic greenstone belts and large felsic granitoids grouped into four categories (Laurent et al., 2014): (1) TTGs (Tonalite – Trondhjemite – Granodiorite) (Moyen and Martin, 2012), (2) Sanukitoids, which are metaluminous (monzo) diorites and granodiorites, (3) Biotite- and two-mica granites, (4) Hybrid granitoids.

The origin of dominant TTGs may be related to melting of a hot subducted slab (like adakitic magma) as described by the classical model of (Martin, 1986). Other models are possible, like melting at the base of a thick oceanic crust, subduction of oceanic plateaus (Hastie et al., 2016) or delaminated portions below a plateau (Bédard, 2006). Alternatively, new models suggest their origin by proto-collision zones in Archean tectonics by melting of hydrated mafic rocks (Moyen et al., 2016). Sanukitoids (< 15% in proportion in the continental crust) are derived from interaction/hybridization between a mantle peridotite and a component rich in incompatible elements. We can cite as sanukitoid, the Rio Maria granodiorite (Carajás Province) dated at *ca.* 2870 Ma as we will see later (Santos and Oliveira, 2016). Biotite- and two-mica granites are crustal-derived granites (partial melting from TTGs and/or metasediments). The hybrid granitoids form a heterogeneous group that contains all kind of intermediate granitoids that cannot be strictly associated to the first three groups. Therefore, they result from interaction (mixing, mingling, or metasomatism) of sources and magmas. Laurent et al. (2014) proposed a long-stage (up to 500 Ma) evolution up to late-Archean granitoids: TTGs formation followed by a short-stage (< 50 Ma) of sanukitoids formation and late crustal granitoids (Figure 1.11). Although diachronic, this evolution is the same in cratons worldwide before 2500 Ma.

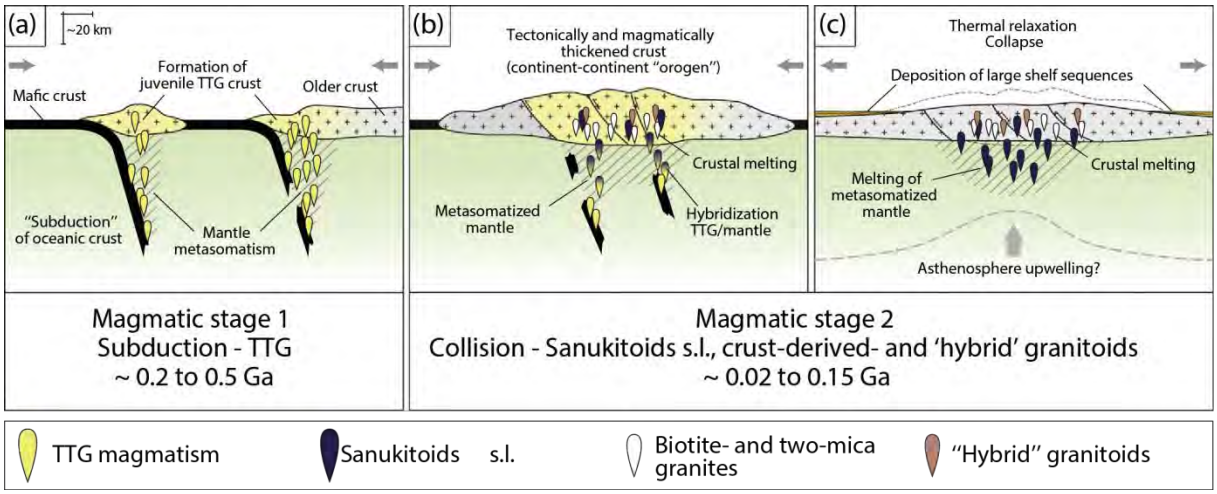

Figure 1.11: Model of Laurent et al. (2014) for the evolution of the granitoids during the Archean (after 3000 Ma).

⇨ ***Proterozoic granitoids***

Evolution of the continental crust after the Archean – Proterozoic transition is marked by the absence of TTGs. In Figure 1.12, decrease in La/Yb suggest decrease in garnet content, therefore a gradual change in the source of granitoids after 2500 Ma. Nevertheless, rare presence of granitoids with TTG-affinity was observed between 2200 – 2150 Ma during the early stages of the Eburnean orogeny in West Africa within the gradual evolution of the continental crust and this suggests episodic returns to Archean conditions (Dioh et al., 2006).

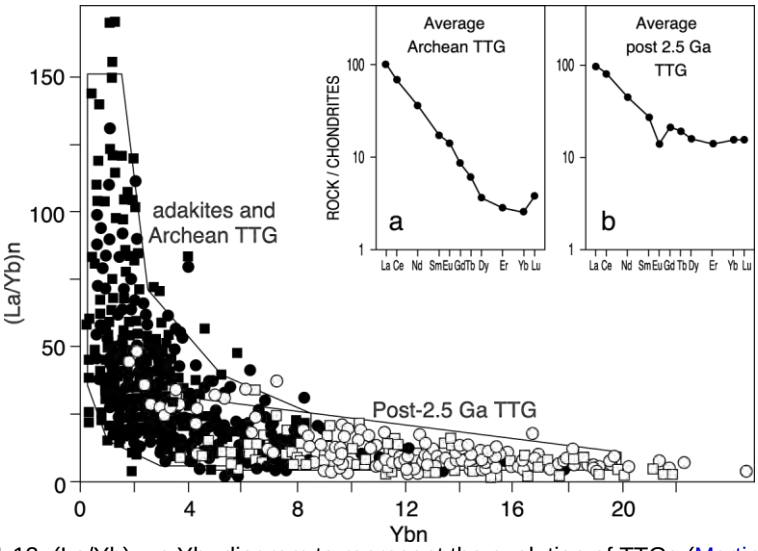

Figure 1.12: $(La/Yb)_n$ vs Yb_n diagram to represent the evolution of TTGs (Martin, 1986).

We observe the dominance of a distinctive magmatic suite specific to the Proterozoic times. The rapakivi granite suites and associated rocks are typical examples of the rocks formed during the Proterozoic times in all cratons and these granites are generally classified as A-type granite (Loiselle and Wones, 1979). The anorthosite, mangerite, charnockite, alkali-feldspar (Rapakivi) granite (AMCG suite) and associated mafic rocks occurred closely in both space and time (Rämö and Haapala, 1995). The Finnish rapakivi granites (Fennoscandia – Baltica) were intruded into the Paleoproterozoic (1900 – 1800 Ma) (Andersen et al., 2009) and during the Mid-Proterozoic in two stages at 1650 – 1620 Ma and 1590 – 1540 Ma (Heinonen et al., 2015). We can observe the same duality in age for the Amazonian craton between the A-type granites of Carajás dated at *ca.* 1880 Ma (Dall'Agnol et al., 2005) and the A-type granites in the southwestern of the craton dated between 1600 – 1400Ma (Sadowski and Bettencourt, 1996). The petrogenetic relationship in the AMCG suite is controversial (Bonin, 2007). The comparison of geochemical data between different lithologies for the North China Craton (NCC) showed that they have different magmatic sources and petrogenetic histories (Liu et al., 2016a). The system is constituted by the anorthosites (A) and norites with magmas from the enriched mantle (fractional crystallization in the lower crust at ~1300°C). The mangerites (M) and charnockites (C) could be related from the partial melting of the lower crust induced by underplating of mafic magmas. The rapakivi granites (G) would be formed by partial melting in the mid/upper crust in shallowing conditions (Figure 1.13.B). Two geological contexts are proposed to form the AMCG suite with an intracontinental rift setting related to the break-up of the Columbia/Nuna supercontinent or in a post-collisional/post-orogenic tectonic setting. The relation between the AMCG suite and the Columbia/Nuna supercontinent was studied by Vigneresse (2005) who proposed a progressive warming of the lithosphere by amalgamation and concentration of zones of juvenile crust during the rotation of the Columbia supercontinent.

In summary, the evolution of the felsic composition of the continental crust can represent the secular decrease of mantle temperature. The evolution from TTG followed by the sanukitoid suite is characteristic of the hot Archean conditions whereas AMCG suite during the Proterozoic could represent a transitional stage before reaching modern conditions (Figure 1.13) (Nédélec and Bouchez, 2015).

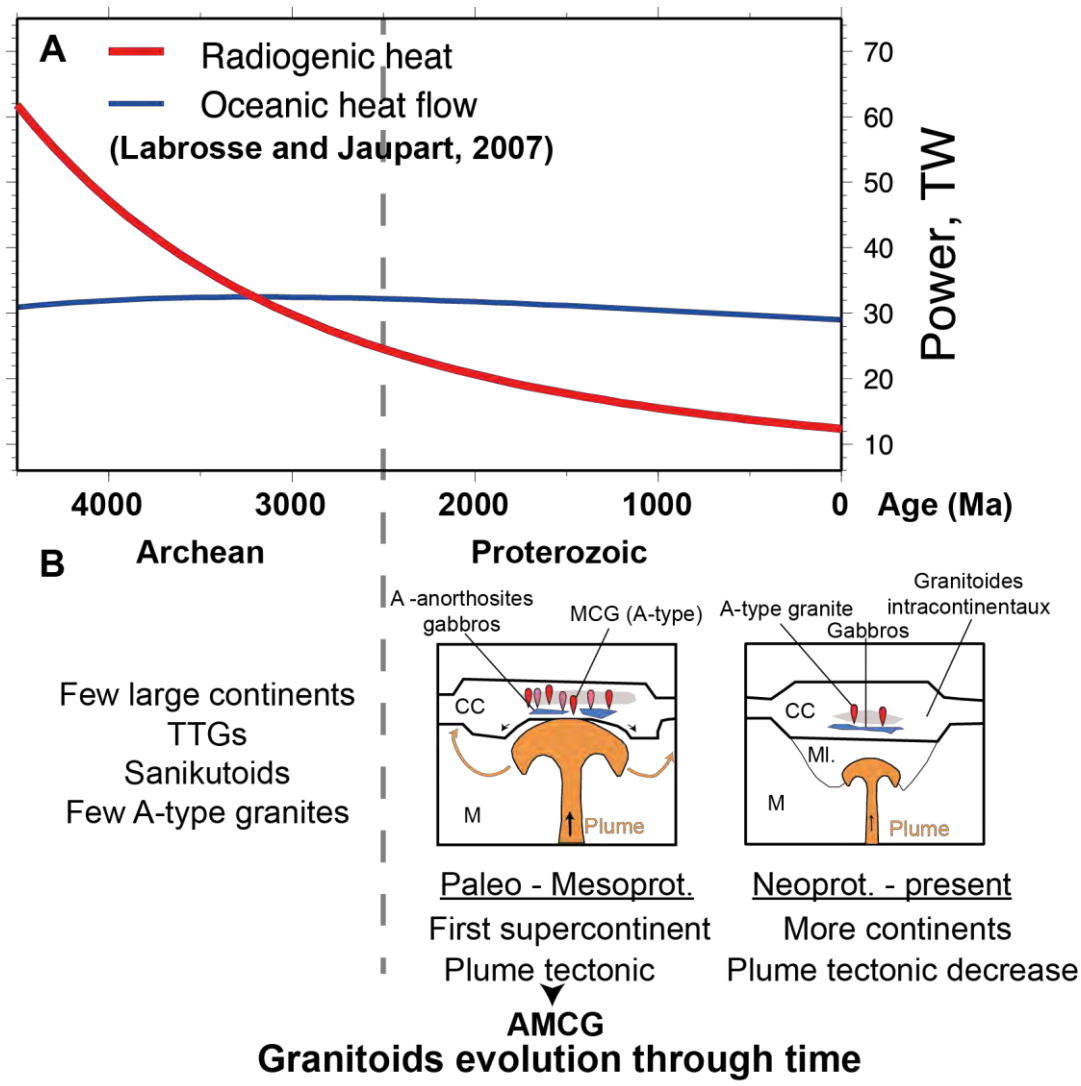

Figure 1.13: Evolution of granitoids with the secular cooling of mantle. A: Model for cooling of mantle, TW = terawatt (Labrosse and Jaupart, 2007). B: Cartoons showing the evolution of granitoids through time.

The distribution of cratons in Earth can influence the mantle temperature through time. Cratons makes easier plate tectonic because they imply a convective stress at the borders and the formation of subductions (Rolf and Tackley, 2011). The establishment of the thick SCLM during the Archean and the presence of supercontinents can play a crucial hole to the onset of plate tectonics on Earth. Indeed, presence of supercontinent may be associated with a thermal blanketing effect (Grigné and Labrosse, 2001) and imply increase of temperature in the underlying mantle up to 150°C (Brandl et al., 2013). After reviewing the geodynamic context, the next sections depict the continental configurations with implications to “the supercontinental Cycle”.

1.2 Definition and evolution of supercontinents

Currently, the only well-defined supercontinent, although still with some inconsistencies, is the Pangaia or Pangea (Domeier et al., 2012) (Figure 1.14). The concept of supercontinent comes from the idea that a large landmass was formed in the late Paleozoic, which included most of the continental areas of the Earth (Wegener, 1912; Wegener and Skerl, 1922). The name of **Pangea** comes from the ancient Greek πᾶν / pân (« all/whole ») and γαῖα / gaîa (« earth/land »), in Latin. A supercontinent was originally defined as the set of a major landmass on Earth (Hoffman, 1989b; Rogers and Santosh, 2002). The term "major landmass", however, is not a good definition for a supercontinent (Bradley, 2011). A new definition has been proposed by Meert (2012), who suggests the use of the term supercontinent only when at least 75 % of the total continental crust is involved in the maximum package. This new definition considers that 75 % of rocks for a given period form the basement of a supercontinent. Therefore **Gondwana (or Pannotia)** cannot be considered a supercontinent, and could be referred as a semi-supercontinent (Evans et al., 2016a).

It is worth noting that during the Earth's History, we had the formation of different supercontinents. Runcorn (1962) was the first to propose four orogenic periods occurring respectively at *ca*. 200 Ma, *ca*. 1000 Ma, *ca*. 1800 Ma and *ca*. 2600 Ma, which could be associated to the formation of supercontinents. It is noteworthy the fact that a recent compilation of U-Pb ages on detrital zircons show the same major periods described by Runcorn (Campbell and Allen, 2008). So, it seems that at several times in the Earth's history, the continents joined together and broke apart in a process known as supercontinental cycle (Condie, 2002b).

Since mid-1970, based on geological, paleontological and paleomagnetic data, arised the idea of an older supercontinent formed at *ca.* 1100 – 1000 Ma which was named **Pangea-I**, "the late Proterozoic supercontinent", **Protopangea** (Burke and Dewey, 1973; Irving et al., 1974; Piper et al., 1976; Sawkins, 1976; Valentine, 1971; Valentine and Moores, 1972) and **Paleopangea** (Piper, 2000). However, the first reconstruction using various evidence received the name **Rodinia** (McMenamin and McMenamin, 1990). The word Rodinia comes from the Russian infinitive "rodit" which means "to grow", because Rodinia will give rise to all the continents and where more complex animals (the rise of metazoans) develop until today (McMenamin and McMenamin, 1990). The name Rodinia was adopted in the literature since the papers published by Powell et al. (1993a); Powell et al. (1993b).

Piper et al. (1976) was the first to suggest an older Paleoproterozoic supercontinent using paleomagnetic data. In the 80s, Paul Hoffman suggested that during 1800 – 1600 Ma the amalgamation of cratonic landmasses of Laurentia may have been contemporaneous with

the formation of a larger landmass, forming a supercontinent (Hoffman, 1988, 1989a; Hoffman, 1989b). But the first attempts of reconstruction began in the 90s. Gower et al. (1990) proposed a reconstruction that brings together Northern Europe and North America, which they called **NENA** (**N**orth **E**urope - **N**orth **A**merica). The Laurentia's amalgamation during the Hudsonian orogenesis, and the occurrence of orogenesis worldwide between 1900 – 1800 Ma (Hoffman, 1989a), gave the name of **Hudsonland** for the first proposal of a Paleoproterozoic supercontinent (Williams et al., 1991). Rogers (1996) updated the reconstruction of NENA (Gower et al., 1990) considering Mesoproterozoic amalgamations of East Antarctica and Baltica to Arctica (composed by Siberia and Laurentia). However, the NENA reconstruction cannot be considered as a supercontinent following the definition of Meert (2012). Hoffman (1997) proposed the name **NUNA** as a substitute for Hudsonland for the reconstruction of the Laurentia-Baltica aggregate. Hoffman (1997) doesn't mention the presence of Siberia, East Antarctica, or any other craton in his reconstruction of **NUNA**, therefore, it is similar to the NENA reconstruction of Gower et al. (1990). **NUNA** is an Eskimo name "Inuktitut" for lands bordering the northern oceans. Hudsonland was also called **Capricornia** by Krapez (1999). The first global reconstruction for the Paleo-Mesoproterozoic supercontinent was called **COLUMBIA** (Rogers and Santosh, 2002). The name is referred from the connection in the model between East India with the Columbia area in North America (NW). In the same year, Meert (2002) published the first set of Euler rotation poles for this supercontinent. In the following years, several studies using geological and paleomagnetic data have refined the model for the Paleo-Mesoproterozoic supercontinent Columbia (Belica et al., 2014; Bispo-Santos et al., 2008; Bispo-Santos et al., 2012; Bispo-Santos et al., 2014b; D'Agrella-Filho et al., 2016; D'Agrella-Filho et al., 2016; Evans et al., 2010; Evans et al., 2016b; Goldberg, 2010; Hou et al., 2008; Kilian et al., 2016; Kusky and Santosh, 2009; Pesonen et al., 2003; Xu et al., 2014; Yakubchuk, 2010; Zhang et al., 2012; Zhao et al., 2002; Zhao et al., 2004).

Piper (2010b) proposed a Archean crescent-shape supercontinent, the **Protopangea** (2700 – 2200 Ma), which appears to have retained internal quasi-integrity until the end of Proterozoic Eon. With only few readjustments, he proposed an evolution toward his Neoproterozoic configuration, the **Paleopangea** (Piper, 2000, 2010a). The **Protopangea-Paleopangea** model of Piper (2014) implies periods of lid tectonic on Earth separated by rapid variations of "loop-shape" Apparent polar wander paths (APWPs). JDA. Piper doesn't use a rigorous paleomagnetic poles selection, and so his model was criticized (Li et al., 2009; Meert and Torsvik, 2004).

Currently, there is a great debate about the name of the Paleoproterozoic supercontinent and three names are normally in use in the literature: **Columbia**, **Nuna**, and **Paleopangea** (Evans, 2013; Evans et al., 2016a). The term Paleopangea was originally used

for the Rodinia supercontinent and is used almost exclusively by J.D.A. Piper (Piper, 2010b; Piper et al., 2011; Piper, 2013b; Piper, 2014). The term Nuna appeared in the literature (Hoffman, 1997) before the term Columbia (Rogers and Santosh, 2002). For this reason Nuna is preferred by some authors (Evans et al., 2016b; Kilian et al., 2016; Mitchell et al., 2014; Pehrsson et al., 2016; Salminen et al., 2014; Zhang et al., 2012). But as Nuna originally refers only to the connection between two landmasses – Laurentia-Baltica –, , Meert (2012) proposed to adopt the name Columbia which refers to the first global reconstruction. We follow in this manuscript the proposal of Meert (2012) to designate this supercontinent as **Columbia**. The existence of an Archean supercontinent (named as **Kenorland**) was also suggested by (Williams et al., 1991). The name Kenorland is referred to the Kenoran orogeny (Laurentia) originated at *ca*. 2700 Ma during the first supercontinental cycle. However, paleomagnetic data do not support an Archean supercontinent (Reddy and Evans, 2009). An alternative model proposes distinct **supercratons** which are drifting independently (Bleeker, 2003). **Superia** would be a supercraton with blocks of Superior-Hearne-Wyoming (Laurentia) associated with blocks of Karelia-Kola (Baltica) (Bleeker, 2003). **Sclavia** (Bleeker, 2001) is associated with the "Slave clan" but we can find also the term **Nunavutia** to design a set of cratons for the Rae's clan including the Slave craton (Pehrsson et al., 2013). The Kaapvaal (Africa) and Pilbara (Australia) cratons would be part of the **Vaalbara** supercraton (Zegers et al., 1998) and Zimbabwe (Africa) and Yilgarn (Australia) cratons would have formed the **Zimgarn** supercraton (Smirnov et al., 2013)..

So, at least 3 supercontinents, and several Archean supercratons are suggested in Earth's History, following the definition of Meert (2012) (Figure 1.14). They are:

- **Pangea** at *ca*. 200 Ma (Wegener, 1912)

- **Rodinia** at *ca*. 1000 Ma (McMenamin and McMenamin, 1990)

- **Columbia** at *ca*. 1800 – 1600Ma (Rogers and Santosh, 2002)

- **Kenorland** (Williams et al., 1991) or **supercratons** (Superia, Sclavia, Nunavutia, Vaalbara, **Zimgarn**) at *ca*. 2700 Ma

Evidence for the formation of the Columbia supercontinent and their different models are the focus of the next section.

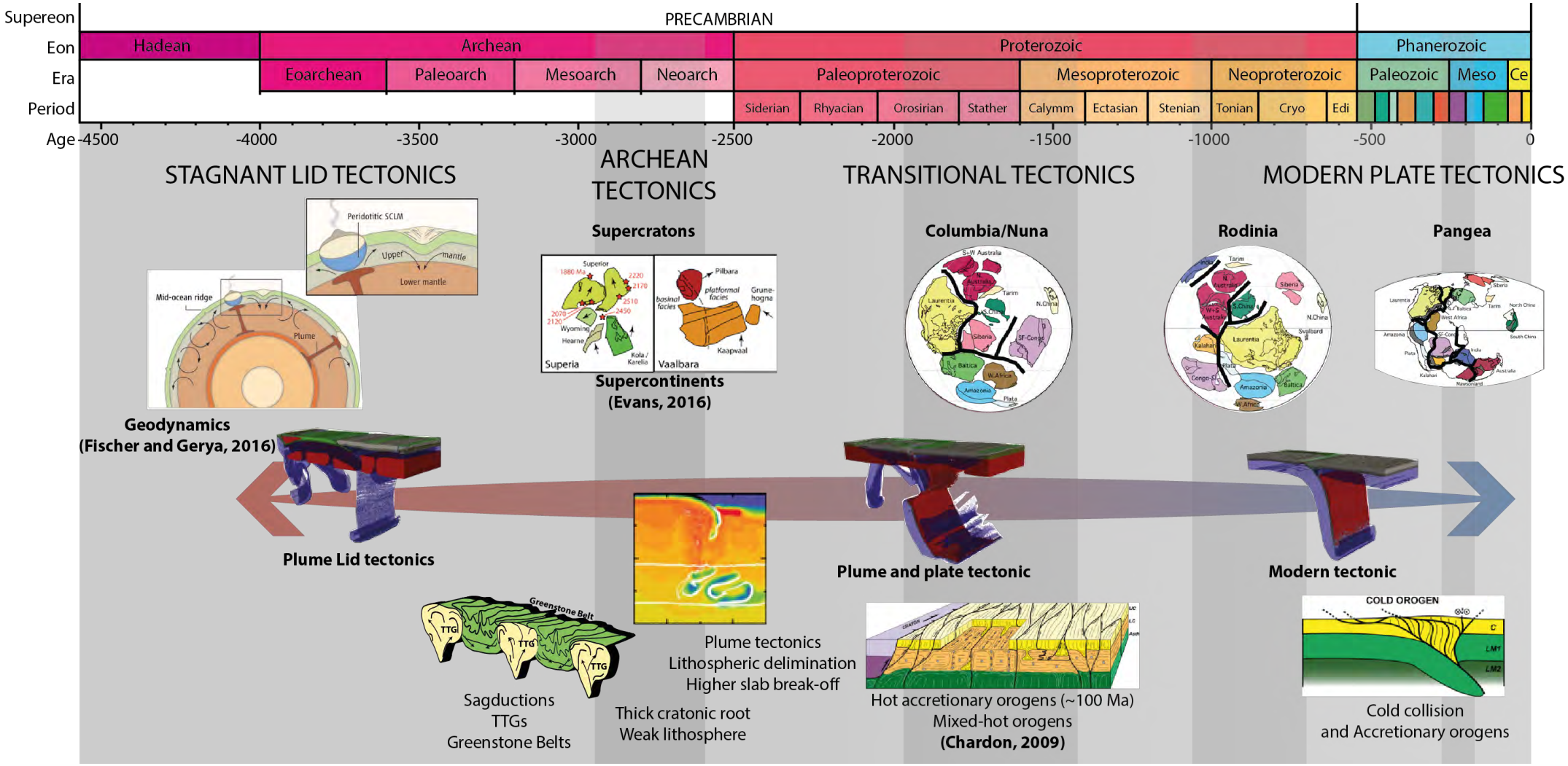

Figure 1.14: Supercontinents in Earth's History and associated geodynamic. Images from Fischer and Gerya (2016), Evans et al. (2016a), and Chardon et al. (2009).

1.3 Evidence for a Paleoproterozoic supercontinent

Dalziel (1999) presented 6 “benchmarks” to evaluate the credibility of a supercontinent:

- Collisions and increase of convergent settings during the amalgamation of the supercontinent.
- Passive margins created during the break-up of an anterior supercontinent.
- Geometric shape of cratons (difficult for Precambrian reconstructions).
- Geological linkages (sutures, large igneous provinces - LIPs, thrusts, faults…) present on different cratons.
- Paleomagnetic data.
- Realistic kinematics towards the Pangea model.

Evidence related to each topic described above will be discussed below for the Columbia supercontinent.

⇨ Collisions

(Hoffman, 1989b) was the first to provide geological evidence for a supercontinent between 2100 and 1800 Ma. Most Rodinia cratons appear to have registered oldest events, especially between 2100 and 1800 Ma. Zhao et al. (2002); Zhao et al. (2004) studied in detail these orogenesis and its role in the agglutination of Columbia supercontinent (Figure 1.15). The relationships of these orogenic belts among the several cratonic blocks constitute the basic problem related to the different paleogeographic reconstruction models proposed for the Columbia supercontinent.

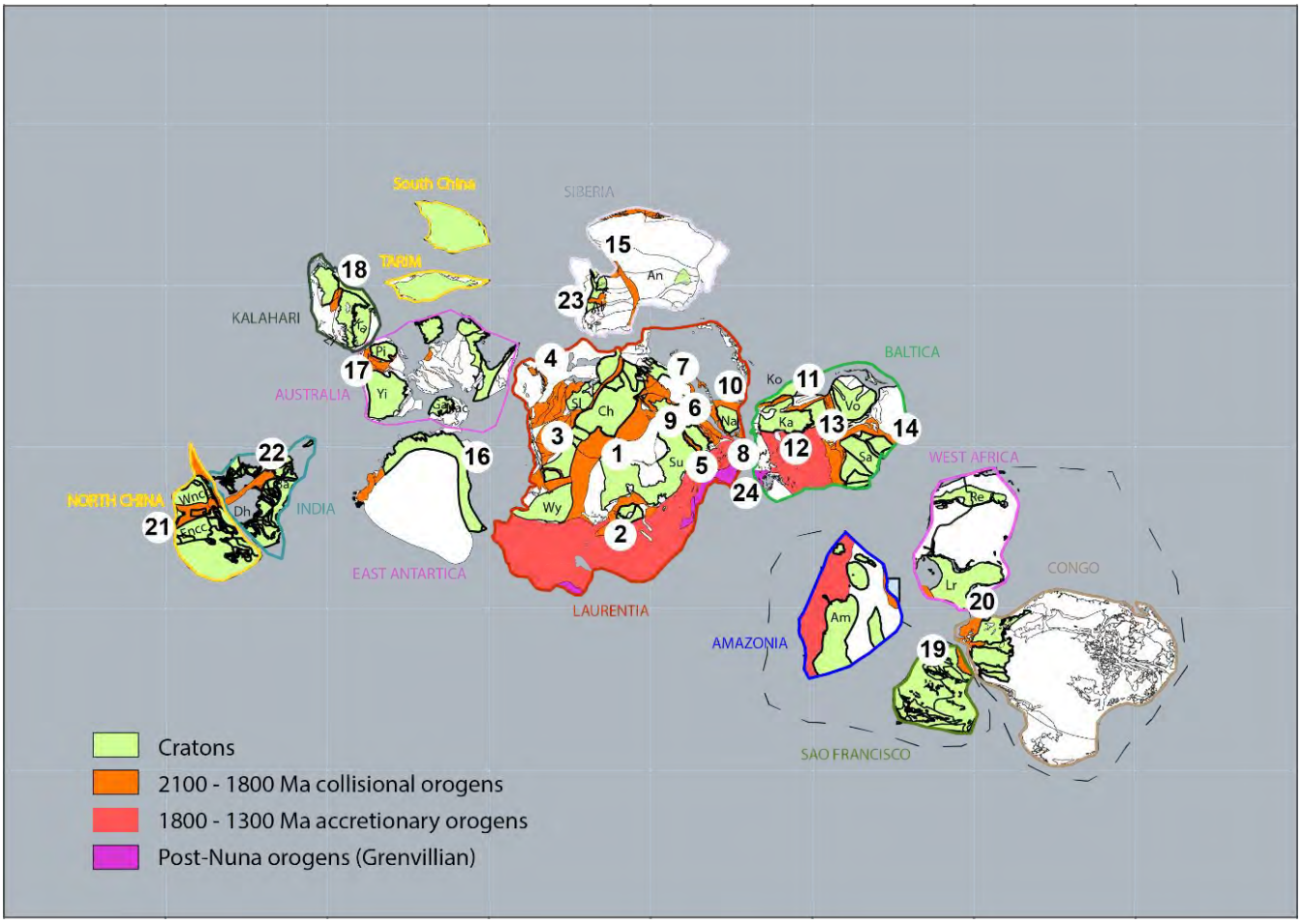

Figure 1.15: Columbia reconstruction after Zhao et al. (2004)). Symbols for orogenesis: (1) Trans-Hudson; (2) Penokean; (3) Taltson– Thelon; (4) Wopmay; (5) New Quebec; (6) Torngat; (7) Foxe; (8) Makkovik– Ketilidian; (9) Ungava; (10) Nugssugtoqidian; (11) Kola– Karelian; (12) Svecofennian; (13) Volhyn– Central Russian Orogen; (14) Pachelma; (15) Akitkan; (16) Transantarctic Orogen; (17) Capricorn; (18) Limpopo Belt; (19) Transamazonian; (20) Eburnean; (21) Trans-North China Orogen; (22) Central Indian Tectonic Zone; (23) Central Aldan Orogen; (24) Halls Creek Orogen.

The evolution of an orogenesis can be considered in two stages: the onset of subduction and the onset of collision according to Condie (2013). The age for the onset of subduction is a maximum age for the closing of oceanic basin, since subduction may begin before. Ages before 2100 Ma reflect only the onset of subductions in convergent settings after the break-up of Kenorland and/or supercratons (Figure 1.16). We can observe ages > 2100 Ma for the 'Birimian – Transamazonian", "Magondi-Keis", "Sutam", "Trans-North China" orogenesis. For ages younger than 2100 Ma, we observe the onset of collisions and accretionary orogens for most cratons. Figure 1.16 shows that the amalgamation of Columbia mainly occurs in a short period between 1900 and 1750 Ma. Continental collision between 1600 and 1550 Ma are located in Australia and Antarctica ("Olarian" and "Kararan") and would show the ultimate closure for Columbia. Break-up for the Columbia would happen in the interval 1500 – 1300 Ma, before or coeval with the "Albany – Fraser" and "Musgrave" orogenesis (1345

– 1330 Ma) in Australia. Figure 1.16 suggests that the final Columbia break-up would be later and partially (1350 – 1200 Ma) before the Grenvillian cycle at *ca*. 1200 Ma.

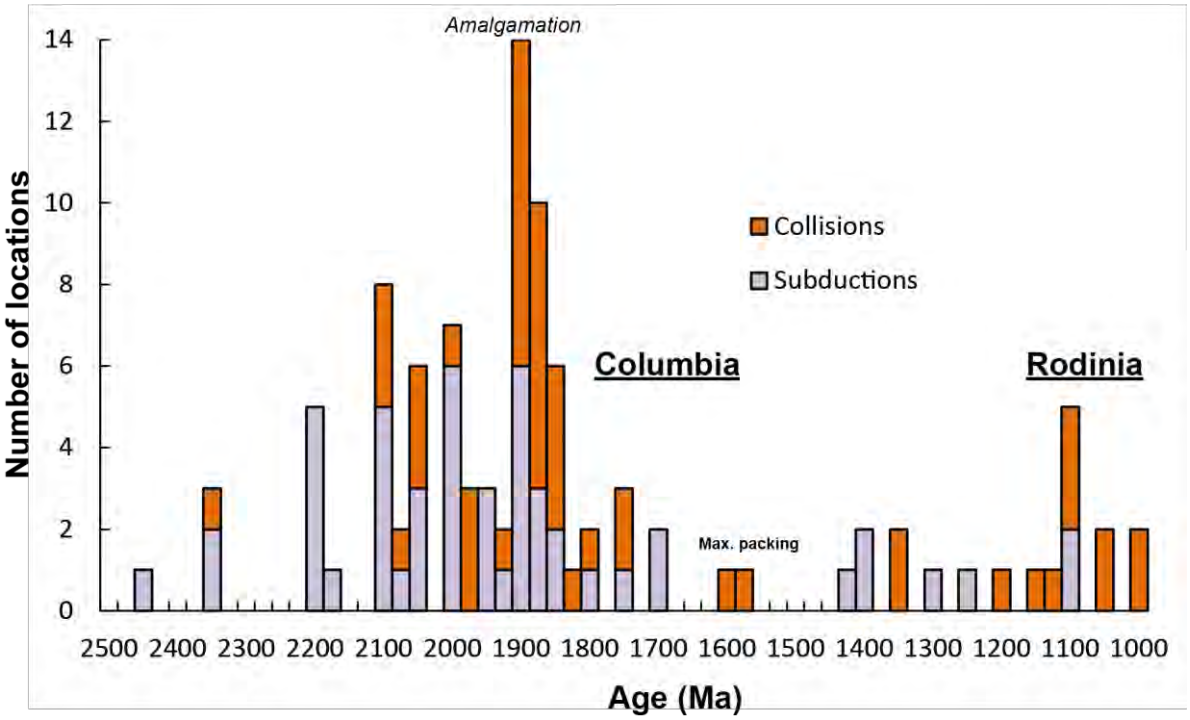

Figure 1.16: Frequency of onset of subduction and collision in Proterozoic orogens, recalculated after Condie (2013).

U-Pb ages on zircons for detrital or igneous rocks show peaks for crystallization ages (Figure 1.17) (Campbell and Allen, 2008; Condie, 1998, 2000, 2004; Condie and Aster, 2010). Five major peak clusters are closely related to supercontinent formation at *ca*. 2700, *ca*. 1870, *ca*. 1000, *ca*. 600, and *ca*. 300 Ma as suggested by Runcorn (1962) (Condie and Aster, 2010). Peak clusters are probably related to preservation of juvenile crust in orogens during supercontinent assembly (Condie and Aster, 2010). The peak could reflect the potential of preservation of zircons during the assembly of supercontinents and not an episodic continental growth (Cawood and Hawkesworth, 2013; Hawkesworth et al., 2013).

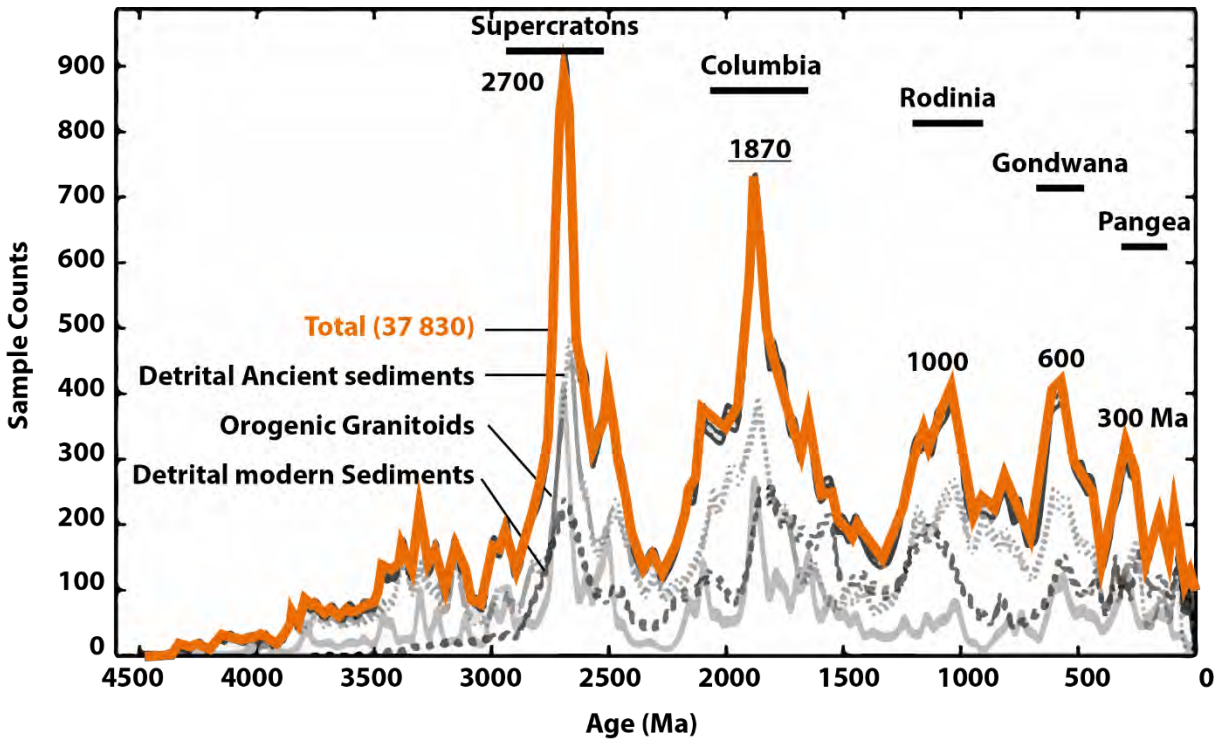

Figure 1.17: Distribution of U-Pb ages on zircons in detrital and granitoid rocks through time after Condie and Aster (2010).

The peak at *ca*. 1870 Ma could be attributed to the collisions forming the supercontinent (mainly due to better preservation). The minimum at *ca*.1500 – 1400 Ma may be assigned when the maximum package is reached.

⇨ **Passive margins**

Passive margins are created during supercontinent break-up and are destroyed during supercontinent assembly and can be used as evidence of the supercontinental cycle (Figure 1.18) (Bradley, 2011). Abundance of passives margin increased between 2300 and 2050 Ma after the break-up of Kenorland and/or supercratons. The peak declined between 1850 and 1750 Ma which is considered as the onset of the supercontinent. The onset for a passive margin is taken as the onset of seafloor spreading (rift -> drift transition) (Bradley, 2008). We don't observe increase of passive margins between the Columbia supercontinent and the Rodinia cycle. Mesoproterozoic times between 1750 and 1000 Ma are characteristic of low amount of passive margins. One would think that the Columbia supercontinent was remained assembled until 1000 Ma without classical break-up before Rodinia.

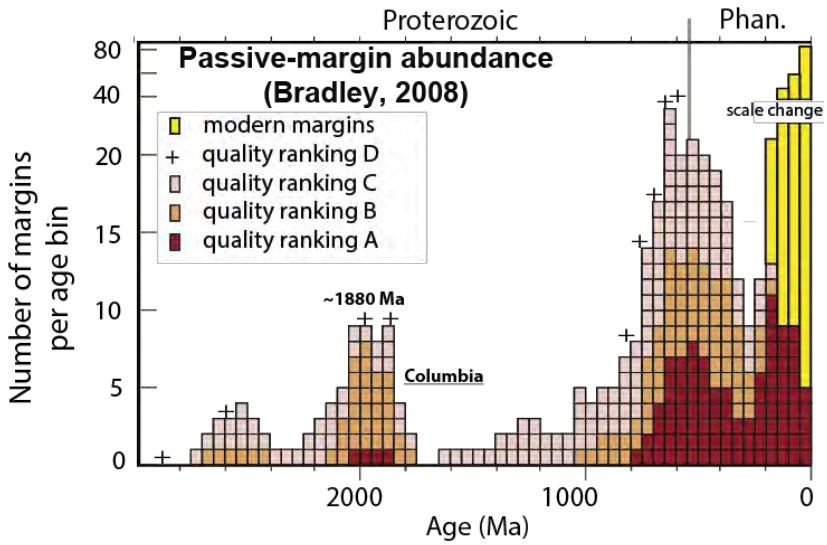

Figure 1.18: Passive-margin abundance through time after Bradley (2008).

⇨ **Geological linkages**

Large igneous provinces (LIPs) are a powerful tool for the reconstruction of supercontinents (Söderlund et al., 2016). LIPs are very large magmatic events where enormous volumes of magma were generated with typical volumes > 100 000 km^3 (Bryan and Ernst, 2008; Coffin and Eldholm, 1994; Ernst, 2014). On the surface of the Earth we can observe thick piles of flood basalts ("traps" on continental LIPs in opposition to the "oceanic plateau"). A felsic magmatism - carbonatites, lamprophyres, lamproites and kimberlites - is associated with the mafic rocks (Ernst, 2014). After erosion of the cratons' surface plumbing system of LIPs with layered intrusions, sills, associated ultramafic rocks, giant dike swarms can be observed. LIPs are characterized by the emplacement of short pulses (1 – 5 Ma) and their formation is classically related to the fusion at the head of a mantle plume (Bryan and Ernst, 2008). **Giant dike swarms** are potentially useful for paleogeographic reconstructions:

- They are associated with the LIP.
- Dikes emplacement with a large extension (300 – 3000 km).
- Emplacement in short pulses which allows a precise dating (U-Pb on baddeleyite/zircon) - maximum lifespan of ~50 Ma for a LIP.
- They can grow inside the craton and are insensitive to uplift (because they are vertical)
- They provide information on the paleo-stress suffered by the craton (radial or linear/parallel, giant-fan-shaped dike swarms).
- They are "piercing points". These characteristics make them priority targets for paleomagnetic studies (Buchan et al., 2000; Buchan, 2013).
- It is possible to reconstruct a larger LIP – Barcode for different cratons having LIPs with the same ages.

These barcodes (Figure 1.19) can be compared between different cratons to recognize an old linkage. Moreover, the geometry can define the relative orientation of cratons while the paleomagnetic data can restrict the paleolatitude and the azimuthal orientation. The geochemistry of magmas can be used to compare LIPs of different blocks and identify those that are genetically related (Ernst et al., 2013a). Different LIPs with the same age (within error) can be find in remote and independent cratonic units. So, a unique "barcode" is insufficient to precisely define the paleogeographic links. But as stated by Bleeker et al. (2008) a common "barcode" over a long period of time (100 – 200 Ma) for two or more cratonic units almost always identify neighboring cratons. Ernst et al. (2013a) use at least three coincident "bars" with time difference within 10 Ma as evidence for a link between different cratons.

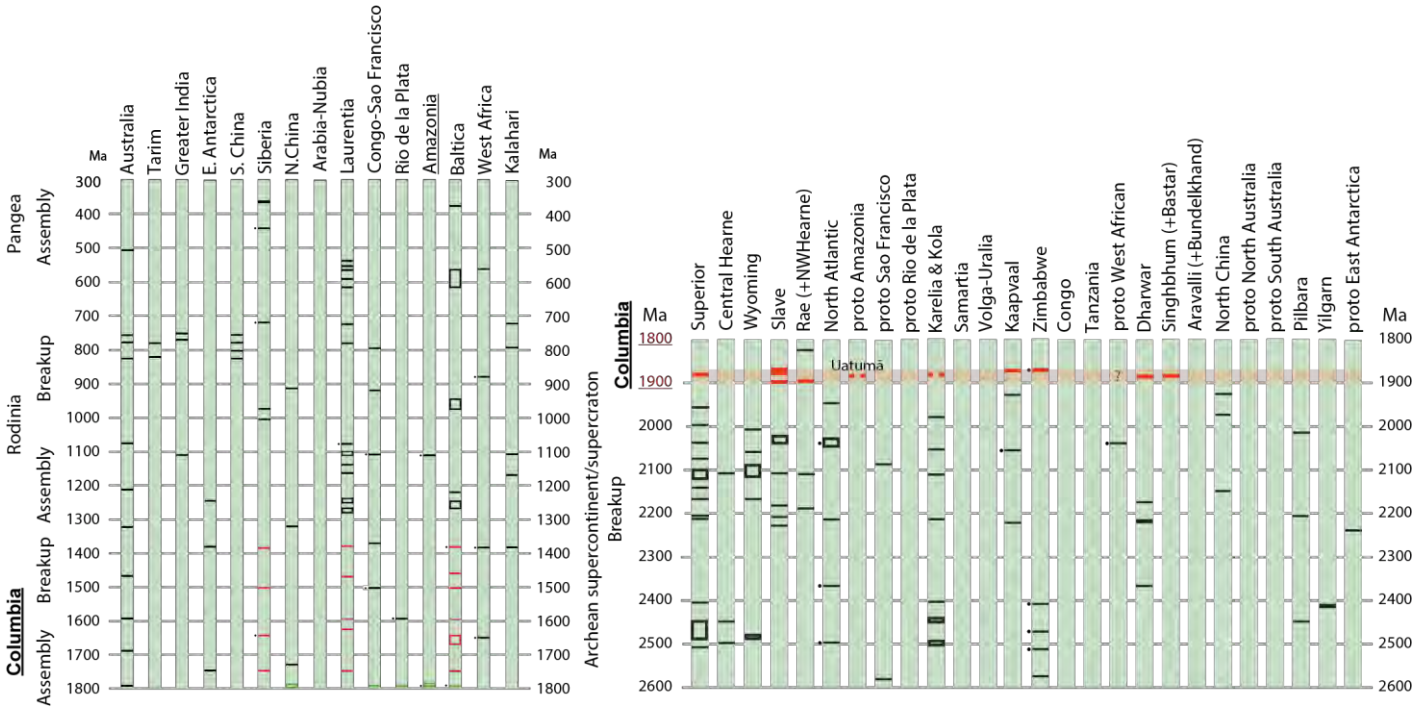

Figure 1.19: LIP barcode modified from Ernst et al. (2013b).

During the amalgamation of Columbia many LIPs are registered but correlations are still very speculative. For example the 1980 – 1950 Ma Pechenga-Onega LIP was recognized in Baltica (Lubnina et al., 2016) and a new paleomagnetic pole was calculated for the Karelian craton at *ca*. 1980 Ma. A coeval event was recognized in the Amazonian craton with the Surumu volcanics dated at *ca*. 1970 Ma (Dreher and Fraga, 2010). A paleomagnetic pole was also calculated for the Amazonian craton at *ca*. 1970 Ma (Bispo-Santos et al., 2014a) and a possible reconstruction at *ca*. 1970 Ma show the position of Baltica relative to Amazonia (Figure 1.20). In this case, in spite of both cratons sharing LIPs with overlapping ages, the paleomagnetic data clearly show that these cratonic units were not together at that time. This

example shows the importance of combining a large dataset in order to establish a real paleogeographic link.

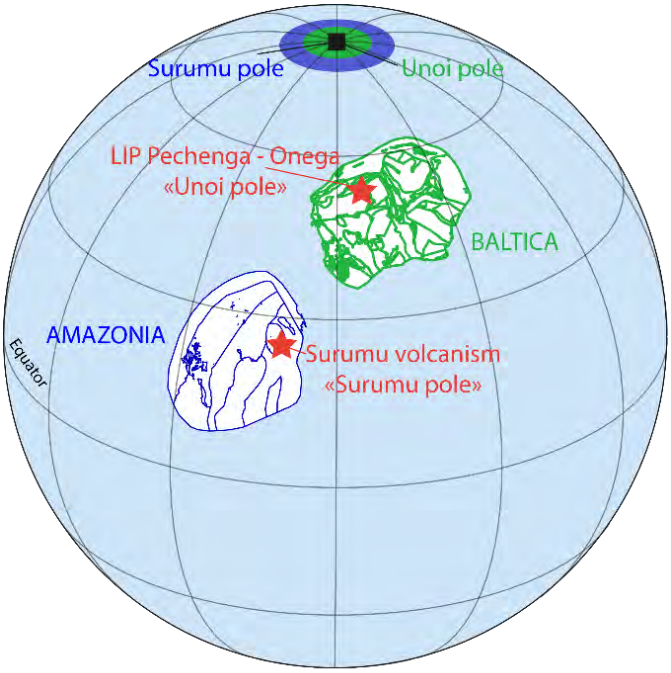

Reconstruction between Baltica and the Amazonian craton at *ca.* 1970 Ma

Figure 1.20: Possible reconstruction for the Amazonian craton and Baltica at *ca.* 1970 Ma.

At *ca*. 1880 Ma, many coeval LIPs across the world are well-recognized. The large amount of LIPs at the same time increases the ambiguity in barcode but at the same time provides several targets for paleomagnetic data acquisition. At *ca*. 1790 Ma, we observe the emplacement of Avanavero LIP in the Amazonian craton (Reis et al., 2013). Coeval LIPs are recognized in other cratons: in the Rio de la Plata craton with the Florida dikes (Teixeira et al., 2013) and in the Ukrainian shield (Baltica) with two magmatic pulses at *ca*. 1790 and *ca*. 1750 Ma (Bogdanova et al., 2015). Magmatic events at *ca*. 1750 Ma are also present in West Africa (Youbi et al., 2013), Siberia (Gladkochub et al., 2010) and Laurentia (Ernst and Bleeker, 2010).

A long-time connection (1800 – 920 Ma) for the São Francisco, Congo, Siberia and North China cratons has been proposed based on the LIPs barcode method (Cederberg et al., 2016; Ernst et al., 2016b). Gladkochub et al. (2016) proposed a superplume under the Siberia craton considered as the center of the Columbia supercontinent to explain the coeval LIPs between these cratons at *ca*. 1500 Ma. Later on, a giant LIP occurred at *ca*. 1380 Ma in Laurentia, Baltica, Siberia, Congo, and West Africa and could represent magmatic events associated to the break-up of the Columbia supercontinent (Ernst et al., 2013a).

The best example of the use of the LIP-barcode method is for the connection between Siberia and Laurentia. Four robust “matches” are identified at ca. 1870, 1750, 1350, and 720 Ma (Figure 1.21) (Ernst et al., 2016a). They leave no doubt about the proximity between these two cratons, which was recently supported by paleomagnetic data (Evans et al., 2016b).

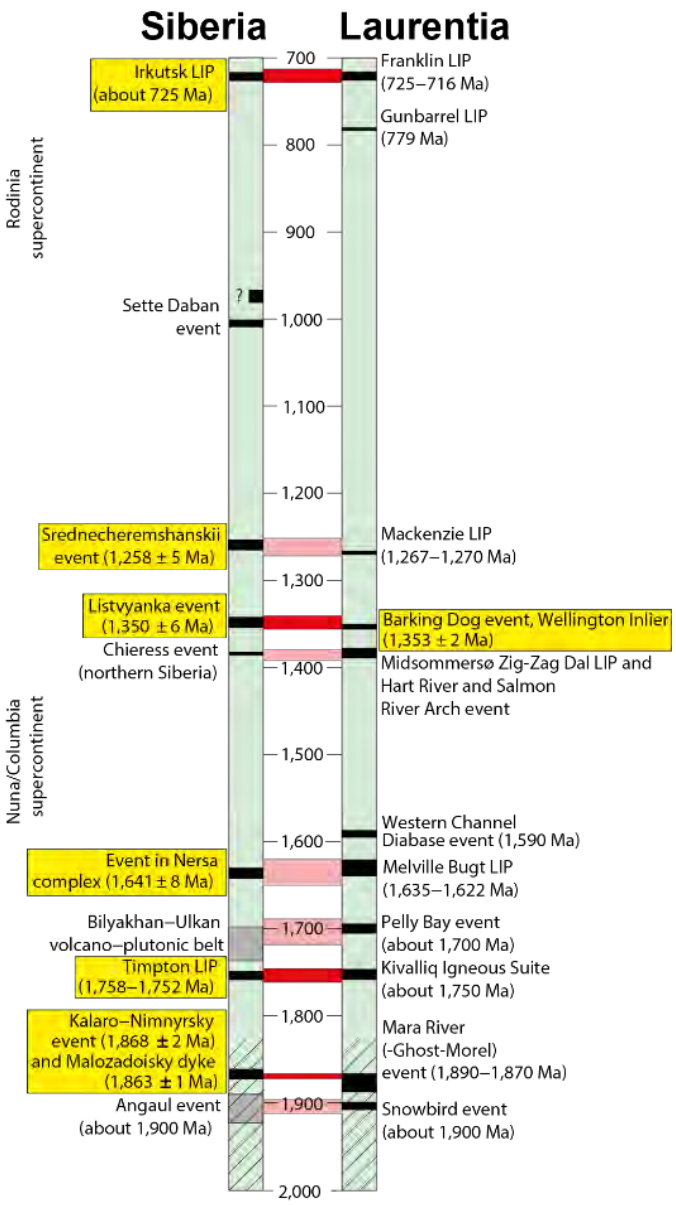

Figure 1.21: LIP barcode between Laurentia and Siberia after Ernst et al. (2016a).

New data on silicic large igneous provinces (SLIPs) show that they can be potential targets in the future to obtain information about paleogeographic reconstructions, including LIP-barcode and paleomagnetic data (Bryan and Ferrari, 2013).

⇨ Paleomagnetic data

Paleomagnetism is known to be the only "quantitative" method to assess the relative positions (paleolatitude and azimuthal orientation) of continental blocks in the past. There are a number of methods by which the paleomagnetic poles can be used to establish or test paleogeographic reconstructions in the Proterozoic (Buchan, 2013) but all methods require a succession of good-quality paleomagnetic poles or “key poles”.

A key pole (Buchan et al., 2000; Buchan, 2013) is defined by well-determined age (U-Pb geochronology with ± 10 Ma), good stepwise demagnetization (by thermal and/or AF), a sufficient number of sites to eliminate secular variation, regional tectonic consistency and positive field tests (baked contact test, intraformational conglomerate test, polarity test) attesting for the primary nature of remanence. Another possibility used for assessing the reliability of a pole is the Q index (1 – 7) of Van der Voo (1990b). The seven reliability criteria are: (1) well-determined rock age and a presumption that magnetization is of the same age, (2) sufficient number of samples and sites (Samples > 24; ~10 sites; no specific number of sites is indicated in Van der Voo criteria, but Fisherian statistics need a minimum of 4 observations, therefore 6 sites) and good statistical parameters ($K > 10$, $A_{95} < 16$), (3) adequate stepwise demagnetization using AF and/or thermal associated with vectorial analysis, (4) field tests, (5) structural and tectonic control on area, (6) presence of reversals, and (7) no resemblance to younger paleopole of the same craton. A problem of this Q index is that not all criteria are of equal value, hence, the association between age and primary remanence are essential to characterize a key pole (Buchan, 2013).

Method 1: Comparison between APWPs (apparent polar wander paths)

Graham et al. (1964) proposed to compare APWP segments which are defined as the succession of paleomagnetic poles (Figure 1.22). This is the most accurate method to compare the positions of cratons and verify if the cratons are moving on the same plate. If two cratons drifted together in the same plate in the past, superimposing their APWPs for the time they were united will result in similar lengths and shapes (Evans and Pisarevsky, 2008). Superimposing APWPs is the only method to obtain a unique reconstruction. Buchan (2013) recalled that only key poles should be used to construct APWPs. It should be emphasize that none paleomagnetic method constrain the paleolongitude. However the APWP method constrains the relative paleolongitude between different cratons. However, this technique is difficult to be employed during the Proterozoic because few key poles are presently available.

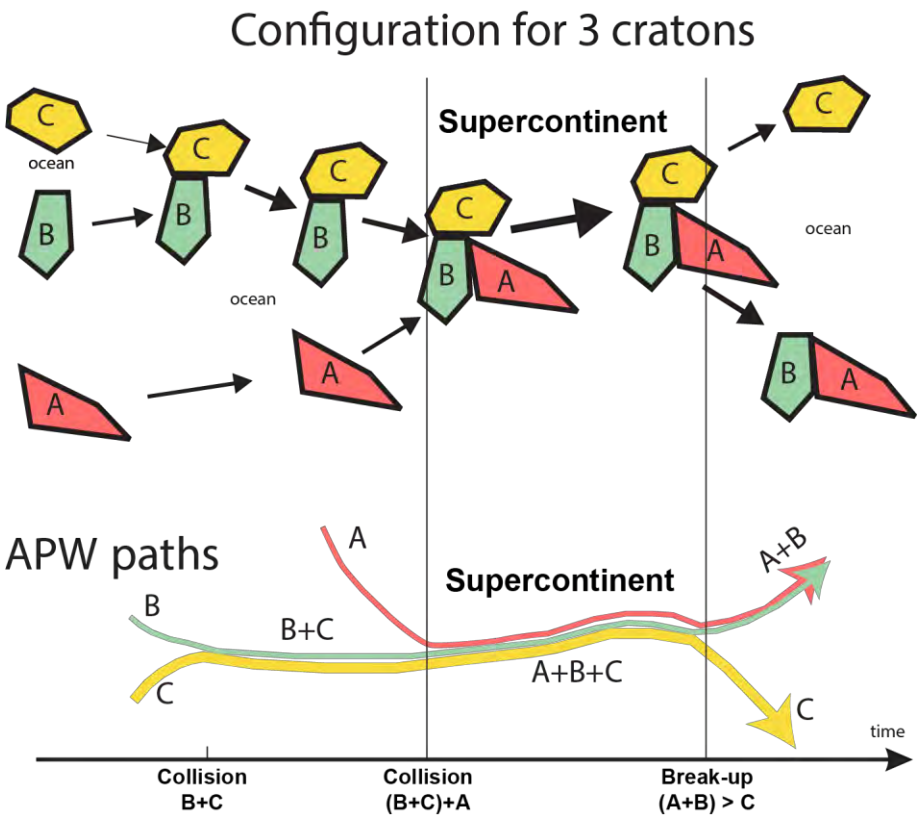

Figure 1.22: Schematic APWPs between 3 cratons to understand the APWPs method, redrawn after Evans and Pisarevsky (2008)

Method 2: Comparison between coeval paleopole

This method is used when there are not enough paleomagnetic poles to trace APWPs, which is the case for Proterozoic times. The procedure consists in comparing coeval key poles from different cratons. After superimposing the key poles we compare the position of the cratons. Figure 1.20 shows a possible reconstruction of the Amazonian craton and Baltica at *ca*. 1970 Ma using the Surumu (Amazonia) and Pechenga–Onega (Karelia craton, Baltica) poles. This method, however, doesn't constrain the relative paleolongitude and, as a consequence, the drift evolution of cratons in time. Moreover, depending on the polarity choice of paleomagnetic poles (polarity ambiguity) we have many alternative for the relative position of the cratons.

Method 3: Comparison of coeval great circle

Always with two cratons as an example, we added two new poles of another age, so we have a basic APWP with two paleomagnetic poles for each craton. This method consists in comparing the lengths of great circles for the two cratons. Thus, we infer if both cratons experienced the same rotation about a unique rotation pole, but we do not have information about vertical rotation for each craton. The problem with this method is that the superimposition

of two great circles can be fortuitous, for example if we choose a pair of poles with very distinct ages (Evans and Pisarevsky, 2008). The same logic is used when analyzing possible true polar wander (TPW) as we will see later.

- **APWP in Paleoproterozoic**

The period between 1850 and 1200 Ma corresponds to the amalgamation and the break-up of Columbia supercontinent (Pesonen et al., 2012). Buchan (2013) identified 50 key poles in the Proterozoic but only 45 are located inside the cratons. Normally, key poles and non-key poles combined with geological data are used to propose consistent reconstructions (Pehrsson et al., 2016; Pisarevsky et al., 2014). Based only on key poles, Buchan (2013) established a common APWP for Laurentia and Baltica between 1840 and 1260 Ma. This common path suggests a connection between these two cratons during 570 Ma at least. The importance of using APWPs segments is evident because the superimposition of two APWPs allows that a single configuration, as NENA, can be well-constrained (Figure 1.23, Evans (2013) (where northern margin of Baltica is adjacent with eastern Greenland/upside-down orientation for Baltica).

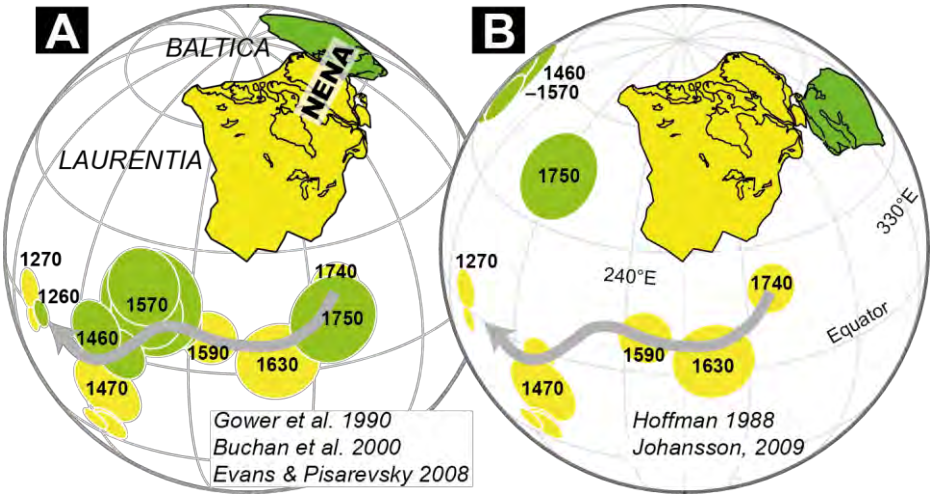

Figure 1.23: APWPs for Laurentia and Baltica. A: In NENA configuration the APWPs are superimposed. B: In the alternative configuration of Hoffman (1988) the APWPs are different. After Evans (2013).

Using key poles and non-key poles, updated APWPs for different cratons superimpose into a common path for the Columbia supercontinent (as proposed by (Zhang et al., 2012)) between 1750 and 1380 Ma (Figure 1.24) (Salminen et al., 2015; Xu et al., 2014). So, robust paleomagnetic data reinforces the existence of a Paleo-Mesoproterozoic supercontinent. However, alternative configurations for most cratons are possible, as proposed in different models that will be discussed in the next section.

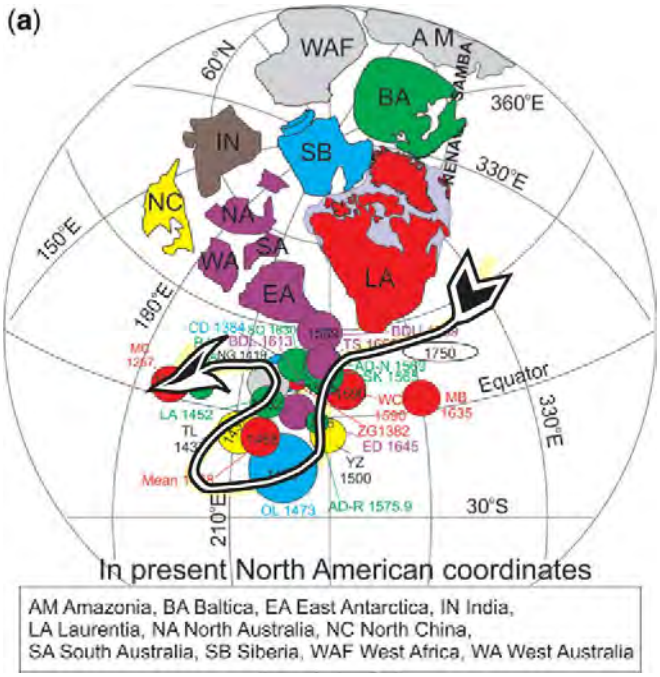

Figure 1.24: APWP of the Columbia supercontinent in a configuration as suggested by Zhang et al. (2012), according to Salminen et al. (2015).

- **How to build a supercontinent?**

Three mechanisms are proposed to explain supercontinent's formation (Figure 1.25). A first mechanism is the **introversion** model (Nance et al., 1988) where the new supercontinent is formed in the same location with closure of oceanic basin (classical Wilson cycle). A second mechanism is the **extroversion** (Hartnady, 1991) where the new supercontinent is formed after the closure of an external large ocean. A third mechanism is the **orthoversion** model (Evans, 2003; Mitchell et al., 2012). This model proposes a closure of oceanic basin to at 90° along the great circle perpendicular to the axis of previous supercontinent. This model can explain the TPW oscillations recorded with paleomagnetic data (Mitchell et al., 2012). The transition of Nuna to Rodinia could be a mixing between extroversion and introversion. The introversion could explain presence of "stranger attractors" of Meert (2014). The extroversion could explain the rotation of Baltica or Amazonian craton (Evans, 2013). Purely extroversion is evoked for the Rodinia – Gondwana transition. These transitions could be associated with some mechanisms of orthoversion and we can use it to calculate paleolongitude for supercontinent as suggested by Mitchell et al. (2012).

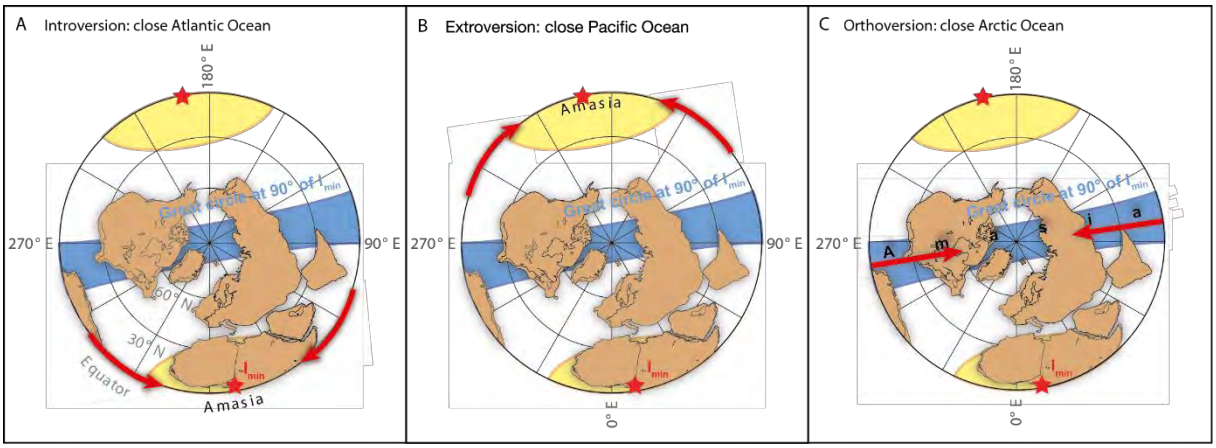

Figure 1.25: Mechanisms for the formation of supercontinents. Example for the future Amasia (Mitchell et al., 2012). Red stars indicate the I_{min} (position of the previous supercontinent – Pangea).

1.4. Models for the Columbia supercontinent

⇨ The first models (2002 – 2004)

During the 90s, research on the Rodinia supercontinent stole the spotlight in relation to tectonic reconstructions of older ages. The Columbia supercontinent was an abstract idea with only some geological evidence. Rogers (1996) introduced a schematic model of the evolution of supercontinents over three billion years of Earth's History. According to him, Rodinia and Pangea were considered as supercontinents but pre-Rodinia landmasses were only speculative. Three large landmasses were identified to be the "initial" continents which remained fixed until the Pangea: **Ur**, **Arctica**, and **Atlantica** (Figure 1.26.A). Ur (3000 – 200 Ma) was constituted by blocks of East – Gondwana (Kaapvaal, Dharwar, Pilbara, East – Antarctica). Arctica (2500 – 1500 Ma) was constituted of Northern America (Slave, Superior…), Greenland, and Siberia. Arctica would evolve in NENA (1500 – 200 Ma) that includes Baltica and other part of East – Antarctica. Atlantica (2000 – 200 Ma) was formed by cratons in South America (Amazonia, Rio de la Plata, São Francisco) and Africa (West Africa, Congo, West Nile). In the 2000s, the first conceptual models on the Columbia supercontinent appeared and will be summarized here.

The first model of Rogers and Santosh (2002) proposed a configuration of Columbia based on evidence of rifting and orogenic activity (Figure 1.26.B). We find the three blocks Ur, Arctica and Atlantica of Rogers (1996). The amalgamation of supercontinent would began around 1900 – 1800 Ma with a maximum package at *ca*. 1600 Ma (Mesoproterozoic supercontinent). The greatest evidence supporting this configuration would be a Mesoproterozoic rifting between eastern India and western North America, and orogenic zones along sutures. The supercontinent's name comes from the connection in a rifting system which was supposed in

the Columbia region in North America. In the latest model of Columbia (Rogers and Santosh (2002, 2009), the authors add only North China Craton (NCC) in a position close to Baltica and Greenland in Figure 1.26.B. It should be noted that new paleomagnetic data of good-quality for India contradict this connection between India and Western Laurentia at *ca*. 1880 Ma (Meert et al., 2011) and ca. 1470 Ma (Pisarevsky et al., 2013).

Zhao et al. (2002); Zhao et al. (2004) proposed a different reconstruction for the Columbia supercontinent in the same year, providing additional details about the orogenic systems (Figure 1.26.C). Thus, the model is based on geological data and some existing paleomagnetic data. In the reconstructions of Rogers and Santosh (2002) and Zhao et al. (2004), most of the supercontinent are represented by NENA with Siberia. South America and “West Africa” (plus Congo craton) are connected in both reconstructions referred to the Atlantica, but Zhao et al. (2004) proposed a position of Atlantica near Baltica. The South China craton is shown as a separate craton by Zhao et al. (2004) and omitted by Rogers and Santosh (2002). Zhao et al. (2004) show a connection between the North China Craton (NCC) with the India craton along the Trans-North China orogeny connected to the "Central India Tectonic Zone" (CITZ), but this association is questioned. A major difference in the model of Zhao et al. (2002); Zhao et al. (2004) is the location of East Antarctica and associated cratons. Rogers and Santosh (2002) proposed an extension of Ur (“in the Pangea configuration”) with South Africa, Australia and East Antarctica connected with Laurentia. Concerning Zhao et al. (2004), East Antarctica (Terre d’Adélie) was connected with southern Australia (Gawler craton) to form a proto-Mawson (Payne et al., 2009). East Antarctica was connected with southwestern of North America whereas Australia was connected to the northwestern of North America (Canada). South Africa (Kalahari) was near Australia and the Tarim craton.

These models were mainly based on geological and structural data. Meert (2002) was the first who performed a paleomagnetic analysis with the available paleomagnetic database (Figure 1.26.D). At that time it was impossible to test all the associations between 1900 and 1400 Ma. At *ca*. 1770 Ma, the difference in paleolatitude between the cratons didn’t allow the presence of a supercontinent. At *ca*. 1500 Ma, paleomagnetic data for Laurentia, Australia, Baltica and Siberia provided a first paleomagnetic evidence for the Columbia supercontinent but slightly different from that based on geological evidence (Zhao et al. (2002). Australia and Baltica are a little further south relative to Laurentia than that proposed by Zhao et al. (2002), and Siberia have a good match with North America. These early models and especially the model proposed by Zhao et al. (2002), based on orogenic connections are the basis of all future models.

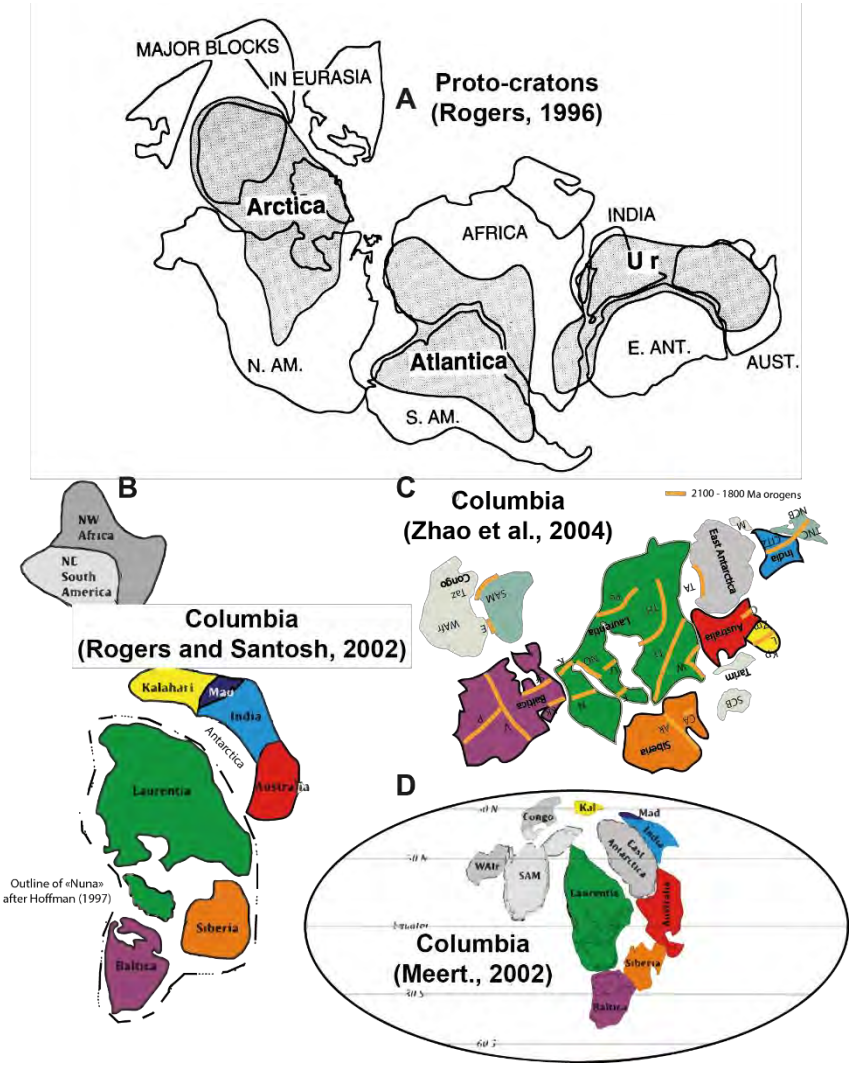

Figure 1.26: First models for the Columbia supercontinent. A: Model of Rogers (1996). B: Model of Rogers and Santosh (2002). C: Model of Zhao et al. (2004).D: Paleomagnetic model of Meert (2002).

⇨ India - North America connection

Paleomagnetic data were limited in previous reconstructions, due to the small amount of good quality data and precise geochronology. So, Hou et al. (2008) used giant radiating dike swarms and orogenic belts to propose a new reconstruction of Columbia supercontinent (Figure 1.27). Coeval dikes at ca. 1850 Ma in North China Craton (NCC), India craton, and North America suggested a unique landmass before break-up. Hou et al. (2008) proposed a plume model between the Xiong'er region in NCC and the Cuddapah Basin to explain radial dikes in the three cratons.

In this model, Hou et al. (2008) proposed a subduction zone on the northern margin of the NCC. The Wopmay orogenic system (1880 – 1840 Ma) in Laurentia can be interpreted in a

subduction setting. A giant subduction zone runs along the southern part of the supercontinent, which continues through Baltica and Amazonia. Kaur and Chaudhri (2013) also adopted this reconstruction in their metallogenic model.

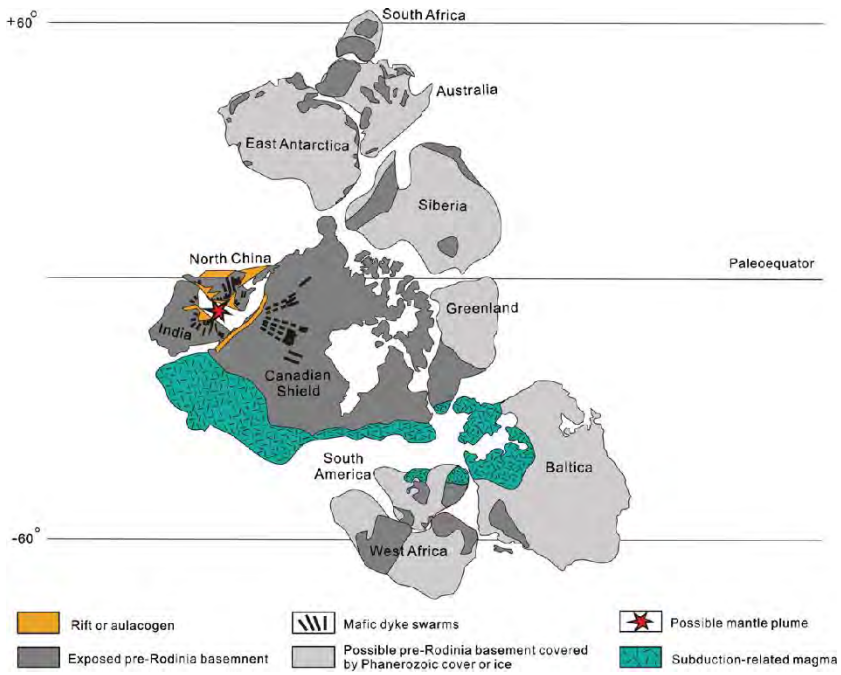

Figure 1.27: Columbia supercontinent according the model of Hou et al. (2008).

⇨ **Baltica – NCC - Amazonia connection**

Wilde et al. (2002) noted similarities between the NCC and Baltica and proposed a speculative reconstruction with the NCC connected by the Kola – Karelian orogeny (in northern Baltica) through the Trans – North China orogeny.

Kusky et al. (2007) proposed that NCC was adjacent to Baltica and Amazonian craton between 2000 – 1700 Ma based on coeval tectonothermal episodes (Figure 1.28.A). According to Kusky et al. (2007), the Northern Hebei orogeny (~1930 Ma) is similar to the Svecofennian orogeny (1840 – 1830 Ma) in Baltica, and the Transamazonian-Eburnian orogenic system (2200 – 1900 Ma) in South America and Africa. Kusky and Santosh (2009), also proposed a connection with the Rio Negro Juruena Province in the Amazonian craton and UHT (Ultra-high-temperature) metamorphism in the three cratons was used as supporting this link until ~1700 Ma.

With the Colíder paleomagnetic pole at *ca*. 1790 Ma for the Amazonian craton, Bispo-Santos et al. (2008) provided the first paleogeographic reconstruction for the Baltica – NCC – Amazonia landmass (Figure 1.28.B). In this model, the connection between Baltica and

Amazonia is through the Trans – North – China belt in NCC rather the North Hebei orogeny and the Ventuari – Tapajos Province in Amazonia.

This scenario was updated by D'Agrella-Filho et al. (2012) who propose a triple junction located between the NCC, the landmass Amazonia / Sarmatia, and Fennoscandia (Figure 1.28.C). Indeed, this model considers a strong connection between Amazonia and Sarmatia whereas rotations takes place between Fennoscandia and Sarmatia (Bogdanova et al., 2013).

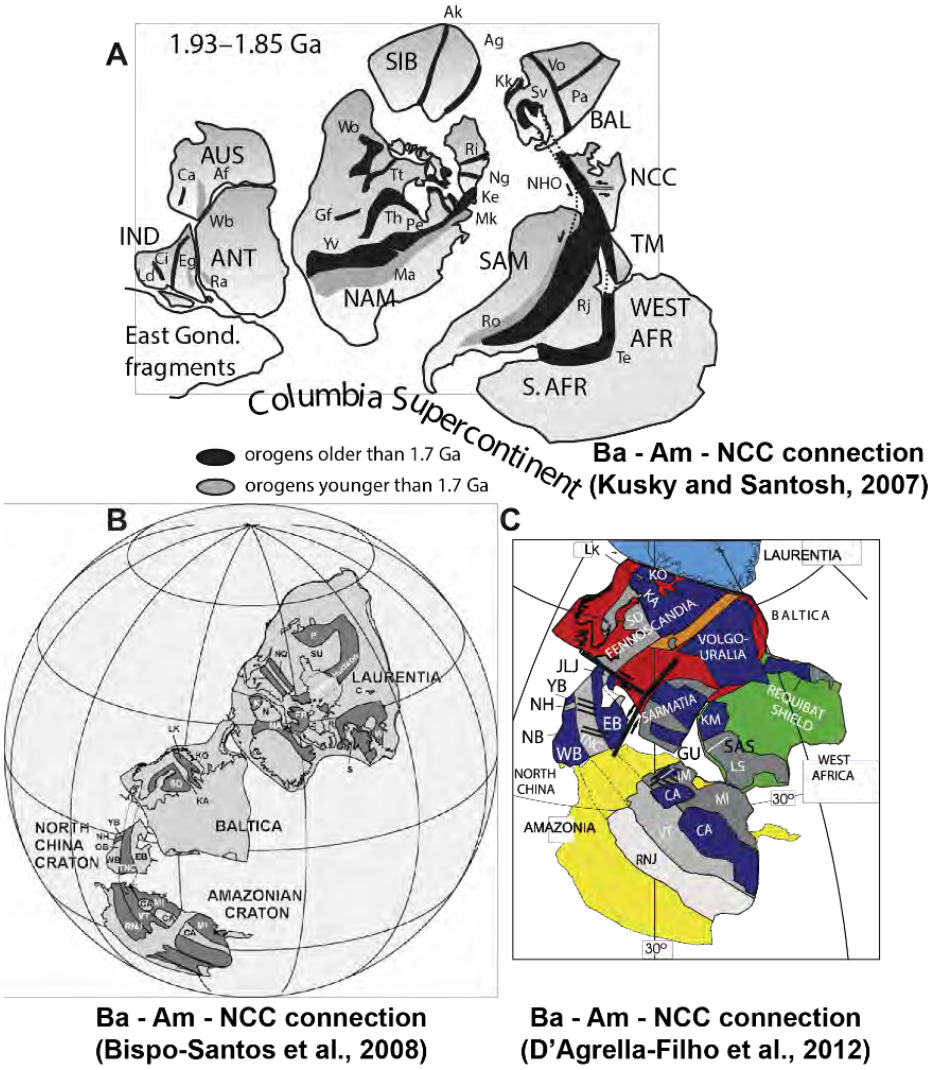

Figure 1.28: Possible connections between Baltica -North China Craton (NCC) – Amazonia. A: Model of Kusky et al. (2007). B: Model of Bispo-Santos et al. (2008). C: Model of D'Agrella-Filho et al. (2012).

⇨ Long lifespan models and lid tectonic

Yakubchuk (2010) proposed a new vision for a long-lived Paleo-Mesoproterozoic supercontinent. He used the traditional method that correlates collisions (internal) and accretionary system (external) through kinematics during the Proterozoic, added to paleomagnetic data. Moreover, he also considers the distribution between the Archean

granulite – gneiss and granite – greenstone terranes. In his model, Columbia supercontinent was a ~30 000 km long supercontinent, composed of Archean terranes (granulite-gneiss), reworked between 1900 and 1800 Ma, and occupying an axial position along its length, forming a "Super horde" (Figure 1.29.A). The core of the Super-Horde is constituted by the lithospheric keels of cratons. The Columbia supercontinent remained intact between 1850 and 1100 Ma without break-up before Rodinia, which was formed only by a rearrangement of block rotations.

In the Protopangea – Paleopangea model of Piper (1982, 2000, 2007, 2010a); Piper (2014), the three initial blocks of Rogers (1996) - Ur, Arctica and Atlantica – are evident (Figure 1.29.B). He proposes a long-lived supercontinent lasting between 2600 – 570 Ma, which does not consider the existence of Rodinia but a dominant lid tectonic until the late Neoproterozoic. This model includes the link between Laurentia, Baltica and Siberia. It also assumes a link between Amazonia and Antarctica rather than between Amazonia and Baltica as observed in other models. The symmetrical crescent-shape of the supercontinent in this reconstruction can be compared to the (Neo)-Pangea. As already stressed, however, this model is widely criticized in the literature.

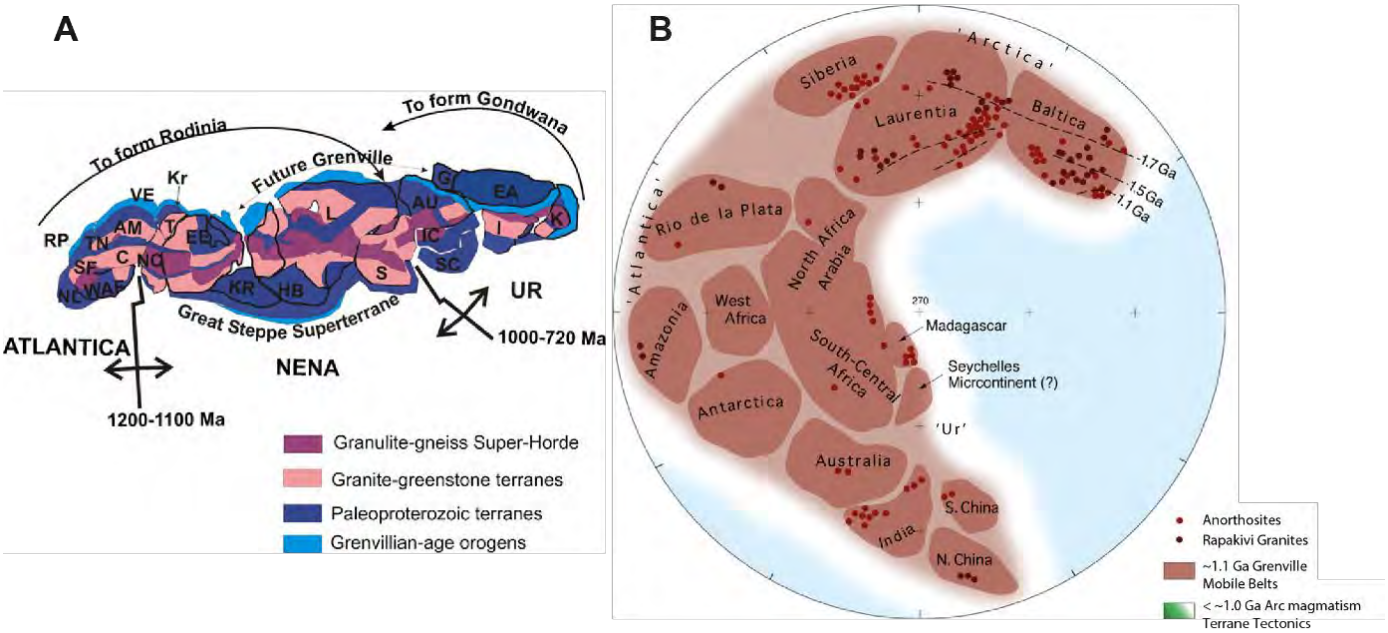

Columbia «Super-Horde» Yakubchub (2010)

Paleopangea between ~ 2000 - 1100 Ma Piper (2013)

Figure 1.29: A: Super-Horde model of Yakubchuk (2010). B: Paleopangea model of Piper (2013b).

⇨ **Baltica – Amazonia – West Africa connection**

Karlstrom et al. (2001) were the first to propose a link between Baltica, Amazonia and Africa. The **SAMBA** (South America – Baltica) model suggests that Baltica, Amazonia and West Africa were linked together, and remained consistent from 1800 Ma until 1300 Ma or even 800 Ma (Figure 1.30) (Johansson, 2009, 2014). Johansson (2009)'s model is mainly based on the distribution of orogenic and magmatic belts to provide a coherent evolution and continuity of these belts along the cratonic blocks, and the repartition of AMCG complexes. This model suggests that the Svecofennian orogenic belt (1900 – 1850 Ma) in Baltica is connected to the coeval Ventuari – Tapajós Province in the Amazonian craton. Moreover, the 1850 – 1650 Ma Transscandinavian Igneous Belt (TIB) and the 1640 – 1520 Ma Gothian belt have their continuation in the Rio Negro-Juruena Province (1780 – 1550 Ma) in the Amazonian craton.

According to this model, Baltica is well-linked with Laurentia but its orientation is different from the NENA "upside-down" configuration (Gower et al., 1990). The "right-way-up" orientation of Baltica relative to Laurentia is adopted based on geological grounds, and this supports a tight fit between SE Greenland and NW Fennoscandia as also suggested by Hoffman (1988) and Bridgwater et al. (1990). However, paleomagnetic data is consistent with a different connection between Baltica and Laurentia (Buchan, 2013).

New paleomagnetic and geochronological data for the Amazonian craton supports the SAMBA model with the 1790 Ma Avanavero pole (Bispo-Santos et al., 2014b). However, 1440 – 1420 Ma paleomagnetic poles - Indiavai pole (D'Agrella-Filho et al., 2012), Nova Guarita pole (Bispo-Santos et al., 2012), Salto do Céu sills pole (D'Agrella-Filho et al., 2012) are located at ca. 30° from the 1460 Ma mean pole for NENA (Laurentia and Baltica) and they don't support the SAMBA model as viewed by (Bispo-Santos et al., 2014b). A possible explanation is that Internal block rotations within the Columbia supercontinent occurred between 1780 and 1400 Ma (See D'Agrella-Filho et al. (2016) for a discussion).

Among the latest models published in the literature, the SAMBA model is widely accepted (Eglington et al., 2013; Evans and Mitchell, 2011; Pehrsson et al., 2016; Salminen et al., 2015; Xu et al., 2014; Zhang et al., 2012).

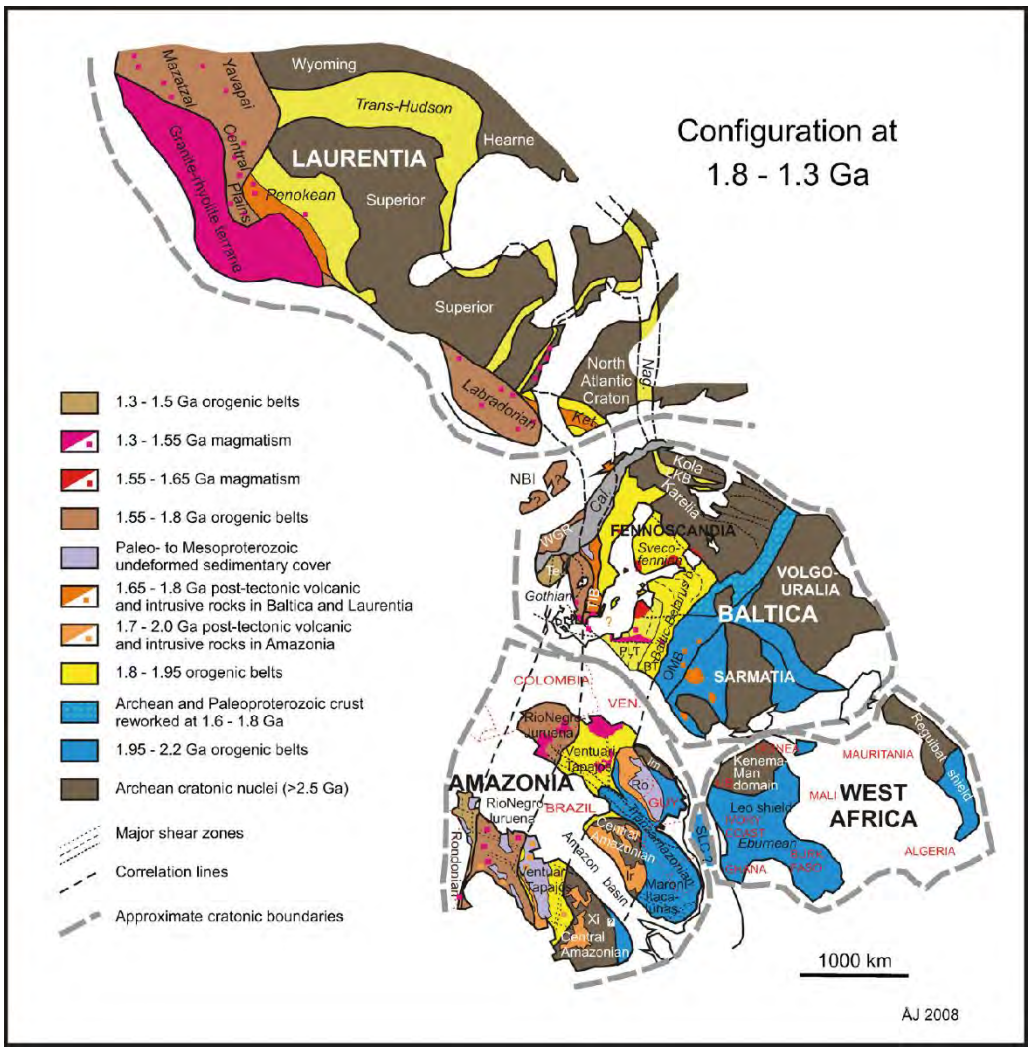

Figure 1.30: SAMBA model according to Johansson (2009).

⇨ Current models for Columbia

Current models are based on a larger paleomagnetic database, seeking to obtain a coherent kinematic evolution. Moreover, these data are combined with geochronological and stratigraphic compilations (Eglington et al., 2009; Pisarevsky et al., 2014). Metallogenic associations are also used (Pehrsson et al., 2016).

Pehrsson et al. (2016) propose a model that takes into account the evolution of cratons over time and which considers each province within the cratons (Figure 1.31). It's not a palinspastic reconstruction because they consider rigid plates. This model is based on the updated paleomagnetic reconstructions of Evans and Mitchell (2011) and Zhang et al. (2012) and propose an evolution until the assembly of Rodinia of Li et al. (2013) and Li et al. (2008). The paleomagnetic "Upside-down" configuration between Baltica and Laurentia is accepted (Buchan, 2013). Siberia is linked to Laurentia in a tight-fit position (Buchan et al., 2016). The

East Antarctica – Australia block is linked to Laurentia in a proto-SWEAT ("Southwest U.S – East Antarctic") configuration (Zhang et al., 2012). Geological data support a tight connection of Australia with Laurentia (Betts et al., 2016; Thorkelson and Laughton, 2015). The SAMBA model is used to form a large landmass with Baltica – Amazonia and West Africa (Johansson, 2009, 2014). North China is near to the São Francisco-Congo craton and India, whereas Kalahari is drifting alone. In their model, Rio de la Plata, Amazonia, West Africa, and Congo/São Francisco formed a large united landmass. They consider India as divided in two parts - South and North India - but such separation is not supported by paleomagnetic data (Radhakrishna et al., 2013a; Radhakrishna et al., 2013b). Most of the Columbia supercontinent amalgamation occurred between 2200 – 1780 Ma, but it was finally assembled at *ca*. 1550 Ma. Finally, Kalahari and India did not took part of this Supercontinent, according to the model.

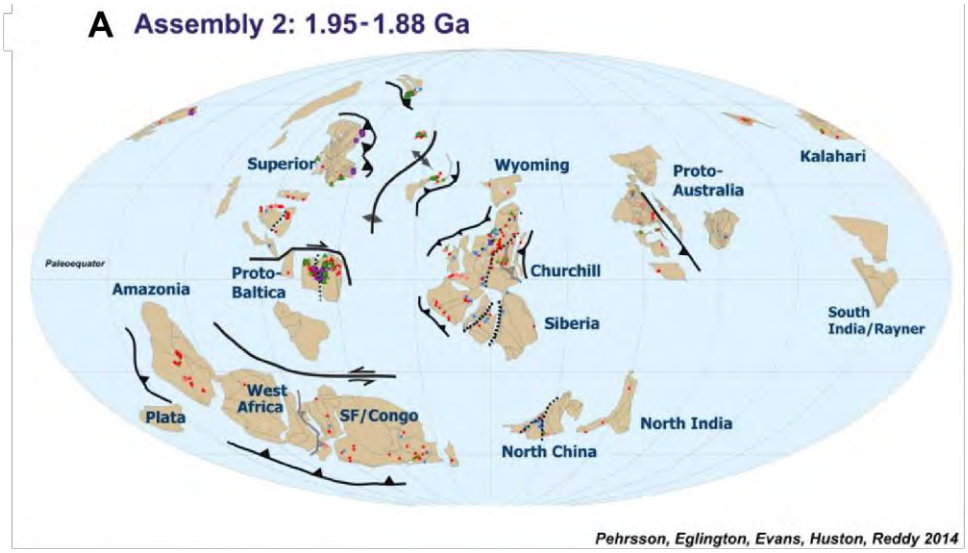

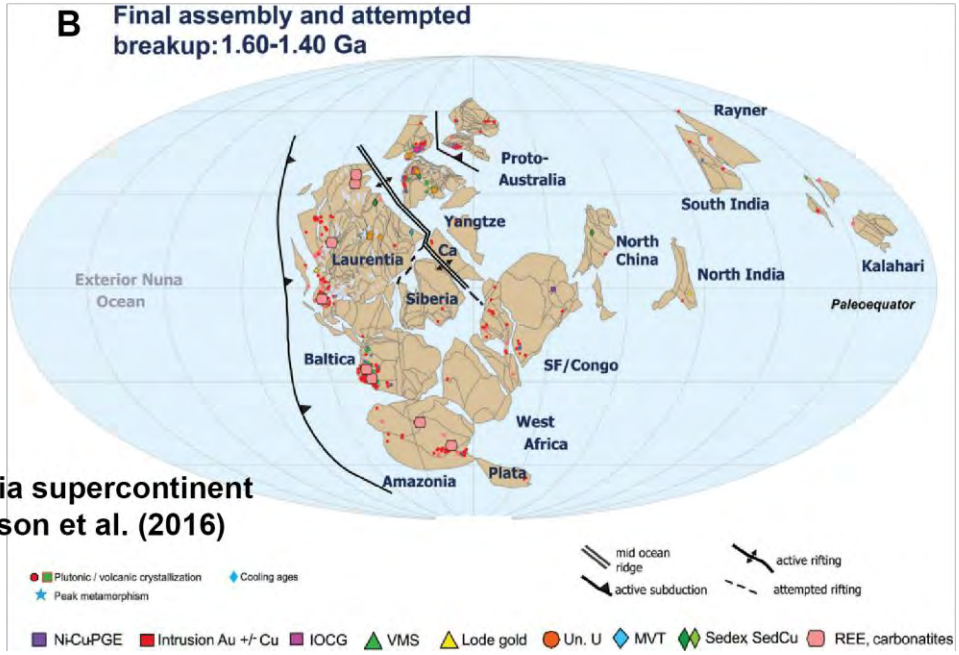

Figure 1.31: Positions of cratons at 1.95 – 1.88 Ga (A) and Columbia supercontinent with its maximum packing at 1.60 – 1.40 Ma (B) (Pehrsson et al., 2016).

Also based on a large paleomagnetic database, Pisarevsky et al. (2014) suggested an alternative model for Columbia supercontinent between 1790 and 1270 Ma (Figure 1.32), the main features of which are summarized below. Like Pehrsson et al. (2016)'s model, Baltica and Laurentia are connected in an "upside-down" position as in NENA (Gower et al., 1990). Siberia was positioned close to the equator but ~2000 km separated from Laurentia between 1740 and 1720 Ma. New paleomagnetic data and LIP barcode strongly support the Laurentia and Siberia connection but some uncertainties on the position and orientation of Siberia persist (Buchan et al., 2016; Ernst et al., 2016a; Pisarevsky et al., 2008). Based on LIPs barcode correlation, Siberia is considered close to the Congo – São Francisco with a mantle plume center under the craton. Cederberg et al. (2016) updated this connection with inclusion of North China Craton (NCC).

In the Pisarevsky et al. (2014)'s model, Australia and East Antarctica are located close to north-western Laurentia in a proto-SWEAT configuration as in the Zhang et al. (2012) and Pehrsson et al. (2016)'s models with a certain distance (before final collision at *ca*. 1580 Ma). India was linked to Baltica during the Mesoproterozoic unlike the SAMBA model proposes. Evans (2013), however, pointed out that this position of India is unlikely because of the great distance it has to move towards Rodinia (Li et al., 2008). Another consequence of their model is the rejection to the SAMBA model. They consider Amazonia and West Africa are not part of the Columbia supercontinent and they drift as a single landmass. In this model we have the formation of proto-cratons between 2000 and 1800 Ma that drifted to form the "West-Nuna" or the "East-Nuna" since 1790 Ma with a final collision of these two large landmasses at *ca*. 1580 Ma. Break-up occurred between 1450 and 1380 Ma.

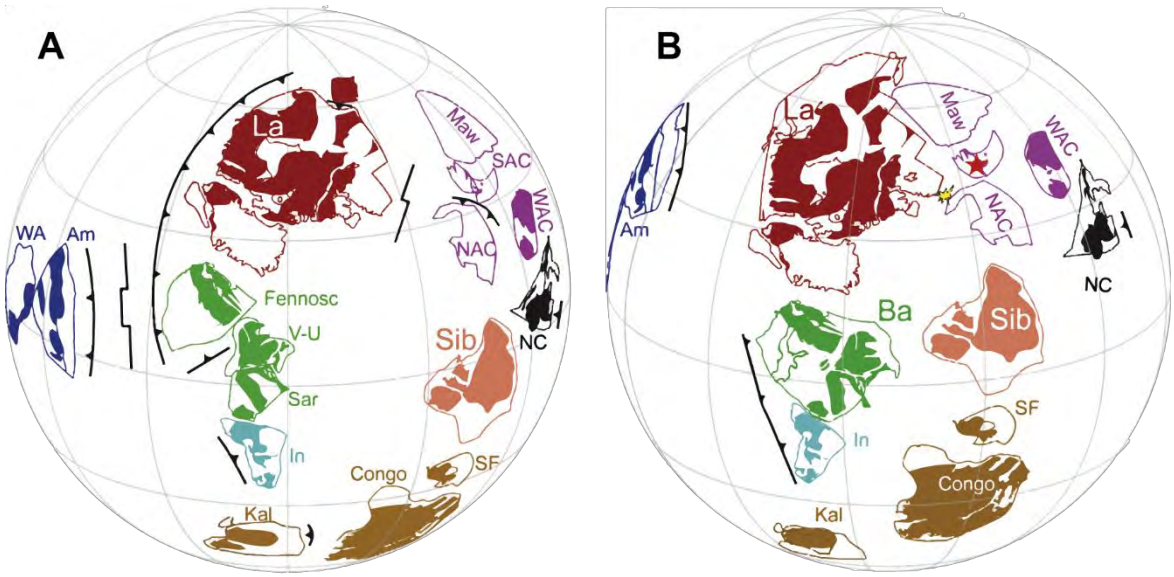

Columbia at *ca.* ~ 1770 Ma (Pisarevsky et al., 2014)

Columbia at *ca.* ~ 1580 Ma (Pisarevsky et al., 2014)

Figure 1.32: Columbia supercontinent between 1770 and 1580 Ma (Pisarevsky et al., 2014).

⇨ Summary

A significant amount of evidence corroborates the existence of the Columbia supercontinent, which was probably the first supercontinent in Earth's history. Many different reconstructions exist for this supercontinent but some specificities are common to all models. The connection between Laurentia and Baltica appears to be strong although their orientations may vary between models. The same can be said for Amazonian craton and West Africa which apper linked together in practically all models. The proto-SWEAT connection is also generally well-accepted between proto-Australia – East Antarctica ("Mawsonland") and Laurentia. Most proto-cratons amalgamated between 2000 and 1800 Ma and the maximum package seems to have occurred at *ca*. 1600 Ma. Break-up seems to have initiated at ca.1400 Ma but alternative models admit a later break-up with the formation of Rodinia. The lack of paleomagnetic data in this period is the main reason for these uncertainties.

Previous discussion shows that the geodynamic context (classified as "transitional") in which this first supercontinent was assembled is different from the classical Phanerozoic plate tectonics. Most models do not take into account the geodynamical aspect. Recently, Meert (2014) observed similarities between the three supercontinents (Columbia, Rodinia, and Pangea). Laurentia, Baltica, and Siberia are always close together in the three supercontinents (in different configurations). With the modern-style plate tectonics, we tend to imagine a random drifting for the cratons through time and the probability to observe the same associations should be low. Meert (2014) called these landmasses as "strange attractors". In opposition, cratons of "West-Gondwana" (South America, Africa) are referred as 'spiritual interlopers" (similarities with large displacement). Some cratons are always isolated in different configurations and are referred to as "lonely wanderers". This very interesting vision could suggest a dominant lid tectonic during the Proterozoic with episodes of true polar wander (TPW) (Meert, 2014).

Despite these new advances many uncertainties still persist. Thus, acquiring new paleomagnetic, geochronological, and structural data, and considering the prevailing geodynamics are essential to improve these models. We have especially seen that position of the Amazonian craton was not yet convincingly set in the different models. In the next section, we will focus on the importance of the Amazonian craton in the Columbia supercontinent.

Chapter 2: Position of the Amazonian craton in Columbia:

The paleomagnetic problem

This section is a brief summary of the published paper **"Amazonian Craton paleomagnetism and paleocontinents"** (D'Agrella-Filho et al., 2016) (see end of section). The evolution of the Amazonian craton has little resemblance to that recorded in other cratonic units of South America. It has more similarities with the evolution of West Africa craton, Laurentia and Baltica (Geraldes et al., 2001; Pesonen et al., 2003). The position of many of the units, especially the Amazonian craton, is yet poorly established due to the low quality of the world paleomagnetic database making reconstruction of the Proterozoic paleogeography highly speculative (Pesonen et al., 2003).

2.1 The Amazonian craton

The Amazonian craton is one of the main tectonic units of the South American Platform consisting of the Guiana and Central-Brazil (or Guaporé) shields, separated by the Amazon and Solimões basins. After the initial model of tectonic subdivision of the Amazonian craton, proposed by Amaral (1974), several other models of tectonic evolution have been proposed, which basically oppose two major theoretical schools: fixist against mobilistic school.

The fixist school considers the craton as a large Archean continental shield, affected by several episodes of crustal reworking through thermal events (Costa and Hasui, 1997; Hasui et al., 1984; Hasui, 1985). These authors defined the Amazonian craton as a mosaic due to the juxtaposition of twelve tectonic blocks (paleo-plates), which were assembled as a large landmass through diachronic collisions during the Archean and Paleoproterozoic. According to this model, at the end of Paleoproterozoic and at the beginning of the early Mesoproterozoic the newly assembled craton would be affected only by intraplate tectonic events, most likely extensional events. The fixist model was based primarily on geophysical data (gravimetric and magnetometric), available geological and structural interpretations at the time, and in a few radiometric data, especially those obtained by the K-Ar and Rb-Sr geochronological methods.

The mobilistic school proposes that the evolution of the Amazonian craton is the result of successive episodes of crustal accretion in Paleo and Mesoproterozoic, around an older core, stabilized at the end of the Archean (Cordani and Sato, 1999; Cordani et al., 1979; Cordani and Neves, 1982; Cordani and Teixeira, 2007; Tassinari and Macambira, 1999; Tassinari et al., 2000; Tassinari and Macambira, 2004; Teixeira et al., 1989).

Among the models in the most recent literature, the tectonic divisions of Vasquez et al. (2008) or Santos et al. (2000) and Cordani and Teixeira (2007) are the most used (Figure 2.1). The models are similar, with some disagreements, especially regarding the boundaries of tectonic (geochronological) provinces.

The model of Vasquez et al. (2008), is a review of models of Santos et al. (2003a); Santos et al. (2000) and is based on the interpretations of new U-Pb and Sm-Nd data. Santos et al. (2003a); Santos et al. (2000) proposed a division of the craton in seven geochronological or tectonic provinces (Figure 2.1.A): the **Transamazonic Province** (2250 – 2000 Ma), Carajás Province (2530 – 3100 Ma), **Central Amazon Province** (1880 – 1700 Ma), **Tapajós – Parima Province** (2100 – 1870 Ma), **Rio Negro Province** (1860 – 1520 Ma), **Rondônia – Juruena Province** (1760 – 1470 Ma), and **Sunsás Province** (1330 – 990 Ma). Vasquez et al. (2008) updated this model based on the geological map of Pará state (Brazil). They proposed new domains: (1) the division of the Carajás Province in the Carajás and Rio Maria domains, (2) the division of Transamazonas Province in Carecuru, Paru, Amapá, Bacajá and Santana do Araguaia domains, (3) the division of the Central Amazonia Province in the Erepecuru – Trombetas (W and E) and Iriri – Xingu domains.

The model of Cordani and Teixeira (2007) is a review of previous models (Figure 2.1.B) (Cordani et al., 1979; Tassinari and Macambira, 1999; Tassinari and Macambira, 2004; Teixeira et al., 1989) with two Archean nuclei and five Proterozoic tectonic provinces. In this model, the core of the Amazonian craton consists in the **Central Amazonian Province** which is formed by two Archean nuclei, the Xingu – Iricoumé and Roraima blocks (3200 – 2600 Ma). The **Maroni – Itacaiunas Province** is constituted by mobile belts of ages between 2250 and 2050 Ma (Ledru et al., 1994) associated to the Siderian – Rhyacian orogenic events ("old-Transamazonian cycle"). The Archean basement of the Amazonian craton is covered by Proterozoic volcano – sedimentary units with little or no deformation. Accretionary belts occurred during the Paleo-Mesoproterozoic along the southwestern margin with the development of the **Ventuari – Tapajós Province** (2000 – 1800 Ma), the **Rio Negro – Juruena Province** (1780 – 1550 Ma), and the **Rondonian – San Ignacio Province** (1500 – 1300 Ma). The latter is characterized by the collision of the Paraguá terrane at *ca*. 1320 Ma (Bettencourt et al., 2010; Rizzotto and Hartmann, 2012). The final orogenic belt occurring to the west of the Amazonian craton is the **Sunsas – Aguapeí** (1250 – 1000 Ma) which highlights the Grenvillian collision between Amazonian and Laurentia cratons.

In this work, we will follow the evolutionary model of Cordani and Teixeira (2007) which is adopted by several other authors (Bettencourt et al., 2010; Cordani et al., 2009; Schobbenhaus et al., 2004).

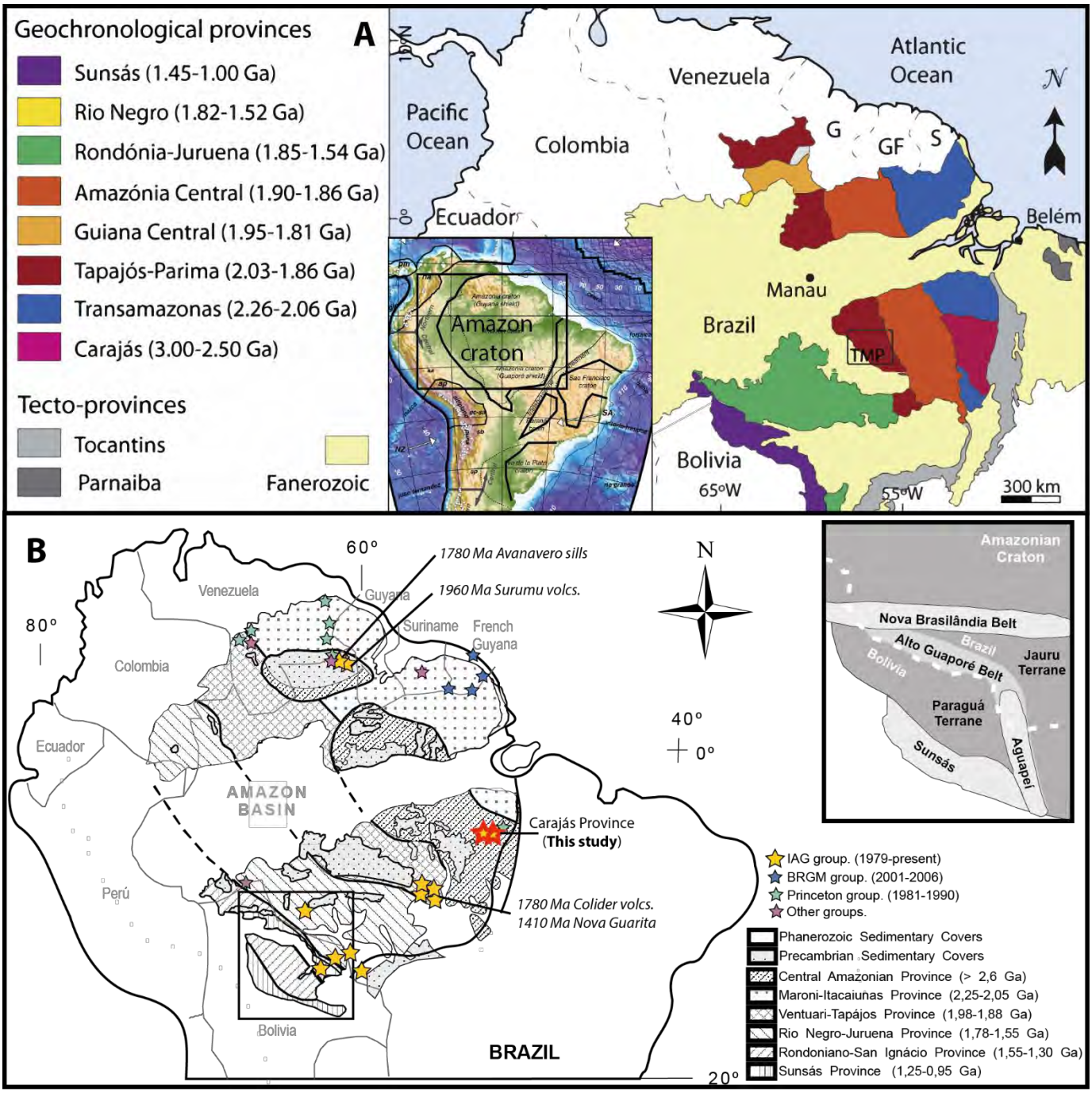

Figure 2.1: Tectonic models for the Amazonian craton. A: Model of Santos et al. (2003a) adapted from Roverato et al. (2016). B: Model of Cordani and Teixeira (2007) with localization of different paleomagnetic studies for the Amazonian craton (D'Agrella-Filho et al., 2016; Teixeira et al., 2016). Inset: Sketch of the southwestern part of the Amazonian Craton showing the Paraguá Terrain and Alto Guaporé, Aguapeí and Nova Brasilândia belts (modified after D'Agrella-Filho et al. (2012)).

2.2 Paleomagnetic database for the Amazonian craton – implications to the paleocontinent Columbia.

We saw in the previous chapter that there are many models for the position of the Amazonian craton in the Columbia supercontinent constrained by paleomagnetic data. All Amazonian paleomagnetic poles from Paleo-Mesoproterozoic times are described in Table 1 of the attached paper (D'Agrella-Filho et al., 2016), which synthesizes their tectonic implications for paleocontinents. The progress in the Amazonian paleomagnetism can be attributed mainly to three research groups (Figure 2.1.B): (i) one carried out by the Princeton group (led by Tullis C. Onstot) in the 1980s. This group worked mainly on Paleoproterozoic rocks from Venezuela (green stars in Figure 2.1.B). (ii) A second group, with paleomagnetic work developed on Paleoproterozoic rocks from the French Guiana (blue stars in Figure 2.1.B), whose paleomagnetic results were published in the 2000s. This group was led by French researchers: Sébastian Nomade (at that time in Berkeley Geochronology Center, USA) and Hervé Théveniaut from BRGM (Bureau de Recherches Géologiques et Minières, France). (iii) The third influential group (and currently in activity) in the history of paleomagnetism of the Amazonian craton is from IAG-USP (Brazil). This group has worked with geological units with ages varying since Paleoproterozoic up to Cambrian (yellow stars in Figure 2.1.B). Adding to these three groups, independent studies (purple stars in Figure 2.1.B) have also achieved significant results (Castillo and Costanzo-Alvarez, 1993; Valdespino and Alvarez, 1997; Veldkamp et al., 1971). Below, we describe a synthesis of the main tectonic implications of the Paleoproterozoic paleomagnetic data on the formation of the Columbia supercontinent. The first paleomagnetic data obtained by the Princeton Group led to the proposition of a possible connection between Amazonian and West African cratons along the Guri (in Amazonia) and Sassandra (West Africa) shear zones (Onstott, 1981a). This proposal was later on corroborated by new paleomagnetic data from Paleoproterozoic igneous and metamorphic rocks from French Guiana (Nomade et al., 2003).

In the 2000s, new paleomagnetic expeditions were carried out in the Guiana shield by the BRGM (Bureau de Recherches Géologiques et Minières, France). They produced a large amount of paleomagnetic data and new poles for the Guiana shield (Costal Late granite, Approuague River granite, Mataroni River granite, Tampok granite, Tumuc granite, Armontabo River granite) (Théveniaut et al., 2006). We can highlight the very good paleomagnetic OYA pole determined by Nomade et al. (2001), and dated by Ar-Ar at *ca*. 2036 ± 14 Ma (cooling age of the tonalite). Théveniaut and Delor (2003) were the first authors to propose a review of the paleomagnetic results and quantify the reliability of data for the Amazonian craton. Based on new paleomagnetic data on well-calibrated in age plutonic and metamorphic rocks,

(Théveniaut et al., 2006) proposed the first apparent polar wander path for the Amazonian craton between 2155 and 1970 Ma.

Recently, Bispo-Santos et al. (2014a) published a robust pole for the well-dated 1980 – 1960 Ma (U-Pb on zircons) Surumu volcanics from northern Roraima State (Brazil). This pole helped to improve the Théveniaut et al. (2006)'s APWP. Bispo-Santos et al. (2014a) argue that the present 2100 – 1960 Ma paleomagnetic data from Amazonian and West African cratons support the connection between these cratons along the Guri and Sassandra lineaments as previously proposed by Onstott et al. (1981) and Nomade et al. (2003). These results imply that a large landmass was probably formed at 2.0 Ga by proto-Amazonia, West Africa, and another cratonic block (probably Sarmatia/Volgo-Uralia from Baltica) that collided during the 2200 – 2000 Ma Maroni – Itacaiunas mobile belt (D'Agrella-Filho et al., 2016). According to these authors, this continental block collided with Fennoscandia to form Columbia at about 1.79 – 1.78 Ga ago.

Bispo-Santos et al. (2008) calculated a paleomagnetic pole for the well-dated 1790 Ma Colíder group from the Central – Brazil shield. They proposed a configuration for the Columbia supercontinent with a connection between Baltica, North China craton and Amazonian craton as we saw previously. It is interesting to note that results from the 1440 – 1420 Ma Nova Guarita mafic dike swarm (Bispo-Santos et al., 2012), Indiavaí Suite (D'Agrella-Filho et al., 2012) and Salto do Céu sills (D'Agrella-Filho et al., 2016) support a similar connection between Baltica – NCC – Amazonia. These geological units are also from the Central – Brazil shield located at the southern part of the Amazonian craton.

Recently, however, Bispo-Santos et al. (2014b) performed a paleomagnetic study on the Avanavero sills from the Guiana shield. These rocks are well-dated by U-Pb on baddeleyite at *ca*. 1790 Ma (Reis et al., 2013). The Avanavero pole passes a baked contact test and supports the SAMBA model (Johansson, 2009) where Baltica was directly linked to Amazonian craton and West Africa. The inconsistence of the 1790 Ma and the 1440 – 1420 Ma poles from the Central – Brazil shield with those from Guiana shield, Baltica and Laurentia (in the Columbia reconstruction of Bispo-Santos et al. (2014b)) may be interpreted as either: (i) dextral strike-slip movements occurred between Central – Brazil shield and Guiana shield, after 1420 Ma (Bispo-Santos et al., 2014b); (ii) counterclockwise rotation of Amazonia/West Africa occurred at some time between 1780 and 1440 Ma inside Columbia (D'Agrella-Filho et al., 2016a, b); or (iii) Amazonia/West Africa did not take part of Columbia (Pisarevsky et al. (2014). The last two alternatives assume that the Colíder pole did not represent a primary magnetization.

2.3 Paleomagnetic problem and birth of this study

Despite the accumulation of new paleomagnetic data obtained for the Amazonian craton during the Paleo – Mesoproterozoic, it is yet difficult to define an apparent polar wander path for this craton for more recent periods than 1960 Ma (Surumu pole). Figure 2.2 shows possible scenarios for the Amazonian craton's APWP according to the use of the Avanavero pole (trajectory 1), Colíder pole (trajectory 2), or yet using their anti-poles which define, respectively, the trajectories 3 and 4. The great age difference between the 1960 Ma Surumu pole and the 1790 Ma Avanavero and Colíder poles shows clearly the need of new poles for this interval. In addition, there is yet a large uncertainty in the position of the Amazonian craton at *ca*. 1790 Ma. Indeed, as discussed above, there were two different poles of the same age, the Colíder pole (Bispo-Santos et al., 2008) and the Avanavero pole (Bispo-Santos et al., 2014b) that involve distinct configurations within the Columbia supercontinent (Figure 5 of the attached paper). Therefore, we need new key poles for the Amazonian craton, particularly between 1960 (Surumu) and 1790 Ma (Avanavero, Colíder) to constrain the position of the craton and establish its APWP. It may be noted that there is no paleomagnetic pole at 1880 Ma for the North China Craton (NCC) to test a possible connection with the Amazonian craton as suggested by Bispo-Santos et al. (2008).

In addition, numerous workers have recognized large APW movements and high continental velocities between 2000 – 1850 Ma (The Coronation and Nagssugtoqidian Loops) (Mitchell et al., 2010; Piper, 2013a). Such rapid APW movements have been attributed to possible (oscillatory) true polar wander (TPW) event where the Earth's silicate outer shell is moving over its liquid core to align the new I_{max} (maximum principal inertia axis) with the Earth's spin axis (Gold, 1955).

Fortunately, a magmatic intracontinental event with A-type granites, rhyolites, ignimbrites occurred in the Amazonian craton during the formation of the Columbia supercontinent (Dall'Agnol et al., 2005). This magmatism is also observed on a global scale in most continents (Vigneresse, 2005). In the Amazonian craton, this event was initially called **Uatumã** and covers a wide area, from the Roraima State, through the Pará State and to the north of the Mato Grosso State, with ages ranging at *ca*. 1880 – 1870 Ma. To study this event is very important because we have just poor-quality paleomagnetic data (Q= 2) for the A-type granites in the Carajás domain (Seringa and Carajás granites) without enough number of samples, without geochronological data, and without field tests (Renne et al., 1988). Thus, this work intends to study the 1880 Ma units situated in the Pará State to get a new key pole for the Amazonian craton trying to solve these paleomagnetic problems and test a potential TPW event during the amalgamation of the Columbia supercontinent.

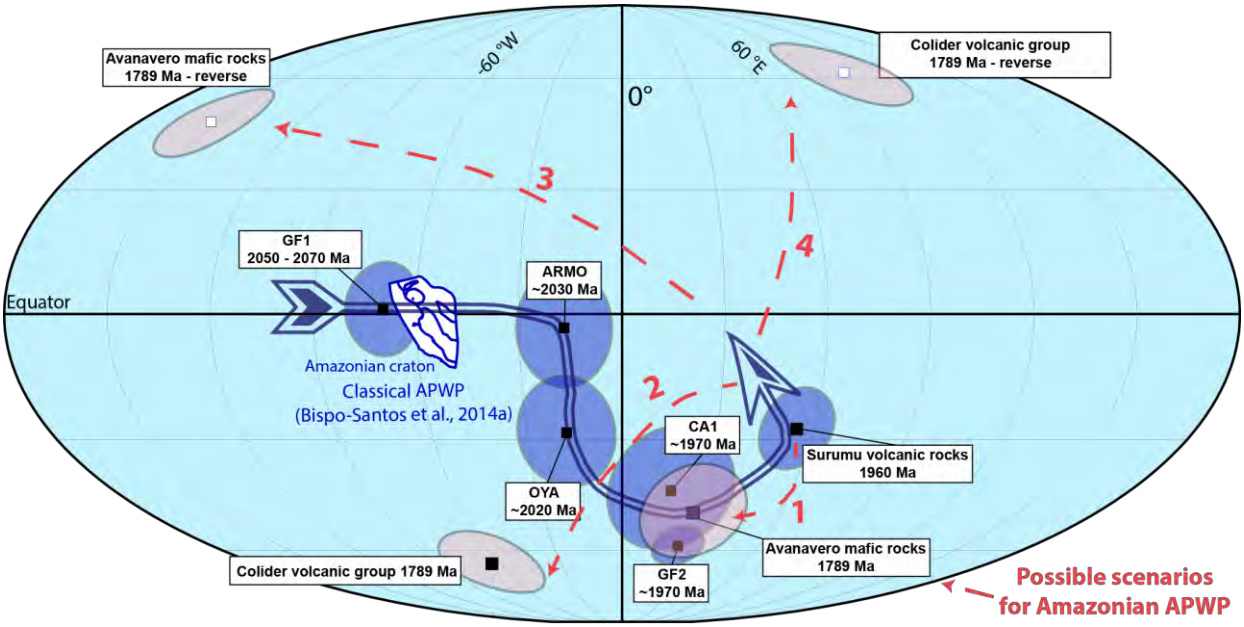

Figure 2.2: Apparent polar wander path for the Amazon craton between 2050 and 1960 Ma after Bispo-Santos et al. (2014a). Position for the Colíder and Avanavero poles at *ca*.1790 Ma. Supposed position for a paleomagnetic pole at *ca*.1880 Ma, see text for more information (in red).

2.4 Paper "Amazonian Craton paleomagnetism and paleocontinents" (co-author)

DOI: 10.1590/2317-4889201620160055

INVITED REVIEW

Paleomagnetism of the Amazonian Craton and its role in paleocontinents

Paleomagnetismo do Cráton Amazônico e sua participação em paleocontinentes

Manoel Souza D'Agrella-Filho[1]*, Franklin Bispo-Santos[1], Ricardo Ivan Ferreira Trindade[1] , Paul Yves Jean Antonio[1,2]

ABSTRACT: In the last decade, the participation of the Amazonian Craton on Precambrian supercontinents has been clarified thanks to a wealth of new paleomagnetic data. Paleo to Mesoproterozoic paleomagnetic data favored that the Amazonian Craton joined the Columbia supercontinent at 1780 Ma ago, in a scenario that resembled the South AMerica and BAltica (SAMBA) configuration. Then, the mismatch of paleomagnetic poles within the Craton implied that either dextral transcurrent movements occurred between Guiana and Brazil-Central Shield after 1400 Ma or internal rotation movements of the Amazonia-West African block took place between 1780 and 1400 Ma. The presently available late-Mesoproterozoic paleomagnetic data are compatible with two different scenarios for the Amazonian Craton in the Rodinia supercontinent. The first one involves an oblique collision of the Amazonian Craton with Laurentia at 1200 Ma ago, starting at the present-day Texas location, followed by transcurrent movements, until the final collision of the Amazonian Craton with Baltica at ca. 1000 Ma. The second one requires drifting of the Amazonian Craton and Baltica away from the other components of Columbia after 1260 Ma, followed by clockwise rotation and collision of these blocks with Laurentia along Grenvillian Belt at 1000 Ma. Finally, although the time Amazonian Craton collided with the Central African block is yet very disputed, the few late Neoproterozoic/Cambrian paleomagnetic poles available for the Amazonian Craton, Laurentia and other West Gondwana blocks suggest that the Clymene Ocean separating these blocks has only closed at late Ediacaran to Cambrian times, after the Amazonian Craton rifted apart from Laurentia at ca. 570 Ma.

KEYWORDS: Amazonian Craton; paleomagnetism; supercontinents; Columbia; Rodinia; Gondwana.

RESUMO: *Dados paleomagnéticos obtidos para o Cráton Amazônico nos últimos anos têm contribuído significativamente para elucidar a participação desta unidade cratônica na paleogeografia dos supercontinentes pré-cambrianos. Dados paleomagnéticos do Paleo-Mesoproterozoico favoreceram a inserção do Cráton Amazônico no supercontinente Columbia há 1780 Ma, em um cenário que se assemelhava à configuração "South AMerica and BAltica" (SAMBA). Estes mesmos dados também sugerem a ocorrência de movimentos transcorrentes dextrais entre os Escudos das Guianas e do Brasil-Central após 1400 Ma, ou que movimentos de rotação do bloco Amazônia-Oeste África ocorreram dentro do Columbia entre 1780 e 1400 Ma. Os dados paleomagnéticos atualmente disponíveis do final do Mesoproterozoico são compatíveis com dois cenários diferentes para a Amazônia no supercontinente Rodínia. O primeiro cenário envolve uma colisão oblíqua da Amazônia com a Laurentia, começando no Texas há 1200 Ma, seguida por movimentos transcorrentes até o final da colisão da Amazônia com a Báltica há 1000 Ma. No segundo cenário, a ruptura da Amazônia e da Báltica do Columbia ocorre após 1260 Ma e é seguida por uma rotação horária e pela colisão desses blocos com a Laurentia ao longo do cinturão Grenville há 1000 Ma. Finalmente, a época em que a Amazônia colidiu com a parte central do Gondwana tem sido objeto de muita disputa. Todavia, os poucos polos paleomagnéticos do final do Neoproterozoico/Cambriano para o Cráton Amazônico, para a Laurentia e outros blocos do Gondwana Ocidental sugerem que o Oceano Clymene que separou estes blocos ocorreu entre o final dos períodos Ediacarano e Cambriano, após a separação do Cráton Amazônico da Laurentia há 570 Ma.*

PALAVRAS-CHAVE: *Cráton Amazônico; paleomagnetismo; supercontinentes; Columbia; Rodínia; Gondwana.*

[1]Departamento de Geofísica, Instituto de Astronomia, Geofísica e Ciências Atmosféricas, Universidade de São Paulo (USP). E-mails: *dagrella@iag.usp.br, frankb@iag.usp.br, rtrindad@iag.usp.br*

[2]Géosciences Environnement Toulouse (GET), Université de Toulouse, Observatoire Midi-Pyrénées, Toulouse, France. E-mail: *paul@iag.usp.br*

*Corresponding author.

Manuscript ID: 20160055. **Received in:** 04/15/2016. **Approved in:** 05/05/2016.

INTRODUCTION

The paleogeography of continental blocks is the key piece of information to understand the geological evolution of our planet and the mechanisms that prevailed in the assembly and rupture of supercontinents, a process known as supercontinental cycle (Condie 2002). Based on the Pangea assembly, Meert (2012) defined that a supercontinent must comprise at least 75% of the existing continental crust. Based on this definition, the continental masses were united in supercontinents at least three times in Earth's history: 200 Ma (Pangea), 1100-1000 Ma (Rodinia), and 1850-1800 Ma (Columbia/NUNA). Note that large continental masses such as Gondwana and Laurasia did not comprise 75% of the continental surface, and therefore cannot be regarded supercontinents according to Meert's definition. The ages of assembly for the three supercontinents imply a periodicity of approximately 750 Ma for the supercontinent cycle (Meert 2012).

If we consider the peaks in U-Pb zircon ages, integrated with Nd isotopic ratios obtained for rocks all over the globe, we can assume the existence of a fourth supercontinent at ca. 2700 Ma (Hawkesworth *et al.* 2010). However, the reconstruction of such Archean supercontinent is a challenge given the scarcity of paleomagnetically viable targets of that age (Evans 2013). Some attempts to correlate Archean units based on geological and paleomagnetic data have been published, such as the formation of Zingarn supercraton made by the link of Zimbabwe/Rhodesia (Africa) and Yilgarn (Australia) blocks (Smirnov *et al.* 2013), or the Vaalbara supercraton formed by Kaapvaal (Africa) and Pilbara (Australia) blocks (de Kock *et al.* 2009). However, the lack of the main paleomagnetic poles for the Archean nuclei make paleogeographic reconstructions for those times very speculative (Buchan *et al.* 2000, Pesonen *et al.* 2003).

Several paleogeographic reconstructions of a Paleoproterozoic supercontinent (1850-1800 Ma) have been proposed in literature (e.g. Rogers 1996, Rogers & Santosh 2002, Zhao *et al.* 2002, 2003, 2004, 2006, Meert 2002, Pesonen *et al.* 2003, Hou *et al.* 2008a, 2008b, Johansson 2009, 2014, Yakubchuck 2010, Piper 2010, Evans & Mitchell 2011, Zhang *et al.* 2012, among others). This supercontinent has received different names: NENA (Gower *et al.* 1990), NUNA (Hoffman 1997), Columbia (Rogers & Santosh 2002), or Paleopangea (Piper 2010). Reddy & Evans (2009) advocate the name NUNA because it is older than the name Columbia. However, Meert (2012) argues that the NUNA paleocontinent defined by Hoffman (1997) differs little from the NENA proposed by Gower *et al.* (1990). Therefore, if precedence should be considered, this Mesoproterozoic supercontinent should be named NENA. In addition, NENA and NUNA originally refer to correlations between Laurentia, Baltica, Siberia, and eventually East Antarctica, so these reconstructions represent only a fraction of the Paleoproterozoic supercontinent. In this way, Meert (2012) states that the name Columbia proposed by Rogers & Santosh (2002) designates the first attempt of a global and testable reconstruction. After Meert's (2012) reasonings, we will call hereafter the Paleoproterozoic supercontinent as Columbia.

The rupture time of Columbia is a subject of intense discussion in literature. Some authors suggest that Columbia broke-up soon after its formation, as evidenced by the significant amount of mafic dykes dated around 1780-1790 Ma found in North China Craton (Kusky *et al.* 2007), Baltica (Pisarevsky & Bylund 2010), and Amazonian Craton (Reis *et al.* 2013). Nevertheless, such global tectonic and magmatic features are usually associated with Statherian taphrogenesis at different cratons, and so they would not represent a complete rupture of the supercontinent (Brito Neves *et al.* 1995). Indeed, paleomagnetic and geochronological data obtained for Baltica and Laurentia, which formed the Columbia core (e.g. Zhao *et al.* 2002), suggest they remained joined from 1800 Ma until at least 1270 Ma (Salminen & Pesonen 2007). A long-lived Columbia is consistent with the unusual tectonic style that prevailed in the Mesoproterozoic, marked by a strong decrease in the subduction flow and subduction related magmatism (Silver & Behn 2008). This is also coherent with the intense intracratonic magmatic activity that is characterized by the emplacement of a voluminous anorogenic rapakivi granitic magmatism, between 1600 and 1300 Ma, which is one of the most striking features of the continental blocks forming Columbia (e.g. Åhäll & Connelly 1998, Anderson & Morrison 1992, Bettencourt *et al.* 1999, Hoffman 1989, Karlstrom *et al.* 2001, Rämö *et al.* 2003, Vigneresse 2005).

Piper (2010) proposes that the demise of Columbia occurred through a series of small intracratonic rotations that are consistent with U-Pb ages (and Nd model ages), obtained for rocks between 1200 and 1000 Ma. Such period is characterized by a small peak in the formation of juvenile crust, when compared with periods related to the formation of other supercontinents (Hawkesworth *et al.* 2010). Recently, Pisarevsky *et al.* (2014) suggested that the Columbia supercontinent began its agglutination at ~1700 Ma, reaching its maximum area between 1650-1580 Ma. They also argued that Columbia broke-up in two stages. The first one occurred between 1450 and 1380 Ma and the second at ca. 1270 Ma. In contrast, Zhao *et al.* (2004) and Rogers & Santosh (2009) postulated that Columbia's break-up occurred almost synchronously at ca. 1500 Ma.

Almost all continental masses involved in Columbia, later assembled to form the Rodinia supercontinent at about

1100 – 1000 Ma ago (McMenamin & McMenamin 1990). Several paleogeographic reconstructions have been proposed for the Neoproterozoic supercontinent (e.g. Hoffman 1991, Weil *et al.* 1998, D'Agrella-Filho *et al.* 1998, Dalziel *et al.* 2000, Tohver *et al.* 2002, 2006, Pisarevsky *et al.* 2003, Meert & Torsvik 2003, Li *et al.* 2008). Li *et al.* (2008) rebuilt Rodinia including all cratonic areas of the world. However, geological evidence show that some continental blocks that formed the West Gondwana (e.g. Congo-São Francisco, Kalahari) did not take part in Rodinia, since a large ocean existed between these units and the Amazonian Craton (Cordani *et al.* 2003, Kröner & Cordani 2003, D'Agrella-Filho *et al.* 2004, and references therein). After Rodinia break-up, their continental fragments gathered in other configurations (e.g. Gondwana), but the details of this process, including the timing and reassembly configuration of the different blocks, are still a subject of debate in literature, mainly due to the almost total absence of key paleomagnetic poles between 900 and 600 Ma for the units that potentially composed these landmasses.

The Amazonian Craton, in the Northwest of South America, surely played a fundamental role in the Earth's geodynamic history and in the paleogeography of Columbia, Rodinia, and Gondwana. In recent years, a wealth of new paleomagnetic data was obtained for this unit with important implications on the formation and rupture of Columbia and Rodinia supercontinents, and on the agglutination of Gondwana. In Table 1, we list all poles between 2100 and 530 Ma available for the Amazonian Craton and corresponding references.

In this paper, we will discuss the recent paleomagnetic and geological evidence for the participation of the Amazonian Craton in different Proterozoic supercontinents. Firstly, we will introduce the reasoning behind paleogeographic reconstructions based on paleomagnetic data. Then, we will present a brief description of the geologic/tectonic compartments of the Amazonian Craton. The following topics discuss the recent paleomagnetic data and their implications for the participation of the Amazonian Craton in pre-Columbia times, in Columbia supercontinent, in Rodinia supercontinent, and in the Gondwana continent. Finally, the most important conclusions regarding the geodynamic evolution of the Amazonian Craton during the Proterozoic will be shown.

PALEOMAGNETIC RECONSTRUCTION OF PALEOCONTINENTS

The Pangea was the first supercontinent to be reconstructed on the basis of the fitting of geological provinces, continent shorelines, paleoclimatic indicators, and the continuity of the paleontological record throughout the ancient continental assembly (Wegener 1912). With the advent of isotope geochemistry, radiometric chronology and geophysics, other approaches were incorporated into the exercises of paleocontinent reconstructions, particularly the pre-Pangea supercontinents (Evans 2013), including the age and continuity of large igneous provinces and paleomagnetic data. From these, the only technique that provides a quantitatve assessment of the past distribution of the continents is paleomagnetism (e.g. Butler 1992).

Paleomagnetic poles are equated to the Earth's spinning poles and therefore provide a geographical reference frame for reconstructions. The paleomagnetic method is based on two premises:

1. the Earth's magnetic field when averaged over 10^4 to 10^5 years is equivalent to that of a dipole centered in the planet, and aligned along its rotation axis;
2. magnetic minerals record and preserve the orientation of the ancient field over geological time scales.

The first premise is also known as the geocentric axial dipole (GAD) hypothesis, and seems to hold for recent and ancient times (Meert 2009, Swanson-Hysell *et al.* 2009). The field sampling must then comprise sites distributed within at least tens to hundreds of thousand years. This is the reason why several dykes or sedimentary strata must be sampled to determine a single paleomagnetic pole.

For ensuring that a paleomagnetic pole calculated for a given geological formation fits the GAD assumption, we must comply with minimum statistical standards (e.g. number of samples larger than 24; confidence circle around the pole smaller than 16°; van der Voo 1990). In addition, paleomagnetic directions for a given target must preferentially include normal and reversed directions, thus proving that enough time has elapsed during the eruption, intrusion or deposition of the studied geological unit. The second premise of paleomagnetism assumes that the orientation of the geomagnetic field, when the rock unit was formed, is preserved until today in its magnetic remanence vector. However, we know that different geological processes, such as metamorphism or diagenesis, can change the original magnetization by re-heating original magnetic grains or creating new ones (van der Voo & Torsvik 2012). Usually, this change overprints the original magnetization only partially and a single sample may therefore record two or more remanence vectors.

Classically, we apply the stepwise demagnetization techniques to deconvolve the different components of the natural remanence vector; the remanence unblocked in more stable magnetic grains is usually interpreted as the primary one (As & Zijderveld 1958). In order to attest to the primary

Table 1. Paleomagnetic poles from the Amazonian Craton between 2100 and 530 Ma.

Rock unit	Plat (°N)	Plong (°E)	d_p/d_m (A_{95}) (°)	Age ± error (Ma)	Q	Ref.
The proto-Amazonian Craton before Columbia						
a) Tumuc Humac Mount. Granite	18.9	273.7	19.2/22.3	2100 ± 1 U-Pb zrn	3	1, 2
b) Tampok River Granite	-6.9	300.1	15.9/16.1	2155 ± 3 U-Pb zrn	3	1, 3
c) Mataroni River Granite	14.9	289.2	40.6/42.7	2115 ± 3 U-Pb zrn	3	1, 2
d) Approuague River Granite	4.5	298.9	19.1/19.2	2093 ± 3 U-Pb zrn	3	1, 2
e) Approuague River Granite	-5.9	296.9	34.3/35.1	2100–2050	3	1
f) Approuague River Granodiorite	-18.5	294.3	21.3/23.0	2089 ± 4 U-Pb zrn	3	1, 3
g) Approuague River Granite	5.3	293.4	16.8/17.2	2050–2070	3	1
Mean (a–g) - GF1 pole	1.8	292.5	(11.2)	2050-2070	3	4
h) Oyapok granitoids – OYA pole	-28.0	346.0	(13.8)	2036 ± 14 Ar-Ar amp	5	1, 5
i) Armontabo River Granite – ARMO pole	-2.7	346,3	(14.2)	2080 ± 4 U-Pb zrn	4	1, 6
j) Imataca Complex – IM1 pole	-49.0	18.0	(18.0)	1960–2050	3	7
k) Imataca Complex – IM2 pole	-29.0	21.0	(18.0)	1960–2050	3	7
l) Encrucijada Pluton – EN1 pole	-55.0	8.0	(6.0)	1972 ± 4 Ar-Ar amp	3	8
m) Encrucijada Pluton – EN2 pole	-37.0	36.0	(18)	1972 ± 4 Ar-Ar amp	3	8
Mean (h-m) - CA1 pole	43.2	21.9	(16,5)	~1970	3	9
n) Costal Late Granite – PESA pole	-56.7	25.1	6.2/12.4	2060 ± 4 U-Pb zrn	3	1, 3
o) Costal Late Granite – ROCO pole	-58.0	26.4	7.9/15.8	2095 ± 6 U-Pb zrn	3	1, 3
p) Costal Late Granite – MATI pole	-58.6	25,5	9.7/19.4	~2050-1970	3	1
q) Costal Late Granite – ORGA pole	-59.7	44.7	10.1/19.5	2069 ± 4 U-Pb zrn	3	1, 3
Mean (n-q) - GF2 pole	-58.5	30.2	(5.8)	~2050-1970	3	4
Roraima Uairen Fm. – U2 pole	-66.5	9.0	(17.8)	1920-1830	2	10, 11
Surumu Group volcanics - SG pole	-27.4	54.8	(9.8)	1966 ± 9 U-Pb zrn	5	9, 12, 13
The Amazonian Craton in the Columbia supercontinent						
Roraima Uairen Fm. - U1 pole	-69.0	17.0	(7.2)	1838 ± 14 U-Pb fl	4	10, 11
Aro-Guaniamo dike (group II)	-42.0	0.0	(6.0)	1820 mean Ar-Ar bi	4	8
Colider Group (rhyolites) – CG pole	-63.3	298.8	(10.2)	1789 ± 7 U-Pb zrn	4	14
Avanavero Sills – AV pole	-48.4	27.9	(9.6)	1788.5 ± 2.5 U-Pb badd	5	15, 16
Basic dykes (group I)	59.0	222.0	(6.0)	1800-1500	4	8
Kabaledo dykes	44.0	210.0	(14.3)	1800-1500	2	17
La Escalera basic dykes (group 1)	55.5	225.5	(11.2)	1800-1500	4	8
Parguaza G3N	10.7	294.7	(25.0)	1545-1393	1	18, 19, 20
Parguaza rapakivi batholith G1R	54.4	173.7	(9.6)	1545-1392	1	18, 19, 20
Mean Mucajai/Parguaza complex	31.7	186.6	(22.8)	~1530	2	21

Continue...

Tabela 1. Continuation.

Rock unit	Plat (°N)	Plong (°E)	d_p/d_m (A_{95}) (°)	Age ± error (Ma)	Q	Ref.
Guadalupe Gabbro (Component A)	38.9	306.2	(13.7)	1531 ± 16 U-Pb zrn	4	22
Roraima dolerites, younger component	63.0	231.0	(8.8)	1468 ± 3 Ar-Ar pl	2	8
Rio Branco sedimentary rocks – A1 pole	-45.5	270.0	(6.5)	1440-1544 U-Pb	4	23, 24
Salto do Céu sills – A2 pole	-56.0	278.5	(7.9)	1439 ± 4 U-Pb badd; 981 ± 2 Ar-Ar wr	5	23, 25, 26
Nova Guarita dykes – A3 pole	-47.9	245.9	(7.0)	1418.5 ± 3.5 Ar-Ar bi	6	27
Indiavai dykes – A4 pole	-57.0	249.7	(8.6)	1415.9 ± 6.9 U-Pb zrn	4	28, 29
Nova Lacerda mafic dykes	-0.5	310.7	(17.9)	1380 ± 32 Rb-Sr	2	30, 31
The Amazonian Craton: Rodinia's prodigal son						
Nova Floresta formation – NF pole	24.6	164.6	(6.2)	1198 ± 3 Ar-Ar bi	5	32
Fortuna formation – FT pole	59.8	155.9	(9.5)	1149 ± 7 U-Pb x	5	33
The Amazonian Craton in Gondwana						
Puga Cap carbonate – A pole	-82.6	292.6	(7.2)	627 ± 30 Pb-Pb wr	4	34
Puga Cap carbonate – B pole	33.6	326.9	(8.4)	530-520*	2	34

Plat: Paleolatitude; Plong: Paleolongitude; d_p/d_m (A_{95}) (in degrees): Fisher's statistical parameters. Geochronological symbols – zrn: zircon; badd: baddeleyite; bi: biotite; pl: plagioclase; fl: fluorapatite; x: xenotime; amp: amphibole; wr: whole rock; Q: quality factor (van der Voo 1990); *: inferred from the Gondwana apparent polar wander path. References of the table: 1 – Théveniaut *et al.* (2006); 2 – Vanderhaeghe *et al.* (1998); 3 – Delor *et al.* (2003); 4 – D'Agrella-Filho *et al.* (2011); 5 – Nomade *et al.* (2001); 6 – Enjolvy (2004); 7 – Onstott & Hargraves (1981); 8 – Onstott *et al.* (1984a); 9 – Bispo-Santos *et al.* (2014a); 10 – Castillo & Costanzo-Alvarez (1993); 11 – Beyer *et al.* (2015); 12 – Fraga & Dreher (2010); 13 – Schobbenhaus *et al.* (1994); 14 – Bispo-Santos *et al.* (2008); 15 – Bispo-Santos *et al.* (2014b); 16 – Reis *et al.* (2013); 17 – Veldkamp *et al.* (1971); 18 – Valdespino & Costanzo-Alvarez (1997); 19 – Gaudette *et al.* (1978); 20 – Bonilla-Pérez *et al.* (2013); 21 – Veikkolainen *et al.* (2011); 22 – Bispo-Santos (2012); 23 – D'Agrella-Filho *et al.* (2016); 24 – Geraldes *et al.* (2014); 25 – Teixeira *et al.* (2016); 26 – Elming *et al.* (2009); 27 – Bispo-Santos *et al.* (2012); 28 – D'Agrella-Filho *et al.* (2012); 29 – Teixeira *et al.* (2011); 30 – Tamura *et al.* (2013); 31 – Girardi *et al.* (2012); 32 – Tohver *et al.* (2002); 33 – D'Agrella-Filho *et al.* (2008); 34 – Trindade *et al.* (2003).

nature of a remanence direction, we use paleomagnetic stability tests, such as the baked contact test, the fold test, and the conglomerate test (see details in Butler 1992). In addition, the direction must be different from the paleomagnetic directions obtained in younger geological units of the same region. van der Voo (1990) summarized the checks conceived to attest if the two basic assumptions of paleomagnetism were valid. Furthemore, van der Voo stablished that a reference paleomagnetic pole must have been obtained in a geological unit in structural continuity to the cratonic block and must have a precise dating (error within 4%).

With reference paleomagnetic poles in hand, one can define the ancient position of continents based on their Euler rotations. The Euler theorem implies that any displacement in the surface of a sphere is equivalent to a single rotation about a fixed axis. Thus, to drive any continental mass back to its ancient position, we just need a rotation pole and the rotation angle around it. In this way, the confirguration of a paleocontinent can be expressed as a series of rotation poles and angles and as such they can be tested with new paleomagnetic poles or through the other approaches cited before. Euler pole reconstructions of continent motions date back to the work of Bullard *et al.* (1965), but until recently several reconstructions are still performed by cutting and pasting continents on flat maps, thus distorting their contours and providing models that are sometimes unrealistic and not testable. Nowadays, several softwares enable to easily reconstruct the global geography in three-dimensions using rotation angles and poles (e.g. GPlates, Williams *et al.* 2012, GMap, Torsvik & Smethurst 1999).

The paleomagnetic approach to paleocontinent reconstructions has nevertheless some drawbacks: the most important is the ambiguity in polarity given the axial symmetry of the GAD model (Fig. 1). Because of that, a paleomagnetic pole allows one to assign a paleolatitude and a paleodeclination (rotation from present-day North) for a continent but not the hemisphere or longitude it belonged to in the past. Therefore, to deduce the paleolongitude and polarity of different continental masses in paleogeographic reconstructions, one must use additional information other than paleomagnetism. In the further discussion, we attempted to complement the paleomagnetic information for the

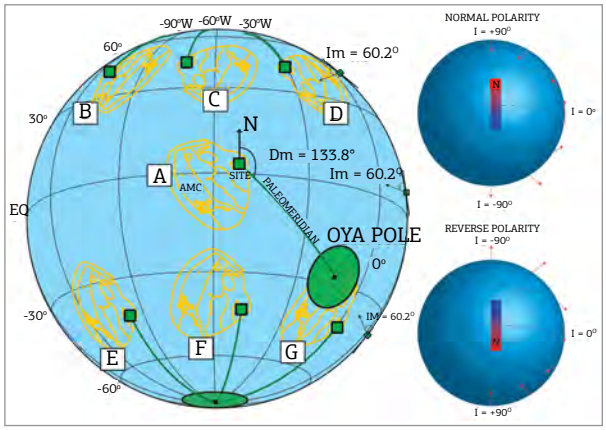

Figure 1. Amazonian craton (AMC) and geologic/geocronological provinces (yellow lines) reconstructed with the OYA pole. Amazonian craton is shown in its present position (A) with South American coastline. Also shown is the local geographic position of the Oyapok granites and their respective pole (with confidence circle) in green. Paleomeridian line passing through the sampling site and paleomagnetic pole is also shown. Positions B to G show that the continent can be moved freely along the same latitude for the two choices of polarity: Normal (B, C and D) or Reverse (E, F and G). D_m and I_m are, respectively, the mean declination and inclination of characteristic remanent magnetization direction calculated for the OYA rocks. "Normal polarity" and "reverse polarity" globes on the right show the configuration of inclination (I, red arrows) for each case.

Amazonia Craton and surrounding cratonic blocks with the most updated geological data available in the literature.

THE AMAZONIAN CRATON

The Amazonian Craton is one of the largest cratonic areas in the world, with about four million square kilometers (Fig. 2a). It is exposed in two major areas divided by the Phanerozoic Amazon Basin: the Guiana Shield to the North and the Brazil-Central Shield (also known as Guaporé Shield) to the South (Schobbenhaus *et al.* 1984, Santos *et al.* 2000, Lacerda-Filho *et al.* 2004). According to recent syntheses of Tassinari *et al.* (2000), Delor *et al.* (2003), Santos *et al.* (2003), and Cordani & Teixeira (2007), the evolution of the Amazonian Craton is marked by successive accretionary events with greater or lesser involvement of the juvenile crust occurred from the Paleoproterozoic to the Neoproterozoic.

Based on geochronological data, Tassinari & Macambira (1999, 2004) proposed an evolutionary model for the Amazonian Craton, which began when Hadean-Archean microcontinents assembled along Paleoproterozoic collisional orogens between 2200 Ma and 1950 Ma. This was followed by the development of a succession of magmatic arcs and collisional processes involving the reactivation and reworking of pre-existing rocks. Two models that subdivide

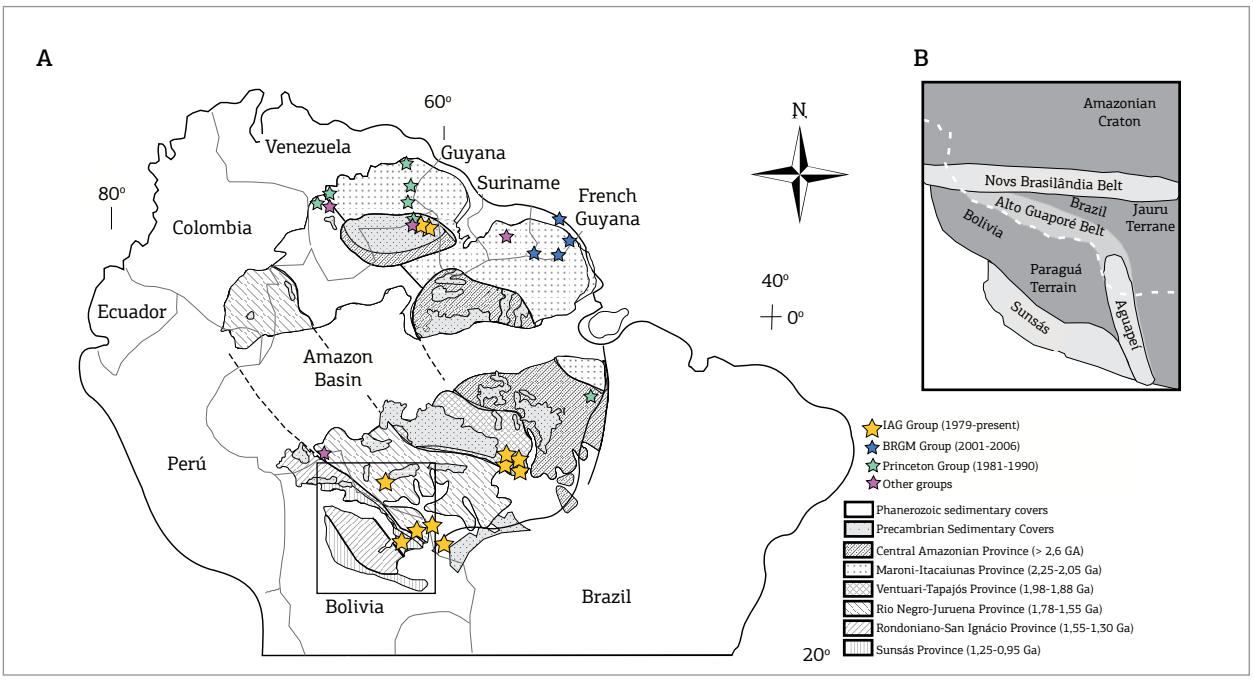

Figure 2. (A) Amazonian Craton and their geologic/geochronological provinces (adapted from Cordani & Teixeira 2007 and Bettencourt *et al.* 2010). The stars indicate approximate geographical locations of geological units studied by the following research groups: Princeton – blue; BRGM – green; IAG-USP – yellow; other groups – purple. (B) Sketch of the southwestern part of the Amazonian Craton showing Paraguá Terrain and Alto Guaporé, Sunsás, Aguapeí, and Nova Brasilândia belts (modified after D'Agrella-Filho *et al.* 2012).

the Amazonian Craton into geochronological provinces have been proposed, one by Tassinari & Macambira (1999, 2004) and the other by Santos *et al.* (2003). We followed the model of Tassinari & Macambira (1999, 2004) (Fig. 2A), which is adopted by several other authors (e.g. Schobbenhaus *et al.* 2004, Cordani & Teixeira 2007, Cordani *et al.* 2010, Bettencourt *et al.* 2010).

The oldest portion (Hadean-Archean) of the Amazonian Craton (Central Amazonian Province) consists of granite-greenstone terrains and high-grade metamorphic rocks exposed in the Brazil-Central and Guiana shields (Tassinari & Macambira 2004, Nadeau *et al.* 2013). The Maroni-Itacaiúnas Belt separates these landmasses, and it is dated around 2250-2050 Ma (Ledru *et al.* 1994). The Hadean-Archean basement is covered by volcano-sedimentary sequences with little or no deformation and ages ranging between 1980 and 1400 Ma. The southwestern part of the Hadean-Archean core was accreted by subduction-related juvenile magmatic arcs, which formed the Ventuari-Tapajós (1980-1810 Ma) and Rio Negro-Juruena (1780 – 1550 Ma) Provinces (Tassinari & Macambira 1999, Tassinari *et al.* 2000, Pinho *et al.* 2003, Schobbenhaus & Brito Neves 2003, Cordani & Teixeira 2007).

During the Mesoproterozoic, subduction-related magmatic arcs were developed between 1600 Ma and 1300 Ma (e.g. Jauru Terrain in Mato Grosso State), forming the Rondoniano-San-Ignacio Province until the final collision of Paraguá Terrain at about 1320 Ma ago (Bettencourt *et al.* 2010). This collisional model has been extended to the northwestern Rondônia State, with the recognition of the Trincheira ophiolite by Rizzotto & Hartmann (2012), who interpreted it as an oceanic crust fragment raised during the Mesoproterozoic as a consequence of the collision between the Paraguá Terrain and the proto-Amazonian Craton along the Alto Guaporé Belt (Fig. 2B). The E-W Nova Brasilândia Belt (NBB – 1100 – 1000 Ma old) at North of the Paraguá Terrain (Fig. 2b) most likely represents intracratonic reactivations that occurred during the development of Sunsás orogen (Sunsás Province – 1250 – 1000 Ma), which is located on the southwestern tip of the Amazonian Craton, in the Bolivian region (Litherland *et al.* 1989, Boger *et al.* 2005, Santos *et al.* 2008, Teixeira *et al.* 2010, Cordani *et al.* 2010). Some authors, however, interpret the NBB as a result of the collision between the proto-Amazonian Craton and the Paraguá Terrain, which would extend to Mato Grosso State, including the Jauru Terrain (Tohver *et al.* 2004a).

The Aguapei Belt (Fig. 2B) is considered a branch to the north of the Sunsas belt, separated from the main part of the orogeny by the Paraguá Terrain. This belt has been interpreted as an aborted continental rift, whose deposition initiated at ca. 1300 Ma, followed by compression and thrusting to the east at ca. 1000 Ma (Litherland *et al.* 1989, Sadowski & Bittencourt 1996).

THE PROTO-AMAZONIAN CRATON BEFORE COLUMBIA

The definition of a crustal paleogeography for the period prior to Columbia formation is yet very speculative, since many continental blocks were still being assembled during this period, including the Amazonian Craton, Laurentia, and Baltica. Well-dated paleomagnetic poles for the different fragments that later were assembled in these cratons are scarce, thus we can only speculate about the possible presence of Archean supercratons, as are the cases of Zingarn (Zimbabwe/Rhodesia/Yilgarn) and Vaalbara (Kaapvaal/Pilbara) supercratons proposed by Smirnov *et al.* (2013) and de Kock *et al.* (2009), respectively. In Amazonia, some authors advocate a relation between the Guiana Shield and the West Africa Craton forming a single, large cratonic block (supercraton) at about 2000 Ma ago (Onstott & Hargraves 1981, Nomade *et al.* 2003, Johansson 2009, Evans & Mitchell 2011).

Despite the general scarcity of Precambrian paleomagnetic data for the Amazonian Craton, the interval between 2100 and 1970 Ma is relatively well represented in the database as a result of studies carried out by two research groups at different times. These studies led to the construction of apparent polar wander paths (APW Paths) for the Amazonian Craton (Guiana Shield) and the West Africa Craton for Orosirian times. In the 1980s, the Princeton group (led by Tullis C. Onstott) conducted a series of paleomagnetic and geochronological studies on intrusive rocks from Guiana Shield (Venezuela and Guyana; see localizations of the studied geological units in Fig. 2 – green stars) and West Africa Craton (Onstott & Hargraves 1981, Onstott *et al.* 1984a, 1984b). Based on the available paleomagnetic data, these authors argued that Guiana Shield was an extension of West Africa Craton, however, it was displaced in relation to the Pangaea reconstruction in such way that the Guri lineament in Guiana Shield and Sassandra lineament in West Africa Craton were aligned (Onstott & Hargraves 1981).

In the beginning of the last decade, researchers from the *Bureau de Recherches Géologiques et Minières* (BRGM, in France) extended the studies of the Princeton group using granitic and metavolcanic rocks exposed in the French Guiana (see localizations of studied geological units in Fig. 2 – blue stars), and also from West Africa Craton (Nomade *et al.* 2001, 2003). APW Paths were constructed for West Africa Craton and Guiana Shield for the time interval 2100 – 1990 Ma (Nomade *et al.* 2003). Such authors showed that both

APW Paths overlap at about 2020 Ma, if the paleogeographic configuration suggested by Onstott & Hargraves (1981) was used. Subsequently, Théveniaut *et al.* (2006), also from the BRGM, presented a comprehensive paleomagnetic and geochronological study regarding plutonic and metamorphic rocks from Guiana Shield, in which they tried to accurately identify the age of magnetization acquisition of the studied rocks, based on several U-Pb and Ar-Ar datings of minerals with different closure temperatures. According to a new group of poles and the reinterpretation of previous paleomagnetic poles, Théveniaut *et al.* (2006) proposed a new APW Path for the Amazonian Craton (Guiana Shield), between 2155 and 1970 Ma. However, they did not discuss the paleogeography proposed by Onstott & Hargraves (1981), which was corroborated by Nomade *et al.* (2003).

Recently, new paleomagnetic data were obtained for felsic volcanic rocks from the Surumu Group (Guiana Shield), which is well dated at 1960-1980 Ma by the U-Pb method (Bispo-Santos *et al.* 2014a). A robust paleomagnetic pole (Tab. 1) was obtained for these rocks, which helps to better define the APW Path traced by Théveniaut *et al.* (2006) between 2070 and 1970 Ma for the Guiana Shield (Fig. 3). This APW Path began being defined by a series of paleopoles concentrated on northern South America, which Théveniaut *et al.* (2006) associated with the Orosirian deformation event (2070-2050 Ma) that affected the French Guiana. An average paleopole designated GF1 (Fig. 3, Tab. 1) was determined for this set of poles (D'Agrella-Filho *et al.* 2011). Eastward, the curve passes over the ARMO and OYA poles (Tab. 1) determined for granites collected over the Armontabo and Oyapok rivers, respectively, whose first letters provided the acronyms of their poles. The age of these poles was defined by dating different minerals (zircon, amphibole and biotite) representing distinct closure temperatures associated with their isotopic systems.

Théveniaut *et al.* (2006) interpret the 2020 ± 4 Ma Ar-Ar age (amphibole) obtained for an Oyapok River granite as the one that best agrees with the blocking temperature of the magnetic mineral (magnetite), which records the geomagnetic field at the time of formation of these rocks, which yielded the OYA pole. The youngest part of the curve is established by two sets of poles: the first corresponds to the poles determined for the Imataca Complex (IM1, IM2 – Tab. 1) and the La Encruzijada Granite (EN1, EN2 – Tab. 1), which are integrated into a single average paleopole called CA1 (Fig. 3, Tab. 1). The second set comprises four poles determined for granitic rocks of northern French Guiana (Théveiaut *et al.* 2006), whose average is represented by GF2 (Fig. 3, Tab. 1). An approximate age of 1970 Ma was suggested by Théveniaut *et al.* (2006) for this part of the curve, based on the 1972 ± 4 Ma age ($^{40}Ar/^{39}Ar$ in amphibole) obtained for the La Encruzijada granite (Onstott *et al.* 1984b). A similar age (ca. 1970 Ma) was also suggested based on the Imataca Complex thermal history, disclosed by hornblende, biotite, and feldspar Ar-Ar dating (Onstott *et al.* 1989).

Finally, the recent ~1960 Ma pole (SG in Tab. 1) determined for the acid volcanic rocks from the Surumu Group (Bispo-Santos *et al.* 2014a) may indicate an extension of the APW Path traced by Théveniaut *et al.* (2006) for the interval 2070-1970 Ma (Fig. 3). In Fig. 3, the APW Path traced by Nomade *et al.* (2003) for West Africa, referring

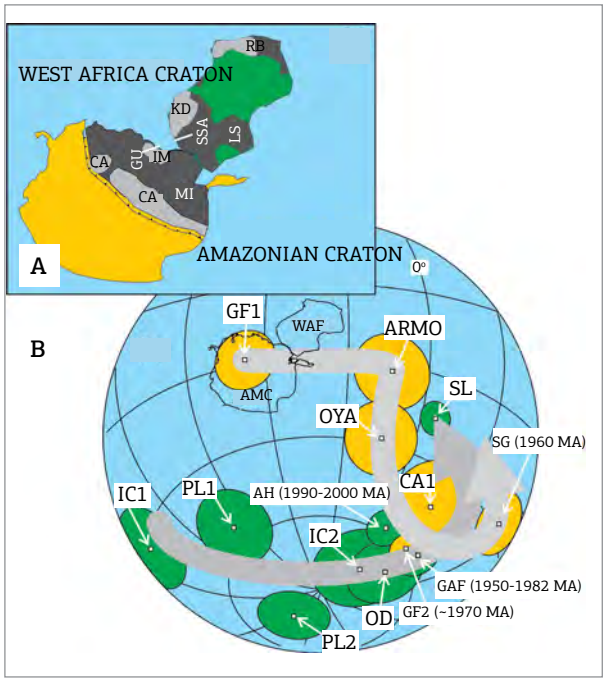

Figure 3. (A) Paleogeographic configuration of the Amazonian Craton and West Africa Craton link at around 2000-1970 Ma ago. Geotectonic provinces: Amazonia (CA – Central Amazonian Province, MI – Maroni-Itacaiúnas Province; GU – Guri lineament); West Africa (LS – Leo Shield, KD – Kenemanan Domain, RB – Requibat Shield, SSA – Sassandra lineament). (B) Comparison of the Amazonian and West African 2070-1960 Ma APW Paths. Pole Acronyms: AMC – Amazonian Craton (yellow); GF1, ARMO, OYA, GF2 and SG poles (Tab. 1); WAF – West Africa Craton (green); IC1 –Ivory Coast Granites (Nomade *et al.* 2003); PL1 – *Abouasi* Amphibolites (Piper & Lomax 1973); PL2 – *Abouasi* Dolerites (Piper & Lomax 1973); OD – Liberia Granites (Onsttot & Dorbor 1987); IC2 – *Ferke* Granites – *Ivory Coast* (Nomade *et al.* 2003); GAF – *Aftout* Granites (Nomade *et al.* 2003); AH – *Harper* Amphibolite – Liberia (Onsttot *et al.* 1984a); SL – *Aftout* Gabbros – Algeria (Nomade *et al.* 2003). West Africa Craton and their corresponding paleomagnetic poles were rotated using the Euler pole at 43.3°N; 330.5°E (rotation angle of -71.5°). Modified after Bispo-Santos *et al.* (2014a).

to the time interval 2080 – 1940 Ma, is also shown, after rotation of West Africa and corresponding paleomagnetic poles using an Euler pole located at 43.3°N; 330.5°E (rotation angle of -71.5°). The proto-Amazonian/West-African paleogeography (Fig. 3) is similar to that proposed by Onstott & Hargraves (1981), in which the Guri (Guiana Shield) and Sassandra (West Africa) shear zones were part of the same tectonic lineament. Despite the poor quality of the poles applied to trace the West Africa Craton's APW Path (Nomade *et al.* 2003), the two paths are clearly different for ages older than 2000 Ma, and seem to joint at younger ages (1980 – 1960 Ma), attesting the validity of the formation of this supercraton at about 1980-2000 Ma (Bispo-Santos *et al.* 2014a) (Fig. 3).

According to Bleeker (2003), during Archean to early Proterozoic transition, there would have been a favorable scenario to the presence of many independent 'supercratons'. Between 2500 and 2000 Ma, a diachronic fragmentation would have occurred in the larger supercratons generating around 35 independent cratons, which later on amalgamated into larger continental blocks (e.g. Laurentia) that ultimately formed the Columbia Paleo-Mesoproterozoic supercontinent (Bleeker 2003).

Based on the available paleomagnetic and geologic-geochronological data, we can attempt to reconstruct a proto-Amazonian Craton and its relation with other cratonic blocks at ca. 2000 Ma. In general, the paleomagnetic poles from the Amazonian Craton are compared with those from Laurentia and Baltica aiming supercontinental reconstructions. As already stressed, at times prior to Columbia formation, however, any reconstruction must be considered very speculative, since the major cratonic masses that would be assembled in Columbia were still not completely formed. For example, most of Laurentia was only assembled at ca. 1850 Ma, after the following collisions: Archean Slave and Rae blocks at 1970 Ma; the Slave/Rae and Hearne blocks at 1920 Ma; and this block with the Superior Craton at 1850 Ma (Mitchell *et al.* 2014). Following well-dated paleomagnetic poles from Slave and Superior cratons in the interval between 2200 Ma and 2000 Ma, Mitchell *et al.* (2014) demonstrate that these blocks were separated by a very large ocean (Manikewan Ocean) at ca. 2000 Ma (see Fig. 7 in Mitchell *et al.* 2014). In their reconstruction, the Slave block was rotated -79° around an Euler pole at 52°N, 356°E relative to the Superior block. Using this reconstruction, we propose a possible paleogeography at 2000 Ma (Fig. 4) that tentatively includes other two cratonic blocks of Laurentia (Rae and Hearne), and also parts of Baltica, Amazonia, and West Africa, partly based on paleomagnetic poles as further described. The relative paleogeographic positions of Slave and Superior cratons (Mitchell *et al.* 2014) are constrained using the 1998 Ma pole determined for the Minto dykes (pole at 30°N, 183°E, A_{95} = 13°) from the Superior Craton. The Rae and Hearne blocks were positioned between these cratonic blocks.

At that time, Central Amazonia had already been assembled with the collision of Archean blocks along the 2250-2050 Ma Maroni-Itacaiúnas mobile belt (MIMB, Cordani & Teixeira 2007). Since other Archean blocks collided with Central Amazonia along the MIMB during and after its assembly, it is very likely that the craton at such time was a larger landmass. Based mainly on geological/geochronological evidence, Johansson (2009) proposed the SAMBA model for Columbia, in which West Africa and Sarmatia/Volgo-Uralia may be the components of this larger cratonic block. As previously discussed, West Africa was linked to the Guiana Shield at least since 1970-2000 Ma in a position

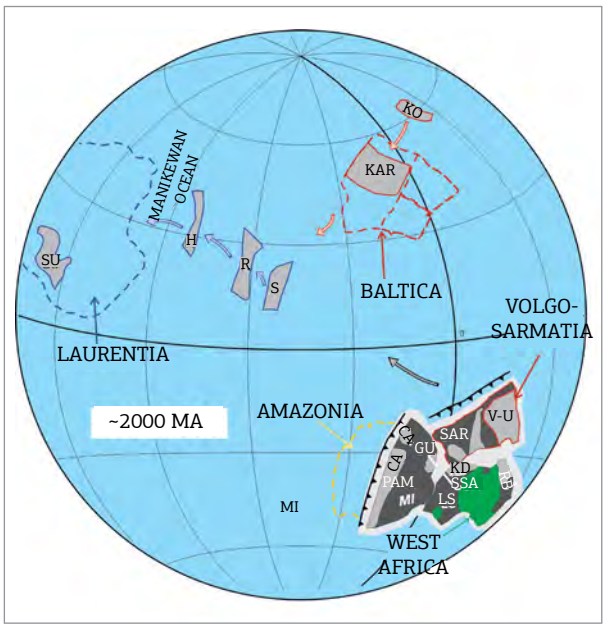

Figure 4. Reconstruction at 2000 Ma partially based on paleomagnetic data. Proto-Amazonia (pAM) was constrained using the OYA pole (Tab. 1). Superior Craton (Su) is constrained using the Minto dykes pole (Buchan *et al.* 1998, Evans & Halls 2010). Superior (Su) and Slave (S) relative positions are the same proposed by Mitchell *et al.* (2014) following paleomagnetic data. Karelia (Kar) is constrained by the 1984 Ma Pudozhgora intrusion pole (Lubnina *et al.* 2016), and Kola (Ko) Craton is tentatively positioned close to Karelia. In this scenario, it is suggested that proto-Amazonia, West Africa, Volgo-Uralia (V-U), and Sarmatia (SAR) formed a single cratonic mass. The curved arrows indicate the possible later drifts of each cratonic block. CA – Central Amazonian Province; MI – Maroni-Itacaiúnas Province; GU – Guri lineament; LS – Leo Shield; KD – Kenemanan Domain; RB – Requibat Shield; SSA – Sassandra lineament.

where the Guri (in Guiana Shield) and Sassandra (in West Africa) lineaments were aligned (Onstott & Hargraves 1981, Nomade *et al.* 2003, Bispo-Santos *et al.* 2014a).

At 2000 Ma ago, Baltica was not yet formed either (see Bogdanova *et al.* 2001, 2013). Collision between Sarmatia and Volgo-Uralia (from South and East of Baltica Shield, respectively) occurred between 2100 and 2000 Ma, forming the Volgo-Sarmatia block. Therefore, based on such arguments, we propose herein that a large landmass was already formed at 2000 Ma composed by Volgo-Uralia, Sarmatia, Central Amazonia, and West Africa agglutinated along Paleoproterozoic mobile belts developed up to 2000 Ma. The position of this landmass is constrained by the OYA pole (Tab. 1) obtained for the Oyapok granitoids with an Ar-Ar (amphibole) age of 2020 ± 4 Ma. At that time, active subduction zones were in progress at the Northern and Western margins of Volgo-Sarmatia and Central Amazonia, respectively (Fig. 4).

Karelia and Kola Archaean areas from north-northwestern part of the Baltica Shield were far from Volgo-Uralia and Sarmatia blocks at 2000 Ma (Bogdanova *et al.* 2013). In Fig. 4, the Karelia position was constrained by the 1984 Ma Pudozhgora Intrusion pole (Lubnina *et al.* 2016), and Kola Craton is tentatively positioned close to Karelia. According to Daly *et al.* (2006), after the formation of the Archean Kernoland supercontinent (Pesonen *et al.* 2003), a Wilson cycle was developed between Kola and Karelia after the break-up of this supercontinent at ca. 2500 Ma. This was followed by the formation of an ocean and its later closure, culminating with the docking of Kola and Karelia along the Lapland-Kola orogen at ca. 1900 Ma.

Between 1830 and 1800 Ma, an oblique collision took place between Volgo-Sarmatia with Fennoscandian terrains (Kola-Karelia) along the NW part of Sarmatia (Bogdanova *et al.* 2013). After this oblique collision, Volgo/Sarmatia (together with Central Amazonia and West Africa in our model) performed a counterclockwise rotation that activated older strike-slip faults (Bogdanova *et al.* 2013). These fault systems accommodated mafic dyke swarms with ages between 1790 and 1750 Ma in the Ukrainian Shield (northwestern Sarmatia). At the same time (1790-1780 Ma), profuse mafic intrusions occurred as dykes and sills at the Guiana Shield, spreading over Venezuela, French Guiana and northern Brazil (Reis *et al.* 2013, Bispo-Santos *et al.* 2014b). After Columbia formation at 1780 Ma (Bispo-Santos *et al.* 2014b), minor internal rotations happened associated with 1750 Ma mafic dykes at the Ukrainian Shield (Bogdanova *et al.* 2013).

THE AMAZONIAN CRATON IN THE COLUMBIA SUPERCONTINENT

According to Rogers & Santosh (2009), the Columbia supercontinent mostly assembled at about 1900-1850 Ma, as suggested by geologic correlations, age constraints, and other lines of evidence, like significant atmospheric changes (Bleeker 2003). However, different paleogeographic scenarios of Columbia were proposed, mainly due to scarcity of high-quality paleomagnetic poles (e.g. Meert 2002, Zhao *et al.* 2002, 2003, 2004, Pesonen *et al.* 2003, 2012, Hou *et al.* 2008a, 2008b, Johansson 2009, Rogers & Santosh 2009, Wingate *et al.* 2009, Yakubchuk 2010, Evans & Mitchell 2011, Zhang *et al.* 2012, Pisarevsky *et al.* 2014; among others).

In recent years, several Paleo-to Mesoproterozoic geological units from the Amazonian Craton were investigated to establish its role in the Columbia Supercontinent. The first paleomagnetic study was conducted on the 1780 Ma felsic volcanic rocks of the Colíder Suite (Bispo-Santos *et al.* 2008), now called Colíder Group, located in northern Mato Grosso State, Brazil-Central (or Guaporé) Shield (Lacerda Filho *et al.* 2004). Based on these results, the paleogeographic scenario visualized for Columbia at 1780 Ma has Laurentia, Baltica, North China and proto-Amazonia aligned in a north to south continental mass forming the core of Columbia Supercontinent (Bispo-Santos *et al.* 2008) (Fig. 5A). Geological evidence favor the hypothesis that proto-Amazonia and North China were laterally disposed at 1780 Ma ago. Subduction-related processes were developed in the western margin of the East Block of North China Craton and along the southwestern proto-Amazonian Craton. This process culminated with the docking of the West Block from North China Craton, along the Trans-North China Belt at ca. 1850 Ma ago, establishing the final configuration of North China Craton. Meanwhile, Ventuari-Tapajós accretion was in progress along the southwestern Amazonian Craton. Cordani *et al.* (2009) restated this interpretation again in a broad discussion on the evolution of the Amazonian Craton and its role in the formation of supercontinents.

Subsequently, paleomagnetic studies on rocks from the Nova Guarita mafic dyke swarm (Bispo-Santos *et al.* 2012) and Indiavaí Intrusive (D'Agrella-Filho *et al.* 2012), also located in Mato Grosso State (Brazil-Central Shield), corroborated the paleogeographic model proposed by Bispo-Santos *et al.* (2008). $^{40}Ar/^{39}Ar$ geochronological dating on biotite and plagioclase minerals separated from four Nova Guarita dykes yielded plateau ages between 1407 ± 8 Ma and 1430 ± 8 Ma. An

average of 1418 ± 3 Ma was calculated, which was interpreted as the intrusion age of the dykes (Bispo-Santos *et al.* 2012). A positive baked contact test obtained for one of the dykes that cut the Paleoproterozoic Matupá granite demonstrates the primary nature of the characteristic remanent magnetization (ChRM) isolated for these rocks (see Bispo-Santos *et al.* 2012). The Indiavaí Intrusive belongs to a set of mafic bodies collectively known as Figueira Branca Intrusive Suite (Bettencourt *et al.* 2010). U-Pb dating performed on zircons extracted from Indiavaí and Figueira Branca Intrusives provided ages of 1425 ± 8 Ma and 1415 ± 6 Ma, respectively, which were interpreted as the crystallization times of these bodies (Teixeira *et al.* 2011). Although a baked contact test performed for the Indiavaí Intrusive resulted inconclusive (D'Agrella-Filho *et al.* 2012), similar radiometric

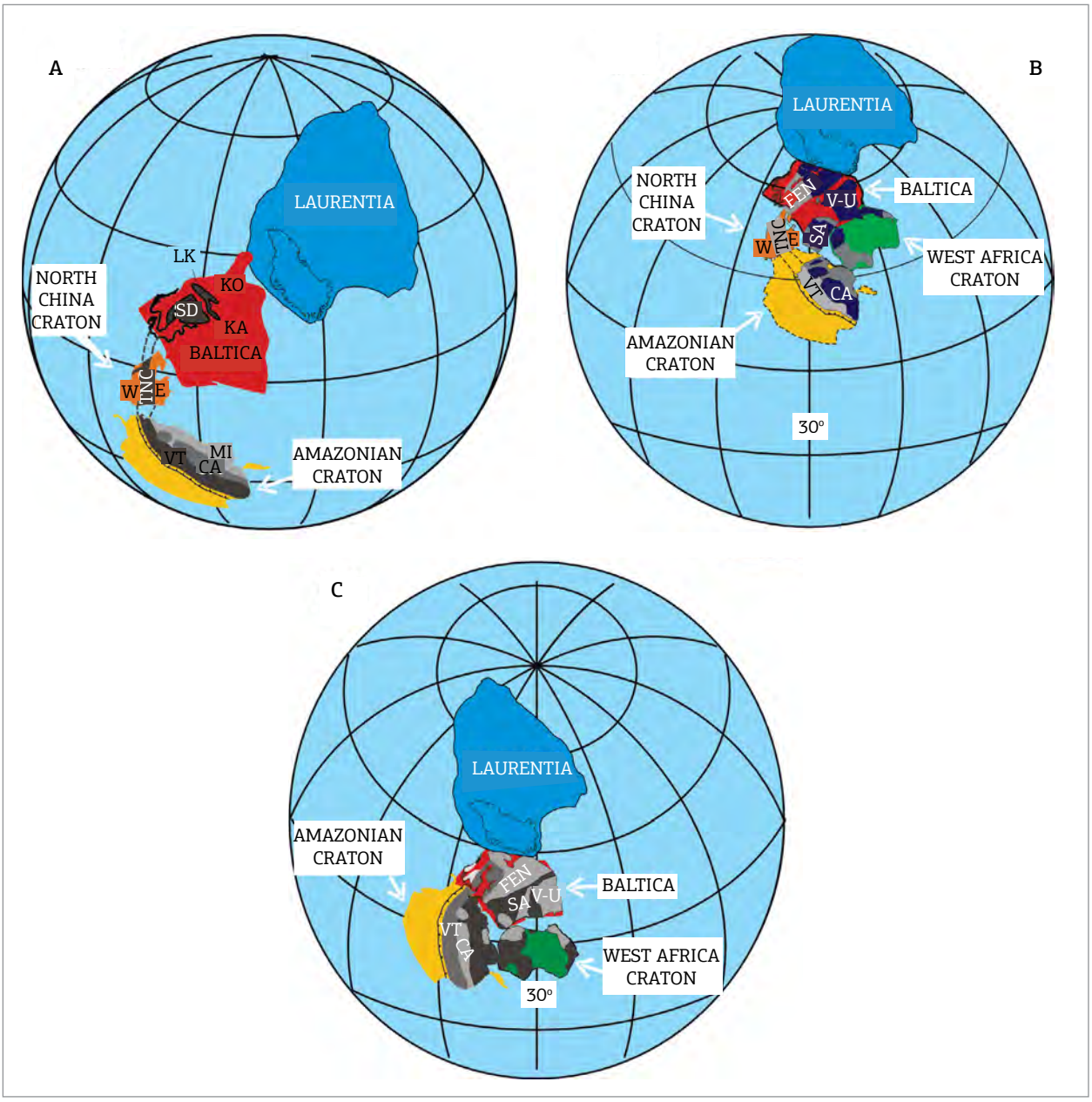

Figure 5. Paleogeographic reconstructions at ~1790 Ma as proposed by: (A) Bispo-Santos *et al.* (2008), (B) D'Agrella-Filho *et al.* (2012), and (C) Bispo-Santos *et al.* (2014b). Baltica (FEN – Fennoscandia; V-U – Volgo-Uralia; SA – Sarmatia; KO – Kola; KA – Karelia; LK – Lapland-Kola; SD – Svecofennian Domain); Amazonia (CA – Central Amazonian Province; MI – Maroni-Itacaiúnas Province; VT – Ventuari-Tapajós Province); and North China Craton (W –West Block; E – East Block; TNC –Trans-North China belt).

ages and ChRM directions obtained for Indiavaí and Nova Guarita rocks strongly suggest they both preserved thermoremanent magnetizations, acquired during rock intrusions at ca. 1415 – 1425 Ma.

These Mesoproterozoic poles (Tab. 1) have important implications regarding the significance of the Nova Brasilândia Belt (NBB – Fig. 2). Based on geophysical data and structural inferences, Tohver *et al.* (2004a) interpreted NBB as a suture zone between the Paraguá Terrain (which, in their view, would also include Mato Grosso area, to the south of NBB) and the proto-Amazonian Craton. This model follows primarily the strong contrast between the monocyclic history of NBB, composed by high pressure and temperature granulites (1090-1060 Ma), and the polycyclic history of the basement rocks to the north, with evidence of sinistral strike-slip deformation dated at 1190 – 1130 Ma (the Ji-Paraná shear zone). Other evidence presented by Tohver *et al.* (2004a) refer to the strong magnetic lineament disclosed by aeromagnetic data, which suggests the continuity of NBB to the east under Serra dos Parecis sedimentary cover. This interpretation, however, contrasts with that of other authors, who suggest that the NBB resulted from intracratonic reactivations during the evolution of Sunsás Belt situated on the southwestern tip of the Amazonian Craton (e.g. Cordani & Teixeira 2007). The similarity of Nova Guarita and Indiavaí poles obtained for geological units situated on opposite sides of NBB supports this latter interpretation (D'Agrella-Filho *et al.* 2012). Nevertheless, the position of these poles, almost perpendicular to NBB, permitted that transcurrent movements along this belt occurred, which might have originated the Ji-Paraná sinistral shear zone previously described.

With regard to the paleogeography of Columbia, the new paleomagnetic data disclosed for Colíder Group (1780 Ma), Nova Guarita dykes (1419 Ma), and Indiavaí Intrusive (1416 Ma) corroborate the model initially proposed by Bispo-Santos *et al.* (2008) (Fig. 5a). In such model, Laurentia, Baltica, North China Craton and proto-Amazonian Craton were laterally disposed, forming the core of Columbia Supercontinent (D'Agrella-Filho *et al.* 2012) (Fig. 5b). West Africa Craton can be included in the model assuming it was linked to the proto-Amazonian Craton (Onstott & Hargraves 1981, Nomade *et al.* 2003, Johansson 2009, Evans & Mitchell 2011, Bispo-Santos *et al.* 2014a). However, some adjustments should be done to accommodate geological information taking into account the uncertainties of the available paleomagnetic poles. Thus, in the Columbia Supercontinent proposed by D'Agrella-Filho *et al.* (2012), Sarmatia was rotated 43° counter-clockwise (Fig. 5b), as suggested by Elming *et al.* (2010), based on paleomagnetic and geological evidence. D'Agrella-Filho *et al.* (2012) also speculated on the presence of a triple junction between Fennoscandia, Sarmatia, North China, and Amazonia (see Fig. 13 in D'Agrella-Filho *et al.* 2012).

According to such model, soon after the formation of Columbia core, around 1850 Ma ago, dextral strike-slip movements occurred between North China and Fennoscandia and sinistral ones between North China and Amazonia/Sarmatia unit. Rupture of North China would be consistent with the profusion of 1780-1790 Ma mafic dykes and sills exposed in northern Brazil, Venezuela and Guyana, known as the Avanavero Large Igneous Province (LIP – Gibbs 1987, Santos *et al.* 2003, Reis *et al.* 2013), with the felsic and mafic dykes from Småland province in southwestern Baltica (Pisarevsky & Bylund 2010); the 1770-1780 Ma gabbros and dolerites belonging to the Ropruchey sills in eastern Fennoscandia (Fedotova *et al.* 1999); and the profusion of similar in age dykes spread over North China (Kusky *et al.* 2007).

Although Paleo to Mesoproterozoic paleomagnetic data of the southeastern Amazonian Craton (Brazil-Central Shield) support a model in which Laurentia, Baltica, North China Craton, and Amazonian/West Africa Cratons were laterally displayed, thus forming the core of Columbia Supercontinent (D'Agrella-Filho *et al.* 2012), in most Columbia models, the Amazonian Craton appears directly linked to Baltica, in a reconstruction called SAMBA connection formally proposed by Johansson (2009).

Recently, a paleomagnetic study was conducted on mafic sills and dykes belonging to the Avanavero LIP, located in northern Roraima State (Guiana Shield). These rocks are very well-dated by the U-Pb method (seven determinations on zircon and baddeleyite), whose 1788 ± 2 Ma mean age is interpreted as the rock crystallization age (Reis *et al.* 2013, Bispo-Santos *et al.* 2014b). A paleomagnetic pole graded with quality factor (Q) five (Tab. 1) was found for the Avanavero event. Studies of magnetic mineralogy, petrography and a positive baked contact test point out to a primary nature of ChRM directions isolated for these rocks (Bispo-Santos *et al.* 2014b).

The Avanavero pole agrees with coeval poles from Baltica and Laurentia, if SAMBA reconstruction is considered, based on geological and geochronological data (Bispo-Santos *et al.* 2014b) (Fig. 5C). Furthermore, we can envisage the agglutination of these masses, starting from the reconstruction at 2000 Ma ago in Fig. 4, in which the landmass formed by proto-Amazonia, West Africa and Volgo-Sarmatia obliquely collided with Fennoscandia, and other cratonic masses that formed Laurentia.

However, the Avanavero pole is very different from the Colider pole, and therefore does not support Columbia's models suggested by Bispo-Santos *et al.* (2008) (Fig. 5A),

based on the Colíder pole, and D'Agrella-Filho *et al.* (2012) (Fig. 5B), according to Paleo- to Mesoproterozoic poles. Two hypotheses could be raised to explain this difference:

1. although the rocks have similar ages, their magnetizations were acquired at different times;
2. their magnetizations were obtained during rock crystallization at 1780 to 1790 Ma, however, a relative movement occurred between the two areas after magnetization was acquired by rocks.

If we accept the first hypothesis, four facts lead us to assume that SAMBA model (Johansson 2009) should prevail over those proposed by Bispo-Santos *et al.* (2008) and D'Agrella-Filho *et al.* (2012). Therefore:

1. the Avanavero pole was obtained for anorogenic rocks emplaced in an intracratonic environment (Guiana Shield), whose Hadean-Archean to Paleoproterozoic basement was only partially affected in its southern part by the 1200 Ma K'Mudku event (Cordani *et al.* 2010);
2. the magnetic and petrographic evidence added to a positive baked contact test obtained for Avanavero rocks suggest that their ChRM directions most likely result from thermo-remanent magnetizations acquired during rock cooling at about 1789 Ma ago;
3. no stability tests were performed for the Colíder rocks; Colíder pole was obtained for 1780-1790 Ma felsic rocks from the southern part of Amazonian Craton, where NW-SE magmatic arcs were being formed along the Jauru Terrain up to the final collision of Paraguá Terrain at 1320 Ma (Bettencourt *et al.* 2010). This makes easier to assume that the Colíder pole represents a secondary magnetization;
4. the presently available 1530 Ma paleomagnetic data for Amazonia, Baltica and Laurentia are also consistent with the SAMBA model (Pesonen *et al.* 2012).

On the other hand, if both magnetic records represent the primary magnetization, a possible explanation for the difference in the paleomagnetic poles from Colíder and Avanavero igneous units could be that after their emplacement at 1780 Ma ago, approximately NW dextral strike-slip motions occurred between the northern part of the craton where the Avanavero sills and dykes crop out, and the southern of the craton, in which the acid volcanic rocks from Colíder Group are housed in (Bispo-Santos *et al.* 2014b).

Another interesting fact emerges when the ~1420 Ma Nova Guarita and Indiavaí poles are compared with coeval poles from Baltica and Laurentia, after their rotation to the SAMBA configuration (see Fig. 12 in Bispo-Santos *et al.* 2014b). In such case, a difference between these poles is also observed, which is similar to that of the Avanavero-Colíder poles and once more point to NW dextral movements between the southern part of the Amazonian Craton and the northernmost portions of the Columbia supercontinent. Therefore, it suggests that if these strike-slip movements are real, they must have occurred after 1420 Ma.

In this scenario, the recent recognition of the Trincheira ophiolite in southwestern Amazonian Craton (Rondônia State) suggests that collision of the Paraguá Terrain with the proto-Amazonian Craton along the Alto Guaporé Belt occurred between ~1470 and 1320 Ma (Bettencourt *et al.* 2010, Rizzotto & Hartmann 2012). This collisional event probably originated the NW-SE lineaments (Buiuçu Shear Zone; Almeida *et al.* 2012) observed to the east of Trincheira ophiolite, where mylonitic rocks were dated at 1466.5 ± 1.4 Ma (Ar-Ar on muscovite) and 1467.8 ± 0.8 Ma (Ar-Ar on sericite). These shear zones are interpreted as the result of the Rondonian-San Ignacio orogeny (Cordani *et al.* 1979, Tassinari *et al.* 1996, Almeida *et al.* 2012) that led to the collision of Paraguá Terrain. In face of these facts, Bispo-Santos *et al.* (2014b) speculated that if both paleomagnetic poles represent primary ChRM directions, reactivation of these faults could be, at least partly, responsible for the NW-SE dextral movements implied by the available paleomagnetic data.

Furthermore, later tectonic events affected the Amazonian Craton, which may have produced relative movements between the northern Guiana Shield and the Brazil-Central Shield. We highlight the Late Mesoproterozoic intracratonic displacements associated with the Amazonian Craton/Laurentia collision along the Sunsás-Grenville orogenic belts – e.g. the 1200-950 Ma Aguapeí mobile belt; the ca. 1100 Ma NBB; and NE-SW shear zones associated with ca. 1200 Ma K'Mudku event that affected the southern part of the Avanavero event (Reis *et al.* 2003, Tohver *et al.* 2004a, Teixeira *et al.* 2010, Cordani *et al.* 2010). ENE-WSW to NE-SW shear zones associated with the Rondônia-San-Ignacio rocks in Rondônia State, which were dated at 1300.1 ± 1.4 Ma (plateau Ar-Ar age in muscovite), may have been caused by Sunsás orogen activity (Almeida *et al.* 2012). Also, the polydeformed basement to the north of the NBB is marked by intense shear zones at about 1150 Ma, although mylonitic rocks formed in the tectonic process display a systematic sinistral shear sense in this case (Tohver *et al.* 2004a).

Pisarevsky *et al.* (2014) also discussed the Paleoproterozoic (Colíder and Avanavero) and Mesoproterozoic (Nova Guarita and Indiavaí) poles from Amazonia. They contested the explanation presented by Bispo-Santos *et al.* (2014b) arguing that displacements between the parts of Amazonia are unlikely, as they would disrupt the linearity of the Ventuary-Tapajós province. Alternatively, they propose that Amazonia/West Africa was positioned outboard of the peripheral subduction system comprised by Laurentia and Baltica at 1770 Ma (see Fig. 7 in Pisarevsky *et al.* 2014).

Other models of Columbia, however, are possible, for which smaller mismatches of the Mesoproterozoic poles from Amazonia, Baltica and Laurentia are observed (e.g. Zhang *et al.* 2012, Xu *et al.* 2014, Pehrsson *et al.* 2016). Recently, D'Agrella-Filho *et al.* (2016) presented new paleomagnetic data about the 1440 Ma Salto do Céu mafic sills and sedimentary rocks cut by the sills. Comparison of selected 1460-1400 Ma poles from Baltica and Laurentia with available Mesoproterozoic poles from Amazonia are shown in Fig. 6 for each reconstruction of Columbia proposed by Bispo-Santos *et al.*

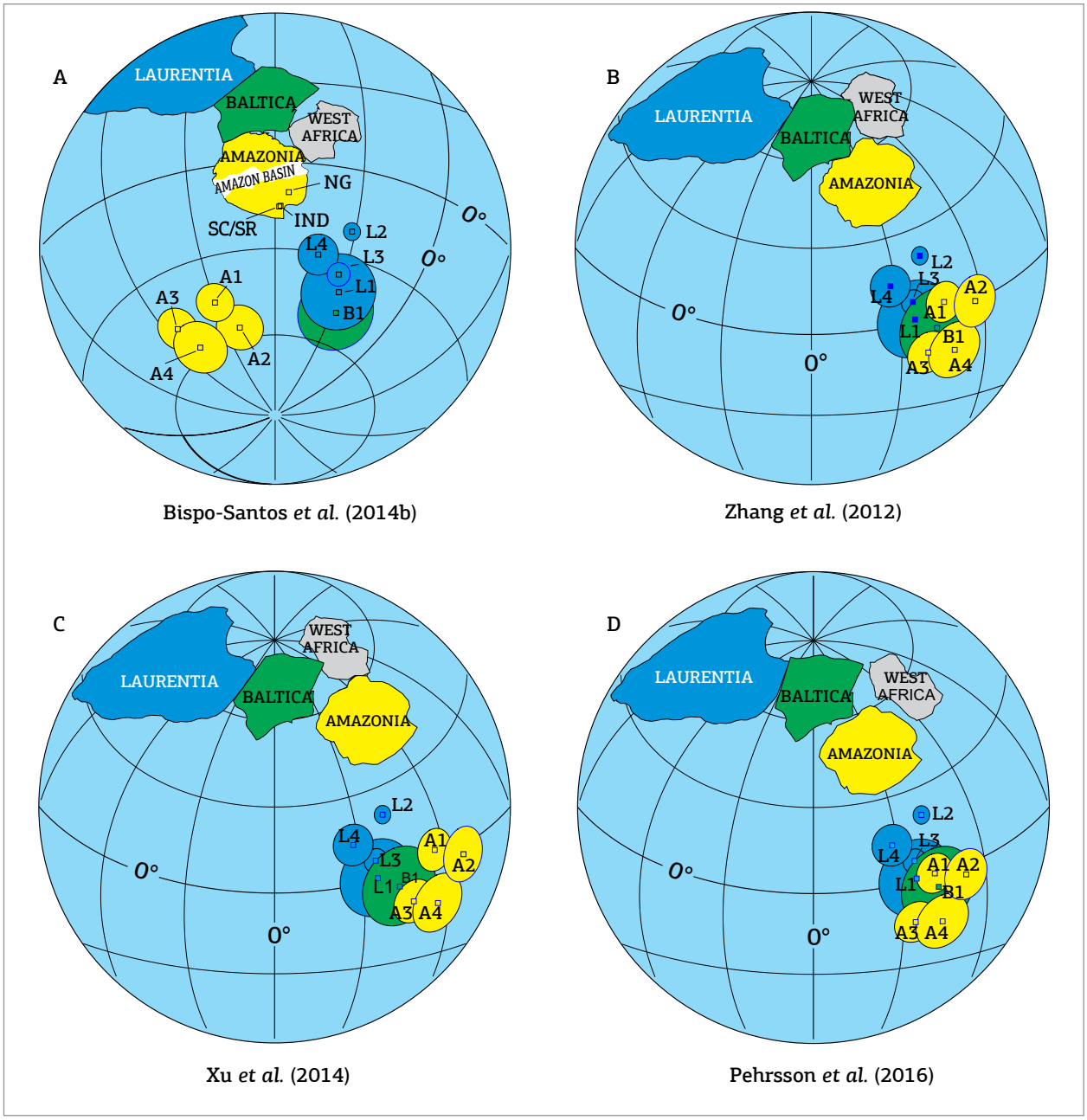

Figure 6. Comparison of Mesoproterozoic poles from the Amazonian Craton, Laurentia, and Baltica considering the reconstruction of Columbia proposed by (A) Bispo-Santos *et al.* (2014b); (B) Zhang *et al.* (2012); (C) Xu *et al.* (2014); and (D) Pehrsson *et al.* (2016) (based on D'Agrella-Filho *et al.* 2016). Mesoproterozoic paleomagnetic poles, and their confidence circles (α_{95}): Amazonia – (A1) Rio Branco Sedimentary rocks; (A2) Salto do Céu sills; (A3) Nova Guarita Dykes; (A4) Indiavaí Intrusive (Tab. 1); Baltica – (B1) 1460 Ma mean pole (Bispo-Santos *et al.* 2014b); Laurentia – (L1) 1460 Ma mean pole; (L2) McNamara pole (1401 ± 6 Ma); (L3) Electra Lake Gabbro (1433 ± 2 Ma); (L4) Laramie Anorthosite (1429 ± 9 Ma) (Bispo-Santos *et al.* 2014b). Paleomagnetic poles are represented in the same color of the respective cratonic blocks. Euler rotation poles used for paleomagnetic poles and cratonic blocks as in D'Agrella-Filho *et al.* (2016). Geographical positions of Salto do Céu sills (SC), Rio Branco sedimentary rocks (SR), Indiavaí Intrusive (IND) and Nova Guarita Dykes (NG) are shown in (A).

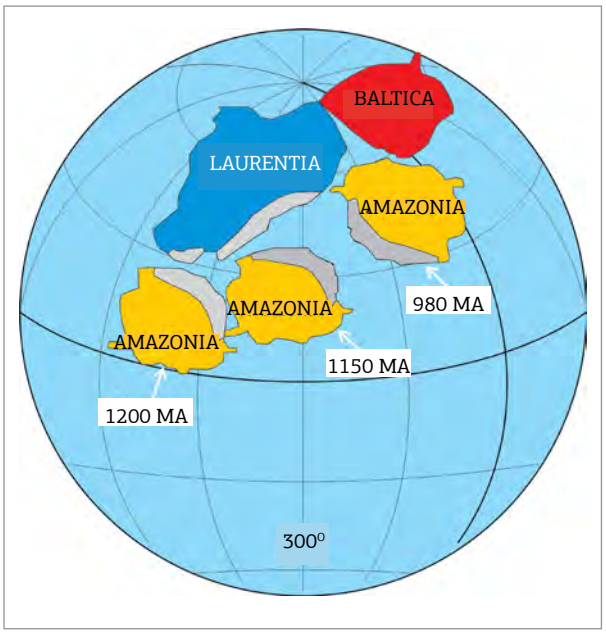

Figure 7. Geodynamical interaction model of the Amazonian Craton and Laurentia between 1200 Ma and 980 Ma (after Elming *et al.* 2009). Amazonian positions relative to Laurentia (North America in its present position) are shown at 1200 Ma (based on Nova Floresta pole – NF pole in Tab. 1), at 1150 Ma (based on Fortuna Formation pole – FT in Tab. 1), and at 980 Ma (based on Aguapeí sills pole of Elming *et al.* 2009).

(2014b), Zhang *et al.* (2012), Xu *et al.* (2014), and Pehrsson *et al.* (2016), as seen in Figs. 6a to 6d, respectively. The best cluster of poles is obtained through the reconstruction of Pehrsson *et al.* (2016), in which Amazonia appears rotated counterclockwise relative to the reconstruction of Bispo-Santos *et al.* (2014b) (Fig. 6a), and may indicate internal plate rotations inside Columbia. Note this reconstruction is similar to that proposed by Bispo-Santos *et al.* (2012). Nevertheless, it is clear that new Mesoproterozoic poles from the Amazonian Craton, mainly from the northern Guiana Shield, are required before we decide the best model proposed for Columbia.

THE AMAZONIAN CRATON: RODÍNIA'S PRODIGAL SON

The Amazonian Craton is one of the largest and most complete fragments of Rodínia's rupture, and possibly the only one of its descendants to take part in the Western Gondwana. Trying to increase our understanding about the paleogeographic evolution and dynamic interaction between Laurentia and the Amazonian Craton, other paleomagnetic investigations were carried out. Sedimentary rocks belonging to the Aguapeí Group and mafic sills cutting these rocks became the targets of paleomagnetic studies performed in western Mato Grosso State by D'Agrella-Filho *et al.* (2008) and Elming *et al.* (2009), respectively. For the study of the Aguapeí Group, redbeds described as belonging to Fortuna Formation (the basal unit) and gray pelitic sedimentary rocks of Vale da Promissão Formation (intermediate unit) were collected close to Vila Bela (next to the Brazil-Bolivia boundary) and Rio Branco (on the other side of the basin) cities, respectively. U-Pb detrital zircon ages ranging from 1453 ± 10 Ma to 1165 ± 27 Ma (n = 89) established the maximum deposition age for the Fortuna Formation at 1165 Ma (Santos *et al.* 2001, Leite & Saes 2003).

The paleomagnetic study of Fortuna Formation rocks enabled isolating ChRM directions carried by diagenetic hematite (D'Agrella-Filho *et al.* 2008). An age of 1149 ± 7 Ma was assigned to Fortuna Formation pole (Tab. 1), based on U-Pb (SHRIMP) dating of authigenic xenotime rims on detrital zircon grains. This paleomagnetic pole, when compared with coeval poles belonging to Laurentia (D'Agrella-Filho *et al.* 2008), seems to support the model proposed by Tohver *et al.* (2004b), which suggests an oblique collision followed by a strike-slip movement between the Amazonian Craton and Laurentia (Fig. 7). A similar model was used to explain the Colombian-Oaxaquian peri-Amazonian fringing arc system (Putumayo orogeny) outboard of Amazonia that evolved during the Amazonia transcurrent movement up to its final collision with Baltica in late Mesoproterozoic times (Ibanez-Mejia *et al.* 2011).

On the other hand, the gray pelitic sedimentary rocks collected near Rio Branco region disclosed reversed ChRM directions, in general, carried by magnetite. The absence of direct geochronological dating of these rocks did not permit to establish the age of the corresponding paleomagnetic pole (D'Agrella-Filho *et al.* 2008).

Paleomagnetic and geochronological studies were also performed on Aguapeí mafic sills (Rio Branco region, Mato Grosso State) cutting the pelitic sedimentary rocks (Elming *et al.* 2009). These sills and dykes belong to Salto do Céu Intrusive Suíte (Araújo-Ruiz *et al.* 2007), but Elming *et al.* called them Aguapeí (hereafter we will use the Salto do Céu original name, see also D'Agrella-Filho *et al.* 2016). In summary, the laboratorial treatments (alternating field – AF and thermal demagnetization) revealed southwest (northeast) directions with downward (upward) inclinations for ten sites (Dm = 11.3°; Im = -57.9°; α_{95} = 8.1°, K = 37), which yielded a paleomagnetic pole (Salto do Céu pole) located at 64.3°S; 271.0°E (A_{95} = 9.2°). An age of 981 ± 2 Ma was determined for one of the sills by ^{40}Ar-^{39}Ar (whole rock). Assigning this age to Salto do Céu pole, Elming *et al.* (2009) proposed a paleogeographic reconstruction, showing the

Amazonian Craton position relative to Laurentia at ~980 Ma ago (Elming *et al.* 2009), which follows the transcurrent model firstly proposed by Tohver *et al.* (2004a, 2004b) and later supported by D'Agrella-Filho *et al.* (2008), as in Fig. 7.

Two facts should be highlighted in this reconstruction:

1. Laurentia paleomagnetic poles in the age range between 1000 and 900 Ma come from high-grade metamorphic rocks related to the Grenville event. The ages of these poles were obtained, in general, from ^{40}Ar-^{39}Ar single-mineral dating (amphibole, biotite, and plagioclase), and it is not always easy to correlate radiometric and rock magnetization ages;
2. The paleogeographic reconstruction proposed by Elming *et al.* (2009) was based on the transcurrent model of Tohver *et al.* (2004a, 2004b), which shows that the Amazonian Craton at 980 Ma (based on Salto do Céu pole) rotated approximately 180° to its position at 1200 Ma (based on Nova Floresta pole of Tohver *et al.* 2002), during the ~3000 km sinistral motion along the Grenvillian margin (see Fig. 7). Although such large rotations may occur, the final position of the Amazonian Craton to Laurentia is very different from that normally admitted in Rodínia reconstructions (see Weil *et al.* 1998, D'Agrella-Filho *et al.* 1998, Li *et al.* 2008, Ibanez-Mejia *et al.* 2011).

A new U-Pb dating on baddeleyite extracted from Salto do Céu sill (Rio Branco region) has recently yielded an upper intercept age of 1439 ± 4 Ma on the U-Pb concordia diagram, which is interpreted as the crystallization age of the rock (Teixeira *et al.* 2016). This age contrasts with the previous 981 ± 2 Ma Ar-Ar age and enables an alternative interpretation for Salto do Céu sills pole. The new baddeleyite age correlates well with the U-Pb zircon ones of 1471 ± 8 Ma and 1427 ± 10 Ma, respectively, for a gabbro and a granophyre belonging to Rio Branco mafic-felsic Suite (Geraldes *et al.* 2001), suggesting that Salto do Céu sills belong to the same event.

Geraldes *et al.* (2014) presented a provenance study on 100 detrital zircons extracted from Rio Branco sedimentary rocks at Salto do Céu region (their AG-1 sample). The U-Pb determinations showed four age populations for these zircons: 1544, 1655, 1812, and 2515 Ma. The younger population (age peak of 1544 Ma) may represent detrital zircons derived from the Cachoeirinha event rocks (from 1580 to 1520 Ma), and indicate the maximum depositional age for that unit (Geraldes *et al.* 2014). The identification by Ruiz (2005) of xenoliths from these sedimentary rocks inside the Rio Branco igneous rocks (age of 1427 ± 10 Ma) also suggests they are older than those near Vila Bela, whose detrital zircon ages indicate a maximum of 1126 Ma for them (Santos *et al.* 2001, Leite & Saes 2003). These results demonstrate that the pelitic sedimentary rocks previously interpreted as the intermediate unit of Aguapeí Group must in fact be correlated with other sedimentary rocks, probably the Dardanelos Group to the north of the Phanerozoic Serra dos Parecis sedimentary cover (Lacerda-Filho *et al.* 2004). In such case, Salto do Céu sills pole (now dated at 1439 Ma) cannot be used to represent the Amazonian Craton position in the context of Rodínia, and the paleogeographic interpretation made by Elming *et al.* (2009) using this pole should be revised.

Trying to prove the primary nature of the magnetization carried by the sills, recently, D'Agrella-Filho *et al.* (2016) sampled eight new paleomagnetic sites from Salto do Céu sills and samples from five profiles of sedimentary rocks close to the contact with the sills for baked contact tests. The results obtained for the sills and sedimentary rocks are similar to those from Elming *et al.* (2009) and D'Agrella-Filho *et al.* (2008), respectively, in the previous studies of these rocks. More statistically robust paleomagnetic poles were calculated for the sedimentary rocks (A1 pole in Tab. 1 – now called Rio Branco sedimentary rocks pole) and for the sills (A2 pole in Tab. 1) that supersede older poles. Although the baked contact test was inconclusive, because no different magnetization direction was disclosed for sedimentary rocks far from the sills, ages around 1440 Ma for these paleomagnetic poles are supported by the Nova Guarita (1419 Ma) and Indiavaí (1416 Ma) poles. Fig. 6A shows the poles for the sedimentary rocks from Rio Branco area (pole A1), Salto do Céu sills (pole A2), the 1419 Ma Nova Guarita dyke swarm (pole A3), and the 1416 Ma Indiavaí Intrusive (pole A4). All these poles plot close together suggesting similar ages for all of them.

Recently, Evans (2013) (followed by Johansson 2014) proposed an alternate scenario for the dynamic interaction between Laurentia, Baltica, and the Amazonian Craton (see Fig. 3 in Evans, 2013) that totally contrasts with that proposed by Tohver *et al.* (2004b), D'Agrella-Filho *et al.* (2008) and Elming *et al.* (2009). Due to the polarity ambiguity, Evans (2013) argues that a different model may be proposed if we use the Amazonian Craton's anti-poles. In the Evans' model, after SAMBA rupture in Columbia, Baltica and Amazonian Craton performed clockwise rotations, and docked again with Laurentia, the Amazonian Craton faced to Grenville Belt in the present Labrador region. Partially based on paleomagnetic data, Fig. 8 shows a possible dynamic scenario for Columbia rupture, clockwise rotation of Amazonia and Baltica, and posterior collision of these blocks with Laurentia. Paleomagnetic data suggest that Laurentia and Baltica behaved as a unique block at least up to 1265 Ma (Salminen & Pesonen 2007). Fig. 8B provides the configuration of SAMBA connection (after Bispo-Santos

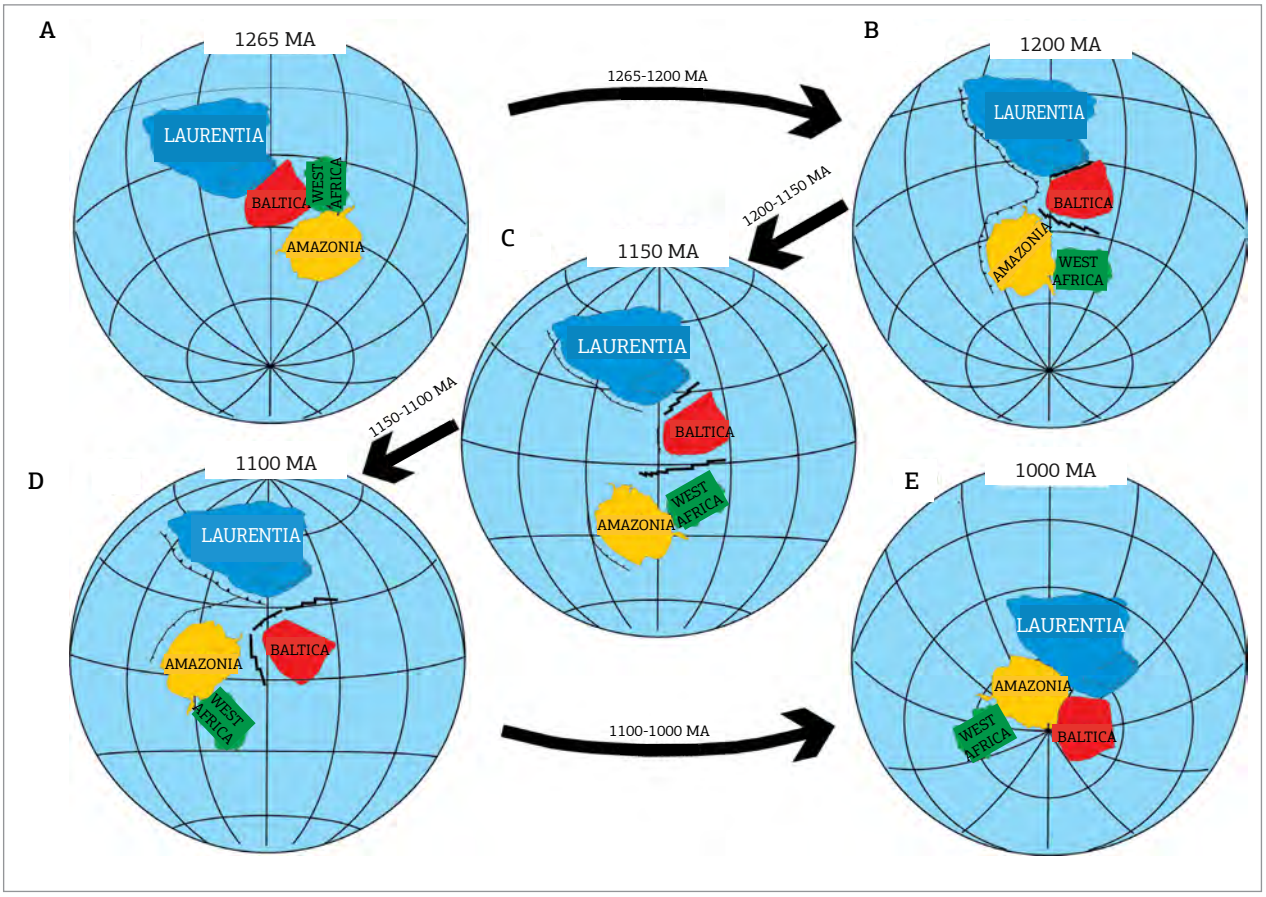

Figure 8. Schematic sketch showing rupture of Columbia core (comprised by Laurentia, Baltica, Amazonia, and West Africa), followed by clockwise rotation of Amazonia/West Africa and Baltica and posterior collision with Laurentia forming Rodínia. (A) Reconstruction at 1265 Ma – Columbia core after Bispo-Santos *et al.* (2014b) and Pehrsson *et al.* (2016), positioned by the MacKenzie dykes pole (Buchan & Halls 1990). (B) Reconstruction at 1200 Ma – Laurentia and Amazonia/West Africa were constrained by the Upper Bylot (Fahrig *et al.* 1981, Kah *et al.* 2001) and Nova Floresta poles (Tab. 1), respectively. (C) Reconstruction at 1150 Ma – Laurentia and Amazonia/West Africa were constrained by the Abitibi dykes (Ernst & Buchan 1993, Krogh *et al.* 1987, Irving & Naldrett 1977) and Fortuna Formation poles (Tab. 1), respectively. (D) Reconstruction at 1100 Ma – Laurentia was constrained by the Logan dykes pole (Halls & Pesonen 1982, Davis & Sutcliffe 1985). (E) Reconstruction at 1000 Ma – Laurentia, Baltica, and Amazonia as shown in the reconstruction of Rodínia proposed by Li *et al.* (2008). Euler poles used: Laurentia (14.27°N; 37.04°E; 107.02°); Baltica (21.17°N; 204.26°E; -176.32°); Amazonia (24.21°N; 175.25°E; -150.19°). West Africa was rotated to Amazonia as in Bispo-Santos *et al.* (2014a).

et al. 2014b and Pehrsson *et al.* 2016) constrained by the 1267 Ma MacKenzie dykes pole (Buchan & Halls 1990). The Baltica-Laurentia link is practically the same as that proposed by Salminen & Pesonen (2007). It is possible that the MacKenzie dyke swarm is the record of the initial rupture of Columbia (Hou *et al.* 2008b). Fig. 8B presents the configuration at 1200 Ma. Amazonia/West Africa Craton and Laurentia are constrained by Nova Floresta (Tab. 1) and Upper Bylot poles (Fahrig *et al.* 1981), respectively. Baltica and Amazonia/West Africa broke-up and initiated their clockwise rotation. Fig. 8C shows the configuration at 1150 Ma, in which Laurentia and Amazonia/West Africa are constrained by Abitibi dyke (Ernst & Buchan 1993, Irving & Naldrett 1977) and Nova Fortuna poles (Tab. 1), respectively. For the reconstruction at 1100 Ma (Fig. 8D), only Laurentia is constrained by Logan sills pole (Halls & Pesonen 1982, Davis & Sutcliffe 1985). Finally, Fig. 8E introduces the configuration at 1000 Ma as proposed by Li *et al.* (2008), in which Rodínia had already been formed.

THE AMAZONIAN CRATON IN GONDWANA

Dynamic processes associated with the Amazonian Craton, Laurentia, and Proto-Gondwana between 900 Ma and 530 Ma have been intensively investigated and debated. The period when the Amazonian Craton separated from

Rodínia Supercontinent, as well as the time of its collision with proto-Gondwana, — composed in its western part by the Paranapanema block, the Central Goiás microplate, the Parnaíba block and other smaller blocks underlying the Paraná and Parnaíba Basins — are still in dispute (see Cordani *et al.* 2013a, 2014, Tohver & Trindade 2014).

Many authors advocate a final collision between Amazonian-West African Craton and proto-Gondwana at around 650-600 Ma, after closure of the great Goiás-Pharusian ocean separating these cratonic units in earlier times (e.g. Trompette 1994, 1997, Cordani *et al.* 2000, Cordani & Teixeira 2007, Cordani *et al.* 2013a, 2013b, Ganade de Araújo *et al.* 2014). In this case, late Neoproterozoic would be characterized by the presence of supercontinent Pannotia (Dalziel 1997), comprising all Gondwana units plus Laurentia, the break-up of Laurentia occurring during the Ediacaran with the formation of the Yapetus Ocean (570 Ma, Cawood *et al.* 2001). However, Pannotia formation was contested by Meert & Van der Voo (1997) who declared that Gondwana agglutination occurred in three distinct periods: 800-650 Ma (formation of the Mozambique Belt due to the collision of India, Madagascar, and Sri Lanka with East Africa); 600-530 Ma (formation of the Brasiliano/Pan-African belts through the collision of the South American and African cratonic blocks); and ~550 Ma (formation of the Kuunga belt, which was the result of the collision of Australia and Antarctica with the rest of Gondwana). Thus, east Gondwana would not be completely agglutinated at the time Pannotia is supposed to have existed.

In recent years, several authors have claimed that the final agglutination of the South American core of Gondwana — formed by the Amazonia/Rio Apa, Congo-São Francisco, Rio de la Plata and several other smaller blocks — could have happened during the Cambrian between 550-520 Ma, with the closure of the Clymene Ocean that separated the Amazonian Craton from other continental blocks (Trindade *et al.* 2006).

The paleomagnetic study on carbonate rocks from Araras Group, conducted by Trindade *et al.* (2003), provided a paleomagnetic pole (Puga Cap carbonate A pole in Tab. 1) for the Amazonian Craton, which has been dated at 627 ± 30 Ma (Pb-Pb whole rock isochron obtained for rocks at the base of Araras Group – Babinski *et al.* 2006). When compared with the paleomagnetic poles of proto-Gondwana (including Congo São Francisco and part of East Gondwana), this suggests that the Amazonian Craton was separated from the rest of Gondwana at Ediacaran times. Otherwise, the close fit of the 525 Ma poles from Amazonia and proto-Gondwana (in a Gondwana pre-drift configuration) might show that complete closure of Clymene Ocean occurred only at Ediacaran times (Trindade *et al.* 2006). In the model proposed by Trindade *et al.* (2006), West Gondwana was formed diachronically, similarly to the East Gondwana whose final amalgamation occurred only at 525 Ma (Meert & Van der Voo 1997).

New evidence supporting this interpretation came from paleomagnetic and geochronological studies from remagnetized carbonate rocks collected along the Paraguay Belt (Tohver *et al.* 2010). Collision along the southeastern margin of the Amazonian Craton along the Paraguay Belt produced folding, trusting, and remagnetization dated at 528 ± 36 Ma. According to Tohver *et al.* (2010), the oroclinal inflection of the Paraguay Belt occurred after 528 Ma, which caused the coherent change observed in the ChRM declinations disclosed for rocks collected in the northern and southern inflection areas. Tohver *et al.* (2012) carried out a review regarding the geological, geochronological and tectonic history related to Araguaia, Paraguay and Pampeano belts. These authors show common features for these belts that reflect a shared geodynamic environment associated with the Clymene Ocean closure, with the occurrence of a transition from accumulated cratonic-origin sediments over a passive margin to a predominated magmatic, metamorphic and deformational phase between 550 to 500 Ma.

Recently, sedimentologic and provenance studies of rocks from two geological formations of Alto Paraguay Group (Paraguay Belt) showed that their evolutions are associated with the Clymene Ocean closure (Bandeira *et al.* 2012, McGee *et al.* 2012, 2015a, 2015b). According to these studies, the top unit of Alto Paraguay Group represents the last transgressive deposits of the Paraguay Basin, resulting from the last stage of marine incursion of this ocean. Meanwhile, pelitic and fine sandstone deposits of Diamantino Formation (Upper Formation from Paraguay Group) are associated with the molassic phase. U-Pb detrital zircons dating of rocks from the basal part of this formation indicates that the deposition of Diamantino Formation occurred after 541 ± 7 Ma (Bandeira *et al.* 2012, McGee *et al.* 2012, 2015a, 2015b). Furthermore, the recent sedimentological and radiometric studies of glaciogenic rocks from Serra Azul Formation (Alto Paraguay Group) indicate that they are probably associated with the 580 Ma Gaskiers event (McGee *et al.* 2013, 2015a). These findings also propose an Ediacaran-Early Cambrian closure of the Clymene Ocean. The age of 518 ± 4 Ma (U-Pb zircon) obtained for the post-tectonic São Vicente Granite (Almeida & Mantovani 1975; McGee *et al.* 2012) establish the minimal age of the deformation and metamorphic phase in the northern part of Paraguay Belt and, therefore, the final time of the South America accretion in the Gondwana continent.

In a recent paper, however, Ganade de Araújo *et al.* (2014) discuss that the Goiás-Pharusian ocean separating the Amazonian-West African block from the proto-West Gondwana (also named as Central African block by Cordani *et al.* 2013a) closed beween 900 and 600 Ma. According to Ganade de Araújo *et al.* (2014),

Himalaya-type mountains more than 2500 km long formed along this mega-suture (the Transbrasiliano-Kandy tectonic corridor, Cordani *et al.* 2013b), thus producing eclogitic rocks at about 130 km depth in the lithosphere, whose exhumation occurred at about 615 Ma. Unfortunately, paleomagnetic data between 900 and 600 Ma are rare for all Gondwana cratonic blocks, which make the tectonic processes involving Rodínia break-up and Gondwana formation undefiened.

FINAL REMARKS

In the last decade, a significant increase of the Amazonian paleomagnetic data brought important implications for the geodynamic evolution of the Amazonian Craton and for its participation in supercontinents, mainly in Paleo to Mesoprotezoic times.

The Surumu Group pole corroborated the idea of a ca. 2000-1960 Ma pre-Columbia proto-Amazonian/West Africa link in a continental paleogeography, in which Guri (Guiana Shield) and Sassandra (West Africa Craton) shear zones were aligned. Similarly, the participation of the Amazonian Craton in the SAMBA model, forming the core of Columbia supercontinent, is constrained by the Avanavero pole, which is a model supported by geological and geochronological data (Johansson 2009). A paleogeography at 2000 Ma (Fig. 4) is also envisaged and comprises cratonic blocks that later on formed Laurentia, Baltica, and Amazonian/West Africa in the core of Columbia.

Paleo- to Mesoproterozoic paleomagnetic poles (Colíder, Nova Guarita, Indiavaí, and Salto do Céu poles) from southeastern Amazonian Craton (Brazil-Central Shield) suggest the occurrence of dextral strike-slip movements between the Guiana and the Brazil-Central Shields. These transcurrent movements could be due to the collision of the Paraguá Terrain with proto-Amazonia along the Alto Guaporé Belt at ca. 1320 Ma ago, although other tectonic events (Sunsás, Nova Brasilândia and Aguapeí orogens) may also be responsible for them. Another possible interpretation is that internal block rotations within Columbia supercontinent occurred between 1790 Ma (or 1530 Ma) and 1420 Ma ago (see Fig. 6).

The importance of Nova Guarita and Indiavaí poles should be highlighted for the significance of the E-W NBB whose origin resulted, most probably, of intracratonic reactivation that occurred during the collision of the Amazonian Craton with Laurentia along the Sunsás/Grenville Belt. Paleomagnetic data from late Mesoproterozoic and early Neoproterozoic are compatible with two scenarios for the collision of the Amazonian Craton with Laurentia in the formation of Rodínia: oblique collision, followed by relative transcurrent movement up to the collision of Amazonian Craton with Baltica at ca. 1000 Ma (Fig. 7), or starting from a SAMBA link, a clockwise rotation of Amazonia/West Africa Craton and Baltica with their final collision with Laurentia along the Grenville Belt (Fig. 8).

Finally, some geochronological and paleomagnetic data suggest that the collision of the Amazonian-West African Craton (plus Rio Apa block) with proto-Gondwana resulted in the formation of Gondwana only in the late Ediacaran and early Cambrian between 550 and 520 Ma. However, this hypothesis is contested by other geologic-geochronological evidence, which defend a prior (650-600 Ma) collision. We understand that only with more key paleomagnetic poles from Gondwana cratonic units in the interval between 900 and 550 Ma, we will be able to solve this issue.

ACKNOWLEDGEMENTS

This work is a synthesis of more than ten years of research on the Amazonian craton, and it has benefited from discussions with several colleagues from *Universidade de São Paulo, Serviço Geológico do Brasil* (CPRM), *Companhia Mato-Grossense de Mineração* (METAMAT), *Universidade Federal do Mato Grosso* (UFMT), *Instituto Nacional de Ciência e Tecnologia de Geociências da Amazônia* (INCT-GEOCIAM), among others. We thank the support provided by research agencies, institutions, and professionals that contributed to the progress of paleomagnetic research in the Amazonian Craton: grants 2007/59531-4, 2007/53177-4, 2011/50887-6 and 2012/50327-3, São Paulo Research Foundation (FAPESP), and grant 554458/2005-5 (CNPq).

REFERENCES

Åhäll K.I. & Connelly J. 1998. Intermittent 1.53-1.13 Ga magmatism in Western Baltica; age constraints and correlations within a postulated supercontinent. *Precambrian Research*, **92**:1-20.

Almeida F.F.M. & Mantovani M.S.M. 1975. Geologia e gechronologia do granito de São Vicente, Mato Grosso. *Anais da Academia Brasileira de Ciências*, **47**:451-458.

Almeida M.E., Costa U.A.P., Betiollo L.M., Reis N.J., Splendor F., Bahia R.B.C., Ruffet G. 2012. Idades Ar-Ar step heating em milonitos do sudeste do Amazonas: implicações na evolução tectonotermal da Província Rondônia-Juruena. *In*: 46° Congresso Brasileiro de Geologia, *Abstract*, CD-ROM, Santos, São Paulo, Brasil.

Anderson J.L. & Morrison L. 1992. The role of anorogenic granites in the Proterozoic crustal development of North America. *In*: Condie K.C. (ed.). *Proterozoic Crustal Evolution*. Amsterdam, Elsevier, p. 263-299.

Araújo-Ruiz L.M.B., Godoy A.M., Ruiz A.S., Sousa M.Z.A., Montano L.F.M. 2007. Geologia e geoquímica do Batólito Rapakivi Rio Branco, SW do Cráton Amazônico – MT. *Geologia USP Série Científica*, **7**:57-72.

As J.A. & Zijderveld J.D.A. 1958. Magnetic cleaning of rocks in palaeomagnetic research. *Geophysical Journal*, **1**:308-319.

Babinski M., Trindade R.I.F., Alvarenga C.J.S., Boggiani P.C., Liu D., Santos R.V., Brito Neves B.B. 2006. Chronology of Neoproterozoic ice ages in Central Brazil. ***In***: V South American Symposium on Isotope Geology, Punta del Este, Uruguay, *Short Papers*, p. 303-306.

Bandeira J., McGee B., Nogueira A.C.R., Collins A.S., Trindade R.I.F. 2012. Sedimentological and provenance response to Cambrian closure of the Clymene ocean: the upper Alto Paraguai Group, Paraguay belt, Brazil. *Gondwana Research*, **21**:323-340.

Bettencourt J.S., Tosdal R.M., Leite Jr. W.B., Payolla B.L. 1999. Mesoproterozoic rapakivi granites of the Rondônia Tin Province, southwestern border of the Amazonian Craton, Brazil – I. Reconnaissance U-Pb geochronology and regional implications. *Precambrian Research*, **95**:41-67.

Bettencourt J.S., Leite Jr. W., Payolla B., Ruiz A.S., Matos R.S., Tosdal R.M. 2010. The Rondonian-San Ignacio Province in the SW Amazonian Craton: an overview. *Journal of South American Earth Sciences*, **29**:28-46.

Beyer S.R., Hiatt E.E., Kyser K., Drever G.L., Marlatt J. 2015. Stratigraphy, diagenesis and geological evolution of the Paleoproterozoic Roraima Basin, Guyana: Links to tectonic events on the Amazon Craton and assessment for uranium mineralization potential. *Precambrian Research*, **267**:227-249.

Bispo-Santos F. 2012. *Estudo paleomagnético de unidades paleoproterozóicas do Cráton Amazônico*. Dissertation, Universidade de São Paulo, São Paulo, 253 p.

Bispo-Santos F., D'Agrella-Filho M.S., Pacca I.I.G., Janikian L., Trindade R.I.F., Elming S-Å., Silva J.A., Barros M.A.S., Pinho F.E.C. 2008. Columbia revisited: Paleomagnetic results from the 1790 Ma Colíder volcanics (SW Amazonian Craton, Brazil). *Precambrian Research*, **164**:40-49.

Bispo-Santos F., D'Agrella-Filho M.S., Trindade R.I.F., Elming S-Å., Janikian L., Vasconcelos P.M., Perillo B.M., Pacca I.I.G., Silva J.A., Barros M.A.S. 2012. Tectonic implications of the 1419 Ma Nova Guarita mafic intrusives paleomagnetic pole (Amazonian Craton) on the longevity of Nuna. *Precambrian Research*, **196-197**:1-22.

Bispo-Santos F., D'Agrella-Filho M.S., Janikian L., Reis N.J., Reis M.A.A.A., Trindade R.I.F. 2014a. Towards Columbia: Paleomagnetism of 1980–1960 Ma Surumu volcanic rocks, Northern Amazonian Craton. *Precambrian Research*, **244**:123-138.

Bispo-Santos F., D'Agrella-Filho M.S., Trindade R.I.F., Janikian L., Reis N.J. 2014b. Was there SAMBA in Columbia? Paleomagnetic evidence from 1790 Ma Avanavero mafic sills (Northern Amazonian craton). *Precambrian Research*, **244**:139-155.

Bleeker W. 2003. The late Archean record: a puzzle in ca. 35 pieces. *Lithos*, **71**:99-134.

Bogdanova S.V., Page L.M., Skridlaite G., Taran L.N. 2001. Proterozoic tectonothermal history in the western part of the east European Craton: $^{40}Ar/^{39}Ar$ geochronological constraints. *Tectonophysics*, **339**:39-66.

Bogdanova S.V., Gintov O.B., Kurlovich D.M., Lubnina N.V., Nilsson M.K.M., Orlyuk M.I.O., Pashkevich I.K., Shumlyanskyy L.V., Starostenko V.I. 2013. Late Palaeoproterozoic mafic dyking in the Ukranian Shield of Volgo-Sarmatia caused by rotation during the assembly of supercontinent Columbia (Nuna). *Lithos*, **174**:196-216.

Boger S.D., Raetz M., Giles D., Etchart E., Fanning C.M. 2005. U-Pb age data from Sunsas region of Eastern Bolivia, evidence for the allochthonous origin of the Paraguá Block. *Precambrian Research*, **139**:121-146.

Bonilla-Pérez A., Frantz J.C., Charão-Marques J., Cramer T., Franco-Victoria J.A., Mulocher E., Amaya-Perea Z. 2013. Petrografia, geoquimica y geocronologia del Granito de Parguaza en Colombia. *Boletín de Geología*, **35**:83-104.

Brito Neves B.B., Sá J.M., Nilson A.A., Botelho N.F. 1995. A Tafrogênese Estateriana nos blocos Paleoproterozóicos da América do Sul e processos subseqüentes. *Geonomos*, **3**(2):1-21.

Buchan K.L. & Halls H.C. 1990. Paleomagnetism of Proterozoic mafic dyke swarms of the Canadian Shiled. ***In***: Parker A.J., Rickwood P.C., Tucker D.H. (eds.). *Mafic dykes and emplacement mechanism*. A.A. Balkema, Rotterdam, p. 209-230.

Buchan K.L., Mertanen S., Park R.G., Pesonen L.J., Elming S-A., Abrahamsen N., Bylund G. 2000. Comparing the drift of Laurentia and Baltica in the Proterozoic: the importance of key palaeomagnetic poles. *Tectonophysics*, **319**:167-198.

Buchan K.L., Mortensen J.K., Card K.D., Percival J.A. 1998. Paleomagnetism and U-Pb geochronology of diabase dyke swarms of Minto Block, Superior Province, Quebec, Canada. *Canadian Journal of Earth Sciences*, **35**:1054-1110.

Bullard E., Everett J.E., Smith A.G. 1965. The fit of the continents around the Atlantic. *Philosophical Transactions of the Royal Society of London A: Mathematical, Physical and Engineering Sciences*, **258**:41-51.

Butler R.F. 1992. *Paleomagnetism: magnetic domains to geologic terranes*. Boston, Blackwell Scientific Publications, 319 p.

Castillo J.H. & Costanzo-Alvarez V. 1993. Paleomagnetism of the Uairen Formation, Roraima Group, southeastern Venezuela: evidence for one of the oldest (Middle Proterozoic) depositional remanent magnetizations. *Canadian Journal of Earth Sciences*, **30**:2380-2388.

Cawood P.A., McCausland P.J.A., Dunning G.R. 2001. Opening Iapetus: Constraints from the Laurentian margin in Newfoundland. *Geological Society of America Bulletin*, **113**:443-453.

Condie K.C. 2002. Continental growth during a 1.9-Ga superplume event. *Journal of Geodynamics*, **34**:249-264.

Cordani U.G. & Teixeira W. 2007. Proterozoic accretionary belts in the Amazonian Craton. *Geological Society, America Memoir*, **200**:297-320.

Cordani U.G., Tassinari C.C.G., Teixeira W., Basei M.A.S., Kawashita K. 1979. Evolução tectônica da Amazônia com base nos dados geocronológicos. ***In***: Congreso Geológico Chileno, Arica, *Actas*, v. 4, p. 137-148.

Cordani U.G., Sato K., Teixeira W., Tassinari C.C.G., Basei M.A.S. 2000. Crustal evolution of the South American platform. *In*: Cordani U.G., Milani E.J., Thomaz-Filho A., Campos D.A. (eds.) *Tectonic evolution of South America*, Rio de Janeiro, p. 19-40.

Cordani U.G., D'Agrella-Filho M.S., Brito-Neves B.B., Trindade R.I.F. 2003. Tearing up Rodinia: the Neoproterozoic paleogeography of South American fragments. *Terra Nova*, **15**:350-359.

Cordani U.G., Teixeira W., D'Agrella-Filho M.S., Trindade R.I.F. 2009. The position of the Amazonian craton in supercontinents. *Gondwana Research*, **15**:396-407.

Cordani U.G., Fraga L.M., Reis N., Tassinari C.C.G., Brito-Neves B.B. 2010. On the origin and tectonic significance of the intra-plate events of Grenvillian-type age in South America: a discussion. *Journal of South American Earth Sciences*, **29**:143-159.

Cordani U.G., Pimentel M.M., Araújo C.E.G., Basei M.A.S., Fuck R.A., Girardi V.A.V. 2013a. Was there an ediacaran Clymene Ocean in central South America? *American Journal of Science*, **313**:517-539.

Cordani U.G., Pimentel M.M., Araújo C.E.G., Fuck R.A. 2013b. The significance of the Transbrasiliano-Kandy tectonic corridor for the amalgamation of West Gondwana. *Brazilian Journal of Geology*, **43**:583-597.

Cordani U.G., Pimentel M.M., De Araújo C.E.G., Basei M.A.S., Fuck R.A., Girardi V.A.V. 2014. Reply to the comment by Tohver E., Trindade R.I.F., on was there a clymene ocean in central South America? 313: 517-539. *American Journal of Science*, **314**(3):814-819.

D'Agrella-Filho M.S., Trindade R.I.F., Siqueira R., Ponte-Neto C.F., Pacca I.I.G. 1998. Paleomagnetic constraints on the Rodinia supercontinent: Implications for its Neoproterozoic break-up and the formation of Gondwana. *International Geology Review*, **40**:171-188.

D'Agrella-Filho M.S., Pacca I.G., Trindade R.I.F., Teixeira W., Raposo M.I.B., Onstott T.C. 2004. Paleomagnetism and $^{40}Ar/^{39}Ar$ ages of mafic dykes from Salvador (Brazil): new constraints on the São Francisco Craton APW path between 1080 and 1010 Ma. *Precambrian Research*, **132**:55-77.

D'Agrella-Filho M.S., Tohver E., Santos J.O.S., Elming S-Å., Trindade R.I.F., Pacca I.G., Geraldes M.C. 2008. Direct dating of paleomagnetic results from Precambrian sediments in the Amazon craton: Evidence for Grenvillian emplacement of exotic crust in SE Appalachians of North America. *Earth and Planetary Science Letters*, **267**:188-199.

D'Agrella-Filho M.S., Trindade R.I.F., Tohver E., Janikian L., Teixeira W., Hall C. 2011. Paleomagnetism and ^{40}Ar-^{39}Ar geochronology of the high-grade metamorphic rocks of the Jequié block, São Francisco Craton: Atlantica, Ur and beyond. *Precambrian Research*, **185**:183-201.

D'Agrella-Filho M.S., Trindade R.I.F., Elming S-Å., Teixeira W., Yokoyama E., Tohver E., Geraldes M.C., Pacca I.I.G., Barros M.A.S., Ruiz A.S. 2012. The 1420 Ma Indiavaí Mafic Intrusion (SW Amazonian Craton): Paleomagnetic results and implications for the Columbia supercontinent. *Gondwana Research*, **22**:956-973.

D'Agrella-Filho M.S., Trindade R.I.F., Queiroz M.V.B., Meira V.T., Janikian L., Ruiz A.S., Bispo-Santos F. 2016. Reassessment of Aguapeí (Salto do Céu) Paleomagnetic pole of the Amazonian Craton and implications for Proterozoic supercontinents. *Precambrian Research*, **272**:1-17.

Daly J.S., Balagansky V.V., Timmerman M.J., Whitehouse M.J. 2006. The Lapland-Kola orogen: Palaeoproterozoic collision and accretion of the northern Fennoscandian lithosphere. ***In***: Gee D.G. & Stephenson R.A. (eds.) *European Lithosphere Dynamics*. Geological Society, 32, London, Memoirs, p. 579-598.

Dalziel I.W.D. 1997. Neoproterozoic-Paleozoic geography and tectonics: Review, hypothesis, environmental speculation. *Geological Society of America Bulletin*, **109**:16-42.

Dalziel I.W.D., Mosher S., Gahagan L.M. 2000. Laurentia-Kalahari collision and the assembly of Rodinia. *The Journal of Geology*, **108**:499-513.

Davis D.W. & Sutcliffe R.H. 1985. U-Pb ages from the Nipigon plate and northern Lake Superior. *Geological Society of America Bulletin*, **96**:1572-1579.

de Kock M.O., Evans D.A.D., Beukes N.J. 2009. Validating the existence of Vaalbara in the Neoarchean. *Precambrian Research*, **174**:145-154.

Delor C., Lahondere D., Egal E., Lafon J.M., Cocherie A., Guerrot C., Rossi P., Truffert C., Theveniaut H., Phillips D., Avelar V.G. 2003. Transamazonian crustal growth and reworking as revealed by the 1:500.000 – scale geological map of French Guiana. ***In***: *Geologie de la France – Special Guiana Shield*, 2. ed., BRGM, SGF Editor, p. 5-58.

Elming S-Å., D'Agrella-Filho M.S., Page L.M., Tohver E., Trindade R.I.F., Pacca I.I.G., Geraldes M.C., Teixeira W. 2009. A palaeomagnetic and $^{40}Ar/^{39}Ar$ study of Late Precambrian sills in the SW part of the Amazonian Craton: Amazonia in the Rodinia reconstruction. *Geophysical Journal International*, **178**:106-122.

Elming S-Å., Shumlyanskyy L., Kravchenko S., Layer P., Söderlund U. 2010. Proterozoic basic dykes in the Ukrainian Shield: A palaeomagnetic, geochronologic and geochemical study-The accretion of the Ukrainian Shield to Fennoscandia. *Precambrian Research*, **178**:119-135.

Enjolvy R. 2004. *Caractérisation géochronologique et pétrologique de l'évènement fini-transamazonien: étude en Guyane française et en Amapá (Brésil)*. Rapport de DEA, Université de Montpellier II, 42 p.

Ernst R.E. & Buchan K.L. 1993. Paleomagnetism of the Abitibi dyke swarm, southern Superior Province and implications for the Logan Loop. *Canadian Journal of Earth Sciences*, **30**:1886-1897.

Evans D.A.D. 2013. Reconstructing pre-Pangean supercontinents. *Geological Society of America Bulletin*, **125**:1735-1751.

Evans D.A.D. & Halls H.C. 2010. Restoring Proterozoic deformation within the Superior craton. *Precambrian Research*, **183**:474-489.

Evans D.A.D. & Mitchell R.N. 2011. Assembly and breakup of the core of Paleoproterozoic–Mesoproterozoic supercontinent Nuna. *Geology*, **39**:443-446.

Fahrig W.F., Christie K.W., Jones D.L. 1981. Paleomagnetism of the Bylot basins: evidence for MacKenzie continental tensional tectonics. *Geological Survey of Canada Paper*, **81-10**:303-312.

Fedotova M.A., Khramov N.A., Pisakin B.N., Priyatkin A.A. 1999. Early Proterozoic palaeomagnetism: new results from the intrusives and related rocks of the Karelian, Belomorian and Kola provinces, eastern Fennoscandian Shield. *Geophysical Journal International*, **137**:691-712.

Fraga L. & Dreher A. 2010. Grupo Surumu. ***In***: CPRM (ed.) *Programa Geologia do Brasil. Programa Cartografia da Amazônia*. Geologia e Recursos Minerais da Folha Vila de Tepequém, NA, 80-94.

Ganade de Araújo C.E.G., Rubatto D., Hermann J., Cordani U.G., Caby R., Basei M.A.S. 2014. Ediacaran 2.500-km-long synchronous deep continental subduction in the West Gondwana orogen. *Nature Communications*, **5**(5198):1-8.

Gaudette H.E., Mendoza V., Hurley P.M., Fairbairn H.W. 1978. Geology and age of the Parguaza rapakivi granite, Venezuela. ***Geological*** *Society of America Bulletin*, **89**:1335-1340.

Geraldes M.C., Van Schmus W.R., Condie K.C., Bell S., Teixeira W., Babinski M. 2001. Proterozoic geologic evolution of the SW part of the Amazonian Craton in Mato Grosso state, Brazil. *Precambrian Research*, **111**:91-128.

Geraldes M.C., Nogueira C., Vargas-Mattos G., Matos R., Teixeira W., Valencia V., Ruiz J. 2014. U-Pb detrital zircon ages from the Aguapeí Group (Brazil): Implications for the geological evolution of the SW border of the Amazonian Craton. *Precambrian Research*, **244**(1):306-316.

Gibbs A.K. 1987. Contrasting styles of continental mafic intrusions in the Guiana Shield. ***In***: Halls H.C. & Fahrig W.F. (eds.) *Mafic dyke swarms*. Geological Association of Canada, Special paper, **34**:457-465.

Girardi V.A.V., Corrêa da Costa P.C., Teixeira W. 2012. Petrology and Sr–Nd characteristics of the Nova Lacerda dike swarm, SW Amazonian Craton: new insights regarding its subcontinental mantle source and Mesoproterozoic geodynamics. *International Geology Review*, **54**(2):165-182.

Gower C.F., Ryan A.F., Rivers T. 1990. Mid-Proterozoic Laurentia-Baltica: an overview of its geological evolution and summary of the contributions made by this volume. ***In:*** Gower C.F., Rivers T., Ryan B. (eds.) *Mid Proterozoic Laurentia-Baltica*. Geological Association of Canada, St. John's Newfoundland, p. 23-40.

Halls H.C. & Pesonen L.J. 1982. Paleomagnetism of Keweenawan rocks. *Geological Society of America Memoirs*, **156**:173-201.

Hawkesworth C.J., Dhuime B., Pietranik A.B., Cawood P.A., Kemp A.I.S., Storey C.D. 2010. The generation and evolution of the continental crust. *Journal of the Geological Society*, **167**:229-248.

Hoffman P.F. 1989. Speculations on Laurentia's first gigayear (2.0 to 1.0 Ga). *Geology*, **17**:135-138.

Hoffman P.F. 1991. Did the breakout of Laurentia turn Gondwanaland inside-out? *Science*, **252**:1409-1412.

Hoffman P.F. 1997. Tectonic genealogy of North America. *In*: van der Pluijm B.A. & Marshak S. (eds.) *An introduction to structural geology and tectonics*. McGraw Hill, New York, p. 459-464.

Hou G., Santosh M., Qian X., Lister G.S., Li J. 2008a. Configuration of the Late Paleoproterozoic supercontinent Columbia: Insights from radiating mafic dyke swarms. *Gondwana Research*, **14**:395-409.

Hou G., Santosh M., Qian X., Lister G.S., Li J. 2008b. Tectonic constraints on 1.3~1.2 Ga final breakup of Columbia supercontinent from a giant radiating dyke swarm. *Gondwana Research*, **14**:561-566.

Ibanez-Mejia M., Ruiz J., Valencia V.A., Cardona A., Gehrels G.E., Mora A.R. 2011. The Putumayo Orogen of Amazonia and its implications for Rodinia reconstructions : New U-Pb geochronological insights into the Proterozoic tectonic evolution of northwestern South America. *Precambrian Research*, **191**:58-77.

Irving E. & Naldrett A.J. 1977. Paleomagnetism in Abitibi greenstone belt, and Abitibi and Matachewan diabase dykes: evidence of the Archean geomagnetic field. *The Journal of Geology*, **85**:157-176.

Johansson Å. 2009. Baltica, Amazonia and the SAMBA connection – 1000 million years of neighbourhood during the Proterozoic? *Precambrian Research*, **175**:221-234.

Johansson Å. 2014. From Rodinia to Gondwana with the 'SAMBA' model – a distant view from Baltica towards Amazonia and beyond. *Precambrian Research*, **244**:226-235.

Kah L.C., Lyons T.W., Chesley J.T. 2001. Geochemistry of a 1.2 Ga carbonate-evaporite succession, northern Baffin and Bylot Islands: implications for Mesoproterozoic marine evolution. *Precambrian Research*, **111**:203-234.

Karlstrom K., Åhäll K.I., Harlan S.S., Williams M.L., McLelland J., Geissman J.W. 2001. Long-Lived (1.8-1.0 Ga) convergent orogen in southern Laurentia, its extensions to Australia and Baltica, and implications for refining Rodinia. *Precambrian Research*, **111**:5-30.

Krogh T.E., Corfu F., Davis D.W., Dunning G.R., Heaman L.M., Kamo S.L., Machado N., Greenough J.D., Nakamura E. 1987. Precise U-Pb isotopic ages of diabase dyke and mafic to ultramafic rocks using trace amounts of baddeleyite and zircon. *In*: Halls H.C. & Fahrig W.F. (eds.) *Mafic dyke swarms*. Geological Association of Canada, Special Paper, **34**, p. 147-152.

Kröner T.M. & Cordani U.G. 2003. African, southern India and South American cratons were not part of the Rodinia supercontinent: evidence from field relationships and geochronology. *Tectonophysics*, **375**:325-352.

Kusky T.M., Li J., Santosh M. 2007. The Paleoproterozoic North Hebei Orogen: North China craton's collisional suture with the Columbia supercontinent. *Gondwana Research*, **12**:4-28.

Lacerda-Filho J.V., Abreu Filho W., Valente C.R., Oliveira C.C., Albuquerque M.C. 2004. *Geologia e Recursos Minerais do Estado do Mato Grosso. Escala 1:1.000.000*. Texto explicativo dos mapas geológicos e de recursos minerais do Estado do Mato Grosso, Convênio CPRM e SICME-MT, 235 p.

Ledru P., Cocherie A., Barbosa J., Johan V., Onstott T. 1994. Ages du métamorphisme granulitique dans le craton du São Francisco (Brésil). Implications sur la nature de l'orogène transamazonien. *Comptes Rendus de l'Academie des Sciences*, Paris II, **318**:251-257.

Leite J.A.D. & Saes G.S. 2003. Geocronologia Pb/Pb de zircões detríticos e análise estratigráfica das coberturas sedimentares Proterozóicas do sudeste do Craton Amazônico. *Revista do Instituto de Geociências da USP*, **3**:113-127.

Li Z.X., Bogdanova S.V., Collins A.S., Davidson A., De Waele B., Ernst R.E., Fitzsimons I.C.W., Fuck R.A., Gladkochub D.P., Jacobs J., Karlstrom K.E., Lu S., Natapov L.M., Pease V., Pisarevsky S.A., Thrane K., Vernikovsky V. 2008. Assembly, configuration, and break-up history of Rodinia: A synthesis. *Precambrian Research*, **160**:179-210.

Litherland M., Annells R.N., Darbyshire D.P.F., Fletcher C.J.N., Hawkins M.P., Klinck B.A., Mitchell W.I., O'Connor E.A., Pitfield P.E.J., Power G., Webb B.C. 1989. The Proterozoic of Eastern Bolivia and its relationship to the Andean mobile belt. *Precambrian Research*, **43**:157-174.

Lubnina N.V., Stepanova A.V., Ernst R.E., Nilsson M., Söderlund U. 2016. New U-Pb baddeleyite age, and AMS and paleomagnetic data for dolerites in the Lake Onega region belonging to the 1.98-1.95 Ga regional Pechenga–Onega Large Igneous Province. *GFF*, **138**(1):54-78.

McGee B., Collins A.S., Trindade R.I.F. 2012. G'day Gondwana – the final accretion of a supercontinent: U-Pb ages from the post-oroigenic São Vicente Granite, northern Paraguay Belt, Brazil. *Gondwana Research*, **21**:316-322.

McGee B., Collins A.S., Trindade R.I. 2013. A glacially incised canyon in Brazil: Further evidence for mid-Ediacaran glaciation? *The Journal of Geology*, **121**(3):275-287.

McGee B., Collins A.S., Trindade R.I.F., Jourdan F. 2015a. Investigating mid-Ediacaran glaciation and final Gondwana amalgamation using coupled sedimentology and ^{40}Ar-^{39}Ar detrital muscovite provenance from the Paraguay Belt, Brazil. *Sedimentology*, **62**:130-154.

McGee B., Collins A.S., Trindade R.I., Payne J. 2015b. Age and provenance of the Cryogenian to Cambrian passive margin to foreland basin sequence of the northern Paraguay Belt, Brazil. *Geological Society of America Bulletin*, **127**(1-2):76-86.

McMenamim M.A.S. & McMenamim D.L.S. 1990. *The emergence of animals: the Cambrian breakthrough*. Columbia University Press, New York, 217 p.

Meert J.G. 2002. Paleomagnetic Evidence for a Paleo-Mesoproterozoic Supercontinent Columbia. *Gondwana Research*, **5**:207-215.

Meert J.G. 2009. Palaeomagnetism: In GAD we trust. *Nature Geoscience*, **2**(10):673-674.

Meert J.G. 2012. What's in a name? The Columbia (Paleopangaea/Nuna) supercontinent. *Gondwana Research*, **21**:987-993.

Meert J.G. & Van der Voo R. 1997. The assembly of Gondwana 800-550Ma. *Journal of Geodynamics*, **23**:223-235.

Meert J.G. & Torsvik T.H. 2003. The making and unmaking of a supercontinent: Rodinia revisited. *Tectonophysics*, **375**:261-288.

Mitchell R.N., Bleeker W., van Breemen O., Lecheminant T.N., Peng P., Nilsson M.K.M., Evans D.A.D. 2014. Plate tectonics before 2.0 Ga: Evidence from Paleomagnetism of cratons within Supercontinent Nuna. *American Journal of Science*, **314**:878-894.

Nadeau S., Chen W., Reece J., Lachhman D., Ault R., Faraco M.T.L., Fraga L.M., Reis N.J., Betiollo L.M. 2013. Guyana: The lost hadean crust of South America? *Brazilian Journal of Geology*, **43**(4):601-606.

Nomade S., Chen Y., Féraud G., Pouclet A., Théveniaut H. 2001. First paleomagnetic and ^{40}Ar/^{39}Ar study of Paleoproterozoic rocks from the French Guyana (Camopi and Oyapok rivers), northeastern Guyana Shield. *Precambrian Research*, **109**:239-256.

Nomade S., Chen Y., Pouclet A., Féraud G., Théveniaut H., Daouda B.Y., Vidal M., Rigolet C. 2003. The Guiana and West African Shield Palaeoproterozoic grouping: new palaeomagnetic data for French Guiana and Ivory Coast. *Geophysical Journal International*, **154**:677-694.

Onstott T.C. & Hargraves R.B. 1981. Proterozoic transcurrent tectonics: palaeomagnetic evidence from Venezuela and Africa. *Nature*, **289**:131-136.

Onstott T.C. & Dorbor J. 1987. $^{40}Ar/^{39}Ar$ and paleomagnetic results from Liberia and the Precambrian APW data base for the West African Shield. *Journal of African Earth Sciences*, **6**:537-552.

Onstott T.C., Hargraves R.B., York D. 1984a. Dating of Precambrian diabase dykes of Venezuela using Paleomagnetic and $^{40}Ar/^{39}Ar$ methods. *Anais II do Simpósio Amazônico*, Manaus, Brasil, DNPM, **2**:513-518.

Onstott T.C., Hargraves R.B., York D., Hall C. 1984b. Constraints on the motions of South American and African shields during the Proterozoic: I. $^{40}Ar/^{39}Ar$ and paleomagnetic correlations between Venezuela and Liberia. *Geological Society of America Bulletin*, **95**:1045-1054.

Onstott T.C., Hall C.M., York D. 1989. $^{40}Ar/^{39}Ar$ thermochronometry of the Imataca Complex, Venezuela. *Precambrian Research*, **42**:255-291.

Pehrsson S.J., Eglington B.M., Evans D.A.D., Huston D., Reddy S. 2016. Metallogeny and its link to orogenic style during the Nuna supercontinent cycle. *In*: Li Z.X., Evans D.A.D., Murphy J.B. *Supercontinent Cycles Through Earth History*. Geological Society, London, Special Publications, **424**:83-94.

Pesonen L.J., Elming S.Å., Mertanen S., Pisarevsky S., D'Agrella-Filho M.S., Meert J.G., Schmidt P.W., Abrahamsen N., Bylund G. 2003. Palaeomagnetic configuration of continents during the Proterozoic. *Tectonophysics*, **375**:289-324.

Pesonen L.J., Mertanen S., Veikkolainen T. 2012. Paleo-Mesoproterozoic Supercontinents – A paleomagnetic view. *Geophysica*, **47**:5-47.

Pinho M.A.S.B., Chemale Jr F., Van Schmus W.R., Pinho F.E.C. 2003. U-Pb and Sm-Nd evidence for 1.76-1.77 Ga magmatism in the Moriru region, Mato Grosso, Brazil: Implications for province boundaries in the SW Amazon Craton. *Precambrian Research*, **126**:1-25.

Piper J.D.A. 2010. Protopangea: Palaeomagnetic definition of Earth´s oldest (mid-Archaean-Palaeoproterozoic) supercontinent. *Journal of Geodynamics*, **50**:154-165.

Piper J.D.A. & Lomax K. 1973. Palaeomagnetism of Precambrian Birrimian and Tarkwaian rocks of West Africa. *Geophysical Journal of the Royal Astronomical Society*, **34**:435-450.

Pisarevsky S.A. & Bylund G. 2010. Paleomagnetism of 1780–1770 Ma mafic and composite intrusions of Småland (Sweden): Implications for the Mesoproterozoic Supercontinent. *American Journal of Science*, **310**:1168-1186.

Pisarevsky S.A., Wingate M.T.D., Powell C., Johnson S., Evans D.A.D. 2003. Models of Rodinia assembly and fragmentation. In: Yoshida M. (ed.) Proterozoic East Gondwana : Supercontinent Assembly and Breaup. *Geological Society, London, Special Publications*, **206**:35-55.

Pisarevsky S.A., Elming S-Å., Pesonen L.J., Li Z.X. 2014. Mesoproterozoic paleogeography: Supercontinent and beyond. *Precambrian Research*, **244**:207-225.

Rämö O.T., McLemore V.T., Hamilton M.A., Kosunen P.J., Heizler M., Haapala I. 2003. Intermittent 1630-1220 Ma magmatism in central Mazatzal Province: new geochronologic piercing points and some tectonic implications. *Geology*, **31**:335-338.

Reddy S.M., Evans D.A.D. 2009. Palaeoproterozoic supercontinents and global evolution: correlations from core to atmosphere. In: Reddy S.M., Mazunder R., Evans D.A.D., Collins A.S. (eds.) Palaeoproterozoic Supercontinents and Global Evolution. *Geological Society of London, Special Publications*, **323**:1-26.

Reis N.J., Fraga L.M.B., Faria M.S.G., Almeida M.E. 2003. Geologia do Estado de Roraima, Brasil. *In: Geology of France and Surrounding Areas – Special Guiana Shield*, BRGM, (2-3-4):121-134.

Reis N.J., Teixeira W., Hamilton M.A., Bispo-Santos F., Almeida M.E., D'Agrella-Filho M.S. 2013. The Avanavero mafic magmatism, a late Paleoproterozoic LIP in the Guiana Shield, Amazonian Craton: U-Pb TIMS baddeleyite, geochemical and paleomagnetic evidence. *Lithos*, **174**:175-195.

Rizzotto G.J. & Hartmann L.A. 2012. Geological and geochemical evolution of the Trincheira Complex, a Mesoproterozoic ophiolite in the southwestern Amazon craton, Brazil. *Lithos*, **148**:277-295.

Rogers J.J.W. 1996. A history of continents in the past three billion years. *The Journal of Geology*, **104**:91-107.

Rogers J.J.W. & Santosh M. 2002. Configuration of Columbia, a Mesoproterozoic Supercontinent. *Gondwana Research*, **5**:5-22.

Rogers J.J.W. & Santosh M. 2009. Tectonics and surface effects of the supercontinent Columbia. *Gondwana Research*, **15**:373-380.

Ruiz A.S. 2005. *Evolução geológica do Sudoeste do Cráton Amazônico na região limítrofe Brasil-Bolívia*. PhD Thesis, Universidade Estadual Paulista, Rio Claro, 259 p.

Sadowski G.R. & Bettencourt J.S. 1996. Neoproterozoic tectonic correlations between east Laurentia and the western border of the Amazon Craton. *Precambrian Research*, **76**:213-227.

Salminen J. & Pesonen L.J. 2007. Paleomagnetic and rock magnetic study of the Meso-proterozoic sill, Valaam island, Russian Karelia. *Precambrian Research*, **159**:212-230.

Santos J.O.S., Hartmann L.A., Gaudette H.E., Groves D.I., McNaugthon N.J., Fletcher I.R. 2000. A new understanding of the Provinces of Amazon Craton based on integration of field mapping and U-Pb and Sm-Nd geochronology. *Gondwana Research*, **3**:453-488.

Santos J.O.S., Rizzotto G.A., Hartmann L.A., McNaughton N.J., Fletcher L.R. 2001. Ages of sedimentary basins related to the Sunsas and Juruena orogenies, Southwest Amazon Craton established by zircon U-Pb geochronology. *In*: Workshop Geology of the SW Amazonian Craton: State-of-the-Art. *Extended Abstract*, São Paulo, p. 114-118.

Santos J.O.S, Potter P.E., Reis N.J., Hartmann L.A., Fletcher I.R., McNaughton N.J. 2003. Age, source, and regional stratigraphy of the Roraima Supergroup and Roraima-like outliers in northern South America based on U-Pb geochronology. *Geological Society of America Bulletin*, **3**:331-348.

Santos J.O.S., Rizzotto G.J., Potter P.E., McNaughton N.J., Matos R.S., Hartmann L.A., Chemale Jr. F., Quadros M.E.S. 2008. Age and autochthonous evolution of the Sunsás Orogen in West Amazon Craton based on mapping and U-Pb geochronology. *Precambrian Research*, **165**:120-152.

Schobbenhaus C. & Brito-Neves B.B. 2003. A geologia do Brasil no Contexto da Plataforma Sul-Americana. *In*: Bizzi L.A., Schobbenhaus C., Vidotti R.M., Gonçalves J.H. (eds.) *Geologia, tectônica e recursos minerais do Brasil: texto, mapas & SIG*. Brasília, CPRM – Serviço Geológico do Brasil, 692 p.

Schobbenhaus C., Campos D.A., Derze G.R., Asmus H.E. 1984. *Geologia do Brasil: Texto explicativo do Mapa Geológico do Brasil e da área oceânica adjacente incluindo depósitos minerais. Escala 1:2.500.000*. Brasília, DNPM, 501 p.

Schobbenhaus C., Hoppe A., Lork A., Baumann A. 1994. Idade U/Pb do magmatismo Uatumã no norte do Cráton Amazônico, Escudo das Guianas (Brasil): primeiros resultados. *In: Congresso Brasileiro de Geologia*, Sociedade Brasileira de Geologia, **38**:395-397.

Schobbenhaus C., Gonçalves J.H., Santos J.O.S., Abram M.B., Leão Neto R., Matos G.M.M., Vidotti R.M., Ramos M.A.B., Jesus J.D.A. 2004. *Carta Geológica do Brasil ao Milionésimo*. Sistema de Informações Geográficas. Folhas Boa Vista (NA-20) e Roraima (NB-20). Escala 1:1,000,000, CPRM.

Silver P.G. & Behn D. 2008. Intermittent plate tectonics. *Science*, **319**:85-88.

Smirnov A.V., Evans D.A.D., Ernst R.E., Söderlund U., Li A.X. 2013. Trading partners: Tectonic ancestry of southern Africa and Western Australia, in Archean supercratons Vaalbara and Zimgarn. *Precambrian Research*, **224**:11-22.

Swanson-Hysell N.L., Maloof A.C., Weiss B.P., Evans D.A. 2009. No asymmetry in geomagnetic reversals recorded by 1.1-billion-year-old Keweenawan basalts. *Nature Geoscience*, **2**:713-717.

Tamura L.N., D'Agrella-Filho M.S., Trindade R.I., Teixeira W., Ruiz A.S. 2013. Estudo paleomagnético do enxame de diques máficos Rancho de Prata. *In*: 13º Simpósio de Geologia da Amazônia, *Anais*, Belém, Pará, CDR (21), 4 p.

Tassinari C.C.G. & Macambira M.J.B. 1999. Geochronological provinces of the Amazonian Craton. *Episodes*, **22**:174-182.

Tassinari C.C.G. & Macambira M.J.B. 2004. A evolução tectônica do Cráton Amazônico. *In*: Mantesso-Neto V., Bartorelli A., Dal Ré Carneiro C., Brito-Neves B.B. (eds.) *Geologia do Continente Sul-Americano*: Evolução da obra de Fernando Flávio Marques de Almeida. São Paulo, Beca, p. 471-485.

Tassinari C.C.G., Cordani U.G., Nutman A.P., van Schmus W.R., Bettencourt J.S., Taylor P.N. 1996. Geochronological systematics on basement rocks from the Rio Negro-Juruena Province (Amazon C Rio Alegre Terrainon) and tectonic implications. *International Geology Review*, **38**:1161-1175.

Tassinari C.C.G., Bettencourt J.S., Geraldes M.C., Macambira M.J.B., Lafon J.M. 2000. The Amazonian Craton. ***In***: Cordani U.G., Milani E.J., Thomaz-Filho A., Campos D.A. (eds.) *Tectonic Evolution of South America*. Rio de Janeiro, 31st International Geological Congress, p. 41-95.

Teixeira W., Geraldes M.C., Matos R., Ruiz A.S., Saes G., Vargas-Mattos G. 2010. A review of the tectonic evolution of the Sunsas belt, SW portion of the Amazonian Craton. *Journal of South American Earth Sciences*, **29**:47-60.

Teixeira W., Geraldes M.C., D'Agrella-Filho M.S., Santos J.O.S., Barros M.S.S., Ruiz A.S., Corrêa da Costa P.C. 2011. Mesoproterozoic juvenile mafic-ultramafic magmatism in the SW Amazonian Craton (Rio Negro-Juruena province): SHRIMP U-Pb geochronology and Nd-Sr constraints of the Figueira Branca Suite. *Journal of South American Earth Sciences*, **32**:309-329.

Teixeira W., Ernst E.E., Hamilton M., Lima G., Ruiz A.S., Geraldes M.C. 2016. Widespread ca. 1.4 Ga intraplate magmatism and tectonics in a growing Amazonia. *GFF*, **138**(1):241-254.

Théveniaut H., Delor C., Lafon J.M., Monié P., Rossi P., Lahondère D. 2006. Paleoproterozoic (2155–1970 Ma) evolution of the Guiana Shield (Transamazonian event) in the light of new paleomagnetic data from French Guiana. *Precambrian Research*, **150**:221-256.

Tohver E. & Trindade R.I.F. 2014. Comment on was there an ediacaran clymene ocean in central South America by Cordani UG and others. *American Journal of Science*, **314**(3):805-813.

Tohver E., van der Pluijm B., van der Voo R., Rizzotto G., Scandolara J.E. 2002. Paleogeography of the Amazon craton at 1.2 Ga: early Grenvillian collision with the Llano segment of Laurentia. *Earth and Planetary Science Letters*, **199**:185-200.

Tohver E., van der Pluijm B., Mezger K., Essene E., Scandolara J. 2004a. Significance of the Nova Brasilândia metasedimentary belt in western Brazil: redefining the Mesoproterozoic boundary of the Amazon Craton. *Tectonics*, **23**(6):TC6004:1-20.

Tohver E., Bettencourt J.S., Tosdal R., Mezger K., Leite W.B., Payolla B.L. 2004b. Terrane transfer during the Grenville orogeny: tracing the Amazonian ancestry of southern Appalachian basement through Pb and Nd isotopes. *Earth and Planetary Science Letters*, **228**:161-176.

Tohver E., D'Agrella-Filho M.S., Trindade R.I.F. 2006. Paleomagnetic record of Africa and South America for the 1200-500 Ma interval, and evaluation of Rodinia and Gondwana assemblies. *Precambrian Research*, **147**:193-222.

Tohver E., Trindade R.I.F., Solum J.G., Hall C.M., Riccomini C., Nogueira A.C. 2010. Closing the Clymene ocean and bending a Brasiliano belt: Evidence for the Cambrian formation of Gondwana, southeast Amazon Craton. *Geology*, **38**:267-270.

Tohver E., Cawood P.A., Rossello E.A., Jourdan F. 2012. Closure of the Clymene Ocean and formation of West Gondwana in the Cambrian: Evidence from the Sierras Australes of the southernmost Rio de la Plata craton, Argentina. *Gondwana Research*, **21**:394-405.

Torsvik T.H. & Smethurst M.A. 1999. Plate tectonic modelling: virtual reality with GMAP1. *Computers & Geosciences*, **25**:395-402.

Trindade R.I.F., Font E., D'Agrella-Filho M.S., Nogueira A.C.R., Riccomini C. 2003. Amazônia at low-latitude by the end of the ~600 Ma Puga glaciation. *Terra Nova*, **15**:441-446.

Trindade R.I.F., D'Agrella-Filho M.S., Epof I., Brito-Neves B.B. 2006. Paleomagnetism of the Early Cambrian Itabaiana mafic dykes, NE Brazil, and implications for the final assembly of Gondwana and its proximity to Laurentia. *Earth and Planetary Science Letters*, **244**:361-377.

Trompette R. 1994. *Geology of Western Gondwana (2000-500 Ma)*. Pan-African-Brasiliano aggregation of South America and Africa. A.A. Balkema, Rotterdam, Brookfield, 366 p.

Trompette R. 1997. Neoproterozoic (~600Ma) aggregation of Western Gondwana: a tentative scenario. *Precambrian Research*, **82**:101-112.

Valdespino O.E.M. & Alvarez V.C. 1997. Paleomagnetic and rock magnetic evidence for inverse zoning in the Parguaza batholith (southwestern Venezuela) and its implications about tectonics of the Guyana shield. *Precambrian Research*, **85**:1-25.

Vanderhaeghe O., Ledru P., Thiéblemeont D., Egal E., Cocherie A., Tegyey M., Milesi J.P. 1998. Contrasting mechanism of crustal growth Geodynamic evolution of the granite-greenstone belts of French Guiana. *Precambrian Research*, **85**:1-25.

Van der Voo R. 1990. The reliability of paleomagnetic data. *Tectonophysics*, **184**:1-9.

Van Der Voo R. & Torsvik T.H. 2012. The history of remagnetization of sedimentary rocks: deceptions, developments and discoveries. *Geological Society, London, Special Publications*, **371**:23-53.

Veikkolainen T., Heinonen A., Pesonen L.J., Fraga L.M., Rämö O.T., Dall'Agnol R. 2011. Mucajaí-kompleksin (Pohjois-Amazonia, Brasilia) paleomagnetismista. *XXV GEOFYSIIKAN PÄIVÄT*, 121-124.

Veldkamp J., Mulder F.G., Zijderveld J.D.A. 1971. Palaeomagnetism of Suriname dolerites. ***Physics of the*** *Earth and Planetary Interiors*, **4**:370-380.

Vigneresse J.L. 2005. The specific case of the Mid-Proterozoic rapakivi granites and associated suite within the context of the Columbia Supercontinent. *Precambrian Research*, **137**:1-34.

Wegener A. 1912. The origin of the continents. *Petermanns Geographische Mitteilungen*, **58**(1):185-195, 253-256, 305-309.

Weil A.B., van der Voo R., Niocaill C.M., Meert J.G. 1998. The Proterozoic supercontinent Rodinia: paleomagnetically derived reconstructions for 1100 to 800 Ma. *Earth and Planetary Science Letters*, **154**:13-24.

Williams S., Müller R.D., Landgrebe T.C.W., Whittaker J.M. 2012. An open-source software environment for visualizing and refining plate tectonic reconstructions using high resolution geological and geophysical data sets. *GSA Today*, **22**(4/5):4-9.

Wingate M.T.D., Pisarevsky S.A., Gladkochub D.P., Donskaya T.V., Konstantinov K.M., Mazukabzov A.M., Stanevich A.M. 2009. Geochronology and paleomagnetism of mafic igneous rocks in the Olenek Uplift, northern Siberia: implications for Mesoproterozoic supercontinents and paleogeography. *Precambrian Research*, **170**:256-266.

Xu H., Yang Z., Peng P., Meert J.G., Zhu R. 2014. Paleo-position of the North China craton within the Supercontinent Columbia: Constraints from new paleomagnetic results. *Precambrian Research*, **255**:276-293.

Yakubchuk A. 2010. Restoring the supercontinent Columbia and tracing its fragments after its breakup: A new configuration and a Super Horde hypothesis. *Journal of Geodynamics*, **50**:166-175.

Zhang S., Li Z.X., Evans D.A.D., Wu H., Li H., Dong J. 2012. Pre-Rodinia supercontinent NUNA shaping up: A global synthesis with new paleomagnetic results from North China. *Earth and Planetary Science Letters*, **353-354**:145-155.

Zhao G., Cawood P.A., Wilde S.A., Sun M. 2002. Review of global 2.1-1.8 Ga orogens: implications for a pre-Rodinia supercontinent. *Earth-Science Reviews*, **59**:125-162.

Zhao G., Sun M., Wilde S.A., Li S. 2003. Assembly, accretion and breakup of the Paleo-Mesoproterozoic Columbia Supercontinent: records in the North China Craton. *Gondwana Research*, **6**:417-434.

Zhao G., Sun M., Wilde S.A., Li S. 2004. A Paleo-Mesoproterozoic supercontinent: assembly, growth and breakup. *Earth-Science Reviews*, **67**:91-123.

Zhao G., Sun M., Wilde S.M., Sanzhong L., Zhang J. 2006. Some key issues in reconstructions of Proterozoic supercontinents. *Journal of Asian Earth Sciences*, **28**:3-19.

Available at www.sbgeo.org.br

Chapter. 3: The Carajás Province, Sampling

3.1 Target of the study: The Uatumã LIP, a Paleoproterozoic SLIP

A large part of the Amazonian craton (1, 500, 000 km^2) located in northern Brazil and neighboring countries, is represented by volcanic and plutonic rocks dated between 1880 and 1860 Ma (Figure 3.1). This magmatic event is located in the Central – Amazonian Province (Cordani and Teixeira, 2007) and is considered as one of the largest continental magmatic event occurred during the Paleoproterozoic Era (Ernst, 2014). These rocks were formed in intracontinental framework and were not affected by younger orogeneses. This large igneous province is usually called the Uatumã event *"sensu stricto"*. Some authors argue for a Uatumã event "*sensu lato*" or Uatumã Supergroup, forming by a single LIP event running between 1980 and 1860 Ma (~100 Ma) (Ferron et al., 2010; Juliani and Fernandes, 2010). The main magmatic activity happened in an interval of 10 Ma, although the magmatic province lasted at least 29 Ma. Its orogenic or anorogenic setting is still debated, but many arguments reinforce the idea that it could be a **SLIP** (Silicic (~felsic) Large Igneous Province) (Ernst, 2014; Ferreira and Lamarão, 2013; Klein et al., 2012) as defined by Bryan and Ferrari (2013). We observe the predominance of ignimbrites and rhyolites associated with mafic and felsic dikes. The chemical signature of the felsic rocks is mainly A-type, but it is possible to find rare calk-alkaline and transitional magmas. This magmatism took place at the end, or immediately after the last orogenic stage in each tectonic domain, which may have favored the crustal melting. The main ore minerals associated with this event are gold and tin of epithermal origin. Many volcanic and plutonic units belonging to different tectonic domains of the craton have been associated with this event and thus carries different names depending on the locality. In the Uatumã – Anaua domain (northern Guiana shield) we find the Mapuera granites associated with the Iricoumé group. In the southwestern of the craton (Iriri – Xingu domain), we can find the Velho Guilherme plutonic suite associated with the Iriri volcanics and Santa Rosa formation in the São Felix do Xingu area. In the Carajás area we observe mainly A-type granites (Jamon, Musa, Serra dos Carajás, Cigano, Rio Branco) and associated dikes, without volcanic rocks. In the Tapajós domain A-type granites belonging to the Maloquinha suite occur. In southern Amazonian craton the Rio Dourado plutonic suite is associated to the Iriri group.

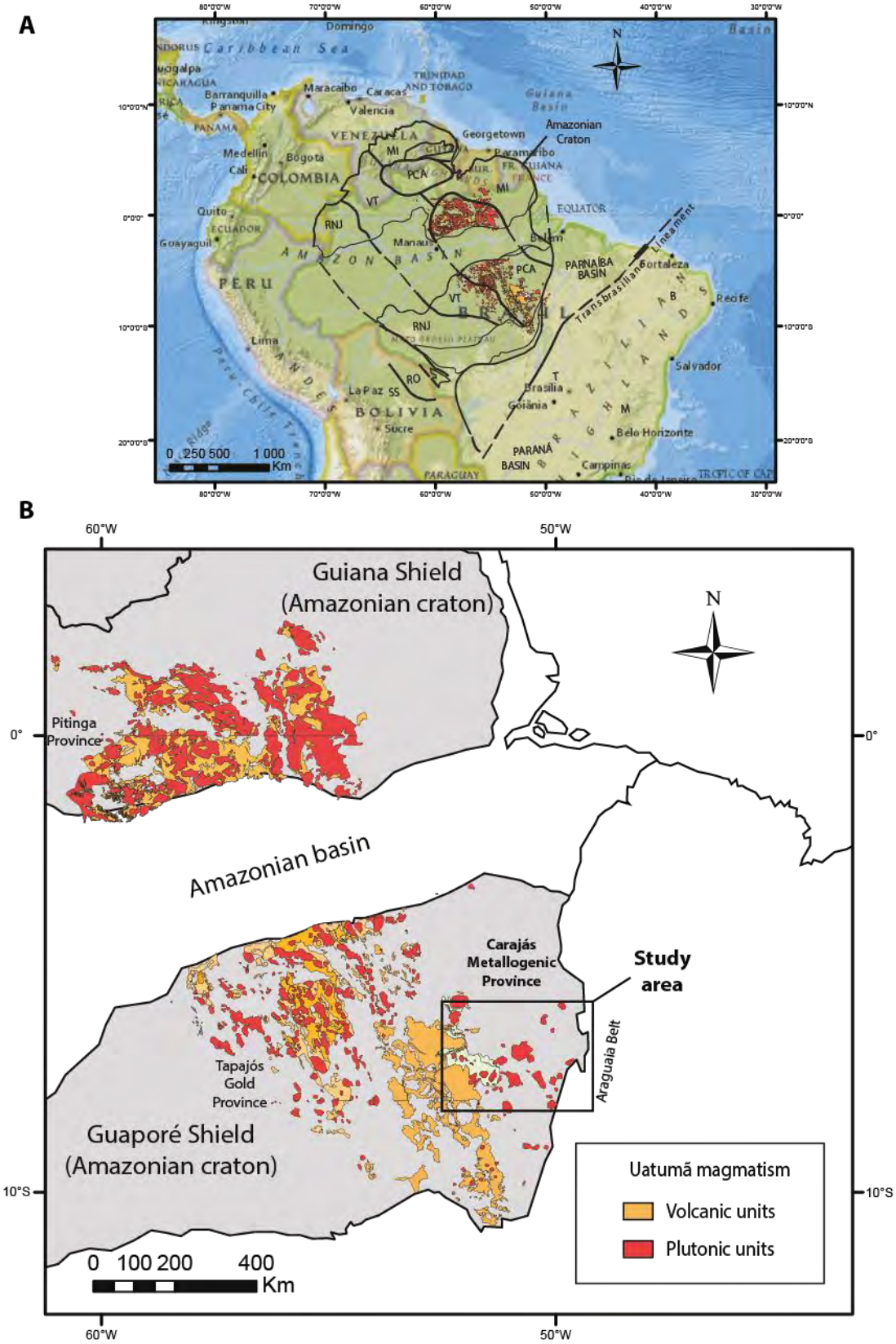

Figure 3.1: A: Uatumã event in the Amazonian craton related with the geochronological provinces (Cordani and Teixeira, 2007). PCA - Central Amazonia Province; MI - Maroni-Itacaiunas Province; VT – Ventuari-Tapajós Province; RNJ – Rio Negro-Juruena Province; RO – Rondonia-San Ignacio Province; SS – Sunsás-Aguapeí Province. B: Distribution of volcanic and plutonic units from the Uatumã event and localization of the Carajás province.

From a petrological standpoint, plutonic units have been studied in detail (Dall'Agnol et al., 1999a; Dall'Agnol et al., 2005), in contrast to the volcanic units and the associated plumbing system (dikes). The size and age of the Uatumã event are not yet well constrained due to the many Pb-Pb ages of low quality.

Furthermore, thanks to the large exposed areas and the large number of geochronological data, the Amazonian craton offers a unique opportunity to characterize this volcanism, associating it to its original plutonism. This work is therefore part of a multidisciplinary research by combining petrology with a paleomagnetic study to help deciphering the Amazonian craton evolution during Paleoproterozoic

3.2 The Carajás Province

The Carajás Province is the oldest and best preserved crustal portion of the Amazonian Craton, located in its southeastern margin. It is part of the Central Amazonian Province (Cordani and Teixeira, 2007; Tassinari and Macambira, 2004), and is considered as a region whose formation and tectonic stability occurred during the Archean, which was not affected by the “Transamazonic orogenic cycle”. According to Brito Neves (2011) the term "Transamazonian cycle" should be avoided because it was used to include all Paleoproterozoic events from the Siderian (2500 – 2300 Ma) to the Statherian (1800 – 1600 Ma). Santos et al. (2003a) divided the Carajás Province into two parts, the Rio Maria (south) and the Carajás domains (north) (Figure 3.2). The boundary between the two areas has been defined using magnetometric anomalies, which do not coincide with a geological unconformity. This limit is located to the northern of Tucumã city.

In the Carajás domain, the Plaquê granite is a lenticular body, preferentially oriented in the E-W direction, which according to Araújo and Maia (1991) is concordant with the Xingu complex (Figure 3.2). Orthogneisses, migmatites and granitoids of the Xingu Complex represent a Mesoarchean Granite – Gneiss - migmatite association, which is the basement of this domain. This domain was affected by Neoarchean events (3000 – 2750 Ma) (Feio et al., 2013). Currently, the Carajás domain was divided into the Canaã and Sapucaia domains reflecting the complexity of Neoarchean events (Figure 3.2) (Dall’Agnoll et al., 2013).

The Rio Maria domain area is an Archean terrane which contains the oldest rocks of the Amazonian craton. It is characterized by a Mesoarchean juvenile crust, with sequences of greenstone belts and TTG-type and sanukitoid granitoids (3000 – 2860 Ma). A striking structural feature is the *ca*. 100 km NW-SE Seringa fault (not visible the map), which cuts across the rocks of the Tucumã Group (greenstone belt).

The Carajás Province was intruded by many Paleoproterozoic anorogenic granites and associated dikes of the Uatumã event at *ca*. 1880 Ma (in red, Figure 3.2) (Dall'Agnol et al., 2005; Dall'Agnol and de Oliveira, 2007). The Jamon, Serra dos Carajás, and Velho Guilherme suites were recognized in the area. They are Paleoproterozoic A – type rapakivi granites with some differences in the degree of oxidation of their magmas and occurrence regions (Dall'Agnol and de Oliveira, 2007). Dall'Agnol et al. (2005) have suggested an extensional event that marks the initial break–up of the Columbia supercontinent. $\varepsilon_{Nd\ (1880\ Ma)}$ values range between -10.5 and -7.9 for the oxidized Jamon suite (Rämö et al., 2002; Teixeira et al., 2002) which suggest an Archean crustal–derived source for these granites. Dall'Agnol et al. (1999b) argued that a possible Archean source for these rocks is a biotite – hornblende quartz diorite, which is different of the Rio Maria composition. These volcanic rocks occur to the west in the São Felix do Xingu area, and are absent to east of this area (Figure 3.2). All Paleoproterozoic units are well-preserved without deformation and no younger orogenic event is recorded into the Carajás Province which is delimited to the east by the Brasiliano Araguaia Belt (~550 Ma).

Three Paleoproterozoic generations of dikes are observed in the Carajás Province, represented by rhyolitic, andesitic and basaltic dikes (Rivalenti et al., 1998). Two U-Pb ages (baddeleyite) confirm that these basaltic dikes are synchronous (1880 ± 2 Ma and 1885 Ma) with the 1880 Ma felsic magmatism (Teixeira et al., 2016). Recent ages obtained for some mafic dikes show that the Carajás region was affected by localized Phanerozoic events (Teixeira et al., 2016) (Table 3.1). Dating of NS - mafic dikes, located in the region of Parauapebas (NE - Carajás), yielded an U-Pb (on baddeleyite) age of 535 ± 1 Ma (Teixeira et al., 2012b). The dikes have the same direction and are coeval to the Araguaia-Pampeana orogenic Belt (540 – 520 Ma). The Neoproterozoic Araguaia fold belt show folding, faulting and low–angle thrust with vergence from W to NW, whose events was recorded by the Tocantins Group and mark the boundary with the Amazonian craton. The origin of this orogenic belt is yet debated but it could be related to the tectonic inversion of a small oceanic basin (Paixão et al., 2008). Low/medium greenschist metamorphism affected the middle portion of the belt and mylonitization and regional metamorphism (large amounts of fluids) of the Araguaia Belt with intrusion of syn-tectonic granites, as the Matança granite, can be observed (Kotschoubey et al., 2016). The true boundary between the Amazonian and São Francisco cratons could be under the Parnaíba Basin along the Transbrasiliano shear zone - TBSZ (de Azevedo et al., 2015). An alternative scenario suggests the presence of Parnaíba block between the Amazonian and the São Francisco cratons, and the Araguaiana fault zone would mark the suture to the west, between the Parnaíba Block and the Amazonian craton, and the TBSZ would be the suture to the east, between the Parnaíba block and the São Francisco Craton (Daly et al., 2014).

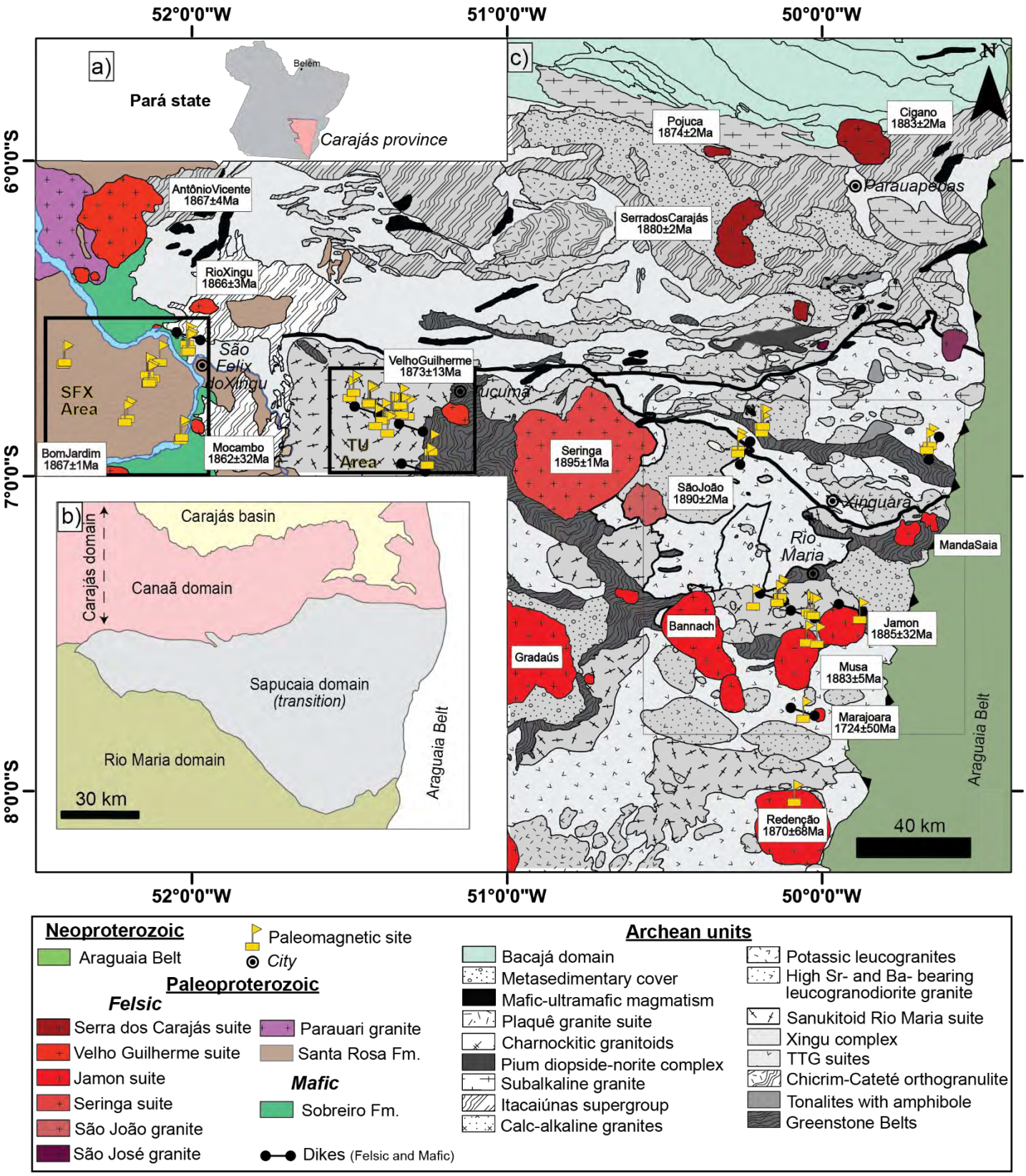

Figure 3.2: a) Localization of Carajás in the Pará state. b) Subdomains in the Carajás domain. c) Geological map of Carajás Province - adapted from the Pará geological map (Vasquez et al., 2008) showing the Paleoproterozoic volcano – plutonic event. The localization on all paleomagnetic sites is indicated as the Tucumã and São Felix do Xingu areas. Tu Area = Tucumã area, SFX Area = São Felix area.

New U-Pb age on baddeleyite extracted from other mafic dikes of the Carajás Province yilded age of 199.3 ± 0.3 Ma (Teixeira et al., 2012a). These dikes may be related to the extent of the continental flood basalts of the Central Magmatic Province (CAMP) (Ernesto et al., 1999; Marzoli et al., 1999). This is one of the largest known Phanerozoic igneous provinces dated at *ca*. 202 – 198 Ma during break–up of Pangea (Font et al., 2011; Marzoli et al., 2011).

Figure 3.3 shows a summary of the recorded events in the Carajás Province. All geochronological data in the Carajás Province were compiled, and only a few may be considered as reference ages (U-Pb dating). Most ages correspond to the Uatumã event and are present in each region in the Amazonian craton. Some data are localized and it seems (until today) difficult to associate them to a major event affecting the region. As example, a U-Pb age of *ca*. 1583 ± 7 Ma obtained for one ~10 m width dike (maybe AMCG magmatism) can be cited (Pimentel et al., 2003). Knowing these events is essential to know that could eventually affect magnetization of ~1880 Ma rocks. At the present knowledge, a remagnetization of these rocks could be at *ca*. 200 Ma (CAMP) and at *ca*. 550 Ma (Araguaia Belt).

The relative tectonic stability since the Paleoproterozoic, the well-defined units, the well-exposed rocks and the good road network makes the Carajás Province an ideal target for a paleomagnetic work. Three areas were sampled from east to west (Figure 3.2): (1) the Rio – Maria area, (2) the Tucumã area, and (3) the São Felix do Xingu area. We sampled 72 sites in the Carajás Province for this paleomagnetic study. Because of the lack of good paleomagnetic results, geochronological data and lack of geological consistency for the sampled dikes in the Rio Maria area (maybe related to the proximity with the Araguaia Belt), this thesis will focus on the Tucumã and São Felix do Xingu areas.

Table 3.1: Geochronological data for the Amazonian craton. *Abbreviations*: zrn= zircons, Ttn = titanite, wr = whole rock, badd = baddeleyite, Al = alunite, disc. = discordant age, int = lower intercept, Bt = biotite, musc = muscovite, iso = isochron, Mn = manganese. Ar – Ar ages of Tavares (2015) are cooling ages for Archean rocks. References: (Almeida et al., 2000; Alves, 2006; Amaral, 1974; Arcanjo et al., 2013; Avelar et al., 1994; Bahia and Quadros, 2000; Barbosa and Lafon, 1996; Cordani, 1981; da Silva et al., 2016; de Mesquita Barros et al., 2009; Feio et al., 2013; Gomes et al., 1975; Grainger et al., 2008; Juliani et al., 2005; Juliani and Fernandes, 2010; Lamarão et al., 2002; Macambira and Vale, 1997; Macambira, 1992; Macambira and Lafon, 1995; Macambira et al., 2000; Machado et al., 1991; Paixão et al., 2008; Pimentel and Machado, 1994; Pimentel et al., 2003; Pinho et al., 2006; Rodrigues, 1992; Roverato, 2016; Santos et al., 2002; Santos et al., 2001; Tavares, 2015; Teixeira et al., 2002; Teixeira et al., 2012a; Teixeira et al., 2012b; Vasconcelos et al., 1994).

Occurrence area	Rock type	Age	Method	References
Tapajos Gold Province (400 Km from SFX)				
Tapajós	Alunite (supergene)	51.3 ± 0.1 Ma	Ar-Ar Al	Juliani et al. (2005)
Cachoeira seca intrusive suite	Gabbro, diabase	1186 ± 12 Ma	U–Pb badd	Bahia and Quadros (2000), Santos et al. (2002)
Crepori diabase	Gabbro, diabase	1780 ± 7 Ma	U–Pb badd	Santos et al. (2002)
Maloquinha granite	Granite	1870 ± 4 Ma	U–Pb zrn	Lamarão et al. (2002)
Salustiano Fm.	Rhyolite	1870 ± 8 Ma	U–Pb zrn	Almeida et al. (2000)
Parauari intrusive suite	Granodiorite	1883 ± 4 Ma	U–Pb zrn	Almeida et al. (2000)
Tapajós	Alunite	1869 ± 2 Ma	Ar-Ar Al	Juliani et al. (2005)
Tapajós	Alunite (shearing)	1805 ± 2 Ma	Ar-Ar Al	Juliani et al. (2005)
Creporização suite	Monzogranite	1957 ± 6 Ma	U-Pb zrn	Santos et al. (2001)
Xingu region				
Cururu	Diabase dike	200 ± ? Ma		Macambira and Vale (1997)
Santa Rosa	Felsic dike	1857.0 ± 8.4 Ma	U–Pb zrn	Rovareto et al. (personal com.)
Mocambo Massif	Granite	1862 ± 32 Ma	Pb–Pb zrn	Teixeira et al. (2002)
Rio Xingu	Granite	1866 ± 3 Ma	Pb–Pb zrn	Teixeira et al. (2002)
Antônio Vicente	Granite	1867 ± 4 Ma	Pb–Pb zrn	Teixeira et al. (2002)
Bom Jardim	Granite	1867 ± 1	Pb–Pb zrn	Lamarão et al. (2012)
Uatumã Supergrpoup	Andesite + rhyolite	1875 ± 158 Ma	Pb–Pb wr	Teixeira et al. (2002)
Serra da Queimada Massif	Granite	1882 ± 12 Ma	Pb–Pb zrn	Pinho et al. (2006)
Sobreiro Formation	Dacite	1880 ± 6 Ma	Pb–Pb zrn	Pinho et al. (2006)
Iriri Formation	Granitic porphyry	1887 ± 2 Ma	Pb–Pb zrn	Pinho et al. (2006)
Iriri Formation	Granitic porphyry	1888 ± 3 Ma	Pb–Pb zrn	Pinho et al. (2006)
Iriri Formation	Granitic porphyry	1881 ± 3 Ma	Pb–Pb zrn	Pinho et al. (2006)
Iriri Formation	Granitic porphyry	1881 ± 2 Ma	Pb–Pb zrn	Pinho et al. (2006)
Santa Rosa Fm.	Ash tuff	1884 ± 1.7 Ma	Pb–Pb zrn	Juliani et al. (2010)
Santa Rosa Fm.	Rhyolite	1879 ± 2 Ma	Pb–Pb zrn	Juliani et al. (2010)
Santa Rosa Fm.	Ignimbrite	1881.5 ± 6.4 Ma	U–Pb zrn	Rovareto et al. (personal com.)
Tucumã region				
Velho Guilherme	Granite	1873 ± 13 Ma	Pb–Pb wr	Rodrigues et al. (1992)
Tucumã dikes	µgranite 54.PY79 (FDB29)	1880.9 ± 3.3 Ma	U–Pb zrn	Fernandes et al. (2016)
Tucumã dikes	µgranite 54.PY79 (FDB29)	1881.9 ± 4.4 Ma	U–Pb zrn	Fernandes et al. (2016)
Rio Maria region				
Marajoara	Granite	1724 ± 50 Ma	Rb–Sr wr	Macambira (1992)
Musa	Granite	1883 ± 5/-2 Ma	U–Pb zrn/Ttn	Machado et al. (1991)
Jamon	Granite	1885 ± 32 Ma	Pb–Pb zrn	Macambira and Dall'Agnol (1997)
Redenção	Granite	1870 ± 68 Ma	Pb–Pb zrn	Barbosa et al. (1995)
Seringa	Granite	1895 ± 1 Ma	Pb–Pb wr	Avelar et al. (1994)
Felsic dike	dike jamon	1885 ± 4	Pb–Pb zrn	Oliveira DC., unpublished data
Felsic dike	dike jamon	1886 ± 2	Pb–Pb zrn	Oliveira DC., unpublished data
Xingu Complex	Tonalitic orthogneisses	2867 ± 18 Ma	Pb–Pb zrn	Macambira et al. (2000)
Rio Maria	Granodiorite	2872 ± 5 Ma	U–Pb zrn/Ttn	Pimentel and Machado (1994)
Carajás region				
Haematite ore	Pebbles	72.6 ± 6	Ar-Ar in K-Mn-ox	Vasconselos et al. (1994)
Mafic dyke swarms	NW-basaltic dyke	1880 ± 2	U–Pb badd	Teixeira et al. (2016)
Mafic dyke swarms	NE-basaltic dyke	1885 (?)	U–Pb badd	Teixeira et al. (2016)
Parauapebas	NW-HTi dyke CJ-2	199.3 ± 0.3 Ma	U–Pb badd	Teixeira et al. (2012)
Parauapebas	NW-HTi dyke CJ-14	234 ± 11 Ma	K–Ar wr	Teixeira et al. (2012)
Parauapebas	NS-HTi dyke CJ-47	535.1 ± 0.9 Ma	U–Pb badd	Teixeira et al. (2012)
Parauapebas	NS-HTi dyke CJ-61	668 ± 14 Ma	K–Ar wr	Teixeira et al. (2012)
Formiga	Granite	600 ± ? Ma	Pb–Pb zrn disc.	Grainger et al. (2008)
Dyke (Salobo)	Diabase dyke	561 ± 16 Ma	Rb–Sr wr	Cordani (1981)
Piranhas	Dike swarm dolerite	512 ± 20 Ma	Rb–Sr wr	Amaral (1974)
Bom Jesus granite 2.87 Ga	leucogranite	525 ± 25	U-Pb zrn int.	Feio et al. (2013)
Gabbro Rio da Onça	Gabbro	507 ± 29	K/Ar wr	Gomes et al. (1975)
Estrela metagranite	K-Feld/hornblende	797 ± 15 Ma	Ar-Ar Fk	Tavares (2015) PhD.
Gameleira Cu–Au deposit	Leucocratic syenogranite	1583 ± 7 Ma	U-Pb zrn	Pimentel et al. (2003)
Sample POJ	Biotite K alteration	1734 ± 8	Ar-Ar Bt	Pimentel et al. (2003)
Cigano	Granite	1883 ± 2 Ma	U–Pb zrn	Machado et al. (1991)
Serra dos Carajás	Granite	1880 ± 2 Ma	U–Pb zrn	Machado et al. (1991)
Pojuca	Granite	1874 ± 2 Ma	U–Pb zrn	Machado et al. (1991)
Estrela metagranite	muscovite/sericite	1877 ± 11 Ma	Ar-Ar musc	Tavares (2015) PhD.
Estrela complex	Granite	2763 ± 7 Ma	Pb–Pb zrn	Barros et al. (2009)
Araguaia Belt (Quatipuru)				
Quatipuru mafic dikes	Gabbro dikes and diabases	775 ± 49	Sm-Nd iso.	Paixão et al. (2008)
Granite Matança, metam.	Metamorphic rocks	547 ± 6	Pb-Pb zrn	Arcanjo et al. (2014)
Ramal do lontra granite	Granite	549 ± 5	Pb-Pb zrn	Alves (2006)

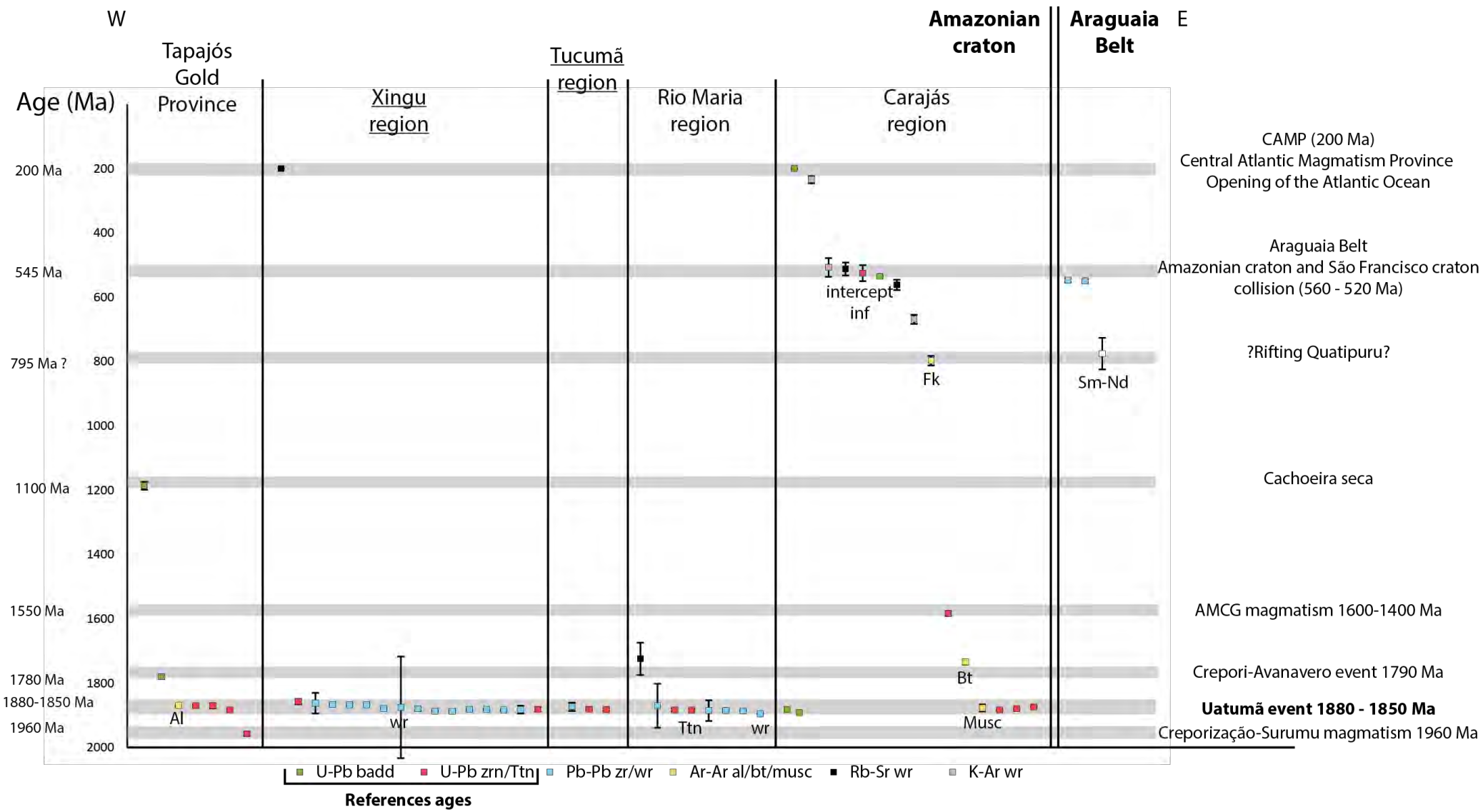

Figure 3.3: Time – space – chart for the Carajás Province. Data and references in Table 3.1.

3.3 Sampling and geological setting

3.3.1 Tucumã area

Tucumã is geologically situated in the area of Rio Maria which is composed by a Neoarchean crustal basement with greenstones and granitoids. The Tucumã group (Figure 3.4) is a "Greenstone Belt" "*sensu stricto*" with metavolcanic and mafic ultramafic rocks dated by Pb-Pb on zircons at *ca*. 2868 ± 8 Ma (De Avelar et al., 1999). The Rio Maria sanukitoid suite is composed by calk – alkaline granodiorites with associated mafic rocks (Santos and Oliveira, 2016) dated at *ca*. 2872 ± 5 Ma (Pb-Pb zrn). Medeiros and Dall'Agnol (1988) emphasized the existence of a sub-vertical foliation with a predominant WNW-ESE direction. The ultimate tectonothermal event related to the cratonization of the Rio Maria domain is marked by the presence of K-rich leucogranites dated to 2880 – 2870 Ma (Xinguara, Mata Surrão, and Rancho de Deus granites).

The Orosirian of the Rio Maria domain is marked by the anorogenic magmatism of the Uatumã event and particularly by the Velho Guilherme granite and associated felsic dikes in the Tucumã area (Figure 3.4). The granitic rocks of the reduced Velho Guilherme suite are monzogranite to syenogranite subordinate alkali – feldspar granite with low contents of TiO_2, Al_2O_3, CaO, MgO, P_2O, Sr, Ba, and Cl (Teixeira et al., 2005).They are metaluminous to peraluminous rocks with A – type affinity classified in the A2 sub-group (Eby, 1992).

The felsic dikes of Tucumã shows a dominant N125 ° direction. The felsic dikes are. *ca.* 15 m in width and a few hundred meters in length in average. They are made of A-type subsolvus microgranite characterized by subhedral phenocrysts of quartz, alkali feldspar and plagioclase in a quartz-feldspar matrix with granophyric texture. These dikes have recently been well-characterized and dated at *ca*. 1882 ± 4 Ma (da Silva et al. (2016), see attached paper). Younger Neoproterozoic or Mesozoic dikes in the Tucumã area have not yet been described in the literature. To the west of Tucumã, in the region of Sao Felix Xingu, Macambira and Vale (1997) described Mesozoic diabase dikes which are known as Cururu diabase, dated by K-Ar at *ca*. 180 ± 9 Ma (Tassinari et al., 1978). New constraints on the geochemistry and geochronology of these dikes will bring new information on the emplacement of these A-type granites related to the Uatumã event. We sampled mainly the felsic dikes and some mafic dikes.

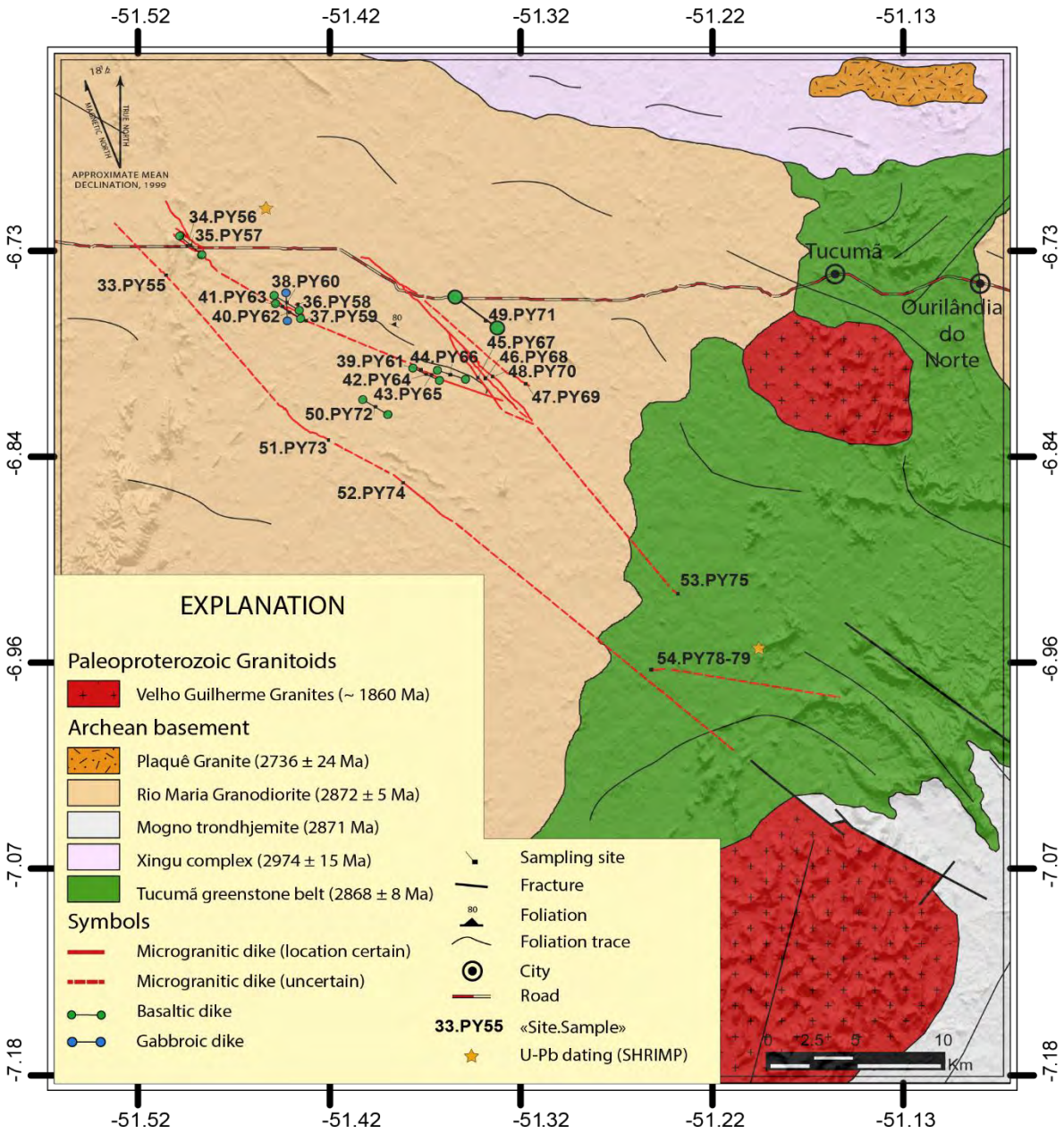

Figure 3.4: Geological map of Tucumã according to Vasquez et al. (2008) with localizations of sites.

207 oriented cylinders and 4 blocks were sampled in 28 sites in the Tucumã area for the paleomagnetic study. Geographic coordinates and names of sites are presented in Table 3.2 From the 28 sites, 16 are from NW - microgranitic dikes and 7 are from NW - associated mafic dikes. In addition, two sites were sampled on a large N-S gabbroic dike. Besides some sites where we could make field tests we also sampled 3 different sites of the Archean Rio Maria sanukitoid (the basement) to verify the regional magnetic remanence consistency.

Generally, dikes are easily found on the field but the "*in situ*" character of the dikes is always difficult to judge with many blocks of metric size, especially for mafic dikes (Figure 3.5.B). This is a recurring problem in the Amazonian craton for a good paleomagnetic study, which is not a problem for the geochronology and geochemistry.

Site	Sample	Localization	Lithology	Geochronology
NW - Felsic dikes				
33	PY55 $_{A-E}$	6.75°S/308.50°E	A-type Microgranite	
34	PY56 $_{A-H}$	6.73°S/308.51°E	A-type Microgranite	1881.9 ± 4.4 Ma U-Pb zrn (Fernandes et al., 2016)
36	PY58 $_{A-F}$	6.76°S/308.56°E	A-type Microgranite	
37	PY59 $_{A-F}$	6.77°S/308.56°E	A-type Microgranite	
39	PY61 $_{A-E}$	6.8°S/308.63°E	A-type Microgranite	
40	PY62 $_{G-Q}$	6.76°S/308.56°E	A-type Microgranite	
41	PY63 $_{H-M}$	6.76°S/308.56°E	A-type Microgranite	
43	PY65 $_{A-G}$	6.8°S/308.63°E	A-type Microgranite	
45	PY67 $_{A-G}$	6.8°S/308.66°E	A-type Microgranite	
46	PY68 $_{A-F}$	6.8°S/308.66°E	A-type Microgranite	
47	PY69 $_{A-H}$	6.81°S/308.68°E	A-type Microgranite	
48	PY70 $_{A-G}$	6.8°S/308.66°E	A-type Microgranite	
51	PY73 $_{A-H}$	6.84°S/308.58°E	A-type Microgranite	
52	PY74 $_{A-G}$	6.86°S/308.62°E	A-type Microgranite	
53	PY75 $_{A-B}$	6.92°S/308.76°E	A-type Microgranite	
54	PY76 - 77- 78 - 79	6.96°S/308.75°E	A-type Microgranite	1880.9 ± 3.3 Ma U-Pb zrn (Fernandes et al., 2016)
NW - Mafic dikes				
35	PY57 $_{A-D}$	6.73°S/308.51°E	Basalte	
38	PY60 $_{A-H}$	6.76°S/308.56°E	Basalte	
40	PY62 $_{A-F}$	6.76°S/308.56°E	Basalte	
42	PY64 $_{A-H}$	6.8°S/308.63°E	Basalte	
44	PY66 $_{A-G}$	6.8°S/308.64°E	Basalte	
49	PY71 $_{A-G}$	6.77°S/308.66°E	Basalte	
50	PY72 $_{A-F}$	6.82°S/308.6°E	Basalte	
NS - Gabbro dike				
38	PY60 $_{I-Q}$	6.76°S/308.56°E	Gabbro	
41	PY63 $_{A-G}$	6.76°S/308.56°E	Gabbro	
Rio Maria Granodiorite (Archean basement)				
36	PY58 $_{G-K}$	6.76°S/308.56°E	Granodiorite	
38	PY60 $_{R-Z}$	6.76°S/308.56°E	Granodiorite	
46	PY68 $_{G-K}$	6.8°S/308.66°E	Granodiorite	

Table 3.2: Site number, sample name, localization and lithology for the sampled sites in the Tucumã area.

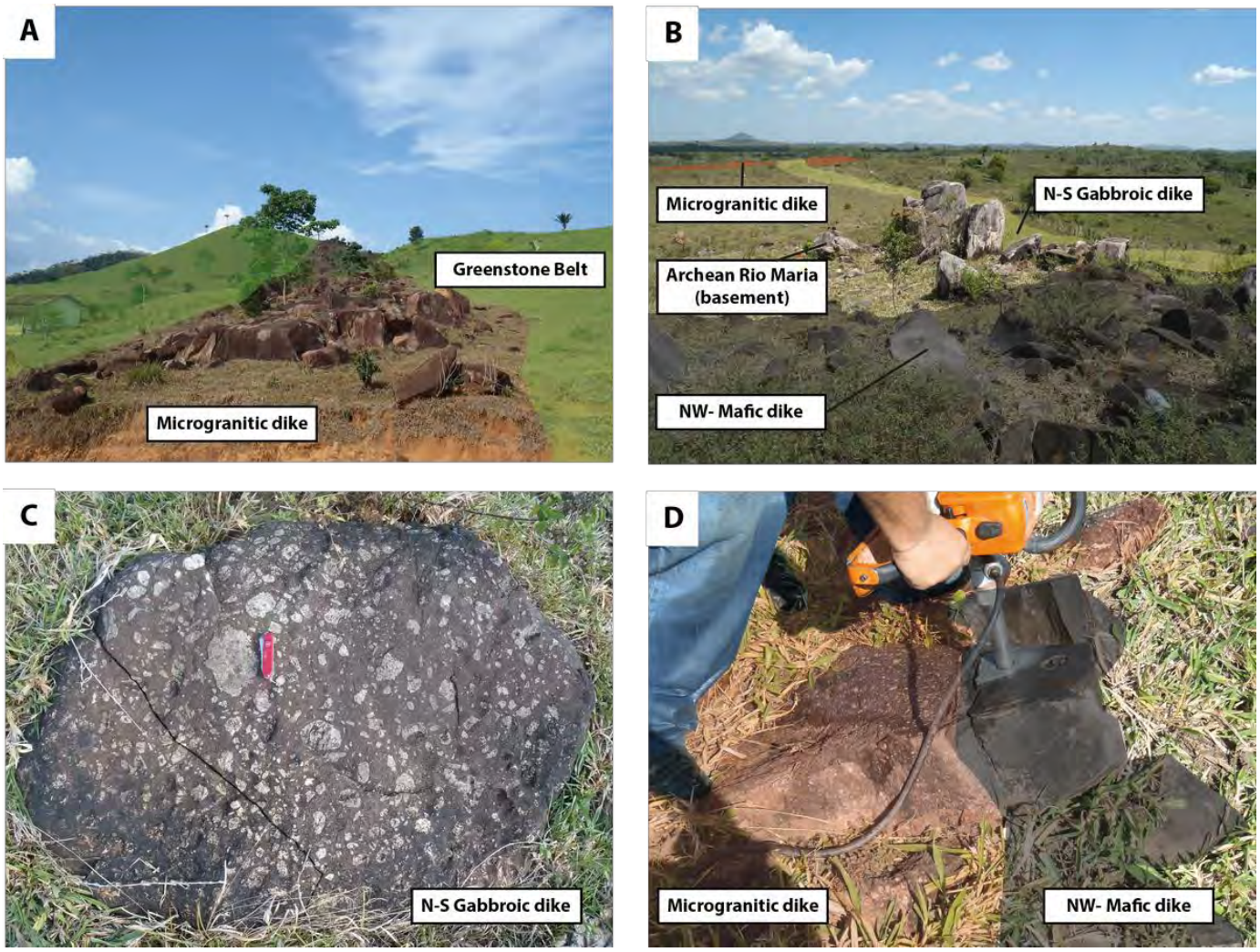

Figure 3.5: A: Microgranitic dike (Site 54) in the Tucumã area crosscutting the Tucumã group (greenstone belt). B: NW- Mafic dike at contact with the Rio Maria granodiorite (Archean basement). C: N-S Gabbroic dike. D: Sampling at contact between microgranitic dike and NW - Mafic dike.

3.3.2 São Felix do Xingu area

As mentioned above, this area is in the western part of the Carajás Province where well-preserved outcrops of the volcanic rocks associated to the Uatumã event can be observed. In the western area of Xingu River, Archean rocks are not exposed. A detailed description of the sampling in São Felix do Xingu is presented in the chapter 7 (Paper submitted to Gondwana research).

In São Felix do Xingu (Figure 3.6), the Paleoproterozoic volcano-plutonic event is represented by the Sobreiro (1880 ± 6 Ma TIMS Pb-Pb zircon) and Santa Rosa (1879 ± 2 Ma TIMS Pb-Pb zircon) Formations (Juliani and Fernandes, 2010; Pinho et al., 2006). The basal Sobreiro Formation is mainly composed by massive andesitic rocks and volcanoclastic facies with a high-K to shoshonitic calk-alkaline signature. These massive andesitic rocks are also

referred to as the Montesbelos mass-flow (Roverato, 2016). No precise age based on U-Pb dating is actually available for the Sobreiro Formation.

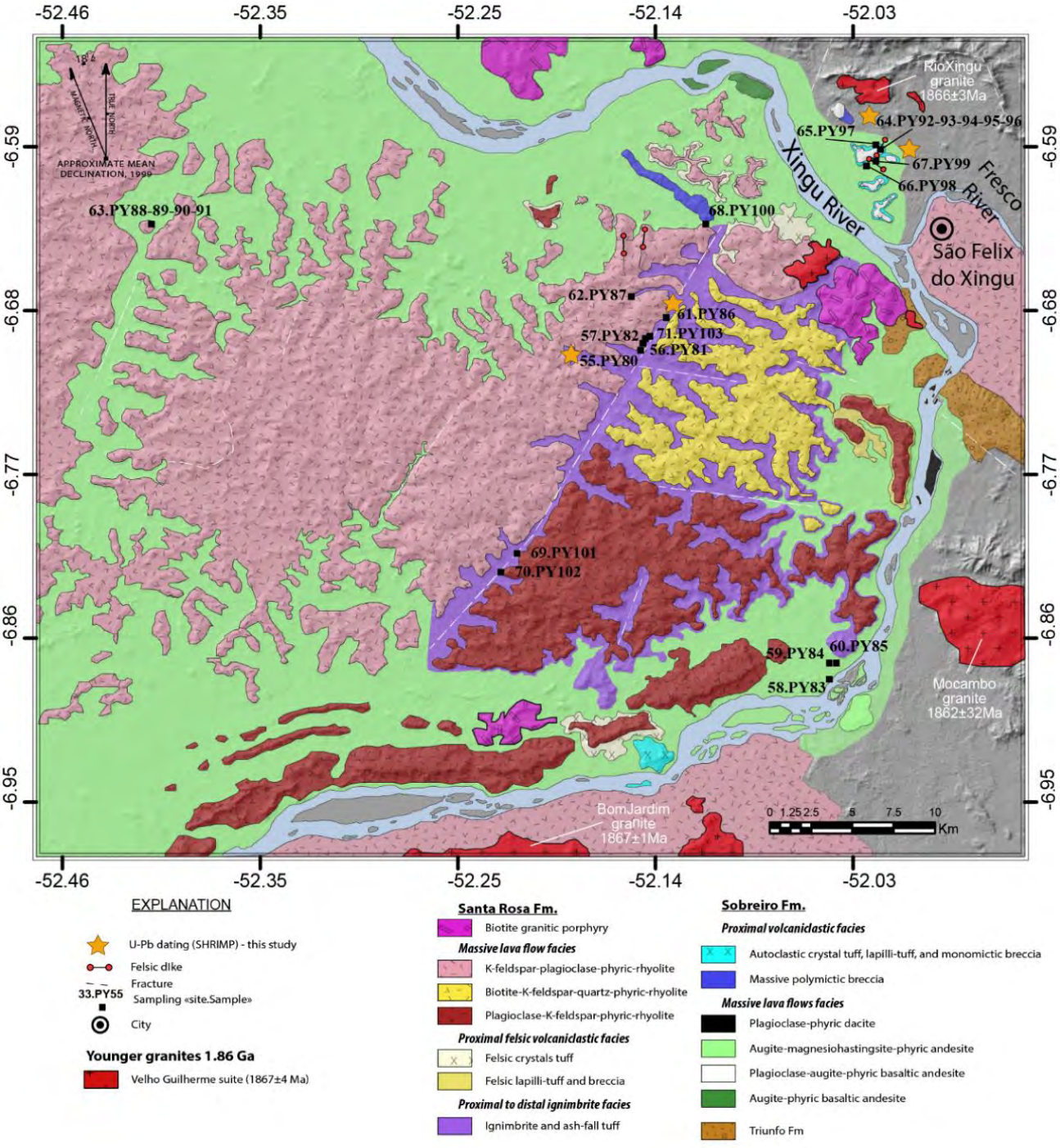

Figure 3.6: Geological map of São Felix do Xingu with localization of sites modified from Juliani and Fernandes (2010).

The upper felsic Santa Rosa Formation is composed by (1) rhyolitic lava-flows, (2) ignimbrites (unwelded ash-fall and/or highly rheomorphic ignimbrites), (3) Volcanic breccia and felsic crystal tuffs, and (4) large felsic dikes (Juliani and Fernandes, 2010). These rocks have a peraluminous composition with A-type anorogenic geochemical signature. The Sobreiro Formation is crossed by granitoid bodies of the Velho Guilherme Suite (VGS) among which Antônio Vicente, Mocambo, Rio Xingu, Benedita, Ubim/Sul, and Velho Guilherme granites. These A-type granites are dated by Pb-Pb on zircon at 1867 ± 4 Ma (Teixeira et al., 2002). The emplacement of these units is associated with an intense hydrothermal alteration (da Cruz et al., 2015; da Cruz et al., 2016). Mesozoic dikes and Quaternary alluvial deposits are the youngest units in the region.

The geodynamic context during emplacement of these Formations in the studied region is yet debated. One single SLIP, the Uatumã event, is proposed to explain the emplacement of these A-type rocks which contrasts with the model of *flat*-subduction migration between the Tapajós Province to the São Felix do Xingu region proposed by Juliani et al. (2009). 18 sites represented by 142 cylindrical samples and 7 oriented block were sampled in São Felix do Xingu area. The most representative sampled unit was the Santa Rosa Formation with 7 sites of rhyolitic lava-flows, 2 sites of ignimbrites, one felsic dike, and one site for volcanic breccia. Six sites of andesitic rocks from the Sobreiro Formation and one site from a felsic dike of the Velho Guilherme Suite (VGS) were also sampled (Table 3.3).

9	Sample	Localization	Lithology	Geochronology
Santa Rosa Formation				
55	PY80	6.7°S/307.85°E	Rhyolite lava flow	1877.4 ± 4.3 Ma U-Pb zrn (this study)
56	PY81	6.69°S/307.85°E	Ignimbrite	
57	PY82	6.69°S/307.85°E	Rhyolite lava flow	
61	PY86	6.68°S/307.87°E	Rhyolite lava flow	
62	PY87	6.67°S/307.85°E	Rhyolite lava flow	
63	PY88 - 89 -90 -91	6.63°S/307.59°E	Rhyolite lava flow	
67	PY99	6.6°S/307.98°E	Felsic microgranite dike - coarse grained	1895 ± 11 Ma U-Pb zrn (this study)
68	PY100	6.63°S/307.89°E	Volcanoclastic breccia	
69	PY101	6.81°S/307.79°E	Rhyolite lava flow	
70	PY102	6.82°S/307.78°E	Rhyolite lava flow	
71	PY103	6.69°S/307.86°E	Ignimbrite	
Sobreiro Formation				
58	PY83	6.88°S/307.96°E	Volcaniclastic deposit (andesitic)	
59	PY84	6.87°S/307.96°E	Volcaniclastic deposit (andesitic)	
60	PY85	6.87°S/307.96°E	Volcaniclastic deposit (andesitic)	
64	PY96 $_{D-R}$	6.59°S/307.98°E	Volcaniclastic deposit (andesitic) - BCT	1880 ± 6 Ma Pb-Pb zrn (Pinho et al., 2006)
65	PY97	6.59°S/307.98°E	Volcaniclastic deposit (andesitic)	
66	PY98	6.6°S/307.98°E	Volcaniclastic deposit (andesitic)	
Velho Guilherme Suite				
64*	PY92 - PY93 - PY96 $_{A-C}$	6.59°S/307.98°E	Felsic microgranite dike - fine grained (Chilled margin)	1853.7 ± 6.2 Ma U-Pb zrn (this study)
	PY94 - PY95	6.59°S/307.98°E	Felsic microgranite dike - coarse grained	

Table 3.3: Site number, sample name, localization and lithology for the sampled sites in the São Felix area.

In contrast to the dikes of Tucumã whose outcrops are exposed as isolated blocks, here the outcrop conditions are exceptionally adequate for a paleomagnetic study because all sampled rocks were undoubtedly '*in situ' at* the different outcrops (Figure 3.7).

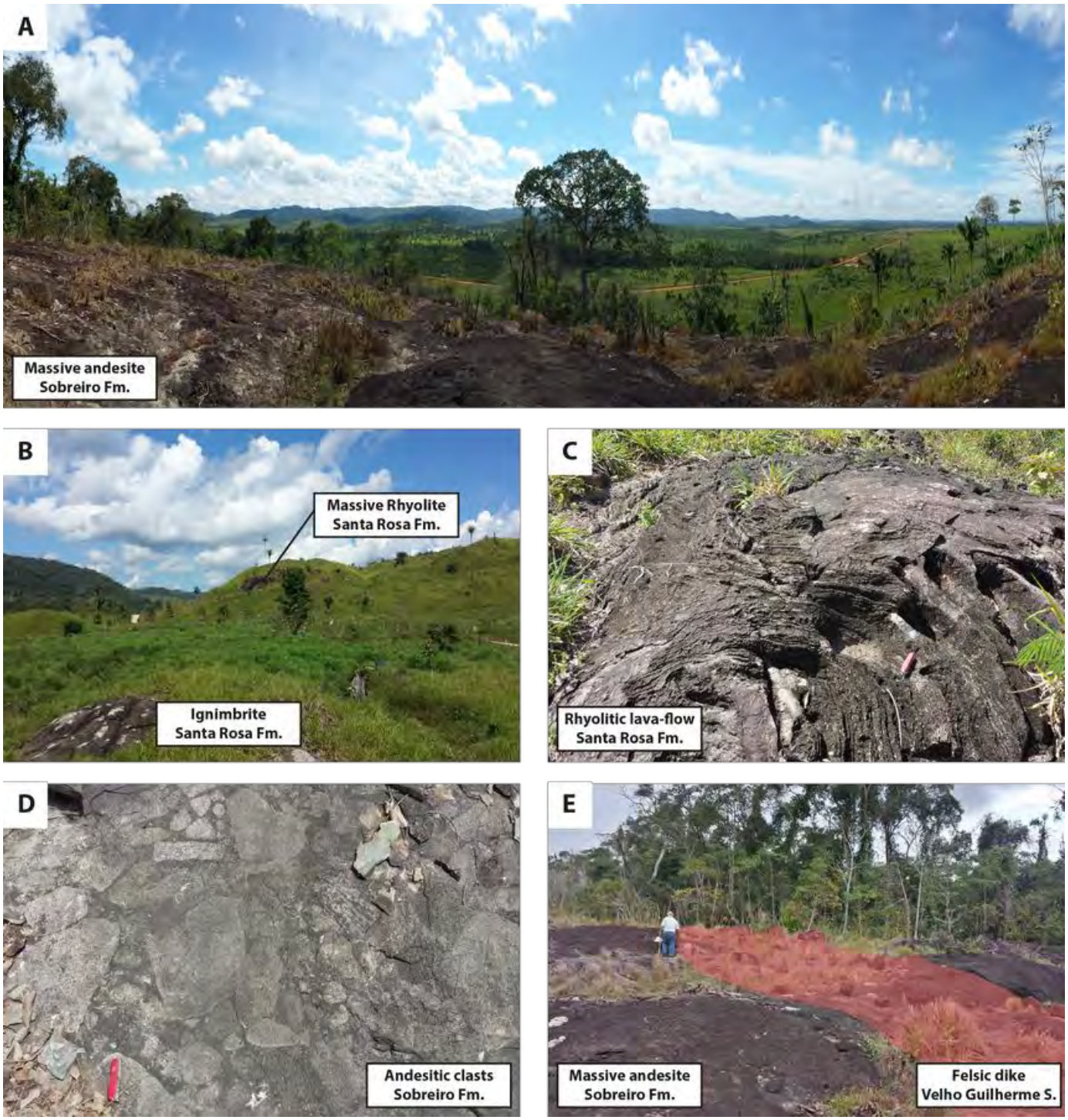

Figure 3.7: A: Massive andesite (Montesbelos – flow). B: Topography of the Santa Rosa Formation with massive rhyolite and ignimbrite *in situ*. C: Magmatic folding (flux lines) in rhyolitic flows. D: Andesitic clasts (up to 1 m) in the Sobreiro Formation. E: Rhyolitic dike of the Velho Guilherme Suite intruding andesitic rocks of the Montesbelos – flow (Sobreiro Formation).

Chapter. 4: Methodology

This paleomagnetic study was performed in the laboratory of IAG-USP (Instituto de Astronomia, Geofísica e Ciências Atmosféricas – Universidade de São Paulo) in São Paulo, Brazil. Geochronology studies were performed in the laboratory of UFOP (Universidade Federal de Ouro Preto) and IGc-USP (Instituto de Geociências da Universidade de São Paulo). Petrographic and chemical analyses were performed in the laboratory of GET (Toulouse, France). This chapter is a description of the methods and techniques used in this research (Figure 4.1).

4.1 Paleomagnetism

4.1.1 Paleomagnetic sampling

In situ oriented samples were collected for this paleomagnetic study using a portable gasoline – powered drilling apparatus with a water-cooled diamond bit (Figure 4.2.A). The diameter of cylinders is usually of 25 mm. Six to eight cylindrical samples were drilled per site and oriented with magnetic and sun compasses (whenever possible) (Figure 4.2.B). During orientation, the azimuth (angle between the sample reference mark and the geographic north) and plunge (angle between local vertical and the axis of the cylindrical sample) are measured and annotated on a field notebook for each drill in the outcrop. Solar compass verifies if azimuth obtained by magnetic compass is correct since rocks carrying a strong magnetization (normally originated by lightning strikes) can deflect the magnetic compass needle. After orientation, sample is removed and the reference mark is traced along the cylindrical sample (Figure 4.2.B). Arrows denote the top of the cylinder. At a few sites oriented block samples were collected due to difficulty in drilling the rocks. Cylindrical cores were extracted from the sample using a machine drill at the IAG-USP laboratory (Figure 4.2.C). The sample collection was named as PY ("Paul Yves"). A number (1, 2, 3…) followed by a letter (A, B, C…) designates, respectively the sampled site and each cylinder drilled in that site. For example, for site 10, the cylinder names will be PY10A, PY10B, PY10C,…. This sequence was only broken if at some site, block samples were collected. In this case, each number represents a collected block sample. So, cylinders drilled from each block sample from the same site are named, for example, as PY11A, PY11B, PY11C, etc…, for block sample 11; PY12A, PY12B, PY12C, etc… for block sample 12, etc…. All field orientation data were integrated in a software named 'ENTRAR' (developed at the IAG-USP laboratory).

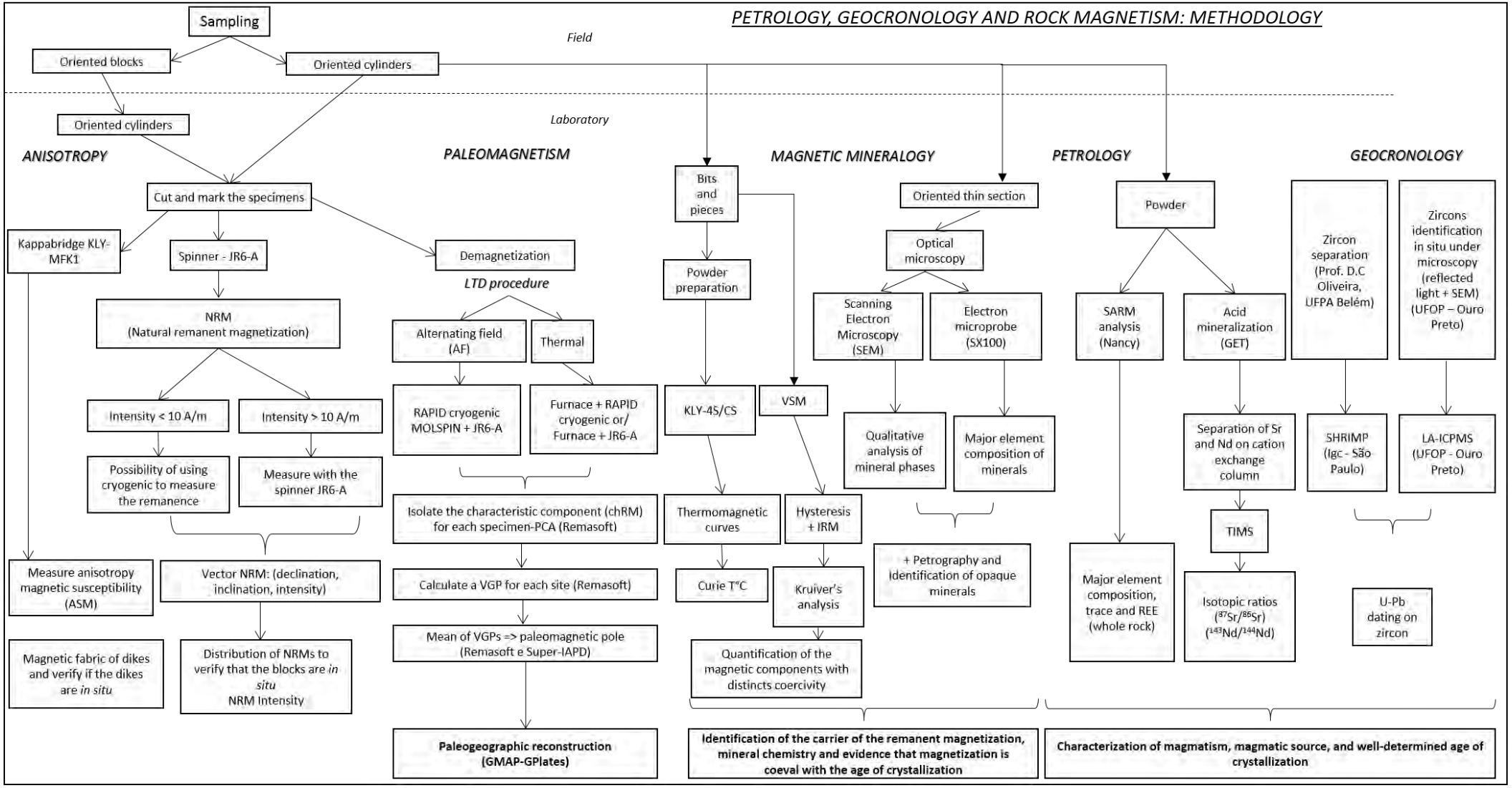

Figure 4.1: Summary of the techniques used in this work.

Using the site geographic coordinates (obtaining through a GPS) and local time each sample was collected, this software calculates solar azimuth and magnetic declination (using the IGRF model). With these values, it corrects (for each sample) the azimuths measured in the field, having the geographic north as reference.

Samples were brought to São Paulo and cut in the laboratory in standard specimen (paleomagnetic sample) (Figure 4.2.D). Thus, the cylinder PY10A will become in three specimens called PY10A1 (bottom of the arrow), PY10A2, and PY10A3 (top of the arrow). The standard specimen size is 22 mm in height and 25 mm in diameter (~11 cm^3). A total of 1728 specimens (72 sites) was produced for this paleomagnetic study.

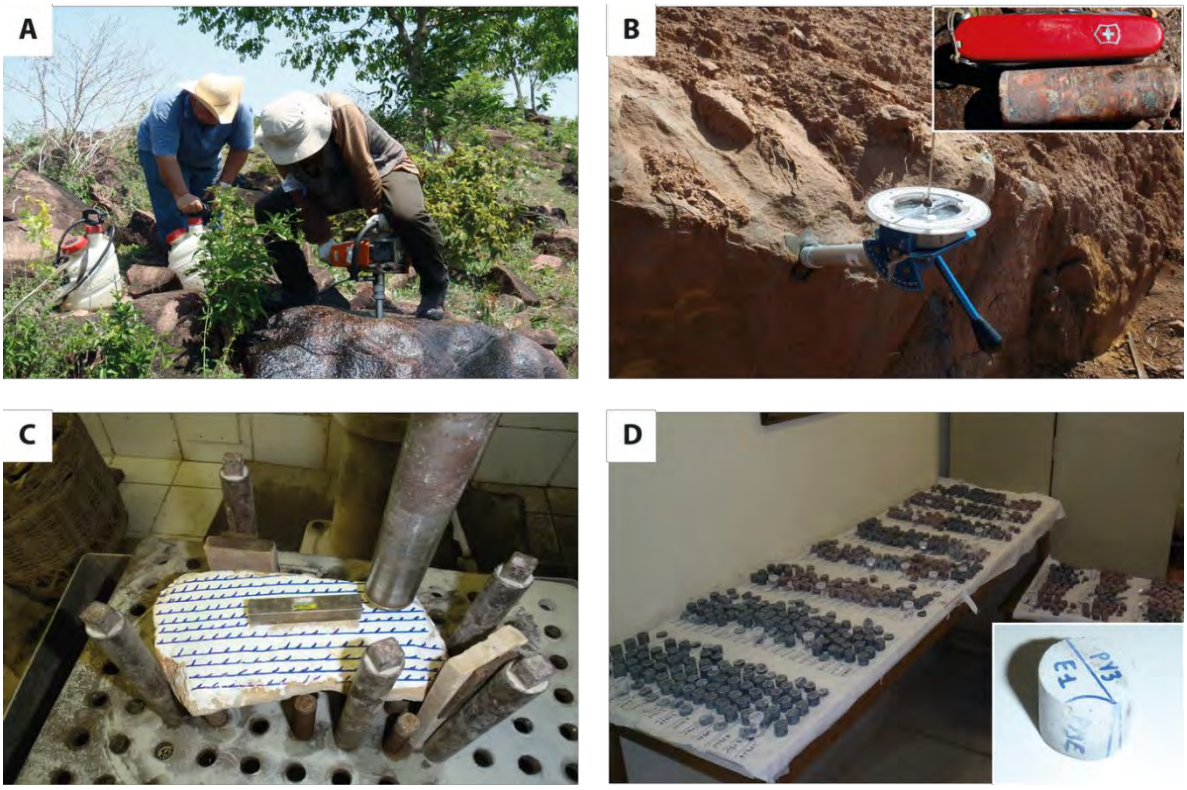

Figure 4.2: A: Sampling with a portable gasoline – powered drilling apparatus to drill a felsic dike (Tucumã). B: Sample orientation. C: Drilling of an oriented block in laboratory. D: Specimens in laboratory after preparation of cylindrical samples.

4.1.2 Anisotropy of magnetic susceptibility (AMS)

Magnetic susceptibility expresses the ability of a body to magnetize (M) when applying a magnetic field (H). The magnetic susceptibility of a sample is rarely isotropic, and has some directional differences. To measure these small differences (anisotropy), we used a Kappabridge MFK1-FA ™ ® AGICO. In weak field, the magnetization (M) is proportional to the inducing magnetic field (H), according to:

$$M = K \times H \tag{4.1}$$

The constant of proportionality K is the magnetic susceptibility. In the international system (SI), the magnetic susceptibility is dimensionless. For anisotropic materials, the susceptibility varies with the direction along which the sample is measured and with the direction of the applied magnetic field, so M and H are not collinear. K is represented by a second rank tensor whose geometric representation is an ellipsoid. The three main components of the tensor axes are K1 (K_{max}), K2 ($K_{int.}$), K3 (K_{min}) representing, respectively, the direction of maximum, intermediate and minimum susceptibility (K1 ≥ K2 ≥ K3). The measurement is semi – automatic (with rotation) and we have to adjust the specimen in three perpendicular positions to characterize the three axis of the ellipsoid. During measurements a 3D adaptor (totally automatic) in the laboratory of GET (Géosciences – Environnement - Toulouse, in France) was also used. The 3 susceptibility axis are represented in a stereographic diagram where K1 is represented by a square (□), K2 is represented by a triangle (Δ), and K3 by a circle (○). Some parameters are usually used to evaluate the shape of the ellipsoid:

(1) The bulk mean susceptibility (Km) is calculated by $Km = \frac{(K1+K2+K3)}{3}$. (4.2)

(2) The anisotropy degree, $P = \frac{K1}{K3}$. (4.3)

(3) The magnetic foliation, $F = \frac{K2}{K3}$. (4.4)

(4) The magnetic lineation, $L = \frac{K1}{K2}$. (4.5)

(5) The Jelinek (1981) parameter (T), the values of which range between -1 (cigar-shape, prolate) to +1 (disk-shaped, oblate). $T = \left[\frac{2\ln(\frac{K2}{K3})}{\ln(\frac{K1}{K3})}\right]$. (4.6)

4.1.3 The remanent magnetization

Paleomagnetism is the study of Earth's magnetic field in the past, recorded by rocks or more precisely, by the ferromagnetic minerals *(sensu lato)*. When a ferromagnetic body is subjected to a magnetic field, it acquires a magnetization. After removing the magnetic field, the ferromagnetic body becomes a new source of the magnetic field as it is able to memorize the field direction through its remanence.

The theory of the remanent magnetization stability over time was established by a French physicist (Néel, 1955). Without magnetic field, a ferromagnetic body composed by single – domain particles (without interactions) has an initial remanent magnetization (M_0) that decreases exponentially with time (t) due to thermal agitation (equation 4.7).

$$M = M_0 e^{\frac{-t}{\tau}} \quad (4.7)$$

where τ is the relaxation time, the time for the initial magnetization decay until 1/e of its initial value. Therefore the relaxation time τ is the mechanism that controls the dynamic equilibrium between the thermal and exchange energy.

$$\tau = (\frac{1}{\lambda})e^{(\frac{KV}{\kappa T})} \tag{4.8}$$

where KV, is the magnetic anisotropy energy within a particle with volume V and κT, is the thermal energy (κ is the Boltzmann constant and T is the temperature). λ is a constant frequency which measures the crystal lattice vibration (~10^8 s^{-1}). In formula (4.8), ***the relaxation time vary exponentially with V and T***.

For a fixed temperature, the variation of the relaxation time depends on volume, V. If the volume is too small (< 20 – 30 nm), relaxation time is also too small (<100 s), and the magnetic moments are unstable due to thermal agitation and will reach an equilibrium very quickly - this is the **superparamagnetic state (SP state)**. As already stressed, relaxation time has an exponential increase with volume (equation 4.8), so that at a critical volume its relaxation time becomes very large and the magnetization will become uniform and stable within the grain, that is, it behaves as a single domain (SD) grain. In the same logic we can now consider a fixed volume and the evolution of temperature following the formula (4.8). If the temperature is very high, we observe a superparamagnetic state for the grain and the relaxation time would be small. We have a critical temperature value, the **blocking temperature (T_b)** where during cooling the relaxation time will quickly increase, the grain magnetic moments are blocked, and magnetization becomes stable. It should be noted that unlike the Curie temperature that is characteristic of each magnetic mineral, blocking temperature depends on magnetic mineral, their grain volumes, grain magnetic properties (their magnetic anisotropies) and ultimately on time. Since the rock may have grains with different volumes and shapes, it may also have a spectrum of blocking temperatures that may extends in a large range below the Curie temperature. For the single-domain grains, blocking temperatures will be very close to the Curie temperature whereas for the multi-domain grains the blocking temperature will be in a range of value that can be very low (low stability).

We can use the diagram V (volume) – K (anisotropy energy density) to represent lines of equal relaxation time. This Figure 4.3 shows the lines where relaxation time is 100 s, 1 Ma, and 4.5 Ga. The blue line (τ < 100 s) limits the transition between superparamagnetic (to the left side of this line) and stable single domain grains (to the right side of this line), which have higher relaxation time (τ).

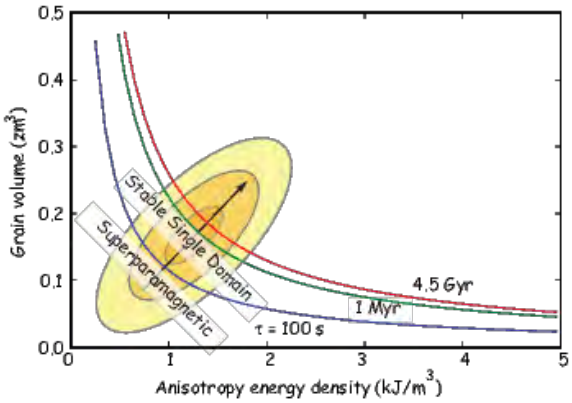

Figure 4.3: Lines of equal blocking energy in the V-K diagram.
(https://earthref.org/MagIC/books/Tauxe/Essentials/WebBook3ch7.html)

For igneous rocks the remanence acquisition is controlled in first order by the decrease in temperature during cooling. When the magma begins to crystallize its temperature is high (above Curie temperature) and the magnetic moments take random directions (**paramagnetic** state). If temperature continues to decrease it passes by the Curie temperature of magnetic minerals, and they acquire their ferromagnetic properties. The **Curie temperature** (temperature at which occurs the transition paramagnetic – ferromagnetic) is characteristic of each mineral: magnetite = 585°C, hematite = 675 °C. However, the magnetic grains behave as superparamagnetic, since their relaxation times are very small at those high temperatures. If a magnetic field (like the Earth's field) is active in the rocks, the magnetic moments will preferably align along this field. Alignment is not perfect due to intrinsic grain anisotropies, but the resultant moment and the field will have the same direction. When the rock cools below blocking temperature (Tb) of the grains, their magnetic moments will freeze in the direction of the magnetic field, and did not change more, even if the field changes its direction. Below blocking temperature, the magnetic energy becomes more important than the thermal energy, grain relaxation times become very large and their magnetization becomes stable. At room temperature, rock has acquired a **thermal remanent magnetization (TRM)** (Figure 4.4).

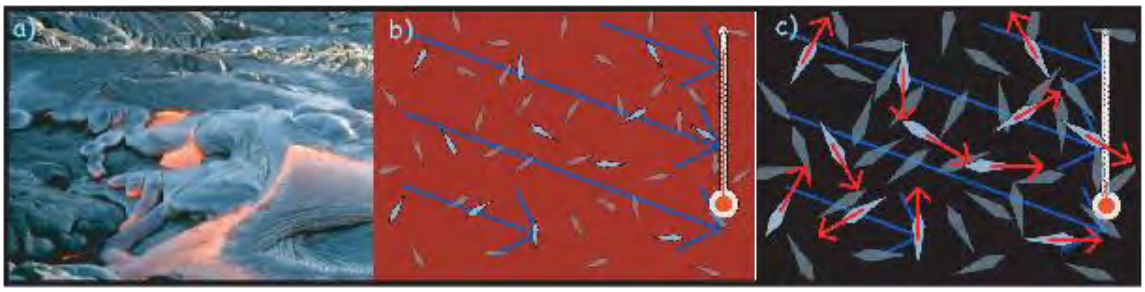

Figure 4.4: Acquisition of a remanent magnetization during cooling of a lava flow. Magnetic moments are acquiring a magnetization through the blocking temperature.
(https://earthref.org/MagIC/books/Tauxe/Essentials/WebBook3ch7.html)

Two possible ways igneous rocks can acquire natural remanent magnetizations (NRMs) were described: the thermal remanent magnetization (TRM) which is acquired during rock cooling and is considered of primary nature, and the viscous remanent magnetization (VRM), which is acquired at room temperature under an ambient field, and is regarded as of secondary nature. However, other processes can originate natural remanent magnetization as, for example, the formation of new minerals following hydrothermal alteration (typical process at the end of intrusive body crystallization) or an increase in temperature (intrusion of dikes or regional metamorphism). The rocks may acquire during these processes a **chemical remanent magnetization (CRM**) or a **partial Thermal Remanent Magnetization (pTRM**) due to the rock partial heating.

In summary, the natural remanent magnetization (NRM) of igneous rocks is often a superimposition of a primary magnetization (NRM I) acquired during rock cooling (TRM) and secondary magnetizations (NRM II) acquired through time (VRM, pTRM and/or CRM).

$$NRM = NRM\ I_{TRM} + NRM\ II_{CRM/pTRM/VRM}$$

All specimens are stored and demagnetized inside a magnetically shielded room in the Laboratory of IAG – USP (São Paulo, Brazil) with an ambient field < 1000 nT (Figure 4.5.A). To measure the magnetization we used a spinner JR6-A™, AGICO® (~2 × 10^{-6} A.m^{-1} of sensitivity) (Figure 4.5.C). This apparatus measure the current induced in its two coils by the sample rotation. We can also use for specimens with lower intensity (< 10 A.m^{-1}) a 2G – Enterprises DC SQUID magnetometer with ~10^{-12} A.m^2 sensitivity per axis in horizontal position (Figure 4.5.A) or a RAPID 2G – Enterprises DC SQUID magnetometer in vertical position (Figure 4.5.E) (Kirschvink et al., 2008).

In a paleomagnetic study we have to check if the measured natural remanent magnetization carried by the specimens is not a superimposition of various magnetic components. To solve this problem, specimens were submitted to the usual progressive stepwise alternating field (AF) and/or thermal demagnetization.

4.1.4 Demagnetization techniques

4.1.4.1 Alternating Field (AF) demagnetization

We applied on the specimen crescent alternating field steps until 120 mT – 160 mT. Steps of 2.5 mT (up to 15 mT) and 5 mT (15 – 100 mT) were selected for AF demagnetization. Demagnetization consists in submitting the sample to a symmetrical alternating field, which linearly decreases to zero in a null field environment. The effect of the AF demagnetization is to unblock magnetization of all grains that have coercivities lower than the applied alternating

field, randomizing them during the process, and so, eliminating their contribution to remanent magnetization. Crescent successive fields are applied until the complete demagnetization of the specimen. We used a three-axis demagnetizer coupled with a cryogenic magnetometer (2G Enterprises) or a spinner demagnetizer apparatus (Molspin) (Figure 4.5.B) where the specimen is placed in a holder sample which rotates along two axis. AF demagnetization is effective for samples with minerals that have coercivities below 100 or 160 mT, the upper limits of demagnetizers.

4.1.4.2 Thermal demagnetization

This method consists in submitting the samples to cycles of heating and cooling in a null field environment using a TD-48 (ASC Scientific) furnace (Figure 4.5.D). Steps of 50°C until 500°C, after which detailed steps of 20°C until 600°C (for magnetite) or 700°C (for hematite) were used to isolate precisely the magnetic components. When the specimen is heated at 100°C, for example, magnetization of all grains which have blocking temperature (T_b) equal or lower than 100°C will be unblocked. Since the samples cools in a null field environment magnetic moments associated with these grains become random and the total magnetization will be zero. This technique is very effective for rocks carrying minerals with high coercivities, as hematite, since they cannot be demagnetized by the AF treatment. A problem with this technique refers to the chemical alterations of minerals during procedure. After each step of heating the specimen magnetic susceptibility is measured in order to detect mineralogical alterations.

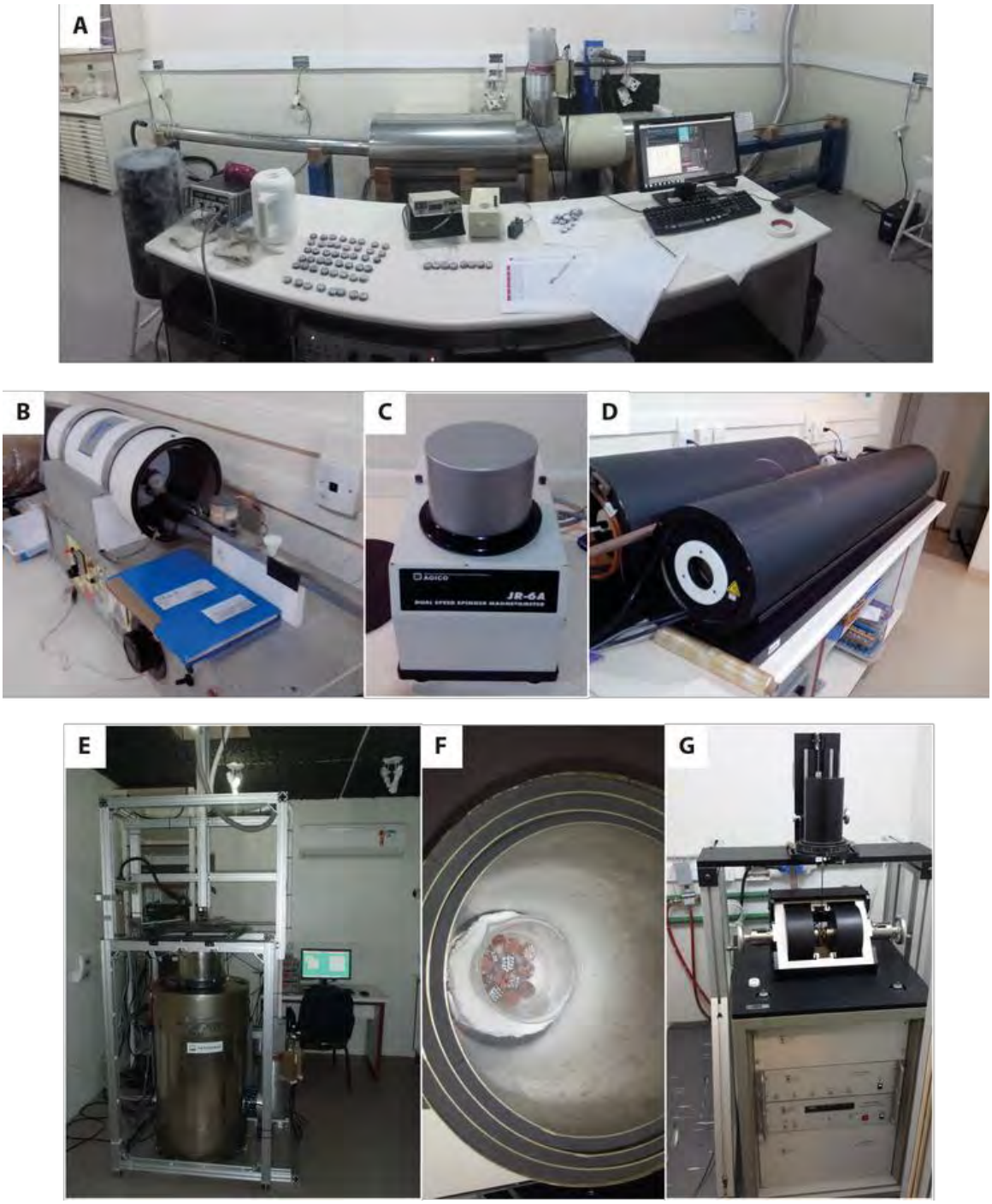

Figure 4.5: A: Magnetically shielded room in the Laboratory of IAG – USP with a 2G – Enterprises DC SQUID magnetometer in horizontal position. B: AF demagnetizer apparatus (Molspin). C: Spinner JR6-A™ magnetometer, AGICO®. D: TD-48 Furnace (ASC Scientific). E: RAPID 2G – Enterprises DC SQUID magnetometer in vertical position. F: Low-temperature demagnetization (LTD) with nitrogen bath. G: MicroMag-VSM, Model 3900.

4.1.4.3 LTD demagnetization

Sometimes it's difficult to isolate the magnetic component during thermal demagnetization. We can evoke presence of multi-domain grains that can hide the primary component as a function of their blocking temperature spectrum. In this case, a pre-treatment that uses the low-

temperature demagnetization technique (LTD) can be applied. The specimens are immersed in liquid nitrogen (77 K), after which they are placed inside a magnetically shielded space (µ-metal recipient) until they reach again room temperature (Borradaile, 1994; Borradaile et al., 2004) (Figure 4.5.F). Three (up to five) immersions are required to have a good effect and destruction of MD magnetization before thermal demagnetization. LTD technique is now used *in routine* for paleomagnetic study of Proterozoic rocks to separate multicomponent remanences.

Progressive AF and thermal demagnetization provide good information (Coercivity spectrum, T_{ub} spectrum…) on the magnetic carriers of remanent magnetization present in the rock. However, further experiments may better characterize the magnetic mineralogy, as will be seen in the next topic.

4.1.5 Magnetic mineralogy

4.1.5.1 Petrographic analysis

To characterize the ferromagnetic minerals we can use polished thin sections observed under transmitted and reflected light microscopy. In addition, scanning electron microscopy (SEM) was used in the laboratory of GET (Toulouse, France) to constrain the mineralogy of accessories minerals.

4.1.5.2 Thermomagnetic analysis

Thermomagnetic experiments are based on the evolution of the magnetic susceptibility in function of temperature, and were conducted in the IAG laboratory. Magnetic susceptibility was measured at argon atmosphere in low and high temperatures using a CS-4 apparatus coupled to the KLY-4S Kappabridge instrument (AGICO, Brno, Czech. Republic). During heating at high temperatures, when Curie temperature of the magnetic minerals are reached, a strong fall in the magnetic susceptibility is observed, as the magnetic minerals lost their ferromagnetic properties and behave as paramagnetic minerals. So, thermomagnetic curves may be used to identify the rock magnetic carriers. When heating and cooling curves are similar, the thermomagnetic curve is called reversible. When this doesn't happen, it is called irreversible and it indicates that mineralogical transformations in the sample occurred during heating. In the Low-temperature experiment samples are immersed in nitrogen liquid (77 K), and magnetic susceptibility is measured during heating to room temperature. These low-temperature thermomagnetic curves characterize the presence of the Verwey transition (-153 °C) for the magnetite or the Morin transition for hematite (~-15°C).

4.1.5.3 Hysteresis and Isothermal remanent magnetization (IRM) curves

Hysteresis curves may be used to evaluate the magnetic domain structures of rocks under study (Dunlop, 2002). Figure 4.6 shows the hysteresis curve (magnetization (M) versus applied field (H)) obtained for magnetite grains with initial zero magnetization. As the field increases (point 1 in the figure), the corresponding magnetization also increases until it reaches saturation (point 2 in the figure), receiving the name saturation magnetization (**Ms**). If the field decreases, magnetization also decreases but when the field is at 0 a remanent magnetization yet remains in the sample (point 3 in the figure), which is named as saturation remanent magnetization (**Mrs**). Now, if a reverse field is applied, magnetization drops until it becomes zero at an applied field H (point 4 in the figure). The field at which magnetization is zero is the bulk coercive force (**Hc**). Increasing more the field will saturate the magnetization on the opposite side. Now, if the field decreases to zero and is inverted again up to saturation magnetization the hysteresis cycle is completed. Other important parameter is remanent bulk coercive force (**Hcr**). This field (point 5 in the figure) corresponds to the field that removes remanent magnetization (that is, magnetization turn back to zero after field (Hcr) is removed).

These four parameters (Ms, Mrs, Hc, Hcr) are characteristic of the magnetic domain structure of the ferromagnetic minerals and they also tell us about their grain sizes. Ms/Mrs are plotted against Hc/Hcr in the Day's plot (Day et al., 1977), which defines the single domain (SD), multi-domain (MD) and mixtures of SD and MD fields (Dunlop, 2002).

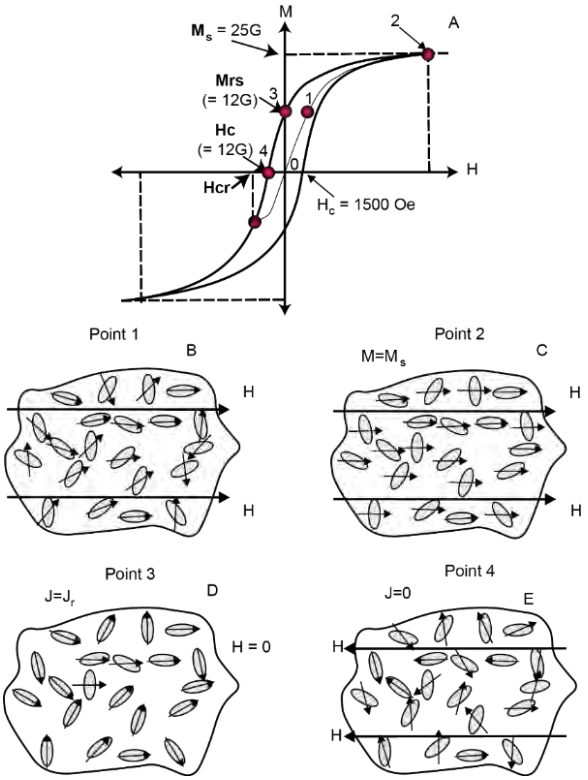

Figure 4.6: Hysteresis curve for SD grains of magnetite (a) and Magnetization direction during the hysteresis acquisition (b, c d, e), adapted from Butler (1992).

In this work a MicroMag-VSM, Model 3900 was used to determine hysteresis curves (Figure 4.5.G). The same apparatus can be used to determine the isothermal remanent magnetization (IRM) curves. To construct the IRM curves, crescent successive increments of remanent magnetizations until the saturation of the rock are obtained by applying step by step crescent magnetic fields at room temperature. After each applied field the corresponding remanent magnetization is measured, and it is plotted against magnetic field. A threshold of saturation is reached quickly for relatively small field (< 300 mT) for rocks carrying magnetite. For hematite we cannot determine the saturation magnetization using the VSM apparatus because hematite coercivities are greater than 1000 mT, the largest field VSM applies. For samples carrying hematite we can use a pulse magnetizer (MMPM10) which can apply fields up to 3 T for standard samples (2.5 cm in diameter x 2.2 cm height) or up to 9 T for smaller samples (1 cm in diameter x 1 cm height). Gaussian analysis was applied to the isothermal remanent magnetization (IRM) curves to quantify the different magnetic coercivity components (Gong et al., 2009; Kruiver et al., 2001).

4.1.6 Analysis of components

After AF and thermal demagnetization, directions must be analyzed to separate magnetic components. In paleomagnetism two kinds of projection are used: stereographic projections (Figure 4.7) and orthogonal projections (Figure 4.8). To represent a direction in stereographic projection, magnetization vector is considered of unit length whose tip, represented over the surface of a sphere of equal unit radius, is linked with the south pole of the sphere (Figure 4.7). Projection is considered the point of intersection with the equator plane of the sphere (open small circle in Figure 4.7). This equator plane is represented in the right side of Figure 4.7. The north (N), east (90°), south (180°) and west (270°) geographic directions are represented. Magnetic declination varies from zero (N direction) up to 360° in a clockwise direction, and magnetic inclination from zero, at the border of the equator plane, to 90°, at the center of the projection.

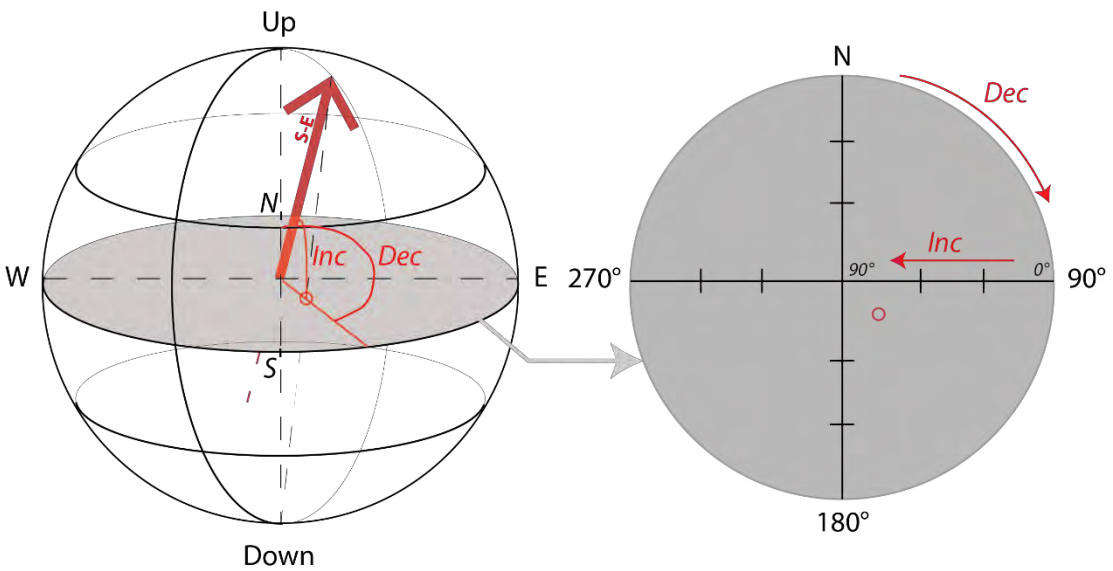

Figure 4.7: Stereographic representation of an upward magnetic direction. The direction is plotted on the *equal-area* projection in grey (Lambert), modified from Bispo-Santos (2012).

Unlike in the structural geology studies, in paleomagnetism the magnetic vector may point downward (positive inclination – magnetic field in the northern hemisphere) or upward (negative inclination – magnetic field in the southern hemisphere). To represent this vector, we use a *net* which represents the projection on an equatorial plane of the considered hemisphere (upper or lower hemisphere). Two types of spherical projections are used in paleomagnetism and there is no convention. The *equal-angle* projection (stereographic projection, Wulff net) where a given angle between two vectors is preserved after the projection. The *equal-area* projection (Lambert projection, Schmidt net) preserves area, therefore grid sectors parallel to

the equator all have the same area. An *equal-area* projection (Lambert) is usually preferred because we are interested by the directional scatter in distributions of paleomagnetic directions. It may be noted that the “stereographic” term is misused when we use a Lambert projection.

By convention, a solid symbol is associated with a downward direction and an open symbol is associated with an upward direction.

During stepwise AF or thermal demagnetization, measured magnetization after each step is plotted in the stereographic projection. Magnetic declination and magnetic inclination can directly be read on the stereographic projection, and so, changes in the NRM direction can easily be observed in stereographic projection. However, intensity variations are not represented in stereographic projections. So, it is always associated with an intensity decay curve.

A more practical representation of magnetic directions was proposed by **Zijderveld (1967)**, based on projections of the tip of the magnetic vector on the orthogonal horizontal and vertical planes of the reference system, where x, y and z axes represent, respectively, the north geographic direction, the east geographic direction and the downward direction. After projection, the horizontal plane is rotated to the vertical plane, and both projections can be seen in the same vertical plane (Figure 4.8). The orthogonal projection (also known as Zijderveld projection) provides information on both, direction and intensity (Dunlop, 1979; Zijderveld, 1967). This figure shows the vector magnetization components (vector tip) plotted in the vertical and horizontal planes, in the course of stepwise demagnetization (AF or thermal). When the natural remanent magnetization (NRM) is represented by only one component the different plotted horizontal and vertical projections during demagnetization steps become aligned, moving to the origin of the coordinate system, as shown in Figure 4.8 (decrease in intensity). Broken lines (Figure 4.9a, b), instead, show that more components with different coercivity/blocking temperature spectra were added to compose NRM. In this case each line represents a distinct component. The last and more stable component (moving to the origin) disclosed in Zijderveld diagram is frequently associated to the primary magnetization. But for Precambrian rocks this correlation is not so simple. Buchan (1978) showed in a gabbro with multicomponents that the older component is carried by minerals with the lower coercivities, and the younger component is carried by the lower blocking temperatures. So, the more stable component isolated by demagnetization is referred to as the **characteristic remanent magnetization (ChRM)**. A field test (baked contact test or conglomerate test) may eventually prove that the isolated ChRM direction represents the primary magnetization (see below).

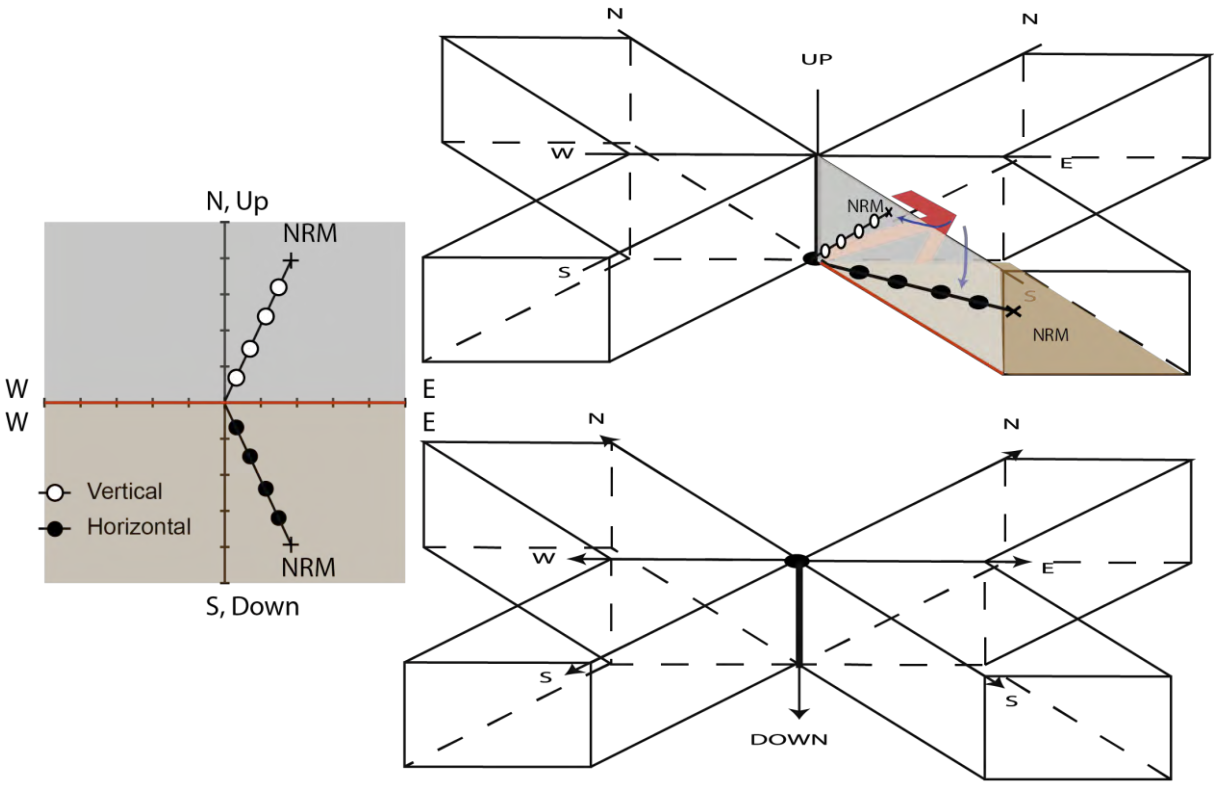

Figure 4.8: Zijderveld diagram and vision in 3D for the vector (it is the same vector, SE-direction with negative inclination, of the stereographic diagram in Figure 4.7. We can see the decomposition in two orthogonal planes.

One major problem in paleomagnetism is when two (or more) components have completely overlapping coercivity (or blocking temperature) spectra (Figure 4.9e). In this case, curved segments in the Zijderveld diagram (Figure 4.9f) avoid any component be calculated. In special cases when a primary magnetization is affected by random secondary components, the alternative technique of remagnetization circles (Halls, 1978) permit primary magnetization to be calculated.

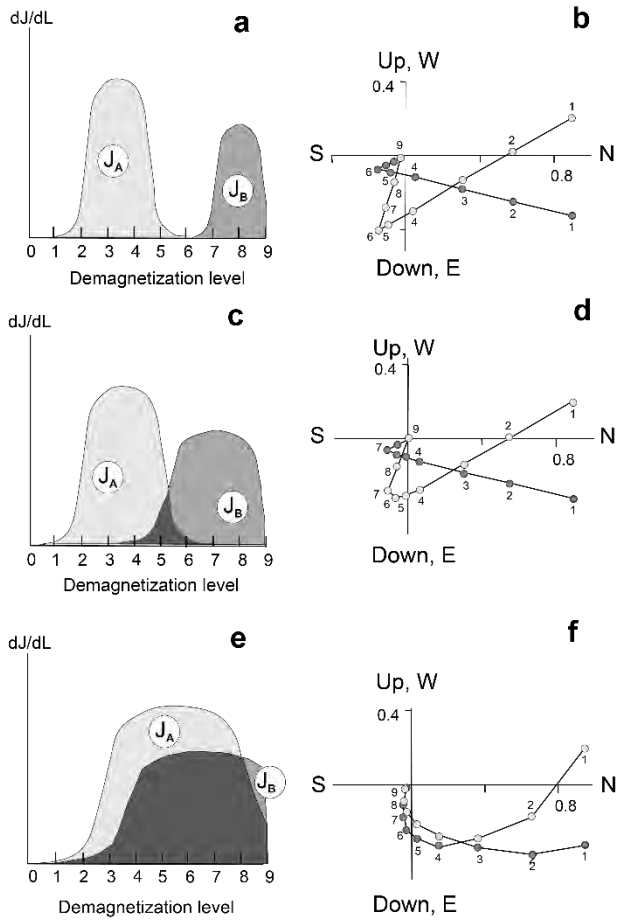

Figure 4.9: Possibility for overlapping demagnetization spectra (H_c or T_b) for 3 examples (a, c, e) and associated Zijderveld diagrams (b, d, f).

Principal component analysis (PCA) developed by Kirschvink (1980) is used to calculate magnetization components. The least squares fit method is applied to the points defining linear trajectories. The **maximum angular deviation (MAD)** provides a quantitative measure for the fit precision. Paleomagnetic directions with MAD < 10° are considered as acceptable.

To calculate mean directions and paleomagnetic poles in paleomagnetism, the Fisher (1953)'s statistics is used. In this statistics, each direction is considered as a unit vector, whose extremity is represented over a sphere of unit radius. The mean of N directions is estimated as the vectorial sum of the N unit vectors, whose modulus is R (R ≤ N). Within the Fisher probability density distribution two statistical parameters can quantify if a mean direction is of good quality.

The precision parameter (K) is a measure of the concentration of the directions distribution over the sphere about the mean direction. Equation 4.9 gives the estimated precision parameter (K) in the Fisher statistics. Therefore, high values for the precision parameter (K) are expected for well grouped directions.

$$K = \frac{N-1}{N-R} \tag{4.9}$$

Where R is the length of the vector sum of N individual unit vectors.

A confidence limit (α_{95}) for the calculated mean direction is estimated by the following formula:

$$\alpha 95 = \frac{140°}{\sqrt{KN}} \tag{4.10}$$

This value depends of the number of directions (N) used in the mean and the precision parameter (K). The significance of α_{95} is that the true direction has 95% of probability to be inside the cone of semi-angle α_{95} about the mean direction. For a good direction we consider only α95 < 16°.

4.1.7 Field tests and paleomagnetic stability

It is crucial to know if the isolated stable direction (ChRM) carried by ferromagnetic minerals with high blocking temperatures or high coercivities was acquired during rock cooling (primary nature). The only way to prove if a direction is primary is by applying field tests (fold test, conglomerate test, reversals test, baked contact test, regional consistency). The studied rocks were not submitted to deformation processes nor conglomerate sedimentary deposits were found. Therefore, only the three later field tests will be described.

4.1.7.1 Reversals test

The geomagnetic field direction can differ by 180° between a normal and reverse polarity interval (during a reversion). During a long cooling of the rocks the ferromagnetic minerals can record these reversions and we can find sites with normal polarity and sites with reverse polarity. Statistical tests are used to establish if the reversals test is positive (McFadden and McElhinny, 1990). A positive reversal test could also indicate that the secular variation was averaged and that secondary components were totally eliminated during demagnetization.

4.1.7.2 Baked contact test

This is a classic test for paleomagnetism that becomes a priority for any studying igneous rocks. As an example, a vertical dike is crosscutting an older country rock (Figure 4.10). During the intrusion, the baked country rock acquires a thermal remanent magnetization (TRM) with the same direction of the dike. In addition, the country rock far from contact (unbaked rock) carries a distinct older direction. These are requirements to consider the dikes's

ChRM direction as primary. In this case the performed baked contact test is considered positive.

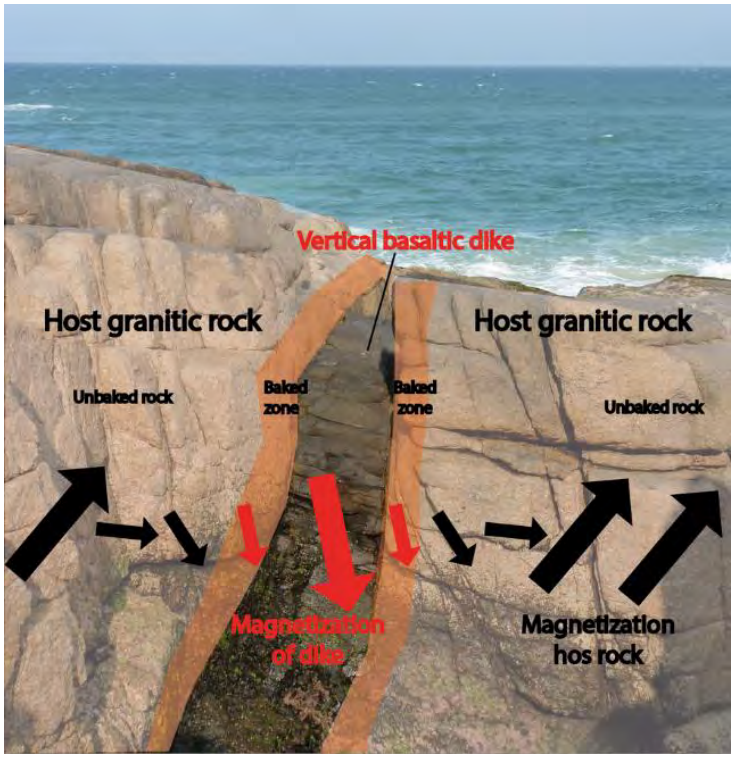

Figure 4.10: Positive baked contact test between a basaltic dike and the granitic basement.*Credits: S. Couzinié* (Florianopolis, Brazil).

4.1.7.3 Regional consistency

This test involves a logic in the sequence of directions observed in the region, *i.e.,* all units of the same age have similar directions. Older rocks could be remagnetized by this event. But more information is necessary because a dominant direction in a region could also indicate a wholescale remagnetization (Buchan, 2013).

4.1.8 Paleomagnetic pole

In paleomagnetism, two assumptions must be considered. (1) The ability of natural rocks to acquire remanence and record the magnetic field during their formations. (2) For long periods (several thousands of years), the mean Earth's magnetic field corresponds to that produced by a dipole located at the center of the Earth and aligned with its rotation spin axis. This is the concept of **Geocentric Axial Dipole (GAD)**. The GAD model implies a basic relation between the inclination and the latitude (see deduction in the frame below).

$$\underline{\boldsymbol{\tan I = 2 \times \tan \lambda}} \tag{4.11}$$

Relation between the inclination and the latitude.

1. We have the magnetic potential of a dipole, W
$$= \frac{\mu_0 \times m \times \cos\theta}{4\pi r^2} \tag{4.12}$$
2. The field of a magnetic dipole is the derivative of the magnetic potential on both radial (B_r) and tangential (B_θ) components:
$$B_r = 2 \times \frac{\mu_0 \times m \times \cos\theta}{4\pi r^3} \; ; \; B_\theta = \frac{\mu_0 \times m \times \sin\theta}{4\pi r^3} \tag{4.13}$$
3. The component B forms an angle **I** with the local horizontal (or tangential component) called the **magnetic inclination**.

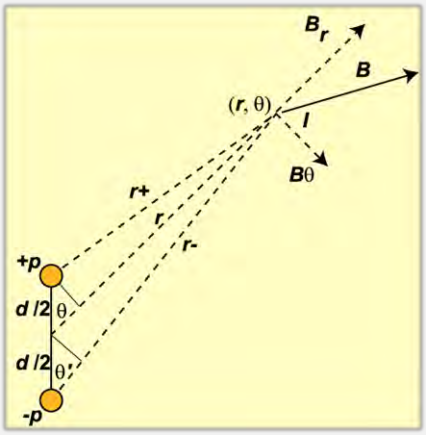

The tangent is:

$$\tan I = \frac{B_r}{B_\theta} = \frac{2 \times \frac{\mu_0 \times m}{4\pi r^3}}{\frac{\mu_0 \times m}{4\pi r^3}} \times \frac{\cos\theta}{\sin\theta} = 2 \times \frac{\cos\theta}{\sin\theta} = 2 \times \cot\theta = \mathbf{2 \times \tan \lambda} \tag{4.16}$$

With m = dipole magnetic moment, r = distance from the dipole and a point in the space (see figure above), μ_0= permeability of free space.

In the laboratory we can determine the paleo-inclination (I) in old rocks and thus calculate the paleo-latitude (λ) for the associated continent.

For each site (dike, lava flow…) a calculated site-mean direction gives rise to a **virtual geomagnetic pole (VGP)**. The mean of the **VGPs** defines a **paleomagnetic pole** which

averages out the secular variation and it coincides with the geographic pole at the time rocks were formed.

To calculate the position of the paleomagnetic pole we need the site geographic coordinates (λ_S, ϕ_S), and the mean of site directions (D_m, I_m) (see Figure 4.11).

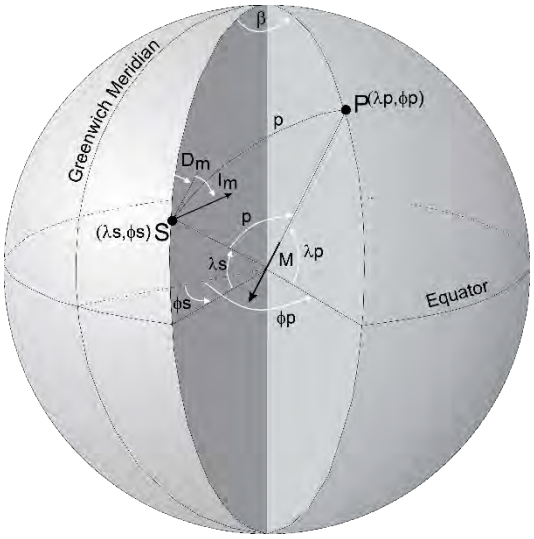

Figure 4.11: Localization of the sample site (S) to calculate the localization of the paleomagnetic pole. From Butler (1992).

Supposing the GAD hypothesis as valid, we calculate the colatitude (p), the great circle distance from site to pole (Figure 4.11).

$$\underline{tan\, Im\ = 2 \times tan\, \lambda} \qquad (4.17)$$

$$\underline{= 2 \times \cot \mathrm{p}}$$

Or,

$$\cot \mathrm{p} = \frac{\tan Im}{2} \Rightarrow \mathrm{p} \qquad (4.18)$$

$$= \frac{1}{\cot}(\frac{\tan Im}{2})$$

$$\mathrm{p} = \cot^{-1}(\frac{\tan I_m}{2}) = \tan^{-1}(\frac{2}{\tan I_m}) \qquad (4.19)$$

The pole latitude (λ_p) is given by:

$$\lambda_p = \sin^{-1}(\sin \lambda_S \times \cos \mathrm{p} + \cos \lambda_S \times \sin \mathrm{p} \times \cos(D_m)) \qquad (4.20)$$

The longitudinal difference between the pole and the sampling site is β (Figure 4.11):

$$\boldsymbol{\beta} = \sin^{-1}\left(\frac{\sin \mathrm{p} \times \sin(D_m)}{\cos \lambda_p}\right) \tag{4.21}$$

To calculate the pole longitude (φ_p) there are two solutions:

– If $\cos \mathrm{p} \geq \sin \lambda_S \times \sin \boldsymbol{\lambda_p}$

$$\varphi_p = \varphi_S + \boldsymbol{\beta} \tag{4.22}$$

– If $\cos \mathrm{p} < \sin \lambda_S \times \sin \boldsymbol{\lambda_p}$

$$\varphi_p = \varphi_S + 180° - \boldsymbol{\beta} \tag{4.23}$$

4.1.9 Paleogeographic reconstruction in the Precambrian

The reliability of paleomagnetic poles was discussed in chapter.1, where 7 criteria establish the Q factor (Van der Voo, 1990) for a paleopole, and whether it can be considered a key pole. Below, some examples show how to use a paleomagnetic pole in the paleogeographic reconstructions.

4.1.9.1 GAD through Precambrian?

As said previously, the GAD hypothesis is the most important assumption in paleomagnetism and its validity in the past is crucial in establishing the paleogeographic reconstructions. Archaeomagnetic studies show that, over the past 10 000 years, Earth's magnetic field is best described by the GAD model (McElhinny et al., 1996) and paleomagnetic data supports a GAD model until 150 Ma (when reconstructions are well-established) with 3 – 5% contribution of an axial quadrupole component (Besse and Courtillot, 2002).

The evolution of the Earth's magnetic field is related to the evolution of the convection processes in the liquid core due to the effect of magnetic convection and solid core growth (Reshetnyak and Pavlov, 2016). Tarduno et al. (2014) proposed the presence of a magnetic field on Earth older than ca. 3400 Ma supported by a conglomerate test in Kaapvaal craton (Usui et al., 2009). Onset for the dynamo is delayed in relation with the core nucleation due to the thermal regime in the mantle (Aubert et al., 2009; Labrosse and Jaupart, 2007). The inner core nucleation (ICN) should have been an important effect on the stability of the dipole (Roberts and Glatzmaier, 2001). Paleomagnetic signal for the ICN is expected using paleointensity database but the effect remains enigmatic (Labrosse and Macouin, 2003). Different models are proposed to evaluate the age of the early ICN (Brandon et al., 2003): ICN

at ~2150 Ma (Aubert et al., 2009), ICN at *ca*. 1500 – 1000 Ma (Biggin et al., 2015) or even younger at ca. 600 – 500 Ma (Driscoll, 2016; Macouin et al., 2004). Olson (2016) published a large review on the age of ICN and proposed a younger ICN at *ca*. 1100 – 400 Ma according to a high heat flux at the core – mantle boundary (CMB). All models depend on the interpretation of the core – mantle interaction and there are many uncertainties today on the behavior of the lower mantle. The recent studies of the post-perovskite phase discovered in 2004 (Murakami et al., 2004) in the CMB, may affect the current interpretations for the thermal interaction between mantle and core (Benešová and Čížková, 2016). Also, the use of paleointensity data to detect the ICN have been questioned by Smirnov et al. (2016), who highlight the lack of quality data to draw a conclusion.

To evaluate the GAD in Precambrian, we can mainly use the frequency analysis of inclinations calculated from the paleomagnetic data distributed over the Earth (Evans, 1976). Veikkolainen et al. (2014a) showed that the Precambrian field was dominantly dipolar with insignificant contributions of quadrupole (2%) and octupole (5%) components (Figure 4.12). Another method is to compare the normal and reverse polarities of the field due to a latitudinal dependence of the GAD (like the reversals test). Such an analysis was performed by Veikkolainen et al. (2014c) and supports the GAD hypothesis in the Precambrian.

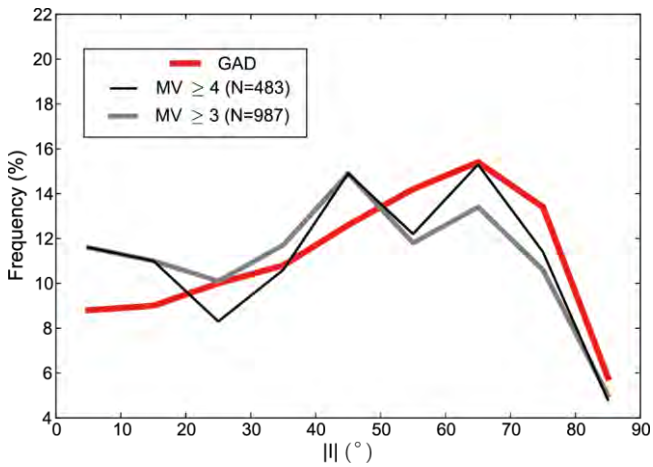

Figure 4.12: Inclination distributions with MV (modified Q_{index} of Van der Voo (1990b). Igneous and metamorphic rocks show a good correlation with the GAD model. Modified from Veikkolainen et al. (2014a).

For some periods anomalous APWPs with fast plate velocities > 20 cm/yr are observed, which question the validity of GAD model. Suggestion of non-axial dipole contribution to the magnetic field in these periods was proposed, for example, at ca. 1100 Ma for North America (Nevanlinna and Pesonen, 1983; Pesonen and Nevanlinna, 1981). New results with symmetric reversals (Swanson-Hysell et al. (2009), however, support a GAD model during these periods. According to these new results, Meert (2009) proposed to use the GAD hypothesis without

worrying about a non-GAD field contribution. We follow in this study the assumption that GAD field prevailed during Precambrian ("in GAD we trust"!), and that eventually anomalous APWPs suggest also the presence of true polar wander (TPW).

4.1.9.2 Paleolatitude reconstruction

A paleomagnetic pole at a given age can be used to reconstruct the position of the continent at its age. For example, the Oyapok granitoids from the Guiana shield (~2036 Ma,) carry a mean magnetic declination of 133.8° and a mean magnetic inclination of 60.2°, and the corresponding paleomagnetic pole is OYA (28°S, 346°E) (Nomade et al., 2001; Théveniaut et al., 2006) (Figure 4.13).

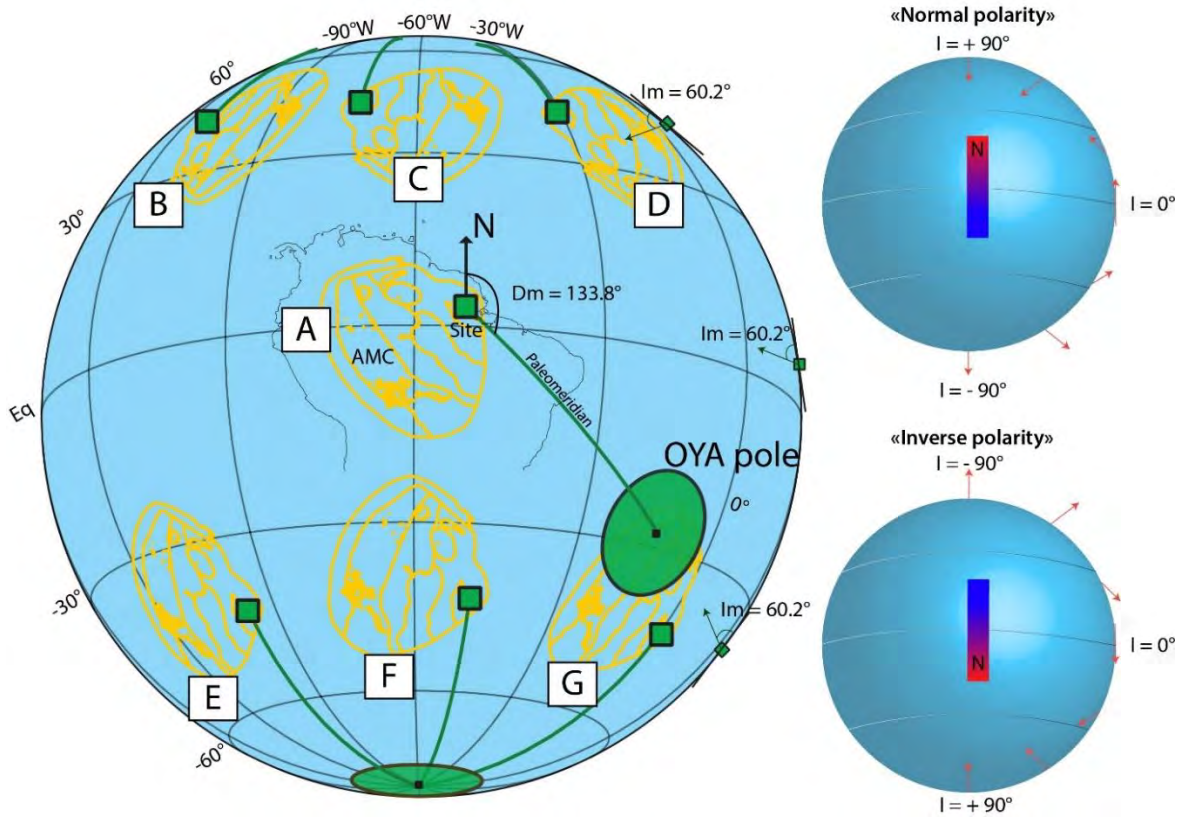

Figure 4.13: Reconstruction for the Amazonian craton at ~2036 Ma with the OYA pole. See text for precisions, adapted from D'Agrella-Filho et al. (2016).

According to the GAD model, the paleomagnetic pole coincided with the geographic pole (North or South) when the rock acquired the Earth's field during formation. So, in paleogeographic reconstruction a rotation pole ($\lambda_p; \varphi_p$), associated to a rotation angle (θ) must be calculated that takes the paleopole to coincide with the geographic pole. The same rotation pole (known as Euler pole) is used to rotate the continent to its paleogeographic position. If the coordinates of the paleomagnetic pole are $(\lambda_p; \varphi_p)$, we can calculate the coordinates of the rotation pole, or Euler pole $(\lambda_E; \varphi_E)$:

$$\varphi_E = \varphi_p + 90° \; ; \; \lambda_E = 0° \tag{4.24}$$

The angle of rotation (θ) is:

$$\theta = \lambda_p - 90° \text{ (north pole)} \tag{4.25}$$

or

$$\theta = \lambda_p + 90° \text{ (South Pole)}$$

Therefore for the OYA pole, the Euler pole is (0°, 76°) and the angle of rotation is 62° for a reconstruction on the South Pole or (0°, 76°) and the angle of rotation is -118° for a reconstruction on the North Pole. . This reflects the ambiguity in polarity due to the GAD model (Figure 4.13) (Buchan et al., 2000). We can reconstruct the position of the craton in the Northern hemisphere (positions B, C, D) or in the Southern hemisphere (positions E, F, G) (Figure 4.13). Based on the *ca*. 2036 Ma Oya pole, this technique provides the position of the Amazonian craton in latitude (constrained by its magnetic inclination) and gives its paleo-orientation (constrained by its magnetic declination). However, paleolongitude is not constrained. So, for a complete paleogeographic reconstruction we need additional information like geological evidence (orogenic belts, mafic dike swarms,…).

4.1.9.3 Comparison between two cratons

We can adopt two different approaches to study the paleo-position of two ideal cratons (A and B) (Figure 4.14.A). First we must have two coeval paleomagnetic poles for the two cratons in their present locations. We can calculate an Euler pole for each craton and transpose the poles on the geographic North Pole to have their paleo-latitudinal positions (Figure 4.14.B-C). After this rotation, we are free to move both cratons in longitude (Figure 4.14.D) around an Euler pole located on the North Pole, due to the symmetry of the GAD model. Note that only the shape of the cratons allows us to find the right configuration at the age of the coeval poles.

An opposite approach can be used to reconstruct the configuration of the cratons. As previously, we can reconstruct the position of one craton (craton A) in latitude (Figure 4.14.B). But looking at the shape of cratons we can assume that these two cratons were together. We can calculate an Euler pole by moving the second craton (craton B) in our supposed configuration with the first (Figure 4.14.E). In this case the paleomagnetic pole of the second craton is placed close to the pole of the first craton which supports this reconstruction but not exactly on the geographic North Pole. With this technique we can test models for cratonic configurations (such as SAMBA or NENA models) over time (see example of SAMBA reconstruction in Bispo-Santos et al. (2014b)).

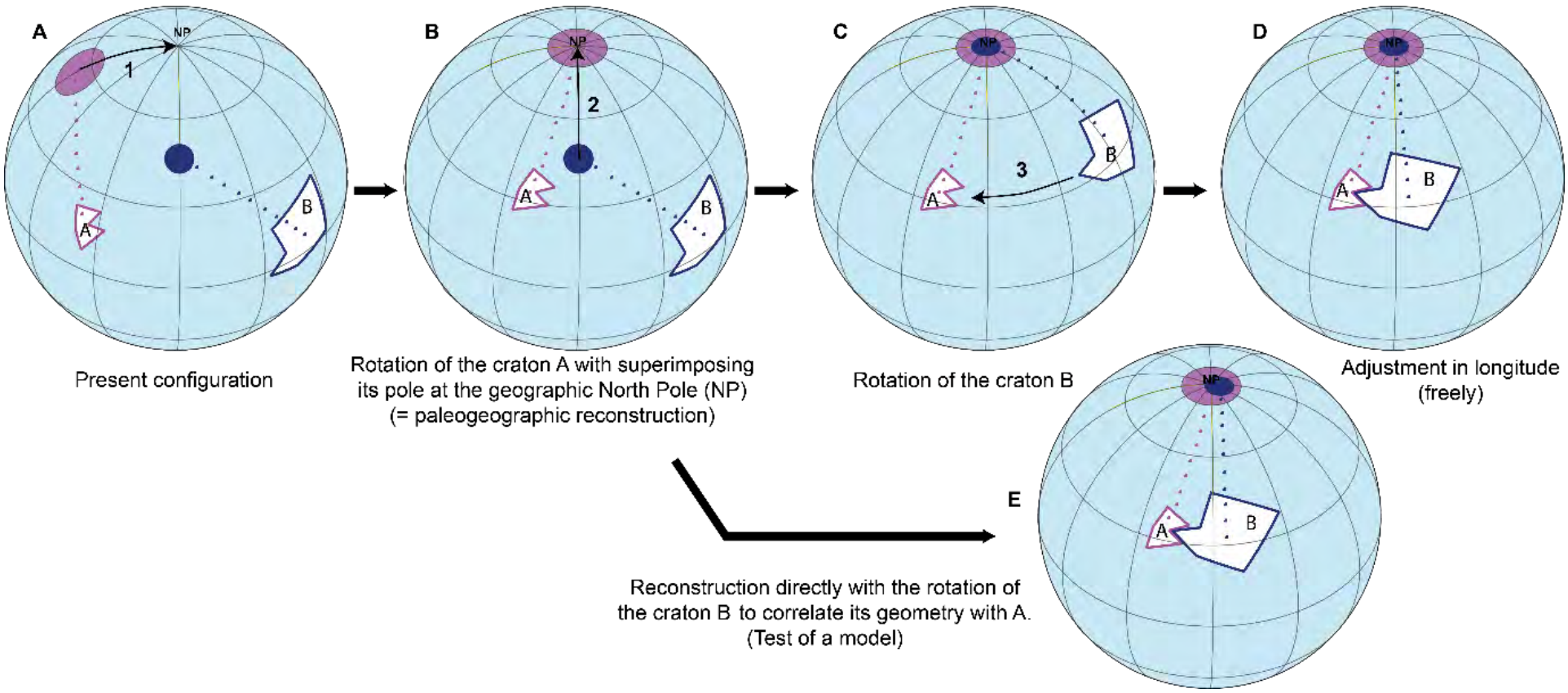

Figure 4.14: Cartoon to represent how we can reconstruct the paleogeography of two cratons (A and B).

More paleomagnetic poles are necessary to establish a precise paleogeographic reconstruction as we saw in chapter 1 by superimposition of APWPs.

4.1.9.4 True Polar Wander (TPW) reconstruction

Two processes can reorient the spin axis of a planetary body (Figure 4.15). The first is the change in obliquity, so the spin axis changes with respect to the celestial sphere (ecliptic). These changes are induced by external torques from the Sun and other planets (and impacts). The second process is by true polar wander (TPW).

True polar wander (TPW) is the large reorientation of the planet with respect to the spin axis (Gold, 1955; Goldreich and Toomre, 1969). In this case we don't have the reorientation of the spin axis with respect to the celestial sphere but to the surface of the planet. These changes are due to the mass distribution within the planetary body. A redistribution of mass inside a body alters its inertial tensor. To minimize energy, the rotation axis will be aligned with the maximum principal axis of inertia (I_{max}). A change of mass will modify the maximum principal axis of inertia (I_{max}) and the planet will tend to reorient to keep the I_{max} aligned with the spin axis. From space (celestial frame) it will look to see the surface of the Earth in rotation around the spin axis during the alignment of I_{max}. Figure 4.16 shows the relation between internal mass anomalies and TPW. A low in the geoid (negative load) may be produced by localized deep mantle cold or subduction zone. A high in the geoid (high topography) is induced by a positive mass anomaly as a mantle plume (or superswells). TPW slip occurs along the planet's largest viscosity discontinuity, at the core-mantle boundary (D"). This viscosity jump is characterized by the presence of seismic anisotropy and ULVZs (ultra-low-velocity zones) (Pradhan et al., 2015).

Here we consider TPW induced only by slow internal geological processes (mainly mantle convection) and we exclude the fast variations (giant impact, earthquake, seasonal, redistribution of ocean, ice-loading).

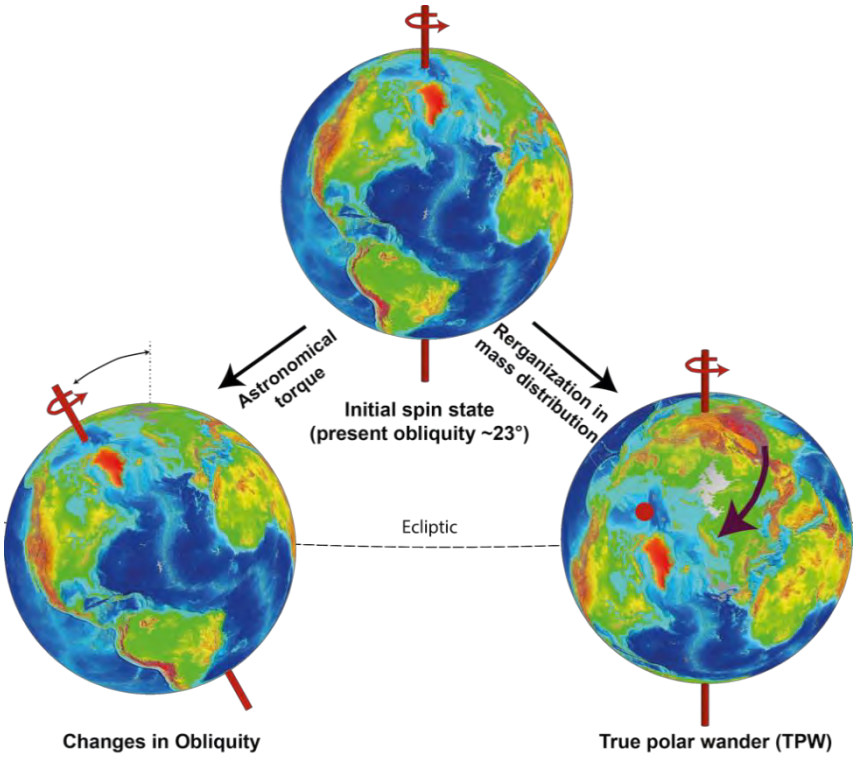

Figure 4.15: Difference between changes in Obliquity and true polar wander (TPW), modified from Siegler et al. (2016).

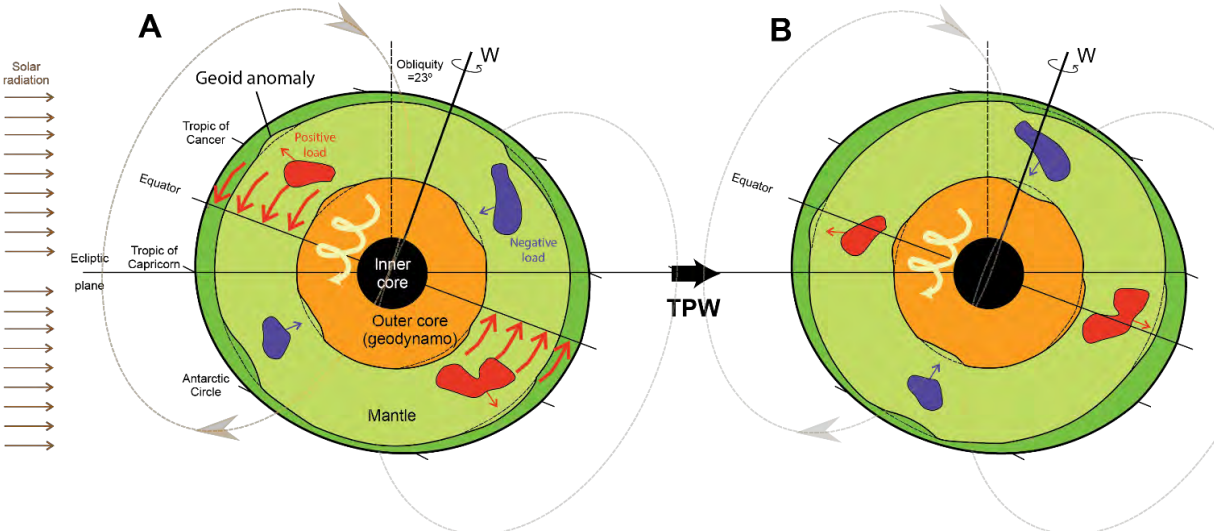

Figure 4.16: Simplified concept of true polar wander (TPW), modified from Evans (2003). The equatorial bulge is exaggerated. A: Density anomalies in the mantle can rising (red) or sinking (blue). B: TPW turns the whole solid earth (mantle and crust) driving positive loads to the equator. The geomagnetic field remains aligned with W (spin axis).

The reorientation of the rotation axis is governed by a competition between the driving force for TPW (loads) and stabilization processes (Chan et al., 2014):

- TPW is driven mainly by loads within the planet in a non-hydrostatic figure. The magnitude of reorientation depends on the initial load latitude (strong reorientation if positive load is at pole). Positive loads move towards the equator, whereas negative loads move towards the rotation axis.
- A first stabilization is the viscous response of the rotational bulge which is related to the centrifugal potential. The hydrostatic response of the planet (Love numbers) in rotation acts to stabilize the pole (Ricard et al., 1993).
- The second stabilization is induced by presence at the surface of a planetary body of an elastic lithosphere. Presence of lithosphere after the gradual cooling of proto-planet would not alter the hydrostatic form of the planet. Elastic stresses induced in the lithosphere during the TPW (reorientation) will prevent the rotational bulge to adjust perfectly (not superimposition of I_{max} and the spin axis) which implies that the positive load will not be at the equator. The lithospheric effect is the remnant bulge (Matsuyama et al., 2006; Willemann, 1984). In Earth presence of plate tectonics implies a broken lithosphere (Creveling et al., 2012).
- A third mechanism can be the figure of the Earth in relation to the mantle convection itself (Creveling et al., 2012). Present mantle convection implies a figure in Earth with two thermochemical domes (superswells) beneath Africa (Tuzo) and Pacific Ocean (Jason) associated with the ring of subduction zones in Pacific. I_{min} is aligned with the superswells and I_{max} with the spin axis. Greff-Lefftz and Besse (2014) showed the possible effect of the growth of thermochemical domes (excess ellipticity) at the equator to stabilize the rotations of poles.

Raub et al. (2007) proposed a classification for the different TPW. Type 0 corresponds to small TPW with short timescale (earthquake, impact…) and Type-1 to TPW in relation with the plate tectonics and mantle reorganization. Raub et al (2007) called type-2, special cases of TPW as episode of inertial interchange true polar wander (IITPW) that requires a 90° rotation, or oscillatory TPW. In this work, TPW is referred to the Type-1 and we don't consider oscillatory TPW or IITPW because of the lack of data to constrain them.

Mitchell (2014) compiled the paleomagnetic database (discordant poles) and shows a correlation between TPW events and supercontinent cycle (Figure 4.17). Large TPW events seem to occur before the formation of the supercontinents (Columbia, Rodinia and Pangea), maybe related with an inelastic lithosphere or a triaxial figure during the orthoversion transitions (memory for old supercontinent / superplume at 90°).

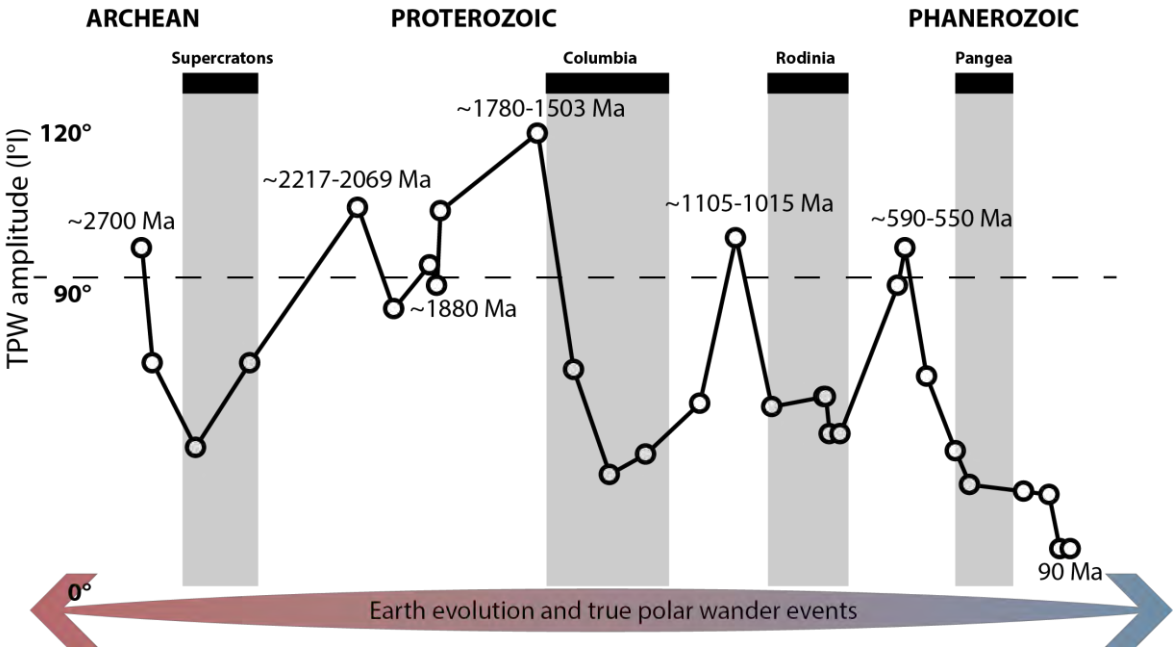

Figure 4.17: Amplitude of true polar wander events (TPW) according the paleomagnetic database for the Earth and supercontinent cycle. Adapted from Mitchell (2014).

- **>How to use paleomagnetic data to reconstruct a TPW event?**

Paleomagnetic reconstructions use apparent polar wander paths (APWPs) for different cratons. With this technique APWP for a craton represents the displacement of the craton/lithosphere over the asthenospheric mantle (plate tectonics). TPW signals were recognized since the 50s (Day and Runcorn, 1955) and were considered as negligible in relation to the plate motion. Evans (2003) summarized in a cartoon the possible effect of TPW signal that can enhance or mask the plate tectonic component in the APWP signal, hence the relation:

$$Apparent\ Polar\ Wander\ (APW) = Plate\ motion + \boldsymbol{TPW}$$

If we consider a rotation of the entire solid Earth, **TPW = APW** and it will mask the plate motion component. To demonstrate an episode of TPW we have to verify the following requirement (Meert, 1999). All the APWPs of all cratons have the similar lengths and shapes during the TPW period. We can in theory verify this requirement with a paleomagnetic database for the considered period.

Raub et al. (2007) proposed to use a reconstruction in a TPW hypothetical frame. For each craton we calculate the best-fit great circle through its APW path and the associated axis with respective errors (Paleomac software of Cogné (2003)). We remember that the APWP is associated to the craton, so we rotate the APWP + craton such that the axis of the great circle is located at 0°; 0° on the projection. This point (0°; 0°) is the center of the new TPW frame, the so-called “spinner diagram”.

Figure 4.18: Cartoon to explain the reconstruction during a hypothetic True Polar Wander event (TPW).

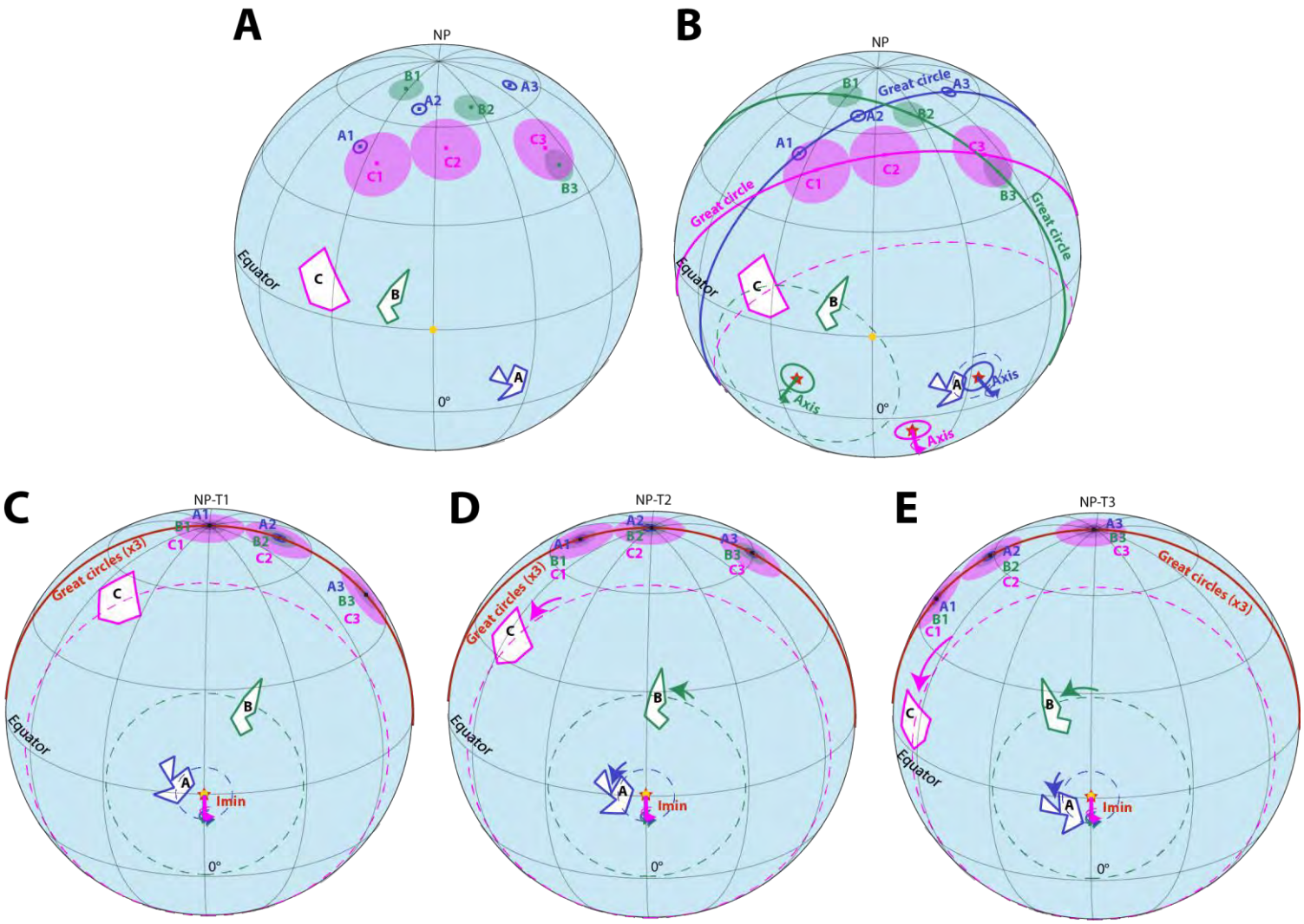

Then it is possible to superimpose all great circles of all cratons, and at the same time all the axis of great circles on 0°; 0° (Figure 4.18). With this reconstruction the center of the projection (0°; 0°) will be the new axis of rotation and consequently all paleomagnetic poles will rotate along the great circle at 90°E. To verify the existence of TPW during the period T1 – T3, we can reconstruct the positions of cratons at T1 by superimposing the paleomagnetic poles dated at T1 in a paleogeographic reconstruction. We can check then that all paleomagnetic poles (T1-T3) have the same localization, *i.e*. they will undergo the same rotation in the interval T1-T3 (TPW).

Many bodies of the solar system seem to have undergone TPW events during their history (Matsuyama et al., 2014). We can cite Mars and the Tharsis dome (Bouley et al., 2016), the Moon (Siegler et al., 2016), Europa (Schenk et al., 2008) and Enceladus (Stegman et al., 2009), which reminds us that TPWs are ubiquitous in planetary histories

4.2 Geochronology

A key pole is by definition a paleomagnetic pole with a precise age (with incertitude < 10 Ma for Precambrian rocks) (Buchan, 2013). In order to obtain precise ages I have used two different methods based on the U-Pb system on zircons. I also tried *in situ* rutile U-Pb dating by laser ablation ICPMS but without positive results.

4.2.1 U-Th-Pb system

During partial melting and fractional crystallization of magma, U and Th are concentrated in the liquid phase (incompatible) and will be incorporated into the more silica-rich phases. Therefore, granitic rocks (and by consequently the continental crust) are more enriched in U and Th than basaltic or ultramafic rocks. The mineral most commonly used to date rocks by the U-Pb system is the zircon ($ZrSiO_4$) (Corfu et al., 2003). Zircon incorporates U^{4+} in its structure in substitution to Zr^{4+} and Th^{4+}, and excludes Pb^{2+} with a larger ionic radius and lower charge.

Uranium has three isotopes and all are radioactive, ^{238}U, ^{235}U and ^{234}U. Thorium exists as a radioactive isotope, ^{232}Th. ^{238}U, ^{235}U and ^{232}Th are each the parents in a chain of radioactive daughters to produce at the end stable isotopes of lead. The element lead has four naturally occurring stable isotopes, ^{204}Pb, ^{206}Pb, ^{207}Pb and ^{208}Pb.

The three U-Th-Pb decay chains:

$$_{92}U^{238} = {}_{82}Pb^{206} + 8\ {}_{2}He^{4} + 6\beta^{-} + Q \tag{4.26}$$

$$_{92}U^{235} = {}_{82}Pb^{207} + 7\ {}_{2}He^{4} + 4\beta^{-} + Q \tag{4.27}$$

$$_{90}Th^{232} = {}_{82}Pb^{208} + 6\ {}_{2}He^{4} + 4\beta^{-} + Q \tag{4.28}$$

Where He = α is an alpha particle, β is a beta particle and Q is energy released during the decay.

The standard decay equations of the three decay systems is normalized to ^{204}Pb because is the only non-radiogenic isotope of lead. We can determine the concentrations of U, Th and Pb along the isotopic composition of Pb and therefore we have three independent systems, which means, three separate age equations (isochron):

$$\left(\frac{^{206}Pb}{^{204}Pb}\right) = \left(\frac{^{206}Pb}{^{204}Pb}\right)_0 + \left(\frac{^{238}U}{^{204}Pb}\right)(e^{\lambda_{238}t} - 1) \tag{4.29}$$

$$\left(\frac{^{207}Pb}{^{204}Pb}\right) = \left(\frac{^{207}Pb}{^{204}Pb}\right)_0 + \left(\frac{^{235}U}{^{204}Pb}\right)(e^{\lambda_{235}t} - 1) \tag{4.30}$$

$$\left(\frac{^{208}Pb}{^{204}Pb}\right) = \left(\frac{^{208}Pb}{^{204}Pb}\right)_0 + \left(\frac{^{232}Th}{^{204}Pb}\right)(e^{\lambda_{232}t} - 1) \tag{4.31}$$

Where 0 is the initial ratio when the system is closed, t is the time since the closure, and λ is the decay constant for the considered system. For zircon mineral, the contribution of initial lead is negligible and we can simplify the equations:

$$\left(\frac{^{206}Pb}{^{238}U}\right) = (e^{\lambda_{238}t} - 1) \tag{4.32}$$

$$\left(\frac{^{207}Pb}{^{235}U}\right) = (e^{\lambda_{235}t} - 1) \tag{4.33}$$

$$\left(\frac{^{208}Pb}{^{232}Th}\right) = (e^{\lambda_{232}t} - 1) \tag{4.34}$$

We represent classically the geochronological results in the Wetherill Concordia plot (Wetherill, 1956) which plots $\left(\frac{^{206}Pb}{^{238}U}\right)$ versus $\left(\frac{^{207}Pb}{^{235}U}\right)$ from the same analyzes (Figure 4.19). Other representations exist for the U-Pb system (Tera-Wasserburg plot for example). Samples yielding the same ratios have the same age and are deemed **concordant**. Samples with concordant ages represent the age of the sample and such samples represent closed systems

since the crystallization of the rock (no lost or gain for U, Th and Pb). Sometimes ages calculated are not concordant and imply a U, Pb, or Th loss during the history of the sample. A line fitted through the discordant zircons give the age of formation of zircons at the intersection with the Concordia. The lower intercept can indicate the time where Pb was lost and sometimes provide information on a metamorphic event. If the Pb-loss is continuous by diffusion the age for the lower intercept is ambiguous.

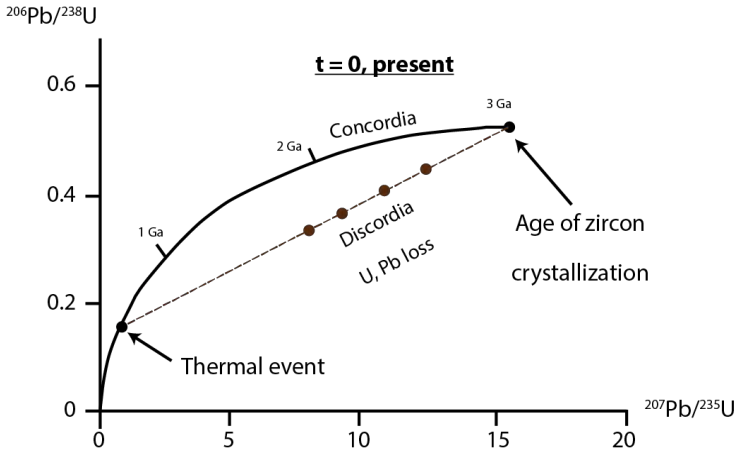

Figure 4.19: Using of the Wetherill diagram for the U-Pb system.

4.2.2 SHRIMP analysis

Samples of rhyolite, felsic dike and andesite were collected for U-Pb geochronological study on zircon (~10 kg by site). Mineral separation of zircons was carried out at Federal University of Pará (UFPA) in Belém. Unfortunately just one felsic dike (PY99) was able to be analyzed by the Sensitive High Resolution Ion Microprobe (SHRIMP IIe/MC) at the Institute of Geosciences of the University of São Paulo (IGc-USP) (Figure 4.20). Cathodoluminescence (CL) and back-scattered electron (BSE) images using a scanning electron microscope (SEM) were performed directly in São Paulo (GeoLab-IGc-USP). Standard used was Temora2 zircon of 416.78 Ma (Black et al., 2004) and results show good value of 416.8 Ma. The primary beam spot size was 30 µm (Sato et al., 2014).

Figure 4.20: SHRIMP II in the IGc laboratory in São Paulo, Brazil.

4.2.3 LA-ICPMS analysis

With only one sample for the SHRIMP analysis, an alternative dating of the study samples was done by U-Pb zircon age by LA-ICP-MS (Laser Ablation Inductively Coupled Plasma Mass Spectrometry) directly *in situ* on polished section at the Federal University of Minas Gerais in Ouro Preto (UFOP) (Figure 4.21). This technique was possible on rhyolites and felsic dikes because the amount of zircons was important. Therefore, I prepared polished sections at the laboratory of IAG-USP and spotted the zircons in optical microscopy under reflected light. The zircons were characterized by cathodoluminescence (CL) and back-scattered electron (BSE) images using a scanning electron microscope (SEM) in Ouro Preto. Analysis was performed in two sessions using a ThermoScientific Element 2 sector field ICP-MS coupled to a LSX-213 $G2_+$ laser (CETAC Technologies) with a 20 µm laser spot size. The data were reducted with the software Glitter (Van Achterbergh et al., 2001) and ages were calculated using the IsoplotEx 4 (Ludwig, 2009) program with uncertainties on the dating at 2 sigma level.

The main advantage of the laser ablation is the shorter analysis time (1 minute) than by SIMS (20 minutes) for precisions generally comparable. The main limitation for the measurement by laser ablation is the digging related to the laser source of 10 – 30 µm in depth (Figure 4.22).

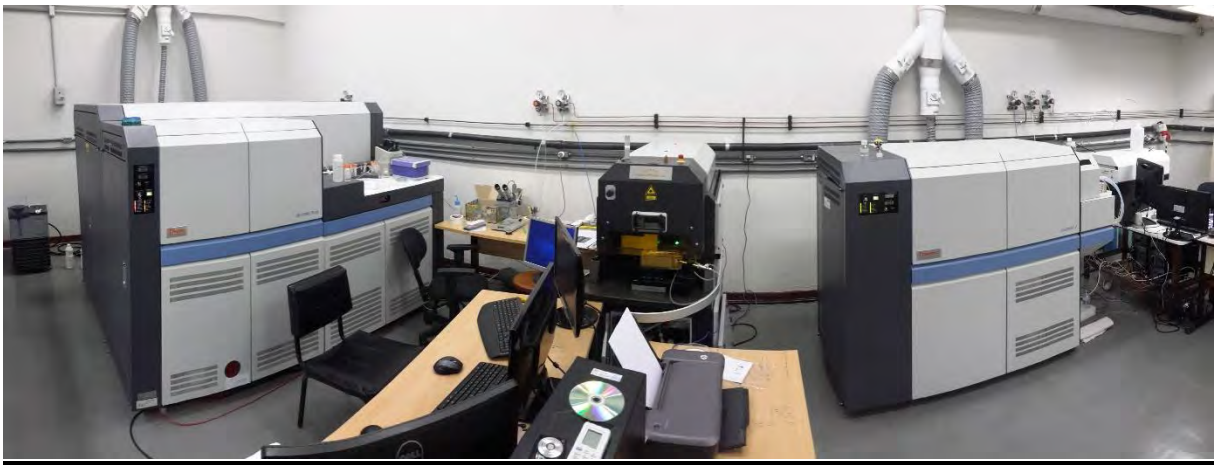

Figure 4.21: LA-ICP-MS in the laboratory of Ouro Preto (UFOP). *Credits: F. Hodel.*

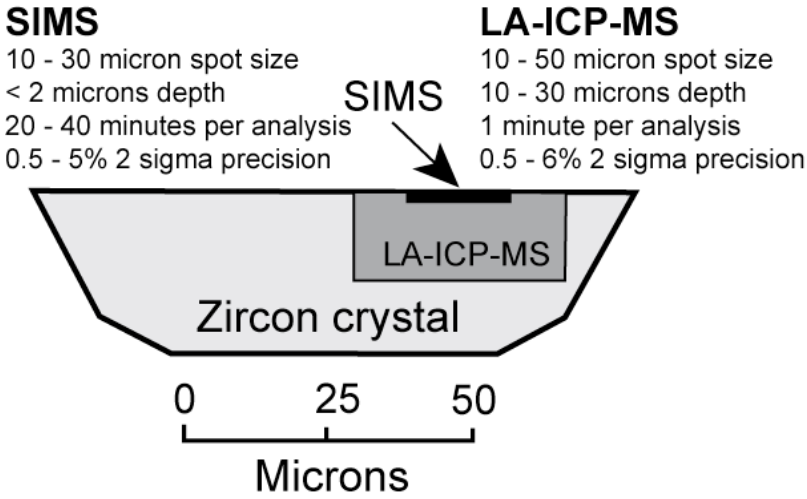

Figure 4.22: Comparison between analysis by SIMS (SHRIMP) and LA-ICP-MS.

4.3 Geochronological and paleomagnetic systems

In paleomagnetism, magnetite and hematite are the main magnetic mineral to record primary remanence (TRM) because they have high Curie temperatures (Tc magnetite= 585°C, Tc hematite= 675°C). A major problem in paleomagnetism is that minerals can be remagnetized even if the rock has undergone no metamorphism or chemical change. Geochronology provides information to recognize the magmatic and/or metamorphic event likely to affect the rocks.

We use the notion of **closure temperature** (**T_c, or blocking temperature)** in geochronology to indicate the temperature under which the minerals have “cooled” and when the diffusion of parent (and daughter) isotopes between the mineral and the external environment stopped. Therefore **T_c** for a mineral may be defined as its temperature at the time

corresponding to its apparent age (Dodson, 1973). The closure temperature varies in function to the cooling rate and the diffusion. Therefore, we have to know the cooling rate to calculate the closure temperature of a mineral for the study rocks (Dodson, 1979). For example, for the zircon $\mathbf{T_c}$ calculated with a cooling rate of 1°C.Ma^{-1}, 5°C.Ma^{-1} and 10°C.Ma^{-1} are 899 ± 7°C, 926 ± 6°C, and 938 ± 5°C respectively (Lee et al., 1997). During dikes emplacement in a cratonic area as the Amazonian craton we can consider a rapid cooling and U-Pb ages on zircons will reflect the age of crystallization of dikes. The closure temperature is always greater than 900°C and above many granitic magma (750 – 850°C), which explains why it indicates the onset of crystallization and why it's a robust geochronometer.

This closure temperature varies according to the minerals. U-Pb geochronology combined with $^{40}Ar/^{39}Ar$ geochronology is classically used to recognize superimpositions of thermal events in cratonic environment (See for the Amazonian craton (Tavares, 2015; Théveniaut et al., 2006)) because amphibole ($\mathbf{T_c}$= 450 – 500°C), muscovite ($\mathbf{T_c}$= *ca*. 450°C), and biotite ($\mathbf{T_c}$= *ca*. 300°C), have lower closure temperature than U-Pb system on zircon ($\mathbf{T_c}$ > 900°C). Concordance between U-Pb and Ar–Ar ages for the same rock suggest a rapid cooling history. Comparison between minerals with distinct closure temperature is useful to estimate a cooling rate (°C.Ma^{-1}) for the rock unit (they define the cooling history of the rock).

Some problems exists in geochronological studies. All methods are dependent from the element diffusion and rocks need to remain in a closed-system (Fresh rocks). We can already consider that whole rock analyzes are not reliable. Distinct minerals do not react in the same way to the considered system. For example, biotite is more sensitive to argon loss than amphibole. Therefore, biotite ages can be ambiguous. A large sampling have to be considered with many ages for comparison because reset (alteration) can be possible on localized analysis. For Ar-Ar geochronology we need weighted age plateau calculated on > 70 % of the argon released (high temperature plateau with more than three concordant incremental heating steps) at minimum, and evidence for minor argon loss. Mini – plateau with 50 – 70 % of the argon released (also known as pseudo-plateau) are considered much less reliable.

Few studies are available for the Carajás Province but recently Tavares (2015) provided new geochronological data and robust Ar-Ar ages for the Carajás domain. Among the robust ages we can cite those for the Itacaiúnas Supergroup (2760 – 2740 Ma, (Machado et al., 1991)), and weighted plateau age of 1930 ± 11 Ma and mini-plateau age of 1877 ± 11 Ma on muscovite (Tavares, 2015). Among the younger ages we observe only one age of 797 Ma on whole rock with mini-plateau so, this age can't be considered as reliable. Many Ar-Ar ages (muscovite/biotite) between 2000 – 1800 Ma indicates resetting during Paleoproterozoic in the Carajás Province (Transamazonic orogenic belts and Uatumã event?). It should be noted

that the lack of younger ages does not mean the absence of thermal events, since emplacement of dike swarms in the area are dated at ~550 Ma and ~200 Ma (Teixeira et al., 2012a; Teixeira et al., 2012b; Teixeira et al., 2016). We can explain the absence of these ages simply because the thermal diffusion in rocks is not an efficient process and difficult into large massive granitoids or greenstone belt. It would be interesting to test new ages in recent weakness zones (dikes, fault ...) where thermal diffusion is easier.

Amphibole with a closure temperature of ~500°C could be the best geochronometer to date a magnetic age (primary magnetization with equivalent high blocking temperatures). Biotite ages (~300°C) could represent ages of thermal perturbations for the considered rocks (secondary magnetization). But we must specify that a rock with an Ar-Ar age (hornblende) of 1880 Ma (for example) comparable to its U-Pb zircon age can carry a younger magnetization.

In paleomagnetism, we saw that the parameter of interest for ferromagnetic grains is the **thermal relaxation time** (τ). Small magnetite grains with a single-domain (SD) are stable with a high relaxation time whereas magnetite with multi-domain (MD) has a low relaxation time and are less stable. Pullaiah et al. (1975) used the relation between the relaxation time and the blocking temperature (**T_b**) to predict the acquisition of secondary magnetizations for single-domain (SD) grains. In practice blocking temperatures are determined through thermal stepwise demagnetization and depends on the heating time in laboratory ($\tau\ labo$). We can calculate and represent the evolution of blocking curves for the magnetite and hematite in a nomogram diagram (or blocking diagram) (Figure 4.23).

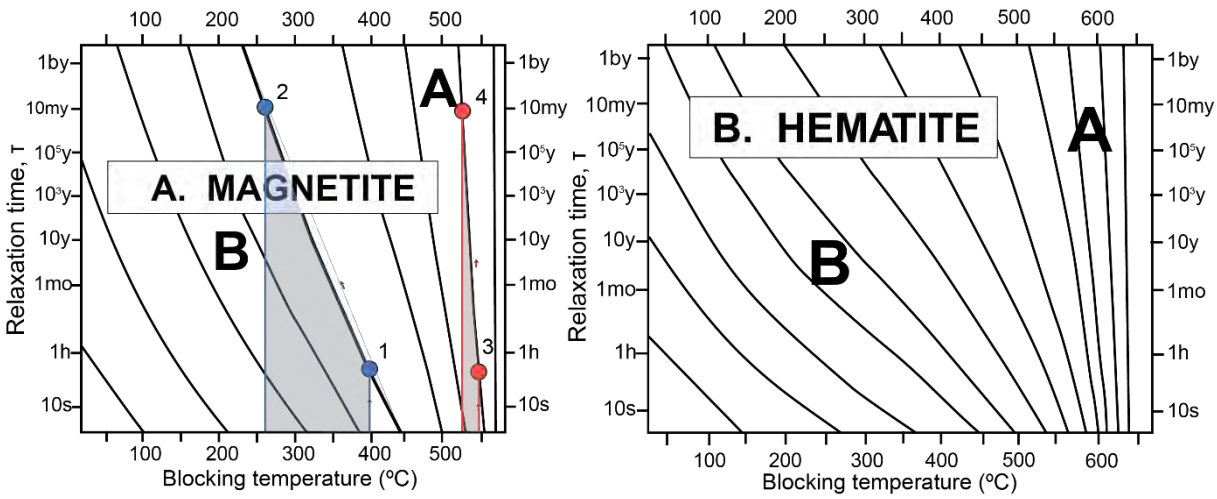

Figure 4.23: Relation between the relaxation time and the blocking temperature for the magnetite (A) and the hematite (B), called the nomogram diagrams (Pullaiah et al., 1975).

Let us take as example a sample with magnetite as carrier of the remanence magnetization and a blocking temperature of 400°C. We can note that 400°C (**T_b**) is below the Curie temperature. We determined a **T_b** of 400°C using thermal demagnetization during ~30 –

40 minutes ($\boldsymbol{\tau = 40\ min}$), **point 1**. Blocking curves (lines on the diagram) represent the conditions to unblock the magnetic grains which are with the same properties (volume, domains…). The **point 1** and **point 2** are on the same curve (in blue), so we can estimate what temperature is required for a determined period of time to unblock the primary magnetization and to remagnetize the sample. This imply that if the sample is heated to 250°C during 10 Ma (dike swarms in the past for example) the same grains could be unblocked and remagnetized (Figure 4.23.A). This example highlights that a remagnetization is possible during heating at relatively low temperature for several millions of years (for grains with low Tb).

A second example show magnetite with high blocking temperature (550°C) during the thermal demagnetization (**point 3**) ($\boldsymbol{\tau = 40\ min}$). In this case, the blocking curve indicates that a higher temperature (~520°C) is necessary during 10 Ma to remagnetize this sample (**point 4**). The nomogram diagram allows us to understand the influence of the blocking temperature on the stability of the magnetization. Region A in the diagram shows $\mathbf{T_b}$ close to the Curie temperature (red area under the curve) and imply stable magnetic grains and difficult to remagnetize, whereas region B (blue area under the curve) shows low-$\mathbf{T_b}$ (> 200°C from Tc) and represents unstable grains, easy to remagnetize. The same theory is used for hematite (Figure 4.23.B).

In summary, the relationship between temperature and thermal relaxation time (τ) indicates some caveats to associate the paleomagnetism with geochronology.

Chapter. 5: Petrology and magnetic mineralogy of the Tucumã dike swarms; overview of the dike swarm of the Uatumã event

This chapter aims to study the dike swarm of Tucumã to make connections between the different parts of the volcano-plutonic system in the Carajás province. Oriented drill core samples and blocks were collected for rock magnetism, geochemistry and isotope geology in collaboration with the University of Belém (Prof. DC. Oliveira). The study of felsic and mafic dikes cutting across the Archean basement near Tucumã (SW-Pará, Brazil) provides new data to constrain this magmatism. The Tucumã felsic dikes likely represent the subvolcanic equivalents of the A-type granites in the area, which were emplaced in relation with the amalgamation of Columbia supercontinent. Note that the exact configuration of Columbia supercontinent is still debated, thus, the relation of this event with the amalgamation of the supercontinent remains a matter of discussion.

A series of thin and polished sections were examined using optical microscopy and scanning electron microscope (SEM) at GET-Toulouse laboratory (France) to determine the location of the different magnetic phases, to observe their mineral associations and to perform a qualitative analysis of the major phases and accessories. Quantification of the major components was performed using the Cameca SX100 microprobe at the analytical Castaing platform (Toulouse). Twenty samples were selected and ground in a planetary mill and sent to SARM (Service d'Analyse des Roches et des Minéraux, Nancy, France), to obtain the composition in major and trace element.

I present here some unpublished (available in supplementary material) results relative to the magnetic mineralogy of the dikes and to their relation with geochemistry. I am co-author of a recently published paper about the petrology and geochronology of dikes (da Silva et al., 2016) (At the end of the chapter).

5.1 Lithology

5.1.1 Field observations

Three types of dikes were observed. The system of felsic dikes shows a main N125 ° direction (Figure 5.1.A). The felsic dikes are *ca*. 15 m in width, and a few hundred meters in length in average. They are clearly visible thanks to their elevated topography (Figure 5.1.A). Felsic dikes are made of microgranite characterized by subhedral phenocrysts of quartz, alkali feldspar and plagioclase in a quartz-feldspar matrix with granophyric texture (Figure 5.1.B). Mafic dikes are less well-preserved and are generally represented by many small blocks. In

most cases, they are found associated with felsic dikes. Mafic dikes are dark gray to dark green and exhibit an aphanitic texture with the same direction of felsic dikes. (Figure 5.1.C). Felsic and mafic dikes display field evidence for mingling (Figure 5.1.E) (mafic enclave in felsic dikes and K-feldspar megacrysts in mafic dikes in Figure 5.1.F) suggesting that mafic and felsic magmas were coeval. It should be noted that the felsic dikes are widely represented in contrast to the mafic dikes, suggesting a more significant contribution of felsic magmatism.

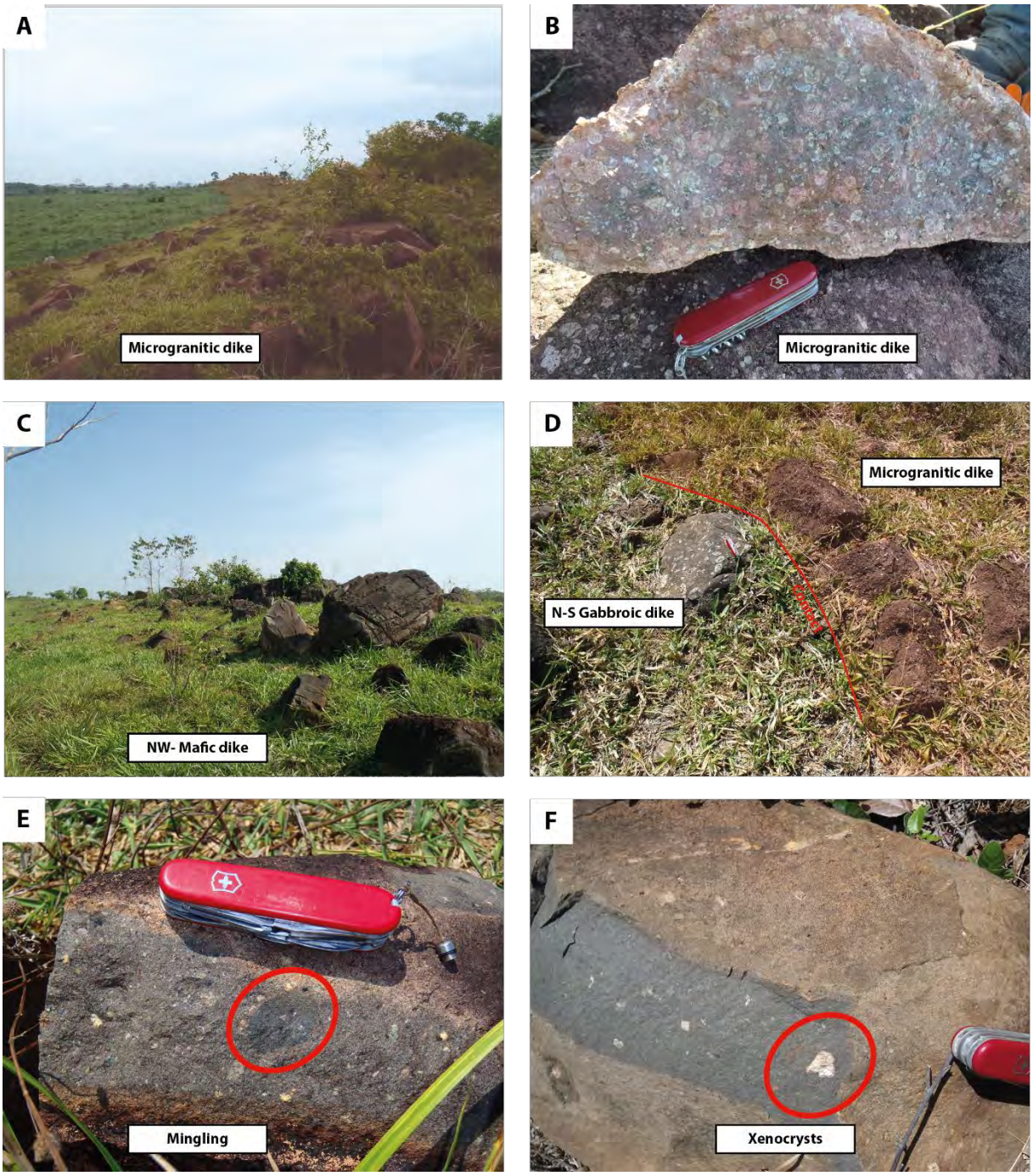

Figure 5.1: A: Felsic dike of site 52. B: Block of microgranite with phenocrysts of feldspar, plagioclase and quartz. C: NW-Mafic dike with many small blocks. D: NS-gabbroic dike at contact with a microgranitic dike. E: Mingling between mafic and felsic dike. F: Xenocrysts of feldspar in a NW-mafic dike.

Only in one area, another type of younger mafic dike was discovered cutting across the felsic and mafic dike association (Figure 5.1.D). This younger dike is *ca*. 10 meters in width and shows an almost N-S strike, very different from the general direction of the NW-dikes. The NS-dike is a gabbroic rock with porphyritic plagioclase (Figure 5.1.D).

5.1.2 Microgranitic dikes

5.1.2.1 Petrography

The optical microscope allows to identify primary (or “first generation”) magmatic minerals, such as euhedral to subhedral phenocrysts formed in subvolcanic environment. It also allows recognizing a second generation of magmatic minerals, which are formed during the last stages of the magma crystallization and develop preferentially anhedral shapes, which form the matrix of the rocks and associated textures with intergrowth and exsolution. After the magmatic stage, the microgranite underwent a hydrothermal alteration. The studied rocks are microgranites with microgranular texture that comprises euhedral to subhedral alkali feldspar, plagioclase and quartz (I) (Figure 5.2.A). Crystals of feldspar are commonly euhedral tabular with irregular edges (Figure 5.2.B). They show Carlsbad twins (Feldspar I) as well as albite exsolution when perthitic (Figure 5.2.A). The only mafic silicate present in thin sections is a biotite with weakly pleochroic green to greenish color (Figure 5.2.C). In the matrix the presence of plagioclase is observed, together with alkali feldspar and quartz (Figure 5.2.D). Symplectic growth texture is recognized between quartz (II) and feldspars forming granophyric textures (Figure 5.2.D).

To study the opaque minerals, we used an ore microscope with reflected light. The iron oxides were also examined using a scanning electron microscope (SEM) to explore their primary character (composition and textural association). Accessory minerals are zircon, magnetite, allanite and titanite. Zircon ($ZrSiO_4$) is present in all microgranite samples (Figure 5.2.E). In the sample PY69B3, zircon is weakly zoned. Subhedral crystals of titanite (Ca Ti (SiO_4) (O, OH, F)) are frequently found in the studied samples (Figure 5.2.F).

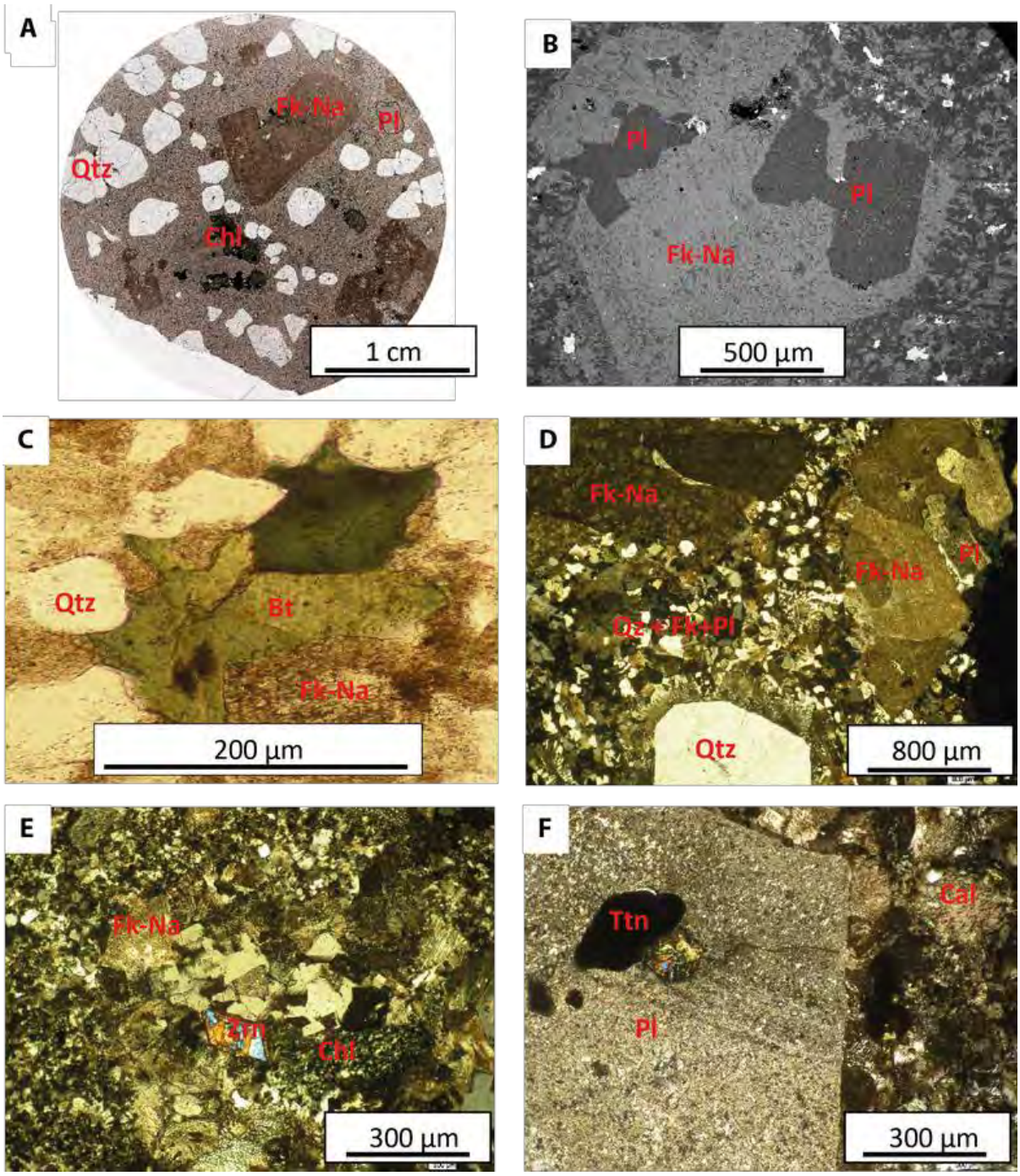

Figure 5.2: A: Polished section of the sample PY69B3. B: SEM image in backscattered electrons (BSE) of perthitic feldspars and plagioclases in a microgranite. C: Photomicrograph of biotite (plane polarized light = PPL). D: Graphyric association in the sample PY65 (cross polarized light = XPL). E: Zircon in the sample PY55 (XPL). F: Subhedral titanite in plagioclase (XPL). Abbreviations: Qtz = quartz, Fk-Na = perthitic feldspar, Pl = plagioclase, Chl = chlorite, Bt = biotite, Ttn = titanite, Cal = calcite.

Magnetite (Fe_3O_4) is the main primary iron oxide and is present in all studied rocks. For example, in the sample PY65, we observe an iron oxide inclusion within an euhedral albite crystal suggesting a primary magmatic origin (Figure 5.3.A). The EDS spectrum shows that the mineral is iron oxide (without Ti), which may be magnetite or hematite, since we cannot see the difference between Fe^{2+} and Fe^{3+} using SEM technique (Figure 5.3.B). Magnetite grains exhibit a very small size (~5 – 10 µm) difficult to observe with the SEM. However, it was

possible to detect octahedral magnetite within a quartz phenocryst, hence the primary character of magnetite (Figure 5.3.C). The EDS spectrum confirmed that this mineral is an iron oxide (Figure 5.3.D).

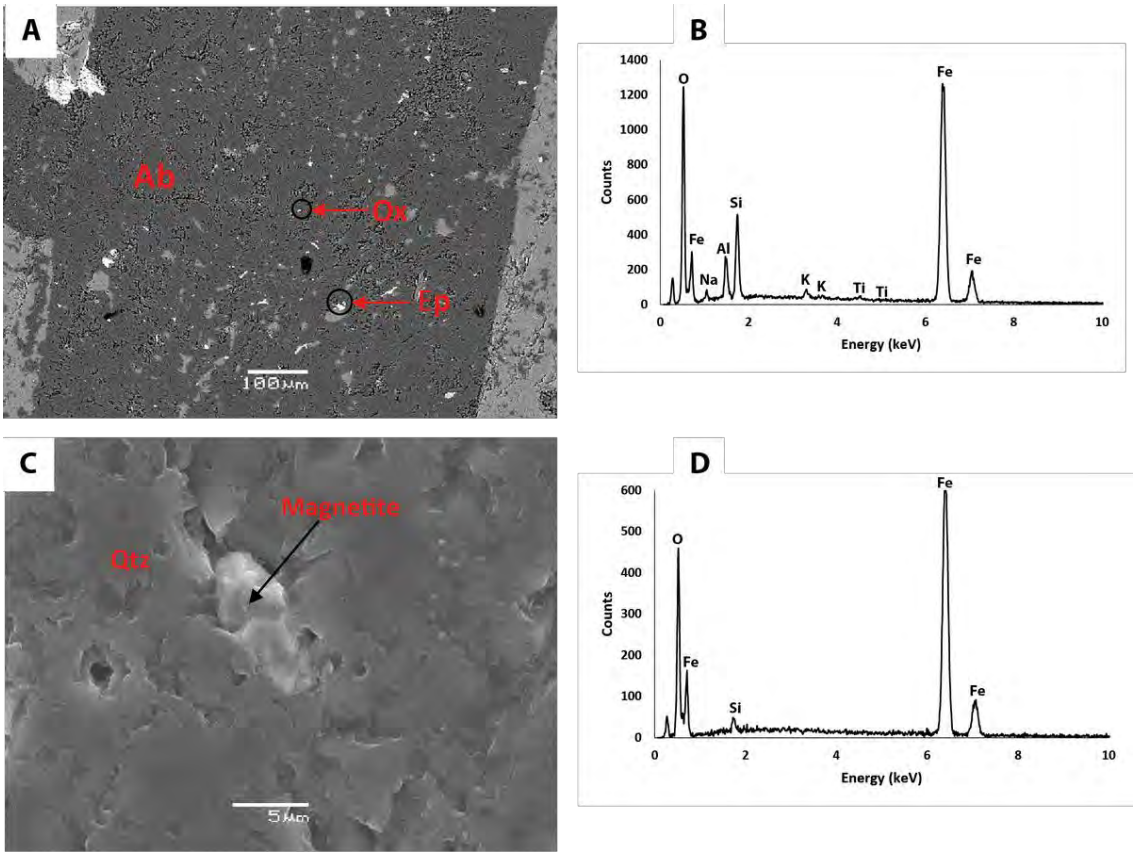

Figure 5.3: Iron oxides in microgranites. A: SEM-BSE micrograph of Iron oxide in plagioclase (albite) in the sample PY65G4. B: EDS spectrum for the iron oxide of the image A. C: SEM-Secondary Electron Image (SEI) of primary euhedral magnetite in inclusion in quartz (PY79C2). D: EDS spectrum of the octahedral magnetite (C). Abbreviations: An = albite, Ox = iron oxide, Ep = epidote, Qtz = quartz.

The secondary paragenesis is characterized by the presence of secondary chlorite (Chl) and muscovite (Ms). Muscovite is associated with epidote (Ep) and albite (Ab), which suggests the hydrothermal alteration of primary plagioclase (Pl I = Ab + Ms + Ep) (Figure 5.4.A). EDS spectrum for epidote is shown in Figure 5.4.B. We can note the presence of iron-rich muscovite (phengite, Ph) in association with chlorite and titanium oxide (Rt / Ant / Brk) which comes from the alteration of biotite (Bt + Rt = Ms + Chl + Rt) in greenschist facies conditions (Figure 5.4.C-D). Chlorite, rich in iron, belongs to the chamosite type (Figure 5.4.E). Secondary iron oxides are also observed. Hematite (αFe_2O_3) crystallized through a process of alteration is responsible for the characteristic red color of the rocks (Boone, 1969; Nédélec and Bouchez, 2015; Nédélec et al., 2015). Presence of hematite is difficult to observe under the microscope because the grains are very small. Ilmenite ($FeTiO_3$) may be observed in association with titanium oxide (TiO_2) in Figure 5.4.A.

Epidote is also present and results from the alteration of plagioclase and allanite- (Ce) ((Ca, Ce)$_2$ (Al, Fe^{2+}, Fe^{3+})$_3$ (SiO_4) (Si_2O_7) O (OH)) (Figure 5.4.F-H). Primary allanite-(Ce) is changed to epidote by substituting (REE^{3+} + Fe^{2+} = Fe^{3+} + Ca^{2+}). In association with allanite we observe parasite-(Ce), a cerium fluoride carbonate of formula Ca (Ce, La)$_2$ (CO_3)$_3$ F_2 (F-REE-Carb) (Figure 5.4). Presence of Nd in the EDS spectrum in Figure 5.4.G suggests the presence of parisite (Nd).

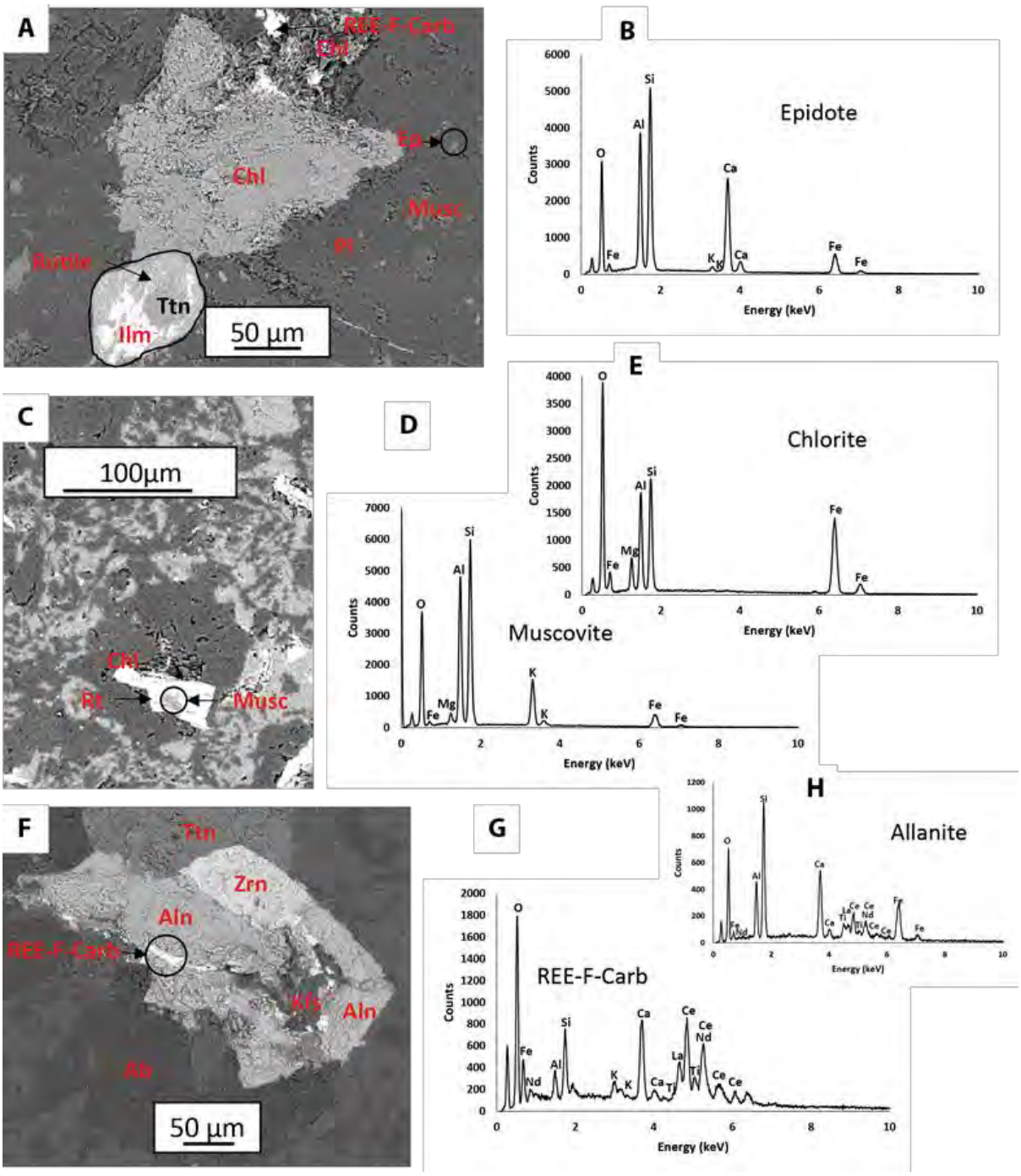

Figure 5.4: A: SEM-BSE image of secondary paragenese for the microgranites (PY55D2). B: EDS spectrum of epidote. C: SEM-BSE image of muscovite (phengite). D: EDS spectrum of muscovite. E: EDS spectrum of chlorite. F: SEM-BSE image of allanite and REE-F-Carb (PY65G4). G: EDS spectrum of parisite. H: EDS spectrum of allanite.

Among phosphates, we note the presence of apatite (which is likely primary; $Ca_5(PO_4)_3$ (OH, F, Cl)). Rare earth element phosphates, such as xenotime (YPO_4), and monazite (Y, La, Nd, Th) PO_4 are also present (Figure 5.5.A). In sample PY79C2, barite ($BaSO_4$), a barium sulphate characteristic of hydrothermal deposits was also recognized (Figure 5.5.A). In sample PY69B3, fluorite (CaF2) infills a crack in the edge of a perthitic feldspar, where we also saw calcite ($CaCO_3$) and allanite (Figure 5.5.B). We observe many inclusions in phenocrysts (Figure 5.5.C). Hydrothermal allanite has been described in altered granites (Ward et al., 1992) but allanite is often primary in A-type granites (Nédélec et al., 1995). Cu-Sn mineral associations were also observed infilling a crack in the same sample (Figure 5.5.D-G).

We note the presence of an iron oxide hydroxide of formula β-Fe_3O (OH,Cl), that is identified as akaganeite (Figure 5.5.E) (sample PY69B3), because of its spectrum showing the presence of Fe, Cl, O (Figure 5.5.F). This mineral is an alteration mineral in meteorites and in human artefacts. Akaganeite requires a crystallization temperature below 500°C (possibly <300°C), because above this limit the mineral is unstable with transformation to hematite (Glotch and Kraft, 2008). In natural conditions, it is generally observed in a fumarole context (Johnston, 1977), because it requires the coexistence of ferrous iron with chloride in low pH conditions (Font et al., 2014; Glotch and Kraft, 2008).

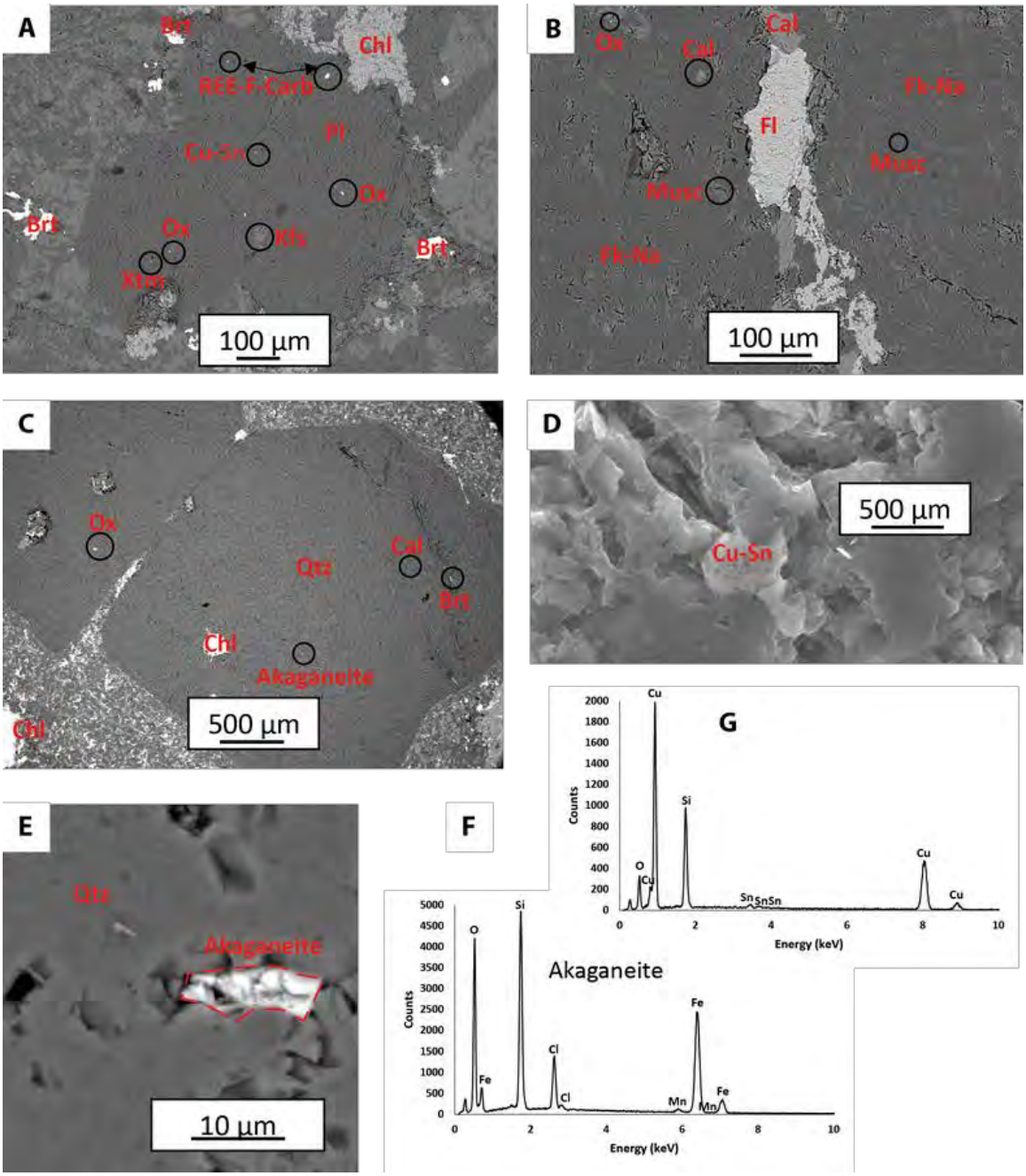

Figure 5.5: A: SEM-BSE image of secondary paragenesis with barite, REE-F-carb, xenotime… in plagioclase (PY79C2). B: SEM-BSE image of fracture with fluorine and calcite (PY69B3). C: SEM-BSE image of quartz with inclusion of akaganeite (PY69B3). D: SEM-SEI of Cu-Sn mineral (PY79C2). E: SEM-SEI image of akaganeite mineral (PY69B3). F: EDS spectrum of Akaganeite. G: EDS spectrum of Cu-Sn mineral. Abbreviations: Brt = barite, Chl = chlorite, Pl = plagioclase, Xtm = xenotime, Ox = iron oxide, Cal = calcite, Musc = muscovite, Fk-Na = perthitic felspar, Qtz = quartz.

5.1.2.4 Sequence of crystallization

It was possible to establish the crystallization sequence, among magmatic and hydrothermal minerals. (Figure 5.6). The textural characteristics indicate crystallization in the uppermost crust for the dikes. Phenocrysts and primary accessory minerals as zircon, titanite, allanite and magnetite crystallized during the first magmatic stage (I). Minerals in the matrix were formed later, during a second magmatic phase. Late phases are titanium oxide, ilmenite,

REE-F-Carbonate, xenotime, barite, fluorite, calcite and monazite. Secondary minerals are chlorite, muscovite, albite, epidote, hematite, and akaganeite pointing to crystallization conditions in the range 500 – 300°C in presence of fluid. Syn- to post magmatic hydrothermal fluids involved minerals containing F, REE, and other HFSE type elements.

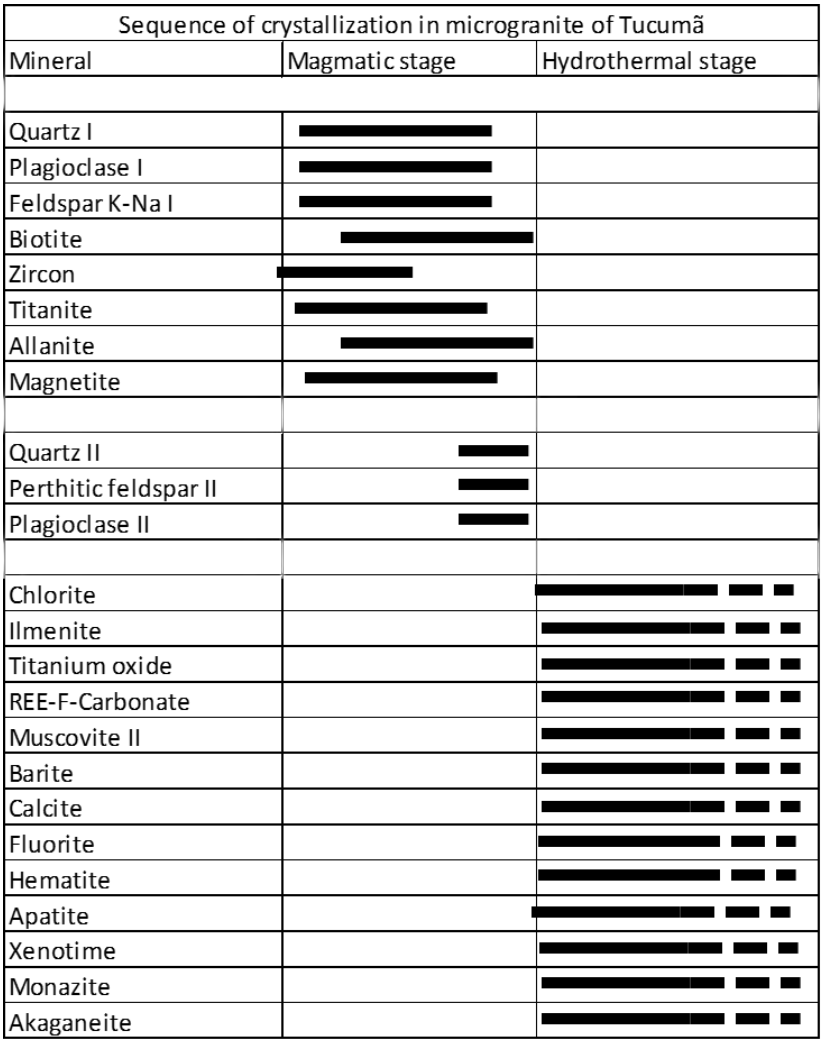

Figure 5.6: Sequence of crystallization for the microgranites.

5.2 Mineral chemistry of microgranites

Composition of feldspars, biotite, epidote and iron oxides of the microgranites were determined using a CAMECA SX100 electron microprobe (Toulouse, France).

Alkali feldspars are perthitic and plagioclase has a composition of albite whose analysis indicates only 0 – 6% Anorthite. The presence of orthose is well-marked in perthitic exsolution of the three samples (Figure 5.7.A). Presence of secondary epidote in plagioclase is characteristic of high-T (500 – 300°C) hydrothermal conditions. The coexistence of perthitic feldspar (FK-Na) with sodic plagioclase as individual crystals is characteristic of the

intermediate situation between hypersolvus and subsolvus granites, called transsolvus granites (Martin and Bonin, 1976).

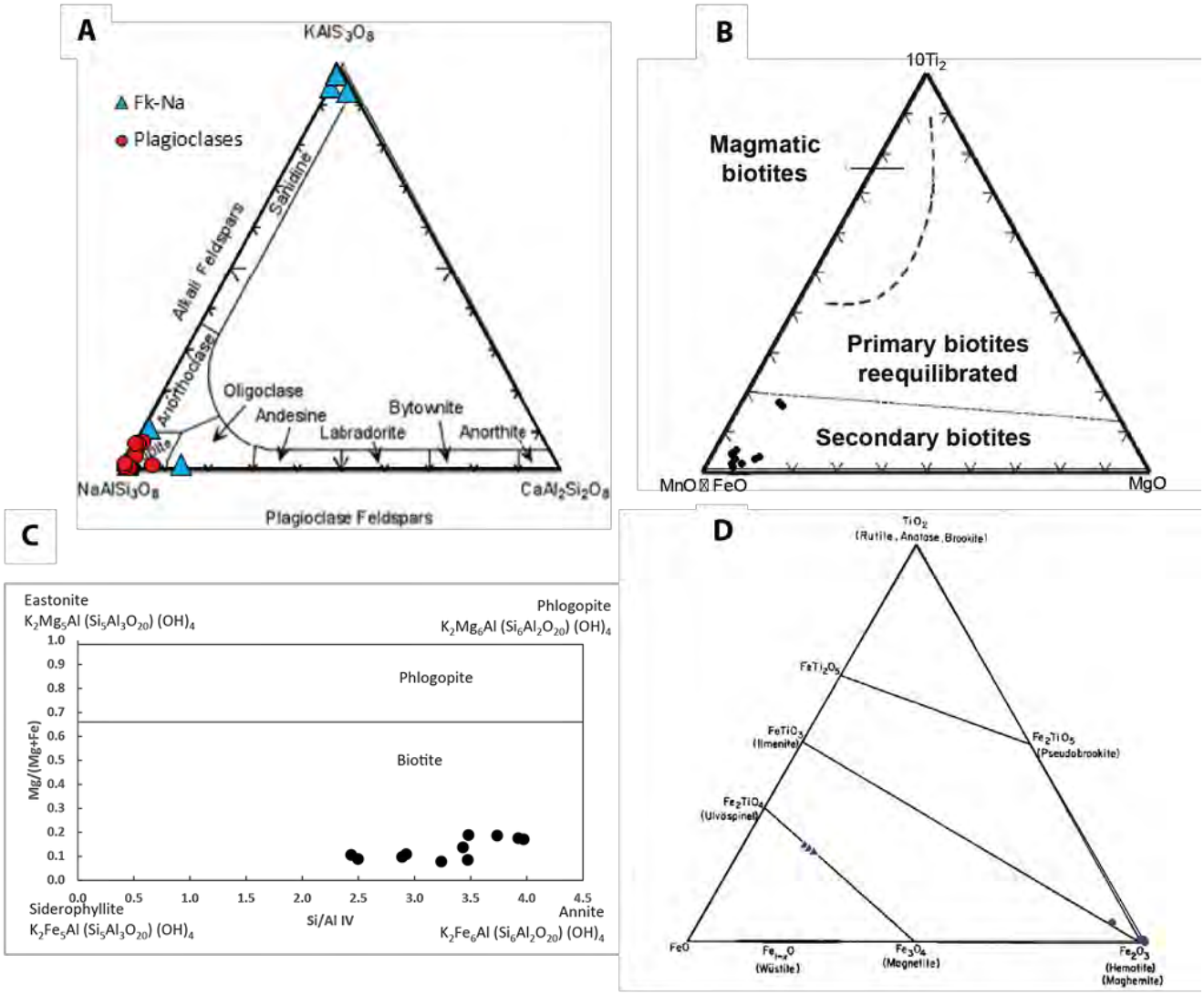

Figure 5.7: A: Ternary classification diagram $KAlSi_3O_8$ – $CaAl_2Si_2O_8$ – $NaAlSi_3O_8$ for feldspar. B: Chemical composition of biotites in the 10*TiO2 – MgO – MnO + FeO ternary diagram (Nachit et al., 2005). C: Classification of micas, (Mg / (Mg + Fe)) versus Si / Al (IV). (Rieder et al., 1999). D: Classification of iron oxides (Buddington and Lindsley, 1964; Teixeira et al., 2016).

Biotite is the only mafic silicate and is mainly altered to chlorite (green). We used the diagram of Nachit et al. (2005) to plot biotite composition. Biotite is rich in FeO which is characteristic of A-type magmas (Figure 5.7.B). Low contents of TiO_2 in biotite are due to the exsolution of a Ti-enriched phase. In the classification chart for micas (Figure 5.7.C), biotite belongs to the solid-solution annite siderophyllite and it is characterized by a high iron content (X_{Mg}= 0.07 – 0.17). Chlorite is the product of alteration of mafic minerals (such as biotite) and

the observed Chlorite is iron-rich chamosite. There are no compositional differences in chlorite from different samples.

Using the pure hematite standard in electronic microprobe, we can distinguish magnetite and hematite through a quantitative analyze. Then, using molar proportions, the results are plotted in the oxides diagram,(Buddington and Lindsley, 1964) (Figure 5.7.D). Analyses of the sample PY65 showed the presence of hematite. Analysis of sample PY69 suggests instead, titanomagnetite close to the solid line of the solution between ulvospinel and magnetite. Therefore, it is highly likely that the iron oxide shown in SEM image (Figure 5.7.A) can be hematite.

5.3 Geochronology

Results of U-Pb ages on zircon (SHRIMP) are published by da Silva et al. (2016). The goal was to determine a crystallization age for the Tucumã microgranites. A Concordia age of 1881.9 ± 8.8 Ma (MSWD = 2) is obtained for the sample FDB2 (= PY56), and a Concordia age of 1880.9 ± 6.7 Ma (MSWD = 2) for the sample FDB29 (= PY79). These robust ages show that the dikes are coeval with the 1880 Ma magmatism of Uatumã event in the Amazonian craton. Evidences (mingling, contacts) show that the emplacement of basaltic rocks is coeval with the well-dated microgranites at ca. 1880 Ma.

5.4 Magnetic properties

5.4.1 Magnetic Mineralogy

The study of magnetic mineralogy was carried out to identify the contribution of different minerals to remanent magnetization of the samples. This part must be linked with the magnetic petrography section. For this study, the following experiments were performed: alternating field demagnetization, hysteresis curves, isothermal remanent magnetization curves (IRM), Kruiver's analysis (Kruiver et al., 2001) and thermomagnetic curves.at the laboratory of IAG-USP.

5.4.1.1 Hysteresis curves

The hysteresis curves for the microgranites of the Tucumã region are shown in Figure 5.8. Hysteresis curves allow to obtain the different parameters (Ms, Mrs, Hc, Hcr) to construct the Day plot (Day et al., 1977). This graph provides information on the structure of the magnetic domains of samples for magnetite. It indicates if the magnetic grains are single domain (SD), pseudo-single (PSD) or multidomain (MD).

For samples PY55B (Figure 5.8.A) and PY59B (Figure 5.8.B), the curves show a wasp-waisted type resulting from the presence of at least two magnetic phases with different coercivities. Sample PY59B (Figure 5.8.B) has a lower coercivity and a high saturation magnetization value. Petrographic analysis indicates that these two phases are magnetite and hematite. Samples PY61B (Figure 5.8.C) and PY75B (Figure 5.8.D) also show wasp-waisted hysteresis curves but with the higher coercivity component much more evident when compared with those from samples PY55B and PY59B. This suggests that the contribution of the high coercivity magnetic phase (probably hematite) is more important. Sample PY63I (Figure 5.8.E) exhibits a thin wast curve typical of low coercivity grains (such as magnetite MD). This sample also has higher magnetization. This sample was collected in a microgranitic dike in contact with a younger gabbroic dike, which probably affected the magnetic properties of the microgranite. Sample PY62I (Figure 5.8. H) shows a narrow hysteresis curve indicating a low coercivity phase and a saturation magnetization of about 200 $A.m^{-1}$, which is typical of titanomagnetite. Most samples have a typical wasp waisted curve behavior indicating mixtures of magnetic phases.

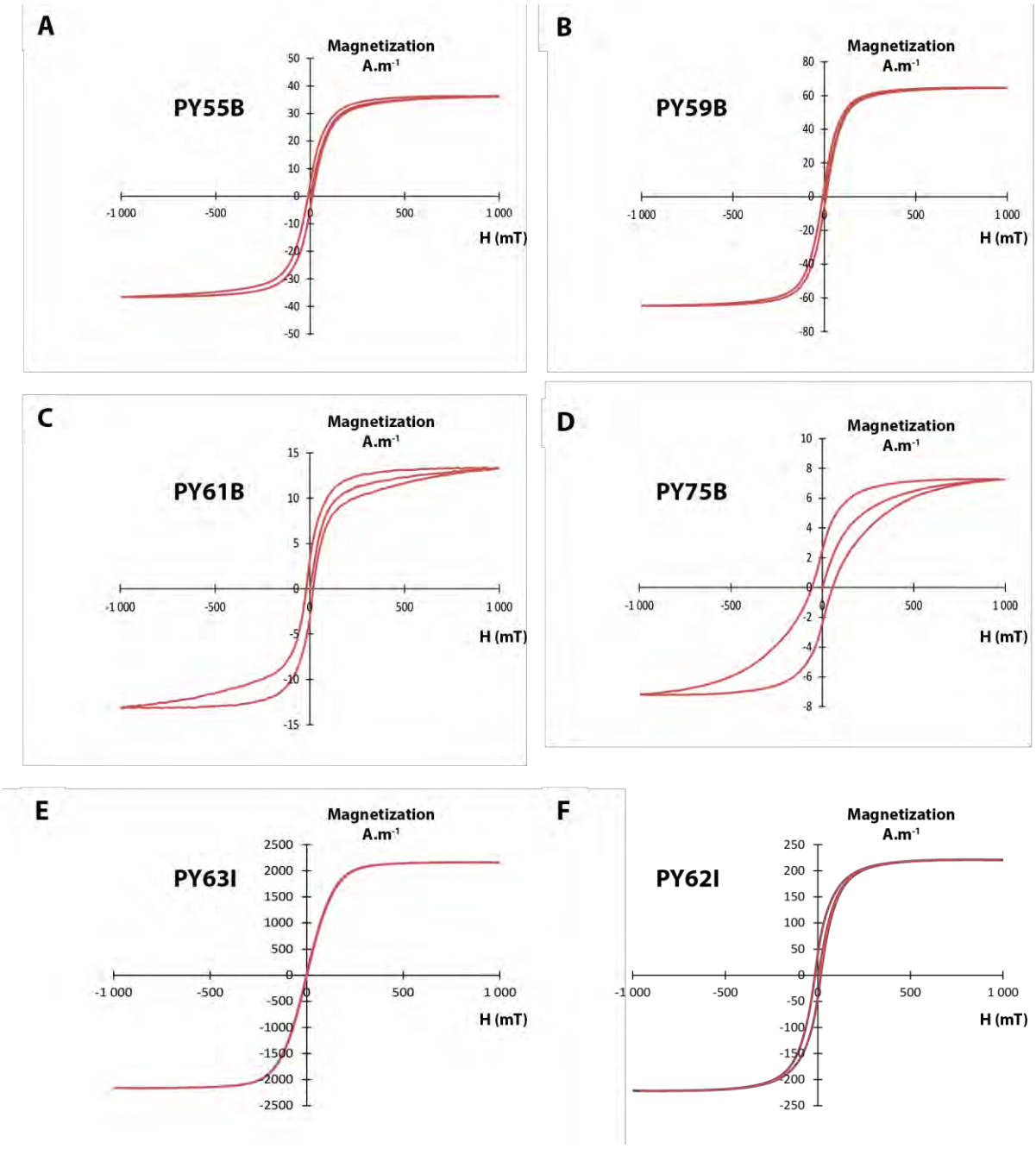

Figure 5.8: Hysteresis curves for the microgranitic dikes.

5.4.1.2 Isothermal remanent magnetization (IRM) curves

Hysteresis and IRM curves, allow us considering four families of magnetic behaviors for the microgranites. Figure 5.9.A shows all IRM curves obtained for microgranites, each color corresponds to a specified magnetic group. The most visible group is constituted by samples with high magnetization values: this is the Group-4 represented by black curves (Figure 5.9.E). These samples are in contact with mafic dikes. They reach saturation quickly and likely represent only one magnetic carrier (magnetite). Samples from Group-1 (Figure 5.9.B) and Group-2 (Figure 5.9.C) do not reach saturation, and are characterized by two magnetic phases, one with low coercivities (likely magnetite) and other with high coercivities (likely hematite).

Group-1 has higher magnetic susceptibility than Group-2. IRMs for Group-3 do not reach the saturation of magnetization and indicate the dominance of the high coercivity phase (hematite) which corresponds to the wasp-waisted hysteresis curves. The color code of Figure 5.9 may recall the color code of the aqueous solutions in chemistry, and represent the intensity of hydrothermal alteration as discussed later.

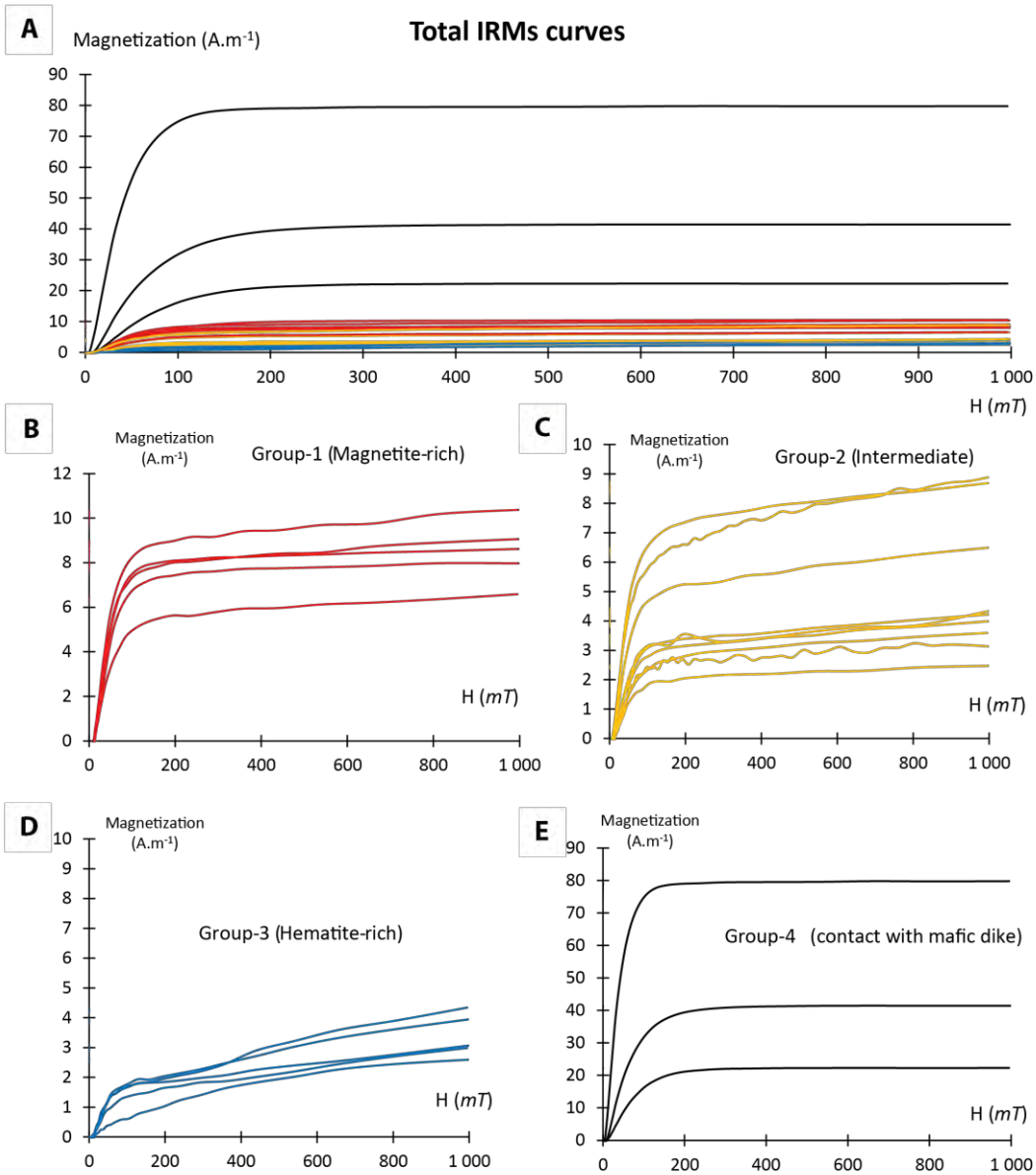

Figure 5.9: A: All IRM curves for microgranites. B: Group-1 (red) = samples with high magnetic susceptibility. C: Group-2 (orange) = intermediate magnetic susceptibility. D: Group-3 (blue) = low magnetic susceptibility. E: Group-4 = very high magnetic susceptibility (contact with mafic dikes).

5.4.1.3 Kruiver's analysis

To quantify the contribution of each magnetic component, we can use the method of Kruiver et al. (2001). This method involves the cumulative log-Gaussian (CLG) analysis of the IRM acquisition curves (Figure 5.10). We can separate groups by their SIRM, the mean coercivity and the dispersion. The SIRM is the saturation isothermal remanent magnetization. For the coercivity we determine the value of the field where the half of SIRM is reached ($B_{1/2}$). The dispersion parameter (DP) represents the width of the distribution. These results are summarized in Table 5.1. Group-1 is characterized by high SIRM values characterized by a magnetic component with lower coercivities (magnetite) and contribution of the second component with higher coercivities (hematite), whose concentration is below 15%. This is consistent with dominance of magnetite in this group and the higher magnetic susceptibility observed in the samples (Figure 5.10 A). Groups 1 and 2 have a $B_{1/2}$ coercivity value of 39.81 mT for the magnetite component. The two magnetic components are well-marked in group 2 (Figure 5.10.B). We can note that for group 3 the hematite component is dominant (Figure 5.10.C), as seen previously, with a $B_{1/2}$ value of 630.95 mT. For samples in contact with the gabbroic dikes (Group 4), the hematite component disappears (Figure 5.10.F), and only a magnetic component (probably magnetite) is detected. In these cases, the recent gabbroic dikes remagnetized the NW-mafic dikes and microgranites (see results in Chapter. 6).

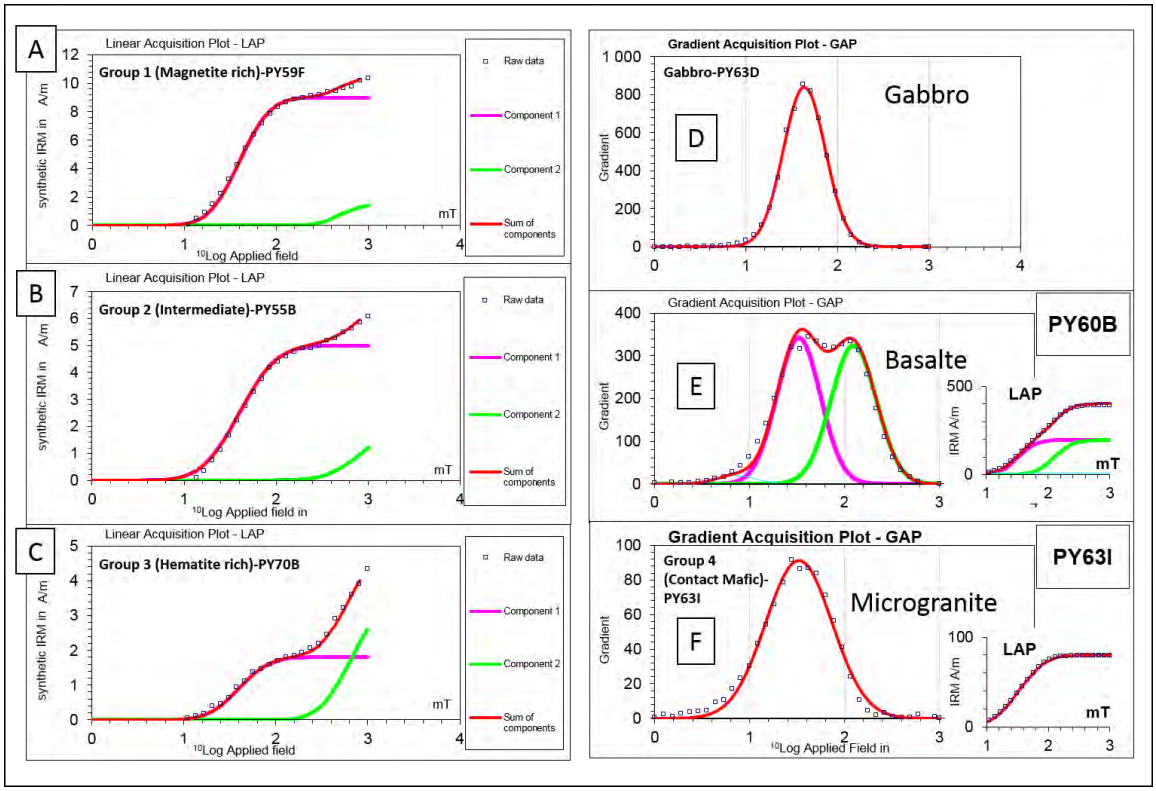

Figure 5.10: Decomposition of IRMs curves by the analysis of Kruiver et al. (2001). IRM acquisition curve on a linear ordinate scale is called the linear acquisition plot (LAP). Analysis using gradient of acquisition plot is referred to the GAP.

5.4.1.4 Day plot

We can plot the parameters of hysteresis curves in a Day's plot using the diagram of Day et al. (1977), as modified by Dunlop (2002), (Figure 5.11). All samples from Group-1 and Group-2 and two samples from Group-4 fall in the PSD domain. One sample (PY63I) from Group 4 falls in the MD domain. We note that the samples of Groups 1, 2 and 4 fall along the curve which represents a mixture of SD-MD grains (PSD) as defined by Dunlop (2002) (Figure 5.11).

Samples of Group 3 (hematite-rich) fall along SP-SD mixing curves of Dunlop (2002) (Figure 5.12). However, the fact that these samples have hematite makes it difficult to determine their saturation magnetizations and we recall that the Day's plot is only valid for titanomagnetites.

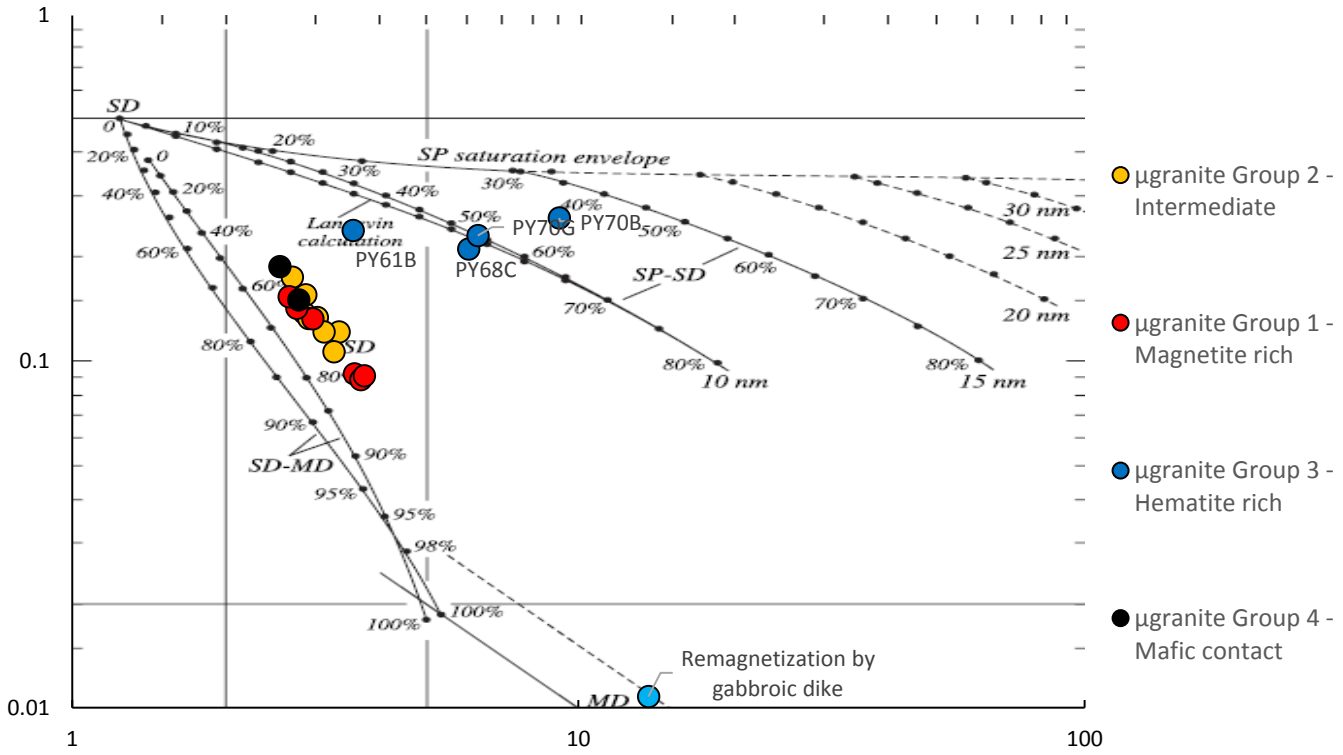

Figure 5.11: Day's plot for Tucumã dikes, after Dunlop (2002).

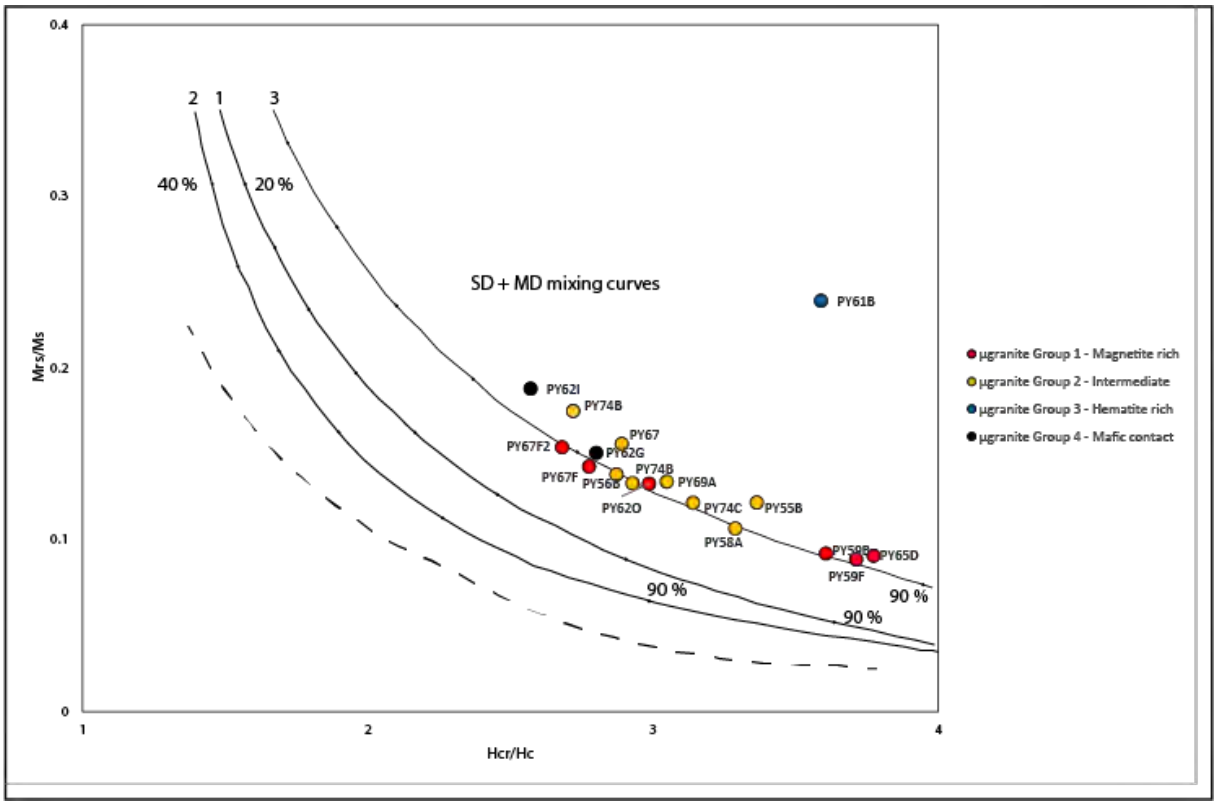

Figure 5.12: Zoom on the PSD domain. Day's plot after Dunlop (2002).

5.4.1.5 Thermomagnetic curves

Some samples in group 1 show reversible behavior (Figure 5.13.A). We can see on these curves the presence of the Hopkinson peak and the Verwey transition at low temperatures, which is characteristic of magnetite. Samples in Group-2 show also the same behavior. Samples from Group-3 show curves with irreversible behavior characterized by different trajectories during heating and cooling (Figure 5.13.B). A small fall around 600° C indicates the presence of magnetite in small quantity in these rocks. The presence of hematite, well-characterized in the previous topics, is not visible on the thermomagnetic curves, which is normal due of its low magnetic susceptibility, compared to that of magnetite. At low temperatures we can see the Morin transition, which is characteristic of hematite (Figure 5.13.B). As already stressed, the high values for the magnetic susceptibility for samples from Group-4 suggest that new magnetite minerals were formed associated to the intrusion of gabbroic dikes.

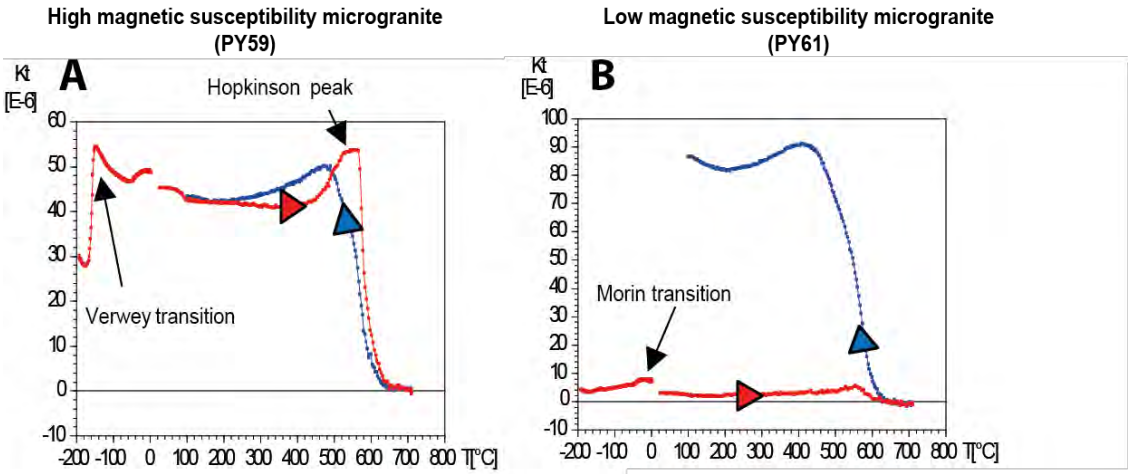

Figure 5.13: Thermomagnetic curves for dikes of Tucumã.

5.4.2 Summary for the magnetic mineralogy

Most samples have a magnetic susceptibility between 200 and 500 μSI (Figure 5.14). Rochette et al. (1992) suggest that susceptibility values below 500 μSI characterize paramagnetic rocks without (or very little) magnetite. We have seen the presence of magnetite even in rocks that have a susceptibility of 250 μSI, suggesting that for Tucumã samples we have a lower limit between paramagnetic and ferromagnetic rocks. Low susceptibility values can also be explained by the low amount of iron oxides and the presence of hematite (low magnetic susceptibility) as was shown through the hysteresis curves and the Kruiver's analysis. In the Tucumã dikes the high susceptibility values are related to the presence of magnetite which controls the magnetic mineralogy of these samples. In summary, the magnetic mineralogy of the microgranites is controlled by a mixture of SD and MD magnetite (PSD) grains and also hematite. The hydrothermal alteration is correlated with the increase of the hematite phase. The magnetic mineralogy of basalts and gabbros is controlled by mixtures of SD and MD (PSD) magnetite grains. These magnetic experiments also show evidence of remagnetization of the Proterozoic dikes by intrusion of gabbroic dikes.

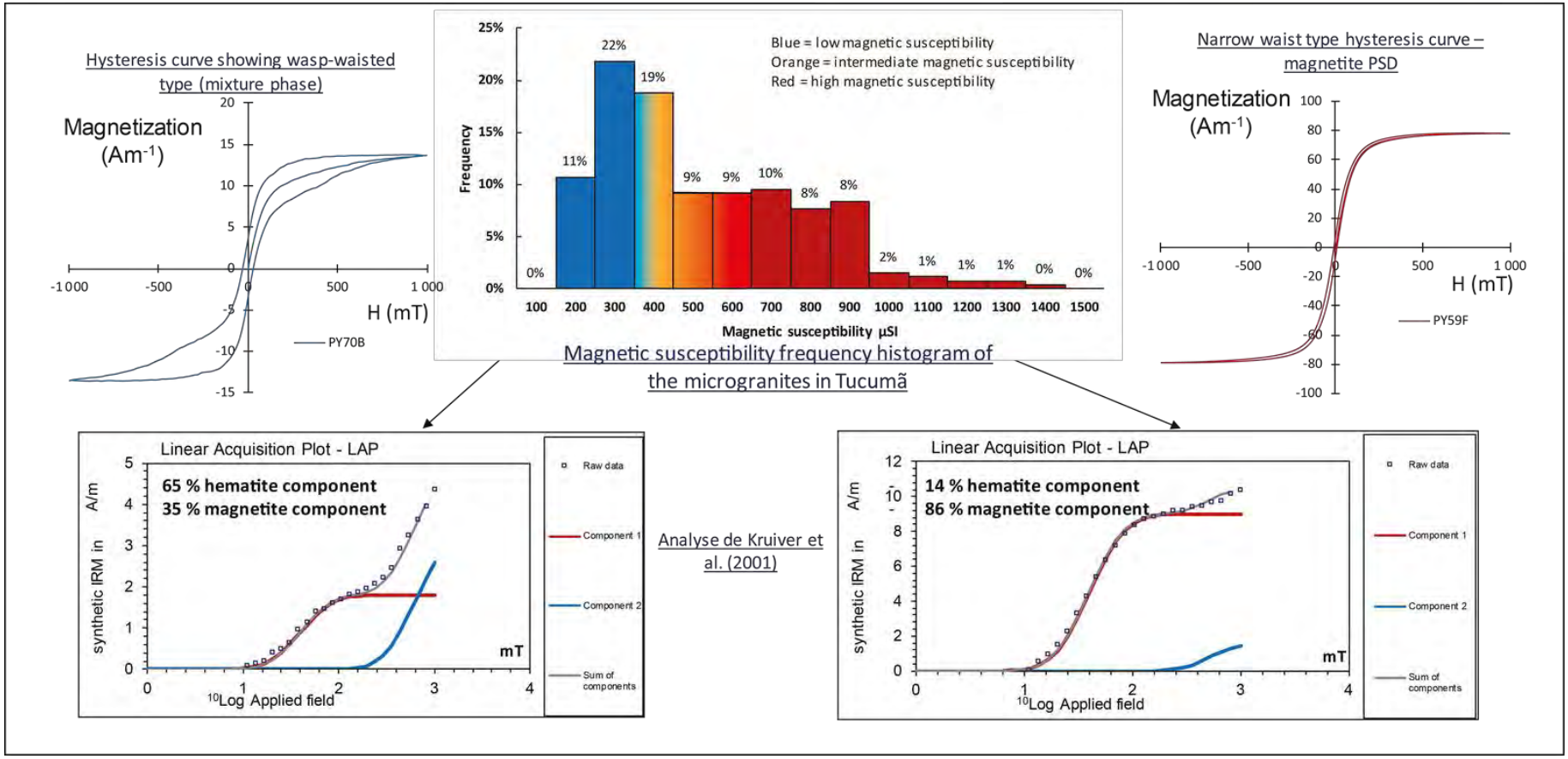

Figure 5.14: Summary for the magnetic mineralogy of microgranitic dikes of Tucumã. Magnetic susceptibility frequency histogram for the microgranites to differentiate samples with low magnetic susceptibility (blue) and high magnetic susceptibility (red). Typical hysteresis curves for these samples are represented in blue and in red, respectively. Decomposition of IRMs curves are also represented.

Table 5.1: Summary of the analysis of Kruiver et al. (2001).

SITE	Name	S ratio		Low coercivity component					Coercivity magnetite component					High Coercivity Hematite component				
		-IRM-0.3T/IRM1T	(1-IRM-0.3T/IRM1T)/2	Contr.(%)	SIRM (A/m)	logB(1/2)	B(1/2) mT	DP	Contr.(%)	SIRM (A/m)	logB(1/2)	B(1/2) mT	DP	Contr.(%)	SIRM (A/m)	logB(1/2)	B(1/2) mT	DP
Group 1-Microgranite (Magnetite rich)																		
37	PY59B	0.816	0.908						86.0215054	8	1.6	39.8107171	0.31	13.97849462	1.3	2.64	436.515832	0.27
37	PY59F	0.768	0.884						85.7142857	9	1.6	39.8107171	0.26	14.28571429	1.5	2.7	501.187234	0.2
40	PY62O	0.942	0.971						90	7.2	1.6	39.8107171	0.26	10	0.8	2.3	199.526231	0.37
51	PY73A	0.918	0.959						91.954023	8	1.6	39.8107171	0.29	8.045977011	0.7	2.6	398.107171	0.37
52	PY74D	0.888	0.944						92.5925926	10	1.77	58.8843655	0.34	7.407407407	0.8	2.67	467.735141	0.37
Group 2-Microgranite (Intermediate)																		
33	PY55B	0.649	0.825						68.4931507	5	1.6	39.8107171	0.32	31.50684932	2.3	2.98	954.992586	0.32
34	PY56B	0.732	0.866						66.6666667	7	1.6	39.8107171	0.28	33.33333333	3.5	3	1000	0.54
36	PY58A	0.714	0.857						73.8372093	2.54	1.6	39.8107171	0.31	26.1627907	0.9	2.67	467.735141	0.37
43	PY65D	0.764	0.882						83.8235294	5.7	1.6	39.8107171	0.32	16.17647059	1.1	2.67	467.735141	0.24
45	PY67	0.586	0.793						64.2857143	2.7	1.65	44.6683592	0.29	35.71428571	1.5	2.8	630.957344	0.37
47	PY69A	0.725	0.862						74.0740741	2	1.6	39.8107171	0.31	25.92592593	0.7	2.8	630.957344	0.4
52	PY74B	0.627	0.813						77.2727273	3.4	1.6	39.8107171	0.28	22.72727273	1	2.8	630.957344	0.2
52	PY74C	0.606	0.803						73.3333333	3.3	1.6	39.8107171	0.29	26.66666667	1.2	2.9	794.328235	0.2
54	PY79C	0.598	0.799						68.4210526	6.5	1.6	39.8107171	0.31	31.57894737	3	2.67	467.735141	0.3
Group 3-Microgranite (Hematite rich)																		
39	PY61B	0.302	0.651						38.3697813	1.93	1.6	39.8107171	0.29	61.63021869	3.1	3.1	1258.92541	0.34
46	PY68C	0.400	0.700	15.19756839	0.5	1.3	19.95262315	0.2	45.2887538	1.49	1.7	50.1187234	0.3	39.51367781	1.3	2.8	630.957344	0.25
48	PY70B	-0.019	0.491						35.0877193	1.8	1.6	39.8107171	0.26	64.9122807	3.33	2.8	630.957344	0.26
48	PY70G	0.125	0.563						35.0877193	1.8	1.6	39.8107171	0.22	64.9122807	3.33	2.8	630.957344	0.3385
53	PY75B	0.134	0.567						19.3548387	0.6	1.6	39.8107171	0.25	80.64516129	2.5	2.61	407.380278	0.4
Group 4-Microgranite (mafic contact)																		
40	PY62G	0.960	0.980						100	22.44	1.76	57.5439937	0.35					
40	PY62I	0.955	0.977						100	42	1.7	50.1187234	0.39					
41	PY63I	0.994	0.997						100	80	1.52	33.1131121	0.35					
Average									66.8251935	4.62947368	1.6168421	41.6127853	0.288947	32.37493447	1.782105263	2.75315789	610.928822	0.3215

5.5 Whole rock geochemistry

5.5.1 Major and trace elements geochemistry

Eleven samples of microgranite, seven samples of mafic rocks, and 2 samples of the younger gabbro intruding the 1880 Ma dikes were chosen to geochemical studies. Whole rock analyzes were carried out at SARM in Nancy (France). On the TAS diagram (Le Maitre et al., 2002), mafic rocks are basalts and andesitic basalts (Figure 5.15.A). Gabbroic rocks show a different group, more rich in TiO_2 compared to basalts, which suggests that the gabbros represent a different mafic magmatism, likely of younger age because of their field relations. Mafic dike with SiO_2 content of 60 wt.% is in contact with the microgranite and was likely contaminated by mixing. Concentrations of SiO_2 in mafic rocks range from 49 to 60 wt.% and TiO_2 concentrations range from 0.8 to 1.1 wt.% (Figure 5.15.A). The gabbros have SiO_2 concentrations of 49 wt.% and TiO_2 of 1.8 – 1.9 wt.%. The microgranites fall on the TAS diagram in the field of "rhyolites". The microgranites have SiO_2 content of 74 wt.% in average.

Microgranite dikes are iron-rich, which implies that they are "ferroan" granites according to the Frost and Frost (2008) classification in Figure 5.15.B. They are metaluminous to peraluminous (Figure 5.15.C).

Trends of the major elements in Harker diagrams are marked by a decrease in Al_2O_3, TiO_2, CaO, and FeO_t with increasing SiO_2. Increase in K_2O with increasing differentiation is observed (Figure 5.15). The decrease in TiO_2 (Figure 5.16.B) suggests fractionation of titanium phases, such as magnetite and / or ilmenite, while the decrease in Al_2O_3 (Figure 5.16.A) is related to plagioclase fractionation, which is sustained by a rather low concentration of CaO and Na_2O.

Among trace elements, vanadium (Figure 5.16.H) shows a strong decrease related to the fractionation of magnetite and the evolution of Sr vs SiO_2, confirms fractionation of plagioclase during magmatic evolution (Figure 5.16.G).

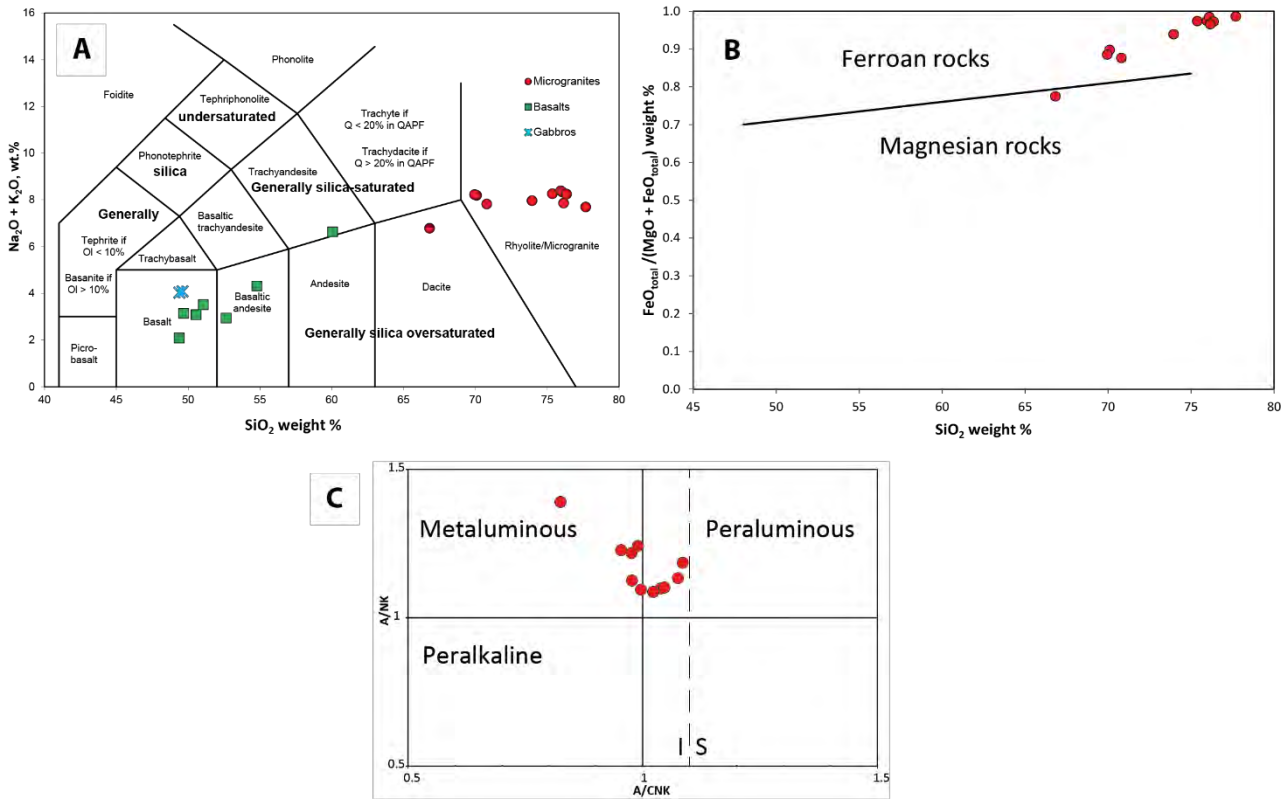

Figure 5.15: A: TAS diagram (Le Maitre et al., 2002). B: Major element variation diagrams showing the range of compositions, FeO_{tot} / (FeO_{tot} + MgO). (Frost et al., 2001; Frost and Frost, 2008). C : Shand diagram, A/NK vs. A/CNK plot (Maniar and Piccoli, 1989).

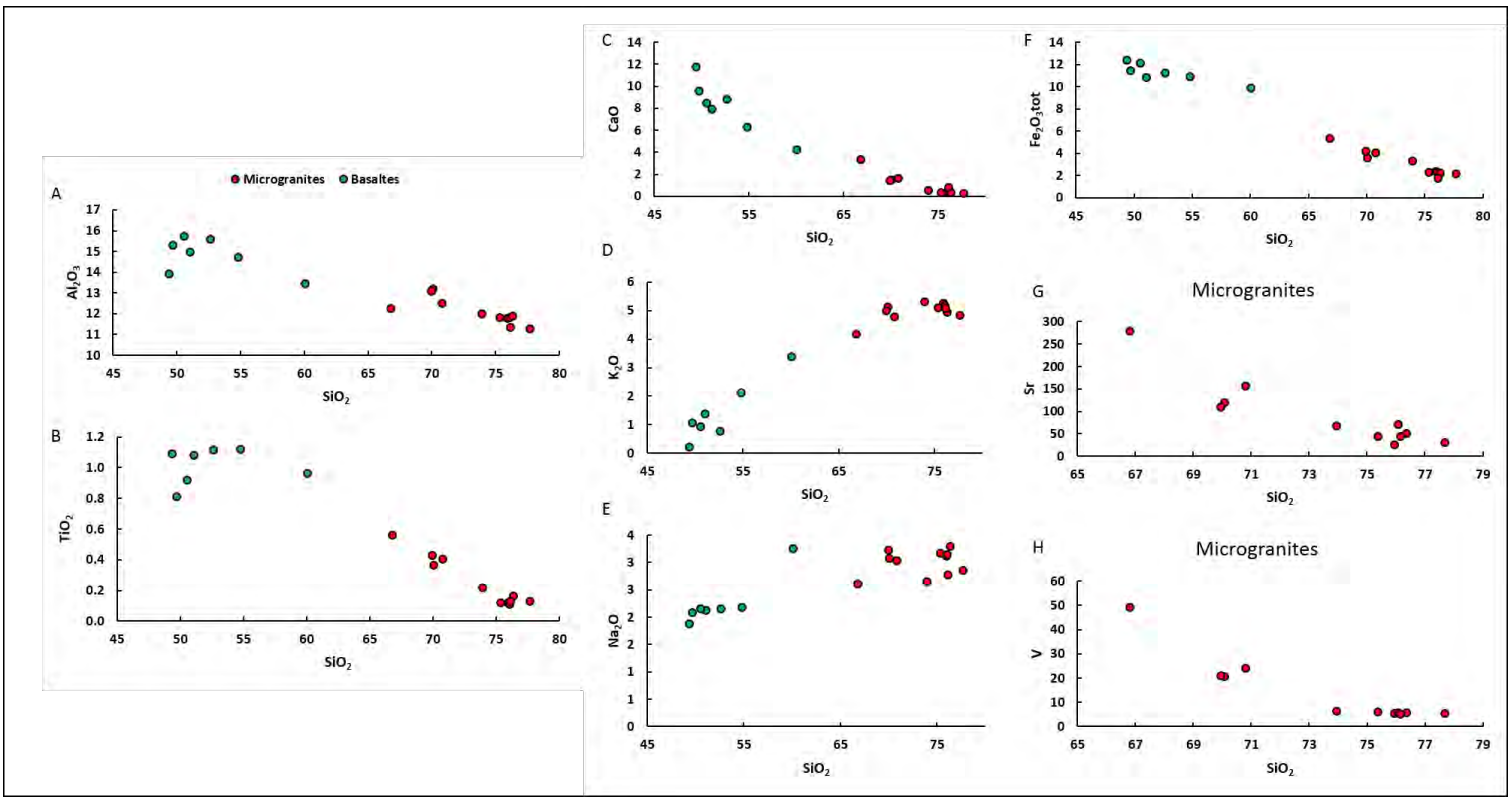

Figure 5.16: Harker diagrams for microgranites and basaltic rocks.

The samples fall within the range of A-type granites in the diagram of Figure 5.17, which shows the concentration of Zr as a function of the Ga / Al ratio (Whalen et al., 1987). The A-type signature was already suggested by high contents of SiO_2, alkali, and iron and low CaO.

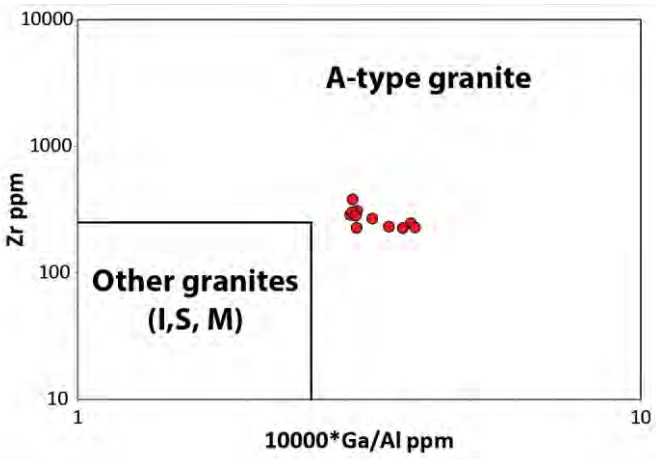

Figure 5.17: Discriminate diagram, Zr vs. 10000*Ga/Al (ppm) of microgranites (Whalen et al., 1987).

The study of HREE indicates two trends as shown in the Y (Yttrium) diagram as a function of SiO_2 (Figure 5.18.A). In this diagram, colors are the same used in Figures 5.9, 5.11, 5.12 and 5.14 to identify samples with different magnetic behaviors, as previously seen. Samples with high magnetic susceptibility values are in red (Group-1 = Magnetite-rich), samples with intermediate magnetic susceptibility are in orange (Group-2 = Intermediate), and sample with low magnetic susceptibility are in blue (Group-3 = Hematite-rich). Increase in Y (HREE) between PY67 and PY61 in the diagram is correlated with a decreased in magnetic susceptibility, and no increase in HREE was observed for samples with high susceptibilities. The other rare earths have the same behavior as Yttrium.

The same color code was used in the REE patterns normalized with chondritic values (Figure 5.18.B). A negative Europium anomaly (Eu / Eu * <1) is observed for all samples. The negative anomaly in Eu is related to the fractionation of plagioclase, which may have occurred through partial melting or fractional crystallization. The fractionation process is crystallization because the increasing Eu anomaly is correlated with the SiO_2 enrichment and the observed mineralogy. It can be noted that Group-1 samples (magnetite-rich) have a low anomaly in Eu. We observe a change in rare earths correlated with magnetic susceptibility. There is a strong enrichment of rare earths (light and heavy) for samples that have a low magnetic susceptibility in blue (PY61 of Group-3 = Hematite-rich). The enrichment in LILE is likely related to magmatic differentiation, and the enrichment if HREE is related to an input of late hydrothermal fluids. Therefore, two processes are superimposed, the magmatic fractionation and the role of the

hydrothermal fluid. These hydrothermal fluids are undoubtedly syn- to post-magmatic, because they carry F, REE, Cl…(Agangi et al., 2010).

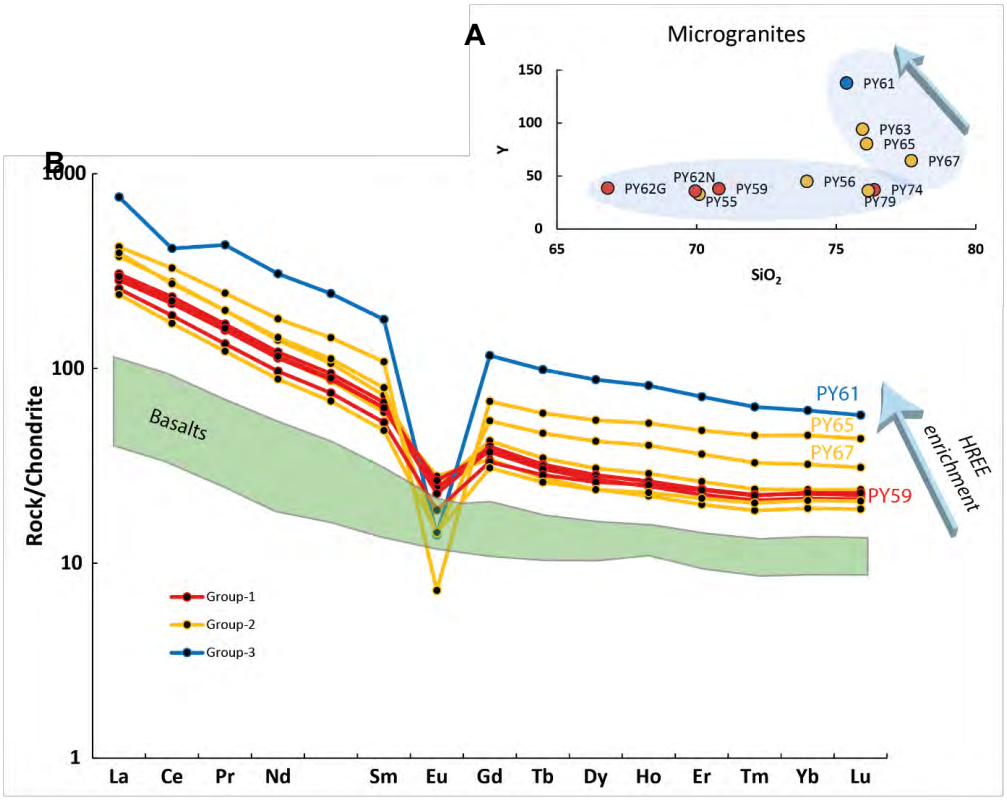

Figure 5.18: A: Y vs. SiO_2 diagram that shows an enrichment in HREE. B: REE patterns of microgranites (normalizing values are from McDonough and Sun (1995)). Basalts are illustrated in green. Color code depends of the magnetic susceptibility. Red = sample with high magnetic susceptibility (magnetite-rich). Orange = sample with intermediate magnetic susceptibility. Blue = sample with low magnetic susceptibility (hematite-rich).

5.5.2 Relation between petrology and magnetism

A-type granites and associated volcanic rocks are frequently described in the literature and compilations of their occurrences and their characteristics have been the subject of numerous studies (Bonin, 2007; Eby, 1990, 1992; Nédélec et al., 2015). For the Tucumã microgranites the typical characters of A-type granites are observed. Porphyric microgranular textures indicate an emplacement in shallow conditions. The presence of two types of feldspar (Perthitic alkali feldspars and sodic plagioclase) shows a transsolvus type granite (Martin and Bonin, 1976). The only mafic silicate is an iron-rich biotite (annite) which is characteristic of A-type magmatism. The felsic dikes are highly silicic (66 – 78 wt.% SiO_2), they also have high Na_2O + K_2O, relatively high FeO, low CaO and very low MgO. They are also enriched in HFSE, and thus are typical A-type magmas.

In addition, magnetic mineralogy and the behavior of trace elements have shown that dikes were affected by hydrothermal fluids syn- to post-magmatic (low temperature), which have modified their magnetic properties. Thus, magnetic mineralogy can be used as a proxy

to quantify the hydrothermal alteration as already shown by Nédélec et al. (2015) for A-type granites. With the precise U-Pb zircon dating (SHRIMP) that provided an age of 1880 Ma, associated with the petrographic and mineralogical study of these microgranites, it is possible to characterize this magmatism as a dike swarm associated with the A-type granite plutonism well-known in the region, whose crustal protolith was determined by Dall'Agnol et al. (1999a); (Dall'Agnol et al., 1999c). We can propose a connection between the volcanic and plutonic units in Carajás province, considering the whole as resulting from the same episode, but corresponding to a different level of erosion (Figure 5.19). It is therefore concluded that all magmatic rocks correspond to the Uatumã event (Dall'Agnol et al., 2005; Dall'Agnol and de Oliveira, 2007). A different level of erosion explain why we don't found volcanic units to the east. Moreover, the increase in the Europium anomaly displayed by the REE patterns of A-type granites from east to west suggests that magmatic differentiation increased when the depth of magma emplacement decreased, therefore evidencing the role of the crustal filter already suggested in a different context by Moyen et al. (2003).

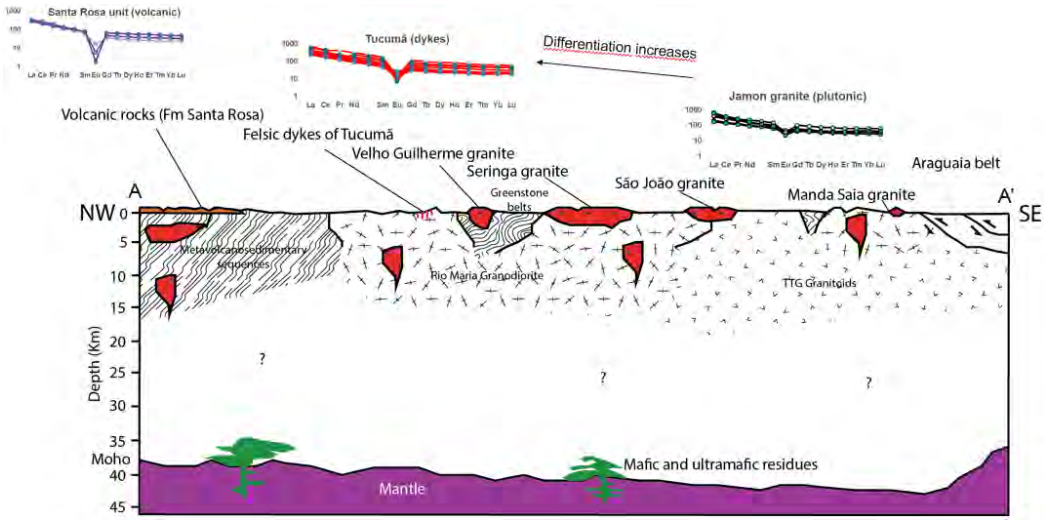

Figure 5.19: Geological cross-section of the Carajás Province showing the A-type magmatism (this study).

The age of 1880 Ma defines not only the phase of magmatic crystallization of these granites, but also the hydrothermal phase, because as we have seen, the magmatic and hydrothermal phases are chronologically indistinguishable. This last point is crucial for the paleomagnetism on these rocks. This suggests that the remanent magnetization isolated for these rocks (next section) is, most probably primary, and acquired at the end of the crystallization of rocks at ca. 1880 Ma. This is the first criteria (Buchan et al., 2000; Buchan, 2013) for the reliability of the paleomagnetic data to qualify a paleomagnetic pole as a key pole.

5.6 Paper of da Silva et al. (2016) (co-author)

Journal of South American Earth Sciences 72 (2016) 95–114

Contents lists available at ScienceDirect

Journal of South American Earth Sciences

journal homepage: www.elsevier.com/locate/jsames

Bimodal magmatism of the Tucumã area, Carajás province: U-Pb geochronology, classification and processes

Fernando Fernandes da Silva [a, *], Davis Carvalho de Oliveira [a], Paul Y.J. Antonio [b], Manoel S. D'Agrella Filho [b], Claudio Nery Lamarão [a]

[a] Grupo de Pesquisa Petrologia de Granitoides (GPPG), Instituto de Geociências (IG), Programa de Pós-Graduação em Geologia e Geoquímica, Universidade Federal do Pará (UFPA). CEP-66075-900, Belém, Pará, Brazil

[b] Instituto de Astronomia, Geofísica e Ciências Atmosféricas (IAG), Universidade de São Paulo, Rua do Matão, 1226, Cidade Universitária, 05508-090, São Paulo, Brazil

ARTICLE INFO

Article history:
Received 17 September 2015
Received in revised form
23 July 2016
Accepted 25 July 2016
Available online 29 July 2016

Keywords:
Carajás province
Dikes
Bimodal magmatism
Magma mixing

ABSTRACT

Geological mapping of the Tucumã area has enabled the identification of dike swarms intruded into an Archean basement. The disposition of these dikes is consistent with the well-defined NW-SE trending regional faults, and they can reach up to 20 km in length. They were divided into three main groups: (i) felsic dikes (70% of the dikes), composed exclusively of porphyritic rhyolite with euhedral phenocrysts of quartz and feldspars immersed in an aphyric felsite matrix; (ii) mafic dikes, with restricted occurrence, composed of basaltic andesite and subordinate basalt, with a mineralogical assembly consisting dominantly of plagioclase, clinopyroxene, orthopyroxene and olivine; and (iii) intermediate rocks, represented by andesite and dacite. Dacites are found in outcrops associated with felsic dikes, representing different degrees of hybridization or mixture of mafic and felsic magmas. This is evidenced by a large number of mafic enclaves in the felsic dikes and the frequent presence of embayment textures. SHRIMP U-Pb zircon dating of felsic dikes yielded an age of 1880.9 ± 3.3 Ma. The felsic dikes are peraluminous to slightly metaluminous and akin to A2, ferroan and reduced granites. The intermediate and mafic dikes are metaluminous and belong to the tholeiitic series. Geochemical modeling showed that mafic rocks evolved by pyroxene and plagioclase crystallization, while K-feldspar and biotite are the fractionate phases in felsic magma. A simple binary mixture model was used to determine the origin of intermediate rocks. It indicated that mixing 60% of rhyolite and 40% basaltic andesite melts could have generated the dacitic composition, while the andesite liquid could be produced by mixing of 60% and 40% basaltic andesite and rhyolite melts, respectively. The mixing of basaltic and andesitic magmas probably occurred during ascent and storage in the crust, where andesite dikes are likely produced by a more homogeneous mixture at high depths in the continental crust (mixing), while dacite dikes can be generated in the upper crust at a lower temperature, providing a less efficient mixing process (mingling). The affinities observed between the felsic to intermediate rocks of the Rio Maria and São Felix do Xingu areas and the bimodal magmatism of the Tucumã area reinforce the hypothesis that in the Paleoproterozoic the Carajás province was affected by processes involving thermal perturbations in the upper mantle, mafic underplating, and associated crustal extension or transtension. The 1.88 Ga fissure-controlled A-type magmatism of the Tucumã area was emplaced ~1.0 to ~0.65 Ga after stabilization of the Archean crust. Its origin is not related to subduction processes but to the disruption of the supercontinent at the end of the Paleoproterozoic.

© 2016 Elsevier Ltd. All rights reserved.

1. Introduction

Dike swarms represent conspicuous extensional structures commonly related with magma ascent and are widespread in cratons throughout the world, where most of them developed in Proterozoic time (Halls et al., 2011; Kumar et al., 2012). The

* Corresponding author.
E-mail addresses: ffernandes@ufpa.br (F.F. Silva), davis@ufpa.br (D.C. Oliveira), antonio_pipot69@hotmail.com (P.Y.J. Antonio), dagrella@iag.usp.br (M.S. D'Agrella Filho), lamarao@ufpa.br (C.N. Lamarão).

http://dx.doi.org/10.1016/j.jsames.2016.07.016
0895-9811/© 2016 Elsevier Ltd. All rights reserved.

Paleoproterozoic Tucumã dikes emplaced in Mesoarchean rocks in the northwest of the Rio Maria Domain, which corresponds to the southern portion of the Carajás Province in the southeast of the Amazonian Craton. The occurrence of hypabyssal bodies in Rio Maria region has been subject of many works that contributed to the understanding of the relationship and genesis of the different types of Proterozoic dikes in this region (Rivalenti et al., 1998; Silva et al., 1999; Oliveira et al., 2008). Hence, this work aims on expand the knowledge to Tucumã region deepen and discussing their relationships and sources. In general, they exhibit NW-SE trends, which are parallel to the contemporaneous regional horizontal maximum compressive stress orientations and perpendicular to the extension direction. Considering these statements, the Tucumã dikes can provide the opportunity of putting constraints on the early stages of the Proterozoic crustal distension processes associated with the Carajás province, such as the relationships between mafic and felsic dikes and their connections with the A-type magmatism.

The purpose of this contribution is to discuss geochemical classification, U-Pb-SHRIMP zircon crystallization age, and emplacement tectonic setting of the Tucumã dikes, in addition to determine themain processes involved in the formation of these rocks. The interpretation of the results will provide newinsights on the genesis of the Paleoproterozoic dike swarms of the Carajás province and their tectonicsignificance.

2. Geological setting

The Tucumã dikes intruded in the Mesoarchean rocks of the Rio Maria domain, which is bounded to the north by the Carajás Meso-Neoarchean domain (Santos, 2003, Fig. 1b). These domains form the Central Amazonian (Tassinari and Macambira, 2004) or Carajás province (Santos et al., 2000) in the southeastern portion of the Amazonian Craton (Fig. 1a), part of the Central Brazilian Shield (Almeida et al., 1981). According Santos et al. (2000), the Carajás province is bounded to the north by the Transamazonas province (Bacajá domain), to the west by Paleo- Mesoproterozoic Amazonia province (Iriri-Xingu domain) and to the East by the Araguaia Belt (Moura and Gaudette, 1993). In the Carajás province, the Archean rocks are commonly intruded by Paleoproterozoic anorogenic granites and associated dikes.

The Archean basement in the Tucumã region includes the Tucumã Group, composed of metaultramafic, metamafic and metasedimentary rocks, which were affected by greenschist facies regional metamorphism (Vasquez et al., 2008). This unit occurs as a large number of NW-SE belts located to the south and southeast of the Paleoproterozoic A-type Seringa pluton occurrence area (Araujo and Maia, 1991). Representative Archean basement granitoids in the Tucumã region comprise the Plaquê granite, which is essentially a suite of two micas granites oriented in an E-W trend; the Mogno Throndjemite that are biotite tonalites and/or trondhjemites, weakly to strongly foliated (Almeida et al., 2011), and the Rio Maria Granodiorite composed of biotite-hornblende granodiorite with associated tonalites and monzogranites, intrusive into the Tucumã greenstone belt (Macambira and Vale, 1997, Fig. 1c).

Paleoproterozoic A-type granites are found across the Carajás Province in the form of discordant batholiths formed of isotropic rocks of monzo- and syenogranite compositions, with moderately alkaline chemistry (Dall'Agnol et al., 2005). U-Pb and Pb-Pb zircon dating indicate ages of 1.88 Ga for these granites (Wirth et al., 1986; Machado et al., 1991; Barbosa et al., 1995, Table 1). In the Rio Maria Domain, they are represented by Seringa, Gradaús, and São João granites in addition to those of the Jamon Suite, which includes Musa, Jamon, Marajoara, Manda Saia, Bannach, and Redenção plutons, and associated felsic and mafic dikes (Rivalenti et al., 1998; Silva et al., 1999; Dall'Agnol and Oliveira, 2007; Oliveira et al., 2008). A representative of this type of magmatism in the Tucumã area is the Velho Guilherme pluton, which is part of a homonymous suite composed of the aforementioned granite and the Antônio Vicente, Mocambo, Xingu, and Bom Jardim plutons. They are part of the Southern Pará Tin Province (Macambira and Vale, 1997; Teixeira et al., 2002a).

These plutons transect the Archean Tucumã and São Félix groups and the TTG's of the Xingu Complex. They are intensely deformed and metamorphosed into an amphibolite facies (Macambira and Vale, 1997). Associated to these, there is the occurrence of felsic dikes with rhyolites of the Iriri Formation, which correspond to an effusive bimodal fissural volcanism formed in the late Paleoproterozoic (Fernandes et al., 2006).

Within the São Félix do Xingu region, well-preserved Paleoproterozoic volcano-plutonic centers form the rocks of the Sobreiro Formation that are mainly composed of basic to intermediate volcanic rocks and volcanoclastic facies, and the Santa Rosa Formation that comprises rhyolites, porphyry granites, volcanoclastic rocks and associated felsic dikes (Fernandes et al., 2011).

3. Field aspects

The Tucumã dike swarms occur in the western portion of the Velho Guilherme granite, and are disposed in kilometers long (may range from about 50 m to nearly 60 km in length with thicknesses that does not exceed 50 m) in a NW-SE pattern. They are intrusive into an older Archean basement formed of leucogranites, granodiorites and a greenstone belt sequence (Fig. 2).

Two main groups of felsic and mafic dikes account for 70% and 10% of the dikes, respectively. A third group of dikes can also be characterized (20% of the total), which is denominated intermediate. Dikes from these three rock-types are found throughout the working area and they are usually associated. The felsic dikes are the longest and show occasional evidence of contamination (Fig. 3a). All of them are rhyolites and show a prominent porphyritic texture with noticeable size reduction in phenocrysts from the core to the rim of the dike as well as an increase in matrix content in the same direction. The mafic dikes are subordinate to the felsic dikes (Fig. 1a). They are shorter than the felsic dikes, but like the latter, present occasional evidences of hybrydization. They are fine-grained without any significant variation in grain size.

The intermediate dikes are the most complex group, given that they plot as andesites and dacites on the TAS diagram and show evidence of magma contamination, suggesting that the felsic magma was hybridized with the mafic magma (Fig. 3b–d). The main evidence for this process is the presence of small round mafic xenoliths (mingling magma) and in some cases it is possible to identify a greater degree of mixture between the two magmas (mixing magma).

A peculiarity of this group of rocks is the considerable presence of mafic to intermediate enclaves. They are generally well rounded and show a significant degree of interaction with the surrounding rock, which is also demonstrated by the presence of minerals originated from felsic magma inside the enclaves, resembling what is commonly described for mingling features. These aspects suggest the coexistence of one or more magmas with low viscosity contrast during ascent into the crust.

4. Methods and analytical procedures

The microscopic study was concentrated on 60 thin sections of the most representative dike samples from the Tucumã area, where textural and mineralogical aspects were characterized in order to reinforce understanding of their genesis. Rock nomenclature in the

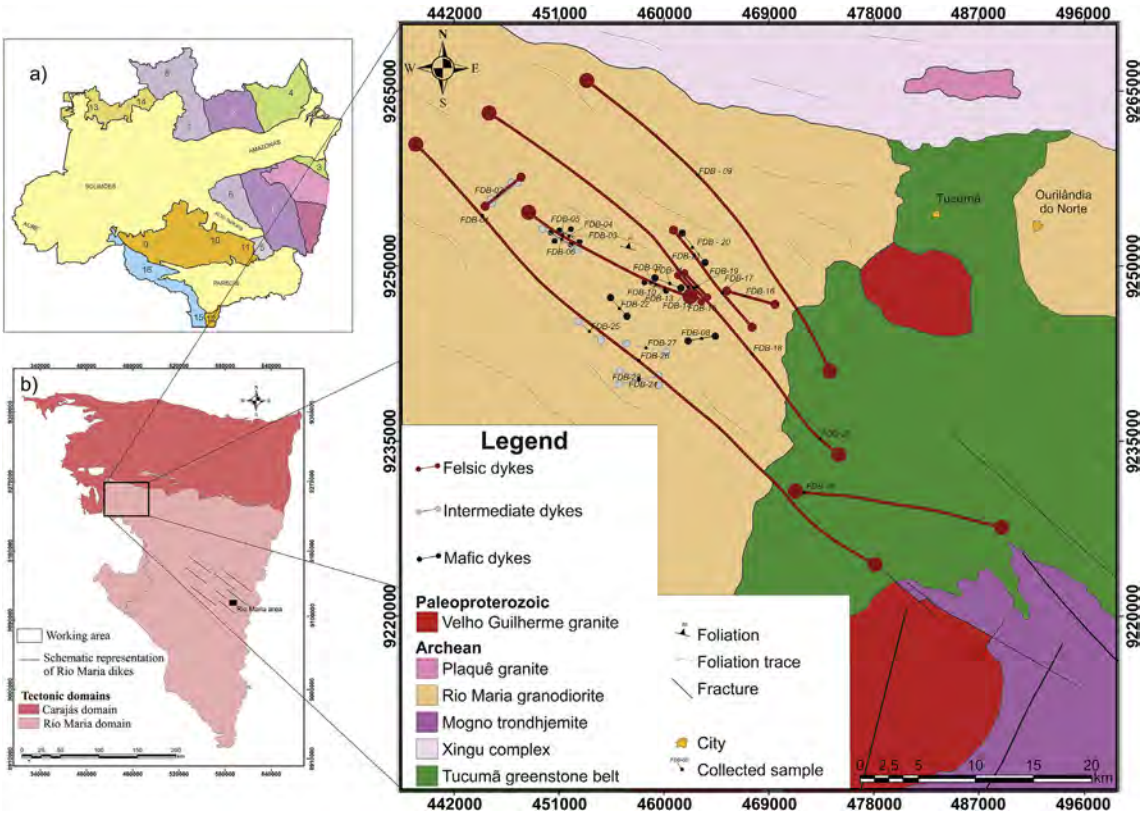

Fig. 1. a) Geochronological provinces of the Amazonian Craton (Santos, 2003). 1, 2 Amazônia central; 3, 4 Transamazonas; 5, 6, 7, 8 Tapajós-Parima; 9, 10, 11, 12 Rondônia-Juruena; 13, 14 Rio Negro; 15, 16 Sunsás. b) Map of tectonic domains with a square to highlight the working area (Modified from Oliveira et al., 2014); c) Geological map of Tucumã region dikes.

Table 1
Proterozoic A type granite geochronology of the Carajás province.

Unit	Method	Analised material	Age/reference
Proterozoic			
Carajás domain			
Cigano Granite	U-Pb	Zircon	1883 ± 2 Ma[(1)]
Serra dos Carajás Granite	U-Pb	Zircon	1880 ± 2 Ma[(1)]
Pojuca Granite	U-Pb	Zircon	1874 ± 2 Ma[(1)]
Rio Maria domain			
Musa Granite	U-Pb	Zircon	1883 ± 52 Ma[(1)]
Jamon Granite	Pb-Pb	Zircon	1885 ± 32 Ma[(2)]
Redenção Granite	Pb-Pb	Zircon	1870 ± 68 Ma[(2)]
Seringa Granite	Pb-Pb	Zircon	1890 ± 2 Ma[(3)]
Marajoara Granite	Rb-Sr	Whole rock	1724 ± 50 Ma[(4)]
São João Granite	Pb-Pb	Zircon	1895 ± 50 Ma[(5)]
Xingu region			
Velho Guilherme Granite	Pb-Pb	Whole rock	1823 ± 13 Ma[(6)]
Antônio Vicente Granite	Pb-Pb	Zircon	1867 ± 4 Ma[(7)]
Mocambo Granite	Pb-Pb	Zircon	1865 ± 4 Ma[(7)]
Dikes			
Felsic dike	Pb-Pb	Zircon	1885±2Ma[(8)]
Felsic dike	Rb-Sr	Whole rock	1707 ± 17Ma[(9)]
Intermediate dike	Rb-Sr	Whole rock	1874 ± 110Ma[(10)]
Mafic dike	K-Ar	Mafic agregate	1802 ± 22Ma[(11)]
Rhyolitic dikes	Pb-Pb	Zircon	1887 ± 2 Ma[(12)]
Rhyolitic dikes	Pb-Pb	Zircon	1879 ± 2 Ma[(12)]

Data source: [(1)]Machado et al. (1991); [(2)]Dall'Agnol et al. (1999); [(3)] Paiva Jr. (2009); [(4)]Macambira (1992); [(5)]Lima 2011; [(6)]Rodrigues et al. (1992); [(7)]Teixeira (1999); [(8)]Oliveira (2006); [(9)]Gastal (1987); [(10)]Rivalenti et al. (1998); [(11)]Silva et al. (1999); [(12)]Ferreira (2009).

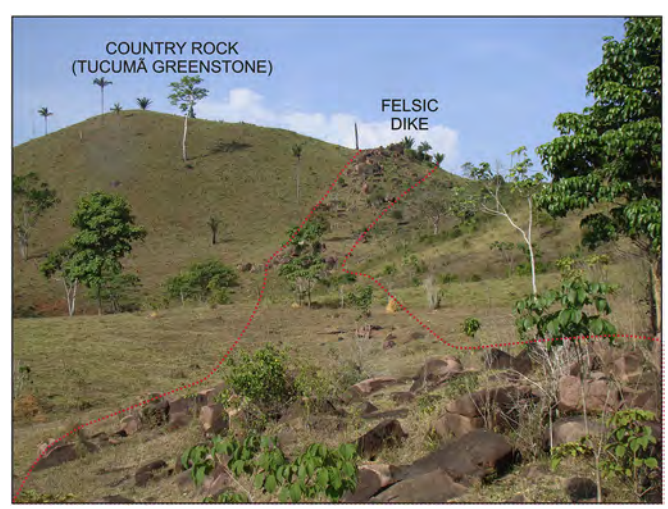

Fig. 2. Felsic dike cutting across the country rock the greenstone belts sequence of Tucumã Group, composed of metaultramafic, metamafic and metasedimentary rocks, which were affected by greenschist facies regional metamorphism (Vasquez et al., 2008).

present study followed International Union of Geological Sciences (IUGS), which recommends chemical classification using the total alkali silica diagram for fine-grained rocks or those whose mineralogical components cannot be identified by microscope.

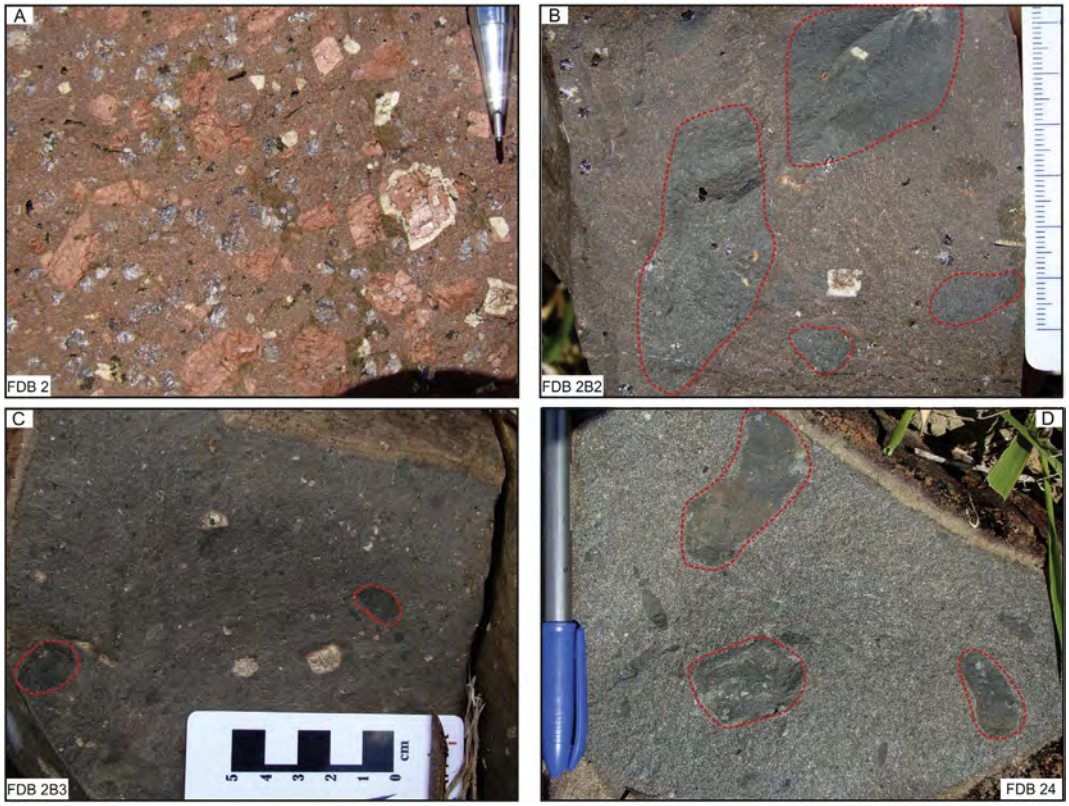

Fig. 3. Field relationship and textural features of the Tucumã dikes: A) Macroscopic appearance of the porphyritic rhyolite showing locally plagioclase mantled K-feldspar phenocrysts (rapakivi texture); B) Dacite with light pink color and large enclaves of mafic/intermediate rocks highlighted in dashed red line; C) Slightly darker dacite with minor enclaves of mafic rocks; D) Andesite with small rounded mafic enclaves. (For interpretation of the references to colour in this figure legend, the reader is referred to the web version of this article.)

For geochemical study rock powders (<200 mesh) of 40 samples considered the most representative of the dike varieties were analyzed by ACME ANALYTICAL LABORATORIES, including whole rock characterization. Major and minor element analyses were performed using ICP-ES, while trace elements and Rare Earth Elements were analyzed by ICP-MS.

The geochronology samples were analyzed by a Sensitive High Resolution Ion Microprobe (SHRIMP II) in the high-resolution geochronology laboratory of Universidade de São Paulo (USP) with analytical procedures and part of the reductions conducted in accordance with Sato et al. (2008), Willians et al. (1998) and Stern (1998). Two mounts were prepared with 70 and 48 zircon grains, respectively, from which 17 for FDB 29 and 16 for FDB 02 were selected and analyzed considering morphology and color, in order to examine all varieties of crystals. Data were plotted on concordia diagrams using ISOPLOT 4 software (Ludwig, 2003, 2009). The concentrations of uranium, lead and thorium were calibrated against the Temora zircon standard (Black et al., 2003) and the equipment had a 30 μm spot diameter. Crystal selection took into account the low disagreement with grains (up to 5%), maximum common lead content of 1.5% and individual error ratio below 7%.

5. Petrography

Among the dikes studied in this work, it was possible to distinguish three main groups based on petrography and geochemical data. The first consists of felsic dikes, which are composed exclusively of rhyolites, the second of intermediate rocks, classified as andesites and dacites, and the third of mafic dikes, represented by basalts and basalt andesites.

5.1. Felsic dikes

Felsic dikes are porphyry rhyolites showing dark purple to pinkish color and usually glomeroporphyritic, holocrystalline to hypocrystalline textures with euhedral to subhedral phenocrysts surrounded by a felsitic matrix. Granophyric and spherulite intergrowths are quite common (Fig. 4a–b). Quartz and feldspars are the only phenocrysts and account for up to 30% of the volume of these rocks. Biotite, zircon, carbonate and chlorite are subordinate matrix components.

Quartz phenocrysts are generally abundant and can reach up to 4 mm in diameter. They show a bipyramidal habit with lower occurrence of rounded shapes due to above-solidus magmatic resorption. They also exhibit engulfment texture, typical of volcanic rocks with high silica content. Plagioclase appears in a lower amount compared to other phenocrysts. They attain typically 3–5 mm in diameter, showing polysynthetic, albite-Carlsbad and albite-pericline twinning, with a tabular habit and euhedral to subhedral forms. Plagioclase crystals usually display normal zoning, evidenced by the more intense sericitic alteration in the Ca-rich inner zone. K-Feldspar is generally euhedric to subhedric with well developed Carlsbad twinning, and perthite and mesoperthite texture. Granophyric intergrowth and spherulites are common on the rims of this mineral. Another common feature of K-feldspar phenocrysts is rapakivi texture (plagioclase-mantled K-feldspar; Fig. 4b), and to a lesser extent, anti-rapakivi texture.

Given that these rocks display mineralogical homogeneity, they are treated as a single unit. However, three main textural variations were identified: porphyritic, glomeroporphyritic and granophyric. The porphyritic rhyolites display quartz and feldspar phenocrysts,

with sizes varying between 0.2 and 1.5 cm, surrounded by a groundmass ranging from fine (~1 mm) to very fine-grained (<1 mm). This groundmass consists of quartz, feldspar, biotite and opaque minerals. The glomeporphyritic texture is characterized by the presence of several smaller quartz and K-feldspar phenocrysts in a felsitic matrix. The granophyric texture is a common aspect in these felsic dikes and the distribution of these intergrowths is heterogeneous, ranging from 10 to 70% by volume. The granophyric texture involves intergrowth of quartz and alkali feldspar on a submicroscopic to microscopic scale, and, according to the classification of Smith (1974), spherulitic, radiate fringe and vermicular types can be observed (Fig. 4a). The presence of these textures could indicate shallow emplacement of these rocks, probably less than 3 km (Thorpe and Brown, 1999). Evidences of hybridization in the felsic magmas are minimum and generally entirely absent.

5.2. Mafic dikes

Mafic dikes are formed predominantly of black to gray basaltic andesite with minor basalt. With respect to petrographic aspects, these two types of rocks have notable textural homogeneity. They are holocrystalline, exhibit ophitic texture and are fine-to medium-grained (Fig. 4c). Plagioclase (labradorite (core) to Ca-andesine (rim)), orthopyroxene (enstatite), clinopyroxene (augite and pigeonite) and minor proportions of olivine are the essential phases. Clinopyroxenes are represented by phenocrysts with prismatic habit. Orthopyroxenes occur mainly as microphenocrysts with prismatic habit, typically zoned and twinned. Chlorite, talc and iron oxide/hydroxide are their alteration products. Epidote and carbonate are also present as secondary phases. Besides that, there is a large presence of primary euhedral iron oxide minerals, mainly magnetite and titanomagnetite, and as occur with the felsic dikes, these rocks do not exhibit noticeable field and petrographic evidence of mixture, except for the occurrence in some rocks of small amounts of K-feldspar phenocrysts, with features that suggest mafic-felsic magma interaction.

5.3. Intermediate dikes

Intermediate dikes are the most complex group of the rocks in the present study, since they show evidence of contamination by mafic magma. This group is composed of andesites and dacites with slight petrographic differences. These rocks range in color from gray, greenish gray, dark gray to darkish brick red. Most are porphyritic with an aphyric matrix. The phenocrysts are represented by quartz, plagioclase, K-feldspar and minor amphibole. Phenocrysts vary from a few millimeters to just over 1 cm; however, the proportion of phenocrysts is lower than that found in rhyolites (15–30% by vol).

The main differences between andesites and dacites lie in the content and degree of amphibole transformation and matrix composition. Andesites exhibit small amphibole crystals (0.1–0.8 mm) that are occasionally displayed as relics. These crystals are subhedral to anhedral, and sometimes zoned and completely replaced by epidote or more rarely by chlorite. Compared to the dacites, the matrix is coarser and composed primarily of plagioclase microliths, preserved or altered by sericite, altered amphibole crystals, chlorite and carbonates. These rocks occasionally have a subophitic texture and flow structures characterized by the orientation of tabular plagioclase crystals, suggesting a trachytic texture. The accessory phases consist predominantly of euhedral to subhedral opaque minerals (mainly hematite) immersed in the fine-grained matrix.

In the dacite dikes the amphibole content are subordinate, they are smaller than the other minerals and difficult to recognize.

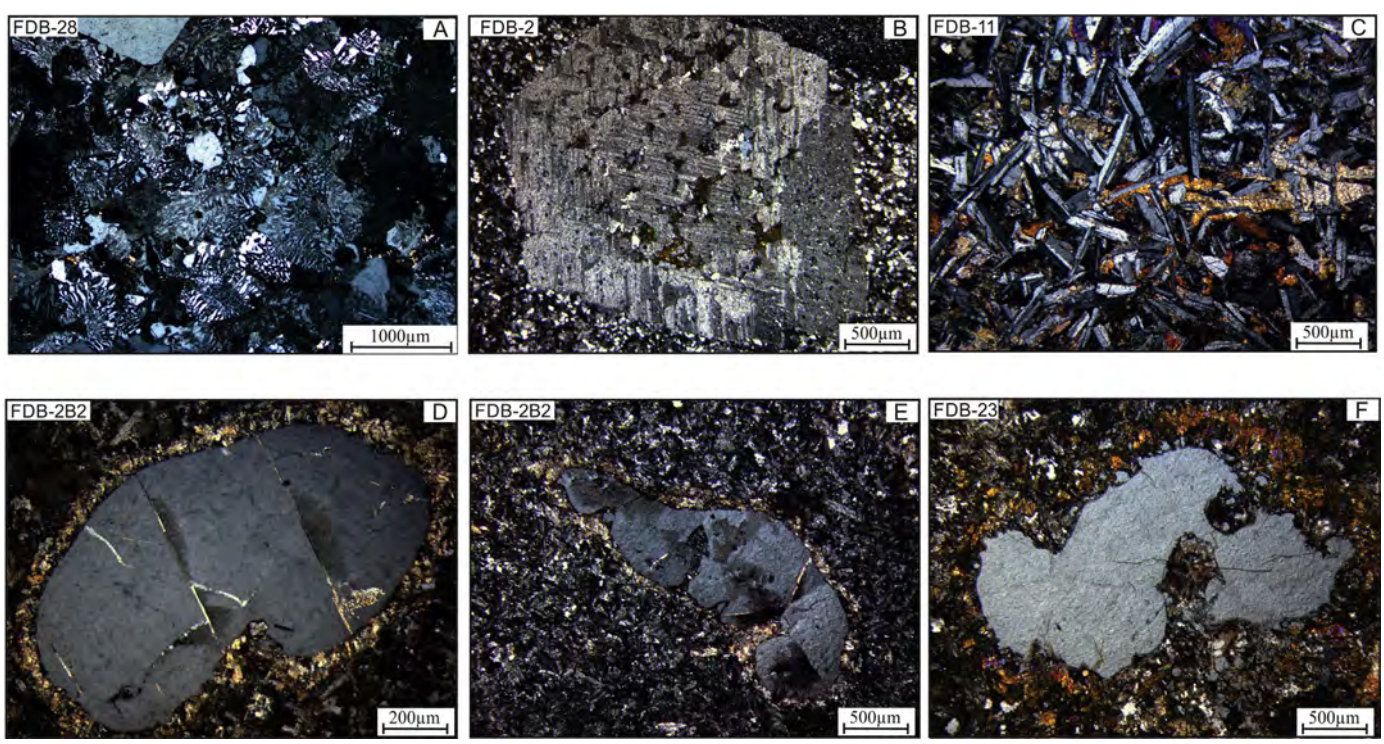

Fig. 4. Microtextural aspects of the Tucumã dikes: A) Radiate fringe and vermicular granophyric texture in rhyolite and an aggregate of quartz forming the glomeporphyritic texture; B) K-feldspar phenocryst with rapakivi texture; C) Subophitic texture, common feature of mafic dikes; D, E, F) Corona texture in quartz crystals with different degrees of embayment/engulfment.

Nevertheless, the form of occurrence is quite similar to that found in the andesites, but prominently altered and appearing as relic minerals. The matrix is very fine-grained (<0.1 mm) and consists mainly of feldspar microliths and opaque minerals. The ferromagnesian minerals as well as plagioclase and alkali feldspar have suffered intense sub-solidus alteration such as, chloritization, saussuritization and argillization, respectively.

Common features of both varieties of this group include the presence of corona textures, also known as reaction rims, which can be observed in quartz and feldspar phenocrysts (Fig. 4d). This texture is a result of the crystals becoming unstable and reacting with its surrounding crystals or melt (Hibbard, 1995; Rämö, 1991). Another common texture is the embayed crystal or engulfment texture (Fig. 4e–f), which consists of a crystal with an irregular cavity penetrating a crystal face. The embayment is often filled with groundmass or another mineral, suggesting that the crystal was out of equilibrium and reacting with the surrounding melt, especially when combined with rounded crystal shapes and reaction rims. Glomeroporphyritic texture is also present, but in lesser amounts compared to rhyolite.

6. Whole-rock geochemistry

6.1. Introduction

The Geochemical analyses of the rocks are shown in Tables 2 and 3. In order to determine comparison parameters with analogous occurrences in the Carajás province, the geochemical data obtained in this work were also confronted with those available in the rocks from the Santa Rosa and Sobreiro formations of the Xingu area (Fernandes et al., 2011), dikes associated with the Jamon suite (Ferreira, 2009; Silva et al., 1999) and granites related to the Velho Guilherme suite (Teixeira et al., 2005).

6.2. Geochemical classification

The Tucumã dikes have a wide composition range, varying from mafic to felsic, displaying a subalkaline trend and plot in basalt to rhyolite fields in the TAS and R1-R2 diagrams (De La Roche et al., 1980, Fig. 5a–b).

The felsic dikes are peraluminous to slightly metaluminous, mainly due to K-feldspar and plagioclase fractionation with a minor contribution of amphibole, while the intermediate and mafic groups are exclusively metaluminous (Fig. 5c). Felsic dikes exhibit high FeOt/(FeOt + MgO) ratios (0.79–0.98), similar to those of ferroan granites (Frost et al., 2001), and, more particularly, with those observed in the Santa Rosa Formation and in the granites of the Velho Guilherme suite (Fig. 5d). Intermediate rocks plot in the magnesian granite field, but they show slightly higher values of FeOt/(FeOt + MgO) ratios (0.67–0.86) compared to those from the Sobreiro Formation, and a clearer scattering than the intermediate dikes of the Jamon Suite.

With respect to the magmatic series, in the AFM diagram (Irvine and Baragar, 1971) mafic dikes plot on the tholeiitic field (Fig. 5e), with a lower Fe content when compared to mafic dikes of the Jamon Suite. Furthermore, the Tucumã mafic dikes exhibit a high-Mg tholeiitic basalts behavior, clearly distinct of the basalts associated with the Jamon Suite that are high-Fe tholeiitic basalts (Fig. 5f). Intermediate rocks show a narrow calc-alkaline behavior, slightly Fe-enriched compared to the Sobreiro Formation. The felsic group exhibits alkalis enrichment that overlaps significantly with the Velho Guilherme Suite, felsic dikes of the Jamon Suite and the Santa Rosa Formation (Fig. 5e). In the cationic diagram developed by Jensen (1976), intermediate dikes display dubious behavior. While the mafic group is in the same field in both diagrams, the dacites plot on the tholeiitic field and the andesites on the calc-alkaline field (Fig. 5f). This incongruous behavior in the two diagrams may indicate that these groups of rocks do not exhibit geochemical continuity.

6.3. Major and trace element behavior

The Tucumã dikes show a wide variation in SiO_2 content, ranging from 49.18% to 78.56% from mafic to felsic, respectively (Tables 2 and 3). Separate analysis of the groups reveals that felsic rocks can be distinguished into two different groups, high SiO_2 (74.00–78.56%) and low SiO_2 (69.16–71.95%) content. The intermediate dikes have the largest variations in SiO_2 (56.76–66.68%), while mafic dikes show a slight variation in SiO_2 content (49.18–53.70%). The global disposition of the rocks analyzed in the Harker variation diagrams (SiO_2 versus oxides) demonstrates a linear decrease in the proportions of TiO_2, Al_3O_2, MgO, CaO, FeO and P_2O_5 with increasing in SiO_2 content (Fig. 6a-b-c-d-f).

The amount of Al_2O_3 in the mafic group is mostly >14.5%, with minor variations (14.37–15.62%), while the intermediate and felsic groups exhibit a broad spectrum, ranging from 11.75 to 15.62% and 10.92–12.36 to high SiO_2 and 12.61–13.07 to low SiO_2, respectively. Despite the negative correlation between Al_2O_3 and SiO_2 observed in all dike groups, the arrangement of the sample sets shows parallel trends, suggesting that these rocks are not comagmatic.

Ferromagnesian oxide and CaO levels in the mafic group [MgO (5–8.37%), Fe_2O_3t (11.13–12.31%) and CaO (5.70–12.21%)] are higher than in the intermediate group [MgO (0.97–3.37%), Fe_2O_3t (5.92–10.82%) and CaO (2.77–5.87%)] and in the felsic group of low-Si [MgO (0.45–1.05%), Fe_2O_3t (3.32–4.53%) and CaO (0.93–1.99%)] and high-Si [MgO (0.04–0.29%), Fe_2O_3t (1.67–2.84%) and CaO (0.11–0.91%)]. The negative correlation of the aforementioned oxides may be explained by the early crystallization of clinopyroxene, hornblende, magnetite, ilmenite and apatite. Ca-plagioclase fractionation plays a significant role in the apparent decline in Al_2O_3 and CaO. On the other hand, A/CNK and K_2O/Na_2O ratios show a clear positive correlation, with a sharp increase towards the most evolved rocks (Fig. 6g–h), indicating that K-feldspar is not an important fractionating phase in these magmas. Despite the negative correlation with SiO_2 in these rocks, TiO_2 and P_2O_5 behavior is slightly discordant with that of other oxides due to their enrichment in the mafic dikes with an increase in SiO_2.

The felsic dikes in the Tucumã area show affinity in major elements with rhyolites from the Santa Rosa Formation, granites of the Velho Guilherme Suite and felsic dikes associated with the Jamon Suite. In this respect, intermediate dikes exhibit good correlation with the Sobreiro Formation and analogous dikes of the Rio Maria area, although intermediate rocks of the Xingu area are more enriched in Al_2O_3, CaO, MgO, FeO and P_2O_5. Mafic dikes do not match those associated with the Jamon Suite, and, despite showing similar trends, those in the Rio Maria area have the highest TiO_2 and FeO.

The variation of trace elements in magmatic series could reflect differentiation and may support the interpretation of the processes responsible for their evolution (Wedepohl, 1970; Hanson, 1978). The behavior of the main trace elements in the different groups of rocks is presented in binary variation diagrams (Fig. 7). Rb and Y contents, whose values range from 161.40 to 289.10 ppm in the high SiO_2 and 167.20–198.30 in the low SiO_2 rhyolites, and 16.40–96.90 ppm in the intermediate rocks, show a clear positive correlation with SiO_2 (Fig. 7a–e).

By contrast, Cr content is very high in the mafic samples (47.90–451.59 ppm), moderate in the intermediate dikes (20.53–130.0 ppm) and extremely low in the rhyolites (13.68–34.21 ppm), exhibiting a negative correlation with the SiO_2

Table 2
Chemical composition of felsic dikes of the Tucumã area.

Variety	Felsic Dikes																					
Rock	Rhyolite porphyry																					
Sample	FDB 6B1	ALC 62	FDB 4A	FDB 1	FDB 3	C2EVP 30B	FDB 26	FDB 2	FDB 10B	FDB 16A	FDB 17	FDB 6A	FDB 7	FDB 10A	FDB 29	FDB 13A	FDB 15A	FDB 14A	FDB 28	FDB 21	FDB 29	AV
SiO_2	69.16	70.37	70.90	71.60	71.95	74.00	74.75	74.83	74.84	75.33	75.37	75.41	75.42	75.56	75.57	75.61	76.03	77.14	77.70	78.24	78.56	74.68
TiO_2	0.47	0.29	0.43	0.42	0.38	0.21	0.19	0.22	0.12	0.15	0.18	0.12	0.12	0.12	0.16	0.12	0.15	0.13	0.12	0.13	0.11	0,21
Al_2O_3	12.85	12.62	12.94	13.07	12.61	12.37	12.17	11.91	12.00	11.83	11.70	11.79	12.06	11.86	11.87	11.98	12.27	11.27	10.92	11.08	11.09	12,01
Fe_2O_3t	4.53	3.36	3.83	3.70	4.00	2.50	2.48	2.84	2.34	2.30	2.60	2.21	2.21	2.23	1.88	2.37	1.77	1.80	1.74	1.81	1.67	2,58
MnO	0.06	0.05	0.09	0.05	0.06	0.03	0.04	0.04	0.02	0.03	0.04	0.02	0.02	0.02	0.02	0.03	0.01	0.02	0.02	0.02	0.01	0,03
MgO	1.05	0.78	0.61	0.45	0.62	0.29	0.10	0.24	0.07	0.10	0.09	0.11	0.06	0.04	0.08	0.05	0.08	0.04	0.09	0.06	0.04	0,24
CaO	1.91	1.99	1.34	1.26	0.93	0.84	0.59	0.83	0.51	0.69	0.91	0.48	0.39	0.52	0.76	0.31	0.18	0.68	0.55	0.15	0.11	0,76
Na_2O	2.69	2.78	3.12	3.03	2.74	3.08	3.34	2.84	3.02	2.56	2.51	2.63	3.20	3.11	2.86	3.11	3.14	2.89	2.41	3.05	2.83	2,9
K_2O	5.09	4.91	4.85	4.92	5.35	5.45	5.11	4.82	5.64	5.83	5.32	5.91	5.37	5.38	5.26	5.27	5.23	4.78	5.35	4.90	4.99	5,23
P_2O_5	0.12	0.04	0.10	0.10	0.07	0.03	0.01	0.03	<0.01	0.01	0.01	0.01	<0.01	0.01	0.02	<0.01	<0.01	<0.01	<0.01	0.01	<0.01	0,04
LOI	1.70	2.60	1.40	1.20	0.90	1.00	1.00	1.10	1.30	1.00	1.10	1.20	1.00	1.00	1.30	1.00	0.90	1.10	0.90	0.40	0.40	1,12
Total	99.63	99.79	99.61	99.8	99.61	99.8	99.78	99.7	99.86	99.83	99.83	99.89	99.85	99.85	99.78	99.85	99.76	99.85	99.8	99.85	99.81	99.79
Ba	1587	774	1442	1180	1232	628	1301	1588	190	709	789	306	112	119	1179	190	705	625	359	690	355	764,76
Rb	167.20	192.30	173.40	193.10	198.30	234.60	161.40	163.80	278.70	221.20	196.10	289.10	266.40	284.10	163.30	272.30	183.60	163.40	185.10	167.60	185.90	206,71
Sr	164.30	127.90	134.70	99.20	113.70	32.00	65.50	68.20	48.20	43.60	37.30	22.70	44.50	63.10	46.70	31.40	33.50	33.80	12.90	35.50	31.00	61,41
Zr	272.50	285.80	309.70	303.40	306.20	240.20	295.80	389.30	217.20	246.90	279.20	216.30	211.60	207.70	247.90	236.80	246.20	214.40	196.80	222.70	203.90	254,79
Nb	11.30	11.70	14.10	14.50	12.60	15.50	9.60	16.70	18.60	15.20	13.30	17.10	17.40	17.60	11.10	18.00	11.60	10.90	11.60	11.30	11.50	13,87
Y	38.10	35.00	45.70	34.20	33.00	57.40	34.20	38.50	67.10	60.30	55.30	69.00	96.90	68.80	29.00	78.30	70.20	38.90	68.70	51.40	53.90	53,52
Ga	19.00	19.60	21.60	21.80	17.80	20.10	19.80	20.30	22.40	19.40	19.00	21.10	20.70	21.80	21.20	22.80	19.00	19.10	18.40	18.80	18.90	20,12
Sc	8.00	6.00	7.00	7.00	7.00	4.00	3.00	4.00	3.00	3.00	4.00	3.00	3.00	3.00	3.00	3.00	3.00	2.00	2.00	2.00	2.00	3,9
Th	27.60	30.40	32.90	32.20	28.50	31.60	13.00	33.60	33.50	27.70	24.90	32.50	33.80	32.50	13.20	32.70	16.50	16.10	17.70	17.30	18.30	26,02
U	7.00	5.40	8.20	6.20	7.20	7.70	3.80	5.10	8.90	7.40	6.20	9.40	10.00	9.00	3.90	9.20	4.10	4.60	4.10	5.30	5.60	6,59
Cr	20.53	nd	20.53	20.53	nd	nd	nd	20.53	20.53	nd	nd	34,21	20,53	20,53	20,53	20,53	20,53	34,21	13,68	34,21	34,21	23,72
V	35.00	26.00	29.00	27.00	20.00	9.00	nd	nd	nd	nd	nd	nd	nd	nd	nd	nd	nd	nd	nd	nd	nd	24,33
La	75.30	77.00	99.30	73.30	70.90	99.60	58.40	90.50	106.00	103.30	101.10	100.70	110.40	105.80	53.90	116.10	160.70	72.40	110.60	107.70	112.60	95,5
Ce	146.60	143.60	188.80	142.30	129.80	188.40	110.30	170.70	208.30	193.60	195.20	203.70	208.10	208.70	103.20	226.20	242.60	132.20	164.70	187.30	180.10	174,97
Pr	15.24	15.05	19.31	15.80	14.21	20.69	11.63	18.63	23.09	21.73	20.94	22.54	23.81	23.22	11.04	24.84	28.59	14.39	20.74	20.28	21.31	19,38
Nd	54.50	55.30	68.80	53.90	49.50	73.40	40.50	65.10	82.40	78.80	74.30	81.00	86.40	82.80	40.10	89.30	103.10	50.90	73.30	69.40	74.20	68,9
Sm	9.15	8.75	11.08	9.26	8.20	12.97	7.16	10.77	15.12	13.35	11.96	14.51	16.71	15.36	6.83	16.45	16.71	8.49	11.95	10.66	12.20	11,79
Eu	1.29	0.70	1.38	1.23	1.03	0.64	0.94	1.30	0.37	0.71	1.03	0.34	0.48	0.40	0.84	0.43	1.25	0.52	0.45	0.59	0.47	0,78
Gd	8.32	7.41	9.58	7.81	6.98	11.05	6.25	8.86	13.70	11.56	10.42	13.44	16.77	13.89	6.03	14.79	14.77	7.45	11.39	9.57	11.21	10,54
Tb	1.17	1.07	1.28	1.09	1.00	1.60	0.95	1.21	2.05	1.74	1.50	2.00	2.63	2.04	0.90	2.24	2.01	1.11	1.66	1.47	1.65	1,54
Dy	6.81	6.28	7.04	6.13	6.06	9.97	5.87	7.01	12.86	10.42	9.29	12.46	16.86	12.96	5.36	13.69	10.90	7.16	10.27	9.02	9.95	9,35
Ho	1.36	1.16	1.46	1.22	1.20	1.85	1.20	1.35	2.48	1.97	1.83	2.38	3.48	2.46	1.06	2.72	2.09	1.46	2.15	1.74	1.91	1,83
Er	3.91	3.46	4.35	3.21	3.32	5.51	3.23	3.67	6.74	5.69	5.22	6.89	9.67	6.95	3.01	7.64	5.69	3.92	6.09	4.67	5.20	5,14
Tm	0.55	0.50	0.62	0.50	0.51	0.78	0.52	0.56	0.99	0.82	0.79	1.02	1.37	1.02	0.46	1.13	0.82	0.62	0.92	0.68	0.76	0,76
Yb	3.55	3.39	4.37	3.26	3.30	4.97	3.46	3.58	6.56	5.23	4.83	6.52	8.29	6.52	3.05	6.95	5.38	3.78	5.56	4.28	4.61	4,83
Lu	0.55	0.51	0.59	0.51	0.49	0.73	0.55	0.55	0.97	0.74	0.72	0.94	1.25	0.94	0.46	1.03	0.81	0.57	0.85	0.62	0.69	0,72
A/CNK	0.96	0.93	1.01	1.04	1.05	0.99	1.01	1.04	1.00	1.00	1.01	1.02	1.02	1.00	1.01	1.05	1.10	1.01	1.02	1.05	1.08	1,02
K_2O/Na_2O	1.89	1.77	1.55	1.62	1.95	1.77	1.53	1.70	1.87	2.28	2.12	2.25	1.68	1.73	1.84	1.69	1.67	1.65	2.22	1.61	1.76	1,82
$FeO_t/(FeO_t + MgO)$	0.8	0.79	0.85	0.88	0.89	0.89	0.96	0.91	0.97	0.95	0.96	0.95	0.97	0.98	0.95	0.98	0.95	0.98	0.95	0.96	0.97	0.93
FeOt	4.08	3.02	3.45	3.33	5.05	2.25	2.23	2.56	2.01	2.07	2.34	1.99	1.99	2.01	1.69	2.13	1.59	1.62	1.57	1.63	1.50	2.39
Rb/Sr	1.02	1.50	1.29	1.95	1.74	7.33	2.46	2.40	5.78	5.07	5.26	12.74	5.99	4.50	3.50	8.67	5.48	4.83	14.35	4.72	6.00	0,16
Ba/Sr	9.66	6.05	10.71	11.90	10.84	19.63	19.86	23.28	3.94	16.26	21.15	13.48	2.52	1.89	25.25	6.05	21.04	18.49	27.83	19.44	11.45	1,44
Nb/Ta	11.30	10.64	14.10	12.08	10.50	11.07	10.67	13.92	10.94	10.13	11.08	10.06	10.24	9.78	12.33	11.25	11.60	9.91	12.89	11.30	10.45	5,08
(La/Yb) N	14.32	15.33	15.34	15.18	14.50	13.53	11.39	17.06	10.91	13.33	14.13	10.42	8.99	10.95	11.93	11.28	20.16	12.93	13.43	16.98	16.49	14,32
ΣETR	328.30	324.18	417.96	319.52	296.50	432.16	250.96	383.79	481.63	449.66	439.13	468.44	506.22	483.06	236.24	523.51	595.42	304.97	420.63	427.98	436.86	4,1
ΣETR Light	302.08	300.40	388.67	295.79	273.64	395.70	228.93	357.00	435.28	411.49	404.53	422.79	445.90	436.28	215.91	473.32	552.95	278.90	381.74	395.93	400.88	11,25
ΣETR Heavy	26.22	23.78	29.29	23.73	22.86	36.46	22.03	26.79	46.35	38.17	34.60	45.65	60.32	46.78	20.33	50.19	42.47	26.07	38.89	32.05	35.98	13,74
Eu/Eu*	0.44	0.26	0.40	0.43	0.41	0.16	0.42	0.40	0.08	0.17	0.28	0.07	0.09	0.08	0.39	0.08	0.24	0.20	0.12	0.18	0.12	0.24

Table 3
Chemical composition of mafic and intermediate dikes of the Tucumã area.

Variety	Intermediate dikes												Mafic Dikes								
Rock	Dacites					Andesites							Basaltic andesite					Basalt			
Sample	FDB 2B3	FDB 2B2	FDB 25B	FDB 2B1	ALC 60	FDB 25A	FDB 6B3	FDB 2C	FDB 27	FDB 23	FDB 24	AV	FDB 10C	FDB 5	FDB 4B	FDB 6B2	FDB 3B	FDB 22	FDB 20	FDB 11A	AV
SiO_2	61.46	61.73	62.55	63.98	66.26	66.68	56.76	57.34	58.02	60.26	61.60	61.52	51.22	51.38	52.26	52.35	53.70	49.18	49.90	50.18	51.27
TiO_2	0.78	0.77	1.06	0.67	0.63	0.66	1.14	1.03	0.69	0.77	0.59	0.80	1.10	1.11	1.27	1.28	1.33	0.72	0.98	0.93	1.09
Al_2O_3	13.24	13.16	12.59	13.11	11.75	12.91	15.12	13.57	14.40	13.78	14.21	13.46	15.14	15.29	15.11	14.88	14.37	15.62	13.73	15.55	14.96
Fe_2O_3t	8.45	8.27	9.06	7.23	6.37	5.92	10.82	10.54	8.52	8.57	7.36	8.28	11.13	11.10	12.24	12.11	10.75	11.53	11.92	12.31	11.64
MnO	0.12	0.14	0.11	0.10	0.08	0.08	0.18	0.14	0.13	0.12	0.10	0.12	0.16	0.16	0.25	0.19	0.17	0.17	0.19	0.18	0.18
MgO	2.66	2.66	2.45	2.09	0.97	1.40	3.17	3.37	3.85	3.00	3.03	2.60	6.79	6.82	5.29	5.31	5.00	7.09	8.37	7.27	6.49
CaO	4.06	3.99	3.65	3.53	3.29	2.77	3.54	5.87	5.57	5.38	4.78	4.24	8.15	8.71	7.24	7.62	5.70	9.50	12.21	8.71	8.48
Na_2O	3.10	3.01	3.26	3.06	2.76	3.09	4.04	3.15	3.20	3.06	2.83	3.15	2.09	2.09	2.37	2.20	3.29	2.05	1.85	2.11	2.26
K_2O	3.37	3.27	3.37	3.45	3.62	4.09	2.34	1.94	2.79	2.74	3.16	3.08	1.36	0.81	1.63	1.35	2.27	0.99	0.17	0.73	1.16
P_2O_5	0.15	0.17	0.16	0.13	0.13	0.10	0.24	0.21	0.14	0.16	0.11	0.16	0.29	0.31	0.25	0.25	0.38	0.08	0.06	0.14	0.22
LOI	2.30	2.50	1.40	2.40	3.80	2.00	2.30	2.50	2.40	1.90	1.90	2.31	2.20	1.90	1.80	2.10	2.60	2.80	0.30	1.60	1.91
Total	99.69	99.67	99.66	99.75	99.66	99.7	99.65	99.66	99.71	99.74	99.67	99.69	99.63	99.68	99.71	99.64	99.56	99.73	99.68	99.71	99.67
Ba	927.00	970.00	1086.00	846.00	1630.00	1329.00	947.00	776.00	708.00	723.00	774.00	978.90	815.00	651.00	923.00	916.00	1352.00	485.00	38.00	452.00	704
Rb	134.80	124.50	133.00	127.10	112.80	152.90	129.60	59.90	156.50	123.00	121.00	124.03	33.40	28.80	67.70	43.30	87.70	34.40	11.70	21.20	41.03
Sr	198.30	213.00	262.40	189.40	110.90	199.40	310.50	211.30	252.90	268.00	171.10	218.89	404.70	379.80	325.50	275.20	388.60	281.50	104.40	206.50	295.78
Zr	233.30	228.20	302.70	269.50	449.00	326.20	203.30	203.30	160.80	203.30	281.80	262.81	158.70	151.80	156.10	145.40	251.00	60.60	52.90	98.60	134.39
Nb	12.80	14.50	9.20	14.90	12.80	10.30	7.90	13.00	10.90	9.70	9.90	11.31	5.70	5.30	5.40	4.50	9.20	1.60	2.30	3.40	4.68
Y	37.80	38.80	35.70	47.30	41.30	35.60	33.00	34.10	38.90	37.50	35.20	37.74	22.40	19.40	27.50	24.80	29.10	18.30	16.40	22.80	22.59
Ga	18.20	21.50	19.20	20.50	21.60	19.90	23.20	21.90	20.80	21.20	19.80	20.96	17.70	17.70	20.50	18.40	20.20	17.30	15.90	16.40	18.01
Sc	17.00	16.00	18.00	14.00	9.00	11.00	23.00	22.00	21.00	19.00	18.00	17.10	26.00	25.00	26.00	26.00	24.00	34.00	41.00	30.00	29
Th	24.20	23.50	15.50	29.60	19.10	22.80	10.30	16.90	19.70	19.90	16.90	19.42	3.90	3.70	4.10	4.20	7.90	2.30	0.20	2.30	3.58
U	4.10	4.30	2.60	4.90	2.90	3.80	2.60	3.40	4.00	3.40	2.40	3.43	0.40	0.50	0.60	0.70	1.10	0.30	<0.1	0.30	0.56
Cr	27.37	34.21	47.9	20.53	54.74	27.37	27.37	130	34.21	41.05	82.11	47.9	47.9	212.11	136.85	307.9	130	294.22	266.85	451.59	230.93
V	145.00	160.00	144.00	122.00	94.00	69.00	160.00	232.00	165.00	176.00	119.00	144.10	194.00	199.00	213.00	205.00	184.00	211.00	295.00	184.00	210,63
La	72.70	83.30	53.90	87.60	70.20	68.20	45.10	59.50	37.70	69.30	55.10	62.99	32.40	29.70	30.40	28.40	54.60	12.00	2.90	18.20	26.08
Ce	143.40	157.30	101.30	166.80	133.00	132.70	87.30	117.30	77.90	133.20	112.40	121.92	64.30	60.60	57.80	57.90	107.90	21.40	7.00	35.20	51.51
Pr	15.46	16.27	11.16	18.52	14.76	13.99	9.53	12.46	9.12	14.08	11.88	13.18	7.45	7.00	6.53	6.45	11.53	2.53	1.12	3.98	5.82
Nd	54.00	59.70	40.10	62.90	52.90	46.60	35.60	42.90	32.00	48.20	42.50	46.34	26.90	26.80	23.80	24.30	44.80	8.80	6.00	15.10	22.06
Sm	9.08	9.49	7.28	10.96	9.72	8.18	6.06	7.16	6.95	8.74	7.39	8.19	5.37	4.92	4.95	4.56	7.72	2.18	1.89	3.27	4.36
Eu	1.12	1.21	1.39	1.10	1.85	1.28	1.33	1.41	0.91	1.18	1.10	1.28	1.43	1.38	1.44	1.28	1.59	0.75	0.72	1.01	1.2
Gd	7.98	9.38	6.94	9.77	8.84	7.44	6.39	7.20	7.23	7.63	6.84	7.77	5.07	4.50	5.10	5.05	6.87	2.67	2.56	3.50	4.42
Tb	1.14	1.28	1.09	1.33	1.27	1.08	0.98	1.06	1.12	1.14	1.04	1.14	0.71	0.68	0.80	0.74	0.91	0.45	0.45	0.58	0.67
Dy	6.68	7.77	6.77	8.12	8.13	6.13	6.20	6.21	6.87	6.76	5.89	6.89	4.15	3.88	5.05	4.75	5.75	2.98	2.83	3.72	4.14
Ho	1.34	1.39	1.26	1.56	1.49	1.20	1.07	1.20	1.48	1.28	1.30	1.32	0.91	0.75	0.97	0.93	1.06	0.65	0.60	0.79	0.83
Er	3.66	4.24	3.69	4.51	4.21	3.83	3.33	3.58	4.07	4.12	3.74	3.93	2.32	1.99	2.63	2.65	2.86	1.83	1.56	2.27	2.26
Tm	0.55	0.59	0.54	0.63	0.62	0.57	0.52	0.56	0.64	0.61	0.48	0.58	0.38	0.32	0.43	0.41	0.42	0.28	0.25	0.34	0.35
Yb	3.66	4.11	3.55	4.27	3.91	3.55	3.10	3.58	3.96	3.74	3.62	3.74	2.37	1.83	2.72	2.43	2.83	1.75	1.62	2.24	2.22
Lu	0.50	0.60	0.56	0.64	0.59	0.54	0.50	0.50	0.55	0.56	0.59	0.56	0.32	0.31	0.40	0.39	0.42	0.27	0.24	0.35	0.34
A/CNK	0.82	0.84	0.80	0.86	0.81	0.89	0.97	0.76	0.78	0.77	0.85	0.83	0.77	0.76	0.80	0.79	0.79	0.72	0.54	0.77	0.74
K_2O/Na_2O	0.92	0.92	0.97	0.89	0.76	0.76	1.73	1.62	1.15	1.12	0.90	1.08	0.65	0.39	0.69	0.61	0.69	0.48	0.09	0.35	0.49
$FeO_t/(FeO_t + MgO)$	0.74	0.74	0.77	0.76	0.86	0.79	0.75	0.74	0.67	0.72	0.69	0.75	0.60	0.59	0.68	0.67	0.66	0.59	0.56	0.60	0.62
Fe_2O_3t	8.45	8.27	9.06	7.23	6.37	5.92	10.82	10.54	8.52	8.57	7.36	8.27	11.13	11.10	12.24	12.11	10.75	11.53	11.92	12.31	10.47
Rb/Sr	0.68	0.58	0.51	0.67	1.02	0.77	0.42	0.28	0.62	0.46	0.71	0.60	0.08	0.08	0.21	0.16	0.23	0.12	0.11	0.10	0.61
Ba/Sr	4.67	4.55	4.14	4.47	14.70	6.66	3.05	3.67	2.80	2.70	4.52	5.13	2.01	1.71	2.84	3.33	3.48	1.72	0.36	2.19	13.09
Nb/Ta	12.80	16.11	11.50	12.42	12.80	10.30	13.17	16.25	13.63	12.13	12.38	13.07	14.25	13.25	13.50	15.00	13.14	16.00	7.67	11.33	0.14
(La/Yb) N	13.41	13.68	10.25	13.85	12.12	12.97	9.82	11.22	6.43	12.51	10.27	11.50	9.23	10.95	7.54	7.89	13.02	4.63	1.21	5.48	2.21
ΣETR	321.27	356.63	239.53	378.71	311.49	295.29	207.01	264.62	190.50	300.54	253.87	279.82	154.08	144.66	143.02	140.24	249.26	58.54	29.74	90.55	1.72
ΣETR Light	295.76	327.27	215.13	347.88	282.43	270.95	184.92	240.73	164.58	274.70	230.37	253.90	137.85	130.40	124.92	122.89	228.14	47.66	19.63	76.76	13.02
ΣETR Heavy	25.51	29.36	24.40	30.83	29.06	24.34	22.09	23.89	25.92	25.84	23.50	25.92	17.66	15.64	19.54	18.63	22.71	11.63	10.83	14.80	7.49
Eu/Eu*	0.39	0.39	0.59	0.32	0.60	0.49	0.65	0.59	0.39	0.43	0.47	0.49	0.84	0.90	0.88	0.82	0.91	1	0.95	0.91	0.87

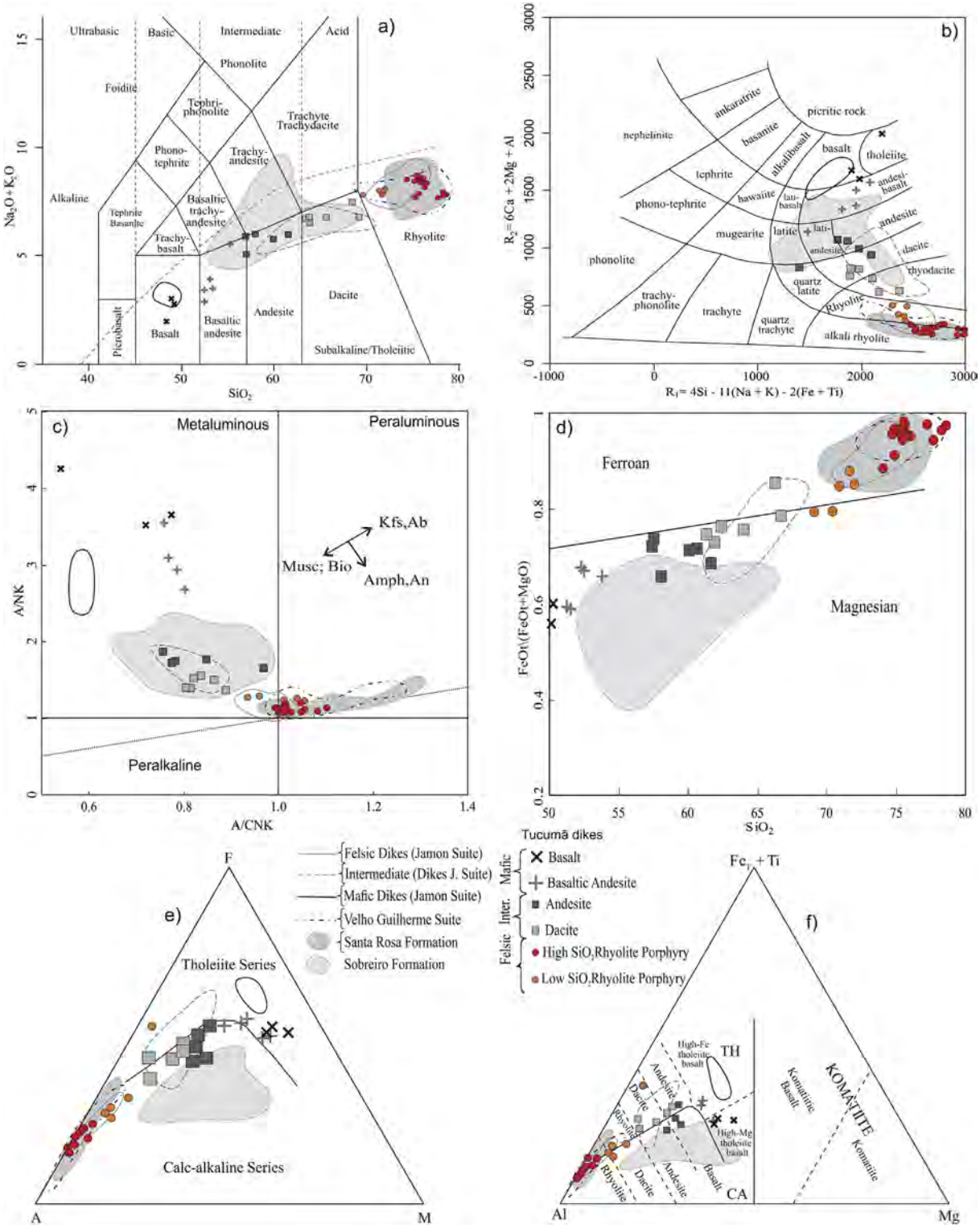

Fig. 5. Geochemical characterization of the Tucumã dikes. a) TAS classification diagram; b) R1-R2 multicationic diagram (De La Roche et al., 1980); c) Molar A/NK vs. A/CNK variation diagram (Shand, 1950), the arrows represent fractionation vectors for mineral phases. (Bio – Biotite; Mus – Muscovite; Amph – Amphibole; An – Anorthite; Kfs – K-feldspar; Ab – Albite) d) SiO2 vs FeOt/(FeOt + MgO) diagram (Frost et al., 2001); e) AFM diagram (Fields of Tholeiite and Calc-alkaline Series of Irvine and Baragar, 1971); f) Al-(Fe + Ti)-Mg cationic diagram (Jensen, 1976).

content (Fig. 7f). Zr and Ba contents increase from mafic [Zr (52.9–158.7 ppm) and Ba (38–1352 ppm)] to intermediate [Zr (160.8–449 ppm) and Ba (708–1630 ppm)] dikes and then decrease from the low-Si rhyolites samples [Zr (272.50–309.70 ppm) and Ba (774–1587 ppm)] to high- Si rhyolite [Zr (196.8–295.8 ppm) and Ba (112–1588 ppm)]. Sr also shows an inflection in its evolutionary trend, where values increase in the mafic samples (104.4–404.7 ppm) and decrease from intermediate

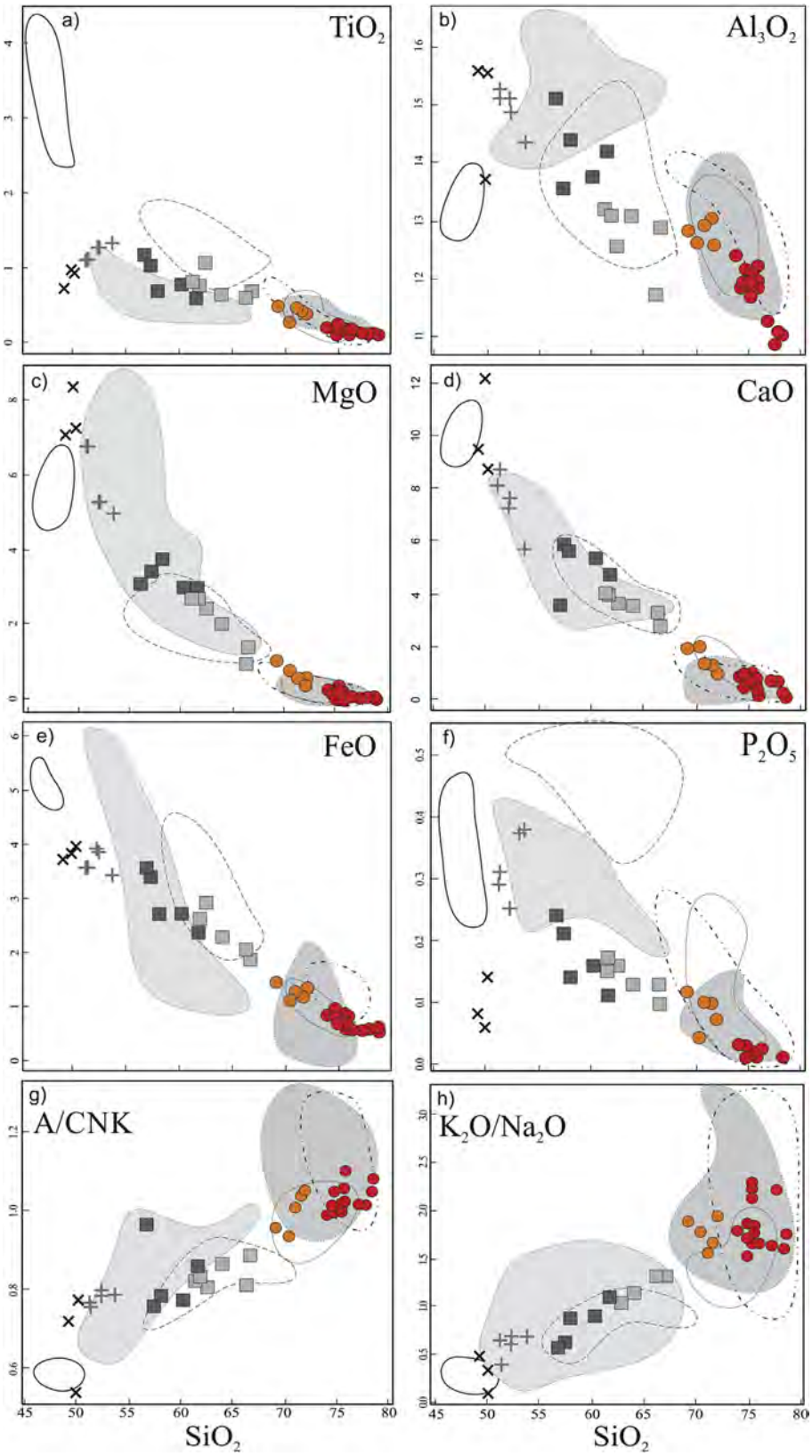

Fig. 6. Harker diagrams for selected major and minor elements of the Tucumã dikes. Tucumã dikes are the symbols red and orange circles for high and low SiO_2 rhyolites; light gray square for dacites; dark gray for andesites; gray cross for basaltic andesites and black x for basalts. The comparisons fields are given by dotted, dashed and solid lines for felsic, intermediate and mafic dikes of Jamon suite; dashed dot line represents the velho Guilherme Suite and the light and dark gray field the Sobreiro and Santa Rosa formations. Symbols as in Fig. 5. (For interpretation of the references to colour in this figure legend, the reader is referred to the web version of this article.)

(110.9–310.5 ppm) to felsic dikes [low-Si (99.2–164.3 ppm) and high-Si (12.9–68.2 ppm)] (Fig. 7b). The dual behavior observed for Ba, Zr and Sr trends may reflect the different fractionating phases during the evolution of these rocks, indicating that Ca-plagioclase ± amphibole commanded the evolution of intermediate dikes, while zircon and biotite ± K-feldspar were important fractionating phases during crystallization of the felsic dikes.

In general, there is a noticeable overlap between trace element contents in the Tucumã area dikes and the established fields for the units used for comparison purposes in the present study, as is also the case for major element behavior, as previously described. However, the Sr content of the Sobreiro Formation clearly diverges from that found in intermediate rocks of the Tucumã and Rio Maria areas, while Rb content is significantly higher in the Velho Guilherme Suite compared to that in felsic rocks from other areas.

Similarly to that described and interpreted by Silva et al. (1999), the frequent compositional gap between the mafic, intermediate and felsic groups, observed in all diagrams, as well as the presence of subparallel trends, support either that these rocks have not been derived by fractional crystallization process from a single parent magma or that fractional crystallization was not an important process in magma evolution. This is consistent with what has been described in field relationships.

6.4. Rare-earth elements

Analytical data on the rare-earth elements (REE; Tables 2 and 3) and corresponding chondrite-normalized plots (Fig. 8a-c-e) for representative samples of the different dikes in the Tucumã area show that felsic dikes display a moderate La/Yb ratio (10.9–20.1), with a nearly HREE flat pattern, and accentuated negative Eu anomaly ($Eu/Eu^* = 0.08–0.44$). The REE pattern of the felsic dikes of the Tucumã area matches both Santa Rosa Formation and felsic dikes of the Jamon Suite, while granites of the Velho Guilherme Suite show a more pronounced negative Eu anomaly. The multi-element diagram for these rocks shows strong depletion of Ti, P and Sr, and moderate Ba, Nb and Ta depletion (Fig. 8b).

Intermediate dikes display a similar pattern to that observed in felsic dikes, although they exhibit a smaller La/Yb ratio (6.43–13.68), slight HREE depletion and a smaller Eu anomaly ($Eu/Eu^* = 0.32–0.65$). When compared with the Sobreiro Formation, the dacites and andesites of the Tucumã area show a similar La/Yb ratio; however, they differ in their higher REE content and accentuated negative Eu anomaly, which is absent in the Sobreiro Formation (Fig. 8c). The intermediate dikes of the Tucumã area exhibit a similar REE pattern to that identified in the Rio Maria area, although the latter dikes show a less pronounced Eu anomaly. Similarly to that observed in the felsic dikes, intermediate rocks show negative though less significant Ti, P and Sr anomalies (Fig. 8d). The negative Nb and Ta anomalies are more pronounced in both intermediate dikes and the Sobreiro Formation when compared to felsic rocks. The Sobreiro Formation differs from the other dikes by the absence of a negative Eu anomaly and presence of a positive Sr anomaly (Fig. 8d).

The mafic dikes of the Tucumã area display an almost flat REE pattern, with low La/Yb ratios (1.21–13.25) and no negative Eu anomaly ($Eu/Eu^* = 0.95–1$). They show no affinity with mafic dikes of the Ja-mon Suite, since the latter dikes are more enriched in HREE and exhibit a flatter REE patterns (Fig. 8e). In the multi-element diagram (Fig. 8f), the mafic dikes of the Tucumã area show moderate to weak negative Ti, P and Sr anomalies, in contrast to what is observed in the intermediate and felsic dikes, and more pronounced negative Nb and Ta anomalies when compared to the last ones. These aspects contrast with that observed in the mafic rocks associated with the Jamon Suite, which show slight flatter spider-gram patterns than those mentioned above, in addition to a slightly P anomaly and absence of negative Ti, Nb and Ta anomalies.

Negative anomalies in Sr, P and Ti are consistent with extensive fractional crystallization of plagioclase, apatite and Fe-Ti oxides, respectively. However, a strong negative anomaly in Nb and Ta contents may be due to contamination of the magma and/or its sources by crustal components (Martin et al., 1997).

6.5. Classification and tectonic affinity

The tectonic setting discrimination diagrams show that both mafic and felsic dikes have within-plate whole rock geochemical affinity, indicating that emplacement of these dikes occurred within an overall extensional tectonic setting. On the Zr vs. Zr/Y discrimination diagram (Pearce and Norry, 1979), the mafic rocks plot in the within-plate basalt field (Fig. 9b), while on the Y vs Nb discrimination diagram (Pearce et al., 1984), the felsic dikes plot in the within-plate granite field and could have been formed in areas of attenuated continental crust (Fig. 9a), as described for the Paleoproterozoic plutons of the Carajás Province (Dall'Agnol et al., 1999; Oliveira et al., 2010).

The felsic dikes show enrichment in high-field-strength elements (e.g. Nb, Y, Zr), allowing their samples to fall in the A-type granite field in the FeO_{tot}/MgO vs. Zr + Nb + Ce + Y plot of Whalen et al. (1987; Fig. 9c). Effective separation of A-type granitoid varieties was recognized by Eby (1992), according to the contents of trace elements (Y, Nb, Ce, and Ga), in particular, Y/Nb. On a Nb-Y-Zr/4 tri-angular plot, samples from Tucumã area felsic dikes plot in the field defined by the granitoid group derived from subcontinental lithosphere or lower crust (A2), reflecting higher Y/Nb ratios (>1.2) than granites interpreted as differentiates of basalt magma derived from an OIB-like source (A1; Fig. 9d).

In the classification scheme of Dall'Agnol and Oliveira (2007), designed to separate calc-alkaline granites from A-type granites, and oxidized A-type granites from reduced A-type granites, felsic dikes of the Tucumã area show a consistent A-type character (Fig. 9e–f). As with typical A-type granites world-wide, the rhyolite dikes under study also show a relatively low CaO/($FeO + MgO + TiO_2$) ratio and low Al_2O_3 content when compared to calc-alkaline granites (Fig. 9e). In the FeOt/(FeOt + MgO) vs. Al_2O_3 diagram (Fig. 9f), the felsic dikes show a moderate (low-Si) to strong (high-Si) enrichment in FeO relative to MgO [$0.9 < FeOt/(FeOt + MgO) > 0.9$), and consequently, reduced A-type characteristics. Affinity with reduced A-type granites can also be observed for both the Santa Rosa Formation and plutons of the Velho Guilherme Suite, while dikes associated with the oxidized A-type Jamon suite exhibit ambiguous behavior, overlapping the fields of reduced and oxidized granites.

7. Geochronology (U-Pb)

Most analyzed zircon grains are prismatic, colorless, transparent and euhedral with some broken parts. Image C1 (Fig. 10) shows obvious oscillatory zoning but no inherited cores, and Th/U ratios ranging from 0.38 to 1.06 (Table 4) that strongly indicate a magmatic origin for these zircons crystals (Belousova et al., 2009; Hoskin and Black, 2000). The zircons of FDB 29 and FDB 2 samples, after all corrections and when plotted in a concordia diagram (Fig. 10), reveal ages of 1880.9 ± 3.3Ma (MSWD = 2.0) and 1881.9 ± 4.4 (MSWD = 2.0) respectively, which can be interpreted as crystallization ages, since these ages refer to a worldwide extensional and metamorphic-free event (Dall'Agnol et al., 2005; Rämö and Haapala, 1995; Dall'Agnol and Oliveira, 2007).

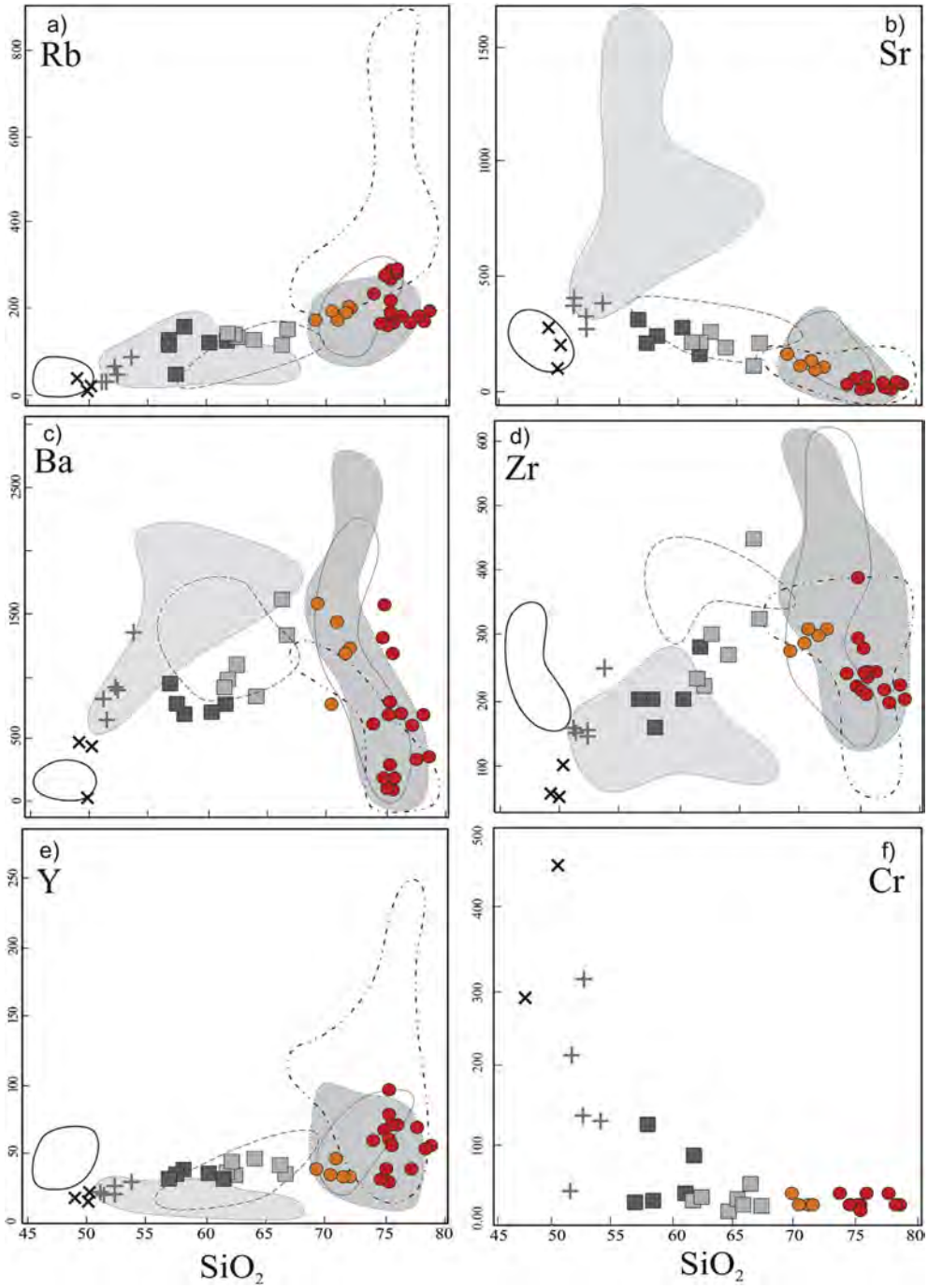

Fig. 7. Harker diagrams for selected trace elements for the Tucumã dikes. Symbols as. Tucumã dikes are the symbols red and orange circles for high and low SiO_2 rhyolites; light gray square for dacites; dark gray for andesites; gray cross for basaltic andesites and black x for basalts. The comparisons fields are given by dotted, dashed and solid lines for felsic, intermediate and mafic dikes of Jamon suite; dashed dot line represents the velho Guilherme Suite and the light and dark gray field the Sobreiro and Santa Rosa formations. Symbols as in Fig. 5. (For interpretation of the references to colour in this figure legend, the reader is referred to the web version of this article.)

8. Discussion

8.1. Fractional crystallization process

Chemical data for the mafic and felsic dikes provide an interpretation on the process that controls the magmatic evolution of these rocks. The fractionation vector calculated by Rayleigh equation (1) for less evolved samples of mafic and felsic dike groups explains the relationship between these rocks.

$$C_{l^a}/c_{l^b} = (c_{o^a}/c_{o^b}) \cdot F^{(D_a - D_b)} \quad (1)$$

where $C_o^{(a,b)}$ and $C_l^{(a,b)}$ are the concentrations of element a and b in the initial and residual liquids, respectively, Da, b are the bulk partition coefficients of a and b and F is the fraction of residual liquid.

The vectors (Fig. 11a–b) displayed in red correspond to the high SiO_2 felsic dikes (rhyolites) and in black, to the mafic dikes (basalts). The Y vs. Rb diagram (Fig. 11a) indicates that the mafic dikes evolve

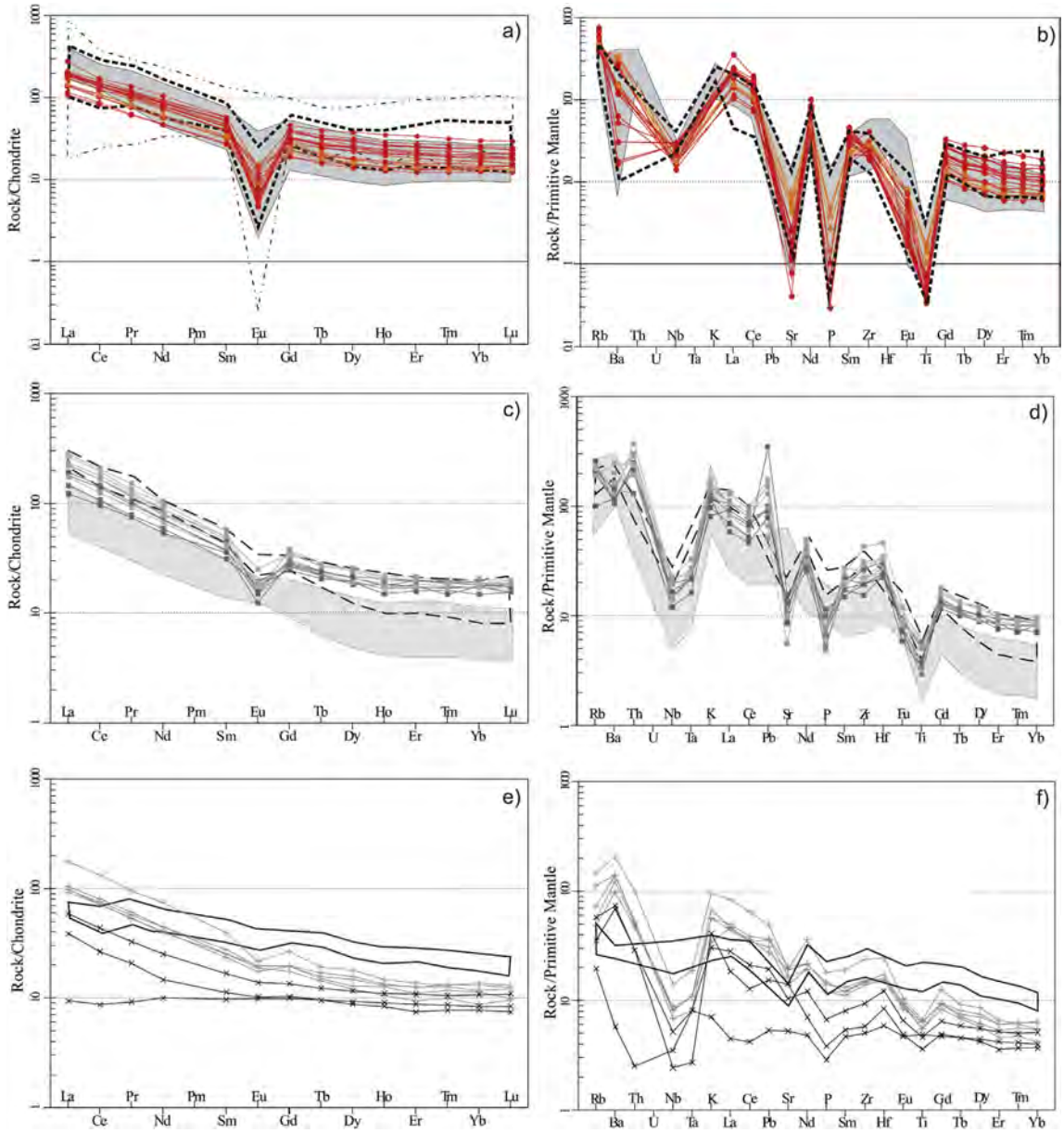

Fig. 8. a and b) Chondrite-normalized REE (Boynton, 1984) and Primitive mantle normalized (McDonough and Sun, 1995) multielements patterns of Tucumã felsic dikes; c and d) Tucumã intermediate dikes; e and f) Tucumã mafic dikes. Symbols as. Tucumã dikes are the symbols red and orange circles for high and low SiO_2 rhyolites; light gray square for dacites; dark gray for andesites; gray cross for basaltic andesites and black x for basalts. The comparisons fields are given by dotted, dashed and solid lines for felsic, intermediate and mafic dikes of Jamon suite; dashed dot line represents the velho Guilherme Suite and the light and dark gray field the Sobreiro and Santa Rosa formations. Symbols as in Fig. 5. (For interpretation of the references to colour in this figure legend, the reader is referred to the web version of this article.)

mainly due to plagioclase and clinopyroxene crystallization and the rhyolites through plagioclase with K-feldspar. This suggests that mafic and felsic dikes may be related to a linear crystallization trend involving plagioclase. However, in the Ba vs. Sr diagram (Fig. 11b) the crystallization vectors exhibit a trend towards clinopyroxene fractionation, with minor contribution of amphibole for the basalts to basaltic andesite, while felsic dikes show a distinct trend, evidencing feldspar and biotite crystallization. This evidence rules out a direct relationship through fractional crystallization for both rock groups.

The K/Ba vs. Ba and Th/Yb vs. SiO_2 diagrams (Fig. 11c–d) show a curvilinear trend in the felsic dikes, which suggests assimilation, or that this variation in rhyolitic magma may be triggered by melting of a heterogeneous crust, also proposed for the Santa Rosa formation (Fernandes et al., 2011). An alternative interpretation was put forth by Sylvester, 1994 and Skjerlie and Johnston, 1993, whereby even though biotite and alkali feldspar are the mineral phases with the highest Kd for Ba in equilibrium with granitic liquid, biotite is the dominant sink for Ba in a restite formed in equilibrium with granite melt, since the alkali feldspar is not stable. Thus, the large variation in Ba content in rhyolites (Fig. 11e) cannot be generated only by fractional crystallization, and may be explained by the biotite content in the restite. In other words, high Ba content in low-Si rhyolite dikes suggests that most of the biotite in their source was consumed at high temperatures. On the other hand, rhyolites with low Ba content (high-Si group) probably have high residual biotite and are associated with low temperatures. This leads to believe that in addition to fractional crystallization the

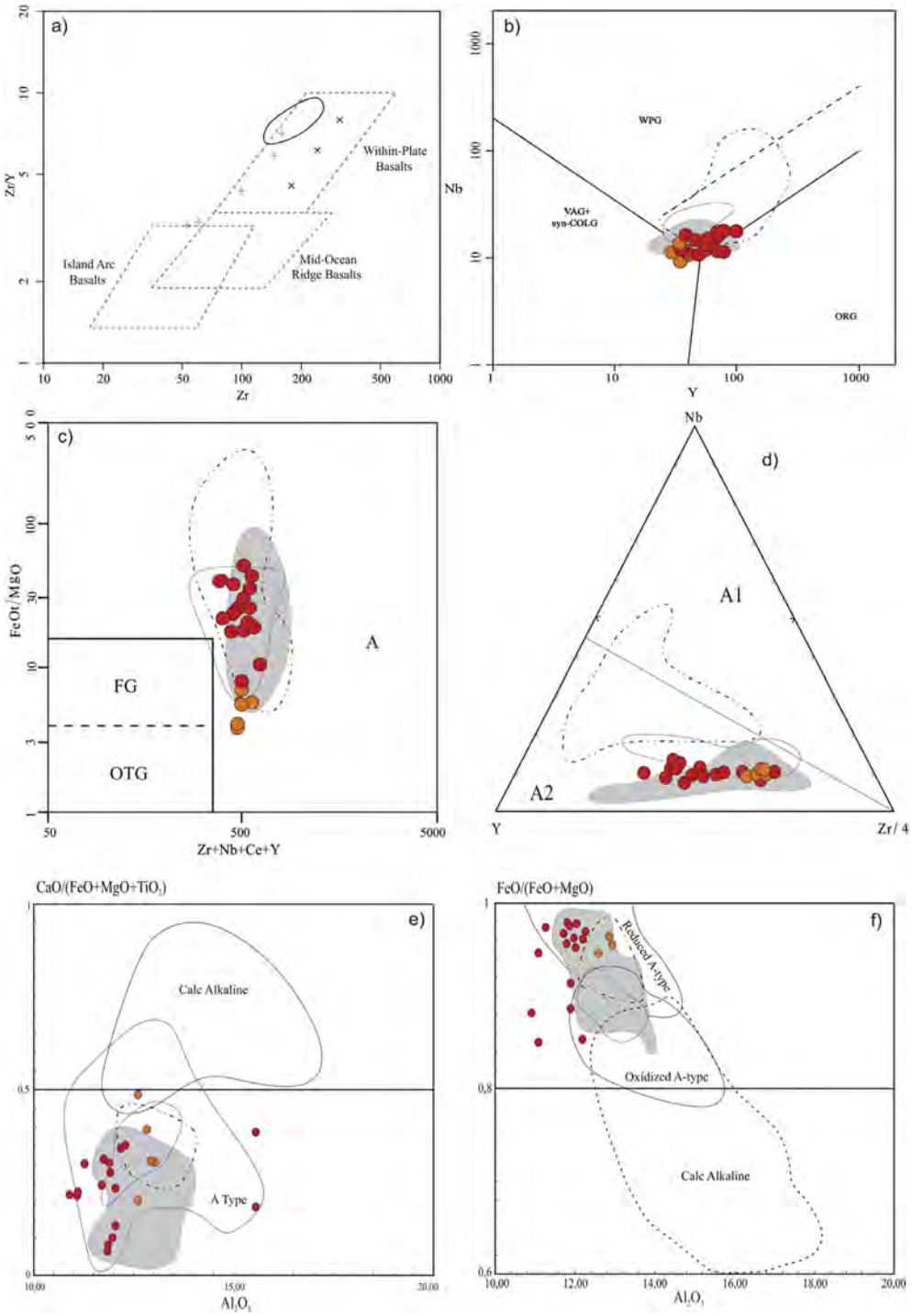

Fig. 9. a) Tectonic classification diagrams of Pearce and Norry (1979) for mafic dikes and b) Pearce et al. (1984) for the felsic dikes. c) Whalen et al. (1987) diagram; d) Eby (1992) diagram. e) Dall'Agnol and Oliveira (2007) diagram to show magmatic series and, f) to evidence their oxidation state. Tucumã dikes are the symbols red and orange circles for high and low SiO2 rhyolites; light gray square for dacites; dark gray for andesites; gray cross for basaltic andesites and black x for basalts. The comparisons fields are given by dotted, dashed and solid lines for felsic, intermediate and mafic dikes of Jamon suite; dashed dot line represents the velho Guilherme Suite and the light and dark gray field the Sobreiro and Santa Rosa formations. Symbols as in Fig. 5. (For interpretation of the references to colour in this figure legend, the reader is referred to the web version of this article.)

felsic dikes may be probably a product of different melting degrees of the continental crust.

8.2. A model for dacite and andesite genesis

In the previous section, we have evaluated if fractional crystallization was the main magmatic process that controlled the evolution of rhyolitic and basaltic rocks; however, dacites and andesites do not fit well in that model. Therefore, to unveil the process that controls the magmatic evolution of intermediate dikes other hypotheses have been tested using geochemical modeling. The hypotheses tested were assimilation and fractional crystallization (AFC), described by De Paolo (1981) in equation (2) and binary mixing, in equation (3).

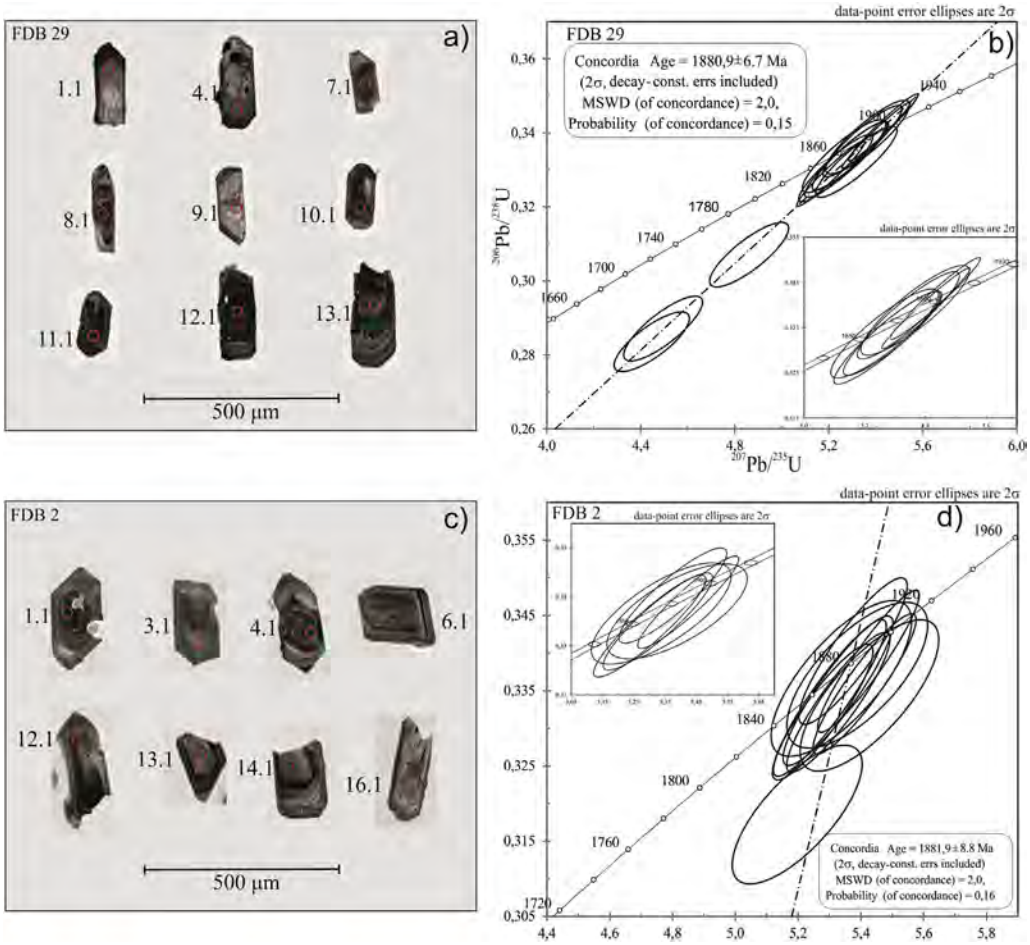

Fig. 10. a, c) Zircon images with a circle representing the laser spot on SHRIMP. The numbers next to the zircon crystals refers to a control number given to each one of them and the second refers to the number of analysis in each zircon crystal; b, d) Concordia diagrams showing U/Pb analyses for zircons crystal from samples of felsic dikes.

Table 4
U-Pb zircon data for felsic dikes of theTucumã region.

Spot name	U (ppm)	Th (ppm)	Th/U	Pb206 (comm) %	$^{206}Pb/^{238}Pb$	err (%) 1	$^{207}Pb/^{235}Pb$	err (%) 1	$^{207}Pb/^{206}Pb$	err (%) 1	$^{207}Pb/^{206}Pb$ age	err (%) 1
FDB-2-1.1	239	229	0.99	0.0562	0.3334	1.1	5.33	1.3	0.1159	0.5	1894	10
FDB-2-3.1	157	101	0.66	−0.0215	0.335	1.2	5.33	1.3	0.1153	0.6	1885	10
FDB-2-4.1	362	308	0.88	0.231	0.3322	1.1	5.28	1.2	0.1153	0.5	1884	10
FDB-2-6.1	238	220	0.95	0.0343	0.3389	1.1	5.42	1.2	0.1161	0.4	1897	8
FDB-2-12.1	192	134	0.72	0.0276	0.334	1.3	5.3	1.4	0.1151	0.5	1881	10
FDB-2-13.1	155	159	1.06	0.2288	0.3371	1.2	5.39	1.7	0.116	1.2	1895	22
FDB-2-14.1	160	149	0.96	0.0481	0.3403	1.2	5.38	1.3	0.1146	0.6	1873	11
FDB-2-16.1	91	66	0.75	0.1642	0.3366	1.3	5.34	1.7	0.115	1.2	1880	21
FDB-29-1.1	133	49	0.38	0.0538	0.3	1.2	5.27	1.4	0.1	0.7	1871	12
FDB-29-4.1	178	65	0.38	0.0402	0.3377	1.2	5.34	1.3	0.1148	0.5	1876	10
FDB-29-7.1	241	130	0.56	0.0628	0.3327	1.3	5.27	1.4	0.115	0.5	1879	9
FDB-29-8.1	283	142	0.52	0.0946	0.3304	1.1	5.23	1.2	0.1148	0.5	1877	9
FDB-29-9.1	135	70	0.54	−0.005	0.3388	1.2	5.37	1.4	0.1149	0.6	1878	12
FDB-29-10.1	661	359	0.56	0.0053	0.3414	1.1	5.43	1.1	0.1154	0.3	1886	5
FDB-29-11.1	625	328	0.54	0.0294	0.329	1.1	5.21	1.1	0.1148	0.3	1877	5
FDB-29-12.1	981	572	0.6	0.008	0.3393	1.1	5.4	1.1	0.1155	0.2	1887	4
FDB-29-13.1	229	92	0.42	0.0795	0.3338	1.1	5.29	1.3	0.115	0.5	1880	9

$$C_{l^c}/C_{l^u} = (r/(r-1+D))\cdot(C_c/C_{l^u}\cdot(1-f))+f \quad (2)$$

where C_l^c and C_l^u is the concentration of trace elements in the contaminated and uncontaminated liquid, respectively, Cc the concentration of trace elements in the contaminant, r the assimilation rate/crystallization rate, D the bulk distribution coefficient for the fractionating assemblage, and f an index described by $f = F^{-(r-1+D)/(r-1)}$; where F = fraction of remaining liquid.

$$X_M = X_A\cdot f + X_B\cdot(1-f) \quad (3)$$

X_A and X_B are the concentration of trace elements in the end members of the mixing, X_M is the concentration of trace elements

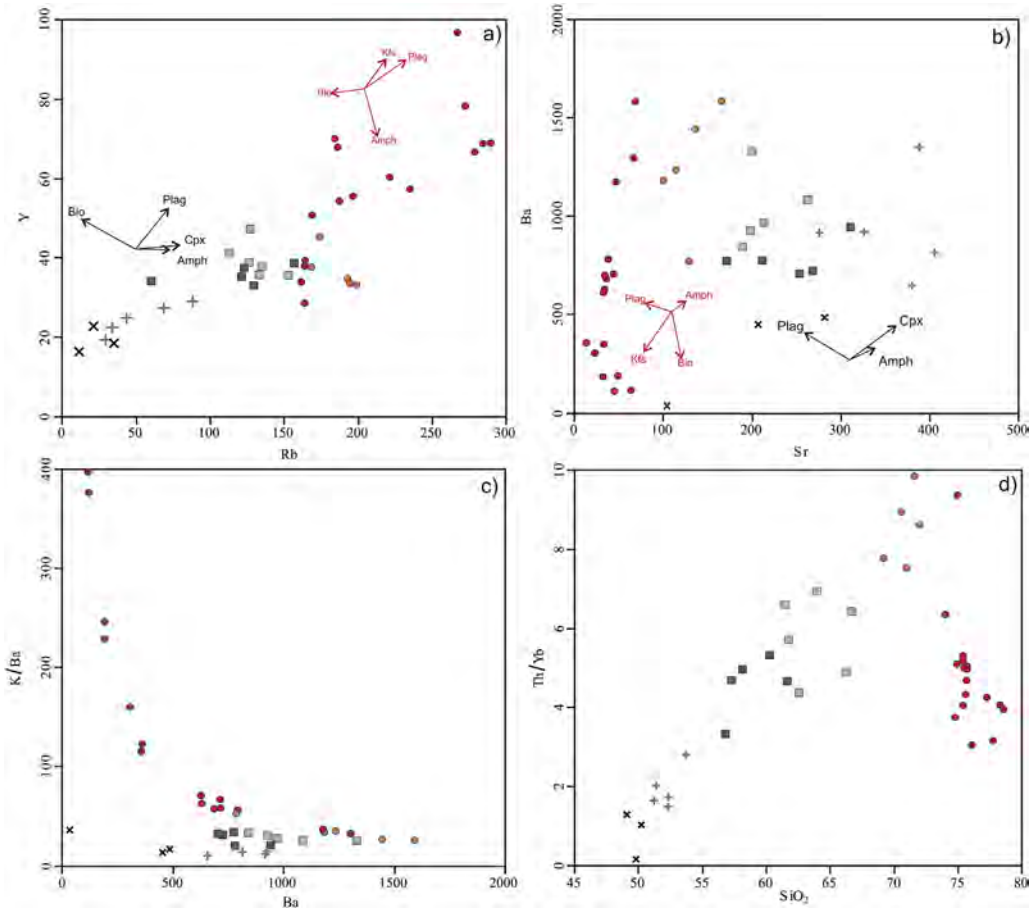

Fig. 11. Variation diagrams with calculated fractionating vectors for felsic and mafic dikes. a) Rb vs. Y; b) Sr vs. Ba; c) K/Ba vs. Ba diagram; d) Th/Yb vs SiO2 diagram. Symbols as in Fig. 5.

in the mixture and f an index described by (A/(A + B)).

Fig. 12a–b shows the curves resulting from the equations presented above. The AFC curve (blue line) was built by taking the basalt, with a fractionating assemblage formed of 20% olivine, 40% plagioclase and 40% clinopyroxene, as the starting point for crystallization and with rhyolite as contaminant. The r index used was 0.4, which is typical of the upper crust, and consistent with dike emplacement levels. The mixing curve (orange line) was built taking basaltic andesite and the rhyolites as end members (X_A) and (X_B), respectively. After these curves were built, the means of basalts, basaltic andesites, andesites, dacites and rhyolites were plotted in the diagram to determine the dominant process involved in the origin of intermediate dikes. Based on this, it is evident to associate the mixing processes with the formation of intermediate rocks, since the Tucumã dikes plot on the mixing curves rather than on AFC trajectories (Fig. 12a–b). The next step was to quantify the degree of mixing of the two components (basaltic andesite and rhyolite) and determine their relative contributions to the mixing process.

A model based on binary mixing to explain the origin of dacite can be seen through normalized REE and multi-element diagrams (Fig. 12c–d). The average composition of basaltic andesite (dark gray line) and rhyolites (red line) are plotted in the diagrams as well as average dacite composition (light gray line); next, by calculating the aforementioned equation it is possible to determine the degree of mixing, denoted by f (orange line). The degree of mixing that most resembles dacite dikes is f = 0.4, which signifies mixing of 60% rhyolite and 40% basaltic andesite, indicating the major contribution of felsic magma in the formation of these rocks. A similar model is used to clarify the generation of andesite dikes (Fig. 12e–f), where f = 0.6 represents mixing of 40% of rhyolite and 60% of basaltic andesite. In this case, the mafic component would theoretically be more important. This is in line with petrographic and geochemical observations, suggesting that andesite liquid represents the product of a more advanced stage of the hybridization process, resulting in more homogeneous and less evolved intermediate rocks.

8.3. Magma formation and tectonic significance

In order to discuss the tectonic significance, Fig. 13 shows a flowchart and schematic model illustrating the processes involved in the generation and emplacement of the Tucumã dikes. The evolutionary history of the dikes consists initially of an extensional tectonic that resulted in decompression, induced mantle melting and basaltic magma generation, which produces a basalt andesite liquid through fractional crystallization. These magmas are trapped while rising to the surface at the Mohorovicic discontinuity or within the crust, supplying sufficient heat for partial melting and the formation of granite magma.

It is known that at ~1.88 Ga the Amazonian Craton underwent a major period of crustal extension (Dall'Agnol et al., 2005; Lamarão et al., 2005; Oliveira et al., 2008, 2010), and in that context, mafic and felsic magmas (basalts and rhyolites) in the Tucumã area ascended to the upper crust through the reactivated deep structure, forming large bimodal dike swarms associated with A-type plutons.

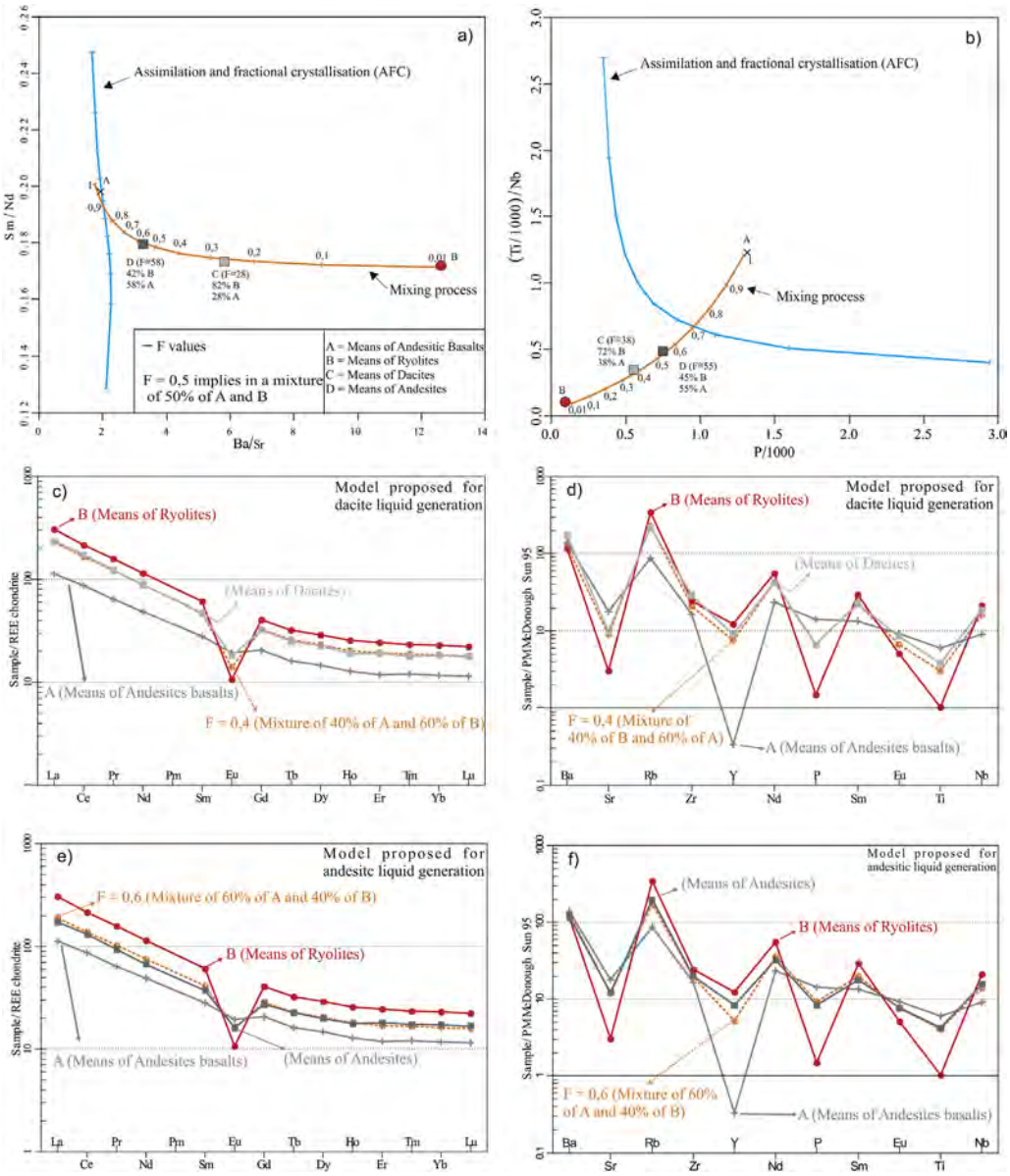

Fig. 12. a) Sm/Nd vs. Ba/Sr, b) ((Ti/100)/Nb)/(P/1000) variation diagrams to determine what process was dominant in intermediate rocks generation, c) e) REE normalized to Boynton (1984) chondrite d) f) multi-element normalized to McDonough & Sun (1995), to evidence a generation model for dacitic and andesitic hybrid rocks.

However, during the ascent of these magmas, mixing processes occurred and changed their original compositions, in order to generate liquids of intermediate compositions. It has been shown that intermediate rocks could be the product of mixing processes, which would more probably occur during transport to the emplacement zone. However, in order to explain how these processes generate a wide range of compositions, Sparks and Marshall (1986) demonstrated that complete hybridization depends on initial magma temperatures and the proportion of mafic magma in the mixture. Thus, andesite dikes are likely generated by a homogenous mixing of mafic and felsic magmas at high depths (Fig. 13), unlike dacites, which are probably produced in the upper crust at a lower temperature, thereby providing a less efficient process (magma mingling).

Similarities of felsic and intermediate dikes with Santa Rosa and Sobreiro formations is remarkable, suggesting a possible manifestation of this wide volcanism in the Rio Maria domain. However, it is also noticeable that the intermediate dikes have some features that distinguish them from the units described in the São Felix do Xingu. The Sr content of these rocks is clearly lower than that of the Sobreiro Formation rocks, stressing an important difference regarding the tectonic settings of these rocks, once the high Al and Sr contents in the Sobreiro Formation led Fernandes et al. (2011) to believe that these rocks were formed into an arc-related setting from the mixing of mantle-derived and anatectic melts of Archean rocks beneath the volcanic sequences in a flat-slab subduction setting. Alternatively, this can be interpreted as bimodal within-plate magmatism with contamination by crustal melts and could be explained by the presence of a thin crust, which favored the presence and continuity of convective systems in the upper mantle.

In the model adopted in this paper, the formation of the 1.88 Ga fissure-controlled A-type magmatism of the Tucumã area could be related to a Paleoproterozoic extensional episode represented by dike swarms, bimodal volcanism, and volcano-plutonic magmatic

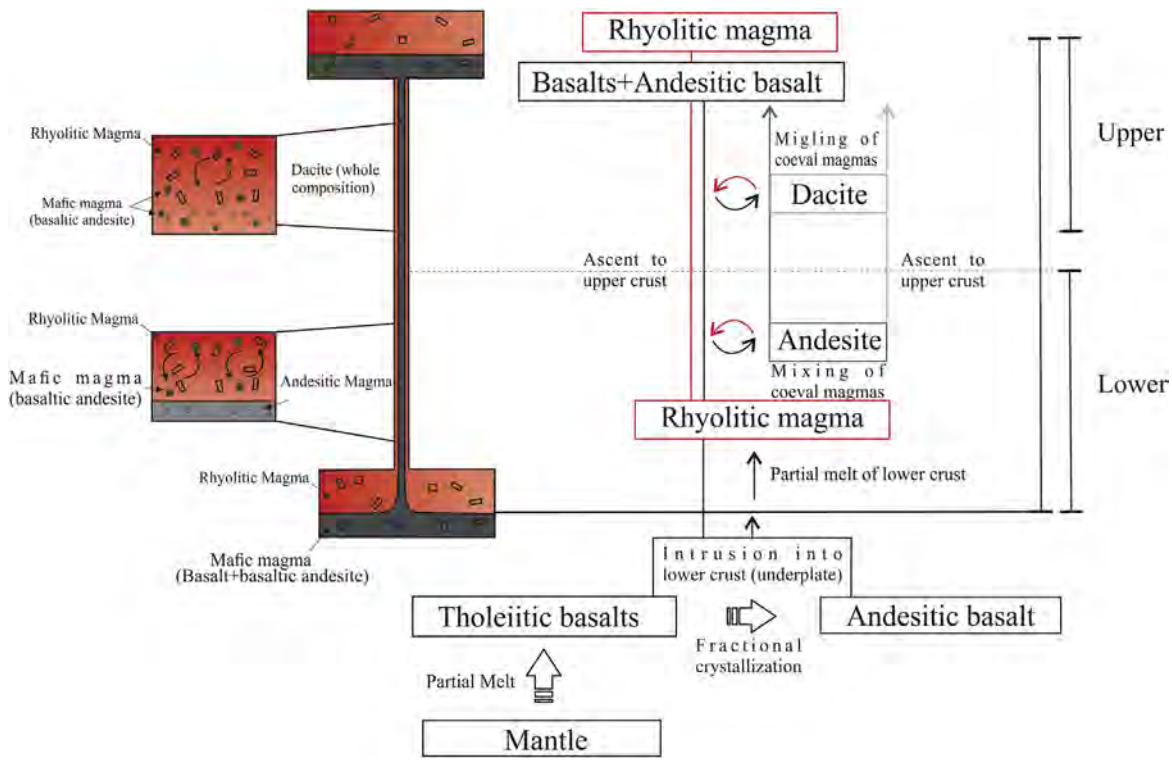

Fig. 13. Flowchart and schematic model for the genesis of mafic and felsic magmas and their emplacement in continental crust in addition to the processes involved in hybridization and subsequent generation of intermediate rocks.

associations in the central and southeastern parts of the Amazonian Craton (Dall'Agnol et al., 2005, Ferron et al., 2010; Fernandes et al., 2011; Marques et al., 2014). In the Carajás province, the Paleoproterozoic magmatism was emplaced ~1.0 to ~0.65 Ga after stabilization of the Archean crust, with its origin related to the disruption of a great continental mass that was the result of the accretion related to the Transamazonian event (Dall'Agnol et al., 2005), not to subduction processes.

9. Summary and conclusions

The Geological mapping of the Tucumã region led to the identification of several dikes aligned in a NW-SE trend and intruded into an older Archean basement. The dikes reach lengths of up to 60 km and three groups were distinguished: felsic (rhyolites), intermediate (andesites and dacites) and mafic (basalt and andesitic basalt). The dacites and andesites are subordinated and occur in association with the felsic dikes. They show evidence of hybridization (quartz phenocrysts mantled by amphibole; mafic microgranular enclaves and alkali feldspar and quartz xenocrysts within a mafic host), suggesting mingling between felsic and mafic magmas. U-Pb zircon ages of 1.88 Ga were obtained for the felsic dikes and are interpreted as crystallization and emplacement age of the different dikes identified in the Tucumã area.

Felsic dikes are essentially peraluminous and have affinity with A-type reduced granites. Intermediate dikes are metaluminous, classified as hybrid rocks with dacitic and andesitic composition. Lastly, mafic dikes are strongly metaluminous and are classified as within-plate tholeiitic basalts.

Geochemical data suggest that rhyolite and basalt magmas are not comagmatic. The basalt liquid evolved due to plagioclase and clinopyroxene crystallization to originate the andesite basalt. On the other hand, even though felsic liquids evolved by fractional crystallization, they show trends in some diagrams (K/Ba vs Ba), suggesting that low-Si and high-Si rhyolites were generated by partial melting at different temperatures during the ascent within the continental crust.

Geochemical modeling demonstrated the viability of mixing between mafic and felsic magmas in generating rocks similar to those of dacitic and andesitic composition described in other areas of Carajás Province. Andesites could be the product of the mixture of 60% mafic magma and 40% rhyolite liquids. This process occurred at deeper crustal levels, resulting in a more homogeneous mixture (magma mixing). Dacites were generated at shallower crustal levels at lower temperatures, where the mixing process was less efficient (magma mingling) and the felsic liquid would have had a more significant contribution (60%).

The compositional differences between the mafic and felsic magmas clearly show that these magmas evolved independently, ruling out their origin from a single liquid. Data presented in this study point to the existence of bimodal magmatism in the Tucumã area, similar to that identified in the Rio Maria region, where a number of studies suggest that the genesis of this magmatism is related to the same tectonic-magmatic event that gave rise to the A-type granites of the Jamon suite (Ramö et al., 2002; Oliveira et al., 2008).

The similar petrography, geochemistry, and geochronological age of the felsic dikes under study and of A-type granites of the Jamon and Velho Guilherme suites suggest that the Paleoproterozoic magmatism of the Tucumã area has also been formed by processes involving thermal perturbations in the upper mantle, mafic underplating, and associated crustal extension or transtension. This is consistent with the broad thermal anomaly associated with the A-type granites of the southwestern United States (Anderson and Cullers, 1999; Frost et al., 1999) and southern Finland (Rämö and Haapala, 1995).

The occurrence of diabase and granite porphyry dike swarms, orientated WNW–ESE to NNW–SSE and coeval with the A-type plutons, demonstrates that tectonic extensional stress was oriented approximately NNE–SSW to ENE–WSW. In this case, the brittle continental crust breakup is also demonstrated by the tabular geometry inferred for A-type plutons of the Jamon suite, and the high viscosity contrast between the granites and their Archean country rocks (Oliveira et al., 2008, 2010). This indicates that dikes were the main mechanism responsible for magma transport and emplacement into the crust. The 1.88 Ga fissure-controlled A-type magmatism of the Tucumã area was emplaced ~1.0 to ~0.65 Ga after stabilization of the Archean crust, with its origin related to the disruption of a large landmass during the Paleoproterozoic, not to subduction processes.

Acknowledgements

The Research Group on Granitoids Petrology (RGGP), for their support in the various stages of this work, the Institute of Geosciences (IG), the Post-Graduate Program in Geology and Geochemistry (PPGG) and the Faculty of Geology, Campus of Marabá, for the support of field activities. This research received financial support from CNPq (D. C. Oliveira – Grants – Proc. 485806/2013-4 and 311610/2012-9; F.F Silva – scholarship — Proc. 133931/2013-7,); FAPESP (P.Y.J. Antonio and M.S. D'Agrella-Filho, grant 2011/50887-6); Vale/FAPESPA (01/2010) ICAAF 053/2011; and Brazilian Institute of Amazonia Geosciences (GEOCIAM – CNPq/MCT/FAPESPA – Grant no 573733/2008-2).

References

Almeida, F.F.M., Hasui, Y., Brito Neves, B.B., Fuck, R.A., 1981. Brazilian structural provinces: an introduction. Earth-Science Rev. 17, 1e29.
Almeida, J.A.C., Dall'Agnol, R., Oliveira, M.A., Macambira, M.J.B., Pimentel, M.M., Rämö, O.T., Guimarães, F.V., Leite, A.A.S., 2011. Zircon geochronology and geochemistry of the TTG suites of the Rio Maria granite-greenstone terrane: implications for the growth of the Archean crust of Carajás Province, Brazil. Precambrian Res. 187, 201–221.
Anderson, J.L., Cullers, R.L., 1999. Paleo- and Mesoproterozoic granite plutonism of Colorado and Wyoming. Rocky Mt. Geol. 34, 149–164.
Araujo, O.J.B., Maia, R.G.N., 1991. Programa de levantamentos geológicos básicos do Brasil, Serra dos Carajás, folha SB-22-Z-A, Estado do Pará. Texto explicativo. DNPM/CPRM, Brasília, p. 164 (in Portuguese).
Barbosa, A.A., Lafon, J.M., Neves, A.P., Vale, A.G., 1995. Geocronologia Rb-Sr e Pb-Pb do Granito Redenção, SE do Pará: Implicações para a evolução do magmatismo Proterozoico da região de Redenção. Boletim do Museu Paraense Emílio Goeldi. Série Ciências Terra 7, 147–164.
Belousova, E.A., Reid, A.J., Griffin, W.L., O'Reilly, S.Y., 2009. Rejuvenation vs. recycling of archean crust in the Gawler craton, south Australia. Evidence from U–Pb and Hf isotopes in detrital zircon. Lithos 113, 570–582.
Black, L.P., Kamo, S.L., Allen, C.M., Aleinikoff, J.N., Davis, D.W., Korsch, R.J., Foudoulis, C., 2003. TEMORA 1: a new zircon standard for Phanerozoic U–Pb geochronology. Chem. Geol. 200, 155–170.
Boynton, W.V., 1984. Cosmochemistry of the rare earth elements; meteorite studies. In: Henderson, P. (Ed.), Rare Earth Element Geochemistry. Elsevier Sci. Publ. Co., Amsterdam, pp. 63–114.
Dall'Agnol, R., Oliveira, D.C., 2007. Oxidized, magnetite-series, rapakivi-type granites of Carajás, Brazil: implications for classification and petrogenesis of A-type granites. Lithos 93, 215–233.
Dall'Agnol, R., Rämö, O.T., Magalhães, M.S., Macambira, M.J.B., 1999. Petrology of the anorogenic, oxidised Jamon and Musa granites, Amazonian craton: implications for the genesis of Proterozoic Atype granites. Lithos 46, 431–462.
Dall'Agnol, R., Teixeira, N.P., Rämö, O.T., Moura, C.A.V., Macambira, M.J.B., Oliveira, D.C., 2005. Petrogenesis of the paleoproterozoic, rapakivi, a-type granites of the Archean Carajás metallogenic province, Brazil. Lithos 80, 01–129.
De La Roche, H., Leterrier, J., Grand Claude, P., Marchal, M., 1980. A classification of volcanic and plutonic rocks using R1R2-diagram and major-element analyses — its relationships with currrent nomenclature. Chem. Geol. 29, 183–210.
De Paolo, D.J., 1981. Trace element and isotopic effects of combined wall-rock assimilation and fractional crystallization. Earth Planet. Sci. Lett. 53, 189–202. http://dx.doi.org/10.1016/0012-821X(81)90153-9.
Eby, G.N., 1992. Chemical subdivision of the A-type granitoids: petrogenetic and tectonic implications. Geology 20, 641–644.
Fernandes, C.M.D., Juliani, C., Monteiro, L.V.S., Lagler, B., Misas, C.M.E., 2011. High-K calc-alkaline to A-type fissure-controlled volcano-plutonism of the São Félix do Xingu region, Amazonian craton, Brazil: exclusively crustal sources or only mixed Nd model ages? J. S. Am. Earth Sci. 32, 351–368.
Fernandes, C.M.D., Lamarão, C.N., Teixeira, N.P., 2006. O vulcanismo bimodal do tipo Uatumã da região de São Felix do Xingu (PA), Província Mineral de Carajás. Rev. Bras. Geociências 36, 565–576.
Ferreira, A.T.R., 2009. Petrografia, geoquímica e geocronologia dos diques da área de Bannach, Terreno Granito-Greenstone de Rio Maria, SE do Pará. Universidade Federal do Pará, Instituto de Geociências, 55f. Trabalho de Conclusão de Curso (graduação).
Ferron, J.M.T.M., Bastos Neto, A.C., Lima, E.F., Nardi, L.V.S., Costi, H.T., Pierosan, R., Prado, M., 2010. Petrology, geochemistry, and geochronology of Paleoproterozoic volcanic and granitic rocks (1.89-1.88 Ga) of the Pitinga Province, Amazonian Craton, Brazil. J. S. Am. Earth Sci. 29, 483–497.
Frost, B.R., Barnes, C., Collins, W., Arculus, R., Ellis, D., Frost, C., 2001. A chemical classification for granitic rocks. J. Petrology 42, 2033–2048.
Frost, C.D., Frost, B.R., Chamberlain, K.R., Edwards, B., 1999. Petrogenesis of the 1.43 Ga Sherman batholith, SE Wyoming, USA: a reduced, rapakivi-type anorogenic granite. J. Petrology 40, 1771–1802.
Gastal, M.C.P., 1987. Mapeamento e Petrologia do Maciço Granítico Musa: Rio Maria, Sudeste do Pará. Belém. UFPA-Centro de Geociências, p. 319. Tese de Mestrado.
Halls, H.C., Hamilton, M.A., Denyszyn, S.W., 2011. The Melville Bugt dyke swarm of Greenland: a connection to the 1.5-1.6 Ga Fennoscandian Rapakivi granite province? In Dyke Swarms: Keys for Geodynamic Interpretation. In: Srivastava, R.K. (Ed.), Proceedings of the 6th International Dyke Symposium, Varanasi, India, February 4 to 7, 2010. Springer-Verlag, Berlin, pp. 509–535, 605 p., (Chapter 27).
Hanson, G.N., 1978. The application of trace elements in the petrogenesis of igneous rocks of granitic composition. Earth Planet. Sci. Lett. 38, 26–43.
Hibbard, M.J., 1995. Petrography to Petrogenesis. Prentice Hall, Englewood Cliffs, New Jersey, p. 587.
Hoskin, P.W.O., Black, L.P., 2000. Metamorphic zircon formation by solid state recrystallization of protolith igneous zircon. J. Metamorph. Geol. 18, 423–439.
Irvine, T.N., Baragar, W.R.A., 1971. A guide to the chemical classification of the common volcanic rocks. Can. J. Earth Sci. 8, 523–547.
Jensen, L.S., 1976. A new cation plot for classifying subalkalic volcanic rocks. Ont. Div. Mines, Misc. Pap. 66, 21.
Kumar, A., Hamilton, M.A., Halls, H.C., 2012. A paleoproterozoic giant radiating dyke swarm in the Dharwar Craton, southern India. Geochem. Geophys. Geosyst, 1029/2011GC003926.
Lamarão, C.N., Dall'Agnol, R., Pimentel, M.M., 2005. Nd isotopic composition of Paleoproterozoic volcanic and granitoid rocks of Vila Riozinho: implications of the crustal evolution of the Tapajós gold province, Amazon craton. J. S. Am. Earth Sci. 18, 277–292.
Lima, P.H.A., 2011. Geologia, Petrografia e Geocronologia do Granito São João, Província Carajás, SSE do Pará. Trabalho de Conclusão de Curso – Graduação em Geologia. Instituto de Geociências, Universidade Federal do Pará, p. 64.
Ludwig, K.R., 2003. Using Isoplot/Ex, Version 3.00, a Geochronological Toolkit for Microsoft Excel. Berkeley Geochronology Center Special Publication, p. 43 no. 1.
Ludwig, K.R., 2009. Isoplot v.4 for Excel 2007. Berkeley Geochronology Center, Berkeley, Calif, p. 71.
Macambira, E.M.B., Vale, A.G., 1997. Programa Levantamentos Geológicos Básicos Do Brasil. São Felix Do Xingu. Folha SB.22-Y-B. Estado Do Pará. DNPM/CPRM, Brasília, p. 384p.
Macambira, M.J.B., 1992. Chronologie U/Pb, Rb/Sr, K/Ar et croissance de la croûte continentale dans L'Amazonie du sud-est; exemple de la région de Rio Maria, Province de Carajas, Brésil. Tese de Doutoramento. Université Montpellier II-France, Montpellier, p. 212.
Machado, N., Lindenmayer, Z., Krogh, T.H., Lindenmayer, D., 1991. U-Pb geochronology of Archaean magmatism and basement reactivation in the Carajás area, Amazon shield. Braz. Precambrian Res. 49, 329–354.
Marques, S.N.S., Souza, V.S., Dantas, E.L., Valério, C.S., Nascimento, R.S.C., 2014. Contributions to the petrography, geochemistry and geochronology (U-Pb and Sm-Nd) of the Paleoproterozoic effusive rocks from Iricoumé Group, Amazonian Craton, Brazil. Braz. J. Geol. ISSN: 2317-4889 44, 121–138 n.1.
Martin, H., Peucat, J.J., Sabaté, J.C., Cunha, J.C., 1997. Crustal evolution in the Archaean of South America: example of the Sete Voltas Massif, Bahia State. Braz. Precam. Res. 82, 35–62.
McDonough, W.F., Sun, S.-S., 1995. Composition of the Earth. Chem. Geol. 120, 223–253. http://dx.doi.org/10.1016/0009-2541(94)00140-4.
Moura, C.A.V., Gaudette, H.E., 1993. Evidence of Brasiliano/Panafrican deformation in the Araguaia Belt: Implicalion for Gondwana evolulion. Revista Brasileira de Geociências 23 (2), 117–123.
Oliveira, D.C., 2006. Modelos de Evolução e Colocação dos Granitos Paleoproterozoicos da Suíte Jamon, SE do Cráton Amazônico. Universidade Federal do Pará, Instituto de Geociências, Belém, p. 186. Tese de Doutorado.
Oliveira, D.C., Dall'Agnol, R., Silva, J.B.C., Almeida, J.A.C., 2008. Gravimetric, radiometric, and magnetic susceptibility study of the Paleoproterozoic Redenção and Bannach plutons: implications for architecture and zoning of A-type granites. J. S. Am. Earth Sci. 25, 100–115.
Oliveira, D.C., Gabriel, E.O., Santos, P.J.L., Sival, C.R.P., Rodrigues, D.S., Santos, R.D., Galarza, M.A., Marangoanha, B., Santos, M.S., Souza, D.B., 2014. Geologia da região de Água Azul do Norte (PA) – Implicações para a compartimentação tectônica do Domínio Carajás. In: SBG, Congresso Brasileiro de Geologia. CDrom, Anais, Salvador, 47.

Oliveira, D.C., Neves, S.P., Trindade, R.I.F., Dall'Agnol, R., Gorki, M., Paulo, B.C., 2010. Magnetic anisotropy of the Redenção granite, eastern Amazonian craton (Brazil): Implications for the emplacement of A-type. Tectonophysics 493, 27–41.

Paiva Júnior, A.L., 2009. Geologia, petrografia, geocronologia e geoquímica do Granito anorogênico Seringa, Província Mineral de Carajás, SSE do Pará. Universidade Federal do Pará. Instituto de geociências, p. 120 (Dissertação de Mestrado).

Pearce, J.A., Harris, N.B.W., Tindle, A.G., 1984. Trace element discrimination diagrams for the tectonic interpretation of granitic rocks. J. Petrology 25, 956–983.

Pearce, J.A., Norry, M.J., 1979. Petrogenetic implications of Ti, Zr, Y and Nb variations in volcanic rocks. Contrib. Mineral. Pet. 69, 33–47.

Rämö, O.T., 1991. Petrogenesis of the proterozoic rapakivi granites and related basic rocks of southeastern Fennoscandia: Nd and Pb isotopic and general geochemical constraints. Geol. Surv. Finl. Bull. 355.

Ramö, O.T., Dall'Agnol, R., Macambira, M.J.B., Leite, A.A.S., Oliveira, D.C., 2002. 1.88 Ga oxidized A-type granites of the Rio Maria region, eastern Amazonian Craton, Brazil: positively anorogenic. J. Geol. 110, 603–610.

Rämö, O.T., Haapala, I., 1995. One hundred years of rapakivi granite. Mineral. Pet. 52, 129–185.

Rivalenti, G., Mazzuchelli, M., Girardi, V.A.V., Cavazzini, G., Finatti, C., Barbieri, M.A., Teixeira, W., 1998. Petrogenesis of the Paleoproterozoic basaltic-andesite-rhyolite dyke association in the Carajás region, Amazonian craton. Lithos 43, 235–265.

Rodrigues, E.S., Lafon, J.M., Scheller, T., 1992. Geocronologia Pb-Pb da Província Mineral de Carajás: primeiros resultados. In: Congresso Brasileiro de Geologia, 37, Boletim de Resumos Expandidos, São Paulo, vol. 2, pp. 183–184.

Santos, J.O.S., 2003. Geotectônica dos Escudos das Guianas e Brasil-Central. In: Bizzi, L.A., Schobbenhaus, C., Vidotti e, R.M., Gonçalves, J.H. (Eds.), Geologia, Tectônica e Recursos Minerais do Brasil. CPRM, Brasília, pp. 169–195 (In portuguese).

Santos, J.O.S., Hartmann, L.A., Gaudette, H.E., Groves, D.I., Mcnaughton, N.J., Fletcher, I.R., 2000. A New Understanding of the Provinces of the Amazon Craton Based on Integration of Field Mapping and U-Pb and Sm-Nd Geochronology. Gondwana Res. 3 (4), 453–488.

Sato, K., Basei, M.A.S., Siga, O.J., 2008. Novas técnicas aplicadas ao método U-Pb no CPGeo -IGc/USP: avanços na digestão química, espectrometria de massa (TIMS) e exemplos de aplicação integrada com SHRIMP [New techniques applied to U-Pb method at CPGeo – Igc/USP: advances in chemical digestion, mass spectrometry (TIMS) and examples of application integrated with SHRIMP]. Geol. USP Série Científica 8, 77–99.

Shand, S.J., 1950. Eruptive Rocks Their Genesis, Composition, Classification and Their Relation to Ore Deposit, 4ed, p. 488. London.

Silva Jr., R.O., Dall'Agnol, R., Oliveira, E.P., 1999. Geologia, petrografia e geoquímica dos diques proterozoicos da região de Rio Maria, sudeste do Pará. Geochim. Bras. 13 (2), 163–181.

Skjerlie, K.P., Johnston, D.A., 1993. Fluid-absent melting behaviour of an F-rich tonalitic gneiss at mid-crustal pressures: implications for the generation of anorogenic granites. J. Pet. 34 (4), 785–815.

Smith, J.V., 1974. Feldspar Minerals. Springer-Verlag, New York, p. 690.

Sparks, R.S.J., Marshall, L.A., September 1986. 1986. Thermal and mechanical constraints on mixing between mafic and silicic magmas. J. Volcanol. Geotherm. Res. ISSN: 0377-0273 29 (1–4), 99–124. http://dx.doi.org/10.1016/0377-0273(86)90041-7.

Stern, R.A., 1998. High resolution SIMS determination of radiogenic trace isotope ratios in minerals. In: Cabri, L.J., Vaughan, D.J. (Eds.), Modern Approaches to Ore and Environmental Mineralogy. Mineralogical Association of Canada, vol. 27, pp. 241–268. Short Course Series.

Sylvester, P.J., 1994. Archaean granite plutons. In: Condie, K.C. (Ed.), The Archaean Crustal Evolution. Elsevier, pp. 261–314.

Tassinari, C.C.G., Macambira, M., 2004. A evolução tectônica do Craton Amazônico. In: Mantesso Neto, V., Bartorelli, A., Carneiro, C.D.R., Brito Neves, B.B. (Eds.), Geologia do Continente Sul Americano: Evolução da obra de Fernando Flávio Marques Almeida. São Paulo, pp. 471–486.

Thorpe, R.S., Brown, G.C., 1999. The Field Description of Igneous Rocks. John Wiley & Sons, p. 154.

Teixeira, N.P., 1999. Contribuição ao estudo das rochas granitoides e mineralizações associadas da Suíte Intrusiva Velho Guilherme, Província Estanífera do Sul do Pará. Instituto de Geociências, Universidade de São Paulo, São Paulo, Tese de Doutoramento, p. 508p.

Teixeira, N.P., Bettencourt, J.S., Dall'Agol, R., Moura, C.A.V., Fernandes, C.M.D., Pinho, S.C.C.P., 2005. Geoquímica dos granitos paleoproterozoicos da Suíte granítica Velho Guilherme, Província Estanífera do Sul do Pará. Rev. Bras. Geociências 35 (2), 217–226.

Teixeira, N.P., Bettencourt, J.S., Moura, C.A.V., Dall'Agnol, R., Macambira, E.M.B., 2002a. Archen crustal sources for paleoproterozoic tin-granites in the Carajás Province, SSE Pará, Brazil: Pb-Pb geochronology and Nd isotope geochemistry. Prec. Res. 119 (1–4), 2257–2275.

Vasquez, L.V., Rosa-Costa, L.R., Silva, C.G., Ricci, P.F., Barbosa, J.O., Klein, E.L., Lopes, E.S., Macambira, E.B., Chaves, C.L., Carvalho, J.M., Oliveira, J.G., Anjos, G.C., Silva, H.R., 2008. Geologia e Recursos Minerais do Estado do Pará: Sistema de Informações Geográficas – SIG: texto explicativo dos mapas Geológico e Tectônico e de Recursos Minerais do Estado do Pará. Organizadores, Vasquez M.L., Rosa-Costa L.T. Escala, 1:1.000.000. CPRM, Belém:

Wedepohl, K.H., 1970. Rubidium, Handbook of Geochemistry. Springer-Verlag, Berlin, 37B-37N.

Whalen, J.B., Currie, K.L., Chappell, B.W., 1987. A-types granites: geochemical characteristics, discrimination and petrogenesis. Contributions Mineralogy Petrology 95, 407–419.

Wirth, K.R., Gibbs, A.K., Olszewski Jr., W.J., 1986. U-Pb zircon ages of the Grão Pará group and Serra dos Carajás granite, Para, Brazil. Rev. Bras. Geociências 16 (2), 195–200.

Chapter. 6: AMS and paleomagnetic data for the Tucumã dike swarms

Petrography, geochemistry and magnetic mineralogy were described in chapter 5. In this chapter complementary AMS and paleomagnetic results obtained for the Tucumã dike swarm are presented.

6.1 Magnetic Mineralogy

In the previous chapter, the magnetic mineralogy study of felsic dikes indicates that magnetization is carried by PSD magnetite and hematite. PSD magnetite is formed during the magmatic stage, so it is primary. Hematite is formed by hydrothermal alteration of the microgranite during a syn-to late emplacement. Therefore, magnetite and hematite would acquire the same primary paleomagnetic direction. Magnetic mineralogy for the NW-basaltic dikes shows that magnetization is carried by PSD magnetite (Figure 6.1). The NS-gabbroic dike has also PSD magnetite as we can see in the Day's plot. The Rio Maria granodiorite is the main rock that constitutes the Archean basement in the Tucumã region (Santos and Oliveira, 2016). This Archean unit is dated at *ca*. 2872 Ma (De Avelar et al., 1999). Magnetic mineralogy for the Archean Rio Maria granodiorite shows large magnetite grains associated with recrystallization (Santos and Oliveira, 2016). According to the Day's plot, samples of granodiorite are mainly multi-domain grains (MD), but a small proportion of single-domain (SD) magnetite grains are also suggested.

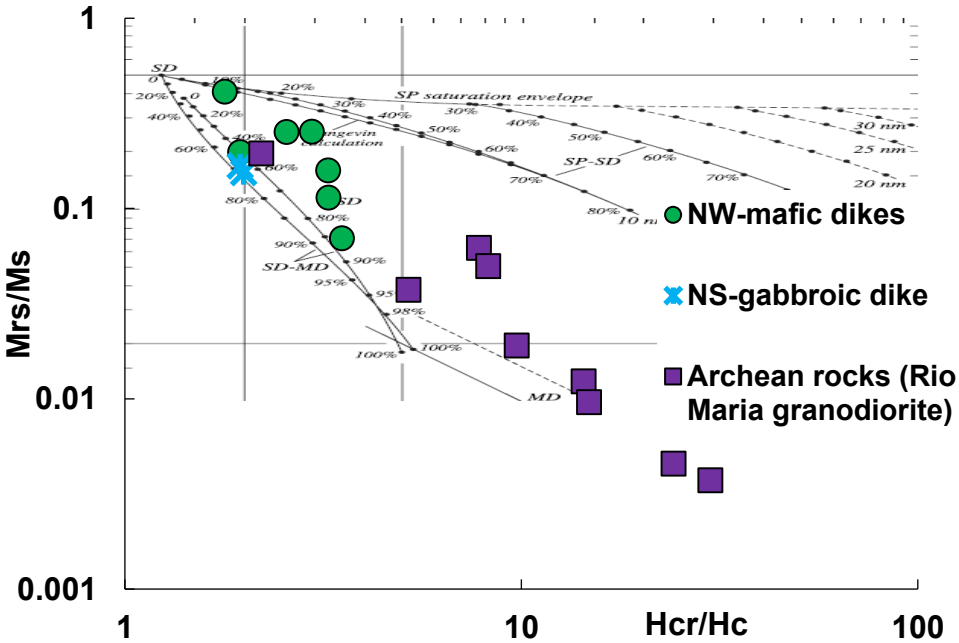

Figure 6.1: Day's plot for NW-mafic dikes, gabbroic dikes and the Rio Maria granodiorite.

6.2 Anisotropy of magnetic susceptibility (AMS)

AMS technique was used to test whether or not the sampled dikes were *in situ* when sampled as many isolated blocks. The Tucumã dike swarms are preferentially NW-oriented (Figure 6.3). They are now well-dated at *ca*. 1880 Ma (da Silva et al., 2016), slightly older (within errors both ages overlap) than the close Velho Guilherme granite dated at *ca*. 1873 ± 13 Ma (Rodrigues, 1992). Field observations show that the NW-microgranitic dikes and associated NW-mafic dikes were intruded by a younger NS-gabbroic dike.

AMS was measured in the laboratory of IAG-USP (São Paulo, Brazil) on each specimen before paleomagnetic investigation. AMS data for Tucumã dikes are presented in Table 6.1. Most felsic samples have a mean magnetic susceptibility (Km) between 200 and 500 µSI. Figure 6.2 shows the anisotropy degree (P) versus mean susceptibility for microgranitic dikes (in red), mafic dikes (in green) and gabbroic dikes (in blue). Most microgranite samples have mean susceptilities lower than 1000 µSI, although values up to 10000 µSI are observed for some samples but in few sites (related to remagnetization). NW-mafic dike have high susceptibilities, between 1000 and 50000 µSI, which is expected for basaltic rocks. For the NS-gabbroic dike, the range of value is concentrated around 15000 µSI. For the Rio Maria granodiorite, we don't have consistency between the three sites with values between 3000 and 30000 µSI (Table 6.1).

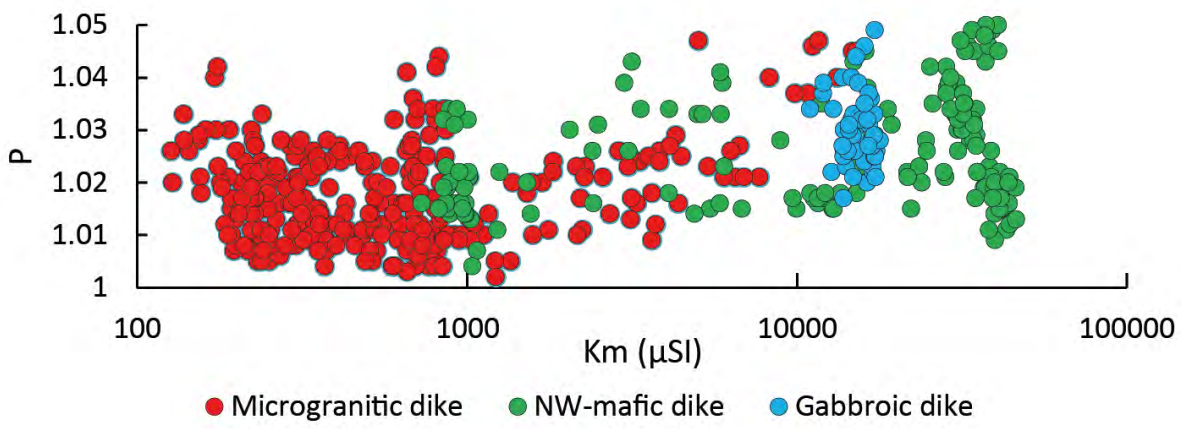

Figure 6.2: P (anisotropy degree) versus. Km (mean magnetic susceptibility).

The anisotropy degree, P is < 1.05 for the microgranite dikes, which indicates a low anisotropy. We also observe low anisotropy degrees (< 1.05) for the NW-mafic and the NS-gabbroic dikes. For the Rio Maria granodiorite higher values are observed (1.15 – 1.27).

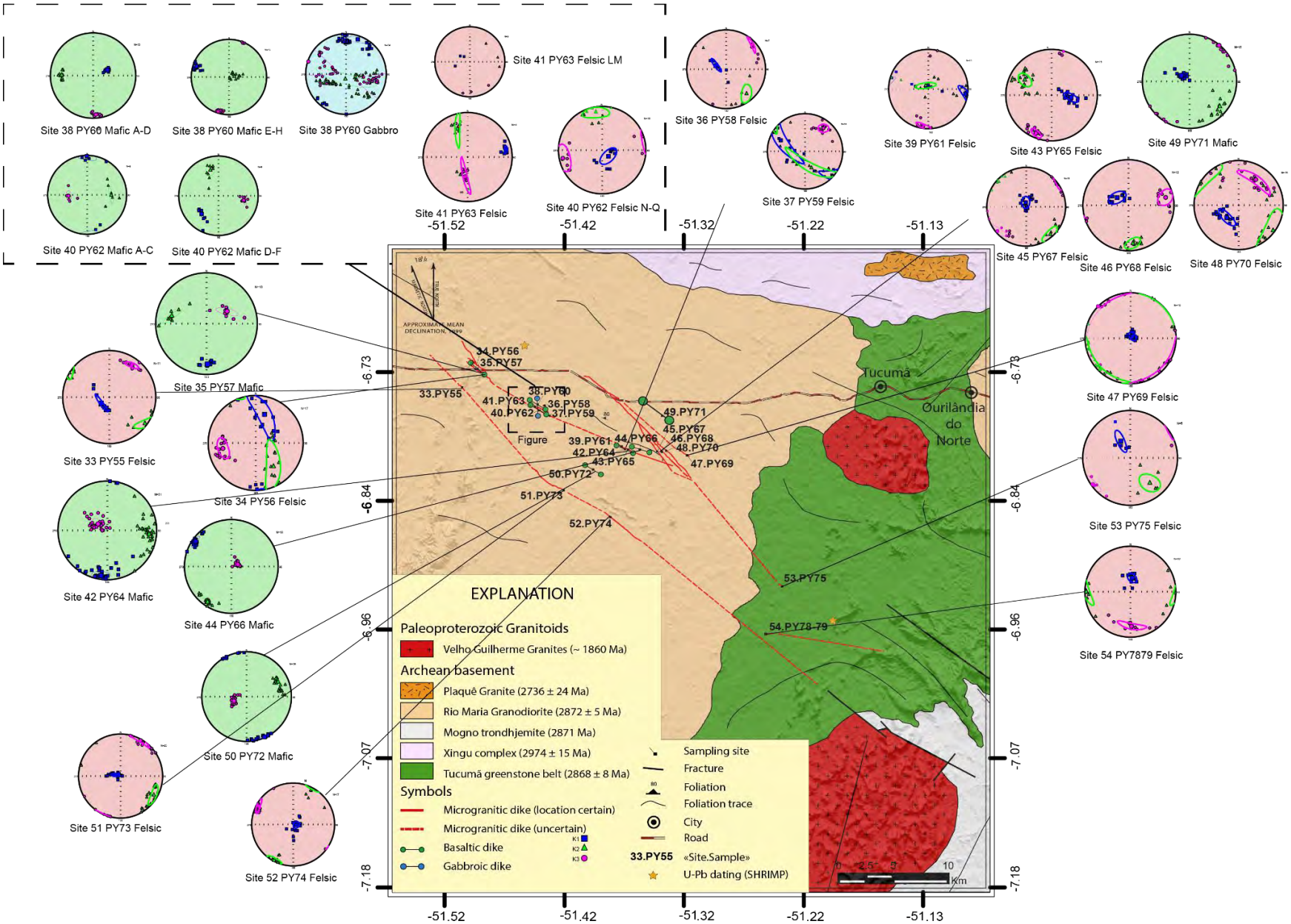

Figure 6.3: AMS fabric types for the dikes of Tucumã.

The Jelinek parameter (T) indicates the shape of the ellipsoid: oblate shape (T > 0) or prolate shape (T < 0). Most microgranitic dikes have an oblate shape but 5 sites have a prolate shape. The oblate shape is dominant also for the NW-mafic dikes in contrary to the NS-gabbroic dike that shows clearly a prolate ellipsoid shape. No clear relation between sites could be observed concerning the T parameter because most of fabrics are triaxial.

We can study the orientation of the ellipsoid (defined by K1-K2-K3) to attempt to determine flow directions of dikes (Ernst and Baragar, 1992; Knight and Walker, 1988; Raposo and D'Agrella-Filho, 2000; Tauxe et al., 1998). Particles normally tend to parallel with magma flux producing maximum susceptibility along magma flux direction. So, K1 axis can be considered as a flow indicator in dike's emplacement. AMS fabric can also reflect the magnetic interaction between particles (Cañón-Tapia et al., 1996; Cañón-Tapia, 2004).

Figure 6.3 presents the AMS fabrics for the Tucumã dike swarms. AMS fabrics have the eigenvectors (K1-K2-K3) well-grouped. We can observe three types of AMS fabrics according the classification of Rochette et al. (1992), as shown in Figure 6.4. A normal fabric defines a fabric where K1 and K2 are aligned along the dike plane and K3 is perpendicular to this plane. This fabric is usually used to determine flow directions. We can also observe intermediate fabric where K1 and K3 are aligned on the dike plane and K2 perpendicular to this plane. Intermediate fabrics can be explained by presence of PSD grains (Rochette et al. (1992) or by vertical compaction of the dike (Park et al., 1988). Sometimes, intermediate fabric is also possible when K2 ~ K3. Few dikes have an inverse fabric where K1 is perpendicular to the dike plane. The origin for an inverse fabric is debated in the literature and related to the presence of SD grains (Rochette et al., 1992; Stephenson et al., 1986) or secondary processes (hydrothermalism, deformation).

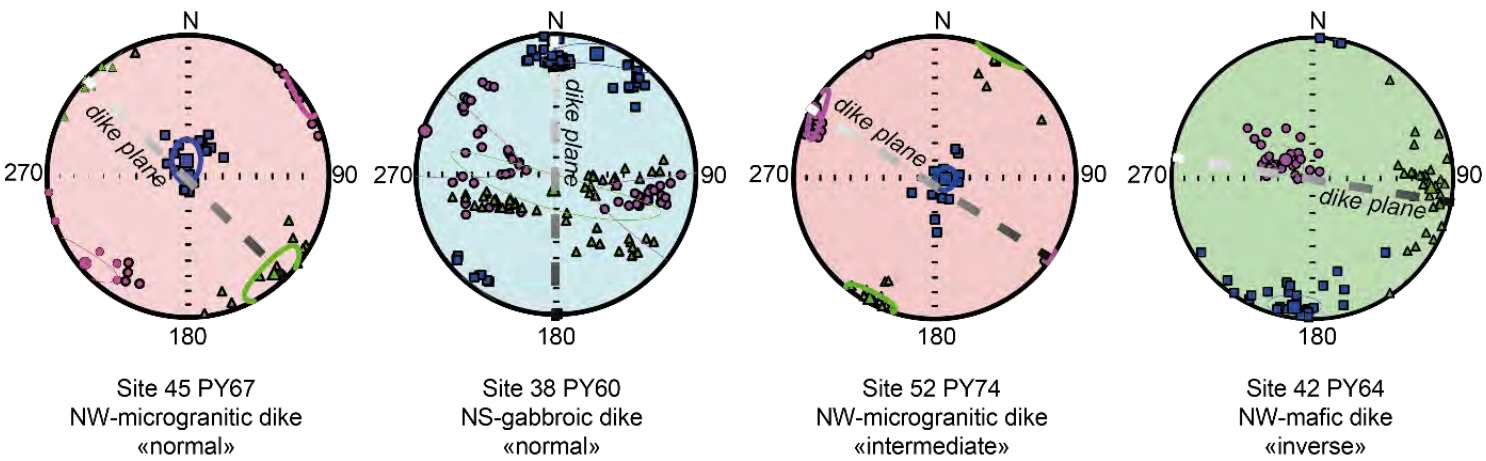

Figure 6.4: Types of AMS fabric in the Tucumã dike swarms.

Sites	Sample	N	AMS parameters						*K1*		*K2*		*K3*	
			Km (µSI)	Km (SI)	L	F	P	T	Dec.	Inc.	Dec.	Inc.	Dec.	Inc.
Microgranitic dikes														
33	PY55	11	511	5.11E-04	1.007	1.017	1.024	0.398	233.2	72.5	126.7	5.1	35.2	16.7
34	PY56	17	545	5.45E-04	1.003	1.01	1.013	0.446	17.1	37.1	143	37.8	260.5	30.7
36	PY58	7	778	7.78E-04	1.006	1.01	1.016	0.134	291.7	67.4	140.3	20	46.7	9.9
37	PY59	14	2000	2.00E-03	1.005	1.008	1.013	0.265	294.5	30.1	159.3	50.8	38.5	22.7
39	PY61	12	234	2.34E-04	1.003	1.006	1.01	0.303	95	5.3	335.8	79.2	185.9	9.4
40	PY62	34	843	8.43E-04	1.004	1.004	1.008	-0.012	205.9	67.3	34	22.5	302.8	2.9
41	PY63	8	11800	1.18E-02	1.016	1.026	1.042	0.236	78.8	13.4	339.7	33.5	187.4	53.3
43	PY65	19	499	4.99E-04	1.004	1.012	1.016	0.44	96.6	54.5	299.5	33.3	202.2	10.9
45	PY67	18	295	2.95E-04	1.009	1.013	1.022	0.202	353.9	80.9	139.1	7.5	229.8	5.1
46	PY68	12	194	1.94E-04	1.007	1.016	1.023	0.373	304.2	65.4	173.6	16.6	78.1	17.6
47	PY69	18	319	3.19E-04	1.01	1.006	1.015	-0.341	44.8	85.5	224.5	4.5	314.5	0
48	PY70	19	216	2.16E-04	1.008	1.006	1.014	-0.114	223.7	58.1	126.6	4.4	33.9	31.5
51	PY73	25	3780	3.78E-03	1.013	1.009	1.023	-0.188	282.1	79.9	120	9.6	29.4	3
52	PY74	17	622	6.22E-04	1.005	1.012	1.017	0.428	96.6	84	208	2.2	298.2	5.6
53	PY75	5	140	1.40E-04	1.013	1.016	1.028	0.08	330.8	56.7	142.2	33	234.7	4
54	PY7677879	12	822	8.22E-04	1.016	1.014	1.03	-0.067	7	65	269.7	3.4	178.1	24.7
Mafic dikes														
35	PY57	10	16500	1.65E-02	1.012	1.007	1.02	-0.209	178.6	21.7	282.3	30.7	59.3	50.9
38	PY60 E-H	16	33100	3.31E-02	1.016	1.019	1.035	0.085	288.4	10.6	85.7	78.5	197.6	4.3
38	PY60 A-D	15	36400	3.64E-02	1.02	1.027	1.048	0.141	68.2	60.7	270.8	27.3	175.8	9.6
40	PY62 D-F	9	9420	9.42E-03	1.008	1.008	1.017	0.038	222.8	37.3	342.4	32.9	99.9	35.5
40	PY62 A-C	6	16100	1.61E-02	1.013	1.022	1.036	0.241	359.5	2.2	91.2	38.9	266.8	51
42	PY64	31	40400	4.04E-02	1.008	1.01	1.018	0.16	188	8.6	95.4	16.4	304.6	71.3
44	PY66	18	28600	2.86E-02	1.014	1.019	1.034	0.136	304.9	7.2	213.7	9.2	72.2	78.3
49	PY71	15	4030	4.03E-03	1.013	1.014	1.028	-0.009	305.5	72.5	129.8	17.5	39.4	1.2
50	PY72	26	919	9.19E-04	1.009	1.011	1.02	0.139	156.2	2.1	65.2	23.9	250.8	66
Gabbroic dike														
38	PY60	9	15700	1.57E-02	1.017	1.006	1.023	-0.493	354.1	7.4	92.2	47.5	257.5	41.5
38	PY60	23	15800	1.58E-02	1.02	1.009	1.029	-0.384	0.3	20.1	243.1	51.3	103.3	31.5
41	PY63	22	14700	1.47E-02	1.019	1.015	1.035	-0.124	40.2	5.6	139.6	59	306.9	30.3
Archean basement (Rio Maria granodiorite)														
36	PY58	13	5250	5.25E-03	1.125	1.028	1.157	-0.625	59.7	48.8	328.7	0.8	238	41.2
38	PY60	14	3440	3.44E-03	1.14	1.113	1.271	-0.051	96.8	64.8	213.3	11.9	308.1	21.9
46	PY68	12	30600	3.06E-02	1.079	1.088	1.173	0.045	234.3	44.1	341.4	16.8	86.6	41.1

Table 6.1: AMS data from the Tucumã dike swarms. K1, K2 and K3 are the maximum, intermediate and minimum susceptibility intensities. N is the number of specimens. Km is the bulk mean magnetic susceptibility. L is the lineation. F is the foliation. P is the anisotropy degree. T is the Jelinek parameter. Dec = declination. Inc = inclination.

Normal fabrics show a NW direction and is consistent with the NW regional lineament. The K1 inclination is used as a flow indicator. For most microgranite dikes, K1 is nearly vertical. These values indicate emplacement of these dikes at *ca*. 1880 Ma along vertical flows (Figure 6.5) and suggest a NE-SW horizontal maximum stress (σH) for the Carajás Province. We can observe for some microgranitic dikes some lower plunges of K1, which suggest a subhorizontal flow. For example, for site 40 (PY63), a plunge of 13.4° is observed. K1 < 20° indicates a subhorizontal flow emplacement of the NS-dike (or the top of the dike) (Figure 6.5). This type of fabric is usually defined for the emplacement of sills. The magnetic fabric for the NS-gabbroic dike, which indicates subhorizontal flow, is consistent with the orientation of plagioclases observed on the field (Figure 3.5.C). This NS-trend in the region was already noted as a tectonic feature by Macambira and Vale (1997) on the geological map of São Felix do Xingu. Paleomagnetic results in the next section permit to associate this NS-gabbroic dike with the emplacement of dikes in the Carajás Province during the CAMP (Central Atlantic Magmatic Province) at *ca*. 200 Ma.

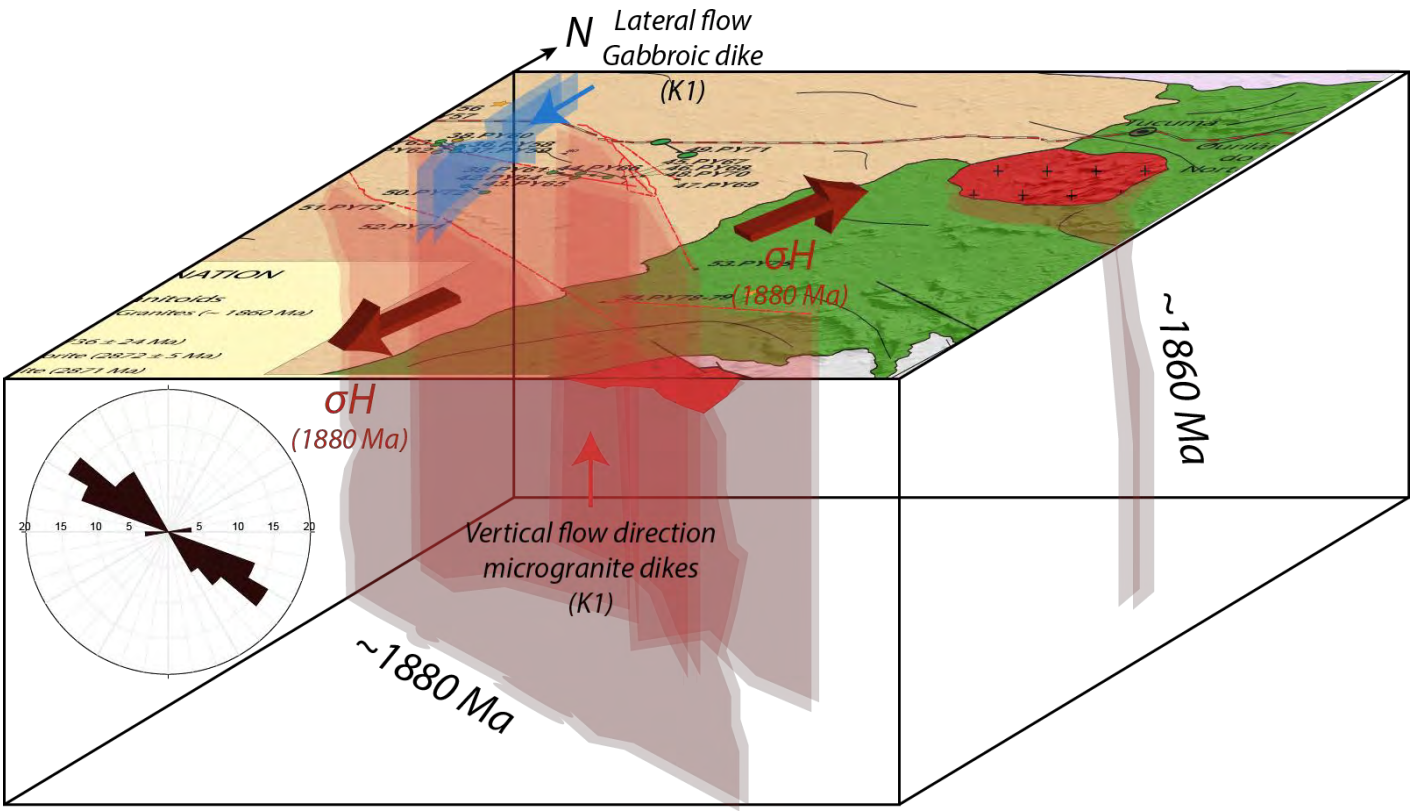

Figure 6.5: Schematic cartoon of dikes emplacement for Tucumã dike swarms. σH is the maximum horizontal stress in the Carajás Province at ~1880 Ma. The NS-gabbroic dike is supposed to be Mesozoic in age.

6.3 Paleomagnetic results

6.3.1 Magnetic components

Component A, a northwestern, moderate downward direction (ChRM), could be isolated in most microgranite dikes and also in associated NW-mafic dikes (Figure 6.6). This component was efficiently isolated after AF treatment in 16 sites, comprising felsic and NW-mafic dikes. The thermal treatment, however, was not efficient to isolate the same component for the microgranite samples. During demagnetization, different directions are observed for the same microgranitic site or magnetization became unstable. Normal (N) and reverse (R) polarities are observed but the classification of the reversal test is indeterminate (McFadden and McElhinny, 1990).

Two sites of the NS-gabbroic dike revealed northern, upward ChRM direction (Figure 6.6), named as component B. Similarly, thermal demagnetization was not efficient to isolate the same component in these rocks. This component was also observed in the basement Rio Maria granodiorite rock collected close to the NS-gabbroic dike, and in microgranitic dikes in the region. Only one polarity (N) is observed.

Two sites of the Archean Rio Maria granodiorite revealed southwestern directions, with low downward inclination (Figure 6.6), named as component C. As already stressed, the third site of Archean basement presented the component B, which, most probably represents a remagnetization of the Archean rock. Component C can be isolated by LTD-AF or thermal demagnetization, and was also observed in microgranitic dikes, as for example, samples from site PY73. Interestingly, this dike presents mingling features, which were not observed in the other felsic dikes. Normal (N) and reverse (R) polarities are observed.

A northern direction with steep upward inclination is observed in a single site (PY72) being unique in the Tucumã area.

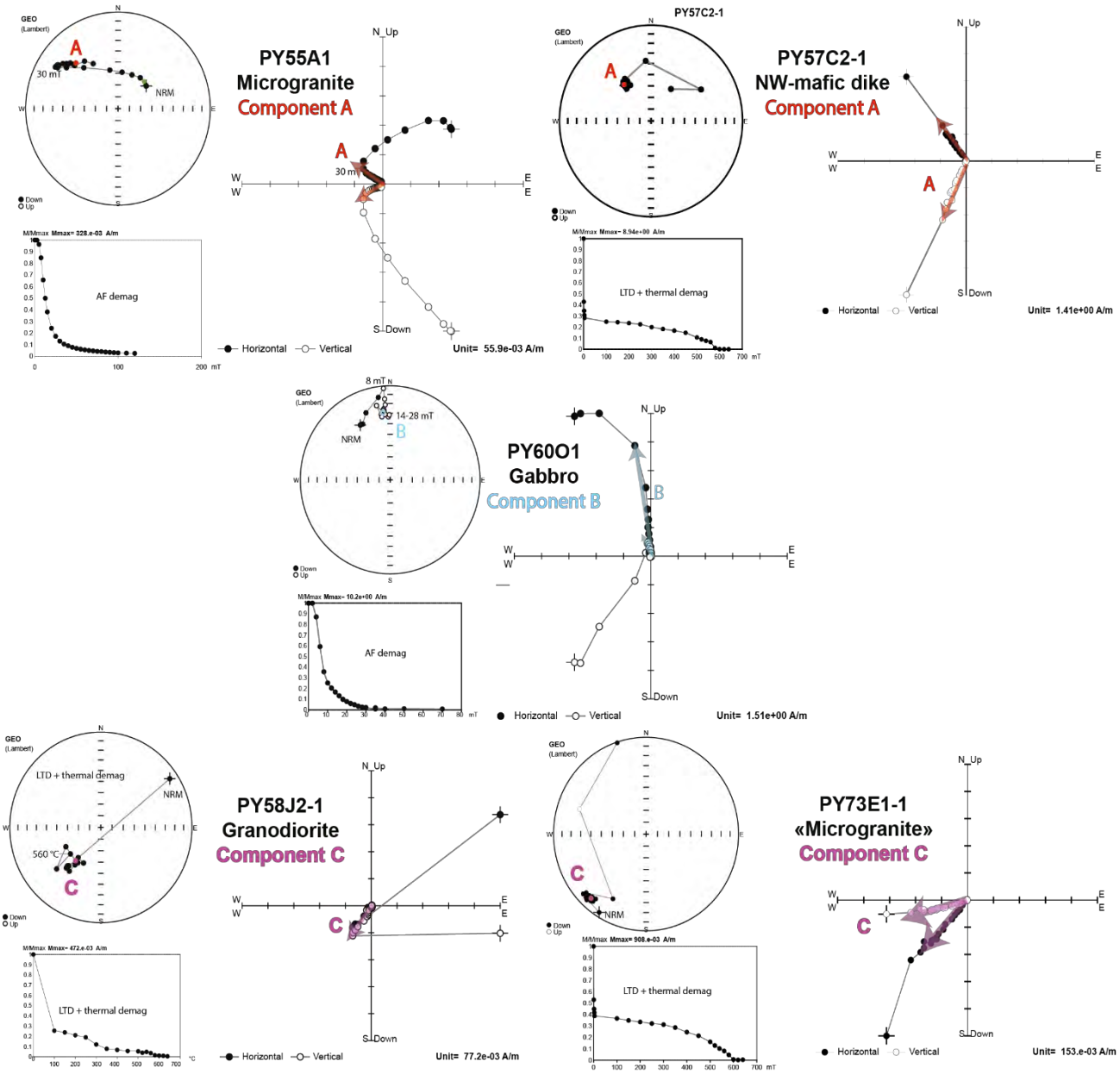

Figure 6.6: Examples of demagnetization behaviors for the Tucumã dike swarms. Figure shows stereographic projections (solid (open)) symbols represent positive (negative) inclinations), normalized intensity curves and Zijderveld diagrams.

6.3.2 Mean directions and paleomagnetic poles

The magnetic components are listed in the Table 6.2. Figure 6.7 shows the site mean directions for components A, B and C. Site mean directions for component A cluster around the mean Dm= 330.5°, Im= 27.9° (N= 16, α_{95}= 11.4°, k= 11.47), which yielded a paleomagnetic pole (TUC-A) located at 52.9°S, 76.4°E (A_{95}= 10.4°, K= 13.52). Mean direction for component B is Dm= 1.4°, Im= -33.7° (N= 9, α_{95}= 12.5°, k= 17.83), and the associated paleomagnetic pole is located at 82.3°S, 317.9°E (A_{95}= 13.7°, K= 15.01). Site mean direction for component C is Dm= 247.3°, Im= 21.5° (N= 6, α_{95}= 17.4°, k= 15.84), which yielded a paleomagnetic pole located at 23.3°S, 228.4°E (A_{95}= 14.8°, K= 21.34).

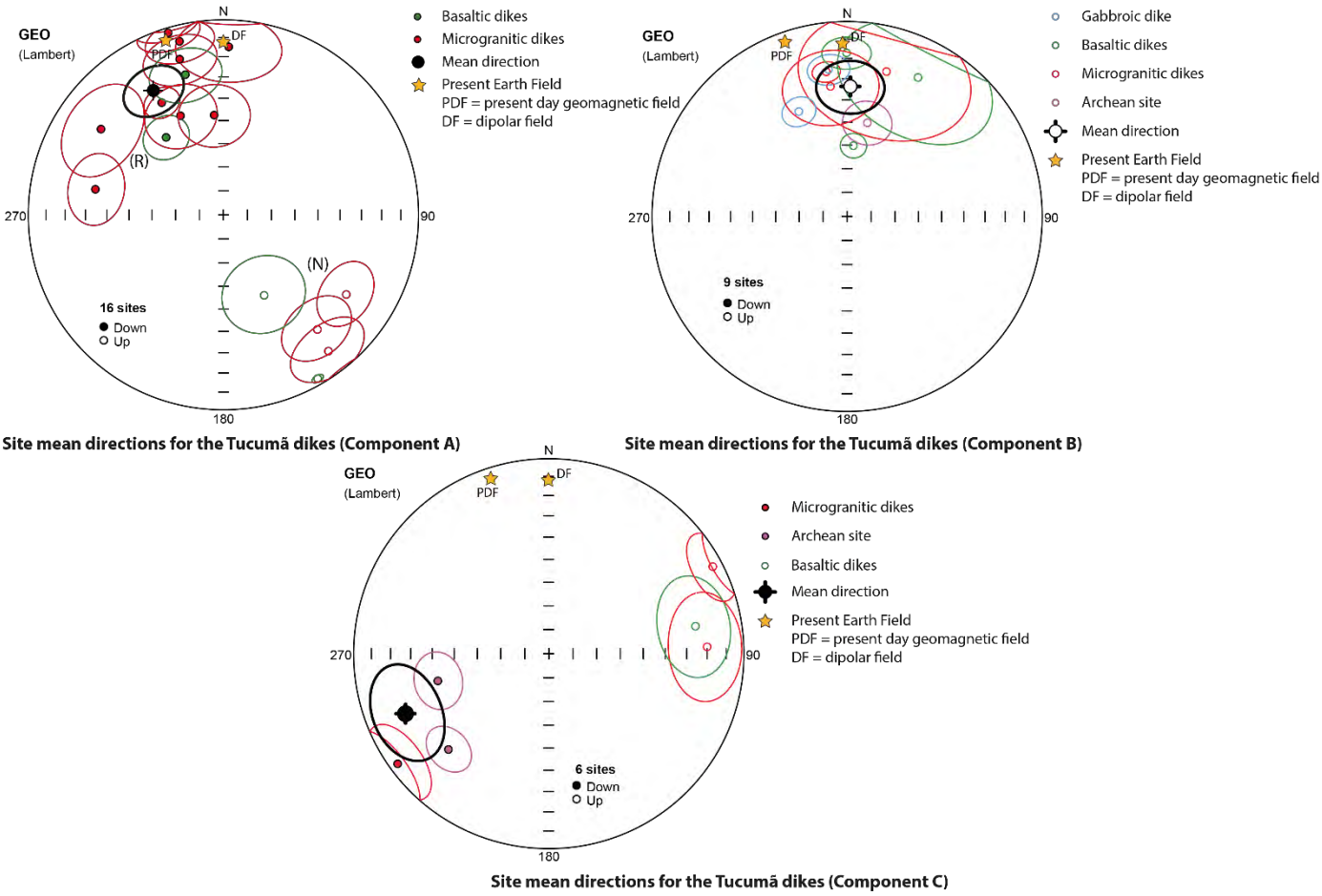

Figure 6.7: Site mean directions for the Tucumã dikes swarms.

Site	Sample	Lat (°N)	Long (°E)	Strike	Lithology	Site Mean direction						VGP	
Component A						n/N	Dec (°)	Inc (°)	R	k	α95 (°)	P. Lat (°N)	P. Long (°E)
Normal polarity (N)													
36	PY58 A-F	-6.76	308.56	N292	Microgranite	7/14	140.7	-25	6.71	20.45	13.7	-46.2	65.5
43	PY65 A-G	-6.8	308.63	N299	Microgranite	10/10	123	-25.9	9.44	16.04	12.4	-29.8	58.6
52	PY74	-6.86	308.62	N309	Microgranite	7/11	142.4	-12.8	6.71	20.38	13.7	-50.2	57.4
38	PY60 A	-6.76	308.56	N277	Basalt	2/7	150.1	-3.5	2	18040	1.9	-59	53.4
40	PY62 A-F	-6.76	308.56	N304	Basalt	3/8	153.2	-51.8	2.96	54.64	16.8	-43.3	97
Mean direction N-polarity						**5**	**141.4**	**-24**	**4.74**	**15.2**	**20.3**		
Reversed polarity (R)													
33	PY55 A-E	-6.75	308.5	N320	Microgranite	6/12	305	24.4	5.67	15.15	17.8	-31.2	58.2
34	PY56 A-H	-6.73	308.51	N315	Microgranite	10/15	1.8	14.9	8.94	8.48	17.6	-75.6	135.7
37	PY59 A-F	-6.77	308.56	N292	Microgranite	9/14	345.8	9.1	8.64	22.23	11.2	-71.8	76.7
39	PY61 A-E	-6.8	308.63	N300	Microgranite	7/10	343.1	2.8	6.85	38.75	9.8	-71.2	63.9
40	PY62 G-Q	-6.76	308.56	N304	Microgranite	11/30	281.3	33.5	10.22	12.77	13.3	-8.5	58.3
41	PY63 H-M	-6.76	308.56	N299	Microgranite	2/12	331.2	34.7	2	1294	6.9	-51.6	81.4
45	PY67 A-G	-6.8	308.66	N325	Microgranite	7/12	336.6	43.9	6.69	19.09	14.2	-50.3	94.6
48	PY70 A-G	-6.8	308.66	N311	Microgranite	10/13	354.7	47.4	9.3	12.8	14	-54.3	120.7
54	PY78 - 79	-6.96	308.75	N262	Microgranite	11/15	344.3	18.2	10.28	13.84	12.7	-67.4	84.6
35	PY57 A-D	-6.73	308.51	N315	Basalt	3/6	323.5	49.1	2.99	171.59	9.4	-39.2	86.8
42	PY64 A-H	-6.8	308.63	N299	Basalt	5/8	344.8	26.4	4.89	35.11	13.1	-64.4	92.7
Mean direction R-polarity						**11**	**335**	**29.5**	**10.04**	**10.45**	**14.8**		
Mean direction (N+R)						**16**	**330.5**	**27.9**	**14.69**	**11.47**	**11.4**		
Paleomagnetic pole										**13.52**	**10.4**	**-52.9**	**76.4**
Component B													
38	PY60 I-Q	-6.76	308.56	N5	Gabbro	10/13	352.8	-25	9.79	42.08	7.5	-80.4	356.2
41	PY63 A-G	-6.76	308.56	N5	Gabbro	5/8	335.3	-40.5	*G.C*	*G.C*	6.6	-61.2	1.4
36	PY58	-6.76	308.56	N292	Microgranite	6/14	351.8	-26.6	*G.C*	*G.C*	5.4	-79.1	355.7
41	PY63 H-M	-6.76	308.56	N299	Microgranite	4/12	15.2	-24	3.69	9.75	31	-74	240.9
47	PY69 A-H	-6.81	308.68	N304	Microgranite	5/12	352.7	-33.2	4.79	19.51	17.8	-76.6	339.7

38	PY60 A-H	-6.76	308.56	N277	Basalt	4/7	27	-21.1	3.74	11.42	28.4	-63	229.4
40	PY62 A-F	-6.76	308.56	N304	Basalt	4/8	359.8	-17.2	3.98	123.69	8.3	-87.9	314.5
50	PY72 A-F	-6.82	308.6	N313	Basalt	10/14	5.1	-60.1	9.89	84.49	5.3	-55.5	301.7
38	PY60 R-Z	-6.76	308.56		Granodiorite	8/11	12.2	-49.3	7.79	33.82	9.7	-63.9	104
Mean direction						**9**	**1.4**	**-33.7**	**8.55**	**17.83**	**12.5**		
Paleomagnetic pole									8.47	**15.01**	**13.7**	**-82.3**	**317.9**
Component C													
Normal polarity (N)													
41	PY63 H-M	-6.76	308.56	N299	Microgranite	6/12	87.5	-19.9	5.64	13.85	18.7	-3.6	228.6
54	PY78 - 79	-6.96	308.75	N262	Microgranite	7/15	62	-5.4	6.79	28.84	11.4	-28.1	218
49	PY71 A-G	-6.77	308.66	N301	Basalt	6/12	79.4	-24.5	5.66	14.75	18	-11.8	230.4
Mean direction N-polarity						**3**	**76**	**-16.9**	**2.92**	**25.6**	**24.9**		
Reversed polarity (R)													
51	PY73 A-H	-6.84	308.58	N301	Microgranite	9/13	233.9	4.7	8.49	15.62	13.4	-36.1	216.6
36	PY58 G-K	-6.76	308.56		Granodiorite	9/11	226.3	29.6	8.75	31.7	9.3	-43.7	234.1
46	PY68 G-K	-6.8	308.66		Granodiorite	7/7	256.2	41.1	6.81	31.13	11	-15.3	241.2
Mean direction R-polarity						**3**	**237.7**	**25.7**	**2.84**	**12.73**	**36.1**		
Mean direction (N+R)						**6**	**247.3**	**21.5**	**5.68**	**15.84**	**17.4**		
Paleomagnetic pole										**21.34**	**14.8**	**-23.3**	**228.4**
***Components not considered**													
46*	PY68 A-F	-6.8	308.66	N326	Microgranite	6/7	93.8	25.1	5.62	13	19.3	-5.3	26
46*	PY68 D-F	-6.8	308.66	N327	Microgranite	5/5	201.3	86.7	4.89	35.85	13	-12.8	306.66
44*	PY66 A-G	-6.8	308.64	N269	Basalt	5/5	86.1	8.8	4.93	60.46	9.9	-3.4	213.8
49*	PY71 A-G	-6.77	308.66	N301	Basalt	5/12	70.2	59.2	*G.C*	*G.C*	2.1	-10.5	175.8

Table 6.2: Paleomagnetic results from Tucumã dikes. Lat (latitude); long (longitude) – site geographical coordinates; Strike – dike direction; n/N is the number of sites. The mean direction is given by its declination (Dec) and inclination (Inc), and the paleomagnetic pole by its latitude (P. Lat.) and longitude (P. Long.). R, α95 and k are the Fisher's (1953) statistical parameters. *G.C* –Great circles analysis. n/N is the ratio of samples with considered direction on the total of measured samples.

6.4 Baked contact tests

Figure 6.8 shows the unique place where it was possible to attempt a field test to determine the chronology of magnetic components. The NS-gabbroic dike cross-cuts a NW-mafic dike and also a NW microgranitic dike. Although outcrop conditions were not good, many small blocks were sampled for the gabbro dike, the NW-mafic dike, the NW microgranitic dike, and the Archean granodiorite.

First baked contact test (BCT-1 on Figure 6.8) was attempted between the NW-mafic dike and the Archean basement. (Figure 6.9). All samples revealed the component B of NS-gabbroic dike and imply a large remagnetization in the area during the intrusion of this dike. This is a negative baked contact test.

A second contact test (BCT-2 on Figure 6.8) was attempted between the NS-gabbroic dike which cross-cuts a NW-microgranitic dike (site 41 PY63) (Figure 6.10).The NS-gabbroic dike show the characteristic component B. At contact (~50 cm) a microgranitic sample revealed the same component B with a northern direction and a low upward inclination. The NS-gabbroic dike remagnetized the microgranitic dike at contact. High values of susceptibility for these sample and the similar magnetic fabrics confirm the remagnetization. At *ca*. 2 m of the contact, the microgranitic dike shows a different component, of northwestern direction with downward inclination, the component A. This contact test is considered as a positive inverse baked contact test for component A. It shows that component A is older than component B but doesn't confirm that component A is primary. The low unblocking temperatures associated with component A in the microgranitic dike (~400°C) is a strong evidence that component A represents a remagnetization.

The third contact test show unexplainable results because the directions are random.

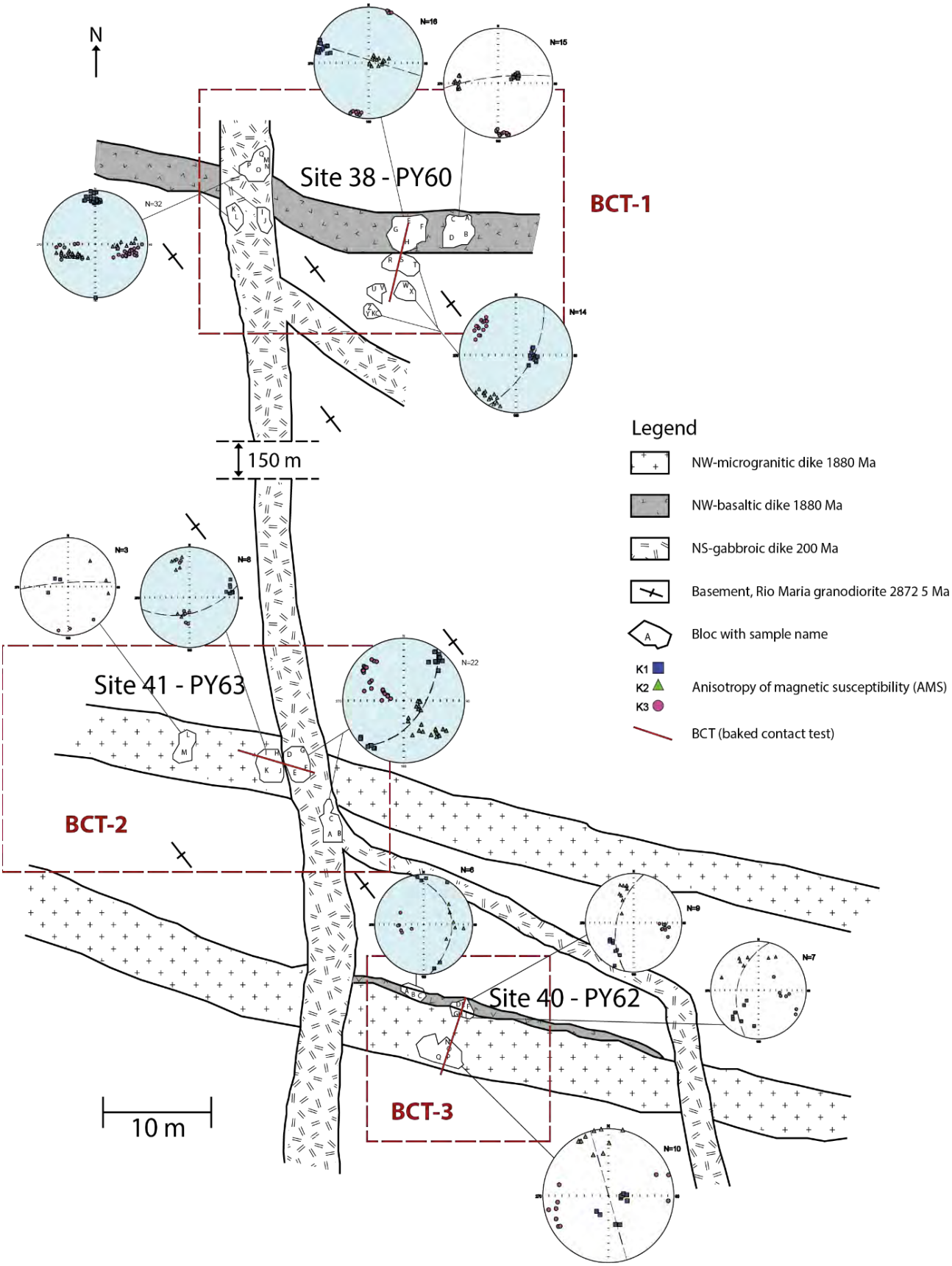

Figure 6.8: Baked contact tests during paleomagnetic investigation in Tucumã area. Localization of baked contact tests is shown. Magnetic fabrics for respective localities are also shown.

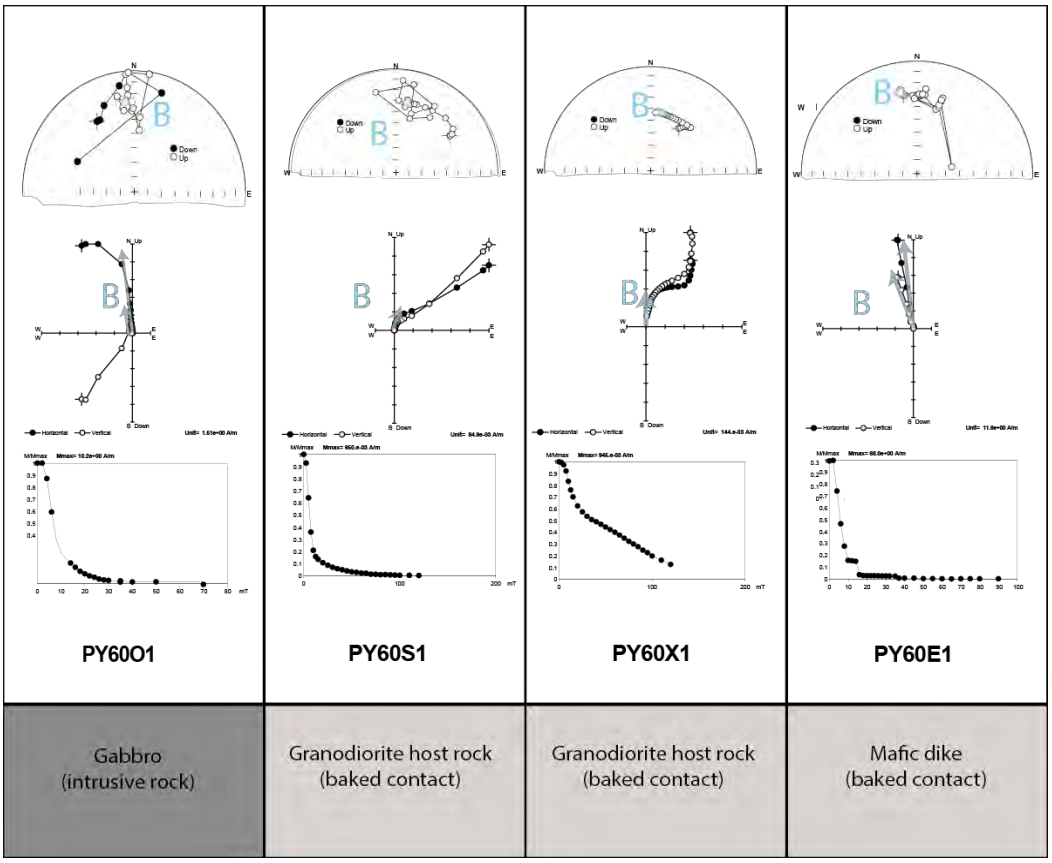

Figure 6.9: BCT-1. Localization in Figure 6.8. Figure shows stereographic projections (solid (open)) symbols represent positive (negative) inclinations), normalized intensity curves and Zijderveld diagrams.

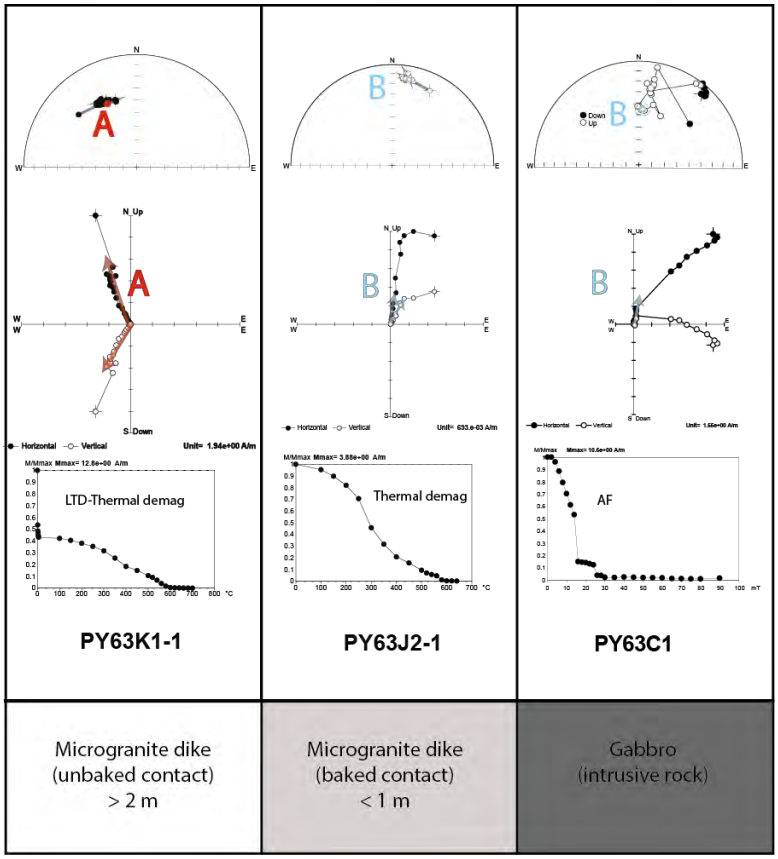

Figure 6.10: BCT-2. Localization in Figure 6.8. Figure shows stereographic projections (solid (open)) symbols represent positive (negative) inclinations), normalized intensity curves and Zijderveld diagrams.

6.5 Reliability of Tucumã poles

Component B yields a paleomagnetic pole close to the Jurassic pole obtained for the French Guyana (Figure 6.11) (Nomade et al., 2000). Mesozoic dikes are common in the studied area, known as the Cururu diabase (Macambira and Vale, 1997). Teixeira et al. (2012a) dated dikes in the Parauapebas area at *ca*. 200 Ma. The NS-gabbroic dike is probably a Mesozoic dike. The Mesozoic dikes are related to the opening of the Atlantic Ocean and the presence of the Central Atlantic Magmatic Province (CAMP). Paleomagnetic poles for the Amazonian craton at *ca*. 200 Ma are well-defined but precise U-Pb geochronology is necessary (De Min et al., 2003; Ernesto et al., 2003).

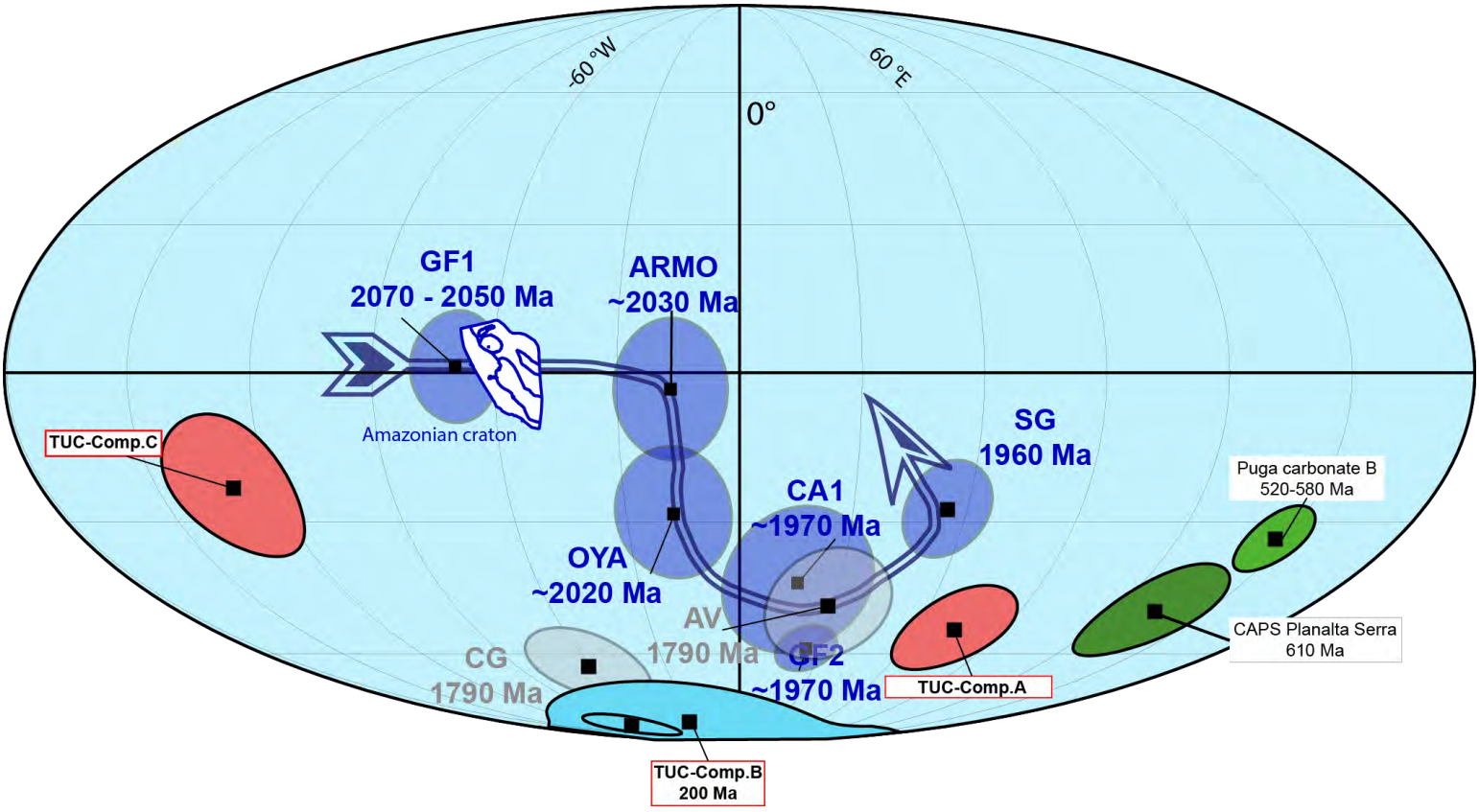

Figure 6.11: Confidence of paleomagnetic poles (A, B and C) in Tucumã (Mollweide projection). Red poles could be Proterozoic in ages. Comparison with Neoproterozoic poles in green (Garcia et al., 2013; Trindade et al., 2003) and a Mesozoic pole in light blue (Nomade et al., 2000) of the Amazonian craton. APW path (2050 – 1960 Ma) for the Amazonian craton is indicated by the blue arrow (Bispo-Santos et al., 2014a).

Presence of component A in NW-microgranitic dikes and associated NW-mafic dikes could represent a primary origin or be due to a large remagnetization process. A positive inverse baked contact test (site 41 PY63) shows that component A is older than component B but doesn't prove its primary origin. Magnetic mineralogy shows that component A is carried by PSD magnetite grains. The paleomagnetic pole associated with component A satisfies 5 (Q= 5) out 7 Van der Voo (1990)'s criteria: (1) Age is precisely defined at *ca*. 1880 Ma by the U-Pb method (SHRIMP) in zircon, although it is not possible to prove that component A has the same age. (2) The pole was determined using a sufficient number of samples and have adequate Fisher statistical parameters, although it is recognized the difficulty for some sites to isolate a well-defined direction. (3) ChRM was isolated by PCA of Kirschvink (1980) after AF, thermal, LTD + AF, LTD + thermal demagnetization. (6) Normal and reverse polarities were observed for the investigated sites. (5) There is no geological evidence of later tectonic events in the area, only intrusions of dikes at *ca*. 530 Ma and *ca*. 200 Ma as suggested by Teixeira et al. (2016). However, this pole does not satisfies the following criteria: (4) its primary origin is not confirmed by the inverse baked contact test, only that this direction is older than component B (Mesozoic). (7) Although pole A falls far from Neoproterozoic poles, Puga B (Trindade et al., 2003) and Complexo Alcalino Planalto da Serra (CAPS) (Garcia et al., 2013), for some sites, the magnetic directions are not too far from the expected Neoproterozoic direction for the Amazonian craton. Therefore, it is possible that this pole is disturbed by: (1) a sampling with many tilted blocks (deviation of directions), (2) a Neoproterozoic remagnetization during the intrusion of dikes dated at *ca*. 530 Ma in the Carajás province (Teixeira et al., 2012b; Teixeira et al., 2016). This is consistent with the fact that component A is older than the Mesozoic component B. Moreover, in the following chapter, close directions (component SF3) have been disclosed for the 1880 Ma Santa Rosa and Sobreiro Formations (São Felix do Xingu area), which are interpreted as a remagnetization in Neoproteroizoic times (Figure 6.11). If a Neoproterozoic thermoviscous remagnetization is possible in the western São Felix do Xingu area, then, we have to observe it in the eastern Tucumã area. In summary, the pole A cannot be considered as a key pole because the age of its magnetization is not well-defined (Buchan et al., 2000; Buchan, 2013).

We will see in the next chapter that a different key pole (SF1) has been determined for rocks of the well-dated (*ca*. 1880 Ma) Santa Rosa Formation. Moreover, studied microgranite dikes in Tucumã area are geochemically related to the felsic rocks from the Santa Rosa Formation as suggested by da Silva et al. (2016). The microgranitic dikes in Tucumã represent the dike swarm associated to the Santa Rosa Formation in São Felix do Xingu, therefore, we can definitely rule out the hypothesis of considering this pole as primary.

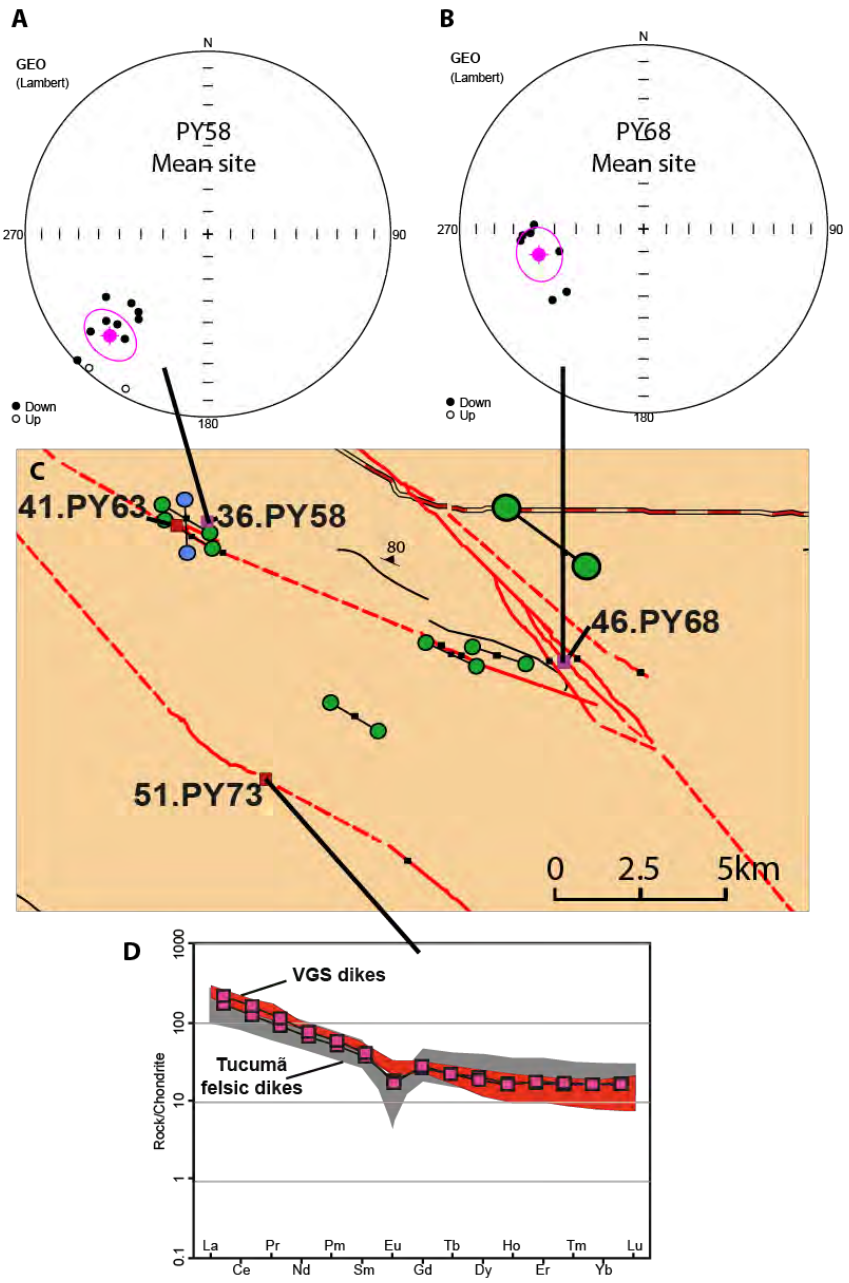

Figure 6.12: A. Mean site direction for PY58 site. B. Site mean direction for PY68 site. C. Geological map and localization of sites of Tucumã. D. REE pattern for rocks of Velho Guilherme Suite (red) and Tucumã felsic dikes (grey) (da Silva et al., 2016). REE pattern for two samples of felsic dikes of Velho Guilherme Suite in Tucumã area are indicated (site PY73).

In the Figure 6.11, we can see the position of pole (TUC-C) associated to the component C in Tucumã. This pole TUC-C is close to component SFX-SF2 pole obtained for a Velho Guilherme granite and other felsic rocks from the Santa Rosa and andesitic rocks from the Sobreiro Formation at the São Felix do Xingu area (See Chapter.7). It will be shown that component SF2 passed a baked contact test, and is considered of primary origin acquired at 1860 Ma, during Velho Guilherme intrusion. We can remember that this pole is associated with two sites of Archean Rio Maria granodiorite and carried by small SD grains of magnetite (LTD demagnetization). This direction has also a regional consistency because we recorded this

direction in two distant (~10 km) sites of the Rio Maria granodiorite (Figure 6.12.A-B-C).It seems unlikely that this direction is Archean because all Archean rocks have MD magnetites. Finally, the last event that affected the Amazonian craton in the Tucumã area, which could likely remagnetize the Archean basement, is the Velho Guilherme Suite *sensu lato,* the last pulse of the Uatumã event at *ca*. 1860 Ma. The Tucumã dike swarms are different in age and in geochemistry from the Velho Guilherme granite (Figure 6.12.D) (da Silva et al., 2016). Except for the sites of the Archean Rio Maria granodiorite, another site revealed component C - site 51 (sample PY73). It is a microgranitic dike and is slightly different from the other felsic dikes with many mingling features. This site is classified as an “intermediate” dacite dike by (da Silva et al., 2016). Furthermore, REE pattern for this dike (PY73 = FDB 25) reveals strong affinity with the Velho Guilherme Suite and rejects an affinity with the Santa Rosa Formation, which is associated to the Tucumã dike swarms dated at *ca*. 1880 Ma (Figure 6.12.D) (da Silva et al., 2016). It thus seems obvious that this dike belongs to the Velho Guilherme Suite (~1860 Ma). So, component C could represent the direction at *ca*. 1860 Ma and suggests a large remagnetization during the final stage of Uatumã event to imprint the Archean basement. These observations reinforce the fact that TUC-C and SFX-SF2 represent a magnetization acquired at ca. 1860 Ma during the Velho Guilherme Suite intrusions.

In São Felix do Xingu area, we calculated a component SF2 very similar to the component C (Figure 6.11) as we will see in the next section. The component SF2 is carried by another dike of the Velho Guilherme Suite (~150 km from Tucumã) well-dated at *ca*. 1855 Ma (this study). In addition, the primary direction of SF2 is supported by a positive baked contact test (next section). This regional coherence more a primary origin for the dike in São Felix do Xingu area (SF2) support that this component C can be related to the primary direction associated with the Velho Guilherme Suite (~1860 Ma).

Chapter. 7: Turmoil before the boring billion: Paleomagnetism of the 1880 – 1860 Ma Uatumã event in the Amazonian craton

Paul Y. J Antonio[1,2], Manoel S. D'Agrella-Filho[1], Ricardo I. F Trindade[1], Anne Nédélec[2], Davis C. de Oliveira[3], Fernando F. da Silva[3], Matteo Roverato[4]

[1]Instituto de Astronomia, Geofísica e Ciências Atmosféricas (IAG), Universidade de São Paulo (USP), Rua do Matão, 1226, 05508-090, São Paulo, SP, Brazil
[2]Geosciences Environnement Toulouse (GET), OMP, Université de Toulouse, France
[3]Grupo de Pesquisa Petrologia de Granitoides (GPPG), Instituto de Geociências (IG), Programa de Pós-Graduação em Geologia e Geoquímica, Universidade Federal do Pará (UFPA). CEP-66075-900, Belém, Pará, Brazil
[4]Universidade de São Paulo, IGC Instituto de Geociências, Departamento de Geologia Sedimentar e Ambiental. Rua do Lago, 562 Cidade Universitária 05508080, São Paulo, SP, Brazil

Abstract

The Uatumã silicic large igneous province (SLIP) has covered about 1.500.000 km^2 of the Amazonian craton at *ca*. 1880 Ma, when the Columbia/Nuna supercontinent has been assembled. Paleomagnetic and geochronological data for this unit were obtained for the Santa Rosa and Sobreiro Formations in the Carajás Province, southwestern Amazonian Craton (Central-Brazil Shield). AF and thermal demagnetizations revealed northern (southern) directions with high upward (downward) inclinations (component SF1), which passes a 'B' reversal test, and is carried by magnetite and SD hematite with high-blocking temperature. This component is present on well-dated 1877.4 ± 4.3 Ma (U-Pb zrn - LA-ICPMS) rhyolitic lava flows, providing the SF1 key paleomagnetic pole (Q= 6) located at 319.7°E, 24.7°S (A_{95}= 16.9°). A second southwestern (northeastern) direction with low inclination (Component SF2) was obtained for a well-dated 1853.7 ± 6.2 Ma (U-Pb zrn - LA-ICPMS) dike of the Velho Guilherme Suite. This component also appears as a secondary component in the host rhyolites of the Santa Rosa Fm and andesites of the Sobreiro Fm at the margins of the dike previously dated. Its primary origin is confirmed by a positive baked contact test, where a Velho Guilherme dike crosscuts the 1880 Ma andesite from the Sobreiro Formation. The corresponding SF2 key pole is located at 220.1°E, 31.1°S (A_{95}= 5°) and is classified with a reliability criterion Q= 7. The large angular distance between the almost coeval (difference of ~25 Ma) SF1 and SF2 poles implies high plate velocities (~39.3 cm/yr) which are not consistent with modern plate tectonics. The similar significant discrepancy of paleomagnetic poles with ages between 1880 and 1860 Ma observed in several cratons could be explained by a true polar wander (TPW) event. This event is the consequence of the reorganization of the whole mantle convection, and is supported by paleomagnetic reconstructions at 1880 Ma and 1860 Ma and also by geological/geochronological evidence.

Keywords: Paleoproterozoic, paleomagnetism, TPW, Columbia, Amazonian craton.

7.1 Introduction

Understanding the position of continents through time is crucial to constrain the geodynamics of the Earth. Supercontinents assembly have punctuated Earth's (Nance et al., 2014) with at least three supercontinents being recognized: Pangea (*ca.* 300 – 200 Ma), Rodinia (*ca.* 1000 – 700 Ma) and Columbia/Nuna (*ca.* 1800 – 1400 Ma). The existence of supercratons during the Archean (*ca.* 2700 Ma) is also speculated (Evans et al., 2016a; Meert, 2012, 2014). While the configurations of Pangea and Rodinia are the object of a relative consensus (Domeier et al., 2012; Li et al., 2013), the timing and the exact configuration of Columbia/Nuna (hereafter called Columbia following Meert (2012)) is still debated. The main geological argument for the existence of this supercontinent is the presence of 2100 – 1800 Ma orogens in most continents (Zhao et al., 2002; Zhao et al., 2004). No changes in ocean and atmosphere composition were observed during the Columbia supercontinent and even more longer (1800 – 800 Ma) which is referred as the "Boring billion" (Holland, 2006). This period is tectonically far from boring and to precisely constrain its paleogeography a more comprehensive paleomagnetic database (such as the PALEOMAGIA) for the Paleo and Mesoproterozoic covering most continental blocks worldwide is needed (Veikkolainen et al., 2014b). Presently, few key poles are available and they are unevenly distributed across the globe. Most models therefore use pairs of coeval poles from cratonic blocks to test reconstructions, but this implies that the models are not unique with many alternatives (For example, see models proposed by Pisarevsky et al. (2014) and Bispo-Santos et al. (2014b) for the Amazonian craton at *ca.* 1790 Ma). Given these uncertainties, the time of maximum packing of Columbia is not a consensus, with some authors proposing it occurred at *ca.* 1780 Ma (Bispo-Santos et al., 2014b; Zhang et al., 2012), while others think it was reached only at around 1580 Ma (Pehrsson et al., 2016; Pisarevsky et al., 2014). The detrital zircon database, however, favors the first hypothesis (Condie and Aster, 2010; Hawkesworth et al., 2010).

The Laurentia-Baltica connection forms the core of Columbia. The extensive paleomagnetic database for these cratons supports a long connection between them, from 1780 to 1260 Ma (Buchan et al., 2000; Pisarevsky and Bylund, 2010; Salminen et al., 2014; Salminen et al., 2015). Recently, paleomagnetic studies on rock units from the Amazonian craton suggest that this cratonic block was also part of Columbia (Bispo-Santos et al., 2008; Bispo-Santos et al., 2012; Bispo-Santos et al., 2014a; Bispo-Santos et al., 2014b; D'Agrella-Filho et al., 2012; D'Agrella-Filho et al., 2015; D'Agrella-Filho et al., 2016). Several lines of evidence suggest a connection between the Amazonian craton and Baltica in a SAMBA (South-America-Baltica) configuration (Johansson, 2009, 2014), which was positively tested by the 1790 Ma Avanavero pole (Bispo-Santos et al., 2014b). Paleomagnetic and geological evidences for alternative models to SAMBA exists (Bispo-Santos et al., 2008; Bogdanova et

al., 2015; Pisarevsky et al., 2014). The Amazonian craton is also usually linked with West Africa, along a connection between the Guri (Guiana Shield) and Sassandra (West Africa) shear zones as updated by Bispo-Santos et al. (2014a) using the new 1960 Ma Surumu pole.

If uncertainties remain in the Columbia configuration, the paleogeography prior to this supercontinent assembly is still more uncertain given the independent drift paths of most continental blocks (e.g. Laurentia, Baltica, Amazonian, West Africa). In such case, match of large igneous provinces (LIPs) can be used as an additional tool to correlate continental blocks, using similarities in their geochronology and geochemistry ("LIP barcode). On the other hand, the orientation of dike swarms can be applied, as they generally herald the break-up of large continental masses (Ernst et al., 2013a; Söderlund et al., 2016). For instance, by ~1880 Ma a large intraplate and plate margin magmatism occurs in numerous Archean cratons worldwide that provides paleomagnetic data that show significant angular distances between poles in the same cratonic unit with only slightly different ages. The best-known example is the Coronation loop for the Slave craton (McGlynn and Irving, 1978; Mitchell et al., 2010), but similarly anomalous results are also noted for Kalahari (Hanson et al., 2004; Hanson et al., 2011) and Superior cratons (Halls and Heaman, 2000; Hamilton et al., 2009), suggesting a true polar wander (TPW) signal (Mitchell et al., 2010). These anomalous apparent polar wander paths (APWPs) have been interpreted as either (i) rapid plate motions, much faster than today, (ii) TPW events when the whole solid Earth (mantle and crust) rotates in relation to the liquid outer core to accommodate a change in global moment of inertia (Mitchell et al., 2010), or (iii) the absence of a stable GAD (geocentric axial dipole) field ("multipolar field"), including the possibility of an equatorial dipole or "hyper" frequent polarity reversals (Abrajevitch and Van der Voo, 2010; Bazhenov et al., 2016; Driscoll, 2016; Halls et al., 2015).

Here we focus on the paleomagnetic record of the Amazonian craton for the *ca.* 1880 – 1860 Ma interval, when a large intraplate magmatism has covered most of its surface defining the Uatumã silicic (~felsic) large igneous province (SLIP) (Klein et al., 2012). We present new paleomagnetic and U-Pb geochronological results for the Santa Rosa and Sobreiro Formations in Pará state, southern Amazonian craton. Our new results for ~1880 Ma help to better define the APW path between 1960 Ma and 1860 Ma for the Amazonian craton as well as to test the possible occurrence of TPW during 1880 – 1860 Ma.

7.2 Geological setting and lithology

The Amazonian Craton (~4.400.000 km^2) is one of the largest cratons in the world (Almeida et al., 1981). It includes the Guiana Shield in the north and the Central-Brazil (or Guaporé) Shield in the south, bisected by the Amazon sedimentary basin (Santos et al., 2000;

Schobbenhaus et al., 1984) (Figure 7.1). Current models for its Precambrian geodynamics primarily based on geochronological data recognize six (Tassinari and Macambira, 1999; Tassinari and Macambira, 2004) or seven/eight (Santos et al., 2003a; Vasquez et al., 2008) geotectonic provinces. In this work, we follow the model of (Tassinari and Macambira, 1999; Tassinari and Macambira, 2004), that is used by several other authors (Cordani and Teixeira, 2007; Cordani et al., 2009; Schobbenhaus et al., 2004). Two ~2500 Ma Archean nuclei are formed by gneissic-granitoid terrains and greenstone belts (Central Amazonian Province) exposed in the southeast of Roraima, northeast of Amazonas, and northwest of Pará states (Cordani and Teixeira, 2007). These nuclei were reworked by Paleoproterozoic events (2260 – 2050 Ma) forming the Maroni-Itacaiúnas Province to the northeast (Tassinari and Macambira, 1999; Tassinari et al., 2000).

One of the most striking characteristic in the Amazonian craton is the abundant A-type intraplate magmatism between 2000 and 1860 Ma (Brito Neves, 2011). The older ~1960 Ma large plutonic and volcanic province includes the "Surumu" magmatism in the Central Amazonian Province in Roraima. The volcanic and plutonic rocks with ages between 1890 and 1860 Ma have generally been referred to as the "Uatumã event" (*sensu stricto*). The associated plutonism (Serra dos Carajás, Cigano, Seringa, Jamon, Musa, Redenção granites, *etc.*) has been studied in detail (See Dall'Agnol et al. (2005) for a review) in the Archean portion of the Central-Brazil Shield. The corresponding volcanic units include the Iriri, Santa Rosa and Iricoumé Formations in northern Brazil. The extension of the Uatumã event may exceed an area larger than 1.500.000 km^2. It forms a 1400 km long NW magmatic belt, considered as a SLIP (Klein et al., 2012). It is worth noting that two younger large intraplate magmatic events also affected the Amazonian Craton: the ~1790 Ma "Avanavero-Crepori" event and the intrusion of an AMCG (anorthosite-mangerite-charnockite-granite) suite between 1600 and 1400 Ma (Sadowski and Bettencourt, 1996; Vigneresse, 2005). The deposition of the ~1870 Ma sedimentary rocks from the Roraima Supergroup in northern Brazil and Venezuela emphasizes the stability of the Amazonian craton (Santos et al., 2003b). To the southwest the Paleo-Mesoproterozoic evolution is marked by the successive accretion of subduction-related juvenile magmatic arcs: the 1980 – 1810 Ma Ventuari-Tapajós, the 1780 – 1600 Ma Rio Negro-Juruena, and the 1550 – 1300 Ma Rondonian-San Ignacio Provinces (Cordani and Teixeira, 2007; Pinho et al., 2003; Schobbenhaus et al., 2003; Tassinari et al., 2000), which culminated with the collision of the Paraguá Terrane at *ca.* 1320 Ma (Bettencourt et al., 2010; Rizzotto and Hartmann, 2012).

The study area (Figure 7.1) is located near to the São Felix do Xingu city in the Rio Maria domain, which corresponds to the southern portion of the Carajás Province (Santos et al., 2003a). This domain is composed by the Archean nucleus of the Central-Brazil Shield in

the Central Amazonian Province (Cordani and Teixeira, 2007), SE of the Pará State. The São Felix do Xingu region is about 300 km far from the ~560 – 520 Ma Araguaia Belt, a Neoproterozoic to Cambrian Brasiliano orogenic system at the eastern border of the Amazonian Craton (Figure 7.1). The Archean TTGs (~2700 Ma Rio Maria granodiorite) and metavolcano-sedimentary units of the Itacaiúnas Supergroup are exposed only to the east of Xingu River (Araújo et al., 1988). Well-preserved ~1880 – 1860 Ma volcanic and plutonic units belonging to the Uatumã SLIP occur across the area. It comprises the 1880 Ma A-type felsic Santa Rosa Formation and the underlying calk-alkaline mafic Sobreiro Formation, which are crosscut by the 1860 Ma A-type tin-bearing granitoid of the Velho Guilherme Suite (Teixeira et al., 2002). The Sobreiro and Santa Rosa Formations were studied in detail by Fernandes et al. (2011), and Juliani and Fernandes (2010). These rocks have been altered by hypogenic hydrothermal fluids (da Cruz et al. (2015); da Cruz et al. (2016)). A brief petrographic review for the Sobreiro and Santa Rosa formations is provided below.

The Sobreiro Formation is the basal unit of the Uatumã event with a flat topography along the Xingu River, but its relation with the Santa Rosa Formation is not well defined (Roverato (2016). The Sobreiro Formation comprises basaltic andesite, andesite and less dacite massive lava flows and volcanoclastic rocks with high-K calk-alkaline signature (Fernandes et al., 2011; Roverato et al., 2017). According to da Cruz et al. (2016) late- to post-magmatic hydrothermal alteration in these rocks is responsible for a secondary paragenesis characterized by epidote, chlorite, carbonate, clinozoisite, sericite, quartz, albite, hematite and pyrite. A prehnite-pumpellyite association is common in the Sobreiro Formation. An age of 1880 ± 6 Ma for this unit was obtained on a dacite by Pb-Pb evaporation on zircon (Pinho et al., 2006).

The Santa Rosa Formation is a thick felsic volcanic formation that usually occupies the topographic highs in the region. Juliani and Fernandes (2010) distinguished four lithological facies: (i) a rhyolitic lava flow and thick dikes of banded rhyolite and ignimbrite, (ii) highly rheomorphic felsic ignimbrite associated with unwelded ash tuff, (iii) felsic crystal tuff, lapilli-tuff, and co-ignimbritic breccias, (iv) granitic porphyry stocks and dikes, and subordinate equigranular granitic intrusions. Two Pb-Pb evaporation ages on zircon of 1884 ± 1.7 Ma and 1879 ± 2 Ma, respectively obtained from an ash tuff and a rhyolite of the Santa Rosa Formation, are reported in Juliani and Fernandes (2010). They interpret the emplacement of these felsic lavas as a dome-shaped structure controlled by two major NE-SW lineaments related to several intrusive episodes. The rocks show an A-type geochemical signature associated with a peraluminous character. They show K-feldspar, euhedral plagioclase, quartz phenocrysts, rare biotite, in a felsic fine-grained groundmass. Spherulitic and granophyric textures are present. Primary accessories are zircon, fluorite, titanite, Fe-Ti oxides, and apatite.

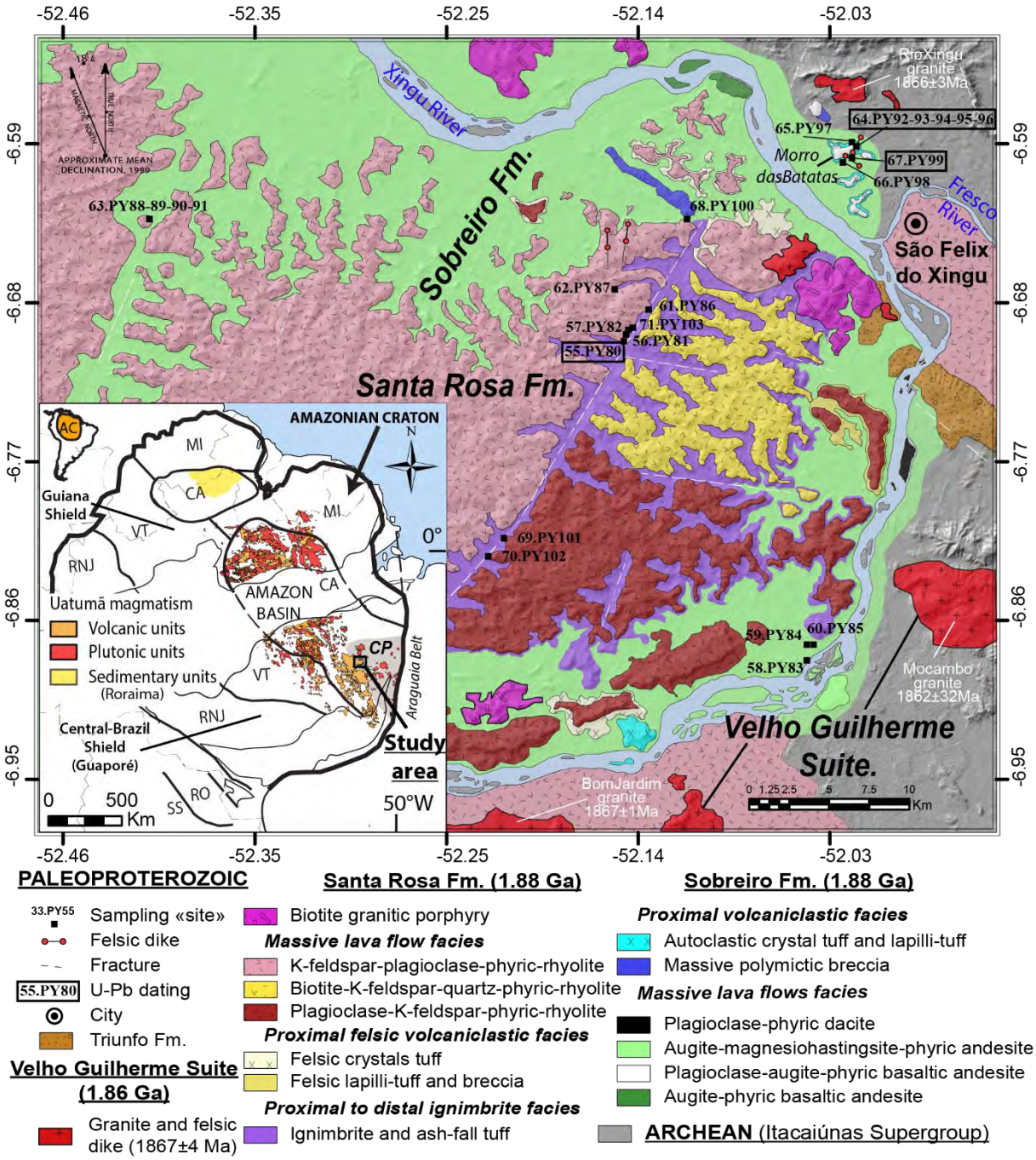

Figure 7.1: Geological map of São Felix do Xingu region with location of sampling sites (Full Square) for Santa Rosa and Sobreiro Formations (adapted from Juliani and Fernandes (2010)). Inset: The ~1880 Ma volcano-plutonic Uatumã event and the main tectonic provinces of the Amazonian craton (adapted from Cordani and Teixeira (2007)). *Abbreviations*: *CP* = Carajás Province (in grey); CA = Central Amazonian Province; MI = Maroni-Itacaiunas Province; VT = Ventuari-Tapájos Province; RNJ = Rio Negro-Juruena Province; RO = Rondonian-San Ignácio Province; SS = Sunsás province.

The ignimbrites show a welded flow-like eutaxitic banded texture. Granite porphyries are massive with a reddish-pink color with K-feldspar, plagioclase, and quartz phenocrysts. Like the Sobreiro Formation, the Santa Rosa Formation shows hydrothermal alteration with secondary minerals such as microcline, sericite, quartz, carbonate, chlorite, gold, clay minerals and Fe-oxides.

The Velho Guilherme Suite (VGS) is represented in the area by plutonic bodies (Antônio Vicente, Serra da Queimada, Rio Xingu, Mocambo, Bom Jardim granites) and associated dikes. These units cut across the volcanics of Santa Rosa and Sobreiro Formations. The Antônio Vicente, Mocambo and Rio Xingu granites are dated at 1867 ± 4 Ma, 1862 ± 16 Ma and 1866 ± 3 Ma, respectively, by Pb-Pb evaporation on zircon (Teixeira et al., 2002).

The geodynamic context for the emplacement of these volcanic rocks is not well established yet. It has been attributed to a large scale extensional magmatic event in the Amazonian craton, hence the notion of SLIP (Ferreira and Lamarão, 2013; Klein et al., 2012). An alternative model involves the migration of a continental magmatic arc from the Tapajós Province to the Xingu Region due to the presence of a E-W flat subduction located to the Serra do Cachimbo region, in the southwestern of the continental plate (Juliani et al., 2009). The A-type nature of most volcanic and granitic rocks favors the intraplate scenario (da Silva et al., 2016).

7.3 Sampling and analytical methods

7.3.1 Paleomagnetism

The São Felix do Xingu region was selected for paleomagnetic sampling because it is one of the most studied areas in the Carajás Province with precise petrology and owns an exceptional amount of *in situ* outcrops (da Cruz et al., 2016; Fernandes et al., 2011; Juliani and Fernandes, 2010). We sampled 18 sites (Table 7.1; Figure 7.1): (i) seven rhyolite lava flows sites (Sites 55, 57, 61, 62, 63, 69, 70), 2 ignimbrite sites (Sites 56, 71), 1 felsic dike (Site 67) and 1 volcanic breccia site (Site 68) from the Santa Rosa Formation, (ii) 6 andesite sites (Sites 58, 59, 60, 64 $_{\text{- samples PY96D-R}}$, 65, 66) from the Sobreiro Formation, (iii) 1 felsic dike from the Velho Guilherme Suite (Site 64 $_{\text{PY92-96A-C}}$). A total of 142 cylindrical samples (~2.54 cm in diameter) and 7 blocks were collected and oriented using in most cases a sun compass and a magnetic compass. Due to the challenging conditions of outcrops (jungle, mature soils), the lithological contacts are difficult to observe in the region. Nevertheless, it was possible to perform a baked contact test (Buchan et al., 2007) at site 64 where a composite NE-trending felsic dike of the Velho Guilherme Suite intrudes a volcanoclastic deposit (andesitic composition) of the Sobreiro Formation at Morro das Batatas (Figure 7.1). The dike is a ~10 m thick composite dike with a complex ramification. A 30 cm thick chilled margin shows that the dike was emplaced into cooler rocks. Three cylindrical cores (PY96$_{\text{A-B-C}}$) and 4 oriented blocks (PY92-93-94-95 in Table 7.1) were sampled from the dike. The host andesite from the Sobreiro Formation is visible across more than 100 meters after the contact which allowed sampling 14

cylindrical cores at several distances from the contact: three at 0 – 5 cm (PY96D, E, R), three at 20 cm (PY96F, G, H), one at 1 m (PY96J), one at 3 m (PY96K), one at 6 m (PY96L), one at 10 m (PY96M), and four at ~20 m (PY96N-Q).

Preparation and analysis of the samples were performed in the Laboratório de Paleomagnetismo - Universidade de São Paulo (USPmag). Extracted cylindrical cores in the field and from sampled blocks were cut in 2.2 cm high standards specimens (total of 505). Magnetic susceptibility and anisotropy of magnetic susceptibility (AMS) were measured using a KLY-4S Kappabridge (AGICO, Czech. Republic) with a sensitivity of 2×10^{-8} SI. In order to isolate a characteristic remanent magnetization (ChRM), conventional stepwise alternating field (AF) and thermal demagnetization were performed in a magnetically-shielded room with ambient field <1000 nT. Steps of 2.5 mT (up to 15 mT) and 5 mT (15 – 100 mT) were selected for AF demagnetization. Devices used were a tumbler Molspin AF demagnetizer coupled to a JR-6A spinner magnetometer (AGICO, Czech Republic) to measure the remanence, an automated three-axis AF demagnetizer coupled to a horizontal 2G-Enterprises™ DC-SQUID magnetometer, and an AF demagnetization coils coupled to a vertical 2G-Enterprises™ DC-SQUID magnetometer with an automatic RAPID sample changer (Kirschvink et al., 2008). Thermal demagnetization comprised steps of 50 °C (until 500 °C) and 20 °C (until 700 °C) using a TD-48 furnace (ASC Scientific). A combination of AF and thermal cleaning was carried out for specimens with a high coercitivity component. Principal component analysis (Kirschvink, 1980) was used to determine the remanence directions using orthogonal vector diagrams (Zijderveld, 1967). Only vectors with mean angular deviation (MAD) smaller than 8° were considered. For some sites, remagnetization great circles analysis (Halls, 1978) was also employed to determine high coercivity/high-blocking temperature components. Site-mean directions and paleomagnetic poles were calculated using Fisher's statistics (Fisher, 1953). Paleomagnetic data processing was carried out using REMASOFT, GMAP, and Super-IAPD software (Chadima and Hrouda, 2006; Torsvik et al., 2000; Torsvik and Smethurst, 1999). Velocity of the different cratons between 2100 – 1200 Ma was calculated using PMTec (Wu et al., 2015) with 20 Ma time windows at 5 Ma steps. Paleomac (Cogné, 2003) and GPlates were used for great circle calculations and paleogeographic reconstructions (Boyden et al., 2011).

Site	Sample	Localization	Lithology	Geochronology
Santa Rosa Formation				
55	PY80	6.7°S/307.85°E	Rhyolite lava flow	1877.4 ± 4.3 Ma U-Pb zrn (**this study**)
56	PY81	6.69°S/307.85°E	Ignimbrite	
57	PY82	6.69°S/307.85°E	Rhyolite lava flow	
61	PY86	6.68°S/307.87°E	Rhyolite lava flow	
62	PY87	6.67°S/307.85°E	Rhyolite lava flow	
63	PY88 - 89 -90 -91	6.63°S/307.59°E	Rhyolite lava flow	
67	PY99	6.6°S/307.98°E	Felsic microgranite dike - coarse grained	1895 ± 11 Ma U-Pb zrn (**this study**)
68	PY100	6.63°S/307.89°E	Volcanoclastic breccia	
69	PY101	6.81°S/307.79°E	Rhyolite lava flow	
70	PY102	6.82°S/307.78°E	Rhyolite lava flow	
71	PY103	6.69°S/307.86°E	Ignimbrite	
Sobreiro Formation				
58	PY83	6.88°S/307.96°E	Volcaniclastic deposit (andesitic)	
59	PY84	6.87°S/307.96°E	Volcaniclastic deposit (andesitic)	
60	PY85	6.87°S/307.96°E	Volcaniclastic deposit (andesitic)	
	PY96 $_{D-R}$	6.59°S/307.98°E	Volcaniclastic deposit (andesitic)	
	PY96 $_{D, E, R}$	6.59°S/307.98°E	Volcaniclastic deposit (andesitic) - *BCT:* < 5 cm at contact	
	PY96 $_{F, G, H}$	6.59°S/307.98°E	Volcaniclastic deposit (andesitic) - *BCT:* 5-20 cm from the contact	
	PY96J	6.59°S/307.98°E	Volcaniclastic deposit (andesitic) - *BCT:* 1 m from the contact	
64*	PY96K	6.59°S/307.98°E	Volcaniclastic deposit (andesitic) - *BCT:* 3 m from the contact	1880 ± 6 Ma Pb-Pb zrn (Pinho et al., 2006)
	PY96L	6.59°S/307.98°E	Volcaniclastic deposit (andesitic) - *BCT:* 6 m from the contact	
	PY96M	6.59°S/307.98°E	Volcaniclastic deposit (andesitic) - *BCT:* 10 m from the contact	
	PY96 $_{N-Q}$	6.59°S/307.98°E	Volcaniclastic deposit (andesitic) - *BCT:* 20 m from the contact	
65	PY97	6.59°S/307.98°E	Volcaniclastic deposit (andesitic)	
66	PY98	6.6°S/307.98°E	Volcaniclastic deposit (andesitic)	
Velho Guilherme Suite				
64*	PY92 - PY93 - PY96 $_{A-C}$	6.59°S/307.98°E	Felsic microgranite dike - fine grained (Chilled margin)	1853.7 ± 6.2 Ma U-Pb zrn (**this study**)
	PY94 - PY95	6.59°S/307.98°E	Felsic microgranite dike - coarse grained	

Table 7.1: Paleomagnetic sampling in São Felix do Xingu region.

*: Site sampled for the baked contact test (BCT) - distances from the contact are indicated.

The magnetic mineralogy was investigated on selected specimens to determine the carriers of magnetic remanence. Hysteresis loops and isothermal remanent magnetization (IRM) curves were determined using a MicroMag-VSM Model 3900 (Princeton Measurements Corporation). Thermomagnetic experiments (susceptibility versus temperature) were conducted in argon atmosphere in low and high temperature conditions using a CS-4 apparatus coupled to the KLY-4S Kappabridge instrument (AGICO, Czech Republic). Thin and polished sections were studied under transmitted and reflected light microscopy and scanning electron microscopy (SEM) for mineralogy and texture analysis.

7.3.2 Geochronology

We selected samples from representative paleomagnetic results for U-Pb age determination to upgrade previously published Pb-Pb ages for the same formations: (i) one rhyolite (PY80B2) and one associated dike (PY99) from Santa Rosa Formation, (ii) one dike (PY92B1) from the Velho Guilherme Suite. Before analysis, zircons were characterized by cathodoluminescence (CL) and back-scattered electron (BSE) images using scanning electron microscopy (SEM) (Figure 7.2).

Two different dating techniques were used in this study: (i) zircon crystals from one dike of the Santa Rosa Formation (PY99) were analyzed by the Sensitive High Resolution Ion Microprobe (SHRIMP) at the Centro de Pesquisas Geocronológicas (CPGeo) of the Instituto de Geociências, Universidade de São Paulo (IGc-USP), (ii) zircon crystals from the Santa Rosa lava flow (PY80B2) and of a Velho Guilherme dike (PY92B1) were analyzed in-situ on polished sections by Laser Ablation Inductively Coupled Plasma Mass Spectrometry (LA-ICP-MS) at the Universidade Federal de Ouro Preto (UFOP), Minas Gerais State, Brazil.

SHRIMP analyzes were performed during one session using a SHRIMP IIe/MC. The primary beam was set with Kohler aperture = 120 µm, spot size = 30 µm, and O-2 beam density = 2.5 – 7 ηA (dependent of brightness aperture), and the secondary beam was set with source slit = 80 µm; mass resolutions for 196 (Zr_2O), ^{206}Pb, ^{207}Pb, ^{208}Pb, ^{238}U, 248 (ThO) and 254 (UO) ranging between 5,000 and 5,500 (1%), and residues < 0.025. Data were reduced with SQUID 1.06 software, and Concordia diagrams were plotted with ISOPLOT 4 (Ludwig, 2009). Common lead corrections usually use ^{204}Pb according to Stacey and Kramers (1975). Temora 2 standard was used as ^{206}Pb/^{238}U ages reference every ten analyses (416.78 Ma, Black et al. (2004)) and provided a weighted mean of standard deviation in Pb/U of 0.003524 (1σ, n= 19, MSWD = 8.60).

ICP-MS analyses were performed during two sessions using a ThermoScientific Element 2 coupled to a LSX-213 G2 laser (CETAC Technologies) with a 20 µm laser spot size. The data were reduced with the software Glitter (Van Achterbergh et al., 2001) and ages were calculated using the ISOPLOT 4 (Ludwig, 2009) program with dating uncertainties at the 2 sigma level. The GJ-1 standard zircon (608.5 ± 0.4 Ma by ID-TIMS) (Jackson et al., 2004) was used for the calibration of the U-Pb analysis in association with the Plešovice secondary standard (337.13 ± 0.37 Ma by ID-TIMS) (Sláma et al., 2008) to test the accuracy of the results each ten analysis. GJ-1 standard zircon gave Concordia ages of 607.00 ± 0.91 Ma (2σ, n= 29, MSWD = 0.42) and 606.1 ± 1.6 Ma (2σ, n= 11, MSWD = 4.3) for the two sessions, respectively. The Plešovice secondary standard gave Concordia ages of 336.80 ± 0.73 Ma (2σ, n= 13, MSWD = 0.87) and 337.6 ± 3.3 Ma (2σ, n= 7, MSWD = 3.4) for the two sessions, respectively. Calculated ages for the two standards are consistent with the reference values.

7.4 U-Pb Geochronology

7.4.1 Zircon morphology

Zircons from the Santa Rosa rhyolite sample PY80B2 are associated with oxides (martite – Fe_2O_3, Mt). They are euhedral to subeuhedral with typical growth zoning in cathodoluminescence (CL) images pointing to a magmatic crystallization (Figure 7.2-A). Zircons separated from the dike of the same unit (sample PY99) are euhedral 250 µm in size and also show growth zoning and inclusions (Figure 7.2-C). Zircons from the Velho Guilherme Suite dike (PY92B1) show a range of morphologies from euhedral to subeuhedral with different types of magmatic zoning and usually contain apatite inclusions suggesting hydrothermal processes during the formation of these rocks (Figure 7.2-B). Zircons studied here, show features of magmatic crystallization without overgrowth and recrystallization, suggesting a magmatic origin.

7.4.2 U-Pb geochronology results

Eight zircons from the rhyolite flow (PY80B2) show ages between 1890 and 1867 Ma (Table 7.2). An upper intercept of 1877.4 ± 4.3 Ma (MSWD = 1.7, probability = 0.099) was calculated for this sample that likely represents the emplacement age of the Santa Rosa rhyolite (Figure 7.2-A). It was also possible to calculate a Concordia age of 1879.6 ± 7.4 Ma (MSWD = 5.2, probability = 0.023) using a cluster of four zircons. The weighted average age for the eight zircons is 1877 ± 14 Ma (MSWD = 0.22, probability = 0.98). The other sample from the Santa Rosa Formation corresponds to the PY99 dike for which SHRIMP analyses were performed. For this sample, nine analyzed zircons yielded an upper intercept of 1895 ± 11 Ma (MSWD = 1.7), which agrees with the weighted age of 1896 ± 17 Ma (MSWD = 1.7)

(Figure 7.2-C). These results are *ca.* 20 – 40 Ma older than the NE-trending dike from the Velho Guilherme Suite (see below), confirming it must belong to the vein system that originated in the Santa Rosa Formation.

The ages for the NE-trending dike of the Velho Guilherme Suite (PY92B1) range between 1867 and 1841 Ma. These ages are slightly younger than those from the rhyolite PY80B2 and from the PY99 felsic dike (Table 7.2). The upper intercept calculated using eight zircons is 1853.7 ± 6.2 Ma (MSWD = 1.2, probability = 0.30) (Figure 7.2B). Recent Pb loss or alteration of zircon grains resulted in three discordant ages. The remaining five concordant zircon ages were used to calculate a Concordia age of 1853.3 ± 3.8 Ma (MSWD = 1.8, probability = 0.18). The weighted average age is 1852 ± 15 Ma (MSWD = 0.20, probability = 0.99).

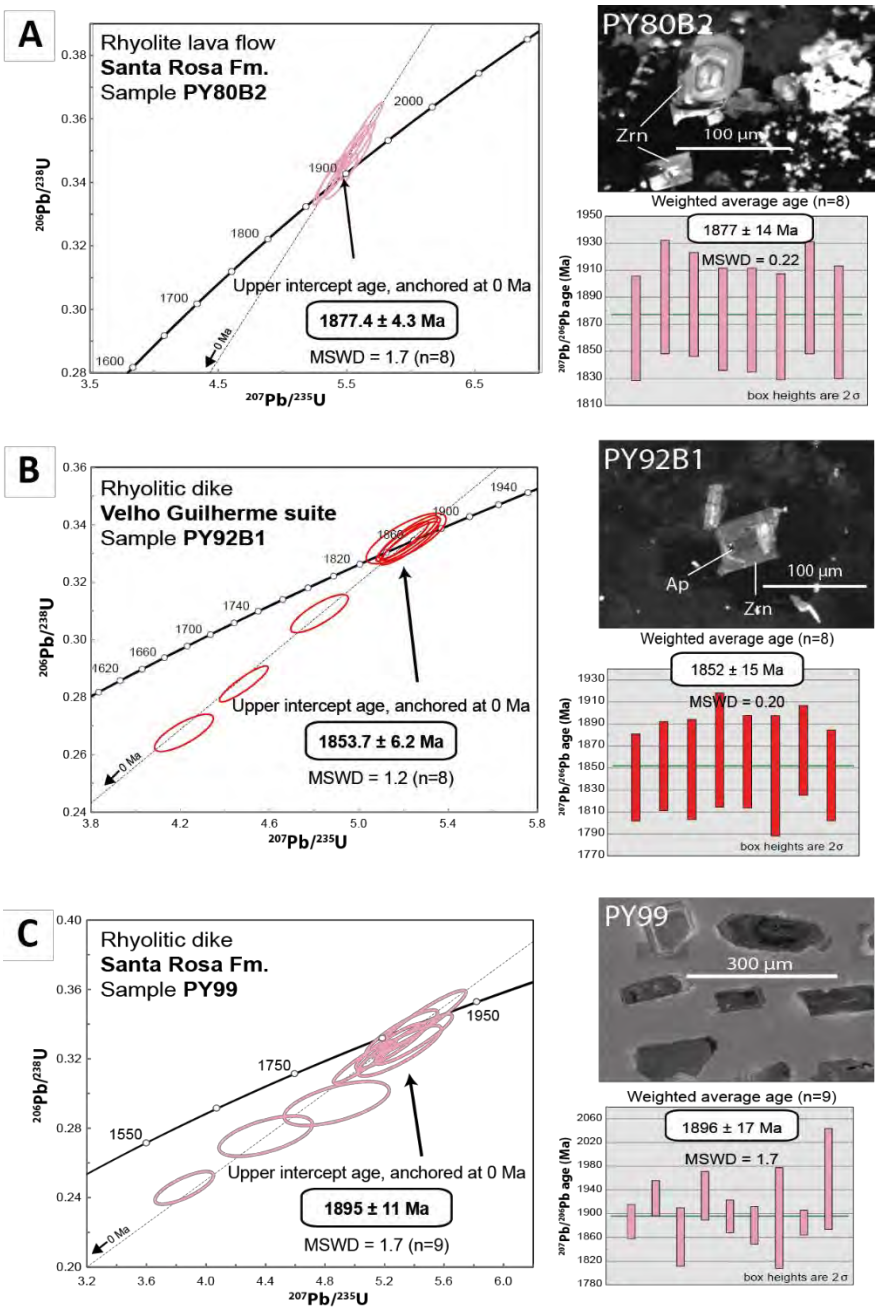

Figure 7.2: (A) Concordia diagrams showing U-Pb zircon LA-ICP-MS results for the rhyolite lava flow sample (PY80B2) and cathodoluminescence (CL) images of typical zircon grains for the sample with the weighted average age. (B) Concordia diagrams showing U-Pb zircon LA-ICP-MS results for the sample of the NE-dike (PY92B1) and cathodoluminescence images of typical zircon grains for the Velho Guilherme Suite with the weighted average age. (C) Concordia diagrams showing U-Pb zircon SHRIMP results for the NW-dike (PY99) and cathodoluminescence images of typical zircon grains for the dike of the Santa Rosa Formation with the weighted average age.

Table 7.2: Zircon U–Pb data obtained by in situ laser ablation ICP-MS and SHRIMP.

Analysis	Th/U	Isotopic ratios							Ages (Ma)				Conc. (%)
		$^{207}Pb/^{206}Pb$	± 1σ	$^{207}Pb/^{235}U$	± 1σ	$^{206}Pb/^{238}U$	± 1σ	ρ	$^{207}Pb/^{206}Pb$	± 1σ	$^{206}Pb/^{238}U$	± 1σ	
***Rhyolite lava flow - Santa Rosa formation* (PY80B2) - LA-ICP-MS**													
PY80B2 #021	0.43	0.1142	0.0012	5.3573	0.0478	0.3399	0.0028	0.94	1867	19	1886	14	100.4
PY80B2 #036	0.46	0.1157	0.0014	5.5540	0.0559	0.3480	0.0031	0.87	1890	21	1925	15	100.8
PY80B2 #039	0.45	0.1153	0.0012	5.5967	0.0511	0.3517	0.0030	0.94	1885	19	1943	14	101.4
PY80B2 #040	0.31	0.1146	0.0012	5.6628	0.0498	0.3579	0.0030	0.96	1874	19	1972	14	102.4
PY80B2 #043	0.42	0.1146	0.0012	5.5412	0.0520	0.3505	0.0031	0.94	1873	19	1937	15	101.5
PY80B2 #044	0.37	0.1143	0.0013	5.3855	0.0487	0.3414	0.0029	0.92	1868	20	1894	14	100.6
PY80B2 #045	0.45	0.1156	0.0013	5.4570	0.0529	0.3419	0.0029	0.88	1890	21	1896	14	100.1
PY80B2 #047	0.47	0.1145	0.0013	5.4090	0.0528	0.3423	0.0030	0.88	1872	21	1898	14	100.6
NE-*Dike* - *Velho Guilherme suite* (PY92B1) - LA-ICP-MS													
PY92B1 #027	1.35	0.1126	0.0012	5.1945	0.0482	0.3342	0.0028	0.91	1841	20	1859	14	100.4
PY92B1 #028	1.00	0.1132	0.0013	5.2353	0.0530	0.3349	0.0031	0.91	1852	20	1862	15	100.2
PY92B1 #029	1.23	0.1130	0.0014	4.8234	0.0526	0.3091	0.0027	0.80	1849	23	1736	13	96.9
PY92B1 #031	0.54	0.1142	0.0017	4.2162	0.0539	0.2676	0.0027	0.78	1867	26	1528	13	90.3
PY92B1 #036	0.78	0.1135	0.0013	5.2250	0.0540	0.3336	0.0031	0.89	1856	21	1856	15	99.9
PY92B1 #037	0.69	0.1127	0.0017	5.2117	0.0730	0.3352	0.0036	0.76	1843	27	1864	17	100.5
PY92B1 #038	0.64	0.1141	0.0013	4.4842	0.0445	0.2846	0.0026	0.90	1866	20	1614	13	93.0
PY92B1 #051	1.02	0.1127	0.0013	5.2209	0.0538	0.3356	0.0031	0.89	1843	21	1866	15	100.5
NW-*Dike* - *Santa Rosa formation* (PY99) - SHRIMP													
PY99 #1.1	1.12	0.1155	0.7900	5.4529	2.2325	0.3425	2.0881	0.94	1887	14	1899	34	100.7
PY99 #3.1	0.97	0.1180	0.8338	5.3993	1.9633	0.3318	1.7775	0.91	1926	15	1847	29	95.3
PY99 #5.1	0.73	0.1138	1.3683	3.8580	2.0808	0.2458	1.5677	0.75	1861	25	1417	20	73.4
PY99 #6.1	1.12	0.1183	1.1394	5.3020	2.1674	0.3251	1.8437	0.85	1931	20	1814	29	93.1
PY99 #7.1	1.17	0.1160	0.7687	5.2441	1.8267	0.3278	1.6571	0.91	1896	14	1828	26	95.9
PY99 #9.1	1.15	0.1151	0.8780	5.3175	1.8610	0.3352	1.6409	0.88	1881	16	1863	27	98.9
PY99 #10.1	1.61	0.1159	2.3562	4.4019	2.9168	0.2756	1.7193	0.59	1893	42	1569	24	80.7
PY99 #12.1	0.66	0.1154	0.5879	5.0709	1.6963	0.3188	1.5912	0.94	1886	11	1784	25	93.8
PY99 #13.1	1.18	0.1202	2.3784	4.8810	2.9597	0.2946	1.7615	0.60	1959	42	1664	26	83.0

7.5 Paleomagnetic results

Rocks from the São Felix do Xingu area show three characteristic components (ChRM) after thermal and AF treatment, with thermal treatment being generally more efficient than AF demagnetization (Figure 7.3). Thermal demagnetization provided better resolution of the trajectories due to the hematite.

Component SF1 was retrieved from eight sites of the Santa Rosa Formation and two sites of the Sobreiro Formation. It corresponds to a stable, steep positive (negative) inclination ChRM isolated after AF and thermal demagnetization (Figure 7.3-A-B-C-D-F). This ChRM direction has unblocking temperatures between 620 °C and 700 °C, the magnetic vector always moving toward the origin in the orthogonal diagram. NRM intensities vary between 0.59 A/m and 1.44 A/m, which are common values for rhyolitic rocks carrying high coercitivity/blocking temperature minerals such as hematite (Dunlop, 1997). Four sites show 'normal' polarity and six sites a 'reverse' polarity so that a reversal test was performed (McFadden and McElhinny, 1990). Nevertheless, despite the similar mean direction for 'normal' (N) and 'reverse' (R) polarities, the test resulted indeterminate, probably due to the small number of sites (10). To circumvent this problem, we used specimen's directions to calculate mean directions for the 'normal' and 'reverse' polarities: Dm= 311.6°, Im= -80.0° (N= 59, R= 55.82) and Dm= 92.7°, Im= 84.6° (N= 29, R= 27.93), respectively. The reversal test now resulted in a critical gamma of 7.3°, which is greater than the angle between the normal and reversed axes. So, it can be considered as positive and classified with quality "B" according to McFadden and McElhinny (1990). Using the specimen directions, the mean SF1 component is Dm= 123.6°, Im= 81.8° (N= 88, α_{95}= 3.5°, k= 19.9). Site mean directions for the 10 sites (N and R polarity) cluster around the mean Dm= 149.2°, Im= 79° (a95= 9.6°, k= 26.4), yielding to a SF1 paleomagnetic pole of Plat= 24.7°S and Plong= 319.7°E (A_{95}= 16.9°) (Table 7.3 – Figure 7.4).

Component SF2 is a southwest/northeast and low inclination direction present in 15 analyzed sites. For rhyolites of the Santa Rosa Formation this component is may be found together with component SF1 (Figure 7.3-A-B-F). It is also observed in four sites of the Sobreiro andesites (Figure 7.3-D), and in the felsic dike of the Velho Guilherme Suite, where it was isolated by the AF treatment (Figure 7.3-E). This component is always characterized by unblocking temperatures between 520 – 580°C, and coercivities between 10 and 100 mT, suggesting it is carried by magnetite, in contrast with component SF1, which is normally carried by hematite. A baked contact test for this component is presented hereafter for site 64. The

mean site for the SF2 component is Dm= 239.2°, Im= 10.6° (N= 15, α_{95}= 12.4°, k= 10.5), yielding to a paleomagnetic pole of Plat= 31.1°S and Plong= 220.1°E (A_{95}= 9.7°) (Figure 7.4).

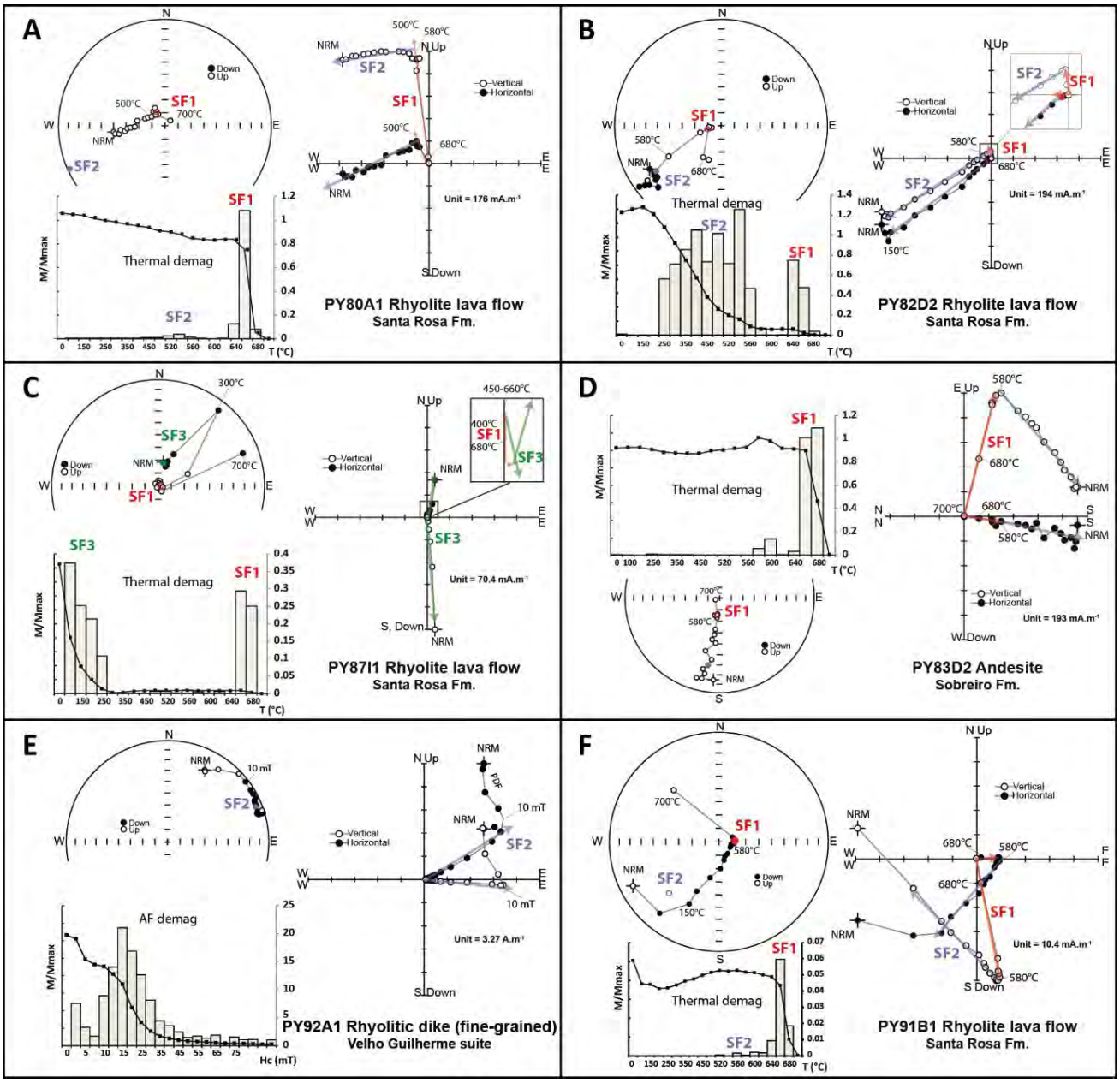

Figure 7.3: Examples of AF (alternating field) and thermal demagnetization for samples of the Santa Rosa Formation, Sobreiro Formation and Velho Guilherme Suite. Demagnetization results presented with stereographic projections, orthogonal projections (Zijderveld plot) and normalized magnetization intensity curves (M/M_0 versus alternating field H).

Component SF3 is a northerly direction with positive inclination (Figure 7.3-C). It was isolated in the NW-trending dike of the Santa Rosa Formation, well-dated at 1895 ± 11 Ma. The component SF3 is different from components SF1 and SF2, despite a possible overlapping between SF1 and SF3. It is found in all the studied units, being usually isolated at lower unblocking temperatures (100 – 200°C) (Figure 7.3-C). The presence of SF3 in 14 sites from different lithologies of different ages suggests that it may be an overprint. The mean for the

SF3 direction is Dm= 0.9° Im= 61.5° (α_{95}= 11.9°, k= 12.2), yielding to a paleomagnetic pole of Plat= 40.7°S and Plong= 128.8°E (A_{95}= 15.6°) (Figure 7.4).

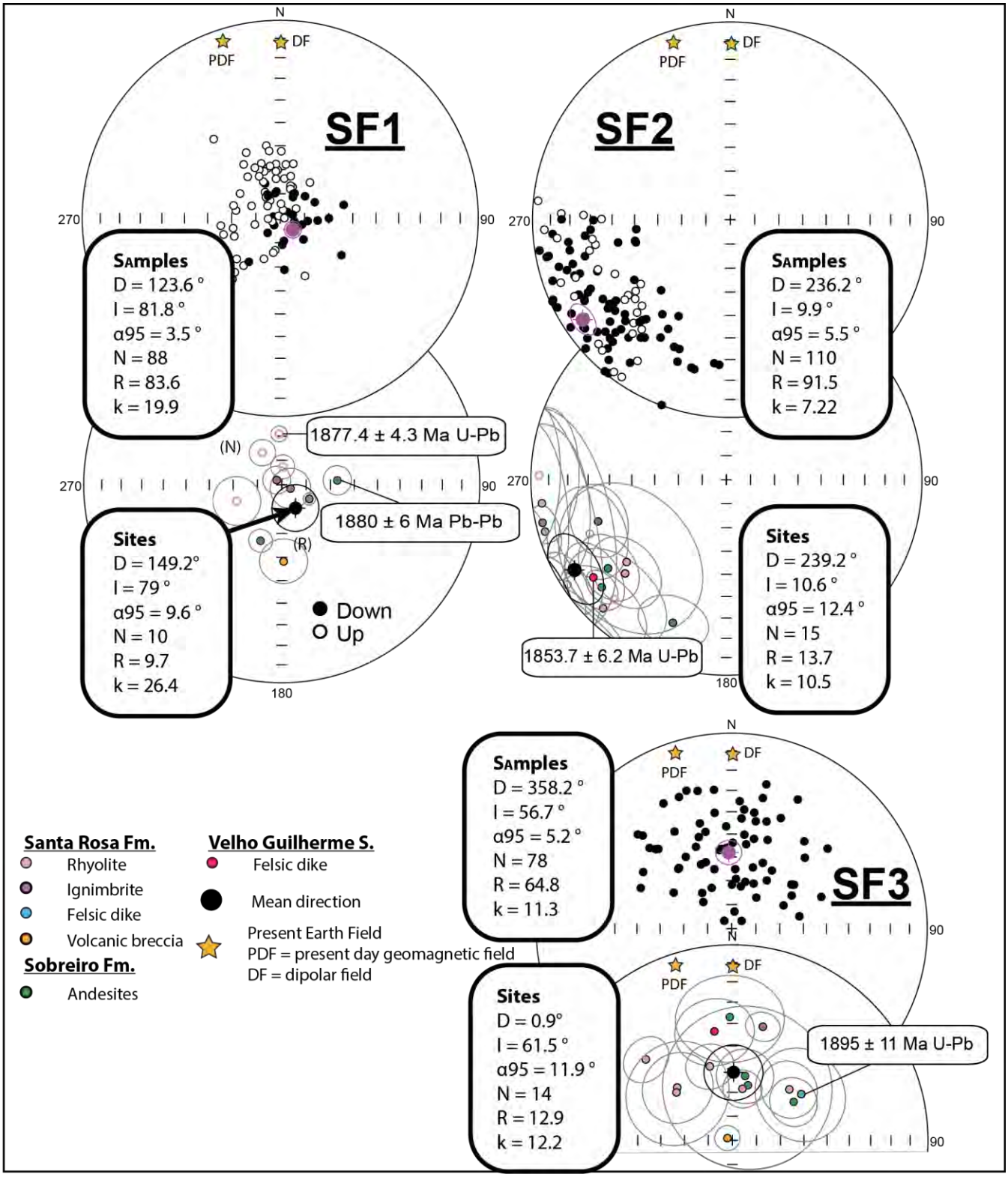

Figure 7.4: Stereographic projections of sample and site mean directions for the sites analyzed. Boxes show mean directions and Fisherian statistical parameters for the four mean directions (SF1, SF2 and SF3).

Site	Sample	Characteristic remanent magnetization (ChRM)					VGP	
		n/N	Dec (°)	Inc (°)	k	α95 (°)	P.Lat (°N)	P.Long (°E)
Component SF1 (~1880 Ma)								
SF1 normal polarity (N)								
55	PY80	13/14	357	-69	154.1	3.3	44.2	130.4
57	PY82	14/14	250.1	70.3	17.2	9.9	-5.8	161.2
61	PY86	10/11	3.2	82.6	97.6	4.9	21.2	127
62	PY87	15/15	328.9	74.6	51.3	5.4	30.8	144.7
Mean sites SF1 N-polarity		4	322.1	78.8	31.7	16.6	23.4	142.2
Mean specimens SF1 N-polarity		**59**	**311.6**	**-80**	**18.3**	**4.4**	**19.2**	**143.2**
SF1 reversed polarity (R)								
63	PY91	8/15	113.2	86.1	45.2	8.3	9.6	134.8
56	PY81	10/14	313.6	87.2	71.8	5.7	2.8	123.8
71	PY103	5/13	117.1	77.3	*G.C*	2.5	17	150.3
68	PY100	12/17	178.6	58.2	*G.C*	9.5	57.7	129.9
58	PY83	10/17	200.7	65.3	*G.C*	4.8	45.8	107.9
64	PY96	12/33	85.5	67	*G.C*	5.9	2.1	168.2
Mean sites SF1 R-polarity		**6**	**154**	**79.1**	**20.4**	**15.2**	**25.4**	**137.9**
Mean specimens SF1 R-polarity		**29**	**92.7**	**84.6**	**26.2**	**5.3**	**7.1**	**138.7**
Component SF2 (~1860 Ma)								
SF2 normal polarity (N)								
64	PY9293949596	8/15	53.7	16.7	19.9	12.7	36.8	43.7
64	PY96	20/33	56.6	3	10.3	10.7	33	31.9
59	PY84	9/11	72	31.6	15.6	13.5	19.2	53.7
65	PY97	6/15	68.4	25.8	16.7	16.9	19.2	21.1
Mean sites SF2 N-polarity		**4**	**62.2**	**-5**	**9.7**	**31.1**	**27.9**	**37.2**
SF2 reversed polarity (R)								
55	PY80	4/14	254	4	126.1	8.2	16.1	38
57	PY82	12/14	223.8	9.7	8.3	16	46.4	37.9
61	PY86	6/11	262.7	5.5	8.5	24.3	7.5	39.8
62	PY87	2/15	271.3	-4.7	145.4	20.9	-1.5	35.7
63	PY91	7/15	223.1	17.3	10.5	19.6	44.3	18.3
69	PY101	5/11	230.5	34.2	7.3	30.5	39.6	56.5
70	PY102	3/12	227.2	30.1	73.7	14.5	42.9	53.6
56	PY81	3/14	256.8	3.9	13.7	34.7	13.4	38.3
58	PY83	15/17	233.2	25.3	9.8	12.9	37.3	49.5
60	PY85	7/10	200.5	22.9	23.9	12.6	69.2	53.5
66	PY98	3/17	229.2	16.9	357.8	6.5	41.2	43.7
Mean sites SF2 R-polarity		**11**	**238.1**	**12.7**	**10.1**	**15.1**	**32.3**	**41.3**
Component SF3 (~550 Ma)								
55	PY80	6/14	48.1	57.9	32.9	11.8	26.5	348.5
61	PY86	4/11	313.8	57.9	40	14.7	27.7	268.3
62	PY87	13/15	343	57.5	19.2	9.7	42.5	289.6
63	PY91	4/15	313.1	39.2	95.8	9.4	35.8	251.1
69	PY101	2/11	310.6	59.1	135.2	21.6	24.8	267.9
70	PY102	3/12	10.9	68.1	240	8	31.2	315.7
56	PY81	9/14	350.1	51	61.3	6.6	50.5	294.6
71	PY103	8/13	15	39.6	71.7	6.6	57.4	334.3
64	PY9293949596	6/15	350.6	42.9	20.4	15.2	57.2	292.2
67	PY99	4/4	56.1	55.1	24.2	19.1	22.6	354.9
59	PY84	2/11	15.8	66.1	52.9	35	33	320.4
64	PY96	4/33	11.1	62.5	64.1	11.6	38.6	318.3
65	PY97	5/15	358.8	37	15.2	20.3	62.7	305.5
66	PY98	2/17	57.8	59.7	625.7	10	19.1	350.9

Poles	Mean direction					Paleomagnetic pole	
	N	D_m (°)	I_m (°)	k/K	α95 (°)/A95 (°)	Lat (°N)	Long (°E)
Pole SF1 (N + R)	10	149.2	79	26.4/9.17	9.6/16.9	-24.7	319.7
Pole SF2 (N + R)	15	239.2	10.6	10.5/16.46	12.4/9.7	-31.1	220.1
Pole SF3	14	0.9	61.5	12.2/6.6	11.9/15.6	-40.7	128.8

Table 7.3: n/N – number of analyzed samples/number of samples used in the mean; Dec. – declination; Inc. – inclination; α_{95}, k – Fisher's confidence cone and precision parameter (Fisher, 1953); *G.C* –Great circles analysis. VGP – Virtual Geomagnetic Pole; P. Long – Paleolongitude; P. Lat – Paleolatitude. VGPs values are indicated after switching to the antipodal position.

7.6 Baked contact test

The baked contact test was performed at site 64 (PY92-93-94-95-96) where a ~10 meters thick NE-trending dike of the Velho Guilherme Suite cuts the volcaniclastic Sobreiro andesites (Table 7.1, Figure 7.5). It is a composite dike system well-dated at 1853.7 ± 6.2 Ma (this study). The host andesites yielded a Pb-Pb age of 1880 ± 6 Ma (Pinho et al., 2006) on zircon. Samples from the dike show northeastern directions with low downward inclinations (PY92A1), corresponding to SF2 component (Figure 7.5). Baked contact rocks present the same SF2 component as shown, for example, in sample PY96D1-1 collected at 0.2 cm from the contact (Figure 7.5). A hybrid zone is represented in sample PY96J1 collected 1 m away from the contact, where a SF2 direction was disclosed between 0 and 15 mT and another more stable component is disclosed at higher coercivities > 50 mT or with unblocking temperatures between 580 – 700°C. This component, carried by hematite, is similar to the SF1 component isolated in the lava flows of the Santa Rosa Formation. At greater distances from the contact, the component SF1 (580 – 700°C) is always observed, as shown by samples PY96-K2 (at 3 m) and PY96P1 (at 20 m in Figure 7.5). Hydrothermal alteration randomly affected the host volcanoclastic rock (andesitic). For specimen PY96J1 we observe an intense alteration with chlorite, hematite and even covellite being formed at the expenses of amphibole. In contrast, in specimen PY96K hematite is absent and the main oxides are large magnetite grains showing exsolution of ilmenite.

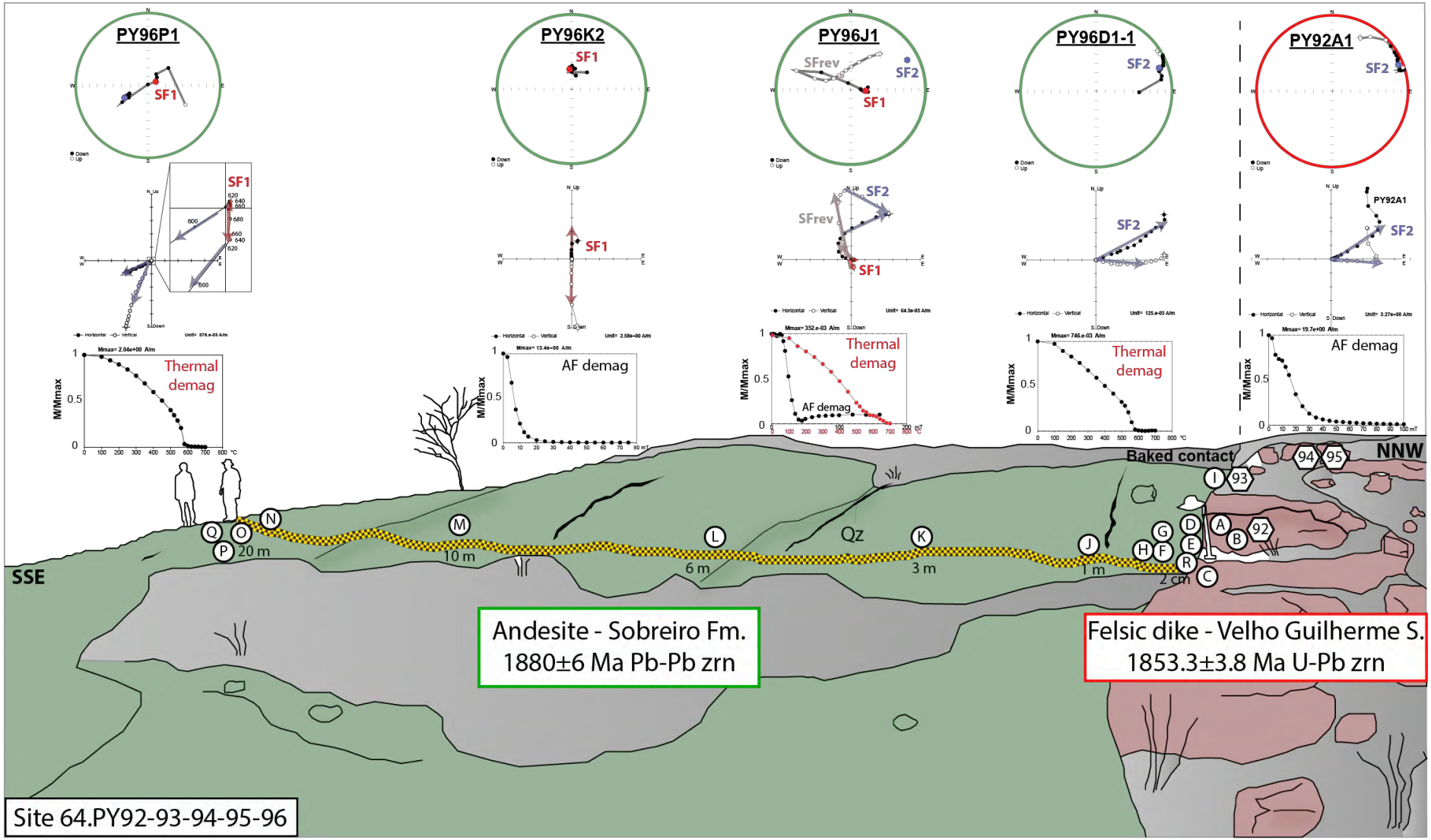

Figure 7.5: Baked contact test for a felsic dike of the Velho Guilherme Suite intruding the Sobreiro Formation. The figure shows the locations of the samples and the distance from the contact, stereographic projections, orthogonal projections, and normalized magnetization intensity curves for samples. The different components are illustrated with arrows.

7.7 Magnetic mineralogy

IRM curves were acquired for 25 specimens and four representative examples are illustrated in Figure 7.6. After unmixing of IRM curves by using cumulative log Gaussian functions (Kruiver et al., 2001), two or three magnetic components of different coercivities were identified. In felsic samples of the Santa Rosa Formation (both rhyolites and ignimbrites) two components are generally identified (Figure 7.6-A). In all samples of rhyolites and ignimbrites the main component has coercivities between 400-1122 mT. This component contributes between 53 – 95% to the total remanence and the values of $B_{1/2}$ and DP (dispersion parameter) are typical of a high coercivity mineral like hematite (Figure 7.6-E). The second magnetic component has a $B_{1/2}$ of 32 mT for the ignimbrite PY81E. The contribution of this magnetic component to the total remanence varies between 3 – 43% except for site PY91C where it reaches 87%. The characteristic association between magnetite and hematite is also found in andesites of the Sobreiro Formation (Figure 7.6–C). In contrast, sample PY96A from the Velho Guilherme Suite dike (Figure 7.6-B) does not contain the high coercivity component, and in the andesite specimen PY96K it is possible to divide the IRM curve into two components "hard magnetite" and "soft magnetite" (Figure 7.6-D).

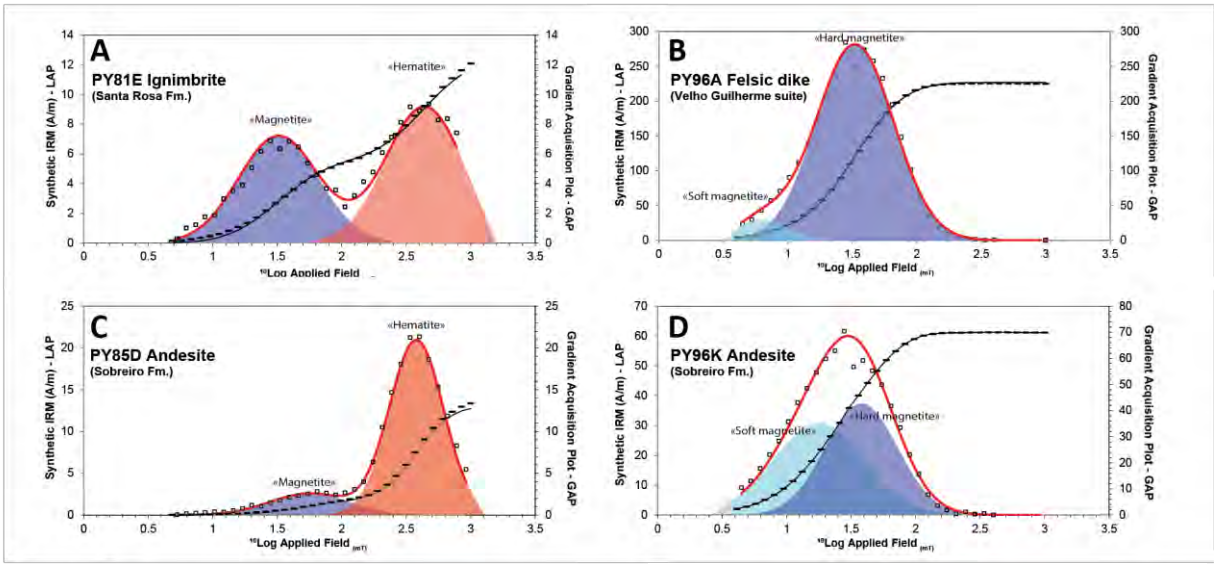

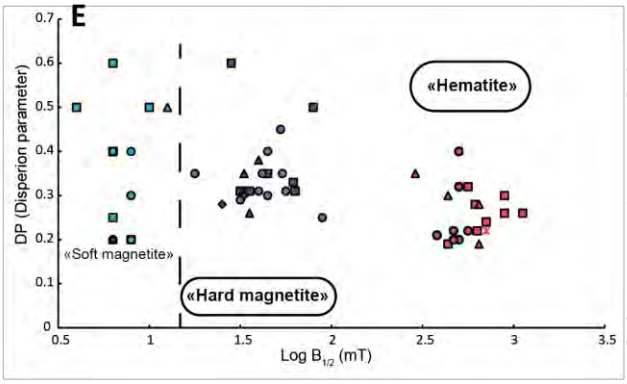

Figure 7.6: Examples of characteristic isothermal remanent magnetization (IRM) after Kruiver's analysis by cumulative log-Gaussian (CLG) function, gradient acquisition plot (GAP) in red. (A) An ignimbrite showing contribution of two ferromagnetic phases with different coercivities (magnetite and hematite). (B) IRM for the felsic dike of the Velho Guilherme Suite with one mean coervity ("hard magnetite") and a very weak component ("soft magnetite"). (C) IRM for an andesite of the Sobreiro Formation with two ferromagnetic phases (magnetite and hematite). (D) IRM for an andesite with two components of near coercivity (soft and hard magnetite). (E) The dispersion parameter in function of the mean coercivity (Log $B_{1/2}$).

Kruiver's parameters DP (dispersion parameter, width of the distribution of the coercivity) and $B_{1/2}$ can be used to separate the samples according to their magnetic properties (Figure 7.6-E). All samples with magnetic behavior dominated by hematite when plotted in Day's diagram (Figure 7.7-A) show values of SD (single-domain) hematite according to the Hcr/Hc limit (of 1.17) between SD and MD (multi-domain) hematite established by Özdemir and Dunlop (2014). The hysteresis curve for rhyolite PY82D is wasp-waisted, typical of a mixture of two magnetic phases (Figure 7.7-B). It shows a large coercivity indicating the predominance of hematite, which is confirmed by Curie/Néel temperature at around 670 – 680°C and a Morin transition (T_M= -20 °C) (Figure 7.7-C). Most samples with predominance of titanomagnetite fall into the pseudo-single domain (PSD) in the Day's diagram (Figure 7.7-D) except for sample PY96Q that plot into the multi-domain (MD) field. These samples are characterized by narrow-waisted hysteresis curves (Figure 7.7-E). In thermomagnetic curves the same samples show an abrupt decrease at around 580-600°C and a sharp increase in susceptibility at the Verwey transition (Tv= -122 °C), both indicative of Ti-poor titanomagnetite (Figure 7.7-F). A small decrease in the heating curve at *ca.* 410 °C is sometimes observed and could be related to maghemite.

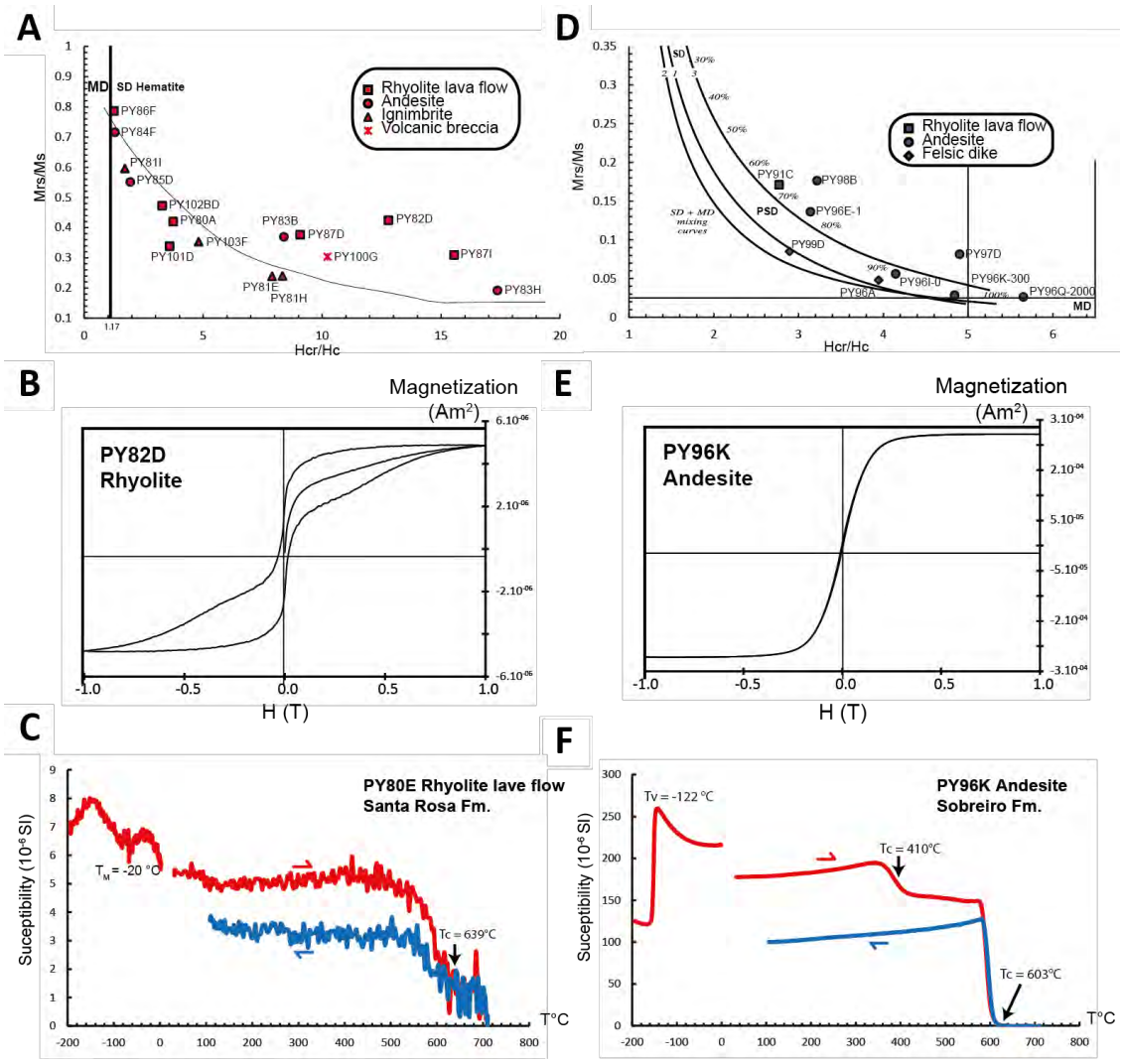

Figure 7.7: (A) Day plot (Day et al., 1977) of the hysteresis ratios Mrs/Ms and Hcr/Hc for samples where the contribution of hematite is > 60 %. The separation between SD and MD hematite is estimated with a ratio Hcr/Hc of 1.17 according to Özdemir and Dunlop (2014). (B) Hysteresis curve for a sample of rhyolite with a strong hematite contribution (PY82D) showing wasp-waisted type (mixture phases). (C) Thermomagnetic curve with low and high temperature dependence of magnetic susceptibility showing the contribution of hematite. (D) Day plot after Dunlop (2002) for samples whose contribution of magnetite is significative, most sample fall in the Pseudo-single domain (PSD) on a typical SD + MD trend. (E) Hysteresis curve for an andesite sample (PY96K) without hematite and associated thermomagnetic curve (F).

7.8 Oxide textural analysis

Petrography of rocks in São Felix do Xingu region is well-known (da Cruz et al., 2016) so we limited our analyses to samples representing different paleomagnetic behavior focusing on iron oxides. The most common iron oxides in rhyolites and ignimbrites for the Santa Rosa Formation are primary titanomagnetite with typical sizes of 10 – 250 µm containing ilmenite lamellae (Figure 7.8-A and B). Figure 7.8-C shows fine (~2 µm) subsolidus exsolution of ilmenite as trellis-lamellae parallel to (111) planes corresponding to the C2-C3 oxidation stages of Haggerty (1991). Sandwich lamellae and some homogeneous oxides have also been observed.

In rhyolites, titanomagnetite is commonly altered to hematite (Martite, Mt) characterized by high anisotropy (Figure 7.8-B). This alteration is regarded as the results of late- to post-magmatic oxidation by hydrothermal fluids (Meller et al., 2014; Nédélec and Borisova, 2015; Nédélec et al., 2015). Indeed, the replacement of magnetite by hematite in A-type granitic magmas emplaced at high levels is a common observation and is regarded as having occurred immediately after emplacement (Nédélec et al., 2015). The recognition of REE-fluoro-carbonate (synchysite) together with fluorine as accessory minerals (Figure 7.8-A and D) in Santa Rosa volcanic rocks is evidence for the existence of a F-rich late-stage magmatic fluid (Agangi et al., 2010). This F-bearing fluid of magmatic derivation, possibly mixed with a lower temperature meteoric fluid, was likely responsible for the transformation of magnetite to hematite (Nédélec and Bouchez, 2015).

Spherulites of 0.2 – 3 cm in size are very common in volcanic facies of Santa Rosa Formation (Figure 7.8-D). These features display a radiating texture of quartz and albite that are described as high-temperature crystallization domains (HTCDs) common in silica-rich volcanic rocks (Breitkreuz, 2013). Castro et al. (2008) pointed that the anhydrous mineral assemblage in spherulites crystallized rapidly at the expense of rhyolitic lava or pyroclastic deposits just after emplacement, and was responsible for expulsion of volatile in the magma at the front of the growing spherulites. The diffusion patterns around spherulites support this interpretation and sometimes evidence limited back-diffusion of water after spherulitic growth. Hematite inclusions observed in spherulites are therefore regarded as a magmatic or late-

magmatic phase formed during or immediately after spherulitic growth, which rules out the formation of hematite by low-temperature weathering.

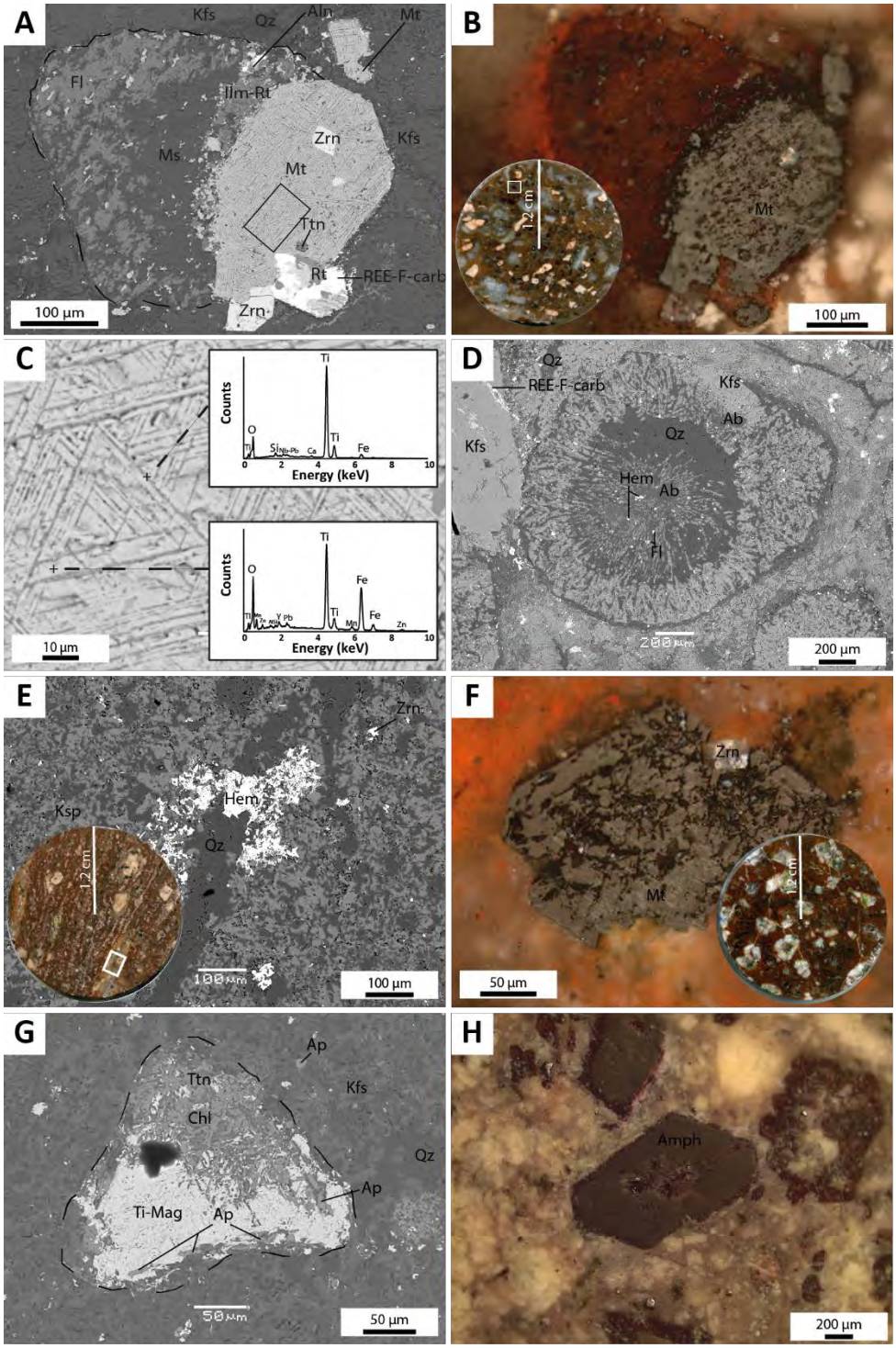

Figure 7.8: Petrography of analyzed samples. (A) SEM-BSE micrograph and (B) reflected light photomicrograph (crossed nicols at 85°) of subeuhedral crystal of titanomagnetite with exsolution lamellae of ilmenite altered in hematite (Martite, Mt) (PY81D1). (C) SEM-BSE micrograph for a detailed view of the exsolutions and energy dispersive spectra EDS associated (PY81D1). (D) SEM-BSE micrograph of hematite-rich spherulite (PY81D1). (E) SEM-BSE micrograph of hematite co-precipitated with quartz veins (PY101A2). (F) Reflected light photomicrograph (crossed nicols at 85°) for a titanomagnetite crystal and (G) SEM-BSE micrograph for hydrothermal alteration in the dike of the Velho Guilherme Suite (PY92). (H) Reflected light photomicrographs (crossed nicols at 85°) of andesite (PY85C1). Mineral abbreviations used from Whitney and Evans (2010).

Hematite can also be found in association with quartz in veins (Figure 7.8-E) as in the site 69.PY101A2 in the plagioclase-K-feldspar-phyric-rhyolite facies. In the dike of the Velho Guilherme Suite, titanomagnetite is also variably altered to hematite (Figure 7.8-F). Figure 7.8-G shows the alteration of a titanomagnetite with titanite filling ilmenite lamellae. Associated chlorite points to alteration in greenschist facies conditions (Figure 7.8-G). Close to the contact of the Velho Guilherme dike this alteration is very well marked. The andesite rocks of the Sobreiro Formation (PY85C1) shows euhedral amphiboles and plagioclase phenocrysts (Figure 7.8-H) with titanomagnetite, rare martite and zircon grains associated.

7.9 Discussion

7.9.1 U-Pb geochronology

The U-Pb results presented in this article are consistent with previous Pb-Pb ages obtained on other same units. Juliani and Fernandes (2010) published two Pb-Pb ages on zircons for the Santa Rosa Formation of 1879 ± 2 Ma and 1884 ± 1.7 for a rhyolite and an ash tuff, respectively. We present here the first U-Pb ages on zircons for the Santa Rosa Formation with 1877.4 ± 4.3 Ma for a rhyolite and 1895 ± 11 Ma for a dike. A similar 1880 ± 6 Ma (Pb-Pb) age was also found for andesites from the Sobreiro Formation (Pinho et al. (2006). All geochronological results support a *ca*. 1880 Ma age for the emplacement of these rocks. The age of 1853.7 ± 6.2 Ma obtained here for the sampled Velho Guilherme dike is consistent with previous Pb-Pb ages of 1867 ± 4 Ma, 1862 ± 16 Ma and 1866 ± 3 Ma obtained for the Antônio Vicente, Mocambo and Rio Xingu granites, respectively (Teixeira et al., 2002), and with a SHRIMP age of 1857 ± 8.4 Ma recently reported for another dike from the same Velho Guilherme dike swarm (Roverato, 2016).

7.9.2 Confidence of the paleomagnetic poles

The ~1880 Ma SF1 component:

Eight sites of felsic rocks of Santa Rosa Formation and two sites of the Sobreiro Formation revealed the SF1 remanence component carried by SD hematite (high coercitivity and high unblocking temperatures). This hematite is regarded as the result of late- to post-magmatic oxidation by hydrothermal fluids, indicating that the magnetization was acquired during and/or shortly after the crystallization of the nearly coeval Sobreiro and Santa Rosa Formations. In some cases, it is also carried by magnetite with high coercivities/high-blocking temperatures (samples PY96-K2, PY96-P1 in Figure 7.5). The pole SF1 (319.7°E, 24.7°S, A_{95}= 16.9°) satisfies 6 out of the 7 quality criteria proposed by Van der Voo (1990b) as reported below:

(1) Rhyolites of the Santa Rosa Formation are now well-dated with a U-Pb zircon age (LA-ICP-MS) of 1877.4 ± 4.3 Ma (this study), which likely corresponds to the age of magnetization.

(2) The component was calculated with 10 sites, (88 specimens) and adequate Fisher's statistical parameters (Dm= 149.2°, Im= 79°, k= 26.4, α_{95}= 9.6°, N= 10).

(3) Remanence was investigated using stepwise AF and thermal treatments, and principal component analysis (Kirschvink, 1980) was used to determine magnetic directions in orthogonal projections.

(4) A positive baked contact test performed for a Velho Guilherme dike (Figure 7.5) attests to the primary nature of SF2 component. This test also serves as a reverse baked test for the SF1 component (carried by host Santa Rosa andesites), proving the SF1 is older than ~1855 Ma (the dike's age).

(5) The Paleoproterozoic units (~1880 – 1855 Ma) in the area of São Felix do Xingu are unmetamorphosed to anchimetamorphic (low-grade metamorphosed) and show no trace of deformation, so the Central Amazonian Province has remained stable since the collision between the Carajás and Rio Maria domains at ~2870 Ma.

(6) The SF1 pole passes the reversal test when the specimen directions are used. The presence of reversals suggests enough time has elapsed to average out secular variation.

(7) This pole is very different from all other poles calculated for younger units in the Amazonian craton (D'Agrella-Filho et al., 2016). but the pole is quite close to the Early Carboniferous South American poles (Rapalini et al., 1994). There is, however, no event of this age to remagnetize these units. Moreover the steep inclination involves a high latitude position for the Amazonian craton whereas previous studies placed the craton in equatorial position at 1960 Ma with the Surumu pole (Bispo-Santos et al., 2014a) and at 1790 Ma with the Avanavero pole (Bispo-Santos et al., 2014b).

This new 1880 Ma SF1 pole can be seen as a very robust pole for the Central-Brazil Shield in the Amazonian craton.

The ~1855 Ma SF2 component:

Component SF2 was disclosed in 110 specimens of 15 sites. This component was observed together with SF1 in rhyolites of the Santa Rosa Formation and andesites from the Sobreiro Formation at lower coercivities or unblocking temperatures, being thus carried by magnetite. The only samples where SF2 directions reach the origin in orthogonal diagram are from the Velho Guilherme Suite dike in Site 64 (PY92-96). The positive baked contact obtained at this site, and the new U-Pb (zircon) dating permit to constrain the age of SF2 component to

ca. 1855 Ma. The mean direction for this component yielded a paleomagnetic pole (SF2) at 220.1°E, 31.1°S (A_{95}= 9.7°, K= 16.5) which may be classified as a key pole with Q= 7:

(1) The positive baked contact test attests that SF2 component was acquired at 1854 Ma (the emplacement age according to this study and consistent with a previous 1857 Ma age of Roverato (2016)).
(2) The SF2 component was calculated with 15 sites and (110 specimens) and is associated with good Fisher's statistical parameters (Dm= 239.2°, Im= 10.6°, k= 10.5, α_{95}= 12.4°, N= 15).
(3) As in the case of SF1 component, adequate demagnetization was performed, and vector diagrams and principal component analysis were employed to isolate and calculate vector directions.
(4) A positive baked contact test was obtained for the dike demonstrating the primary nature of SF2 pole.
(5) No deformation or metamorphism is observed in the dike and neither in the rhyolites and andesites in the area. This component SF2 is also present in some dikes related to the poorly dated Velho Guilherme granite located ~100 km to the east of the study area (Antonio et al., 2016).
(6) Both polarities were disclosed in the studied samples (Table 7.3).
(7) No similar younger paleomagnetic pole is described for the Amazonian craton.

Neoproterozoic to Cambrian remagnetization SF3:

Component SF3 is present in 78 specimens of 14 sites from all units in the area. When it occurs together with SF1 and/or SF2, this component is the less stable, occurring at low coercivities and low unblocking temperatures. It is normally present in rocks with coarser-grained texture. IRM, hysteresis, and thermomagnetic curves show that the magnetic carrier is large multi-domain magnetite grains. The corresponding SF3 pole (128.8°E, 40.7°S, A_{95}= 15.6°) is similar to the Cambrian Puga B pole (146.9°E, 33.6°S, A_{95}= 8.4°) (Trindade et al., 2003). No younger geological event is presently known in São Felix do Xingu area that could be responsible for a remagnetization of the study rocks. A thermoviscous origin for this component is suggested and may be related to the influence of the Neoproterozoic Araguaia Belt located ~300 – 400 km to the east of the study area or to mafic dikes similar to those described in the Carajás domain that yielded U-Pb (on baddeleyite) ages of 535.1 ± 0.9 Ma (unpublished data, Teixeira et al. (2012b); Teixeira et al. (2016)). The SF3 pole (Q= 3) is thus interpreted as a remagnetization due to the Neoproterozoic Brasiliano event (~600 – 530 Ma) developed at the border of the Amazonian craton.

7.9.3 Paleomagnetic discrepancies between 1.9 – 1.8 Ga

With the two new poles SF1 and SF2 we can tentatively extend the APWP traced for the Amazonian craton to 1855 Ma (Bispo-Santos et al., 2014a; Théveniaut et al., 2006) (Figure 7.9). In doing so, we selected the polarities that implied in the shortest APWP between 1960 and 1855 Ma. The Amazonian APWP shown in Figure 7.9 defines a loop, named here the Uatumã loop and indicates a fast motion, *ca.* 39.3 cm/yr, of the Amazonian craton during the interval 1880 – 1855 Ma.

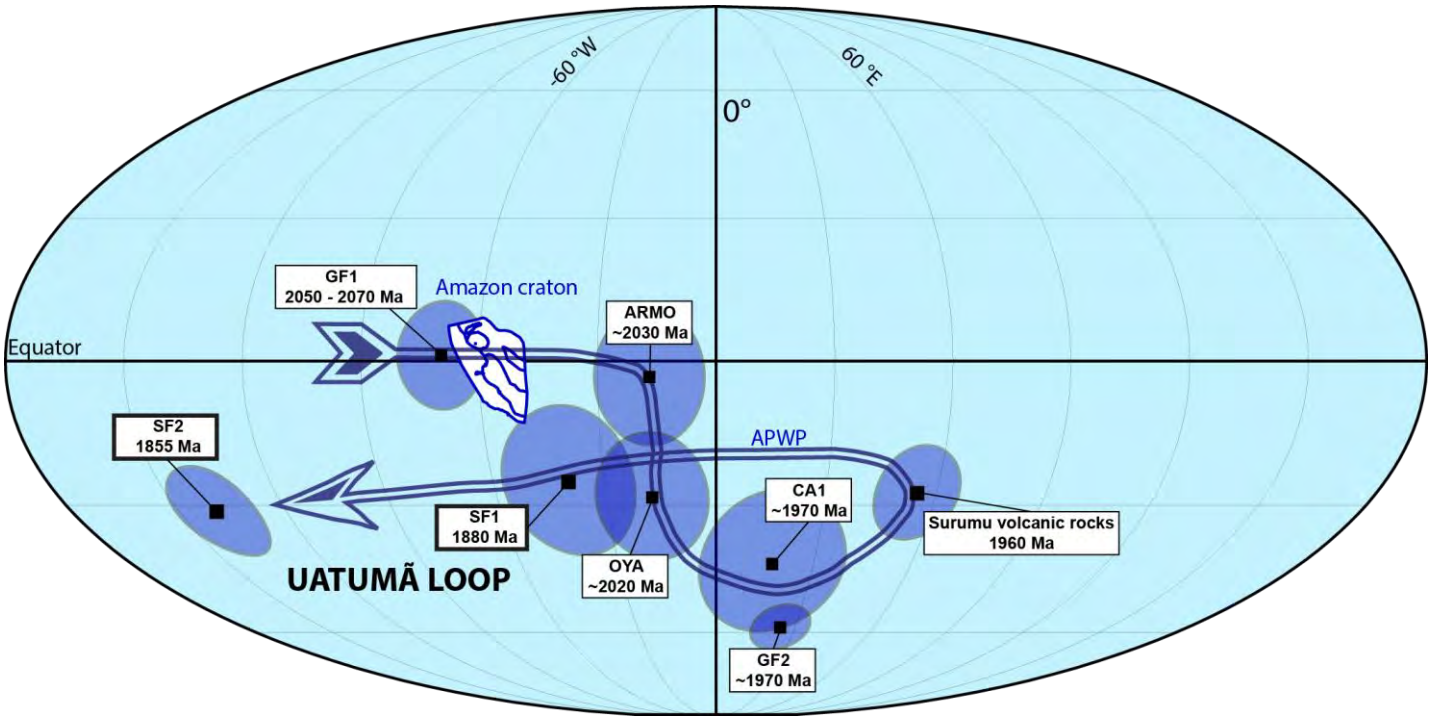

Figure 7.9: APW path traced for the Amazonian craton between 2100 and 1860 Ma (paleomagnetic poles before 1880 Ma in Bispo-Santos et al. (2014a) . Amazonia is in its present position.

The paleomagnetic record of the Amazonian craton implies in rapid motions between a semi-equatorial position at 1960 Ma (Surumu pole), a polar position at 1880 Ma (SF1 pole) and a return to an equatorial position at 1855 Ma (SF2 pole). This behavior is similar to the paleomagnetic record of other cratons at around ~1880 Ma (Table 4).

The Slave craton in Laurentia provides the best database between 1900 – 1800 Ma. Their paleomagnetic poles (listed in the Table 4) form a ~110° loop well-known as "The Coronation loop" (McGlynn and Irving, 1978). Mitchell et al. (2010) revised data for the Slave craton and demonstrated that the loop cannot be explained parsimoniously by large or local vertical-axis rotations and interpreted the "Coronation loop" as a signal of rapid, oscillatory true polar wander (TPW). Still in Laurentia, the Superior craton provides three high quality paleomagnetic poles, all with positive magnetic stability tests. The Flaherty volcanics and Haig intrusives poles are dated at 1870 ± 1 Ma by U-Pb on baddeleyite (Hamilton et al., 2009;

Schmidt, 1980) and differ by 38° from the Molson dikes B + C2 pole with an age of 1884 – 1877 Ma (Evans and Halls, 2010; Heaman et al., 2009). Mitchell et al. (2010) also interpret this discrepancy as a possible TPW.

Semami et al. (2016) refined the APW path of the Kaapvaal craton in South Africa during the late Paleoproterozoic (2200 – 1840 Ma) using a model where the Kaapvaal craton was not linked with the Zimbabwe craton. This model is based on the difference of ~38° between the Mashanaland sills pole dated at ~1883 Ma (Hanson et al., 2011; Söderlund et al., 2010) from the Zimbabwe craton and the Post-Waterberg dolerites pole dated at ~1875 Ma (Hanson et al., 2004) from the Kaapvaal craton. These authors proposed a large-scale post-1880 Ma displacement of >2000 km between the two cratons along the Limpopo Belt. The first argument against this model is the age of collision between the Zimbabwe and Kaapvaal cratons along the Limpopo Belt that occurred between 2700 – 2000 Ma (Barton et al., 2006; Nicoli et al., 2015) and no deformation is documented after 1800 Ma to accommodate a > 2000 km displacement. A second argument against the model is the existence of the Sebanga-2 Virtual geomagnetic pole (Seb-2 VGP) obtained for the Zimbabwe craton (Bates and Jones, 1996). The slightly younger ~1880 Ma Sebanga dikes cross-cut the Mashanaland dolerite (~1883 Ma) but the VGP position is close to the Post-Waterberg dolerite pole (~1875 Ma) from the Kaapvaal craton (see Figure 12 of Hanson et al. (2004)). Therefore, these results preclude any eventual displacement between Zimbabwe and the Kaapvaal cratons as proposed by Hanson et al. (2011), and the discrepancy between paleomagnetic poles are better explained by TPW.

Baltica, together with Laurentia, is the craton with the largest available paleomagnetic database. Baltica was not yet assembled at 1880 Ma and comprehend Fennoscandia (Karelia-Kola-Norbotten), Volgo-Uralia and Sarmatia cratons (Bogdanova et al., 2013). The position of Fennoscandia at 1880 Ma is well established, based on a mean paleomagnetic pole obtained from several Svecofennian gabbroid bodies (Vittangi, Kiuruvesi, Pohjanmaa- Ylivieska, Jalokoski) (Pesonen et al., 2003) and the Keuruu diabase dikes (Klein, 2016; Klein et al., 2016). The slightly younger *ca*. 1860 Ma Loftahammar gabbro pole is the only pole that can be used for comparison. A difference of ~48° is observed between the 1880 and 1860 Ma poles, but despite recent geochronological constraints Bergström et al. (2002), the Loftahammar gabbro pole cannot be considered as a key pole due to poor-quality paleomagnetic data (Poorter, 1976).

Didenko et al. (2015) revised the Paleoproterozoic APWP for the Siberia craton and four 1878 – 1850 Ma paleomagnetic poles with positive magnetic stability tests were selected for the time-interval of interest (Table 7.4). All poles have very similar geographic coordinates

and therefore suggest small dislocations or rotations for Siberia in the 1880 – 1850 Ma interval. The ~1878 Ma Lower Akitkan pole (Malaya Fm.) is the most reliable paleomagnetic pole since it owns positive intra-formational conglomerate and fold tests. All other poles for the 1880-1850 interval were also obtained for the Akitkan volcano-plutonic belt, which was slightly deformed and metamorphosed (Zorin et al., 2008). The analysis of the data is thus complicated because this region has undergone remagnetizations as indicated by some negative conglomerate tests (Didenko et al., 2009).

Belica et al. (2014) performed the latest paleomagnetic study for the India craton and calculated a 1880 Ma mean pole for this block (Dharwar dikes). According to the authors, the high-quality of this mean pole is supported by a positive baked contact test and by a precise U-Pb age on baddeleyite. However, this pole represents an average between dikes of different ages and different directions. For example, site 74 is dated at 1885.4 ± 3.1 and site 19 at 1847 ± 6 Ma (U-Pb on baddeleyite). Here we will use instead the study of Radhakrishna et al. (2013b), which published two different poles for 1880 Ma and 1860 Ma for the Cuddapah Basin.

In summary, several cratons show conspicuous discrepancies between paleomagnetic poles dated between 1880 – 1860 Ma. Using the paleomagnetic database in the interval 2100 – 1200 Ma (Table SM9 - Supplementary material) we can estimate the Precambrian continental drift rate for six cratons with the PMTec package of Wu et al. (2015) based on the method of McFadden and McElhinny (1995). As the paleolongitude is unconstrained in paleomagnetism, we can determine only the minimum motion in paleolatitude. Increments with time windows of 20 Ma and 5 Ma were chosen to identify any large polar wander deviations between 2100 – 1200 Ma. Figure 7.10 shows the APWP velocity (cm/year) for six cratons in the interval 2100 – 1200 Ma. The velocity increases for all cratons in the interval 1890 – 1850 Ma and some of them show very large velocities (> 50 cm/yr). Note that velocities are much smaller after 1800 – 1750 Ma. Piper (2013a) had already noted that during the 2000 – 1800 Ma period, APW paths traced for the cratons are problematic in terms of velocity and paleomagnetic results and did not exclude the possible existence of true polar wander episodes.

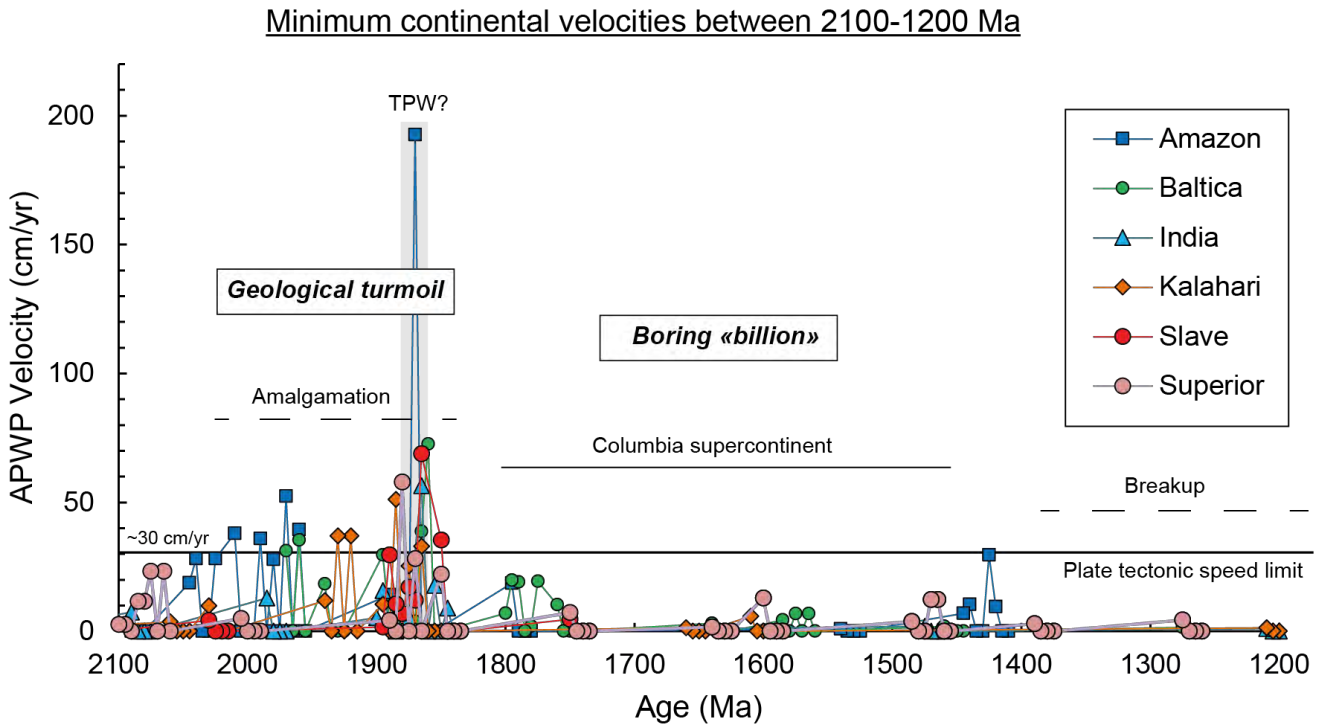

Figure 7.10: Minimum continental velocities calculated between 2100 – 1200 Ma for six cratons during the Columbia supercontinental cycle. Plate tectonic speed limit is marked by a line according to the value of ~30 cm/yr (Gordon et al., 1979; Tarduno, 1990). Paleomagnetic data between 2100 – 1200 Ma is available in supplementary material.

The first possibility to explain this period of high APWP velocity is to consider that plate motions were much faster than today. Zahirovic et al. (2015) carried an analysis of plate speeds and show that fast plate motions (> 10 cm/yr) are linked to plates with large subduction zones and low continental areas. They estimated a speed limit of ~20 cm/yr for Archean/Proterozoic cratonic plates which contained less than 50% of present continental areas. This speed limit is at the same order of previous estimates of 18 cm/yr (Meert et al., 1993) and 30 cm/yr (Gordon, 1990; Tarduno, 1990). Rapid acceleration can be linked to anomalously hot mantle and a possible influence of plume head arrival. The most famous example is for India during the Tethyan subduction reaching a ~18 cm/yr speed (van Hinsbergen et al., 2011), which is still well slower than the suggested speeds for 1890 – 1850 Ma (Figure 7.10).

Another possibility is to consider the absence of a stable GAD (geocentric axial dipole) field during the 1890 – 1850 Ma time interval. A global axial dipole field is the necessary and mandatory condition for using paleomagnetic data in paleogeographic reconstructions (Meert, 2009). Several lines of evidence suggest that the geocentric axial dipole (GAD) hypothesis is viable during the Precambrian (Evans, 1976). According to Veikkolainen et al. (2014a), new results support the existence of a GAD field in Precambrian times with a small octupolar

component (5 % of GAD) and a quadrupole component (2 % of GAD). Using our compilation (Table SM9 – supplementary material), we performed an inclination asymmetry test with a small number of reversals (N= 12) during the 1880 – 1840 Ma period. Values with strong anomalies (> 20°) are not visible during this interval and would support a GAD field with low contamination of non-dipole-terms (Figure SM1 – supplementary material). We performed also an inclination frequency analysis during the interval 2100 – 1200 Ma to detect a non-dipolar contamination but a small number of data (N= 122) was available in this compilation to be statistically representative (Figure SM2 – supplementary material).

The existence of a GAD field depends primarily of the geodynamo's history that can be analyzed through the global paleointensity record. Numerical simulations over two billion years show that the geodynamo could have transitioned from a multipolar to a dipolar regime around 1700 Ma (Driscoll, 2016), with another weak dipolar period around 1000 Ma and the inner core nucleation around 650 Ma. But our knowledge about the global heat balance between core and mantle and the geodynamo are caveats for the reality on this model (Driscoll, 2016). Nonetheless, Smirnov et al. (2016) argue that paleointensity data should be used with caution to constrain inner growth or the long-term evolution of the core because of the poor quality of the database.

The last possibility involves true polar wander (TPW) events with the rotation of the whole lithosphere and mantle (on D") with respect to the Earth's rotation axis (Raub et al., 2007). Possible signals of TPW have already been reported in the literature to explain the anomalous APWP between 1890 – 1850 Ma (Mitchell et al., 2010).

7.9.4 True polar wander and paleogeography at 1880 – 1860 Ma.

Our new data are used to test whether paleogeographic reconstructions are consistent with the TPW episodes proposed by Mitchell et al. (2010). Relative motion (only in latitude) and rotation of cratons with respect to the spin axis of the earth is classically determined with paleomagnetism using the APWPs. In the TPW hypothesis, the motion of the entire lithosphere may be faster than plate tectonics, and the APWPs will reflect the amount of true polar wander (APW = TPW). The motion of cratons is thus determined with respect to the TPW reference axis (I_{min}- minimum inertia axis) and all cratons must undergo identical TPW. The TPW reference axis is determined by the overlapping of APWPs, so the relative longitudinal position between the cratons is fixed (Kirschvink et al., 1997). Therefore, with the Precambrian database (Table 7.4) we can test if the APWPs from all cratons show nearly the same length and shape during the proposed TPW episode (1880 – 1860 Ma). We used the technique of Meert (1999) to compare APWs and evaluate the errors.

The APW path for the "Coronation loop" is the most complete and the most complex (Figure 7.11) (Mitchell et al., 2010). In our paleogeographic reconstructions we used the well-dated 1887 ± 5 Ma pole of Ghost dikes with a positive baked contact test (Buchan et al., 2016) and the youngest pole of Stark Formation (~1876 ± 10 Ma) with a positive conglomerate test (Evans and Hoye, 1981; Mitchell et al., 2010). The angular distance between the two poles is 56° (± 13) which implies a velocity of 56.7 $\frac{+27}{-38}$ cm/yr (interval of 11 ± 15 Ma). The calculated great circle includes all poles of Mitchell et al. (2010) with the axis (P_{lat} = -76.9°N, P_{long} = 56°E, A_{95} = 17.3).

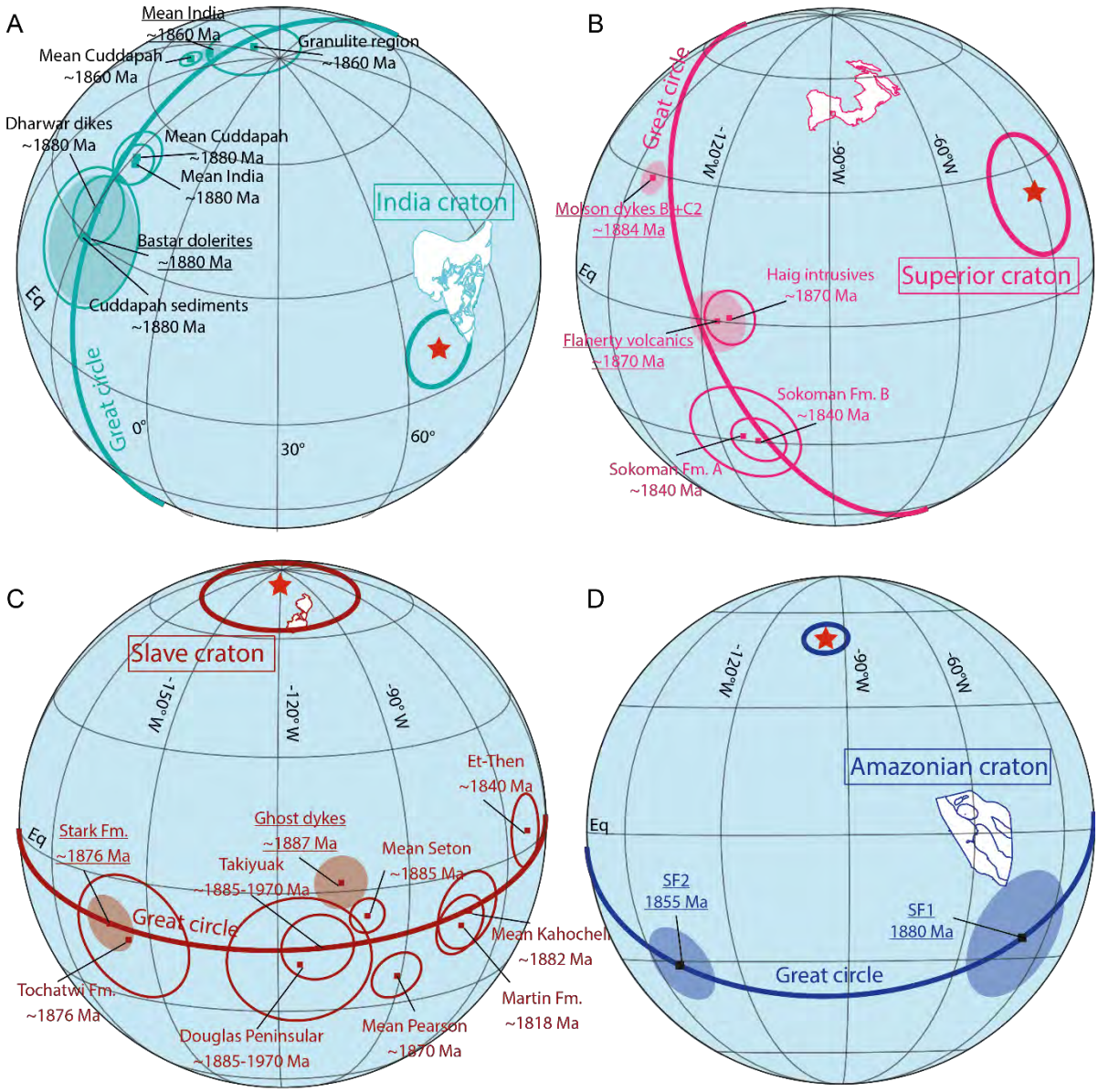

Figure 7.11: Apparent polar wander paths (APWPs) length of India (A), Superior (B), Slave (C) and Amazonia (D). Paleomagnetic poles indicated are listed in Table 4 and poles used in reconstructions are underlined. Great circles calculated for each craton are indicated by thick lines and axis by red stars with their corresponding cone of confidence circles (Table 7.4).

For the Amazonian craton we calculated a great circle between poles SF1 (~1880 Ma) and SF2 (~1855 Ma). With only two poles, we have necessarily a great circle and it is not possible to estimate the error (P_{lat}= 50.3°N, P_{long}= 263.4°E) but the angular distance between poles of 85° ± 25 in the time interval of 24 ± 10 Ma yields a velocity of ~39.3 $\frac{+48}{-19}$ cm/yr . The greatest angular distance can be attributed to the fact that the considered time interval is longer than for the Slave craton.

A great circle was calculated for the Superior craton using three paleomagnetic poles between 1880 Ma (Molson B+C2 dikes pole) and 1870 Ma (Flaherty volcanics pole) (P_{lat}= 40.3°N, P_{long}= 336°E, A_{95}= 4.1). The angular distance between the poles is 38.2° ± 11 during a short time interval of 7 ± 8 Ma (velocity of ~61 $\frac{+78}{-19}$ cm/yr). Considering the associated errors, this distance is close to that of the Slave craton.

A similar angular separation of 38.8° ± 14 is calculated for the Kalahari craton between the Mashonaland sills pole (Hanson et al., 2011) and the Post-Waterberg dolerites pole (Hanson et al., 2004). The angular distance between the ~1880 Ma mean Baltica pole (Pesonen et al., 2003) and the Loftahammar gabbro pole (1859 ± 9 Ma) (Poorter, 1976) is 48.34° ± 9.6 which is very similar to Indian angular distance (48.49° ± 18.2) between the mean 1880 Ma and 1860 Ma poles (Radhakrishna et al., 2013b). Australia has a very poor database (Schmidt, 2014). Only two poles with relatively good quality could be used, despite the much younger age of the Plum Tree volcanic pole (1825 ± 4 Ma) when compared to the poles used for other cratons. Siberia is the only craton without any significant difference between the 1880 and 1850 Ma poles (angular distance of ~10°±10). So, a great circle for its poles provides a large uncertainty (A_{95}= 32.2). The fact that Siberian poles are similar across the time interval of 1880 – 1850 Ma may be explained either as a failure of the TPW hypothesis or as a problem with the paleomagnetic data because the sampling area was not geologically stable at ~1880 – 1850 Ma. In summary, most cratons have angular distances around 40 – 50° between 1880 Ma and 1860 Ma poles except for the Amazonian craton with ~85° and Siberia (<10°).

After calculating the best-fit great circles for each craton and rotating them to the center of a Mollweide projection (spinner projection, P_{lat}= 0°, P_{long}= 0°), we can superimpose the great circle axes (Raub et al., 2007). Thus, the paleolongitude of all considered cratons are constrained. We used this hypothesized TPW axis for two reconstructions at ~1880 Ma and ~1860 Ma (Figure 7.12) where the paleolatitude of any craton is constrained by the corresponding pole with two possibilities due to geomagnetic polarity ambiguity.

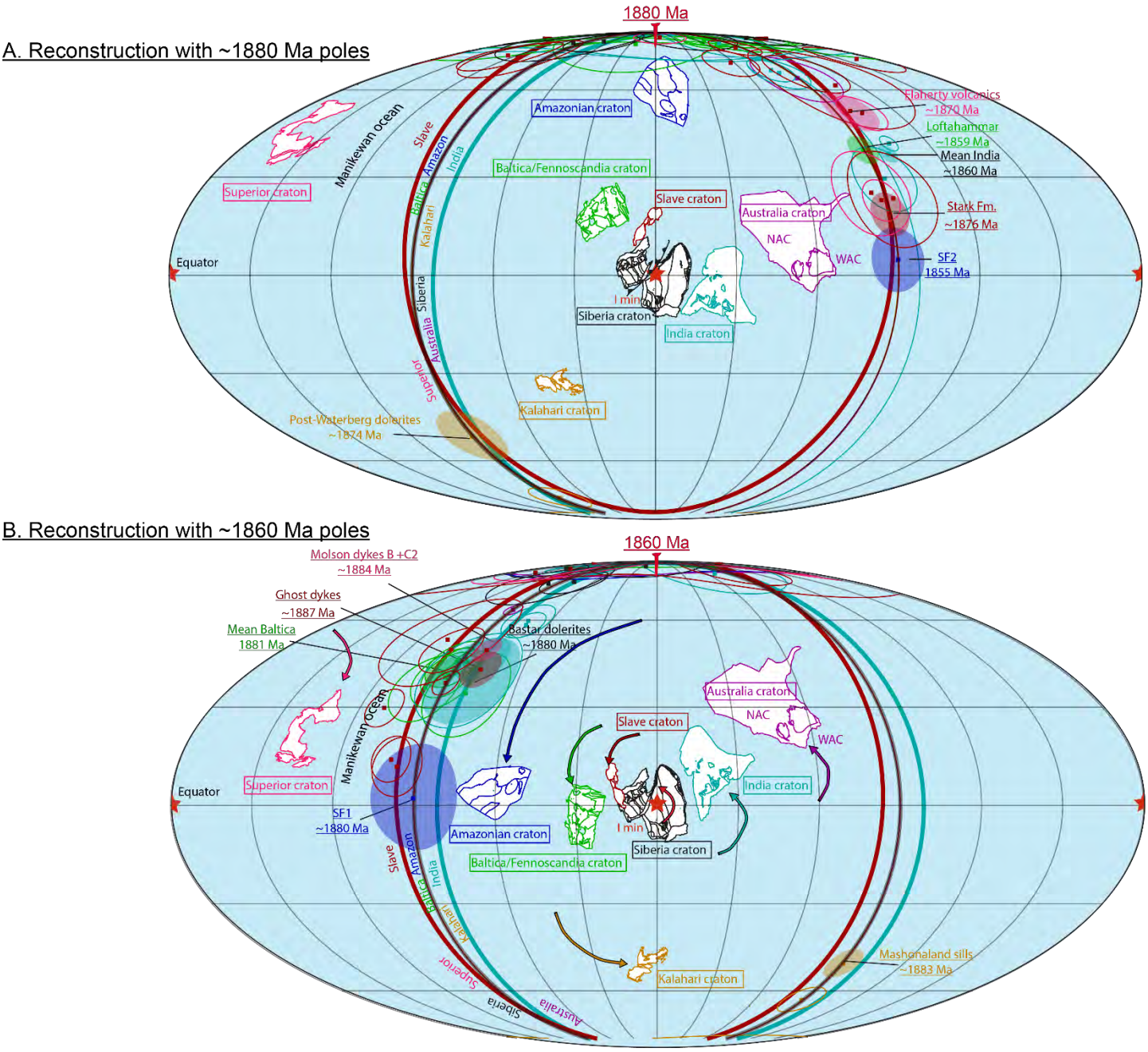

Figure 7.12: Possible paleogeographic reconstructions at 1880 Ma (A) and 1860 Ma (B) during the proposed true polar wander. The reconstructions are established with the true polar wander spin axis (I_{min}) as a red star in the center (spinner diagram) and the great circles associated at each craton with the repartition of paleomagnetic poles. Cone of confidence circles for the error of great circle axis are not illustrated for visibility. Paleomagnetic poles used for the reconstructions are labeled with semitransparent filled ellipse. The sense of motion is indicated by a red arrow. *Abbreviations:* NAC = North Australian craton, WAC = West Australian craton.

In the ~1880 Ma reconstruction (Figure 7.12-A), all APWPs are aligned on the same great circle with a consistent distribution of poles depending on ages. The Amazonian craton is in polar position constrained by the SF1 pole (this study) and differs from the usual equatorial position in different models of supercontinent Columbia (Bispo-Santos et al., 2014b; Evans and Mitchell, 2011; Pehrsson et al., 2016; Pisarevsky et al., 2014). Siberia is situated at the center of the projection, and close to the Slave craton. Siberia is considered as the center of the future Columbia supercontinent (Evans and Mitchell, 2011; Gladkochub et al., 2016), and recent studies support a Slave-Siberia connection (Buchan et al., 2016; Ernst et al., 2016a; Evans et al., 2016b). Reconstruction of Figure 7.12 supports a large ocean between the Slave and the Superior cratons, the so-called Manikewan Ocean (Corrigan et al., 2009); the large distance between these cratons being already pointed by Mitchell et al. (2014) based on distinct Paleoproterozoic Slave and Superior APWPs.

In the ~1860 Ma reconstruction (Figure 7.12-B) we represent a counterclockwise rotation of all cratons indicated by the arrows. The position of the Amazonian craton is equatorial and close to Baltica (Fennoscandia) consistent with a SAMBA-type connection (see D'Agrella-Filho et al. (2016) for a review). After rotation, the Siberia-Slave connection is possible and continental blocks appear to converge towards an assembled supercontinental configuration. The collision between Slave and Superior occurred during the development of the Trans-Hudson orogeny (1860 – 1830 Ma). The final assembly of Laurentia would be at *ca.* 1715 Ma after the collision of Wyoming craton with the Superior craton. This reconstruction does not support a connection between Baltica and India as supposed by Pisarevsky et al. (2014). The longitudinal position of Australia craton is consistent with a future connection with Laurentia at ~1650 – 1600 Ma along the Racklan orogeny (Thorkelson and Laughton, 2015). Finally, Kalahari is considered in this model as an isolated block without evidence of connection with any other craton. It is interesting to note that in our model, where paleolongitude (with respect to TPW) is constrained, positions of the different cratons are not so different from those in reconstructions based on individual paleomagnetic poles alone (Pehrsson et al., 2016; Zhang et al., 2012)

Despite the small amount of available data, our results support a TPW event between 1880 Ma and 1860 Ma with the rotation of all continental blocks around a minimum inertia axis located on the paleo-equator, through Siberia (I_{min} – Figure 7.12).

Name	Plat (°N)	Plong (°E)	A_{95}	Age ± error (Ma)	Q	Ref
SLAVE (The Coronation Loop)						
Ghost dykes	2	254	6	1887 ± 5 U-Pb badd	6	1
Mean Seton/Akaitcho/Mara	-6	260	4	1885 ± 5 U-Pb corr.	5	2
Mean Kahochella/Peacock Hills	-12	285	7	1882 ± 4 U-Pb zrn corr.	4	2
Douglas Peninsular	-17	245	16	~1885-1870	4	2
Takiyuak Fm.	-13	249	8	~1885-1871	5	2
Stark Fm.	-11	199	6.7	1876 ± 10 corr.	5	2
Tochatwi formation	-14	204	15	~1876 corr.	5	2
Mean Pearson/Peninsular sills (PS)	-22	269	6	1870 ± 4 U-Pb	4	2
Et-Then Fm. (Group C)	4	310	8	~1840	6	3
Martin Fm.	-9	287	9	1818 ± 4 U-Pb badd	4	4, 5
Great Circle Calculation	*-76.9*	*56*	*17.3*			
Analysis Ghost vs Stark Fm.	***56.2° ± 13[1]***			***11 ± 15 Ma[2]***	***56.7 cm/yr (247-38)[3]***	
SUPERIOR						
Molson dykes B + C2	29	218	4	1884 ± 2 U-Pb badd	5	6
Flaherty volcanics	0	244	7	1870 ± 1 U-Pb badd	6	7, 8
Haig intrusives	1	247	6.1	1870 ± 1 U-Pb badd	6	7, 8
Sokoman Fm. A	-28.6	247	13.2	~1840-1830	4	9, 10
Sokoman Fm. B	-29.6	250.9	6.4	~1840-1831	5	9, 10
Great Circle Calculation	*23.9*	*329.1*	*14*			
Analysis Molson vs Flaherty	***38.2° ± 11[1]***			***7 ± 8 Ma[2]***	***60.6 cm/yr (78-43)[3]***	
AMAZONIA						
SF1	-24.7	319.7	16	1877.4 ± 4.3 U-Pb zrn	6	11
SF2	-31.1	220.1	9.7	1853.7 ± 6.2 U-Pb zrn	6	11
Great Circle Calculation	*50.3*	*263.4*	*0.2*			
Analysis SF1 vs SF2	***85° ± 25[1]***			***25 ± 10 Ma[2]***	***39.3 cm/yr (48-19)[3]***	
KALAHARI		158.5				
Mashonaland sills (Zimbabwe)	6.5	338.5	5	1883 ± 2 U-Pb badd	4	12, 13
Post-Waterberg dolerites (Kaapvaal)	15.6	17.1	8.9	~1879-1872 U-Pb badd	4	14
Black Hills dyke swarm (Kaapvaal)	9.4	352	5	~1875-1835	5	15, 16
Great Circle Calculation	*-72*	*49.3*	*1.5*			
Analysis Mash vs Post-Waterberg	***38.8° ± 14[1]***			***9 ± 3 Ma[2]***	***47.9 cm/yr (49-27)[3]***	
SIBERIA						
Lower Akitkan, Malaya Fm.	-30.8	98.7	5	1878 ± 4 U-Pb zrn corr.	5	17
Chaya Fm. Upper Akitkan Group (Anabar) Red beds	-22.1	97.5	6.9	1863 ± 9 U-Pb zrn corr.	4	18, 19
Shumikhin granite	-23.7	110	5.7	1855 ± 5 U-Pb zrn	3	20, 21
Okun Fm.	-28.5	111	9.6	~1850	3	22, 19
Great Circle Calculation	*-63.4*	*291.3*	*32.2*			
Analysis Lower Akitkan vs Okun Fm.	***10.9° ± 15[1]***			***28 ± 9 Ma[2]***	***4.3 cm/yr (7-5)[3]***	
INDIA						
Cuddapah Basin sediments	29.3	332.9	14.4	~1880	3	23
Bastar dolerite dykes -C (Group. 3)	29.3	331.7	15.7	1883 ± 1.5 U-Pb badd	5	24, 25
Dharwar 1.88 Ga dykes -C (Overall mean 1.88-1.86 Ga)	35.9	331.1	7.7	~1883-1847 U-Pb badd	4	26
11. Mean around Cuddapah basin 1.88 Ga direction	50.5	331.4	6.4	1880	4	27
12. Overall mean India 1.97-1.88 Ga direction	49.2	332.9	4.8	~1991-1885 U-Pb badd	4	27
13. Mean around Cuddapah basin (~1860 Ma)	69.6	286.7	2.5	1847 ± 6 U-Pb badd	4	27
14. Granulite region (South - Dharmapuri)	82.5	259.1	10.3	1855 ± 9 Ar-Ar phl	5	28
15. Overall mean NNW-N shallow direction in India	73.7	282.6	2.9	1847 ± 6 U-Pb badd	4	27
Great Circle Calculation	10.6	69.1	8.7			

Analysis Bastar dolerites-Mean 1.86 Ga	**48.49° ± 18.2[1]**			**~20 Ma[2]**	**26.9 cm/yr (32-14)[3]**	
BALTICA						
Vittangi gabbro	42.6	227.9	4.9	1886 ± 14 U-Pb zrn	2	29, 30
Kiuruvesi intrusions (mean)	43.1	235.2	10	1886 ± 5 U-Pb zrn	2	31, 32
Pohjanmaa-Ylivieska gabbro	38.6	239.8	10.9	1879 ± 5 U-Pb zrn	3	33, 34
Jalokoski gabbro	43.1	233.9	7.6	1871 ± 4 U-Pb zrn	2	35, 36
Mean Baltica SVF1	41	233	5	~1881	3	37
Svecofennian volcanics and intrusions	46	227	4.1	~1880	4	38
Keuruu diabase dyke swarm	45.4	230.9	5.5	1870 ± 9 U-Pb zrn	?	39
Loftahammar gabbro	23	179	4.6	1859 ± 9 U-Pb zrn	3	40, 41
Great Circle Calculation	45	64.5	15			
Analysis Mean Baltica vs Loftahammar	**48.34° ± 9.6[1]**			**~22 Ma[2]**	**24.4 cm/yr (190-4)[3]**	
AUSTRALIA	**Plat rot.**	**Plong rot.**	**(Li & Evans (2011) correction)**			
Frere Formation red beds (WAC)	-8.26	209.3	1.8	Mean 1891 ± 8 U-Pb zrn	6	42, 43
Plum Tree volcanics (NAC)	-29	195	9.3	1825 ± 4 U-Pb zrn	?	44
Great circle	30.8	124.3	0.5			
Analysis FF vs Plum Tree	**25.2° ± 11.1[1]**			**~62 Ma[2]**	**4.3 cm/yr (8-2.3)[3]**	

Table 7.4: Compilation of paleomagnetic poles used in the TPW analysis. Plat, Paleolatitude; Plong, Paleolongitude; A_{95}, semiangle of the cone of 95 % confidence about the pole. Geochronological symbols: corr.- correlation with related unit; zrn- zircon; badd- baddeleyite; pl- plagioclase; phl- phlogopite; Q- Quality factors (Van der Voo, 1990b). Analysis of TPW; [1]: Angular separation of poles (°). [2]: Time separation of poles (Ma). [3]: Conservative APW rate (cm/yr) with error associated (velocity maximum-velocity minimum).

References: 1, Buchan et al. (2016); 2, Mitchell et al. (2010); 3, Irving et al. (1972b); 4, Evans and Bingham (1973); 5, Morelli et al. (2009); 6, Evans and Halls (2010); 7, Schmidt (1980); 8, Hamilton et al. (2009); 9, Williams and Schmidt (2004); 10, Findlay et al. (1995); 11, **This study**; 12, Hanson et al. (2011); 13, Söderlund et al. (2010); 14, Hanson et al. (2004); 15, Lubnina et al. (2010a); 16, Olsson et al. (2015); 17, Didenko et al. (2009); 18, Donskaya et al. (2007); 19 Vodovozov (2010); 20, Didenko et al. (2006); 21, Larin et al. (2003); 22, Vodovozov et al. (2007); 23, Prasad et al. (1987); 24, Meert et al. (2011); 25, French et al. (2008); 26, Belica et al. (2014); 27, Radhakrishna et al. (2013b); 28, Radhakrishna et al. (2013a); 29, Elming (1985); 30, Skiöld (1988); 31, Neuvonen et al. (1981); 32, Marttila (1981); 33, Pesonen and Stigzelius (1972); 34, Helovuori (1979); 35, Mertanen and Pesonen (1992); 36, Mertanen (2013) unpublished; 37, Pesonen et al. (2003); 38, Elming (1994); 39, Klein (2016); 40, Poorter (1976); 41, Bergström et al. (2002); 42, Williams et al. (2004); 43, Rasmussen et al. (2012); 44, Idnurm and Giddings (1988).

7.9.5 Geological turmoil during the amalgamation of the Supercontinent Columbia

U-Pb ages of Precambrian detrital zircons define major peaks at 2700, 2500, 2100, 1880 and 1100 – 1000 Ma (Figure 7.13-A) (Belousova et al., 2010; Condie and Aster, 2010). These peaks immediately follow times of enhanced mantle activity and witness steps of increased crustal growth. Moreover, Hf isotope compositions in zircons help to determine their provenance, either from juvenile (mantle-derived) material or from recycled continental crust (Figure 7.13-B) (Kemp et al., 2006). Whereas a juvenile origin predominates at 2700 and 2500 Ma, a recycled source predominates at 2100 and 1880 Ma (Arndt and Davaille, 2013). We regard this observation as evidence that amalgamation of the Columbia supercontinent was already ongoing during the time interval of interest (1880 – 1860 Ma). Indeed, the time interval between 2100 and 1800 Ma corresponds to several collisional/accretional orogenic belts in many Precambrian terranes worldwide (Condie, 2002a; Hoffman, 1988; Zhao et al., 2002).

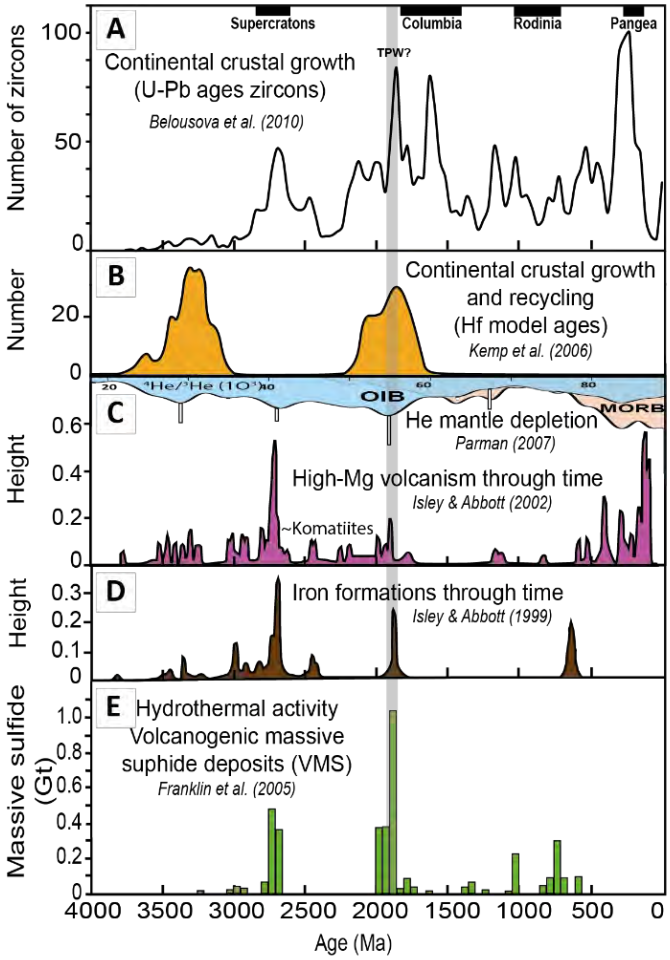

Figure 7.13: Geological features during the Precambrian record between 4000 and 500 Ma. (A) Histogram for the crustal zircon age distribution of Belousova et al. (2010).(B) Peaks in Hf model ages in orange show times of juvenile crustal addition (Kemp et al., 2006). (C) $^{4}He/^{3}He$ probability density function from Parman (2007) with peaks of OIB (ocean island basalt) and MORB (mid-ocean ridge basalt) correlated to the frequency of the High-Mg melts though time (Isley and Abbott, 2002). (D) Frequency of iron formations (BIFs) through time (Isley and Abbott, 1999). (E) Distribution of the volcanogenic massive sulphide deposits (VMS) from Franklin et al. (2005).

Figure 7.13-C also shows the frequency of mantle-derived melts through time (Isley and Abbott (2002). The most important peak in high-MgO magmatism is at 2700 Ma, and is well-known for its abundant komatiites. The 1880 Ma peak also corresponds to a peak in the komatiite record, being the last ultramafic volcanic pulse of Precambrian times. The global LIP record on all cratons is available in (Condie et al., 2015; Ernst, 2014). For the period of interest, we can cite the 1880 Ma NE-trending Ghost dike swarm in the Slave craton, the 1880 Ma Circum-Superior LIP (Molson dikes and Flaherty volcanics) in the Superior craton (Minifie et al., 2013), the 1880 Ma Southern Bastar-Cuddapah LIP in India (French et al., 2008), the Mashonaland sills and the Post-Waterberg dolerites in Kalahari craton (Hanson et al., 2004), Svecofennian A-type magmatism in Baltica and in Siberia, and the Uatumã LIP in Amazonia craton (this study). Figure 7.13-E shows a major peak in the formation of volcanogenic massive sulphide (VMS) deposits related to a strong hydrothermal activity around 1880 Ma also suggesting an important production of mantle-derived magmas. This period also coincides with a major peak in orogenic gold resources (Goldfarb et al., 2001) and iron formations (BIFs and GIFs) (Figure 7.13-D) (Bekker et al., 2010; Isley and Abbott, 1999). So, understanding the geodynamic of this period has an economic interest.

In summary, the Precambrian geological record suggests a high production of mantle-derived magmas at around 1880 Ma, together with the beginning of the Columbia amalgamation and a peak in the magmatic recycling of continents. Both mantle superswells and thermal insulation under an amalgamating supercontinent are causes of density perturbations that alter the Earth's inertia tensor, potentially provoking TPW episodes. These events will place the supercontinent and/or the superswells at the Equator. These conditions could be linked to a whole mantle reorganization following magmatic latency between 2400 and 2200 Ma (Arndt and Davaille, 2013; Condie et al., 2009).

7.10 Conclusions

The following conclusions can be drawn from this work:

(1) Two new paleomagnetic poles considered as primary are found for the Amazonian craton. The SF1 pole from rhyolites is dated at 1877.4 ± 4.3 Ma (U-Pb zrn, LA-ICP-MS) and its primary origin is supported by an inverse contact test, reversal polarities and the late-to post-magmatic hydrothermal origin of hematite as its carrier. The SF2 pole is a secondary component in the ~1880 Ma rhyolites and a primary component in the dike of Velho Guilherme Suite dated at 1853.7 ± 6.2 Ma (U-Pb zrn, LA-ICP-MS). Its primary origin is supported by a positive baked contact test and implies a remagnetization of magnetite at ~1855 Ma in the rhyolites.

(2) The SF3 pole is considered as a widespread remagnetization event in the area affecting the low-coercivity and low-blocking temperature phases in all units of the region. The SF3 component is interpreted to be related to a Neoproterozoic remagnetization during the Araguaia Belt development.

The significant discrepancy of Paleoproterozoic poles between 1880 – 1860 Ma could be explained by a true polar wander (TPW) event which is supported by paleomagnetic reconstructions at 1880 Ma and 1860 Ma and geological/geochronological evidence. This is a likely consequence of the reorganization of mantle convection. If this model is confirmed, some reevaluation will be required about the paleomagnetic approach and the geology and paleogeography of the Columbia Supercontinent.

Acknowledgements

We thank Universidade Federal do Pará (UFPA) for the field trip logistical support and FAPESP (grants 2011/50887-6, 2012/20335-4, 2013/22957-5, 2016/13689-5) for financial support. Prof. Cristiano Lana acknowledges funding from CNPq (401334/2012-0- 302058/2015-0-402852/2012-5) and FAPEMIG (APQ03943 - RPQ-0067-10) grants. We also thank Thierry Aigouy for SEM analysis in the University of Paul Sabatier (Toulouse, France). Special thanks to the technicians of the laboratory of the IAG-USP (USPmag - São Paulo, Brazil) for assistance and discussions. We appreciate comments of Editor J.G Meert and the contribution of L.J Pesonen more an anonymous reviewer, which significantly improved the original manuscript.

Conclusions (English)

This thesis is the first multidisciplinary study on units of the Uatumã event in Carajás Province. This work combines petrology, geochronology and paleomagnetism to define the space-time framework of the Uatumã event (SLIP) of the Amazonian craton within the Columbia supercontinent. Two study areas with good outcrops of the investigated rocks were sampled in the southwestern province of Carajás Province, in the Tucumã and São Felix do Xingu areas.

We studied felsic and mafic dike swarms near Tucumã (SW – Pará, Brazil). Three types of dikes have been identified in this area that cut across the Archean basement represented by, the Rio Maria granodiorite. Felsic dikes of N125° direction represent 70% of observed dikes in the region. They are subsolvus microgranites characterized by subhedral phenocrysts of quartz, alkali feldspar and plagioclase in a quartz-feldspar matrix with granophyric texture. Felsic dikes are highly silicic (66 – 78 wt. % SiO_2), with high Na_2O + K_2O, relatively high FeO, low CaO, and very low MgO. They are also enriched in HFSE, and thus are typical A-type magmas. They are peraluminous to metaluminous granite classified as A2 type (Eby, 1990). Two dikes were precisely dated by U-Pb zircon (SHRIMP) at 1881.9 ± 8.8 and 1880.9 ± 6.7 Ma (da Silva et al., 2016). These new ages allow to associate this dike swarm with the important A-type plutonism represented by the granites of the Jamon Suite in the Amazonian craton (Dall'Agnol et al., 2005). The Tucumã dike swarms are genetically linked to the volcanic rocks (rhyolites, ignimbrites) of the Santa Rosa Formation (~150 km westwards) and allow the connection between the different parts of volcano-plutonic system in the Carajás province. Presence of volcanic rocks only to the west can be explained by a lower level of erosion. Rare associated basaltic dikes (49 – 54 wt. % SiO_2) are tholeiitic in composition. Felsic and mafic dikes display field evidence for mingling (mafic enclave in felsic dikes and K-feldspar megacrysts in mafic dikes) suggesting that mafic and felsic magmas were coeval. A model of mixing between basaltic and felsic dikes can lead to the formation of intermediate rocks (da Silva et al., 2016). Among the intermediate dikes, the PY73 sample shows a strong geochemical affinity with the Velho Guilherme granitic suite. Therefore, this dike does not belong to the Tucumã dike swarms dated at ~1880 Ma but rather to the slightly younger Velho Guilherme Suite (~1860 Ma). All these data suggest that the origin of these dikes is related to a process of underplating in the crustal base, which would generate more felsic than mafic magma and not to a subduction process.

Magnetization results from the contribution of a low-coercivity component (primary PSD magnetite) and a high-coercivity component (secondary hematite produced by syn- to post-

hydrothermal alteration). The magnetic mineralogy is used here as a proxy to quantify hydrothermal alteration. Magnetic mineralogy of mafic dikes (basalts and gabbros) is carried only by pseudo-single-domain (PSD) magnetite. The Archean basement, the Rio Maria granodiorite, has multi-domain magnetite (MD).

Demagnetization treatments revealed three characteristic magnetic components for the Tucumã area. Component B shows a northerly direction with a low negative inclination. This direction is carried by a NS-gabbroic dike similar to the Mesozoic dikes of the Amazonian craton (Ernesto et al., 2003; Nomade et al., 2000). This dike is therefore of Mesozoic age and associated with the Large Igneous Province (LIP) of the CAMP (Central Atlantic Magmatic Province). A component A is defined on most microgranitic and mafic dikes. This component has a northwesterly direction with positive inclination and the associated paleomagnetic pole is located at 52.9°S, 76.4°E (A_{95}= 10.4°, K= 13.52). And finally, a component C has a direction towards the southwest of low positive inclination. This component C is carried by the Rio Maria granodiorite (~2875 Ma) as well as by the dike PY73, which shows a strong affinity with the Velho Guilherme Suite (~1860 Ma).

Field contact tests were carried out only in an area where a NS-gabbroic dike crosscuts Proterozoic dikes. Most of the field tests are negative and show a large Mesozoic remagnetization during the intrusion of the dikes related to the CAMP. A positive inverse baked contact test was obtained between microgranitic dikes intersected by the Mesozoic NS-gabbroic dike. At the contact (~1 m), the microgranitic dike shows the direction of component B, while at a greater distance (~2 m) the component A is revealed. This inverse baked contact test shows that component A is older than the Mesozoic component B but in no way proves its primary origin. Petrographic and geochemical evidence suggest that component C is related with 1860 Ma Velho Guilherme Suite, and so this age is possibly the time this component was acquired. The fact that Component C is similar to Component SF2 isolated for a dike from the Velho Guilherme rocks (see below) in the São Felix do Xingu area corroborates this interpretation.

We sampled three facies in São Felix do Xingu: (1) 11 sites for the Santa Rosa Formation composed by rhyolitic lava flows, ignimbrites, felsic dikes and volcanic breccias. (2) 6 sites for the Sobreiro Formation composed by volcanoclastic rocks (andesitic in composition). (3) One microgranitic dike related to the Velho Guilherme Suite.

First U-Pb zircon dating (LA-ICPMS) were performed for the Santa Rosa Formation with an age of 1877.4 ± 4.3 Ma for a rhyolitic lava flow, and one age of 1895 ± 1.7 Ma for a felsic dike. U-Pb age on zircon (LA-ICPMS) of 1853.7 ± 6.2 Ma was obtained for the dike of the

Velho Guilherme Suite. These first U-Pb zircon ages are consistent with the previous Pb-Pb ages (Juliani and Fernandes, 2010; Teixeira et al., 2002).

Magnetic mineralogy of the rhyolitic lava flows of the Santa Rosa Formation shows that the magnetization is carried by hematite SD (high coercivity component with high blocking temperature). This hematite is related to syn- to post magmatic hydrothermal fluids. The paleomagnetic pole SF1 (319.7°E, 24.7°S, A_{95}= 16.9 °) obtained on the rhyolitic lava flows can be considered as a key pole for the Amazon craton dated at *ca*. 1880 Ma. This pole satisfies 6 of the 7 criteria (Q= 6) proposed by Van der Voo (1990b).

A second key pole SF2 (220.1°E, 31.1°S, A_{95}= 5°) was determined on both the rhyolites of the Santa Rosa Formation and andesites of the Sobreiro Formation. This direction is also well-defined by the felsic dike of the Velho Guilherme Suite dated at 1853.7 ± 6.2 Ma (this study). This direction is the same as the component C observed in Tucumã and also carried by a dike with affinity of the Velho Guilherme Suite. In addition to the regional consistency, the primary origin of the SF2 direction is confirmed by a positive baked contact test with the volcanoclastic rocks of the Sobreiro Formation (1880 ± 6 Ma Pb-Pb (Pinho et al., 2006)). This test allow to constrain the age of the SF1 direction which is observed far from the contact between ~1880 Ma and ~1853 Ma, which strongly suggests that SF1 is primary.

As SF1 is probably primary, the component A obtained on the Tucumã dike swarms is necessarily secondary because these dikes form a dike swarm related to the Santa Rosa Formation. A secondary direction carried by grains with low coercivity and low blocking temperature was observed for the rocks of São Felix do Xingu and gives the pole SF3 (128.8°E, 40.7°S, A_{95}= 15.6°). This pole is superimposed on the Neoproterozoic poles of the Amazonian craton, Puga B (Trindade et al., 2003) and CAPS (Garcia et al., 2013) and therefore is considered secondary. This pole is probably associated with a thermoviscous remagnetization during the Araguaia orogenic belt located at *ca*. 400 km to the east of the studied region.

These two key Paleoproterozoic poles (SF1 and SF2) obtained in this study show a significant angular difference. The difference of ~25 Ma between the poles and this large angular distance imply relatively high plate velocities, which are not consistent with plate tectonics. Such differences between 1880 and 1850 Ma poles are observed for many cratons around the world. These new data allowed testing a reconstruction which supports a True Polar Wander (TPW) event at ~1880 – 1860 Ma in order to explain these high plate velocities. This True Polar Wander (TPW) event is supported by geological evidence (peak of zircons, last Proterozoic Komatiites, LIPs on all cratons), and is surely the consequence of a whole reorganization of the mantle convection.

New paleomagnetic key poles have to be obtained for the Amazonian craton in order to verify this hypothesis and the validity of the Geocentric Axial Dipole (GAD) model during this period. A potential target might be the sedimentary rocks from the Roraima Supergroup in the northern Amazonian craton (Bispo-Santos et al., 2016). These non-deformed sedimentary rocks would be ideal for a detailed paleomagnetic study, as well as to study the variations of the magnetic field along the deposition of the almost 400 m height sedimentary pile on. ~100 Ma…

Conclusions (French)

Cette thèse constitue la première étude pluridisciplinaire sur les unités de l'événement Uatumã dans la Province Carajás. Ce travail associe la pétrologie, la géochronologie, et le paléomagnétisme afin de définir le cadre spatio-temporel de la grande province magmatique siliceuse Uatumã du craton Amazonien au sein du Supercontinent Columbia. Deux zones d'étude où affleurent des roches génétiquement liées à l'événement Uatumã ont été échantillonnées dans le sud-ouest de la Province de Carajás, la région de Tucumã et celle de São Felix do Xingu.

Dans la région de Tucumã, on observe, des essaims de filons felsiques et mafiques. On a identifié trois types de filons qui recoupent le socle archéen du domaine Rio Maria. Les filons felsiques de direction N125 représentent 70 % des filons de la région. Ce sont des filons de microgranites composés de phénocristaux automorphes de quartz et feldspaths dans une matrice felsique. Ces filons felsiques sont riches en silice (66 – 78 wt.% SiO_2), en Na_2O + K_2O, en FeO, pauvres en CaO, et très pauvres en MgO. Ils sont aussi enrichis en HFSE et sont ainsi des magmas granitiques de type A. Ce sont des microgranites peralumineux à métalumineux, que l'on peut classer comme A2 dans la classification de (Eby, 1990). Deux filons ont été datés précisément par U-Pb sur zircons (SHRIMP) à 1881.9 ± 8.8 et 1880.9 ± 6.7 Ma (da Silva et al., 2016). Ces nouveaux âges permettent ainsi d'associer ces filons avec l'important plutonisme de type A représenté par les granites de la suite Jamon dans le craton Amazonien (Dall'Agnol et al., 2005). Ces filons de microgranites sont génétiquement liés à la formation Santa Rosa comme le suggèrent les données géochimiques sur roches totales. La formation Santa Rosa est constituée par des roches volcaniques, des rhyolites et des ignimbrites, qu'on observe à l'ouest de Tucumã (~150 km) dans la région de São Felix do Xingu. Les filons de Tucumã représentent donc le système filonien associé aux roches volcaniques observées seulement dans la partie ouest de la région. Cette répartition peut s'expliquer par une différence de niveau d'érosion qui apparaît plus superficiel vers l'ouest. Les filons mafiques associés aux filons de microgranite sont rares dans la région de Tucumã et sont composés de roches basaltiques. Ces filons sont contemporains des filons microgranitiques comme en témoignent les figures de mélange incomplet (mingling) et les enclaves mafiques dans les microgranites. Un modèle de mélange complet (mixing) entre les filons basaltiques et les filons felsiques peut conduire à former des roches intermédiaires (da Silva et al., 2016). Parmi les filons intermédiaires, l'échantillon PY73 montre une forte affinité géochimique avec la Suite granitique Velho Guilherme. Le filon en question n'appartient donc pas à l'essaim de filons de Tucumã daté à ~1880 Ma mais plutôt à la Suite Velho Guilherme considérée comme 20 Ma plus jeune. Toutes ces données pétrographiques et géochimiques

suggèrent que les filons étudiés résultent d'un processus de sous-placage magmatique (« underplating ») en base de croûte, qui se manifesterait par la production de plus de magma felsique que mafique dans la croûte supérieure.

L'étude détaillée de la minéralogie magnétique montre que l'aimantation des filons de microgranite est portée par la contribution de deux composantes, une à coercivité faible (magnétite primaire pseudo-mono-domaines (PSD)) et une de plus forte coercivité (hématite secondaire). On a montré que des fluides syn- à post-magmatiques ont modifié la minéralogie de ces filons et donc leurs propriétés magnétiques. L'importance de l'hématite (et d'autres minéraux secondaires) nous permet de quantifier l'altération hydrothermale correspondante. La minéralogie magnétique des filons mafiques (basaltes et gabbros) est représentée uniquement par des grains de magnétite pseudo-mono-domaines (PSD). L'encaissant archéen, à savoir la granodiorite Rio Maria, possède des magnétites multi-domaines (MD).

Le paléomagnétisme de la région de Tucumã a permis d'isoler trois composantes magnétiques caractéristiques. La composante B porte une direction vers le nord avec une faible inclinaison négative. Cette direction est portée par un filon gabbroïque d'orientation nord-sud similaire aux filons mésozoïques du craton amazonien (Ernesto et al., 2003; Nomade et al., 2000). Ce filon est donc d'âge mésozoïque et associé à la province magmatique géante de la CAMP (Central Atlantic Magmatic Province). Une composante A est définie sur la plupart des filons microgranitiques et mafiques. Cette composante porte une direction dirigée vers le nord-ouest avec une inclinaison positive et le pôle paléomagnétique associé est localisé à 52.9°S, 76.4°E (A_{95} = 10.4°, K = 13.52). Et enfin une composante C possède une direction vers le sud-ouest de faible inclinaison positive. Cette composante C est portée par la granodiorite archéenne Rio Maria (~2875 Ma) ainsi que par le filon PY73 qui montre une affinité avec la suite granitique Velho Guilherme (~1860 Ma).

Des tests de contact ont été réalisés seulement dans une région où on a pu observer des filons qui se recoupent La plupart des tests sont négatifs et montrent une large réaimantation mésozoïque lors de l'intrusion du filon associé à la CAMP. Un test inverse positif a été obtenu pour un filon microgranitique recoupé par le filon gabbroïque mésozoïque. Au contact (~1 m), le filon de microgranite montre la direction de la composante B alors qu'à une distance plus grande (~2 m) on observe la composante A. Ce test inverse montre que la composante A est plus ancienne que la composante B d'âge mésozoïque, mais en aucun cas ne prouve son origine primaire. L'âge de la composante C reste énigmatique si l'on observe seulement les résultats de Tucumã. On va retrouver cette composante C dans la deuxième région étudiée, c'est-à-dire à São Felix do Xingu.

A São Felix do Xingu, on a échantillonné trois faciès : (1) 11 sites pour la formation Santa Rosa composés de laves rhyolitiques, d'ignimbrites, des filons felsiques et des brèches volcaniques (2) 6 sites de la formation Sobreiro essentiellement constituée de roches volcanoclastiques de nature andésitique, (3) un filon de microgranite associé à la suite granitique Velho Guilherme.

Les datations U-Pb sur zircon (LA-ICPMS) des laves rhyolitiques de la formation Santa Rosa ont donné un âge de 1877.4 ± 4.3 Ma pour une rhyolite et 1895 ± 1.7 Ma pour un filon felsique. Un âge U-Pb sur zircon (LA-ICPMS) de 1853.7 ± 6.2 Ma a été obtenu pour le filon de la Suite Velho Guilherme. Ces âges U-Pb sur zircon sont cohérents avec les âges antérieurs Pb-Pb sur zircon des unités étudiées (Juliani and Fernandes, 2010; Teixeira et al., 2002).

La minéralogie magnétique des laves rhyolitiques de la formation Santa Rosa montre que l'aimantation est portée par de l'hématite mono-domaine (très coercitive avec une haute température de blocage). Cette hématite est le résultat de l'altération syn- à post-magmatique lors du passage de fluides hydrothermaux oxydants. Le pôle paléomagnétique SF1 (319.7°E, 24.7°S, A_{95} = 16.9°) obtenu sur les laves rhyolitiques peut être considéré comme un pôle de référence pour le craton Amazonien à 1880 Ma. En effet, ce pôle satisfait 6 des 7 critères de qualité (Q = 6) proposés par Van der Voo (1990b).

Un deuxième pôle de référence SF2 (220.1°E, 31.1°S, A_{95} = 5°) a été déterminé à la fois sur les rhyolites de la formation Santa Rosa et sur les andésites de la formation Sobreiro. Cette direction est aussi portée par le filon felsique de la Suite Velho Guilherme bien daté à 1853.7 ± 6.2 Ma. Cette direction est la même que la composante C observée à Tucumã et portée aussi par un filon présentant une affinité avec la Suite Velho Guilherme. En plus de la cohérence régionale, l'origine primaire de cette direction est contrainte par un test de contact positif avec les roches volcanoclastiques de la formation Sobreiro (1880 ± 6 Ma Pb-Pb (Pinho et al., 2006)). Ce test permet aussi de contraindre l'âge de la direction SF1 qui est observée loin du contact entre ~1880 Ma et ~1853 Ma ce qui suggère aussi que SF1 est primaire.

Par conséquent, la composante A obtenue à Tucumã sur l'essaim de filons est forcément secondaire, car ces filons forment le complexe filonien associé à la formation Santa Rosa. Une direction secondaire portée par des grains à faible coercivité et faible température de blocage a été observée pour les roches de São Felix do Xingu et donne un pôle SF3 (128.8°E, 40.7°S, A_{95} = 15.6°). Ce pôle se superpose aux pôles néoproterozoïques du craton Amazonien, Puga B (Trindade et al., 2003) et CAPS (Garcia et al., 2013) et par conséquent est considéré comme secondaire. Ce pôle est probablement associé à une réaimantation thermovisqueuse durant l'orogénèse Araguaia localisée à 400 km à l'est de la région étudiée.

Les deux pôles paléoprotérozoïques de référence (SF1 et SF2) obtenus dans cette étude montrent une différence de distance angulaire significative. La différence d'âge de ~25 Ma entre les pôles et cette grande distance angulaire implique des vitesses relatives de déplacement bien supérieures aux vitesses observées pour la tectonique des plaques. On retrouve de telles différences sur tous les cratons entre 1880 et 1850 Ma. Ces nouvelles données ont permis de tester une reconstruction qui supporte la présence d'une Vrai Dérive des pôles (VDP) à ~1880 – 1860 Ma afin d'expliquer ces vitesses si élevées. Cette Vrai Dérive des pôles est associée à des phénomènes géologiques remarquables (pic de zircons, donc pic de production magmatique, dernières komatiites protérozoïques, PMG (Province Magmatique géante) sur tous les cratons). Ce VDP est sûrement la conséquence d'une réorganisation de la convection mantellique ayant entraîné une production magmatique exceptionnelle.

De nouveaux pôles paléomagnétique de référence doivent être obtenus pour le craton Amazonien afin de vérifier cette hypothèse et de tester si le modèle du dipôle axial centré (DAC) est valide pour cette période. Une cible potentielle pourrait être la formation sédimentaire de Roraima dans le nord du craton Amazonien (Bispo-Santos et al., 2016). Ces roches sédimentaires non déformées seraient idéales pour une étude paléomagnétique détaillée, ainsi que pour étudier les variations du champ magnétique le long de la pile sédimentaire sur quasiment 400 m d'épaisseur, déposée en 100 Ma…

List of Figures

Figure 1.1 A: Evolution of Earth's atmospheric oxygen content through time according Lyons et al. (2014). Two models are illustrated: the red curve show two sharp steps for the rise of the oxygen and the blue curve is the emerging model with more fluctuation. Blue arrows are possible rise of O_2 in the atmosphere. B: Summary of carbon (black) and sulphur (red and grey) isotope data in Earth History (Lyons et al., 2014). C: Two models for the oxygenation of the ocean with the model 1 of Holland (2006) and the model 2 of Canfield (1998) with anoxie until 540 Ma. Glaciations and possible snowball earth are represented. Eukaryotes and metazoans apparitions are indicated. p. 23

Figure 1.2 Diagram of Jackson (2015) showing variation in the Mn/Fe ratio (proxy for the oxide-reduction) in non-detrital sedimentary rocks (chert dolomite) through time. p. 25

Figure 1.3 Thermal evolution modeling modified from Korenaga (2013). (A) Evolution of mantle heat production (H in red) with low present-day Urey ratio (0.34) and Ur (0.84) related to the potential mantle temperature, T_p. (B) Evolution of mantle heat flux (Q in blue) during the transition between a stagnant lid convection toward a plate tectonics convection (simulation at 3 Ga, 2 Ga and 1 Ga) with the relation to the potential mantle temperature, T_p. (C) Thermal evolution modeling with the effect of water in plate tectonics in open-system or close-system. Solid circles denote petrological estimates on past potential temperature (Herzberg et al., 2010). p. 27

Figure 1.4 Komatiites through time. A: Time series of occurrences of komatiites modified after Isley and Abbott (1999). B: Secular variation in MgO in komatiites (Condie et al., 2016). In purple – MgO content; In red – aveage MgO content with respective error bars. p. 28

Figure 1.5 Ni/Fe mole ratios for iron banded formation (BIF) through time after Konhauser et al., (2009). Inset: Evolution of the temperature is deduced by calculation of the MgO content of komatiite liquids (T°C = 1000 + 20MgO). p. 29

Figure 1.6 Nb/Yb through time in non-arc oceanic basalts modified from Condie and O'Neill (2010). p. 29

Figure 1.7 Localization of the different cratons in the world, modified from Ernst et al. (2013a). p. 30

Figure 1.8 Models for the formation of the subcontinental lithospheric mantle (SCLM) adapted from Lee (2006). p. 31

Figure 1.9 Crustal growth models for the continental crust, adapted from Cawood et al. (2013). p. 32

Figure 1.10 Evolution for crustal processes modified from Nicoli et al. (2016). The Archean – Proterozoic transition shows the first evidence for continental collisions in convergent settings wth the onset of plate tectonics. Ar-Pr = Archean – Proterozoic transition. Pr-Ph = Proterozoic – Phanerozoic transition. PT = Onset for the plate tectonics in this model. p. 33

Figure 1.11 Model of Laurent et al. (2014) for the evolution of the granitoids during the Archean (after 3000 Ma). p. 35

Figure 1.12 $(La/Yb)_n$ vs Yb_n diagram to represent the evolution of TTGs (Martin, 1986). p. 35

Figure 1.13 Evolution of granitoids with the secular cooling of mantle. A: Model for cooling of mantle, TW = terawatt (Labrosse and Jaupart, 2007). B: Cartoons showing the evolution of granitoids through time. p. 37

Figure 1.14 Supercontinents in Earth's History and associated geodynamic. Images from Fischer and Gerya (2016), Evans et al. (2016a), and Chardon et al. (2009). p. 41

Figure 1.15 Columbia reconstruction after Zhao et al. (2004)). Symbols for orogenesis: (1) Trans-Hudson; (2) Penokean; (3) Taltson– Thelon; (4) Wopmay; (5) New Quebec; (6) Torngat; (7) Foxe; (8) Makkovik– Ketilidian; (9) Ungava; (10) Nugssugtoqidian; (11) Kola– Karelian; (12) Svecofennian; (13) Volhyn– Central Russian Orogen; (14) Pachelma; (15) Akitkan; (16) Transantarctic Orogen; (17) Capricorn; (18) Limpopo Belt; (19) Transamazonian; (20) Eburnean; (21) Trans-North China Orogen; (22) Central Indian Tectonic Zone; (23) Central Aldan Orogen; (24) Halls Creek Orogen. p. 43

Figure 1.16 Frequency of onset of subduction and collision in Proterozoic orogens, recalculated after Condie (2013). p.44

Figure 1.17 Distribution of U-Pb ages on zircons in detrital and granitoid rocks through time after Condie and Aster (2010). p. 45

Figure 1.18 Passive-margin abundance through time after Bradley (2008). p. 46

Figure 1.19 LIP barcode modified from Ernst et al. (2013b). p. 47

Figure 1.20 Possible reconstruction for the Amazonian craton and Baltica at *ca.* 1970 Ma. p. 48

Figure 1.21 LIP barcode between Laurentia and Siberia after Ernst et al. (2016a). p. 49

Figure 1.22 Schematic APWPs between 3 cratons to understand the APWPs method, redrawn after Evans and Pisarevsky (2008). p. 51

Figure 1.23 APWPs for Laurentia and Baltica. A: In NENA configuration the APWPs are superimposed. B: In the alternative configuration of Hoffman (1988) the APWPs are different. After Evans (2013). p. 52

Figure 1.24 APWP of the Columbia supercontinent in a configuration as suggested by Zhang et al. (2012), according to Salminen et al. (2015). p. 53

Figure 1.25 Mechanisms for the formation of supercontinents. Example for the future Amasia (Mitchell et al., 2012). Red stars indicate the I_{min} (position of the previous supercontinent – Pangea). p. 54

Figure 1.26 First models for the Columbia supercontinent. A: Model of Rogers (1996). B: Model of Rogers and Santosh (2002). C: Model of Zhao et al. (2004).D: Paleomagnetic model of Meert (2002). p. 56

Figure 1.27 Columbia supercontinent according the model of Hou et al. (2008). p. 57

Figure 1.28 Possible connections between Baltica -North China Craton (NCC) – Amazonia. A: Model of Kusky et al. (2007). B: Model of Bispo-Santos et al. (2008). C: Model of D'Agrella-Filho et al. (2012). p. 58

Figure 1.29 A: Super-Horde model of Yakubchuk (2010). B: Paleopangea model of Piper (2013b). p. 59

Figure 1.30 SAMBA model according to Johansson (2009). p. 61

Figure 1.31 Positions of cratons at 1.95 – 1.88 Ga (A) and Columbia supercontinent with its maximum packing at 1.60 – 1.40 Ma (B) (Pehrsson et al., 2016). p. 62

Figure 1.32 Columbia supercontinent between 1770 and 1580 Ma (Pisarevsky et al., 2014). p. 63

Figure 2.1 Tectonic models for the Amazonian craton. A: Model of Santos et al. (2003a) adapted from Roverato et al. (2016). B: Model of Cordani and Teixeira (2007) with localization of different paleomagnetic studies for the Amazonian craton (D'Agrella-Filho et al., 2016). Inset: Sketch of the southwestern part of the Amazonian Craton showing the Paraguá Terrain and Alto Guaporé, Aguapeí and Nova Brasilândia belts (modified after D'Agrella-Filho et al. (2012)). p. 67

Figure 2.2 Apparent polar wander path for the Amazon craton between 2050 and 1960 Ma after Bispo-Santos et al. (2014a). Position for the Colíder and Avanavero poles at *ca*.1790 Ma. Supposed position for a paleomagnetic pole at *ca*.1880 Ma, see text for more information (in red). p. 71

Figure 3.1 A: Uatumã event in the Amazonian craton related with the geochronological provinces (Cordani and Teixeira, 2007). PCA - Central Amazonia Province; MI - Maroni-Itacaiunas Province; VT – Ventuari-Tapajós Province; RNJ – Rio Negro-Juruena Province; RO – Rondonia-San Ignacio Province; SS – Sunsás-Aguapeí Province. B: Distribution of volcanic and plutonic units from the Uatumã event and localization of the Carajás province. p. 98

Figure 3.2 a) Localization of Carajás in the Pará state. b) Subdomains in the Carajás domain. c) Geological map of Carajás Province - adapted from the Pará geological map (Vasquez et al., 2008) showing the Paleoproterozoic volcano – plutonic event. The localization on all paleomagnetic sites is indicated as the Tucumã and São Felix do Xingu areas. Tu Area = Tucumã area, SFX Area = São Felix area. p. 101

Figure 3.3 Time – space – chart for the Carajás Province. Data and references in Table 3.1. p. 104

Figure 3.4 Geological map of Tucumã according to Vasquez et al. (2008) with localizations of sites. p. 106

Figure 3.5 A: Microgranitic dike (Site 54) in the Tucumã area crosscutting the Tucumã group (greenstone belt). B: NW- Mafic dike at contact with the Rio Maria granodiorite (Archean basement). C: N-S Gabbroic dike. D: Sampling at contact between microgranitic dike and NW - Mafic dike. p. 108

Figure 3.6 Geological map of São Felix do Xingu with localization of sites modified from Juliani and Fernandes (2010). p. 109

Figure 3.7 A: Massive andesite (Montesbelos – flow). B: Topography of the Santa Rosa Formation with massive rhyolite and ignimbrite *in situ*. C: Magmatic folding (flux lines) in rhyolitic flows. D: Andesitic clasts (up to 1 m) in the Sobreiro Formation. p. 112

E: Rhyolitic dike of the Velho Guilherme Suite intruding andesitic rocks of the Montesbelos – flow (Sobreiro Formation).

Figure 4.1 Summary of the techniques used in this work. p. 114

Figure 4.2 A: Sampling with a portable gasoline – powered drilling apparatus to drill a felsic dike (Tucumã). B: Sample orientation. C: Drilling of an oriented block in laboratory. D: Specimens in laboratory after preparation of cylindrical samples. p. 115

Figure 4.3 Lines of equal blocking energy in the V-K diagram. p. 118

Figure 4.4 Acquisition of a remanent magnetization during cooling of a lava flow. Magnetic moments are acquiring a magnetization through the blocking temperature.

Figure 4.5 A: Magnetically shielded room in the Laboratory of IAG – USP with a 2G – Enterprises DC SQUID magnetometer in horizontal position. B: AF demagnetizer apparatus (Molspin). C: Spinner JR6-A™ magnetometer, AGICO®. D: TD-48 Furnace (ASC Scientific). E: RAPID 2G – Enterprises DC SQUID magnetometer in vertical position. F: Low-temperature demagnetization (LTD) with nitrogen bath. G: MicroMag-VSM, Model 3900. p. 121

Figure 4.6 Hysteresis curve for SD grains of magnetite (a) and Magnetization direction during the hysteresis acquisition (b, c d, e), adapted from Butler (1992). p. 124

Figure 4.7 Stereographic representation of an upward magnetic direction. The direction is plotted on the *equal-area* projection in grey (Lambert), modified from Bispo-Santos (2012) p. 125

Figure 4.8 Zijderveld diagram and vision in 3D for the vector (it is the same vector, SE-direction with negative inclination, of the stereographic diagram in Figure 4.7. We can see the decomposition in two orthogonal planes. p. 127

Figure 4.9 Possibility for overlapping demagnetization spectra (H_c or T_b) for 3 examples (a, c, e) and associated Zijderveld diagrams (b, d, f). p. 128

Figure 4.10 Positive baked contact test between a basaltic dike and the granitic basement.*Credits: S. Couzinié* (Florianopolis, Brazil). p. 130

Figure 4.11 Localization of the sample site (S) to calculate the localization of the paleomagnetic pole. From Butler (1992). p. 132

Figure 4.12 Inclination distributions with MV (modified Q_{index} of Van der Voo (1990b). Igneous and metamorphic rocks show a good correlation with the GAD model. Modified from Veikkolainen et al. (2014a). p. 134

Figure 4.13 Reconstruction for the Amazonian craton at ~2036 Ma with the OYA pole. See text for precisions, adapted from D'Agrella-Filho et al. (2016). p. 135

Figure 4.14 Cartoon to represent how we can reconstruct the paleogeography of two cratons (A and B). p. 137

Figure 4.15 Difference between changes in Obliquity and true polar wander (TPW), modified from Siegler et al. (2016). p. 139

Figure 4.16 Simplified concept of true polar wander (TPW), modified from Evans (2003). The equatorial bulge is exaggerated. A: Density anomalies in the mantle can rising p. 139

(red) or sinking (blue). B: TPW turns the whole solid earth (mantle and crust) driving positive loads to the equator. The geomagnetic field remains aligned with W (spin axis).

Figure 4.17 Amplitude of true polar wander events (TPW) according the paleomagnetic database for the Earth and supercontinent cycle. Adapted from Mitchell (2014). p. 141

Figure 4.18 Cartoon to explain the reconstruction during a hypothetic True Polar Wander event (TPW). p. 142

Figure 4.19 Using of the Wetherill diagram for the U-Pb system. p. 145

Figure 4.20 SHRIMP II in the IGc laboratory in São Paulo, Brazil. p. 146

Figure 4.21 LA-ICP-MS in the laboratory of Ouro Preto (UFOP). *Credits: F. Hodel.* p. 147

Figure 4.22 Comparison between analysis by SIMS (SHRIMP) and LA-ICP-MS. p. 147

Figure 4.23 Relation between the relaxation time and the blocking temperature for the magnetite (A) and the hematite (B), called the nomogram diagrams (Pullaiah et al., 1975). p. 149

Figure 5.1 A: Felsic dike of site 52. B: Block of microgranite with phenocrysts of feldspar, plagioclase and quartz. C: NW-Mafic dike with many small blocks. D: NS-gabbroic dike at contact with a microgranitic dike. E: Mingling between mafic and felsic dike. F: Xenocrysts of feldspar in a NW-mafic dike. p. 152

Figure 5.2 A: Polished section of the sample PY69B3. B: SEM image in backscattered electrons (BSE) of perthitic feldspars and plagioclases in a microgranite. C: Photomicrograph of biotite (plane polarized light = PPL). D: Graphyric association in the sample PY65 (cross polarized light = XPL). E: Zircon in the sample PY55 (XPL). F: Subhedral titanite in plagioclase (XPL). Abbreviations: Qtz = quartz, Fk-Na = perthitic feldspar, Pl = plagioclase, Chl = chlorite, Bt = biotite, Ttn = titanite, Cal = calcite. p. 154

Figure 5.3 Iron oxides in microgranites. A: SEM-BSE micrograph of Iron oxide in plagioclase (albite) in the sample PY65G4. B: EDS spectrum for the iron oxide of the image A. C: SEM-Secondary Electron Image (SEI) of primary euhedral magnetite in inclusion in quartz (PY79C2). D: EDS spectrum of the octahedral magnetite (C). Abbreviations: An = albite, Ox = iron oxide, Ep = epidote, Qtz = quartz. p. 155

Figure 5.4 A: SEM-BSE image of secondary paragenese for the microgranites (PY55D2). B: EDS spectrum of epidote. C: SEM-BSE image of muscovite (phengite). D: EDS spectrum of muscovite. E: EDS spectrum of chlorite. F: SEM-BSE image of allanite and REE-F-Carb (PY65G4). G: EDS spectrum of parisite. H: EDS spectrum of allanite. p. 156

Figure 5.5 A: SEM-BSE image of secondary paragenesis with barite, REE-F-carb, xenotime… in plagioclase (PY79C2). B: SEM-BSE image of fracture with fluorine and calcite (PY69B3). C: SEM-BSE image of quartz with inclusion of akaganeite (PY69B3). D: SEM-SEI of Cu-Sn mineral (PY79C2). E: SEM-SEI image of akaganeite mineral (PY69B3). F: EDS spectrum of Akaganeite. G: EDS spectrum of Cu-Sn mineral. Abbreviations: Brt = barite, Chl = chlorite, Pl = plagioclase, Xtm = xenotime, Ox = iron oxide, Cal = calcite, Musc = muscovite, Fk-Na = perthitic felspar, Qtz = quartz. p. 158

Figure 5.6 Sequence of crystallization for the microgranites. p. 159

Figure 5.7 A: Ternary classification diagram $KAlSi_3O_8$ – $CaAl_2Si_2O_8$ – $NaAlSi_3O_8$ for feldspar. B: Chemical composition of biotites in the 10*TiO2 – MgO – MnO + FeO ternary diagram (Nachit et al., 2005). C: Classification of micas, (Mg / (Mg + Fe)) versus Si / Al (IV). (Rieder et al., 1999). D: Classification of iron oxides (Buddington and Lindsley, 1964). p. 160

Figure 5.8 Hysteresis curves for the microgranitic dikes. p. 163

Figure 5.9 A: All IRM curves for microgranites. B: Group-1 (red) = samples with high magnetic susceptibility. C: Group-2 (orange) = intermediate magnetic susceptibility. D: Group-3 (blue) = low magnetic susceptibility. E: Group-4 = very high magnetic susceptibility (contact with mafic dikes). P 164

Figure 5.10 Decomposition of IRMs curves by the analysis of Kruiver et al. (2001). IRM acquisition curve on a linear ordinate scale is called the linear acquisition plot (LAP). Analysis using gradient of acquisition plot is referred to the GAP. p. 165

Figure 5.11 Day's plot for Tucumã dikes, after Dunlop (2002). p. 166

Figure 5.12 Zoom on the PSD domain. Day's plot after Dunlop (2002). p. 167

Figure 5.13 Thermomagnetic curves for dikes of Tucumã. p. 168

Figure 5.14 Summary for the magnetic mineralogy of microgranitic dikes of Tucumã. Magnetic susceptibility frequency histogram for the microgranites to differentiate samples with low magnetic susceptibility (blue) and high magnetic susceptibility (red). Typical hysteresis curves for these samples are represented in blue and in red, respectively. Decomposition of IRMs curves are also represented. p. 169

Figure 5.15 A: TAS diagram (Le Maitre et al., 2002). B: Major element variation diagrams showing the range of compositions, FeO_{tot} / (FeO_{tot} + MgO). (Frost et al., 2001; Frost and Frost, 2008). C : Shand diagram, A/NK vs. A/CNK plot (Maniar and Piccoli, 1989). p. 172

Figure 5.16 Harker diagrams for microgranites and basaltic rocks. p. 172

Figure 5.17 Discriminate diagram, Zr vs. 10000*Ga/Al (ppm) of microgranites (Whalen et al., 1987). p. 173

Figure 5.18 A: Y vs. SiO_2 diagram that shows an enrichment in HREE. B: REE patterns of microgranites (normalizing values are from McDonough and Sun (1995)). Basalts are illustrated in green. Color code depends of the magnetic susceptibility. Red = sample with high magnetic susceptibility (magnetite-rich). Orange = sample with intermediate magnetic susceptibility. Blue = sample with low magnetic susceptibility (hematite-rich). p. 174

Figure 5.19 Geological cross-section of the Carajás Province showing the A-type magmatism (this study). p. 175

Figure 6.1 Day's plot for NW-mafic dikes, gabbroic dikes and the Rio Maria granodiorite. p. 196

Figure 6.2 P (anisotropy degree) versus. Km (mean magnetic susceptibility). p. 197

Figure 6.3 AMS fabric types for the dikes of Tucumã. p. 198

Figure 6.4 Types of AMS fabric in the Tucumã dike swarms. p. 199

Figure 6.5 Schematic cartoon of dikes emplacement for Tucumã dike swarms. σH is the maximum horizontal stress in the Carajás Province at ~1880 Ma. The NS-gabbroic dike is supposed to be Mesozoic in age. p. 201

Figure 6.6 Examples of demagnetization behaviors for the Tucumã dike swarms. Figure shows stereographic projections (solid (open)) symbols represent positive (negative) inclinations), normalized intensity curves and Zijderveld diagrams. p. 203

Figure 6.7 Site mean directions for the Tucumã dikes swarms. p. 204

Figure 6.8 Baked contact tests during paleomagnetic investigation in Tucumã area. Localization of baked contact tests is shown. Magnetic fabrics for respective localities are also shown. p. 208

Figure 6.9 BCT-1. Localization in Figure 6.8. Figure shows stereographic projections (solid (open)) symbols represent positive (negative) inclinations), normalized intensity curves and Zijderveld diagrams. p. 209

Figure 6.10 BCT-2. Localization in Figure 6.8. Figure shows stereographic projections (solid (open)) symbols represent positive (negative) inclinations), normalized intensity curves and Zijderveld diagrams. p.209

Figure 6.11 Confidence of paleomagnetic poles (A, B and C) in Tucumã (Mollweide projection). Red poles could be Proterozoic in ages. Comparison with Neoproterozoic poles in green (Garcia et al., 2013; Trindade et al., 2003) and a Mesozoic pole in light blue (Nomade et al., 2000) of the Amazonian craton. APW path (2050 – 1960 Ma) for the Amazonian craton is indicated by the blue arrow (Bispo-Santos et al., 2014a). p. 210

Figure 6.12 A. Mean site direction for PY58 site. B. Site mean direction for PY68 site. C. Geological map and localization of sites of Tucumã. D. REE pattern for rocks of Velho Guilherme Suite (red) and Tucumã felsic dikes (grey) (da Silva et al., 2016). REE pattern for two samples of felsic dikes of Velho Guilherme Suite in Tucumã area are indicated (site PY73). p. 212

Figure 7.1 Geological map of São Felix do Xingu region with location of sampling sites (Full Square) for Santa Rosa and Sobreiro Formations (adapted from Juliani and Fernandes (2010)). Inset: The ~1880 Ma volcano-plutonic Uatumã event and the main tectonic provinces of the Amazonian craton (adapted from Cordani and Teixeira (2007)). *Abbreviations*: *CP* = Carajás Province (in grey); CA = Central Amazonian Province; MI = Maroni-Itacaiunas Province; VT = Ventuari-Tapájos Province; RNJ = Rio Negro-Juruena Province; RO = Rondonian-San Ignácio Province; SS = Sunsás province. p. 219

Figure 7.2 (A) Concordia diagrams showing U-Pb zircon LA-ICP-MS results for the rhyolite lava flow sample (PY80B2) and cathodoluminescence (CL) images of typical zircon grains for the sample with the weighted average age. (B) Concordia diagrams showing U-Pb zircon LA-ICP-MS results for the sample of the NE-dike (PY92B1) and cathodoluminescence images of typical zircon grains for the Velho Guilherme Suite with the weighted average age. (C) Concordia diagrams showing U-Pb zircon SHRIMP results for the NW-dike (PY99) and cathodoluminescence p. 225

images of typical zircon grains for the dike of the Santa Rosa Formation with the weighted average age.

Figure 7.3 Examples of AF (alternating field) and thermal demagnetization for samples of the Santa Rosa Formation, Sobreiro Formation and Velho Guilherme Suite. Demagnetization results presented with stereographic projections, orthogonal projections (Zijderveld plot) and normalized magnetization intensity curves (M/M_0 versus alternating field H). p. 228

Figure 7.4 Stereographic projections of sample and site mean directions for the sites analyzed. Boxes show mean directions and Fisherian statistical parameters for the four mean directions (SF1, SF2 and SF3). p. 229

Figure 7.5 Baked contact test for a felsic dike of the Velho Guilherme Suite intruding the Sobreiro Formation. The figure shows the locations of the samples and the distance from the contact, stereographic projections, orthogonal projections, and normalized magnetization intensity curves for samples. The different components are illustrated with arrows. p. 232

Figure 7.6 Examples of characteristic isothermal remanent magnetization (IRM) after Kruiver's analysis by cumulative log-Gaussian (CLG) function, gradient acquisition plot (GAP) in red. (A) An ignimbrite showing contribution of two ferromagnetic phases with different coercivities (magnetite and hematite). (B) IRM for the felsic dike of the Velho Guilherme Suite with one mean coervity ("hard magnetite") and a very weak component ("soft magnetite"). (C) IRM for an andesite of the Sobreiro Formation with two ferromagnetic phases (magnetite and hematite). (D) IRM for an andesite with two components of near coercivity (soft and hard magnetite). (E) The dispersion parameter in function of the mean coercivity (Log $B_{1/2}$). p. 233

Figure 7.7 (A) Day plot (Day et al., 1977) of the hysteresis ratios Mrs/Ms and Hcr/Hc for samples where the contribution of hematite is > 60 %. The separation between SD and MD hematite is estimated with a ratio Hcr/Hc of 1.17 according to Özdemir and Dunlop (2014). (B) Hysteresis curve for a sample of rhyolite with a strong hematite contribution (PY82D) showing wasp-waisted type (mixture phases). (C) Thermomagnetic curve with low and high temperature dependence of magnetic susceptibility showing the contribution of hematite. (D) Day plot after Dunlop (2002) for samples whose contribution of magnetite is significative, most sample fall in the Pseudo-single domain (PSD) on a typical SD + MD trend. (E) Hysteresis curve for an andesite sample (PY96K) without hematite and associated thermomagnetic curve (F). p. 235

Figure 7.8 Petrography of analyzed samples. (A) SEM-BSE micrograph and (B) reflected light photomicrograph (crossed nicols at 85°) of subeuhedral crystal of titanomagnetite with exsolution lamellae of ilmenite altered in hematite (Martite, Mt) (PY81D1). (C) SEM-BSE micrograph for a detailed view of the exsolutions and energy dispersive spectra EDS associated (PY81D1). (D) SEM-BSE micrograph of hematite-rich spherulite (PY81D1). (E) SEM-BSE micrograph of hematite co-precipitated with quartz veins (PY101A2). (F) Reflected light photomicrograph (crossed nicols at 85°) for a titanomagnetite crystal and (G) SEM-BSE micrograph for hydrothermal alteration in the dike of the Velho Guilherme Suite (PY92). (H) Reflected light photomicrographs (crossed nicols at 85°) of andesite (PY85C1). Mineral abbreviations used from Whitney and Evans (2010). p. 236

Figure 7.9 APW path traced for the Amazonian craton between 2100 and 1860 Ma (paleomagnetic poles before 1880 Ma in Bispo-Santos et al. (2014a) . Amazonia is in its present position. p. 240

Figure 7.10 Minimum continental velocities calculated between 2100 – 1200 Ma for six cratons during the Columbia supercontinental cycle. Plate tectonic speed limit is marked by a line according to the value of ~30 cm/yr (Gordon et al., 1979; Tarduno, 1990). Paleomagnetic data between 2100 – 1200 Ma is available in supplementary material. p. 243

Figure 7.11 Apparent polar wander paths (APWPs) length of India (A), Superior (B), Slave (C) and Amazonia (D). Paleomagnetic poles indicated are listed in Table 4 and poles used in reconstructions are underlined. Great circles calculated for each craton are indicated by thick lines and axis by red stars with their corresponding cone of confidence circles (Table 7.4). p. 245

Figure 7.12 Possible paleogeographic reconstructions at 1880 Ma (A) and 1860 Ma (B) during the proposed true polar wander. The reconstructions are established with the true polar wander spin axis (I_{min}) as a red star in the center (spinner diagram) and the great circles associated at each craton with the repartition of paleomagnetic poles. Cone of confidence circles for the error of great circle axis are not illustrated for visibility. Paleomagnetic poles used for the reconstructions are labeled with semitransparent filled ellipse. The sense of motion is indicated by a red arrow. *Abbreviations:* NAC = North Australian craton, WAC = West Australian craton. p. 247

Figure 7.13 Geological features during the Precambrian record between 4000 and 500 Ma. (A) Histogram for the crustal zircon age distribution of Belousova et al. (2010).(B) Peaks in Hf model ages in orange show times of juvenile crustal addition (Kemp et al., 2006). (C) $^{4}He/^{3}He$ probability density function from Parman (2007) with peaks of OIB (ocean island basalt) and MORB (mid-ocean ridge basalt) correlated to the frequency of the High-Mg melts though time (Isley and Abbott, 2002). (D) Frequency of iron formations (BIFs) through time (Isley and Abbott, 1999). (E) Distribution of the volcanogenic massive sulphide deposits (VMS) from Franklin et al. (2005). p. 251

List of Tables

Table 1.1 Summary of the events in the Late Archean – Early Paleoproterozoic (See (Condie, 2015) for an exhaustive review). p.21

Table 3.1 Geochronological data for the Amazonian craton. *Abbreviations*: zrn= zircons, Ttn = titanite, wr = whole rock, badd = baddeleyite, Al = alunite, disc. = discordant age, int = lower intercept, Bt = biotite, musc = muscovite, iso = isochron, Mn = manganese. Ar – Ar ages of Tavares (2015) are cooling ages for Archean rocks. References: (Almeida et al., 2000; Alves, 2006; Amaral, 1974; Arcanjo et al., 2013; Avelar et al., 1994; Bahia and Quadros, 2000; Barbosa and Lafon, 1996; Cordani, 1981; da Silva et al., 2016; de Mesquita Barros et al., 2009; Feio et al., 2013; Gomes et al., 1975; Grainger et al., 2008; Juliani et al., 2005; Juliani and Fernandes, 2010; Lamarão et al., 2002; Macambira and Vale, 1997; Macambira, 1992; Macambira and Lafon, 1995; Macambira et al., 2000; Machado et al., 1991; Paixão et al., 2008; Pimentel and Machado, 1994; Pimentel et al., 2003; Pinho et al., 2006; Rodrigues, 1992; Roverato, 2016; Santos et al., 2002; Santos et al., 2001; Tavares, 2015; Teixeira et al., 2002; Teixeira et al., 2012a; Teixeira et al., 2012b; Teixeira et al., 2016; Vasconcelos et al., 1994). p.103

Table 3.2 Site number, sample name, localization and lithology for the sampled sites in the Tucumã area. p. 107

Table 3.3 Site number, sample name, localization and lithology for the sampled sites in the São Felix area. p. 111

Table 5.1 Summary of the analysis of Kruiver et al. (2001) p. 170

Table 6.1 AMS data from the Tucumã dike swarms. K1, K2 and K3 are the maximum, intermediate and minimum susceptibility intensities. N is the number of specimens. Km is the bulk mean magnetic susceptibility. L is the lineation. F is the foliation. P is the anisotropy degree. T is the Jelinek parameter. Dec = declination. Inc = inclination p. 200

Table 6.2 Paleomagnetic results from Tucumã dikes. Lat (latitude); long (longitude) – site geographical coordinates; Strike – dike direction; n/N is the number of sites. The mean direction is given by its declination (Dec) and inclination (Inc), and the paleomagnetic pole by its latitude (P. Lat.) and longitude (P. Long.). R, α95 and k are the Fisher's (1953) statistical parameters. *G.C* –Great circles analysis. n/N is the ratio of samples with considered direction on the total of measured samples. p. 205

Table 7.1 Paleomagnetic sampling in São Felix do Xingu region. p. 222

*: Site sampled for the baked contact test (BCT) - distances from the contact are indicated.

Table 7.2 Zircon U–Pb data obtained by in situ laser ablation ICP-MS and SHRIMP. p. 226

Table 7.3 n/N – number of analyzed samples/number of samples used in the mean; Dec. – declination; Inc. – inclination; α_{95}, k – Fisher's confidence cone and precision parameter (Fisher, 1953); *G.C* –Great circles analysis. VGP – Virtual Geomagnetic Pole; P. Long – Paleolongitude; P. Lat – Paleolatitude. VGPs values are indicated after switching to the antipodal position. p. 230

Table 7.4 Compilation of paleomagnetic poles used in the TPW analysis. Plat, Paleolatitude; Plong, Paleolongitude; A_{95}, semiangle of the cone of 95 % confidence about the pole. Geochronological symbols: corr.- correlation with related unit; zrn- zircon; badd- baddeleyite; pl- plagioclase; phl- phlogopite; Q- Quality factors (Van der Voo, 1990b). Analysis of TPW; [1]: Angular separation of poles (°). [2]: Time separation of poles (Ma). [3]: Conservative APW rate (cm/yr) with error associated (velocity maximum-velocity minimum). p. 249

References: 1, Buchan et al. (2016); 2, Mitchell et al. (2010); 3, Irving et al. (1972b); 4, Evans and Bingham (1973); 5, Morelli et al. (2009); 6, Evans and Halls (2010); 7, Schmidt (1980); 8, Hamilton et al. (2009); 9, Williams and Schmidt (2004); 10, Findlay et al. (1995); 11, **This study**; 12, Hanson et al. (2011); 13, Söderlund et al. (2010); 14, Hanson et al. (2004); 15, Lubnina et al. (2010a); 16, Olsson et al. (2015); 17, Didenko et al. (2009); 18, Donskaya et al. (2007); 19 Vodovozov (2010); 20, Didenko et al. (2006); 21, Larin et al. (2003); 22, Vodovozov et al. (2007); 23, Prasad et al. (1987); 24, Meert et al. (2011); 25, French et al. (2008); 26, Belica et al. (2014); 27, Radhakrishna et al. (2013b); 28, Radhakrishna et al. (2013a); 29, Elming (1985); 30, Skiöld (1988); 31, Neuvonen et al. (1981); 32, Marttila (1981); 33, Pesonen and Stigzelius (1972); 34, Helovuori (1979); 35, Mertanen and Pesonen (1992); 36, Mertanen (2013) unpublished; 37, Pesonen et al. (2003); 38, Elming (1994); 39, Klein (2016); 40, Poorter (1976); 41, Bergström et al. (2002); 42, Williams et al. (2004); 43, Rasmussen et al. (2012); 44, Idnurm and Giddings (1988).

REFERENCES

Abrajevitch, A., Van der Voo, R., 2010. Incompatible Ediacaran paleomagnetic directions suggest an equatorial geomagnetic dipole hypothesis. Earth and Planetary Science Letters 293, 164-170.

Agangi, A., Kamenetsky, V.S., McPhie, J., 2010. The role of fluorine in the concentration and transport of lithophile trace elements in felsic magmas: Insights from the Gawler Range Volcanics, South Australia. Chemical Geology 273, 314-325.

Allègre, C.J., Rousseau, D., 1984. The growth of the continent through geological time studied by Nd isotope analysis of shales. Earth and Planetary Science Letters 67, 19-34.

Almeida, F.F.M., Hasui, Y., Neves, B.B.D., Fuck, R.A., 1981. Brazilian Structural Provinces: An Introduction. Earth-Science Reviews 17, 1-29.

Almeida, F.F.M.d., Brito Neves, B.B.d., Dal Ré Carneiro, C., 2000. The origin and evolution of the South American Platform. Earth-Science Reviews 50, 77-111.

Alves, C., 2006. Petrologia, geoquímica e geocronologia do granito Ramal do Lontra e sua relação com a tectônica e metamorfismo do Cinturão Araguaia, Xambioá (TO). Unpublished MSc. Thesis Universidade Federal do Pará.

Amaral, G., 1974. Geologia Pré-Cambriana da região amazônica. Universidade de São Paulo.

Andersen, T., Andersson, U.B., Graham, S., Åberg, G., Simonsen, S.L., 2009. Granitic magmatism by melting of juvenile continental crust: new constraints on the source of Palaeoproterozoic granitoids in Fennoscandia from Hf isotopes in zircon. Journal of the Geological Society 166, 233-247.

Antonio, P.Y., D'Agrella-Filho, M.S., Da Trindade, R.I., Nédélec, A., De Oliveira, D.C., Da Silva, F.F., 2016. Paleomagnetismo e magnetismo das rochas do enxame de diques felsicos e maficos do evento Uatumã hà 1.88 Ga (Para), In: Letters, L. (Ed.), Latinmag Letters, São Paulo, pp. B03, 01-07.

Araújo, O., Maia, R., 1991. Serra dos Carajás. Folha SB.

Araújo, O.d., Maia, R., Jorge João, X.d.S., Costa, J., 1988. A megaestruturação arqueana da folha Serra dos Carajás, Congresso Latino-Americano de Geologia. SBG-NO Belém, pp. 324-333.

Arcanjo, S.H.d.S., Abreu, F.d.A.M.d., Moura, C.A.V., 2013. Evolução geológica das sequências do embasamento do Cinturão Araguaia na região de Paraíso do Tocantins (TO), Brasil. Brazilian Journal of Geology 43, 501-514.

Armstrong, R.L., Harmon, R.S., 1981. Radiogenic Isotopes: The Case for Crustal Recycling on a Near-Steady-State No-Continental-Growth Earth [and Discussion]. Philosophical Transactions of the Royal Society of London. Series A, Mathematical and Physical Sciences 301, 443-472.

Armstrong, R.L., 1991. The persistent myth of crustal growth. Australian Journal of Earth Sciences 38, 613-630.

Arndt, N., Davaille, A., 2013. Episodic Earth evolution. Tectonophysics 609, 661-674.

Arndt, N.T., Coltice, N., Helmstaedt, H., Gregoire, M., 2009. Origin of Archean subcontinental lithospheric mantle: Some petrological constraints. Lithos 109, 61-71.

Asael, D., Tissot, F.L.H., Reinhard, C.T., Rouxel, O., Dauphas, N., Lyons, T.W., Ponzevera, E., Liorzou, C., Chéron, S., 2013. Coupled molybdenum, iron and uranium stable isotopes as oceanic paleoredox proxies during the Paleoproterozoic Shunga Event. Chemical Geology 362, 193-210.

Aubert, J., Labrosse, S., Poitou, C., 2009. Modelling the palaeo-evolution of the geodynamo. Geophysical Journal International 179, 1414-1428.

Avelar, V.d., Lafon, J., Scheller, T., Araujo, O.d., Macambira, E., 1994. Geocronologia Pb-Pb por evaporação de zircão e Rb-Sr em rocha total do Granito Seringa, Província Mineral do Carajás, 38 CONGRESSO BRASILEIRO DE GEOLOGIA. SBG Balneário Camboriú.

Bahia, R., Quadros, M., 2000. Geologia e recursos minerais da Folha Caracol (SB. 21-XC). Estado do Pará. Escala 1.

Bao, H., Lyons, J.R., Zhou, C., 2008. Triple oxygen isotope evidence for elevated CO2 levels after a Neoproterozoic glaciation. Nature 453, 504-506.

Barbosa, Lafon, J.M., 1996. Geocronologia Pb-Pb e Rb-Sr de granitóides arqueanos da região de Redenção-sul do Pará. Revista Brasileira de Geociências 26, 255-264.

Barton, J.M., Klemd, R., Zeh, A., 2006. The Limpopo Belt: A result of Archean to Proterozoic, Turkic-type orogenesis? Geological Society of America Special Papers 405, 315-332.

Bates, M.P., Jones, D.L., 1996. A palaeomagnetic investigation of the Mashonaland dolerites, north-east Zimbabwe. Geophysical Journal International 126, 513-524.

Bazhenov, M.L., Levashova, N.M., Meert, J.G., Golovanova, I.V., Danukalov, K.N., Fedorova, N.M., 2016. Late Ediacaran magnetostratigraphy of Baltica: Evidence for Magnetic Field Hyperactivity? Earth and Planetary Science Letters 435, 124-135.

Bédard, J.H., 2006. A catalytic delamination-driven model for coupled genesis of Archaean crust and sub-continental lithospheric mantle. Geochimica et Cosmochimica Acta 70, 1188-1214.

Bekker, A., Slack, J.F., Planavsky, N., Krapež, B., Hofmann, A., Konhauser, K.O., Rouxel, O.J., 2010. Iron formation: the sedimentary product of a complex interplay among mantle, tectonic, oceanic, and biospheric processes. Economic Geology 105, 467-508.

Belica, M.E., Piispa, E.J., Meert, J.G., Pesonen, L.J., Plado, J., Pandit, M.K., Kamenov, G.D., Celestino, M., 2014. Paleoproterozoic mafic dyke swarms from the Dharwar craton; paleomagnetic poles for India from 2.37 to 1.88 Ga and rethinking the Columbia supercontinent. Precambrian Research 244, 100-122.

Belousova, E.A., Kostitsyn, Y.A., Griffin, W.L., Begg, G.C., O'Reilly, S.Y., Pearson, N.J., 2010. The growth of the continental crust: Constraints from zircon Hf-isotope data. Lithos 119, 457-466.

Benešová, N., Čížková, H., 2016. Effect of post-perovskite rheology on the thermal evolution of the Earth. Physics of the Earth and Planetary Interiors 251, 1-10.

Bergström, U., Juhojuntti, N., Kero, L., Lundqvist, L., Stephens, M., Sukotjo, S., Wik, N., Wikman, H., Delin, H., 2002. Projekt Småland, regionalt berg. Regional berggrundsgeologisk undersökning. Sammanfattning av pågående undersökningar. Geological Survey of Sweden, Uppsala, 65-83.

Berry, A.J., Danyushevsky, L.V., St C. O/'Neill, H., Newville, M., Sutton, S.R., 2008. Oxidation state of iron in komatiitic melt inclusions indicates hot Archaean mantle. Nature 455, 960-963.

Besse, J., Courtillot, V., 2002. Apparent and true polar wander and the geometry of the geomagnetic field over the last 200 Myr. Journal of Geophysical Research: Solid Earth 107, EPM 6-1-EPM 6-31.

Bettencourt, J.S., Leite Jr, W.B., Ruiz, A.S., Matos, R., Payolla, B.L., Tosdal, R.M., 2010. The Rondonian-San Ignacio Province in the SW Amazonian Craton: An overview. Journal of South American Earth Sciences 29, 28-46.

Betts, P.G., Armit, R.J., Stewart, J., Aitken, A.R.A., Ailleres, L., Donchak, P., Hutton, L., Withnall, I., Giles, D., 2016. Australia and Nuna. Geological Society, London, Special Publications 424, 47-81.

Biggin, A.J., Piispa, E.J., Pesonen, L.J., Holme, R., Paterson, G.A., Veikkolainen, T., Tauxe, L., 2015. Palaeomagnetic field intensity variations suggest Mesoproterozoic inner-core nucleation. Nature 526, 245-248.

Bispo-Santos, F., D'Agrella-Filho, M.S., Pacca, I.I.G., Janikian, L., Trindade, R.I.F., Elming, S.-A., Silva, J.A., Barros, M.A.S., Pinho, F.E.C., 2008. Columbia revisited: Paleomagnetic results from the 1790 Ma colider volcanics (SW Amazonian Craton, Brazil). Precambrian Research 164, 40-49.

Bispo-Santos, F., 2012. Estudo Paleomagnético de Unidades Paleoproterozóicas do Cráton Amazônico. Universidade de São Paulo.

Bispo-Santos, F., D'Agrella-Filho, M.S., Trindade, R.I.F., Elming, S.-Å., Janikian, L., Vasconcelos, P.M., Perillo, B.M., Pacca, I.I.G., da Silva, J.A., Barros, M.A.S., 2012. Tectonic implications of the 1419Ma Nova Guarita mafic intrusives paleomagnetic pole (Amazonian Craton) on the longevity of Nuna. Precambrian Research 196-197, 1-22.

Bispo-Santos, F., D'Agrella-Filho, M.S., Janikian, L., Reis, N.J., Trindade, R.I.F., Reis, M.A.A.A., 2014a. Towards Columbia: Paleomagnetism of 1980–1960 Ma Surumu volcanic rocks, Northern Amazonian Craton. Precambrian Research 244, 123-138.

Bispo-Santos, F., D'Agrella-Filho, M.S., Trindade, R.I.F., Janikian, L., Reis, N.J., 2014b. Was there SAMBA in Columbia? Paleomagnetic evidence from 1790 Ma Avanavero mafic sills (northern Amazonian Craton). Precambrian Research 244, 139-155.

Bispo-Santos, F., D'Agrella Filho, M.S., Trindade, R.I.F., 2016. PRELIMINARY PALEOMAGNETIC POLE FROM SEDIMENTARY ROCKS OF RORAIMA SUPERGROUP, NORTHERN AMAZONIAN CRATON, In: Letters, L. (Ed.), Latinmag Letters, São Paulo, pp. B05, 01-05.

Black, L.P., Kamo, S.L., Allen, C.M., Davis, D.W., Aleinikoff, J.N., Valley, J.W., Mundil, R., Campbell, I.H., Korsch, R.J., Williams, I.S., Foudoulis, C., 2004. Improved 206Pb/238U microprobe geochronology by the monitoring of a trace-element-related matrix effect; SHRIMP, ID–TIMS, ELA–ICP–MS and oxygen isotope documentation for a series of zircon standards. Chemical Geology 205, 115-140.

Bleeker, W., 2001. Evolution of the Slave craton and the search for supercratons, Program with Abstracts, Geological Association of Canada, p. 14.

Bleeker, W., 2003. The late Archean record: a puzzle in ca. 35 pieces. Lithos 71, 99-134.

Bleeker, W., Hamilton, M., Söderlund, U., Ernst, R., 2008. Towards a complete magmatic event ''barcode''for the Slave craton, I: A precise U–Pb baddeleyite age for the Hearne swarm with implications for a newly recognized Paleoproterozoic LIP across the western Canadian Shield, Annual Meeting, Abstracts, p. 23.

Bogdanova, S., Gorbatschev, R., Skridlaite, G., Soesoo, A., Taran, L., Kurlovich, D., 2015. Trans-Baltic Palaeoproterozoic correlations towards the reconstruction of supercontinent Columbia/Nuna. Precambrian Research 259, 5-33.

Bogdanova, S.V., Gintov, O.B., Kurlovich, D.M., Lubnina, N.V., Nilsson, M.K.M., Orlyuk, M.I., Pashkevich, I.K., Shumlyanskyy, L.V., Starostenko, V.I., 2013. Late Palaeoproterozoic mafic dyking in the Ukrainian Shield of Volgo-Sarmatia caused by rotation during the assembly of supercontinent Columbia (Nuna). Lithos 174, 196-216.

Bonin, B., 2007. A-type granites and related rocks: Evolution of a concept, problems and prospects. Lithos 97, 1-29.

Boone, G.M., 1969. Origin of clouded red feldspars; petrologic contrasts in a granitic porphyry intrusion. American Journal of Science 267, 633-668.

Borradaile, G.J., 1994. Low-temperature demagnetization and ice-pressure demagnetization in magnetite and haematite. Geophysical Journal International 116, 571-584.

Borradaile, G.J., Lucas, K., Middleton, R.S., 2004. Low-temperature demagnetization isolates stable magnetic vector components in magnetite-bearing diabase. Geophysical Journal International 157, 526-536.

Bouley, S., Baratoux, D., Matsuyama, I., Forget, F., Séjourné, A., Turbet, M., Costard, F., 2016. Late Tharsis formation and implications for early Mars. Nature 531, 344-347.

Boyden, J.A., Müller, R.D., Gurnis, M., Torsvik, T.H., Clark, J.A., Turner, M., Ivey-Law, H., Watson, R.J., Cannon, J.S., 2011. Next-generation plate-tectonic reconstructions using GPlates. Geoinformatics: cyberinfrastructure for the solid earth sciences, 95-114.

Bradley, D.C., 2008. Passive margins through earth history. Earth-Science Reviews 91, 1-26.

Bradley, D.C., 2011. Secular trends in the geologic record and the supercontinent cycle. Earth-Science Reviews 108, 16-33.

Brandl, P.A., Regelous, M., Beier, C., Haase, K.M., 2013. High mantle temperatures following rifting caused by continental insulation. Nature Geosci 6, 391-394.

Brandon, A.D., Walker, R.J., Puchtel, I.S., Becker, H., Humayun, M., Revillon, S., 2003. 186Os–187Os systematics of Gorgona Island komatiites: implications for early growth of the inner core. Earth and Planetary Science Letters 206, 411-426.

Brasier, M.D., Antcliffe, J., Saunders, M., Wacey, D., 2015. Changing the picture of Earth's earliest fossils (3.5–1.9 Ga) with new approaches and new discoveries. Proceedings of the National Academy of Sciences 112, 4859-4864.

Breitkreuz, C., 2013. Spherulites and lithophysae—200 years of investigation on high-temperature crystallization domains in silica-rich volcanic rocks. Bulletin of Volcanology 75, 1-16.

Bridgwater, D., Austrheim, H., Hansen, B.T., Mengel, F., Pedersen, S., Winter, J., 1990. The Proterozoic Nagssugtoqidian mobile belt of southeast Greenland: A link between the eastern Canadian and Baltic shields. 1990.

Brito Neves, B.B.d., 2011. The Paleoproterozoic in the South-American continent: Diversity in the geologic time. Journal of South American Earth Sciences 32, 270-286.

Brown, M., 2006. Duality of thermal regimes is the distinctive characteristic of plate tectonics since the Neoarchean. Geology 34, 961-964.

Bryan, S.E., Ernst, R.E., 2008. Revised definition of Large Igneous Provinces (LIPs). Earth-Science Reviews 86, 175-202.

Bryan, S.E., Ferrari, L., 2013. Large igneous provinces and silicic large igneous provinces: Progress in our understanding over the last 25 years. Geological Society of America Bulletin 125, 1053-1078.

Buchan, K., Halls, H., 1990. Paleomagnetism of Proterozoic mafic dyke swarms of the Canadian Shield. Mafic Dykes and Emplacement Mechanisms. Balkema, Rotterdam, 209-230.

Buchan, K.L., 1978. Magnetic overprinting in the Thanet gabbro complex, Ontario. Canadian Journal of Earth Sciences 15, 1407-1421.

Buchan, K.L., Mertanen, S., Park, R.G., Pesonen, L.J., Elming, S.Å., Abrahamsen, N., Bylund, G., 2000. Comparing the drift of Laurentia and Baltica in the Proterozoic: the importance of key palaeomagnetic poles. Tectonophysics 319, 167-198.

Buchan, K.L., Goutier, J., Hamilton, M.A., Ernst, R.E., Matthews, W.A., 2007. Paleomagnetism, U–Pb geochronology, and geochemistry of Lac Esprit and other dyke swarms, James Bay area, Quebec, and implications for Paleoproterozoic deformation of the Superior Province. Canadian Journal of Earth Sciences 44, 643-664.

Buchan, K.L., LeCheminant, A.N., van Breemen, O., 2009. Paleomagnetism and U-Pb geochronology of the Lac de Gras diabase dyke swarm, Slave Province, Canada: implications for relative drift of Slave and Superior provinces in the Paleoproterozoic. Canadian Journal of Earth Sciences 46, 361-379.

Buchan, K.L., N., L.A., Otto., v.B., 2012. Malley diabase dykes of the Slave craton, Canadian Shield: U–Pb age, paleomagnetism, and implications for continental reconstructions in the early Paleoproterozoic1Geological Survey of Canada Contribution 20110114. Canadian Journal of Earth Sciences 49, 435-454.

Buchan, K.L., 2013. Key paleomagnetic poles and their use in Proterozoic continent and supercontinent reconstructions: A review. Precambrian Research 238, 93-110.

Buchan, K.L., Mitchell, R.N., Bleeker, W., Hamilton, M.A., LeCheminant, A.N., 2016. Paleomagnetism of ca. 2.13-2.11 Ga Indin and ca. 1.885 Ga Ghost dyke swarms of the Slave craton: Implications for the Slave craton APW path and relative drift of Slave, Superior and Siberian cratons in the Paleoproterozoic. Precambrian Research 275, 151-175.

Buddington, A.F., Lindsley, D.H., 1964. Iron-Titanium Oxide Minerals and Synthetic Equivalents. Journal of Petrology 5, 310-357.

Burke, K., Dewey, J., 1973. Plume-generated triple junctions: key indicators in applying plate tectonics to old rocks. The Journal of Geology, 406-433.

Butler, R.F., 1992. Paleomagnetism: magnetic domains to geologic terranes. Blackwell Scientific Publications.

Campbell, I.H., Allen, C.M., 2008. Formation of supercontinents linked to increases in atmospheric oxygen. Nature Geosci 1, 554-558.

Canfield, D., 1998. A new model for Proterozoic ocean chemistry. Nature 396, 450-453.

Cañón-Tapia, E., Walker, G.P.L., Herrero-Bervera, E., 1996. The internal structure of lava flows—insights from AMS measurements I: Near-vent a'a. Journal of Volcanology and Geothermal Research 70, 21-36.

Cañón-Tapia, E., 2004. Anisotropy of magnetic susceptibility of lava flows and dykes: A historical account. Geological Society, London, Special Publications 238, 205-225.
Carlson, R.W., 2005. Application of the Pt–Re–Os isotopic systems to mantle geochemistry and geochronology. Lithos 82, 249-272.
Castillo, J.H., Costanzo-Alvarez, V., 1993. Paleomagnetism of the Uairen Formation, Roraima Group, southeastern Venezuela: evidence for one of the oldest (Middle Proterozoic) depositional remanent magnetizations. Canadian Journal of Earth Sciences 30, 2380-2388.
Castro, J.M., Beck, P., Tuffen, H., Nichols Alexander, R.L., Dingwell Donald, B., Martin Michael, C., 2008. Timescales of spherulite crystallization in obsidian inferred from water concentration profiles, American Mineralogist, p. 1816.
Cawood, P.A., Hawkesworth, C.J., 2013. Temporal relations between mineral deposits and global tectonic cycles. Geological Society, London, Special Publications 393.
Cawood, P.A., Hawkesworth, C.J., Dhuime, B., 2013. The continental record and the generation of continental crust. Geological Society of America Bulletin 125, 14-32.
Cederberg, J., Söderlund, U., Oliveira, E.P., Ernst, R.E., Pisarevsky, S.A., 2016. U-Pb baddeleyite dating of the Proterozoic Pará de Minas dyke swarm in the São Francisco craton (Brazil) – implications for tectonic correlation with the Siberian, Congo and North China cratons. GFF, 1-22.
Chadima, M., Hrouda, F., 2006. Remasoft 3.0 a user-friendly paleomagnetic data browser and analyzer. Travaux Géophysiques 27, 20-21.
Chan, N.H., Mitrovica, J.X., Daradich, A., Creveling, J.R., Matsuyama, I., Stanley, S., 2014. Time-dependent rotational stability of dynamic planets with elastic lithospheres. Journal of Geophysical Research: Planets 119, 169-188.
Chardon, D., Rey, P., Teyssier, C., Whitney, D.L., 2009. Hot orogens. Tectonophysics 477, 103-104.
Christensen, U.R., 1985. Thermal evolution models for the Earth. Journal of Geophysical Research: Solid Earth 90, 2995-3007.
Coffin, M.F., Eldholm, O., 1994. Large igneous provinces: Crustal structure, dimensions, and external consequences. Reviews of Geophysics 32, 1-36.
Cogné, J.P., 2003. PaleoMac: A Macintosh™ application for treating paleomagnetic data and making plate reconstructions. Geochemistry, Geophysics, Geosystems 4, 1007.
Condie, K., 2013. Preservation and Recycling of Crust during Accretionary and Collisional Phases of Proterozoic Orogens: A Bumpy Road from Nuna to Rodinia. Geosciences 3, 240-261.
Condie, K.C., 1998. Episodic continental growth and supercontinents: a mantle avalanche connection? Earth and Planetary Science Letters 163, 97-108.
Condie, K.C., 2000. Episodic continental growth models: afterthoughts and extensions. Tectonophysics 322, 153-162.
Condie, K.C., 2002a. Continental growth during a 1.9-Ga superplume event. Journal of Geodynamics 34, 249-264.
Condie, K.C., 2002b. The supercontinent cycle: are there two patterns of cyclicity? Journal of African Earth Sciences 35, 179-183.
Condie, K.C., 2004. Supercontinents and superplume events: distinguishing signals in the geologic record. Physics of the Earth and Planetary Interiors 146, 319-332.
Condie, K.C., O'Neill, C., Aster, R.C., 2009. Evidence and implications for a widespread magmatic shutdown for 250 My on Earth. Earth and Planetary Science Letters 282, 294-298.
Condie, K.C., Aster, R.C., 2010. Episodic zircon age spectra of orogenic granitoids: The supercontinent connection and continental growth. Precambrian Research 180, 227-236.
Condie, K.C., O'Neill, C., 2010. The Archean-Proterozoic boundary: 500 my of tectonic transition in Earth history. American Journal of Science 310, 775-790.
Condie, K.C., 2015. Earth as an evolving planetary system. Academic Press.

Condie, K.C., Davaille, A., Aster, R.C., Arndt, N., 2015. Upstairs-downstairs: supercontinents and large igneous provinces, are they related? International Geology Review 57, 1341-1348.

Condie, K.C., 2016. A planet in transition: The onset of plate tectonics on Earth between 3 and 2 Ga? Geoscience Frontiers.

Condie, K.C., Aster, R.C., van Hunen, J., 2016. A great thermal divergence in the mantle beginning 2.5 Ga: Geochemical constraints from greenstone basalts and komatiites. Geoscience Frontiers 7, 543-553.

Cooper, C., Lenardic, A., Levander, A., Moresi, L., 2006. Creation and preservation of cratonic lithosphere: Seismic constraints and geodynamic models, Archean Geodynamics and Environments. AGU, Washington, DC, pp. 75-88.

Cordani, Sato, 1999. Crustal evolution of the South American Platform, based on Nd isotopic systematics on granitoid rocks. Episodes-Newsmagazine of the International Union of Geological Sciences 22, 167-173.

Cordani, U., Tassinari, C., Teixeira, W., Basei, M., Kawashita, K., 1979. Evolução tectônica da Amazônia com base nos dados geocronológicos, Congresso Geológico Chileno, pp. 137-148.

Cordani, U., 1981. Comentários sobre as determinações geocronológicas da região da Serra dos Carajás. Report, Universidade de São Paulo-Docegeo.

Cordani, U., Neves, B.B., 1982. The geologic evolution of South America during the Archean and Early Proterozoic. Revista Brasileira de Geociências 12, 78-88.

Cordani, U.G., Teixeira, W., 2007. Proterozoic accretionary belts in the Amazonian Craton. Geological Society of America Memoirs 200, 297-320.

Cordani, U.G., Teixeira, W., D'Agrella-Filho, M.S., Trindade, R.I., 2009. The position of the Amazonian Craton in supercontinents. Gondwana Research 15, 396-407.

Corfu, F., Hanchar, J.M., Hoskin, P.W.O., Kinny, P., 2003. Atlas of Zircon Textures. Reviews in Mineralogy and Geochemistry 53, 469-500.

Corrigan, D., Pehrsson, S., Wodicka, N., de Kemp, E., 2009. The Palaeoproterozoic Trans-Hudson Orogen: a prototype of modern accretionary processes. Geological Society, London, Special Publications 327, 457-479.

Costa, J., Hasui, Y., 1997. Evolução geológica da Amazônia. Costa MLC & Angélica RS (coords.) Contribuição à Geologia da Amazônia. SBG-NO, 15-90.

Creer, K.M., Irving, E., Runcorn, S.K., 1954. The Direction of the Geomagnetic Field in Remote Epochs in Great Britain. Journal of geomagnetism and geoelectricity 6, 163-168.

Creveling, J.R., Mitrovica, J.X., Chan, N.H., Latychev, K., Matsuyama, I., 2012. Mechanisms for oscillatory true polar wander. Nature 491, 244-248.

D'Agrella-Filho, M.S., Trindade, R.I.F., Elming, S.-Å., Teixeira, W., Yokoyama, E., Tohver, E., Geraldes, M.C., Pacca, I.I.G., Barros, M.A.S., Ruiz, A.S., 2012. The 1420 Ma Indiavaí Mafic Intrusion (SW Amazonian Craton): Paleomagnetic results and implications for the Columbia supercontinent. Gondwana Research 22, 956-973.

D'Agrella-Filho, M.S., Bispo-Santos, F., Trindade, R.I.F., 2015. O Cráton Amazônico em Supercontinentes - Uma visão com base em dados paleomagnéticos. Contribuições à Geologia da Amazônia 9, 287-304.

D'Agrella-Filho, M.S., Bispo-Santos, F., Trindade, R.I.F., Antonio, P.Y.J., 2016. Paleomagnetism of the Amazonian Craton and its role in paleocontinents. Brazilian Journal of Geology 46, 275-299.

D'Agrella-Filho, M.S., Trindade, R.I.F., Tohver, E., Janikian, L., Teixeira, W., Hall, C., 2011. Paleomagnetism and 40Ar/39Ar geochronology of the high-grade metamorphic rocks of the Jequié block, São Francisco Craton: Atlantica, Ur and beyond. Precambrian Research 185, 183-201.

D'Agrella-Filho, M.S., Trindade, R.I.F., Queiroz, M.V.B., Meira, V.T., Janikian, L., Ruiz, A.S., Bispo-Santos, F., 2016. Reassessment of Aguapeí (Salto do Céu) Paleomagnetic pole of the Amazonian Craton and implications for Proterozoic supercontinents. Precambrian Research 272, 1-17.

da Cruz, R.S., Fernandes, C.M.D., Villas, R.N.N., Juliani, C., Monteiro, L.V.S., de Almeida, T.I.R., Lagler, B., de Carvalho Carneiro, C., Misas, C.M.E., 2015. A study of the hydrothermal alteration in Paleoproterozoic volcanic centers, São Félix do Xingu region, Amazonian Craton, Brazil, using short-wave infrared spectroscopy. Journal of Volcanology and Geothermal Research 304, 324-335.

da Cruz, R.S., Fernandes, C.M.D., Villas, R.N.N., Juliani, C., Monteiro, L.V.S., Lagler, B., Misas, C.M.E., 2016. Paleoproterozoic volcanic centers of the São Félix do Xingu region, Amazonian craton, Brazil: Hydrothermal alteration and metallogenetic potential. Journal of Volcanology and Geothermal Research 320.

da Silva, F.F., de Oliveira, D.C., Antonio, P.Y.J., D'Agrella Filho, M.S., Lamarão, C.N., 2016. Bimodal magmatism of the Tucumã area, Carajás province: U-Pb geochronology, classification and processes. Journal of South American Earth Sciences 72, 95-114.

Dall'Agnol, R., Costi, H.T., da S. Leite, A.A., de Magalhães, M.S., Teixeira, N.P., 1999a. Rapakivi granites from Brazil and adjacent areas. Precambrian Research 95, 9-39.

Dall'Agnol, R., Rämö, O.T., de Magalhães, M.S., Macambira, M.J.B., 1999b. Petrology of the anorogenic, oxidised Jamon and Musa granites, Amazonian Craton: implications for the genesis of Proterozoic A-type granites. Lithos 46, 431-462.

Dall'Agnol, R., Scaillet, B., Pichavant, M., 1999c. An Experimental Study of a Lower Proterozoic A-type Granite from theEastern Amazonian Craton, Brazil. Journal of Petrology 40, 1673-1698.

Dall'Agnol, R., Teixeira, N.P., Rämö, O.T., Moura, C.A.V., Macambira, M.J.B., de Oliveira, D.C., 2005. Petrogenesis of the Paleoproterozoic rapakivi A-type granites of the Archean Carajás metallogenic province, Brazil. Lithos 80, 101-129.

Dall'Agnol, R., de Oliveira, D.C., 2007. Oxidized, magnetite-series, rapakivi-type granites of Carajás, Brazil: Implications for classification and petrogenesis of A-type granites. Lithos 93, 215-233.

Dall'Agnoll, R., Oliveira, D., Guimarães, F., Gabriel, E., Feio, G., Lamarão, C., Althoff, F., Santos, P., Teixeira, M., Silva, A., 2013. Geologia do subdomínio de transição do Domínio Carajás–Implicações para a evolução arqueana da Província Carajás–Pará. 13º Simpósio de Geologia da Amazônia, Anais.

Daly, M.C., Andrade, V., Barousse, C.A., Costa, R., McDowell, K., Piggott, N., Poole, A.J., 2014. Brasiliano crustal structure and the tectonic setting of the Parnaíba basin of NE Brazil: Results of a deep seismic reflection profile. Tectonics 33, 2102-2120.

Dalziel, I., 1999. Global Paleotectonics: reconstructing a credible supercontinent, Nordic Palaeomagnetic Symposium. Aarhus Geosci 8, 37-40.

Davies, G.F., 2009. Effect of plate bending on the Urey ratio and the thermal evolution of the mantle. Earth and Planetary Science Letters 287, 513-518.

Day, A., Runcorn, S., 1955. Polar wandering: some geological, dynamical and palaeomagnetic aspects. Nature 176, 422-426.

Day, R., Fuller, M., Schmidt, V.A., 1977. Hysteresis properties of titanomagnetites: Grain-size and compositional dependence. Physics of the Earth and Planetary Interiors 13, 260-267.

De Avelar, V.G., Lafon, J.-M., Correia JR, F.C., Macambira, E.M.B., 1999. O Magmatismo arqueano da região de Tucumã-Província Mineral de Carajás: novos resultados geocronológicos. Brazilian Journal of Geology 29, 453-460.

de Azevedo, P.A., Rocha, M.P., Soares, J.E.P., Fuck, R.A., 2015. Thin lithosphere between the Amazonian and São Francisco cratons, in central Brazil, revealed by seismic P-wave tomography. Geophysical Journal International 201, 61-69.

de Kock, M.O., Evans, D.A.D., Dorland, H.C., Beukes, N.J., Gutzmer, J., 2006. Paleomagnetism of the lower two unconformity-bounded sequences of the Waterberg Group, South Africa: Towards a better-defined apparent polar wander path for the Paleoproterozoic Kaapvaal Craton. South African Journal of Geology 109, 157-182.

de Mesquita Barros, C.E., Sardinha, A.S., de Oliveira Barbosa, J.d.P., Macambira, M.J.B., Barbey, P., Boullier, A.-M., 2009. STRUCTURE, PETROLOGY, GEOCHEMISTRY AND ZIRCON U/Pb AND Pb/Pb GEOCHRONOLOGY OF THE SYNKINEMATIC

ARCHEAN (2.7 Ga) A-TYPE GRANITES FROM THE CARAJÁS METALLOGENIC PROVINCE, NORTHERN BRAZIL. The Canadian Mineralogist 47, 1423-1440.

De Min, A., Piccirillo, E.M., Marzoli, A., Bellieni, G., Renne, P.R., Ernesto, M., Marques, L.S., 2003. The Central Atlantic Magmatic Province (CAMP) in Brazil: petrology, geochemistry, 40Ar/39Ar ages, paleomagnetism and geodynamic implications. Geophysical Monograph Series 136, 91-128.

Dhuime, B., Hawkesworth, C.J., Cawood, P.A., Storey, C.D., 2012. A Change in the Geodynamics of Continental Growth 3 Billion Years Ago. Science 335, 1334-1336.

Didenko, A.N., Vodovozov, V.Y., Gladkochub, D.P., Donskaya, T.V., Mazukabzov, A.M., Kozakov, I.V., Bibikova, E.V., Kirnozova, T.I., Stanevich, A.M., 2006. Paleomagnetism of the Early Proterozoic southern Siberian craton. In: Sklyarov, E.V.(Ed.), Evolution of the Southern Part of the Siberian Craton in the Precambrian,Novosibirsk., p. 367 (in Russian).

Didenko, A.N., Vodovozov, V.Y., Pisarevsky, S.A., Gladkochub, D.P., Donskaya, T.V., Mazukabzov, A.M., Stanevich, A.M., Bibikova, E.V., Kirnozova, T.I., 2009. Palaeomagnetism and U-Pb dates of the Palaeoproterozoic Akitkan Group (South Siberia) and implications for pre-Neoproterozoic tectonics. Geological Society, London, Special Publications 323, 145-163.

Didenko, A.N., Vodovozov, V.Y., Peskov, A.Y., Guryanov, V.A., Kosynkin, A.V., 2015. Paleomagnetism of the Ulkan massif (SE Siberian platform) and the apparent polar wander path for Siberia in late Paleoproterozoic–early Mesoproterozoic times. Precambrian Research 259, 58-77.

Dioh, E., Béziat, D., Debat, P., Grégoire, M., Ngom, P.M., 2006. Diversity of the Palaeoproterozoic granitoids of the Kédougou inlier (eastern Sénégal): Petrographical and geochemical constraints. Journal of African Earth Sciences 44, 351-371.

Dodson, M.H., 1973. Closure temperature in cooling geochronological and petrological systems. Contrib Mineral Petrol 40, 259-274.

Dodson, M.H., 1979. Theory of Cooling Ages, In: Jäger, E., Hunziker, J.C. (Eds.), Lectures in Isotope Geology. Springer Berlin Heidelberg, Berlin, Heidelberg, pp. 194-202.

Domeier, M., Van der Voo, R., Torsvik, T.H., 2012. Paleomagnetism and Pangea: The road to reconciliation. Tectonophysics 514–517, 14-43.

Donnelly, C.L., Griffin, W.L., Yang, J.-H., O'Reilly, S.Y., Li, Q.-L., Pearson, N.J., Li, X.-H., 2012. In situ U–Pb Dating and Sr–Nd Isotopic Analysis of Perovskite: Constraints on the Age and Petrogenesis of the Kuruman Kimberlite Province, Kaapvaal Craton, South Africa. Journal of Petrology 53, 2497-2522.

Donskaya, T.V., Mazukabzov, A.M., Bibikova, E.V., Gladkochub, D.P., Didenko, A.N., Kirnozova, T.I., Vodovozov, V.Y., Stanevich, A.M., 2007. Stratotype of the Chaya Formation of the Akitkan Group in the North Baikal volcanoplutonic belt: age and time of sedimentation. Russian Geology and Geophysics 48, 707-710.

Dorland, H.C., Beukes, N.J., Gutzmer, J., Evans, D.A.D., Armstrong, R.A., 2006. Precise SHRIMP U-Pb zircon age constraints on the lower Waterberg and Soutpansberg Groups, South Africa. South African Journal of Geology 109, 139-156.

Dreher, A., Fraga, L., 2010. Grupo Surumu. CPRM (Ed.), Programa Geologia do Brasil. Programa Cartografia da Amazônia. Geologia e Recursos Minerais da Folha Vila de Tepequém, NA, 80-94.

Driscoll, P.E., 2016. Simulating 2 Ga of geodynamo history. Geophysical Research Letters 43, 5680-5687.

Dunlop, D.J., 1979. On the use of Zijderveld vector diagrams in multicomponent paleomagnetic studies. Physics of the Earth and Planetary Interiors 20, 12-24.

Dunlop, D.J., 1997. Ozdemir, 0.(1997) Rock Magnetism, Fundamentals, and Frontiers. Cambridge Studies in Magnetism 3, 573.

Dunlop, D.J., 2002. Theory and application of the Day plot (Mrs/Ms versus Hcr/Hc). 2. Application to data for rocks, sediments, and soils. Journal of geophysical research 107, EPM5.1-EPM5.15.

Eby, G.N., 1990. The A-type granitoids: A review of their occurrence and chemical characteristics and speculations on their petrogenesis. Lithos 26, 115-134.

Eby, G.N., 1992. Chemical subdivision of the A-type granitoids:Petrogenetic and tectonic implications. Geology 20, 641-644.

Eglington, B.M., Reddy, S.M., Evans, D.A.D., 2009. The IGCP 509 database system: design and application of a tool to capture and illustrate litho- and chrono-stratigraphic information for Palaeoproterozoic tectonic domains, large igneous provinces and ore deposits; with examples from southern Africa. Geological Society, London, Special Publications 323, 27-47.

Eglington, B.M., Pehrsson, S.J., Ansdell, K.M., Lescuyer, J.L., Quirt, D., Milesi, J.P., Brown, P., 2013. A domain-based digital summary of the evolution of the Palaeoproterozoic of North America and Greenland and associated unconformity-related uranium mineralisation. Precambrian Research.

Elming, S.-Å., 1985. A palaeomagnetic study of Svecokarelian basic rocks from northern Sweden. Geologiska Föreningen i Stockholm Förhandlingar 107, 17-35.

Elming, S.-Å., 1994. Palaeomagnetism of Precambrian rocks in northern Sweden and its correlation to radiometric data. Precambrian Research 69, 61-79.

Elming, S.-Å., Mattsson, H., 2001. Post Jotnian basic Intrusions in the Fennoscandian Shield, and the break up of Baltica from Laurentia: a palaeomagnetic and AMS study. Precambrian Research 108, 215-236.

Elming, S.-Å., D'Agrella-Filho, M.S., Page, L.M., Tohver, E., Trindade, R.I.F., Pacca, I.I.G., Geraldes, M.C., Teixeira, W., 2009a. A palaeomagnetic and 40Ar/39Ar study of late precambrian sills in the SW part of the Amazonian craton: Amazonia in the Rodinia reconstruction. Geophysical Journal International 178, 106-122.

Elming, S.Å., Moakhar, M.O., Layer, P., Donadini, F., 2009b. Uplift deduced from remanent magnetization of a proterozoic basic dyke and the baked country rock in the Hoting area, Central Sweden: a palaeomagnetic and 40Ar/39Ar study. Geophysical Journal International 179, 59-78.

Emslie, R.F., Irving, E., Park, J.K., 1976. Further paleomagnetic results from the Michikamau Intrusion, Labrador. Canadian Journal of Earth Sciences 13, 1052-1057.

Ernesto, M., Raposo, M.I.B., Marques, L.S., Renne, P.R., Diogo, L.A., de Min, A., 1999. Paleomagnetism, geochemistry and 40Ar/39Ar dating of the North-eastern Paraná Magmatic Province: tectonic implications. Journal of Geodynamics 28, 321-340.

Ernesto, M., Bellieni, G., Piccirillo, E., Marques, L., De Min, A., Pacca, I., Martins, G., Macedo, J., 2003. Paleomagnetic and geochemical constraints on the timing and duration of the CAMP activity in northeastern Brazil. The Central Atlantic Magmatic Province: Insights from Fragments of Pangea, 129-149.

Ernst, R., Bleeker, W., 2010. Large igneous provinces (LIPs), giant dyke swarms, and mantle plumes: significance for breakup events within Canada and adjacent regions from 2.5 Ga to the Present. Canadian Journal of Earth Sciences 47, 695-739.

Ernst, R.E., Baragar, W.R.A., 1992. Evidence from magnetic fabric for the flow pattern of magma in the Mackenzie giant radiating dyke swarm. Nature 356, 511-513.

Ernst, R.E., Bleeker, W., Söderlund, U., Kerr, A.C., 2013a. Large Igneous Provinces and supercontinents: Toward completing the plate tectonic revolution. Lithos.

Ernst, R.E., Pereira, E., Hamilton, M.A., Pisarevsky, S.A., Rodriques, J., Tassinari, C.C.G., Teixeira, W., Van-Dunem, V., 2013b. Mesoproterozoic intraplate magmatic ‘barcode’ record of the Angola portion of the Congo Craton: Newly dated magmatic events at 1505 and 1110 Ma and implications for Nuna (Columbia) supercontinent reconstructions. Precambrian Research 230, 103-118.

Ernst, R.E., 2014. Large igneous provinces. Cambridge University Press, p. 304.

Ernst, R.E., Hamilton, M.A., Soderlund, U., Hanes, J.A., Gladkochub, D.P., Okrugin, A.V., Kolotilina, T., Mekhonoshin, A.S., Bleeker, W., LeCheminant, A.N., Buchan, K.L., Chamberlain, K.R., Didenko, A.N., 2016a. Long-lived connection between southern Siberia and northern Laurentia in the Proterozoic. Nature Geoscience 9, 464-469.

Ernst, R.E., Okrugin, A.V., Veselovskiy, R.V., Kamo, S.L., Hamilton, M.A., Pavlov, V., Soderlund, U., Chamberlain, K.R., Rogers, C., 2016b. The 1501 Ma Kuonamka Large Igneous Province of northern Siberia: U-Pb geochronology, geochemistry, and links with coeval magmatism on other crustal blocks. Russian Geology and Geophysics 57, 653-671.

Evans, D., 2003. True polar wander and supercontinents. Tectonophysics.

Evans, D.A., Beukes, N.J., Kirschvink, J.L., 1997. Low-latitude glaciation in the Palaeoproterozoic era. Nature 386, 262-266.

Evans, D.A., Pisarevsky, S.A., 2008. Plate tectonics on early Earth? Weighing the paleomagnetic evidence. When did plate tectonics begin, 249-263.

Evans, D.A., Mitchell, R.N., Kilian, T.M., Panzik, J.E., 2010. Reconstruction of Nuna: A working hypothesis.

Evans, D.A.D., Beukes, N.J., Kirschvink, J.L., 2002. Paleomagnetism of a lateritic paleoweathering horizon and overlying Paleoproterozoic red beds from South Africa: Implications for the Kaapvaal apparent polar wander path and a confirmation of atmospheric oxygen enrichment. Journal of Geophysical Research: Solid Earth 107, EPM 2-1-EPM 2-22.

Evans, D.A.D., Halls, H.C., 2010. Restoring Proterozoic deformation within the Superior craton. Precambrian Research 183, 474-489.

Evans, D.A.D., Mitchell, R.N., 2011. Assembly and breakup of the core of Paleoproterozoic-Mesoproterozoic supercontinent Nuna. Geology 39, 443-446.

Evans, D.A.D., 2013. Reconstructing pre-Pangean supercontinents. Geological Society of America Bulletin.

Evans, D.A.D., Li, Z.-X., Murphy, J.B., 2016a. Four-dimensional context of Earth's supercontinents. Geological Society, London, Special Publications 424, 1-14.

Evans, D.A.D., Veselovsky, R.V., Petrov, P.Y., Shatsillo, A.V., Pavlov, V.E., 2016b. Paleomagnetism of Mesoproterozoic margins of the Anabar Shield: A hypothesized billion-year partnership of Siberia and northern Laurentia. Precambrian Research 281, 639-655.

Evans, M., Hoye, G., 1981. Paleomagnetic results from the lower Proterozoic rocks of Great Slave Lake and Bathurst inlet areas, Northwest Territories. Proterozoic Basins of Canada: Geological Survey of Canada Paper, 81-10.

Evans, M.E., Bingham, D.K., 1973. Paleomagnetism of the Precambrian Martin Formation, Saskatchewan. Canadian Journal of Earth Sciences 10, 1485-1493.

Evans, M.E., 1976. Test of the dipolar nature of the geomagnetic field throughout Phanerozoic time. Nature 262, 676-677.

Evans, M.E., Bingham, D.K., 1976. Paleomagnetism of the Great Slave Supergroup, Northwest Territories, Canada: the Tochatwi Formation. Canadian Journal of Earth Sciences 13, 555-562.

Farquhar, J., Bao, H., Thiemens, M., 2000. Atmospheric Influence of Earth's Earliest Sulfur Cycle. Science 289, 756-758.

Fedotova, M.A., Khramov, A.N., Pisakin, B.N., Priyatkin, A.A., 1999. Early Proterozoic palaeomagnetism: new results from the intrusives and related rocks of the Karelian, Belomorian and Kola provinces, eastern Fennoscandian Shield. Geophysical Journal International 137, 691-712.

Feio, G.R.L., Dall'Agnol, R., Dantas, E.L., Macambira, M.J.B., Santos, J.O.S., Althoff, F.J., Soares, J.E.B., 2013. Archean granitoid magmatism in the Canaã dos Carajás area: Implications for crustal evolution of the Carajás province, Amazonian craton, Brazil. Precambrian Research 227, 157-185.

Fernandes, C.M.D., Juliani, C., Monteiro, L.V.S., Lagler, B., Echeverri Misas, C.M., 2011. High-K calc-alkaline to A-type fissure-controlled volcano-plutonism of the São Félix do Xingu region, Amazonian craton, Brazil: Exclusively crustal sources or only mixed Nd model ages? Journal of South American Earth Sciences 32, 351-368.

Ferreira, A.T.R., Lamarão, C.N., 2013. Geologia, petrografia e geoquímica das rochas vulcânicas Uatumã na área sul de São Félix do Xingu (PA), Província Carajás. Brazilian Journal of Geology 43, 152-167.

Ferron, J.M.T.M., Bastos Neto, A.C., Lima, E.F., Nardi, L.V.S., Costi, H.T., Pierosan, R., Prado, M., 2010. Petrology, geochemistry, and geochronology of Paleoproterozoic volcanic and granitic rocks (1.89–1.88 Ga) of the Pitinga Province, Amazonian Craton, Brazil. Journal of South American Earth Sciences 29, 483-497.

Findlay, J.M., Parrish, R.R., Birkett, T.C., Watanabe, D.H., 1995. U–Pb ages from the Nimish Formation and Montagnais glomeroporphyritic gabbro of the central New Québec Orogen, Canada. Canadian Journal of Earth Sciences 32, 1208-1220.

Fischer, R., Gerya, T., 2016. Regimes of subduction and lithospheric dynamics in the Precambrian: 3D thermomechanical modelling. Gondwana Research 37, 53-70.

Fisher, R., 1953. Dispersion on a Sphere. Proceedings of the Royal Society of London. Series A. Mathematical and Physical Sciences 217, 295-305.

Font, E., Youbi, N., Fernandes, S., El Hachimi, H., Kratinová, Z., Hamim, Y., 2011. Revisiting the magnetostratigraphy of the Central Atlantic Magmatic Province (CAMP) in Morocco. Earth and Planetary Science Letters 309, 302-317.

Font, E., Fabre, S., Nédélec, A., Adatte, T., Keller, G., Veiga-Pires, C., Ponte, J., Mirão, J., Khozyem, H., Spangenberg, J.E., 2014. Atmospheric halogen and acid rains during the main phase of Deccan eruptions: Magnetic and mineral evidence. Geological Society of America Special Papers 505.

Franklin, J.M., Gibson, H., Jonasson, I., Galley, A., 2005. Volcanogenic massive sulfide deposits. Economic Geology 100th anniversary volume 98, 523-560.

French, J.E., Heaman, L.M., Chacko, T., Srivastava, R.K., 2008. 1891–1883 Ma Southern Bastar–Cuddapah mafic igneous events, India: A newly recognized large igneous province. Precambrian Research 160, 308-322.

Frost, B.R., Barnres, C.G., Collins, W.J., Arculus, R.J., Ellis, D.J., Frost, C.D., 2001. A Geochemical Classification for Granitic Rocks. Journal of Petrology 42, 2033-2048.

Frost, B.R., Frost, C.D., 2008. A Geochemical Classification for Feldspathic Igneous Rocks. Journal of Petrology 49, 1955-1969.

Fyfe, W.S., 1978. The evolution of the earth's crust: Modern plate tectonics to ancient hot spot tectonics? Chemical Geology 23, 89-114.

Gansser, A., Dietrich, V.J., Cameron, W.E., 1979. Palaeogene komatiites from Gorgona Island. Nature 278, 545-546.

Gao, S., Rudnick, R.L., Carlson, R.W., McDonough, W.F., Liu, Y.-S., 2002. Re–Os evidence for replacement of ancient mantle lithosphere beneath the North China craton. Earth and Planetary Science Letters 198, 307-322.

Garcia, M.S., Trindade, R.I., Manoel, S., Pinho, F.E., 2013. Paleomagnetismo do complexo alcalino Planalto da Serra (Mato Grosso): Implicações para a formação do Gondwana, In: Letters, L. (Ed.), Latinmag Letters, Montevideo, pp. OB19, 11-18.

Geraldes, M.C., Van Schmus, W.R., Condie, K.C., Bell, S., Teixeira, W., Babinski, M., 2001. Proterozoic geologic evolution of the SW part of the Amazonian Craton in Mato Grosso state, Brazil. Precambrian Research 111, 91-128.

Gerya, T., 2014. Precambrian geodynamics: Concepts and models. Gondwana Research 25, 442-463.

Gladkochub, D.P., Pisarevsky, S.A., Donskaya, T.V., Ernst, R.E., Wingate, M.T.D., Söderlund, U., Mazukabzov, A.M., Sklyarov, E.V., Hamilton, M.A., Hanes, J.A., 2010. Proterozoic mafic magmatism in Siberian craton: An overview and implications for paleocontinental reconstruction. Precambrian Research 183, 660-668.

Gladkochub, D.P., Donskaya, T.V., Mazukabzov, A.M., Pisarevsky, S.A., Ernst, R.E., Stanevich, A.M., 2016. The Mesoproterozoic mantle plume beneath the northern part of the Siberian craton. Russian Geology and Geophysics 57, 672-686.

Glotch, T., Kraft, M., 2008. Thermal transformations of akaganéite and lepidocrocite to hematite: assessment of possible precursors to Martian crystalline hematite. Phys Chem Minerals 35, 569-581.

Gold, T., 1955. Instability of the Earth's Axis of Rotation. Nature 175, 526-529.
Goldberg, A.S., 2010. Dyke swarms as indicators of major extensional events in the 1.9–1.2 Ga Columbia supercontinent. Journal of Geodynamics 50, 176-190.
Goldfarb, R., Groves, D., Gardoll, S., 2001. Rotund versus skinny orogens: Well-nourished or malnourished gold? Geology 29, 539-542.
Goldreich, P., Toomre, A., 1969. Some remarks on polar wandering. Journal of Geophysical Research 74, 2555-2567.
Gomes, C.B., Cordani, U.G., Basei, M.A.S., 1975. Radiometric Ages from the Serra dos Carajás Area, Northern Brazil. Geological Society of America Bulletin 86, 939-942.
Gong, Z., Dekkers, M.J., Heslop, D., Mullender, T.A.T., 2009. End-member modelling of isothermal remanent magnetization (IRM) acquisition curves: A novel approach to diagnose remagnetization. Geophysical Journal International 178, 693-701.
Gordon, R.G., McWilliams, M.O., Cox, A., 1979. Pre-tertiary velocities of the continents: A lower bound from paleomagnetic data. Journal of Geophysical Research: Solid Earth 84, 5480-5486.
Gordon, R.G., 1990. Test for bias in paleomagnetically determined paleolatitudes from Pacific Plate Deep Sea Drilling Project sediments. Journal of Geophysical Research: Solid Earth 95, 8397-8404.
Gower, C., Ryan, A., Rivers, T., 1990. Mid-Proterozoic Laurentia-Baltica: an overview of its geological evolution and a summary of the contributions made by this volume. Mid-Proterozoic Laurentia-Baltica 38, 1-20.
Graham, K.W.T., Helsley, C.E., Hales, A.L., 1964. Determination of the relative positions of continents from paleomagnetic data. Journal of Geophysical Research 69, 3895-3900.
Grainger, C.J., Groves, D.I., Tallarico, F.H.B., Fletcher, I.R., 2008. Metallogenesis of the Carajás Mineral Province, Southern Amazon Craton, Brazil: Varying styles of Archean through Paleoproterozoic to Neoproterozoic base- and precious-metal mineralisation. Ore Geology Reviews 33, 451-489.
Gray, R., Pysklywec, R.N., 2010. Geodynamic models of Archean continental collision and the formation of mantle lithosphere keels. Geophysical Research Letters 37, n/a-n/a.
Greff-Lefftz, M., Besse, J., 2014. Sensitivity experiments on True Polar Wander. Geochemistry, Geophysics, Geosystems 15, 4599-4616.
Grigné, C., Labrosse, S., 2001. Effects of continents on Earth cooling: Thermal blanketing and depletion in radioactive elements. Geophysical Research Letters 28, 2707-2710.
Haggerty, S.E., 1991. Oxide textures; a mini-atlas. Reviews in Mineralogy and Geochemistry 25, 129-219.
Halls, H.C., 1978. The use of converging remagnetization circles in palaeomagnetism. Physics of the Earth and Planetary Interiors 16, 1-11.
Halls, H.C., Heaman, L.M., 2000. The paleomagnetic significance of new U-Pb age data from the Molson dyke swarm, Cauchon Lake area, Manitoba. Canadian Journal of Earth Sciences 37, 957-966.
Halls, H.C., Hamilton, M.A., Denyszyn, S.W., 2011. The Melville Bugt Dyke Swarm of Greenland: A Connection to the 1.5-1.6 Ga Fennoscandian Rapakivi Granite Province?, Dyke Swarms:Keys for Geodynamic Interpretation: Keys for Geodynamic Interpretation. Springer Berlin Heidelberg, Berlin, Heidelberg, pp. 509-535.
Halls, H.C., Lovette, A., Hamilton, M., Söderlund, U., 2015. A paleomagnetic and U–Pb geochronology study of the western end of the Grenville dyke swarm: Rapid changes in paleomagnetic field direction at ca. 585 Ma related to polarity reversals? Precambrian Research 257, 137-166.
Hamilton, M., Buchan, K., Ernst, R., Scott, G., 2009. Widespread and Short-Lived 1870 Ma Mafic Magmatism Along the Northern Superior Craton Margin, American Geophysical Union-Geological Association of Canada, Joint Meeting (abstract# GA11A-01).
Hamilton, M.A., Buchan, K.L., 2010. U–Pb geochronology of the Western Channel Diabase, northwestern Laurentia: Implications for a large 1.59 Ga magmatic province, Laurentia's APWP and paleocontinental reconstructions of Laurentia, Baltica and Gawler craton of southern Australia. Precambrian Research 183, 463-473.

Hanson, R.E., Gose, W.A., Crowley, J.L., Ramezani, J., Bowring, S.A., Bullen, D.S., Hall, R.P., Pancake, J.A., Mukwakwami, J., 2004. Paleoproterozoic intraplate magmatism and basin development on the Kaapvaal Craton: Age, paleomagnetism and geochemistry of ~1.93 to ~1.87 Ga post-Waterberg dolerites. South African Journal of Geology 107, 233-254.

Hanson, R.E., Rioux, M., Gose, W.A., Blackburn, T.J., Bowring, S.A., Mukwakwami, J., Jones, D.L., 2011. Paleomagnetic and geochronological evidence for large-scale post–1.88 Ga displacement between the Zimbabwe and Kaapvaal cratons along the Limpopo belt. Geology 39, 487-490.

Hapgood, C.H., 1958. Earth's shifting crust: A key to some basic problems of earth science. Pantheon books.

Harada, M., Tajika, E., Sekine, Y., 2015. Transition to an oxygen-rich atmosphere with an extensive overshoot triggered by the Paleoproterozoic snowball Earth. Earth and Planetary Science Letters 419, 178-186.

Hargraves, R.B., Onstott, T.C., 1980. Paleomagnetic results from some southern African kimberlites, and their tectonic significance. Journal of Geophysical Research: Solid Earth 85, 3587-3596.

Hargraves, R.B., 1989. Paleomagnetism of mesozoic kimberlites in southern Africa and the cretaceous apparent polar wander curve for Africa. Journal of Geophysical Research: Solid Earth 94, 1851-1866.

Hartnady, C.J., 1991. About turn for supercontinents. Nature 352, 476-478.

Hastie, A.R., Fitton, J.G., Bromiley, G.D., Butler, I.B., Odling, N.W.A., 2016. The origin of Earth's first continents and the onset of plate tectonics. Geology 44, 855-858.

Hasui, Y., Haraly, N., Schobbenhaus, C., 1984. Elementos geofísicos e geológicos da região amazônica: subsídios para o modelo geotectônico. SBG, Simp. Geol. Amaz 2, 129-148.

Hasui, Y., 1985. The Central Brazil Shield Reviewed.

Hawkesworth, C., Cawood, P., Dhuime, B., 2013. Continental growth and the crustal record. Tectonophysics.

Hawkesworth, C.J., Dhuime, B., Pietranik, A.B., Cawood, P.A., Kemp, A.I.S., Storey, C.D., 2010. The generation and evolution of the continental crust. Journal of the Geological Society 167, 229-248.

Heaman, L.M., Peck, D., Toope, K., 2009. Timing and geochemistry of 1.88 Ga Molson Igneous Events, Manitoba: Insights into the formation of a craton-scale magmatic and metallogenic province. Precambrian Research 172, 143-162.

Heinonen, A., Andersen, T., Rämö, O.T., Whitehouse, M., 2015. The source of Proterozoic anorthosite and rapakivi granite magmatism: evidence from combined in situ Hf–O isotopes of zircon in the Ahvenisto complex, southeastern Finland. Journal of the Geological Society 172, 103-112.

Helovuori, O., 1979. Geology of the Pyhasalmi ore deposit, Finland. Economic Geology 74, 1084-1101.

Herzberg, C., Condie, K., Korenaga, J., 2010. Thermal history of the Earth and its petrological expression. Earth and Planetary Science Letters 292, 79-88.

Hoffman, P., 1997. Tectonic genealogy of North America. Earth Structure: An Introduction to Structural Geology and Tectonics, 459-464.

Hoffman, P.F., 1988. United Plates of America, the birth of a craton-Early Proterozoic assembly and growth of Laurentia. Annual Review of Earth and Planetary Sciences 16, 543-603.

Hoffman, P.F., 1989a. Precambrian geology and tectonic history of North America. The geology of North America—An overview: Boulder, Colorado, Geological Society of America, Geology of North America, v. A, 447-512.

Hoffman, P.F., 1989b. Speculations on Laurentia's first gigayear (2.0 to 1.0 Ga). Geology 17, 135-138.

Holland, H.D., 1984. The chemical evolution of the atmosphere and oceans. Princeton University Press.

Holland, H.D., 2006. The oxygenation of the atmosphere and oceans. Philosophical Transactions of the Royal Society B: Biological Sciences 361, 903-915.

Hou, G., Santosh, M., Qian, X., Lister, G.S., Li, J., 2008. Configuration of the Late Paleoproterozoic supercontinent Columbia: Insights from radiating mafic dyke swarms. Gondwana Research 14, 395-409.

Hurley, P.M., Hughes, H., Faure, G., Fairbairn, H.W., Pinson, W.H., 1962. Radiogenic strontium-87 model of continent formation. Journal of Geophysical Research 67, 5315-5334.

Hurley, P.M., Rand, J.R., 1969. Pre-Drift Continental Nuclei. Science 164, 1229-1242.

Idnurm, M., Giddings, J.W., 1988. The Early to Middle Proterozoic of Australia Australian Precambrian polar wander: a review. Precambrian Research 40, 61-88.

Irving, E., Donaldson, J.A., Park, J.K., 1972a. Paleomagnetism of the Western Channel Diabase and Associated Rocks, Northwest Territories. Canadian Journal of Earth Sciences 9, 960-971.

Irving, E., Park, J.K., McGlynn, J.C., 1972b. Paleomagnetism of the Et-Then Group and Mackenzie Diabase in the Great Slave Lake Area. Canadian Journal of Earth Sciences 9, 744-755.

Irving, E., Emslie, R.F., Ueno, H., 1974. Upper Proterozoic paleomagnetic poles from Laurentia and the history of the Grenville Structural Province. Journal of Geophysical Research 79, 5491-5502.

Irving, E., Baker, J., Hamilton, M., Wynne, P.J., 2004. Early Proterozoic geomagnetic field in western Laurentia: implications for paleolatitudes, local rotations and stratigraphy. Precambrian Research 129, 251-270.

Isley, A.E., Abbott, D.H., 1999. Plume-related mafic volcanism and the deposition of banded iron formation. Journal of Geophysical Research: Solid Earth 104, 15461-15477.

Isley, A.E., Abbott, D.H., 2002. Implications of the Temporal Distribution of High-Mg Magmas for Mantle Plume Volcanism through Time. The Journal of Geology 110, 141-158.

Jackson, S.E., Pearson, N.J., Griffin, W.L., Belousova, E.A., 2004. The application of laser ablation-inductively coupled plasma-mass spectrometry to in situ U–Pb zircon geochronology. Chemical Geology 211, 47-69.

Jackson, T.A., 2015. Variations in the abundance of photosynthetic oxygen through Precambrian and Paleozoic time in relation to biotic evolution and mass extinctions: evidence from Mn/Fe ratios. Precambrian Research 264, 30-35.

Jelinek, V., 1981. Characterization of the magnetic fabric of rocks. Tectonophysics 79, T63-T67.

Johansson, Å., 2009. Baltica, Amazonia and the SAMBA connection—1000 million years of neighbourhood during the Proterozoic? Precambrian Research 175, 221-234.

Johansson, Å., 2014. From Rodinia to Gondwana with the 'SAMBA' model—A distant view from Baltica towards Amazonia and beyond. Precambrian Research 244, 226-235.

Johnston, D.T., 2011. Multiple sulfur isotopes and the evolution of Earth's surface sulfur cycle. Earth-Science Reviews 106, 161-183.

Johnston, J.H., 1977. Jarosite and akaganéite from White Island volcano, New Zealand: An X-ray and Mössbauer study. Geochimica et Cosmochimica Acta 41, 539-544.

Jones, D.L., McElhinny, M.W., 1966. Paleomagnetic correlation of basic intrusions in the Precambrian of southern Africa. Journal of Geophysical Research 71, 543-552.

Juliani, C., Rye, R.O., Nunes, C.M.D., Snee, L.W., Corrêa Silva, R.H., Monteiro, L.V.S., Bettencourt, J.S., Neumann, R., Neto, A.A., 2005. Paleoproterozoic high-sulfidation mineralization in the Tapajós gold province, Amazonian Craton, Brazil: geology, mineralogy, alunite argon age, and stable-isotope constraints. Chemical Geology 215, 95-125.

Juliani, C., Fernandes, C., Monteiro, L., Misas, C., Lagler, B., 2009. Possível zonamento metalogenético associado ao evento vulcano-plutônico de~ 2, 0 a 1, 88 Ga na parte sul do Cráton Amazônico. II Simpósio Brasileiro de Metalogenia 2, Gramado.ANAIS.

Juliani, C., Fernandes, C.M.D., 2010. Well-preserved Late Paleoproterozoic volcanic centers in the São Félix do Xingu region, Amazonian Craton, Brazil. Journal of Volcanology and Geothermal Research 191, 167-179.

Karlstrom, K.E., Åhäll, K.-I., Harlan, S.S., Williams, M.L., McLelland, J., Geissman, J.W., 2001. Long-lived (1.8–1.0 Ga) convergent orogen in southern Laurentia, its extensions to Australia and Baltica, and implications for refining Rodinia. Precambrian Research 111, 5-30.

Kaur, P., Chaudhri, N., 2013. Metallogeny associated with the Palaeo-Mesoproterozoic Columbia supercontinent cycle: A synthesis of major metallic deposits. Ore Geology Reviews.

Kemp, A.I.S., Hawkesworth, C.J., Paterson, B.A., Kinny, P.D., 2006. Episodic growth of the Gondwana supercontinent from hafnium and oxygen isotopes in zircon. Nature 439, 580-583.

Kilian, T.M., Chamberlain, K.R., Evans, D.A.D., Bleeker, W., Cousens, B.L., 2016. Wyoming on the run—Toward final Paleoproterozoic assembly of Laurentia. Geology.

Kirschvink, J.L., 1980. The least-squares line and plane and the analysis of palaeomagnetic data. Geophysical Journal International 62, 699-718.

Kirschvink, J.L., Ripperdan, R.L., Evans, D.A., 1997. Evidence for a Large-Scale Reorganization of Early Cambrian Continental Masses by Inertial Interchange True Polar Wander. Science 277, 541-545.

Kirschvink, J.L., Gaidos, E.J., Bertani, L.E., Beukes, N.J., Gutzmer, J., Maepa, L.N., Steinberger, R.E., 2000. Paleoproterozoic snowball Earth: Extreme climatic and geochemical global change and its biological consequences. Proceedings of the National Academy of Sciences 97, 1400-1405.

Kirschvink, J.L., Kopp, R.E., Raub, T.D., Baumgartner, C.T., Holt, J.W., 2008. Rapid, precise, and high-sensitivity acquisition of paleomagnetic and rock-magnetic data: Development of a low-noise automatic sample changing system for superconducting rock magnetometers. Geochemistry, Geophysics, Geosystems 9, n/a-n/a.

Klein, E.L., Almeida, M.E., Rosa-Costa, L.T., 2012. The 1.89-1.87 Ga Uatumã Silicic Large Igneous Province, northern South America. Large Igneous Provinces Commission novembre 2012.

Klein, R., 2016. Baltica from the Svecofennian until the Ediacaran: A Paleomagnetic study of Precambrian formations of Finland. PhD thesis, Faculty of Science, Department of Physics. University of Helsinki, p. 64.

Klein, R., Pesonen, L.J., Mänttäri, I., Heinonen, J.S., 2016. A late Paleoproterozoic key pole for the Fennoscandian Shield: A paleomagnetic study of the Keuruu diabase dykes, Central Finland. Precambrian Research 286, 379-397.

Knight, M.D., Walker, G.P.L., 1988. Magma flow directions in dikes of the Koolau Complex, Oahu, determined from magnetic fabric studies. Journal of Geophysical Research: Solid Earth 93, 4301-4319.

Knoll, A.H., Bergmann, K.D., Strauss, J.V., 2016. Life: the first two billion years. Philosophical Transactions of the Royal Society B: Biological Sciences 371.

Konhauser, K.O., Pecoits, E., Lalonde, S.V., Papineau, D., Nisbet, E.G., Barley, M.E., Arndt, N.T., Zahnle, K., Kamber, B.S., 2009. Oceanic nickel depletion and a methanogen famine before the Great Oxidation Event. Nature 458, 750-753.

Kopp, R.E., Kirschvink, J.L., Hilburn, I.A., Nash, C.Z., 2005. The Paleoproterozoic snowball Earth: A climate disaster triggered by the evolution of oxygenic photosynthesis. Proceedings of the National Academy of Sciences of the United States of America 102, 11131-11136.

Korenaga, J., 2006. Archean Geodynamics and the Thermal Evolution of Earth, Archean Geodynamics and Environments. American Geophysical Union, pp. 7-32.

Korenaga, J., 2008. Urey ratio and the structure and evolution of Earth's mantle. Reviews of Geophysics 46, n/a-n/a.

Korenaga, J., 2011. Thermal evolution with a hydrating mantle and the initiation of plate tectonics in the early Earth. Journal of Geophysical Research: Solid Earth 116, n/a-n/a.

Korenaga, J., 2013. Initiation and Evolution of Plate Tectonics on Earth: Theories and Observations. Annual Review of Earth and Planetary Sciences 41, 117-151.

Kotschoubey, B., Villas, R.N., Aires, B., 2016. Chloritites of the Tocantins Group, Araguaia fold belt, central-northern Brazil: Vestiges of basaltic magmatism and metallogenetic implications. Journal of South American Earth Sciences 69, 171-193.

Krapez, B., 1999. Stratigraphic record of an Atlantic-type global tectonic cycle in the Palaeoproterozoic Ashburton Province of Western Australia. Australian Journal of Earth Sciences 46, 71-87.

Kruiver, P.P., Dekkers, M.J., Heslop, D., 2001. Quantification of magnetic coercivity components by the analysis of acquisition curves of isothermal remanent magnetisation. Earth and Planetary Science Letters 189, 269-276.

Kumar, A., Parashuramulu, V., Nagaraju, E., 2015. A 2082 Ma radiating dyke swarm in the Eastern Dharwar Craton, southern India and its implications to Cuddapah basin formation. Precambrian Research 266, 490-505.

Kusky, T., Li, J., Santosh, M., 2007. The Paleoproterozoic North Hebei Orogen: North China craton's collisional suture with the Columbia supercontinent. Gondwana Research 12, 4-28.

Kusky, T.M., Santosh, M., 2009. The Columbia connection in North China. Geological Society, London, Special Publications 323, 49-71.

Labrosse, S., Macouin, M., 2003. The inner core and the geodynamo. Comptes Rendus Geoscience 335, 37-50.

Labrosse, S., Jaupart, C., 2007. Thermal evolution of the Earth: Secular changes and fluctuations of plate characteristics. Earth and Planetary Science Letters 260, 465-481.

Lamarão, C.N., Dall'Agnol, R., Lafon, J.-M., Lima, E.F., 2002. Geology, geochemistry, and Pb–Pb zircon geochronology of the Paleoproterozoic magmatism of Vila Riozinho, Tapajós Gold Province, Amazonian craton, Brazil. Precambrian Research 119, 189-223.

Larin, A., Sal'nikova, E., Kotov, A., Kovalenko, V., Rytsk, E.Y., Yakovleva, S., Berezhnaya, N., Kovach, V., Buldygerov, V., Sryvtsev, N., 2003. North-Baikal volcanoplutonic belt: timing and tectonic setting. Doklady Akademii Nauk-Rossijskaya Akademiya Nauk 392, 506-511.

Laurent, O., Martin, H., Moyen, J.F., Doucelance, R., 2014. The diversity and evolution of late-Archean granitoids: Evidence for the onset of “modern-style” plate tectonics between 3.0 and 2.5 Ga. Lithos 205, 208-235.

Layer, P.W., Kröner, A., McWilliams, M., Clauer, N., 1988. Regional magnetic overprinting of Witwatersrand Supergroup Sediments, South Africa. Journal of Geophysical Research: Solid Earth 93, 2191-2200.

Le Maitre, R.W., Streckeisen, A., Zanettin, B., Le Bas, M., Bonin, B., Bateman, P., 2002. Igneous rocks: a classification and glossary of terms: recommendations of the International Union of Geological Sciences Subcommission on the Systematics of Igneous Rocks. Cambridge University Press.

Ledru, P., Cocherie, A., Barbosa, J., Johan, V., Onstott, T., 1994. Ages du métamorphisme granulitique dans le craton du São Francisco (Brésil). Implications sur la nature de l'orogène transamazonien. Comptes rendus de l'Académie des sciences. Série 2. Sciences de la terre et des planètes 318, 251-257.

Lee, C.-T.A., 2006. Geochemical/Petrologic Constraints on the Origin of Cratonic Mantle, Archean Geodynamics and Environments. American Geophysical Union, pp. 89-114.

Lee, J.K.W., Williams, I.S., Ellis, D.J., 1997. Pb, U and Th diffusion in natural zircon. Nature 390, 159-162.

Letts, S., Torsvik, T.H., Webb, S.J., Ashwal, L.D., Eide, E.A., Chunnett, G., 2005. Palaeomagnetism and 40Ar/39Ar geochronology of mafic dykes from the eastern Bushveld Complex (South Africa). Geophysical Journal International 162, 36-48.

Li, Z.-X., Evans, D.A.D., Halverson, G.P., 2013. Neoproterozoic glaciations in a revised global palaeogeography from the breakup of Rodinia to the assembly of Gondwanaland. Sedimentary Geology 294, 219-232.

Li, Z.X., Bogdanova, S.V., Collins, A.S., Davidson, A., De Waele, B., Ernst, R.E., Fitzsimons, I.C.W., Fuck, R.A., Gladkochub, D.P., Jacobs, J., Karlstrom, K.E., Lu, S., Natapov, L.M., Pease, V., Pisarevsky, S.A., Thrane, K., Vernikovsky, V., 2008. Assembly, configuration, and break-up history of Rodinia: A synthesis. Precambrian Research 160, 179-210.

Li, Z.X., Bogdanova, S.V., Collins, A.S., Davidson, A., De Waele, B., Ernst, R.E., Evans, D.A.D., Fitzsimons, I.C.W., Fuck, R.A., Gladkochub, D.P., Jacobs, J., Karlstrom, K.E., Lu, S., Natapov, L.M., Pease, V., Pisarevsky, S.A., Thrane, K., Vernikovsky, V., 2009. How not to build a supercontinent: A reply to J.D.A. Piper. Precambrian Research 174, 208-214.

Liu, J.-f., Li, J.-y., Qu, J.-f., Hu, Z.-c., Feng, Q.-w., Guo, C.-l., 2016a. Late Paleoproterozoic tectonic setting of the northern margin of the North China Craton: Constraints from the geochronology and geochemistry of the mangerites in the Longhua and Jianping areas. Precambrian Research 272, 57-77.

Liu, J., Riches, A.J.V., Pearson, D.G., Luo, Y., Kienlen, B., Kjarsgaard, B.A., Stachel, T., Armstrong, J.P., 2016b. Age and evolution of the deep continental root beneath the central Rae craton, northern Canada. Precambrian Research 272, 168-184.

Loiselle, M., Wones, D., 1979. Characteristics and origin of anorogenic granites, Geological Society of America Abstracts with Programs, p. 468.

Lubnina, N., Ernst, R., Klausen, M., Söderlund, U., 2010a. Paleomagnetic study of NeoArchean–Paleoproterozoic dykes in the Kaapvaal Craton. Precambrian Research 183, 523-552.

Lubnina, N.V., Mertanen, S., Söderlund, U., Bogdanova, S., Vasilieva, T.I., Frank-Kamenetsky, D., 2010b. A new key pole for the East European Craton at 1452 Ma: Palaeomagnetic and geochronological constraints from mafic rocks in the Lake Ladoga region (Russian Karelia). Precambrian Research 183, 442-462.

Lubnina, N.V., Stepanova, A.V., Ernst, R.E., Nilsson, M., Söderlund, U., 2016. New U–Pb baddeleyite age, and AMS and paleomagnetic data for dolerites in the Lake Onega region belonging to the 1.98–1.95 Ga regional Pechenga–Onega Large Igneous Province. GFF, 1-25.

Ludwig, K., 2009. Isoplot 4.1. A geochronological toolkit for Microsoft Excel. Berkeley Geochronology Center Special Publication 4, 76.

Lyons, T.W., Reinhard, C.T., Planavsky, N.J., 2014. The rise of oxygen in Earth/'s early ocean and atmosphere. Nature 506, 307-315.

Macambira, E., Vale, A., 1997. Programa levantamentos geologicos basicos do Brasil: Sao Felix do Xingu-Folha SB. 22-YB: Estado do Para. CPRM.

Macambira, M., 1992. Chronologie U-Pb, Rb-Sr, K-Ar et croissance de la croûte continentale dans l'Amazonie de Se. Exemple de la région de Rio Mario, province de Carajas, Brésil.

Macambira, M., Lafon, J., 1995. Geocronologia da Província Mineral de Carajás: síntese dos dados e novos desafios. Boletim do Museu Paraense Emílio Goeldi 7, 263-288.

Macambira, M., Costa, J., Althoff, F., Lafon, J., Melo, J., Santos, A., 2000. New geochronological data for the Rio Maria TTG terrane; implications for the time contraints of the crustal formation of the Carajás province, Brazil, SBG, International Geological Congress, 31st, Rio de Janeiro, CD-ROM.

Machado, N., Lindenmayer, Z., Krogh, T.E., Lindenmayer, D., 1991. U-Pb geochronology of Archean magmatism and basement reactivation in the Carajás area, Amazon shield, Brazil. Precambrian Research 49, 329-354.

Macouin, M., Valet, J.-P., Besse, J., 2004. Long-term evolution of the geomagnetic dipole moment. Physics of the Earth and Planetary Interiors 147, 239-246.

Maniar, P.D., Piccoli, P.M., 1989. Tectonic discrimination of granitoids. Geological Society of America Bulletin 101, 635-643.

Margulis, L., Walker, J., Rambler, M., 1976. Reassessment of roles of oxygen and ultra-violet light in Precambrian evoludon. Nature, 264,620-624.

Martin, A.P., Condon, D.J., Prave, A.R., Lepland, A., 2013. A review of temporal constraints for the Palaeoproterozoic large, positive carbonate carbon isotope excursion (the Lomagundi–Jatuli Event). Earth-Science Reviews 127, 242-261.
Martin, H., 1986. Effect of steeper Archean geothermal gradient on geochemistry of subduction-zone magmas. Geology 14, 753-756.
Martin, R., Bonin, B., 1976. Water and magma genesis; the association hypersolvus granite-subsolvus granite. The Canadian Mineralogist 14, 228-237.
Marttila, E., 1981. Pre-Quaternary Rocks of the Kiuruvesi Map-Sheet area. Geological Map of Finland 1: 100000: Explanation to the Maps of Pre-Quaternary Rocks, Sheet 3323. Geological Survey of Finland.
Marzoli, A., Renne, P.R., Piccirillo, E.M., Ernesto, M., Bellieni, G., Min, A.D., 1999. Extensive 200-Million-Year-Old Continental Flood Basalts of the Central Atlantic Magmatic Province. Science 284, 616-618.
Marzoli, A., Jourdan, F., Puffer, J.H., Cuppone, T., Tanner, L.H., Weems, R.E., Bertrand, H., Cirilli, S., Bellieni, G., De Min, A., 2011. Timing and duration of the Central Atlantic magmatic province in the Newark and Culpeper basins, eastern U.S.A. Lithos 122, 175-188.
Matsuyama, I., Mitrovica, J.X., Manga, M., Perron, J.T., Richards, M.A., 2006. Rotational stability of dynamic planets with elastic lithospheres. Journal of Geophysical Research: Planets 111, n/a-n/a.
Matsuyama, I., Nimmo, F., Mitrovica, J.X., 2014. Planetary Reorientation. Annual Review of Earth and Planetary Sciences 42, 605-634.
McDonough, W.F., Sun, S.s., 1995. The composition of the Earth. Chemical Geology 120, 223-253.
McElhinny, M.W., McFadden, P.L., Merrill, R.T., 1996. The time-averaged paleomagnetic field 0–5 Ma. Journal of Geophysical Research: Solid Earth 101, 25007-25027.
McFadden, P.L., McElhinny, M.W., 1990. Classification of the reversal test in palaeomagnetism. Geophysical Journal International 103, 725-729.
McFadden, P.L., McElhinny, M.W., 1995. Combining groups of paleomagnetic directions or poles. Geophysical Research Letters 22, 2191-2194.
McGlynn, J.C., Irving, E., 1978. Multicomponent magnetization of the Pearson Formation (Great Slave Supergroup, N.W.T.) and the Coronation loop. Canadian Journal of Earth Sciences 15, 642-654.
McGovern, P.J., Schubert, G., 1989. Thermal evolution of the Earth: effects of volatile exchange between atmosphere and interior. Earth and planetary science letters 96, 27-37.
McMenamin, M., McMenamin, D., 1990. S. 1990. The emergence of animals: The Cambrian Breakthrough. New York: Columbia University Press.
Medeiros, H., Dall'Agnol, R., 1988. Petrologia da porção leste do Batólito Granodiorítico Rio Maria, sudeste do Pará. SBG, Congr. Brasileiro Geol 35, 1488-1499.
Meert, J.G., Voo, R.V.d., Powell, C.M., Li, Z.-X., McElhinny, M.W., Chen, Z., Symons, D.T.A., 1993. A plate-tectonic speed limit? Nature 363, 216-217.
Meert, J.G., 1999. A paleomagnetic analysis of Cambrian true polar wander. Earth and Planetary Science Letters 168, 131-144.
Meert, J.G., 2002. Paleomagnetic Evidence for a Paleo-Mesoproterozoic Supercontinent Columbia. Gondwana Research 5, 207-215.
Meert, J.G., Stuckey, W., 2002. Revisiting the paleomagnetism of the 1.476 Ga St. Francois Mountains igneous province, Missouri. Tectonics 21, 1-1-1-19.
Meert, J.G., Torsvik, T.H., 2004. Reply to JDA Piper on "The making and unmaking of a supercontinent: Rodinia revisited". Tectonophysics 383, 99-103.
Meert, J.G., 2009. Palaeomagnetism: In GAD we trust. Nature Geosci 2, 673-674.
Meert, J.G., Pandit, M.K., Pradhan, V.R., Kamenov, G., 2011. Preliminary report on the paleomagnetism of 1.88 Ga dykes from the Bastar and Dharwar cratons, Peninsular India. Gondwana Research 20, 335-343.

Meert, J.G., 2012. What's in a name? The Columbia (Paleopangaea/Nuna) supercontinent. Gondwana Research 21, 987-993.
Meert, J.G., 2014. Strange attractors, spiritual interlopers and lonely wanderers: The search for pre-Pangean supercontinents. Geoscience Frontiers 5, 155-166.
Melezhik, V.A., Fallick, A.E., Filippov, M.M., Lepland, A., Rychanchik, D.V., Deines, Y.E., Medvedev, P.V., Romashkin, A.E., Strauss, H., 2009. Petroleum surface oil seeps from a Palaeoproterozoic petrified giant oilfield. Terra Nova 21, 119-126.
Meller, C., Kontny, A., Kohl, T., 2014. Identification and characterization of hydrothermally altered zones in granite by combining synthetic clay content logs with magnetic mineralogical investigations of drilled rock cuttings. Geophysical Journal International 199, 465-479.
Mertanen, S., Pesonen, L., 1992. Palaeomagnetism of the Early to Middle Proterozoic mafic intrusions in northern Finland, International Symposium, IGCP Project, pp. 57-59.
Mertanen, S., Pesonen, L.J., 1994. Preliminary results of a palaeomagnetic and rock magnetic study of the Proterozoic Tsuomasvarri intrusions, northern Fennoscandia. Precambrian Research 69, 25-50.
Minifie, M.J., Kerr, A.C., Ernst, R.E., Hastie, A.R., Ciborowski, T.J.R., Desharnais, G., Millar, I.L., 2013. The northern and southern sections of the western ca. 1880 Ma Circum-Superior Large Igneous Province, North America: The Pickle Crow dyke connection? Lithos 174, 217-235.
Mitchell, R.N., Hoffman, P.F., Evans, D.A.D., 2010. Coronation loop resurrected: Oscillatory apparent polar wander of Orosirian (2.05–1.8Ga) paleomagnetic poles from Slave craton. Precambrian Research 179, 121-134.
Mitchell, R.N., Kilian, T.M., Evans, D.A., 2012. Supercontinent cycles and the calculation of absolute palaeolongitude in deep time. Nature 482, 208-211.
Mitchell, R.N., 2014. True polar wander and supercontinent cycles: Implications for lithospheric elasticity and the triaxial earth. American Journal of Science 314, 966-979.
Mitchell, R.N., Bleeker, W., van Breemen, O., Lecheminant, T.N., Peng, P., Nilsson, M.K.M., Evans, D.A.D., 2014. Plate tectonics before 2.0 Ga: Evidence from paleomagnetism of cratons within supercontinent Nuna. American Journal of Science 314, 878-894.
Morelli, R.M., Hartlaub, R.P., Ashton, K.E., Ansdell, K.M., 2009. Evidence for enrichment of subcontinental lithospheric mantle from Paleoproterozoic intracratonic magmas: Geochemistry and U–Pb geochronology of Martin Group igneous rocks, western Rae Craton, Canada. Precambrian Research 175, 1-15.
Morgan, G.E., 1985. The paleomagnetism and cooling history of metamorphic and igneous rocks from the Limpopo Mobile Belt, southern Africa. Geological Society of America Bulletin 96, 663-675.
Moyen, J.-F., Nédélec, A., Martin, H., Jayananda, M., 2003. Syntectonic granite emplacement at different structural levels: the Closepet granite, South India. Journal of Structural Geology 25, 611-631.
Moyen, J.-F., Martin, H., 2012. Forty years of TTG research. Lithos 148, 312-336.
Moyen, J.F., Laurent, O., Chelle-Michou, C., Couzinié, S., Vanderhaeghe, O., Zeh, A., Villaros, A., Gardien, V., 2016. Collision vs. subduction-related magmatism: two contrasting ways of granite formation and implications for crustal growth. Lithos.
Mukherjee, I., Large, R.R., 2016. Pyrite trace element chemistry of the Velkerri Formation, Roper Group, McArthur Basin: Evidence for atmospheric oxygenation during the Boring Billion. Precambrian Research 281, 13-26.
Murakami, M., Hirose, K., Kawamura, K., Sata, N., Ohishi, Y., 2004. Post-Perovskite Phase Transition in MgSiO3. Science 304, 855-858.
Nachit, H., Ibhi, A., Abia, E.H., Ben Ohoud, M., 2005. Discrimination between primary magmatic biotites, reequilibrated biotites and neoformed biotites. Comptes Rendus Geoscience 337, 1415-1420.
Nance, D., Worsley, T.R., Moody, J.B., 1988. The supercontinent cycle. Scientific American 259, 72-79.

Nance, R.D., Murphy, J.B., Santosh, M., 2014. The supercontinent cycle: A retrospective essay. Gondwana Research 25, 4-29.

Nédélec, A., Stephens, E.W., Fallick, A.E., 1995. The Panafrican Stratoid Granites of Madagascar: Alkaline Magmatism in a Post-Collisional Extensional Setting. Journal of Petrology 36, 1367-1391.

Nédélec, A., Borisova, A.Y., 2015. Commentary "Is the Neoproterozoic oxygen burst a supercontinent legacy?". Frontiers in Earth Science 3, 80.

Nédélec, A., Bouchez, J.-L., 2015. Granites: Petrology, Structure, Geological Setting, and Metallogeny. OUP Oxford.

Nédélec, A., Trindade, R., Peschler, A., Archanjo, C., Macouin, M., Poitrasson, F., Bouchez, J.-L., 2015. Hydrothermally-induced changes in mineralogy and magnetic properties of oxidized A-type granites. Lithos 212–215, 145-157.

Néel, L., 1955. Some theoretical aspects of rock-magnetism. Advances in Physics 4, 191-243.

Neuvonen, K., Korsman, K., Kouvo, O., Paavola, J., 1981. Paleomagnetism and age relations of the rocks in the main sulphide ore belt in central Finland. Bull. Geol. Soc. Finland 53, 109-133.

Neuvonen, K., 1986. On the direction of remanent magnetization of the quartz porphyry dikes in SE Finland. Bull. geol. Soc. Finland 58, 195-201.

Nevanlinna, H., Pesonen, L.J., 1983. Late Precambrian Keweenawan Asymmetric Polarities as analyzed by axial offset dipole geomagnetic models. Journal of Geophysical Research: Solid Earth 88, 645-658.

Nicoli, G., Stevens, G., Moyen, J.F., Frei, D., 2015. Rapid evolution from sediment to anatectic granulite in an Archean continental collision zone: the example of the Bandelierkop Formation metapelites, South Marginal Zone, Limpopo Belt, South Africa. Journal of Metamorphic Geology 33, 177-202.

Nicoli, G., Moyen, J.-F., Stevens, G., 2016. Diversity of burial rates in convergent settings decreased as Earth aged. Scientific Reports 6, 26359.

Nisbet, E.G., Arndt, N., 1982. Komatiites. Chapman and Hall.

Nomade, S., Théveniaut, H., Chen, Y., Pouclet, A., Rigollet, C., 2000. Paleomagnetic study of French Guyana Early Jurassic dolerites: hypothesis of a multistage magmatic event. Earth and Planetary Science Letters 184, 155-168.

Nomade, S., Chen, Y., Féraud, G., Pouclet, A., Théveniaut, H., 2001. First paleomagnetic and 40Ar/39Ar study of Paleoproterozoic rocks from the French Guyana (Camopi and Oyapok rivers), northeastern Guyana Shield. Precambrian Research 109, 239-256.

Nomade, S., Chen, Y., Pouclet, A., Féraud, G., Théveniaut, H., Daouda, B.Y., Vidal, M., Rigolet, C., 2003. The Guiana and the West African Shield Palaeoproterozoic grouping: new palaeomagnetic data for French Guiana and the Ivory Coast. Geophysical Journal International 154, 677-694.

O'Neill, C., Lenardic, A., Weller, M., Moresi, L., Quenette, S., Zhang, S., 2016. A window for plate tectonics in terrestrial planet evolution? Physics of the Earth and Planetary Interiors 255, 80-92.

Olson, P., 2016. Mantle control of the geodynamo: Consequences of top-down regulation. Geochemistry, Geophysics, Geosystems, n/a-n/a.

Olsson, J.R., Klausen, M.B., Hamilton, M.A., März, N., Söderlund, U., Roberts, R.J., 2015. Baddeleyite U–Pb ages and gechemistry of the 1875–1835 Ma Black Hills Dyke Swarm across north-eastern South Africa: part of a trans-Kalahari Craton back-arc setting? GFF 138, 183-202.

Onstott, T., 1981a. Proterozoic transcurrent tectonics: palaeomagnetic evidence from Venezuela and Africa. Nature 289, 131-136.

Onstott, T., Hargraves, R.B., York, D., Hall, C., 1984. Constraints on the motions of South American and African Shields during the Proterozoic: I. 40Ar/39Ar and paleomagnetic correlations between Venezuela and Liberia. Geological Society of America Bulletin 95, 1045-1054.

Onstott, T.C., 1981b. Paleomagnetism of the Guayana Shield, Venezuela and its implications concerning Proterozoic tectonics of South America and Africa.

Özdemir, Ö., Dunlop, D.J., 2014. Hysteresis and coercivity of hematite. Journal of Geophysical Research: Solid Earth 119, 2582-2594.

Paixão, M.A.P., Nilson, A.A., Dantas, E.L., 2008. The Neoproterozoic Quatipuru ophiolite and the Araguaia fold belt, central-northern Brazil, compared with correlatives in NW Africa. Geological Society, London, Special Publications 294, 297-318.

Park, J.K., Tanczyk, E.I., Desbarats, A., 1988. Magnetic Fabric and Its Significance in the 1400 Ma Mealy Diabase Dykes of Labrador, Canada. Journal of Geophysical Research: Solid Earth 93, 13689-13704.

Parman, S.W., Grove, T.L., 2005. Komatiites in the plume debate. Geological Society of America Special Papers 388, 249-256.

Parman, S.W., 2007. Helium isotopic evidence for episodic mantle melting and crustal growth. Nature 446, 900-903.

Pasenko, A.N., Lubnina, N.V., 2014. The Karelian Craton in the Paleoproterozoic: New paleomagnetic data. Moscow Univ. Geol. Bull. 69, 189-197.

Payne, J.L., Hand, M., Barovich, K.M., Reid, A., Evans, D.A.D., 2009. Correlations and reconstruction models for the 2500-1500 Ma evolution of the Mawson Continent. Geological Society, London, Special Publications 323, 319-355.

Pehrsson, S.J., Berman, R.G., Eglington, B., Rainbird, R., 2013. Two Neoarchean supercontinents revisited: The case for a Rae family of cratons. Precambrian Research.

Pehrsson, S.J., Eglington, B.M., Evans, D.A.D., Huston, D., Reddy, S.M., 2016. Metallogeny and its link to orogenic style during the Nuna supercontinent cycle. Geological Society, London, Special Publications 424, 83-94.

Pesonen, L., Mertanen, S., Veikkolainen, T., 2012. Paleo-Mesoproterozoic Supercontinents–A Paleomagnetic View. Geophysica 48, 5-47.

Pesonen, L.J., Stigzelius, E., 1972. On petrophysical and paleomagnetic investigations of the gabbros of the Pohjanmaa region, Middle-West Finland, Geological Survey of Finland. Bulletin, p. 27.

Pesonen, L.J., Nevanlinna, H., 1981. Late Precambrian Keweenawan asymmetric reversals. Nature 294, 436-439.

Pesonen, L.J., Elming, S.Å., Mertanen, S., Pisarevsky, S., D'Agrella-Filho, M.S., Meert, J.G., Schmidt, P.W., Abrahamsen, N., Bylund, G., 2003. Palaeomagnetic configuration of continents during the Proterozoic. Tectonophysics 375, 289-324.

Pimentel, M., Machado, N., 1994. Geocronologia U-Pb dos terrenos granito-greenstone de Rio Maria, Pará, SBG, Congresso Brasileiro de Geologia, pp. 390-391.

Pimentel, M.M., Lindenmayer, Z.G., Laux, J.H., Armstrong, R., de Araújo, J.C., 2003. Geochronology and Nd isotope geochemistry of the Gameleira Cu–Au deposit, Serra dos Carajás, Brazil: 1.8–1.7 Ga hydrothermal alteration and mineralization. Journal of South American Earth Sciences 15, 803-813.

Pinho, M.A.S.B., Chemale Jr, F., Van Schmus, W.R., Pinho, F.E.C., 2003. U–Pb and Sm–Nd evidence for 1.76–1.77 Ga magmatism in the Moriru region, Mato Grosso, Brazil: implications for province boundaries in the SW Amazon Craton. Precambrian Research 126, 1-25.

Pinho, S., Fernandes, C., Teixeira, N., Paiva Jr, A., Cruz, V., Lamarão, C., Moura, C., 2006. O magmatismo paleoproterozóico da região de São Félix do Xingu, Província Estanífera do sul do Pará: Petrografia e Geocronologia. Revista Brasileira de Geociências 36, 724-732.

Piper, J.D.A., Beckmann, G.E.J., Badham, J.P.N., 1976. Palaeomagnetic Evidence for a Proterozoic Super-Continent [and Discussion]. Philosophical Transactions of the Royal Society of London. Series A, Mathematical and Physical Sciences 280, 469-490.

Piper, J.D.A., 1982. The Precambrian palaeomagnetic record: the case for the Proterozoic Supercontinent. Earth and Planetary Science Letters 59, 61-89.

Piper, J.D.A., 2000. The Neoproterozoic Supercontinent: Rodinia or Palaeopangaea? Earth and Planetary Science Letters 176, 131-146.

Piper, J.D.A., 2007. The Neoproterozoic supercontinent Palaeopangaea. Gondwana Research 12, 202-227.
Piper, J.D.A., 2010a. Palaeopangaea in Meso-Neoproterozoic times: The palaeomagnetic evidence and implications to continental integrity, supercontinent form and Eocambrian break-up. Journal of Geodynamics 50, 191-223.
Piper, J.D.A., 2010b. Protopangaea: Palaeomagnetic definition of Earth's oldest (mid-Archaean-Palaeoproterozoic) supercontinent. Journal of Geodynamics 50, 154-165.
Piper, J.D.A., Jiasheng, Z., Huang, B., Roberts, A.P., 2011. Palaeomagnetism of Precambrian dyke swarms in the North China Shield: The ~1.8 Ga LIP event and crustal consolidation in late Palaeoproterozoic times. Journal of Asian Earth Sciences 41, 504-524.
Piper, J.D.A., 2013a. Continental velocity through Precambrian times: The link to magmatism, crustal accretion and episodes of global cooling. Geoscience Frontiers 4, 7-36.
Piper, J.D.A., 2013b. A Planetary perspective on Earth evolution: Lid Tectonics before Plate Tectonics. Tectonophysics.
Piper, J.D.A., 2014. The Precambrian supercontinent Palaeopangaea: two billion years of quasi-integrity and an appraisal of geological evidence. International Geology Review, 1-29.
Pisarevsky, S.A., Sokolov, S.J., 1999. Palaeomagnetism of the Palaeoproterozoic ultramafic intrusion near Lake Konchozero, Southern Karelia, Russia. Precambrian Research 93, 201-213.
Pisarevsky, S.A., Natapov, L.M., Donskaya, T.V., Gladkochub, D.P., Vernikovsky, V.A., 2008. Proterozoic Siberia: A promontory of Rodinia. Precambrian Research 160, 66-76.
Pisarevsky, S.A., Bylund, G., 2010. Paleomagnetism of 1780–1770 Ma mafic and composite intrusions of Småland (Sweden): implications for the mesoproterozoic supercontinent. American Journal of Science 310, 1168-1186.
Pisarevsky, S.A., Biswal, T.K., Wang, X.-C., De Waele, B., Ernst, R., Söderlund, U., Tait, J.A., Ratre, K., Singh, Y.K., Cleve, M., 2013. Palaeomagnetic, geochronological and geochemical study of Mesoproterozoic Lakhna Dykes in the Bastar Craton, India: Implications for the Mesoproterozoic supercontinent. Lithos 174, 125-143.
Pisarevsky, S.A., Elming, S.-Å., Pesonen, L.J., Li, Z.-X., 2014. Mesoproterozoic paleogeography: Supercontinent and beyond. Precambrian Research 244, 207-225.
Poorter, R.P.E., 1976. Palaeomagnetism of the Svecofennian Loftahammar gabbro and some Jotnian dolerites in the Swedish part of the Baltic Shield. Physics of the Earth and Planetary Interiors 12, 51-64.
Powell, C.M., Li, Z.X., McElhinny, M.W., 1993a. Palaeomagnetic tests of tectonic models of the Tasman Fold Belt during the Neoproterozoic and palaeozoic. Exploration Geophysics 24, 243-246.
Powell, C.M., Li, Z.X., McElhinny, M.W., Meert, J.G., Park, J.K., 1993b. Paleomagnetic constraints on timing of the Neoproterozoic breakup of Rodinia and the Cambrian formation of Gondwana. Geology 21, 889-892.
Pradhan, G.K., Fiquet, G., Siebert, J., Auzende, A.-L., Morard, G., Antonangeli, D., Garbarino, G., 2015. Melting of MORB at core–mantle boundary. Earth and Planetary Science Letters 431, 247-255.
Pradhan, V.R., Pandit, M.K., Meert, J.G., 2008. A cautionary note on the age of the paleomagnetic pole obtained from the Harohalli dyke swarms, Dharwar craton, southern India. Indian Dykes: Geochemistry, Geophysics, and Geochronology. Narosa Publishing Ltd., New Delhi, India, 339-352.
Pradhan, V.R., Meert, J.G., Pandit, M.K., Kamenov, G., Mondal, M.E.A., 2012. Paleomagnetic and geochronological studies of the mafic dyke swarms of Bundelkhand craton, central India: Implications for the tectonic evolution and paleogeographic reconstructions. Precambrian Research 198–199, 51-76.
Prasad, C., Pulla Reddy, V., Subbarao, K., Radhakrishnamurthy, C., 1987. Palaeomagnetism and the crescent shape of the Cuddapah basin. Purana Basins of Peninsular India, Mem. Geol Soc. Ind 6, 331-347.

Pullaiah, G., Irving, E., Buchan, K.L., Dunlop, D.J., 1975. Magnetization changes caused by burial and uplift. Earth and Planetary Science Letters 28, 133-143.

Radhakrishna, T., Chandra, R., Srivastava, A.K., Balasubramonian, G., 2013a. Central/Eastern Indian Bundelkhand and Bastar cratons in the Palaeoproterozoic supercontinental reconstructions: A palaeomagnetic perspective. Precambrian Research 226, 91-104.

Radhakrishna, T., Krishnendu, N.R., Balasubramonian, G., 2013b. Palaeoproterozoic Indian shield in the global continental assembly: Evidence from the palaeomagnetism of mafic dyke swarms. Earth-Science Reviews 126, 370-389.

Rämö, O.T., Haapala, I., 1995. One hundred years of rapakivi granite. Mineralogy and Petrology 52, 129-185.

Rämö, O.T., Dall'Agnol, R., Macambira, M.J., Leite, A.A., de Oliveira, D.C., 2002. 1.88 Ga Oxidized A-Type Granites of the Rio Maria Region, Eastern Amazonian Craton, Brazil: Positively Anorogenic! The Journal of geology 110, 603-610.

Rapalini, A.E., Tarling, D.H., Turner, P., Flint, S., Vilas, J.F., 1994. Paleomagnetism of the Carboniferous Tepuel Group, central Patagonia, Argentina. Tectonics 13, 1277-1294.

Raposo, M.I.B., D'Agrella-Filho, M.S., 2000. Magnetic fabrics of dike swarms from SE Bahia State, Brazil: their significance and implications for Mesoproterozoic basic magmatism in the São Francisco Craton. Precambrian Research 99, 309-325.

Rasmussen, B., Fletcher, I.R., Bekker, A., Muhling, J.R., Gregory, C.J., Thorne, A.M., 2012. Deposition of 1.88-billion-year-old iron formations as a consequence of rapid crustal growth. Nature 484, 498-501.

Raub, T., Kirschvink, J., Evans, D., 2007. True polar wander: Linking deep and shallow geodynamics to hydro-and bio-spheric hypotheses. Treatise on Geophysics 5, 565-589.

Reddy, S.M., Evans, D.A.D., 2009. Palaeoproterozoic supercontinents and global evolution: correlations from core to atmosphere. Geological Society, London, Special Publications 323, 1-26.

Reis, N.J., Teixeira, W., Hamilton, M.A., Bispo-Santos, F., Almeida, M.E., D'Agrella-Filho, M.S., 2013. Avanavero mafic magmatism, a late Paleoproterozoic lip in the Guiana Shield, Amazonian Craton: U–Pb ID-TIMS baddeleyite, geochemical and paleomagnetic evidence. Lithos.

Renne, P., Onstott, T., Jorge João, X., 1988. 40Ar/39Ar and paleomagnetic results from the Guaporé Shield: further implications for the nature of Middle-Late Proterozoic mobile belts of Gondwanaland. SBG, Congr. Lat.-Amer. Geol 7, 348-362.

Reshetnyak, M.Y., Pavlov, V.E., 2016. Evolution of the dipole geomagnetic field. Observations and models. Geomagnetism and Aeronomy 56, 110-124.

Ricard, Y., Richards, M., Lithgow-Bertelloni, C., Le Stunff, Y., 1993. A geodynamic model of mantle density heterogeneity. Journal of Geophysical Research: Solid Earth 98, 21895-21909.

Rieder, M., Cavazzini, G., D'yakonov, Y.S., Frank-Kamenetskii, V.A., Gottardi, G., Guggenheim, S., Koval, P.V., Müller, G., Neiva, A.M., Radoslovich, E.W., 1999. Nomenclature of the micas. Mineral. Mag 63, 79.

Rivalenti, G., Williamson, A., Feyer, A.M., Mazzucchelli, M., Girardi, V.A.V., Cavazzini, G., Finatti, C., Barbieri, M.A., Teixeira, W., 1998. Petrogenesis of the Paleoproterozoic basalt-andesite-rhyolite dyke association in the Carajas region, Amazonian craton. Lithos 43, 235-265.

Rizzotto, G.J., Hartmann, L.A., 2012. Geological and geochemical evolution of the Trincheira Complex, a Mesoproterozoic ophiolite in the southwestern Amazon craton, Brazil. Lithos 148, 277-295.

Roberts, P.H., Glatzmaier, G.A., 2001. The geodynamo, past, present and future. Geophysical & Astrophysical Fluid Dynamics 94, 47-84.

Rochette, P., Jackson, M., Aubourg, C., 1992. Rock magnetism and the interpretation of anisotropy of magnetic susceptibility. Reviews of Geophysics 30, 209-226.

Rodrigues, E., 1992. Implantação da metodologia Pb-Pb em rocha total: exemplos de aplicação na província mineral de carajás (PA). Belém, 128p. Tese (Mestrado)-Centro de Geociências, Universidade Federal do Pará.

Rogers, J.J., 1996. A history of continents in the past three billion years. The journal of geology, 91-107.

Rogers, J.J.W., Santosh, M., 2002. Configuration of Columbia, a Mesoproterozoic Supercontinent. Gondwana Research 5, 5-22.

Rogers, J.J.W., Santosh, M., 2009. Tectonics and surface effects of the supercontinent Columbia. Gondwana Research 15, 373-380.

Rolf, T., Tackley, P.J., 2011. Focussing of stress by continents in 3D spherical mantle convection with self-consistent plate tectonics. Geophysical Research Letters 38, n/a-n/a.

Roverato, M., 2016. The Montesbelos mass-flow (southern Amazonian craton, Brazil): a Paleoproterozoic volcanic debris avalanche deposit? Bulletin of Volcanology 78, 1-6.

Roverato, M., Giordano, D., Echeverri-Misas, C.M., Juliani, C., 2016. Paleoproterozoic felsic volcanism of the Tapajós Mineral Province, Southern Amazon Craton, Brazil. Journal of Volcanology and Geothermal Research.

Roverato, M., Juliani, C., Marcelo Dias-Fernandes, C., Capra, L., 2017. Paleoproterozoic andesitic volcanism in the southern Amazonian craton, the Sobreiro Formation: new insights from lithofacies analysis of the volcaniclastic sequences. Precambrian Research 289, 18-30.

Runcorn, S., 1962. Convection currents in the earth's mantle. Nature 195, 1248-1249.

Runcorn, S.K., 1965. Palaeomagnetic Comparisons between Europe and North America. Philosophical Transactions of the Royal Society of London. Series A, Mathematical and Physical Sciences 258, 1-11.

Sadowski, G.R., Bettencourt, J.S., 1996. Mesoproterozoic tectonic correlations between eastern Laurentia and the western border of the Amazon Craton. Precambrian Research 76, 213-227.

Salminen, J., Pesonen, L.J., Reimold, W.U., Donadini, F., Gibson, R.L., 2009. Paleomagnetic and rock magnetic study of the Vredefort impact structure and the Johannesburg Dome, Kaapvaal Craton, South Africa—Implications for the apparent polar wander path of the Kaapvaal Craton during the Mesoproterozoic. Precambrian Research 168, 167-184.

Salminen, J., Mertanen, S., Evans, D.A.D., Wang, Z., 2014. Paleomagnetic and geochemical studies of the Mesoproterozoic Satakunta dyke swarms, Finland, with implications for a Northern Europe – North America (NENA) connection within Nuna supercontinent. Precambrian Research 244, 170-191.

Salminen, J.M., Klein, R., Mertanen, S., Pesonen, L.J., Fröjdö, S., Mänttäri, I., Eklund, O., 2015. Palaeomagnetism and U–Pb geochronology of c. 1570 Ma intrusives from Åland archipelago, SW Finland – implications for Nuna. Geological Society, London, Special Publications 424.

Santos, Joao Orestes Schneider, Tassinari, C.C.G., 2003a. Geotectônica do Escudo das Guianas e Brasil-Central, Geologia, Tectônica e Recursos Minerais do Brasil. Texto, mapas & SIG: CPRM—Serviço Geológico do Brasil, pp. 169-226.

Santos, J.O.S., Hartmann, L.A., Gaudette, H.E., Groves, D.I., McNaughton, N.J., Fletcher, I.R., 2000. A New Understanding of the Provinces of the Amazon Craton Based on Integration of Field Mapping and U-Pb and Sm-Nd Geochronology. Gondwana Research 3, 453-488.

Santos, J.O.S., Hartmann, L.A., McNaughton, N.J., Fletcher, I.R., 2002. Timing of mafic magmatism in the Tapajós Province (Brazil) and implications for the evolution of the Amazon Craton: evidence from baddeleyite and zircon U–Pb SHRIMP geochronology. Journal of South American Earth Sciences 15, 409-429.

Santos, J.O.S., Potter, P.E., Reis, N.J., Hartmann, L.A., Fletcher, I.R., McNaughton, N.J., 2003b. Age, source, and regional stratigraphy of the Roraima Supergroup and

Roraima-like outliers in northern South America based on U-Pb geochronology. Geological Society of America Bulletin 115, 331-348.

Santos, M.N.S.d., Oliveira, D.C., 2016. Rio Maria granodiorite and associated rocks of Ourilândia do Norte – Carajás province: Petrography, geochemistry and implications for sanukitoid petrogenesis. Journal of South American Earth Sciences 72, 279-301.

Santos, S.J.O., Groves, I.D., Hartmann, A.L., Moura, A.M., McNaughton, J.N., 2001. Gold deposits of the Tapajós and Alta Floresta Domains, Tapajós–Parima orogenic belt, Amazon Craton, Brazil. Miner Deposita 36, 278-299.

Sato, K., Tassinari, C.C.G., Basei, M.A.S., Siga Júnior, O., Onoe, A.T., Souza, M.D.d., 2014. Sensitive High Resolution Ion Microprobe (SHRIMP IIe/MC) of the Institute of Geosciences of the University of São Paulo, Brazil: analytical method and first results. Geologia USP. Série Científica 14, 3-18.

Sawkins, F.J., 1976. Widespread continental rifting: Some considerations of timing and mechanism. Geology 4, 427-430.

Schenk, P., Matsuyama, I., Nimmo, F., 2008. True polar wander on Europa from global-scale small-circle depressions. Nature 453, 368-371.

Schmidt, P.W., 1980. Paleomagnetism of igneous rocks from the Belcher Islands, Northwest Territories, Canada. Canadian Journal of Earth Sciences 17, 807-822.

Schmidt, P.W., 2014. A review of Precambrian palaeomagnetism of Australia: Palaeogeography, supercontinents, glaciations and true polar wander. Gondwana Research 25, 1164-1185.

Schobbenhaus, C., Campos, D.A., Derze, G.R., Asmus, H.E., 1984. Geologia do Brasil: texto explicativo do mapa geológico do Brasil e da área oceânica adjacente incluindo depósitos minerais, escala 1: 2 5000 000. Divisão de Geologia e Mineralogia, Departamento Nacional da Produção Mineral.

Schobbenhaus, C., Brito Neves, B., Bizzi, L., Schobbenhaus, C., Vidotti, R., Gonçalves, J., 2003. A geologia do Brasil no contexto da Plataforma Sul-Americana. Geologia, Tectônica e Recursos Minerais do Brasil. Brasília, CPRM, 5-25.

Schobbenhaus, C., Gonçalves, J., Santos, J., Abram, M., Leão Neto, R., Matos, G., Vidotti, R., Ramos, M., Jesus, J., 2004. Carta Geológica do Brasil ao Milionésimo: Teresina. Sistema de Informações Geográficas.Folhas Boa Vista (NA-20) e Roraima (NB-20). Escala 1:1,000,000. CPRM.

Schrag, D.P., Higgins, J.A., Macdonald, F.A., Johnston, D.T., 2013. Authigenic Carbonate and the History of the Global Carbon Cycle. Science 339, 540-543.

Semami, F.A., de Kock, M., Söderlund, U., Gumsley, A., da Silva, R., Beukes, N., Armstrong, R., 2016. New U–Pb geochronologic and palaeomagnetic constraints on the late Palaeoproterozoic Hartley magmatic event: evidence for a potential large igneous province in the Kaapvaal Craton during Kalahari assembly, South Africa. GFF 138, 164-182.

Shirey, S.B., Richardson, S.H., 2011. Start of the Wilson Cycle at 3 Ga Shown by Diamonds from Subcontinental Mantle. Science 333, 434-436.

Siegler, M.A., Miller, R.S., Keane, J.T., Laneuville, M., Paige, D.A., Matsuyama, I., Lawrence, D.J., Crotts, A., Poston, M.J., 2016. Lunar true polar wander inferred from polar hydrogen. Nature 531, 480-484.

Simon, N.S.C., Carlson, R.W., Pearson, D.G., Davies, G.R., 2007. The Origin and Evolution of the Kaapvaal Cratonic Lithospheric Mantle. Journal of Petrology 48, 589-625.

Skiöld, T., 1988. Implications of new U-Pb zircon chronology to early proterozoic crustal accretion in northern Sweden. Precambrian Research 38, 147-164.

Sláma, J., Košler, J., Condon, D.J., Crowley, J.L., Gerdes, A., Hanchar, J.M., Horstwood, M.S.A., Morris, G.A., Nasdala, L., Norberg, N., Schaltegger, U., Schoene, B., Tubrett, M.N., Whitehouse, M.J., 2008. Plešovice zircon — A new natural reference material for U–Pb and Hf isotopic microanalysis. Chemical Geology 249, 1-35.

Smirnov, A.V., Evans, D.A.D., Ernst, R.E., Söderlund, U., Li, Z.-X., 2013. Trading partners: Tectonic ancestry of southern Africa and western Australia, in Archean supercratons Vaalbara and Zimgarn. Precambrian Research 224, 11-22.

Smirnov, A.V., Tarduno, J.A., Kulakov, E.V., McEnroe, S.A., Bono, R.K., 2016. Paleointensity, core thermal conductivity and the unknown age of the inner core. Geophysical Journal International 205, 1190-1195.

Sobolev, A.V., Asafov, E.V., Gurenko, A.A., Arndt, N.T., Batanova, V.G., Portnyagin, M.V., Garbe-Schönberg, D., Krasheninnikov, S.P., 2016. Komatiites reveal a hydrous Archaean deep-mantle reservoir. Nature 531, 628-632.

Söderlund, U., Hofmann, A., Klausen, M.B., Olsson, J.R., Ernst, R.E., Persson, P.-O., 2010. Towards a complete magmatic barcode for the Zimbabwe craton: Baddeleyite U–Pb dating of regional dolerite dyke swarms and sill complexes. Precambrian Research 183, 388-398.

Söderlund, U., Klausen, M.B., Ernst, R.E., Bleeker, W., 2016. New advances in using large igneous provinces (LIPs) to reconstruct ancient supercontinents. GFF 138, 1-5.

Solomatov, V.S., 2001. Grain size-dependent viscosity convection and the thermal evolution of the Earth. Earth and Planetary Science Letters 191, 203-212.

Stacey, J.S., Kramers, J.D., 1975. Approximation of terrestrial lead isotope evolution by a two-stage model. Earth and Planetary Science Letters 26, 207-221.

Stegman, D.R., Freeman, J., May, D.A., 2009. Origin of ice diapirism, true polar wander, subsurface ocean, and tiger stripes of Enceladus driven by compositional convection. Icarus 202, 669-680.

Stephenson, A., Sadikun, S., Potter, D.K., 1986. A theoretical and experimental comparison of the anisotropies of magnetic susceptibility and remanence in rocks and minerals. Geophysical Journal International 84, 185-200.

Swanson-Hysell, N.L., Maloof, A.C., Weiss, B.P., Evans, D.A.D., 2009. No asymmetry in geomagnetic reversals recorded by 1.1-billion-year-old Keweenawan basalts. Nature Geosci 2, 713-717.

T. Veikkolainen, A. Heinonen, L.J. Pesonen, L.M. Fraga, O.T. Rämö, Dall'Agnol, R., 2011. Mucajaí-kompleksin (Pohjois-Amazonia, Brasilia) paleomagnetismista. XXV GEOFYSIIKAN PÄIVÄT, 121-124.

Tang, M., Chen, K., Rudnick, R.L., 2016. Archean upper crust transition from mafic to felsic marks the onset of plate tectonics. Science 351, 372-375.

Tarduno, J.A., 1990. Absolute inclination values from deep sea sediments: A reexamination of the Cretaceous Pacific record. Geophysical Research Letters 17, 101-104.

Tarduno, J.A., Blackman, E.G., Mamajek, E.E., 2014. Detecting the oldest geodynamo and attendant shielding from the solar wind: Implications for habitability. Physics of the Earth and Planetary Interiors 233, 68-87.

Tassinari, C., Teixeira, W., Siga Jr, O., 1978. Considerações crono-estratigráficas de região das chapadas do Cachimbo e Dardanelos, Anais XXX Congresso Brasileiro de Geologia, pp. 477-490.

Tassinari, C.C., Macambira, M.J., 1999. Geochronological provinces of the Amazonian Craton. Episodes-Newsmagazine of the International Union of Geological Sciences 22, 174-182.

Tassinari, C.C.G., Bettencourt, J.S., Geraldes, M.C., Macambira, M.J.B., Lafon, J.M., 2000. The Amazonian Craton. In: Cordani, U. G., Milani, E. J., Thomaz-Filho, A., Campos, D. A., (Eds), Tectonic Evolution of South America, Rio de Janeiro, 31st International Geological Congress, pp. p. 41-95.

Tassinari, C.C.G., Macambira, M., 2004. A evolução tectonica do Craton Amazonico, In: (Org.), V.M.-N.A.B.C.D.R.C.B.B.d.B.N. (Ed.), Geologia do Continente Sul Americano: Evolução da obra de F.F.M. de Ameida. BECA, São Paulo, pp. p. 471-486.

Tauxe, L., Gee, J.S., Staudigel, H., 1998. Flow directions in dikes from anisotropy of magnetic susceptibility data: The bootstrap way. Journal of Geophysical Research: Solid Earth 103, 17775-17790.

Tauxe, L., Kodama, K.P., 2009. Paleosecular variation models for ancient times: Clues from Keweenawan lava flows. Physics of the Earth and Planetary Interiors 177, 31-45.

Tavares, F.M., 2015. Evolução Geotectônica do Nordeste da Província Carajás. Tese de Doutorado, Instituto de Geociências, Universidade Federal do Rio de Janeiro, 115p.

Taylor, S.R., McLennan, S.M., 1985. The continental crust: its composition and evolution.

Teixeira, N.P., Bettencourt, J.S., Moura, C.A.V., Dall'Agnol, R., Macambira, E.M.B., 2002. Archean crustal sources for Paleoproterozoic tin-mineralized granites in the Carajás Province, SSE Pará, Brazil: Pb–Pb geochronology and Nd isotope geochemistry. Precambrian Research 119, 257-275.

Teixeira, N.P., Bettencourt, J.S., Dall'agnol, R., Moura, C.A.V., Fernandes, C.M.D., Pinho, S.C.C., 2005. Geoquímica dos granitos paleoproterozóicos da Suíte granítica Velho Guilherme, Província Estanífera do Sul do Pará. Revista Brasileira de Geociências 35.

Teixeira, W., Tassinari, C.C.G., Cordani, U.G., Kawashita, K., 1989. A review of the geochronology of the Amazonian Craton: Tectonic implications. Precambrian Research 42, 213-227.

Teixeira, W., Hamilton, M.A., Ernst, R.E., Girardi, V.A.V., 2012a. 200 Ma dyke swarm in the Carajás province, Amazonian craton, South America: distal part of the CAMP event, Reconstruction of Supercontinents Back To 2.7 Ga Using The Large Igneous Province (LIP) Record: With Implications For Mineral Deposit Targeting, Hydrocarbon Resource Exploration, and Earth System Evolution.

Teixeira, W., Hamilton, M.A., Ernst, R.E., Girardi, V.A.V., Evans, D.A.D., 2012b. 535 Ma dyke swarm in the Carajás province, Amazonian craton, South America: potential part of a regional intraplate event, Reconstruction of Supercontinents Back To 2.7 Ga Using The Large Igneous Province (LIP) Record: With Implications For Mineral Deposit Targeting, Hydrocarbon Resource Exploration, and Earth System Evolution, pp. 1-11.

Teixeira, W., D'Agrella-Filho, M.S., Hamilton, M.A., Ernst, R.E., Girardi, V.A.V., Mazzucchelli, M., Bettencourt, J.S., 2013. U–Pb (ID-TIMS) baddeleyite ages and paleomagnetism of 1.79 and 1.59 Ga tholeiitic dyke swarms, and position of the Rio de la Plata Craton within the Columbia supercontinent. Lithos.

Teixeira, W., Hamilton, M.A., Girardi, V.A.V., Faleiros, F.M., 2016. Key Dolerite Dyke Swarms of Amazonia: U-Pb Constraints on Supercontinent Cycles and Geodynamic Connections with Global LIP Events Through Time. Acta Geologica Sinica - English Edition 90, 84-85.

Théveniaut, H., Delor, C., 2003. Le paléomagnétisme du bouclier des Guyanes: état des connaissances et analyses critiques des données. Géologie de la France 2, 3-4.

Théveniaut, H., Delor, C., Lafon, J.M., Monié, P., Rossi, P., Lahondère, D., 2006. Paleoproterozoic (2155–1970 Ma) evolution of the Guiana Shield (Transamazonian event) in the light of new paleomagnetic data from French Guiana. Precambrian Research 150, 221-256.

Thorkelson, D.J., Laughton, J.R., 2015. Paleoproterozoic closure of an Australia–Laurentia seaway revealed by megaclasts of an obducted volcanic arc in Yukon, Canada. Gondwana Research 33, 115-133.

Torsvik, T., Briden, J., Smethurst, M., 2000. Super-IAPD Interactive analysis of palaeomagnetic data. World Wide Web Address: http://www. geodynamics. no/software. htm.

Torsvik, T.H., Smethurst, M.A., 1999. Plate tectonic modelling: virtual reality with GMAP. Computers & Geosciences 25, 395-402.

Trindade, R.I.F., Font, E., D'Agrella-Filho, M.S., Nogueira, A.C.R., Riccomini, C., 2003. Low-latitude and multiple geomagnetic reversals in the Neoproterozoic Puga cap carbonate, Amazon craton. Terra Nova 15, 441-446.

Usui, Y., Tarduno, J.A., Watkeys, M., Hofmann, A., Cottrell, R.D., 2009. Evidence for a 3.45-billion-year-old magnetic remanence: Hints of an ancient geodynamo from conglomerates of South Africa. Geochemistry, Geophysics, Geosystems 10, n/a-n/a.

Valdespino, O.E.M., Alvarez, V.C., 1997. Paleomagnetic and rock magnetic evidence for inverse zoning in the Parguaza batholith (southwestern Venezuela) and its implications about tectonics of the Guyana shield. Precambrian Research 85, 1-25.

Valentine, J.W., 1971. Plate Tetonics and Shallow Marine Diversity and Endemism, An Actualistic Model. Systematic Biology 20, 253-264.

Valentine, J.W., Moores, E.M., 1972. Global tectonics and the fossil record. The Journal of Geology, 167-184.
Van Achterbergh, E., Ryan, C., Jackson, S., Griffin, W., 2001. Data reduction software for LA-ICP-MS. Laser-Ablation-ICPMS in the earth sciences—principles and applications. Miner Assoc Can (short course series) 29, 239-243.
Van der Voo, R., 1990a. Phanerozoic paleomagnetic poles from Europe and North America and comparisons with continental reconstructions. Reviews of Geophysics 28, 167-206.
Van der Voo, R., 1990b. The reliability of paleomagnetic data. Tectonophysics 184, 1-9.
van Hinsbergen, D.J.J., Steinberger, B., Doubrovine, P.V., Gassmöller, R., 2011. Acceleration and deceleration of India-Asia convergence since the Cretaceous: Roles of mantle plumes and continental collision. Journal of Geophysical Research 116, 1-20.
Vasconcelos, P.M., Renne, P.R., Brimhall, G.H., Becker, T.A., 1994. Direct dating of weathering phenomena by 40Ar39Ar and K-Ar analysis of supergene K-Mn oxides. Geochimica et Cosmochimica Acta 58, 1635-1665.
Vasquez, L., Rosa-Costa, L., Silva, C., Ricci, P., Barbosa, J., Klein, E., Lopes, E., Macambira, E., Chaves, C., Carvalho, J., 2008. Geologia e Recursos Minerais do Estado do Pará: Sistema de Informações Geográficas-SIG: texto explicativo dos mapas Geológico e Tectônico e de Recursos Minerais do Estado do Pará. Organizadores, Vasquez ML, Rosa-Costa LT Escala 1, 000.
Veikkolainen, T., Evans, D.A.D., Korhonen, K., Pesonen, L.J., 2014a. On the low-inclination bias of the Precambrian geomagnetic field. Precambrian Research 244, 23-32.
Veikkolainen, T., Pesonen, L., Evans, D.D., 2014b. PALEOMAGIA: A PHP/MYSQL database of the Precambrian paleomagnetic data. Studia Geophysica et Geodaetica. 58, 425-441.
Veikkolainen, T., Pesonen, L., Korhonen, K., 2014c. An analysis of geomagnetic field reversals supports the validity of the Geocentric Axial Dipole (GAD) hypothesis in the Precambrian. Precambrian Research 244, 33-41.
Veizer, J., xe, Jansen, S.L., 1979. Basement and Sedimentary Recycling and Continental Evolution. The Journal of Geology 87, 341-370.
Veizer, J., xe, Jansen, S.L., 1985. Basement and Sedimentary Recycling-2: Time Dimension to Global Tectonics. The Journal of Geology 93, 625-643.
Veldkamp, J., Mulder, F.G., Zijderveld, J.D.A., 1971. Palaeomagnetism of Suriname dolerites. Physics of the Earth and Planetary Interiors 4, 370-380.
Vigneresse, J.L., 2005. The specific case of the Mid-Proterozoic rapakivi granites and associated suite within the context of the Columbia supercontinent. Precambrian Research 137, 1-34.
Vodovozov, V.Y., Didenko, A.N., Gladkochub, D.P., Mazukabzov, A.M., Donskaya, T.V., 2007. Results of paleomagnetic study of Early Proterozoic rocks in the Baikal Range of the Siberian craton. Izv., Phys. Solid Earth 43, 855-867.
Vodovozov, V.Y., 2010. Paleomagnetism of the Early Proterozoic Formations South of the Siberian Craton andGeotectonic Investigation., Lomonosov Moscow State University. Moscow, p. pp. 35 (in Russian).
Ward, C., McArthur, J., Walsh, J., 1992. Rare earth element behaviour during evolution and alteration of the Dartmoor granite, SW England. Journal of Petrology 33, 785-815.
Wegener, A., 1912. Die entstehung der kontinente. Geologische Rundschau 3, 276-292.
Wegener, A., Skerl, J.G.A., 1922. The origin of continents and oceans. Dutton.
Wetherill, G.W., 1956. Discordant uranium-lead ages, I. Eos, Transactions American Geophysical Union 37, 320-326.
Whalen, J., Currie, K., Chappell, B., 1987. A-type granites: geochemical characteristics, discrimination and petrogenesis. Contrib Mineral Petrol 95, 407-419.
Whitney, D.L., Evans, B.W., 2010. Abbreviations for names of rock-forming minerals. American Mineralogist 95, 185-187.

Wilde, S.A., Zhao, G., Sun, M., 2002. Development of the North China Craton During the Late Archaean and its Final Amalgamation at 1.8 Ga: Some Speculations on its Position Within a Global Palaeoproterozoic Supercontinent. Gondwana Research 5, 85-94.

Willemann, R.J., 1984. Reorientation of planets with elastic lithospheres. Icarus 60, 701-709.

Williams, G.E., Schmidt, P.W., 2004. Paleomagnetism of the 1.88-Ga Sokoman Formation in the Schefferville–Knob Lake area, Québec, Canada, and implications for the genesis of iron oxide deposits in the central New Québec Orogen. Precambrian Research 128, 167-188.

Williams, G.E., Schmidt, P.W., Clark, D.A., 2004. Palaeomagnetism of iron-formation from the late Palaeoproterozoic Frere Formation, Earaheedy Basin, Western Australia: palaeogeographic and tectonic implications. Precambrian Research 128, 367-383.

Williams, G.E., 2005. Subglacial meltwater channels and glaciofluvial deposits in the Kimberley Basin, Western Australia: 1.8 Ga low-latitude glaciation coeval with continental assembly. Journal of the Geological Society 162, 111-124.

Williams, H., Hoffman, P.F., Lewry, J.F., Monger, J.W., Rivers, T., 1991. Anatomy of North America: thematic geologic portrayals of the continent. Tectonophysics 187, 117-134.

Wu, L., Kravchinsky, V.A., Potter, D.K., 2015. PMTec: A new MATLAB toolbox for absolute plate motion reconstructions from paleomagnetism. Computers & Geosciences 82, 139-151.

Xu, H., Yang, Z., Peng, P., Meert, J.G., Zhu, R., 2014. Paleo-position of the North China Craton within the supercontinent Columbia: Constraints from new paleomagnetic results. Precambrian Research.

Yakubchuk, A., 2010. Restoring the supercontinent Columbia and tracing its fragments after its breakup: A new configuration and a Super-Horde hypothesis. Journal of Geodynamics 50, 166-175.

Youbi, N., Kouyaté, D., Söderlund, U., Ernst, R.E., Soulaimani, A., Hafid, A., Ikenne, M., El Bahat, A., Bertrand, H., Rkha Chaham, K., Ben Abbou, M., Mortaji, A., El Ghorfi, M., Zouhair, M., El Janati, M.h., 2013. The 1750 Ma Magmatic Event of the West African Craton (Anti-Atlas, Morocco). Precambrian Research 236, 106-123.

Young, G.M., 2013. Precambrian supercontinents, glaciations, atmospheric oxygenation, metazoan evolution and an impact that may have changed the second half of Earth history. Geoscience Frontiers.

Zahirovic, S., Müller, R.D., Seton, M., Flament, N., 2015. Tectonic speed limits from plate kinematic reconstructions. Earth and Planetary Science Letters 418, 40-52.

Zegers, De, W., Dann, White, 1998. Vaalbara, Earth's oldest assembled continent? A combined structural, geochronological, and palaeomagnetic test. Terra Nova 10, 250-259.

Zhang, S., Li, Z.-X., Evans, D.A.D., Wu, H., Li, H., Dong, J., 2012. Pre-Rodinia supercontinent Nuna shaping up: A global synthesis with new paleomagnetic results from North China. Earth and Planetary Science Letters 353–354, 145-155.

Zhao, G., Cawood, P.A., Wilde, S.A., Sun, M., 2002. Review of global 2.1–1.8 Ga orogens: implications for a pre-Rodinia supercontinent. Earth-Science Reviews 59, 125-162.

Zhao, G., Sun, M., Wilde, S.A., Li, S., 2004. A Paleo-Mesoproterozoic supercontinent: assembly, growth and breakup. Earth-Science Reviews 67, 91-123.

Zijderveld, J., 1967. AC demagnetization of rocks: analysis of results. Methods in paleomagnetism 3, 254.

Zorin, Y.A., Mazukabzov, A.M., Gladkochub, D.P., Donskaya, T.V., Presnyakov, S.L., Sergeev, S.A., 2008. Silurian age of major folding in Riphean deposits of the Baikal-patom zone. Dokl. Earth Sc. 423, 1235-1239.

SUPPLEMENTARY MATERIAL

Table SM 1: Major, trace and Rare earth element contents of microgranitic, mafic and gabbroic dikes of Tucumã.

Table SM 2: Representative feldspar analyses and structural formula on the basis of 8 O of microgranitic dikes (PY55D2).

Table SM 3: Representative feldspar analyses and structural formula on the basis of 8 O of microgranitic dikes (PY65G4).

Table SM 4: Representative feldspar analyses and structural formula on the basis of 8 O of microgranitic dikes (PY65G4, continued).

Table SM 5: Representative feldspar analyses and structural formula on the basis of 8 O of microgranitic dikes (PY69B3).

Table SM 6: Representative biotite analyses and structural formula on the basis of 22 O of microgranitic dikes.

Table SM 7: Representative chlorite analyses and structural formula on the basis of 28 O of microgranitic dikes.

Table SM 8: Representative iron oxide analyses and structural formula of microgranitic dikes.

Figure SM1: Values of inclination asymmetries plotted as a function of absolute paleolatitude. Polynomial fit (order 2) is indicated but a small number of data is available. Solid black curve is a best fit using G2 = 0.04 and G3 = 0.05. Dashed grey curve is a best fit using G2 = 0.17 and G3 = 0.03.

Figure SM2: Inclination frequency distributions during the interval 2100-1200 Ma. Observed distribution, GAD field and GAD + (G2 = 0.15, G3 = 0.19) of Tauxe and Kodama (2009) are shown.

Table SM 9: Paleomagnetic database between 2100 – 1200 Ma (code used are below the table).

Table SM 9: Major, trace and Rare earth element contents of microgranitic, mafic and gabbroic dikes of Tucumã.

	Microgranitic dike											Mafic dike							Gabbroic dike	
	PY55	**PY56**	**PY59**	**PY61**	**PY62G**	**PY62N**	**PY63**	**PY65**	**PY67**	**PY74**	**PY79**	**PY57**	**PY60b**	**PY62b**	**PY64**	**PY66**	**PY71**	**PY72**	**PY60x**	**PY63x**
SiO_2 (wt.%)	70.09	73.95	70.80	75.37	66.82	69.95	75.95	76.09	77.69	76.36	76.15	60.07	52.65	54.80	51.07	50.56	49.39	49.70	49.62	49.39
TiO_2	0.37	0.22	0.40	0.12	0.56	0.43	0.12	0.11	0.13	0.16	0.13	0.96	1.11	1.12	1.08	0.92	1.09	0.81	1.81	1.94
Al_2O_3	13.17	12.00	12.50	11.80	12.26	13.07	11.79	11.81	11.27	11.89	11.35	13.43	15.59	14.71	14.96	15.72	13.93	15.30	15.81	14.73
Fe_2O_{3tot}	3.59	3.28	4.08	2.28	5.32	4.20	2.34	2.31	2.13	2.25	1.76	9.86	11.21	10.89	10.85	12.11	12.36	11.43	13.37	14.52
Fe_2O_3	0.54	0.49	0.61	0.34	0.80	0.63	0.35	0.35	0.32	0.34	0.26	1.48	1.68	1.63	1.63	1.82	1.85	1.71	2.01	2.18
FeO	3.05	2.79	3.46	1.94	4.52	3.57	1.99	1.97	1.81	1.91	1.49	8.38	9.53	9.25	9.22	10.29	10.51	9.71	11.36	12.34
MnO	0.05	0.06	0.06	0.02	0.08	0.06	0.02	0.03	0.04	0.05	0.02	0.14	0.16	0.16	0.15	0.17	0.21	0.17	0.18	0.20
MgO	0.41	0.21	0.57	0.06	1.54	0.54	0.06	0.04	0.03	0.06	0.06	3.18	6.79	4.88	6.90	7.09	7.79	6.74	4.47	4.97
CaO	1.48	0.51	1.61	0.35	3.32	1.46	0.38	0.59	0.30	0.32	0.84	4.23	8.78	6.30	7.90	8.49	11.78	9.57	8.60	8.28
Na_2O	3.08	2.65	3.04	3.18	2.60	3.23	3.12	3.14	2.85	3.29	2.78	3.25	2.15	2.18	2.13	2.15	1.87	2.09	2.92	2.90
K_2O	5.11	5.31	4.78	5.08	4.18	4.99	5.26	5.18	4.85	4.95	5.08	3.37	0.78	2.12	1.38	0.93	0.21	1.05	1.16	1.13
P_2O_5	0.09	N.A	0.09	N.A	0.12	0.10	N.A	N.A	N.A	N.A	N.A	0.20	0.30	0.20	0.28	0.16	0.07	0.09	0.25	0.26
LOI	1.33	0.85	1.52	0.65	1.68	1.37	0.59	0.56	0.61	0.61	1.14	2.30	1.68	2.30	2.41	1.78	0.87	2.68	0.63	0.39
Total	**98.76**	**99.04**	**99.43**	**98.91**	**98.49**	**99.40**	**99.63**	**99.86**	**99.89**	**99.93**	**99.31**	**100.99**	**101.21**	**99.66**	**99.11**	**100.07**	**99.57**	**99.62**	**98.81**	**98.70**
Be (ppm)	2.38	2.995	1.841	1.986	1.643	1.785	1.956	4.372	3.74	1.917	1.231	1.909	0.819	1.39	0.816	0.422	L.D.	0.4	0.955	1.034
Sc	6.19	4.16	7.75	3.45	11.21	8.46	3.53	3.34	2.29	3.1	2.71	21.13	27.84	26.14	28.04	32.73	43.76	38.07	27.94	30.18
V	20.6	6.501	23.96	5.994	49.33	20.81	5.57	5.752	5.474	5.649	5.08	188.5	182	166.7	183.4	172.2	293	204.2	191.2	211.4
Cr	263.9	271.4	364.8	349.2	218.4	143.5	300	388.1	307.5	201.4	239.6	190.1	401.4	237.4	378.8	314.1	418.2	298.8	83.62	94.95
Co	5.266	3.218	6.001	1.621	12.16	5.571	1.091	1.539	1.857	1.464	1.214	28.83	43.43	38.28	40.56	47.82	49.77	45.44	43.61	49.3
Ni	62.03	27.04	53.86	39.27	23.07	11.76	29.26	69.5	34.64	5.665	41.99	25.32	118.4	74.12	117.9	107.7	122.1	116.8	58.01	68.18
Cu	15.58	9.403	18.37	10.96	12.18	6.905	11.03	11.41	14.37	L.D.	10.75	22.68	45.97	32.71	45.1	43.15	156.3	84.76	56.77	67.91
Zn	74.01	113.1	92.98	54.74	82.58	111.3	79.14	64.16	138.5	91.89	53.31	130	115.5	142.4	126.4	157.2	104	96.32	150.9	145.1
Ga	21.23	19.55	20.75	24.41	19.94	21.56	23.58	24.82	21.31	20.98	18.8	19.84	19.41	20.23	19.28	18.25	18.94	17.86	22.04	22.66
Rb	215.9	192.8	193.2	288.3	158.8	181.6	262.2	288.8	175	176.2	164.1	121.7	29.6	127.3	42.6	36.26	9.814	38.08	38.89	37.65
Sr	118.8	66.88	156.2	43.85	279.6	110.1	26.23	70.8	29.97	50.32	43.75	223.4	373.1	235.7	354.7	220.6	115.3	315.9	274.7	266.4

Y	32.65	44.78	38.05	137.7	38.49	35.72	94.14	80.24	64.31	37.07	36.08	37.72	22.93	27.49	22.6	22.48	19.66	19.56	27.7	30.64
Zr	286.9	380.2	308.9	247.2	301	283	226	227.9	231.5	267.9	226.5	220.6	159.9	166.4	155.5	94.23	52.5	61.23	154.5	171.9
Nb	9.952	14.17	12	18.14	11.08	10.93	16.98	18.12	10.72	9.028	7.52	11.19	5.389	5.88	5.251	3.166	2.441	1.926	8.549	9.424
Mo	17.22	20.49	22.02	22.09	9.307	7.806	16.17	23.99	16.02	8.385	13.85	8.6	3.889	4.957	2.7	1.97	2.174	1.787	1.862	2.099
Sn	3.214	2.458	3.099	2.723	3.462	2.867	4.42	2.144	3.703	2.322	1.723	2.508	1.068	1.43	1.077	0.763	0.77	0.651	1.439	1.627
Cs	0.633	0.62	1.013	1.022	0.542	0.617	0.61	0.794	1.106	0.778	0.927	0.466	0.907	0.72	0.66	1.132	0.34	1.393	2.405	1.851
Ba	1433	1837	1359	113.6	1691	1436	167.3	104.3	656.4	1348	1178	1017	596.2	909.2	727.5	490.6	38.84	422.3	380.4	417.1
La	72.12	89.22	72.57	179.9	67.37	70.31	139	99.79	92.85	60.86	56.84	66.07	30.82	30.63	29.74	17.75	2.916	12.17	21.44	23.76
Ce	139.7	170.7	142.9	253.3	132.2	136.3	266.7	201.1	167	114.8	104.5	129.4	63.37	65.99	61.6	36.67	7.914	24.98	46.38	51.25
Pr	14.96	18.45	15.69	39.99	14.61	14.95	12.12	22.64	18.45	12.44	11.4	14.24	7.466	7.543	7.272	4.215	1.275	2.848	5.668	6.232
Nd	51.96	63.82	55.57	140	51.67	52.89	109.8	82.13	66	44.3	40.32	50.68	28.88	28.38	28.25	16.59	6.82	11.11	23.38	25.91
Sm	8.803	10.78	9.917	26.45	9.324	9.314	20.61	16.03	11.8	7.822	7.114	8.933	5.4	5.466	5.294	3.553	2.395	2.594	5.401	5.973
Eu	1.578	1.376	1.368	0.788	1.285	1.499	0.526	0.408	0.802	1.057	0.812	1.34	1.49	1.383	1.464	1.095	0.913	0.892	1.776	1.877
Gd	6.806	8.474	7.908	23.19	7.606	7.418	18.46	13.49	10.72	6.611	6.144	7.418	4.611	4.987	4.61	3.57	2.951	2.902	5.223	5.765
Tb	0.99	1.253	1.163	3.564	1.141	1.1	2.642	2.129	1.68	1.026	0.942	1.105	0.685	0.776	0.676	0.59	0.515	0.503	0.817	0.913
Dy	5.903	7.558	6.988	21.58	6.936	6.639	16.1	13.36	10.41	6.432	5.873	6.75	4.195	4.911	4.164	3.915	3.441	3.417	5.107	5.661
Ho	1.21	1.577	1.439	4.463	1.436	1.357	3.32	2.863	2.203	1.377	1.259	1.41	0.875	1.05	0.871	0.868	0.768	0.772	1.075	1.21
Er	3.205	4.206	3.846	11.48	3.839	3.607	8.694	7.704	5.817	3.807	3.45	3.799	2.339	2.794	2.312	2.353	1.998	2.091	2.815	3.15
Tm	0.461	0.593	0.555	1.569	0.552	0.52	1.223	1.119	0.81	0.55	0.504	0.547	0.333	0.406	0.328	0.348	0.288	0.308	0.403	0.455
Yb	3.086	3.848	3.66	9.816	3.699	3.466	7.878	7.306	5.187	3.709	3.384	3.612	2.226	2.711	2.191	2.349	1.905	2.064	2.705	3.011
Lu	0.467	0.587	0.551	1.419	0.562	0.524	1.139	1.073	0.763	0.565	0.514	0.549	0.339	0.409	0.334	0.363	0.29	0.313	0.413	0.462
Hf	7.858	9.879	8.268	8.944	8.138	7.708	8.276	8.523	6.97	7.253	6.302	6.13	3.905	4.324	3.805	2.657	1.628	1.897	3.989	4.52
Ta	1.095	1.251	1.311	2.146	1.197	1.222	2.022	2.236	1.077	0.908	0.816	0.954	0.378	0.515	0.362	0.249	0.218	0.15	0.702	0.768
W	18.63	12.56	15.58	14.38	11.17	7.734	13.43	15.84	13.13	9.714	8.966	9.547	3.921	5.686	2.466	1.742	2.457	1.705	1.44	1.642
Pb	15.124	25.2671	18.0102	8.5601	18.8821	21.9471	16.9958	17.9955	19.37	8.809	5.3358	25.8049	6.9803	11.4848	6.5005	4.7016	2.2858	3.7396	7.3631	8.2494
Th	27.33	27.84	27.88	32.42	23.93	26.54	30.93	31.06	15.55	12.33	12.02	18.22	3.642	7.193	3.424	2.116	0.246	2.278	4.334	4.864
U	5.857	4.9	7.297	11.67	6.119	6.954	9.249	9.961	5.22	4.31	3.681	3.398	0.477	1.62	0.47	0.322	0.07	0.41	0.776	0.865
Fe_2O_3 /FeO	0.18	0.18	0.18	0.18	0.18	0.18	0.18	0.18	0.18	0.18	0.18	0.18	0.18	0.18	0.18	0.18	0.18	0.18	0.18	0.18
FeO_t/ ($MgO+FeO_t$)	0.90	0.94	0.88	0.97	0.78	0.89	0.97	0.98	0.99	0.97	0.97	0.76	0.62	0.69	0.61	0.63	0.61	0.63	0.75	0.75

Table SM 10: Representative feldspar analyses and structural formula on the basis of 8 O of microgranitic dikes (PY55D2).

Sample	**PY55D2D2**			
Analysis	**C11X-1**	**C11X-2**	**C2X-1**	**C2X-2**
SiO_2	62.64	64.06	68.23	66.64
Al_2O_3	17.97	18.01	19.40	19.25
CaO	0.00	0.00	0.54	1.52
Na_2O	0.15	0.18	11.72	11.63
K_2O	15.89	16.02	0.06	0.19
Total	97.32	99.03	100.09	99.37
Si	2.99	3.01	2.98	2.95
Al	1.01	1.00	1.00	1.01
Ca	0.00	0.00	0.03	0.07
Sr	0.00	0.00	0.00	0.00
Na	0.01	0.02	0.99	1.00
K	0.97	0.96	0.00	0.01
Sum cations	4.99	4.98	5.01	5.05
Ab	1	2	97	92
An	0	0	2	7
Or	99	98	0	1

Table SM 11: Representative feldspar analyses and structural formula on the basis of 8 O of microgranitic dikes (PY65G4).

Sample	**PY65G4**													
Analysis	**C5-1**	**C1-2**	**C16-1**	**C5-2**	**C6-1**	**C6-2**	**C6-3**	**C6-4**	**C6-6**	**C7-1**	**C7-2**	**C7-3**	**C7-4**	**C7-5**
SiO_2	64.25	64.64	67.36	68.20	67.40	68.44	68.20	68.61	68.11	66.04	68.80	68.38	68.60	68.06
Al_2O_3	17.96	18.26	20.55	19.51	19.28	19.76	19.76	19.71	19.36	20.49	19.49	19.30	19.47	19.73
CaO	0.00	0.00	0.35	0.25	0.18	0.21	0.19	0.16	0.17	0.34	0.33	0.25	0.38	0.30
Na_2O	0.49	0.17	10.43	11.76	11.50	11.49	11.62	11.55	11.70	11.08	11.59	11.50	11.66	11.65
K_2O	15.34	16.31	1.21	0.21	0.40	0.18	0.30	0.07	0.04	0.64	0.03	0.03	0.04	0.04
Total	98.54	99.59	100.39	100.32	99.31	100.29	100.43	100.21	99.49	98.68	100.25	99.54	100.19	99.84
Si	3.00	3.00	2.95	2.98	2.98	2.98	2.98	2.99	2.99	2.94	3.00	3.00	2.99	2.98
Al	0.99	1.00	1.06	1.00	1.00	1.02	1.02	1.01	1.00	1.07	1.00	1.00	1.00	1.02
Ca	0.00	0.00	0.02	0.01	0.01	0.01	0.01	0.01	0.01	0.02	0.02	0.01	0.02	0.01
Sr	0.00	0.00	0.00	0.00	0.00	0.00	0.00	0.00	0.00	0.00	0.00	0.00	0.00	0.00
Na	0.04	0.02	0.88	1.00	0.99	0.97	0.98	0.98	1.00	0.96	0.98	0.98	0.99	0.99
K	0.91	0.97	0.07	0.01	0.02	0.01	0.02	0.00	0.00	0.04	0.00	0.00	0.00	0.00
Sum cations	4.97	4.99	4.99	5.02	5.02	5.00	5.01	4.99	5.00	5.02	4.99	4.99	5.00	5.01
Ab	5	2	91	98	97	98	98	99	99	95	98	99	98	98
An	0	0	2	1	1	1	1	1	1	2	2	1	2	1
Or	95	98	7	1	2	1	2	0	0	4	0	0	0	0

Table SM 12: Representative feldspar analyses and structural formula on the basis of 8 O of microgranitic dikes (PY65G4, continued).

Sample	**PY65G4**														
Analysis	**C8-1**	**C8-2**	**C8-3**	**C8-4**	**C8-5**	**C9-2**	**C9-3**	**C9-4**	**C9-5**	**C10-3**	**C10-4**	**C10-5**	**C10-6**	**C13-1**	**C13-2**
SiO_2	67.87	69.47	68.35	66.55	68.38	67.50	64.13	63.81	62.62	68.75	64.91	68.24	67.27	68.43	68.01
Al_2O_3	19.18	19.75	19.78	20.63	19.37	19.05	18.12	17.90	19.76	19.65	18.27	20.01	20.45	19.67	19.22
CaO	0.28	0.17	0.29	0.17	0.17	0.26	0.00	0.00	2.50	0.33	0.00	0.53	0.34	0.42	0.38
Na_2O	11.16	11.93	11.77	10.81	11.52	10.34	0.17	0.20	9.05	11.67	0.18	11.60	11.14	11.46	11.65
K_2O	0.63	0.04	0.06	1.10	0.08	1.81	16.09	15.98	0.19	0.09	16.06	0.04	0.61	0.06	0.05
Total	99.22	101.47	100.30	99.61	99.57	99.26	98.80	98.66	97.80	100.54	99.51	100.43	99.88	100.09	99.31
Si	3.00	2.99	2.98	2.94	3.00	2.99	3.00	3.00	2.85	2.99	3.01	2.97	2.95	2.99	2.99
Al	1.00	1.00	1.02	1.07	1.00	1.00	1.00	0.99	1.06	1.01	1.00	1.03	1.06	1.01	1.00
Ca	0.01	0.01	0.01	0.01	0.01	0.01	0.00	0.00	0.12	0.02	0.00	0.02	0.02	0.02	0.02
Sr	0.00	0.00	0.00	0.00	0.00	0.00	0.00	0.00	0.00	0.00	0.00	0.00	0.00	0.00	0.00
Na	0.95	1.00	0.99	0.93	0.98	0.89	0.02	0.02	0.80	0.98	0.02	0.98	0.95	0.97	0.99
K	0.04	0.00	0.00	0.06	0.00	0.10	0.96	0.96	0.01	0.00	0.95	0.00	0.03	0.00	0.00
Sum cations	5.00	5.00	5.01	5.02	4.99	5.00	4.98	4.99	4.96	5.00	4.97	5.01	5.01	4.99	5.01
Ab	95	99	98	93	99	89	2	2	86	98	2	97	95	98	98
An	1	1	1	1	1	1	0	0	13	2	0	2	2	2	2
Or	4	0	0	6	0	10	98	98	1	0	98	0	3	0	0

Table SM 13: Representative feldspar analyses and structural formula on the basis of 8 O of microgranitic dikes (PY69B3).

Sample	**PY69B3**						
Analysis	**C1-7**	**C1-8**	**C1-9**	**C3-8**	**C9-2**	**C10-1**	**C10-2**
SiO_2	64.07	63.56	62.89	64.10	68.00	68.40	66.60
Al_2O_3	17.75	18.08	17.47	17.73	18.91	19.27	20.27
CaO	0.00	0.00	0.91	0.07	0.03	0.04	0.07
Na_2O	0.19	0.18	0.15	10.07	11.53	11.63	10.97
K_2O	16.23	16.15	15.69	0.12	0.11	0.26	1.12
Total	98.53	98.46	97.46	92.27	98.97	99.75	99.54
Si	3.01	3.00	3.00	3.02	3.01	3.00	2.94
Al	0.98	1.01	0.98	0.99	0.99	1.00	1.06
Ca	0.00	0.00	0.05	0.00	0.00	0.00	0.00
Sr	0.00	0.00	0.00	0.00	0.00	0.00	0.00
Na	0.02	0.02	0.01	0.92	0.99	0.99	0.94
K	0.97	0.97	0.95	0.01	0.01	0.01	0.06
Sum cations	4.99	4.99	4.99	4.95	4.99	5.00	5.02
Ab	2	2	1	99	99	98	93
An	0	0	5	0	0	0	0
Or	98	98	94	1	1	1	6

Table SM 14: Representative biotite analyses and structural formula on the basis of 22 O of microgranitic dikes.

Sample	**PY65G4**								**PY69B3**		
Analysis	**C11-2**	**C11-3**	**C5-6**	**C12-1**	**C12-2**	**C12-3**	**C12-4**	**C12-5**	**C3-2**	**C9-5**	**C9-7**
SiO_2	36.384	41.834	40.276	45.629	46.304	46.032	46.136	39.904	46.218	37.116	45.926
TiO_2	0.075	0.01	0.03	0.029	0.036	0.031	0.015	0.026	0.125	0.115	0.099
Al_2O_3	22.484	25.504	24.003	29.991	25.515	27.946	27.216	22.075	26.631	24.857	29.39
FeO	24.103	16.082	18.943	6.338	9.355	8.086	9.686	8.417	5.503	20.66	4.604
MnO	0.788	0.316	0.386	0	0.142	0	0.11	0.138	0.012	0.222	0
MgO	1.595	1.105	1.151	0.303	1.204	0.424	0.867	1.008	0.636	1.133	0.6
CaO	0.071	0.042	0.089	0.018	0.016	0.008	0	0.18	0.083	0.09	0.079
Na_2O	0.051	0.023	0.05	0.08	0.041	0.023	0.03	0.017	0.06	0.084	0.067
K_2O	5.299	8.172	6.252	10.768	9.94	10.53	10.192	9.577	9.712	4.819	10.044
Total	95.59	99.81	97.26	101.23	100.69	101.19	102.42	87.05	97.07	94.09	98.89
Si	5.67	5.96	5.94	6.11	6.31	6.21	6.19	6.38	6.39	5.71	6.21
Al iv	2.33	2.04	2.06	1.89	1.69	1.79	1.81	1.62	1.61	2.29	1.79
Si/Al IV	2.44	2.92	2.89	3.24	3.74	3.47	3.43	3.92	3.97	2.50	3.48
Al vi	1.80	2.25	2.12	2.85	2.41	2.66	2.50	2.53	2.73	2.22	2.90
Ti	0.01	0.00	0.00	0.00	0.00	0.00	0.00	0.00	0.01	0.01	0.01
Fe	3.14	1.92	2.34	0.71	1.07	0.91	1.09	1.12	0.64	2.66	0.52
Mn	0.10	0.04	0.05	0.00	0.02	0.00	0.01	0.02	0.00	0.03	0.00
Mg	0.37	0.23	0.25	0.06	0.24	0.09	0.17	0.24	0.13	0.26	0.12
Li*	0.56	1.41	1.19	1.91	2.05	1.99	1.99	1.22	2.06	0.68	1.97
Ca	0.01	0.01	0.01	0.00	0.00	0.00	0.00	0.03	0.01	0.01	0.01
Na	0.02	0.01	0.01	0.02	0.01	0.01	0.01	0.01	0.02	0.03	0.02
K	1.05	1.49	1.18	1.84	1.73	1.81	1.75	1.95	1.71	0.95	1.73
OH*	3.98	3.87	4.00	4.00	4.00	4.00	4.00	4.00	4.00	4.00	4.00
F	0.02	0.13	0.00	0.00	0.00	0.00	0.00	0.00	0.00	0.00	0.00
Sum cations	21.50	22.27	22.05	22.64	23.27	22.94	22.95	23.06	23.29	21.34	22.77
XFe	0.89	0.89	0.90	0.92	0.81	0.91	0.86	0.82	0.83	0.91	0.81

Table SM 15: Representative chlorite analyses and structural formula on the basis of 28 O of microgranitic dikes.

Sample	**PY65G4**																**PY69B3**							
Analysis	**C1-3**	**C2-1**	**C2-2**	**C3-1**	**C3-2**	**C11-1**	**C5-4**	**C5-5**	**C12-6**	**C15-1**	**C15-2**	**C15-3**	**C15-4**	**C15-5**	**C15-6**	**C15-7**	**C1-1**	**C1-2**	**C1-3**	**C1-4**	**C1-5**	**C1-6**	**C9-4**	**C9-6**
SiO_2	23.01	23.10	23.56	22.75	21.60	23.49	22.59	24.17	25.01	23.42	24.07	24.02	21.13	24.63	23.62	21.44	23.92	23.55	22.16	22.29	21.32	22.95	21.88	22.91
TiO_2	0.00	0.04	0.09	0.01	0.06	0.23	0.11	0.01	0.01	0.12	0.06	0.57	0.23	0.62	0.00	0.00	0.09	0.09	0.08	0.07	0.00	0.05	0.04	0.01
Al_2O_3	17.84	18.20	17.58	17.55	17.90	17.50	16.68	18.22	17.33	17.06	17.10	16.40	14.49	17.02	19.16	16.69	16.52	16.79	18.35	18.24	19.06	19.43	18.58	18.85
FeO	42.76	43.27	44.21	44.61	43.47	42.96	40.92	41.33	37.38	43.96	43.90	43.47	43.46	41.91	42.40	43.12	42.90	42.52	41.74	43.09	41.96	42.57	41.89	42.05
MnO	0.84	0.91	0.83	0.86	0.75	0.75	0.78	0.77	0.94	0.76	0.76	0.68	0.73	0.73	0.70	0.74	0.51	0.52	0.68	0.85	0.79	0.27	0.36	0.59
MgO	1.48	1.31	1.07	0.88	1.11	1.06	1.03	1.11	2.18	0.92	0.87	0.98	0.83	1.07	0.84	0.79	1.72	1.68	1.44	1.30	1.58	1.16	1.47	1.35
CaO	0.09	0.06	0.04	0.07	0.09	0.06	0.19	0.09	0.22	0.03	0.09	0.04	0.04	0.16	0.13	0.11	0.03	0.02	0.04	0.00	0.04	0.02	0.08	0.18
Na_2O	0.03	0.03	0.06	0.06	0.06	0.07	0.14	0.10	0.03	0.03	0.05	0.05	0.06	0.19	0.05	0.12	0.05	0.05	0.03	0.00	0.09	0.07	0.21	0.02
K_2O	0.06	0.04	0.03	0.01	0.03	0.24	0.15	0.17	0.51	0.05	0.03	0.21	0.07	0.42	0.17	0.18	0.09	0.09	0.18	0.10	0.10	0.09	0.05	0.06
F	0.00	0.00	0.14	0.03	0.00	0.06	0.00	0.00	0.00	0.00	0.00	0.00	0.00	0.00	0.00	0.05	0.00	0.00	0.08	0.00	0.00	0.00	0.00	0.00
O=F	0.00	0.00	0.06	0.01	0.00	0.02	0.00	0.00	0.00	0.00	0.00	0.00	0.00	0.00	0.00	0.02	0.00	0.00	0.04	0.00	0.00	0.00	0.00	0.00
H_2O	9.98	10.07	10.00	9.93	9.75	9.96	9.57	10.09	9.99	9.94	10.05	9.98	9.13	10.13	10.17	9.44	9.95	9.90	9.78	9.91	9.82	10.11	9.81	10.03
Total	96.16	97.06	97.60	96.80	94.85	96.36	92.18	96.11	93.65	96.31	97.01	96.40	90.16	96.96	97.26	92.66	95.79	95.19	94.60	95.86	94.76	96.72	94.39	96.08
Si	5.53	5.51	5.61	5.49	5.32	5.64	5.66	5.75	6.01	5.65	5.75	5.77	5.55	5.83	5.57	5.43	5.77	5.71	5.41	5.39	5.21	5.45	5.35	5.48
Ti	0.00	0.01	0.02	0.00	0.01	0.04	0.02	0.00	0.00	0.02	0.01	0.10	0.05	0.11	0.00	0.00	0.02	0.02	0.02	0.01	0.00	0.01	0.01	0.00
Al	5.05	5.11	4.94	4.99	5.19	4.95	4.93	5.11	4.91	4.85	4.81	4.64	4.49	4.75	5.32	4.98	4.69	4.80	5.28	5.20	5.49	5.43	5.35	5.31
Fe	8.60	8.62	8.81	9.00	8.95	8.63	8.58	8.22	7.51	8.87	8.77	8.74	9.55	8.30	8.36	9.14	8.65	8.62	8.53	8.72	8.57	8.45	8.56	8.41
Mn	0.17	0.18	0.17	0.18	0.16	0.15	0.17	0.15	0.19	0.16	0.16	0.14	0.16	0.15	0.14	0.16	0.10	0.11	0.14	0.18	0.16	0.06	0.08	0.12
Mg	0.53	0.47	0.38	0.32	0.41	0.38	0.38	0.40	0.78	0.33	0.31	0.35	0.32	0.38	0.30	0.30	0.62	0.61	0.53	0.47	0.57	0.41	0.54	0.48
Ca	0.02	0.01	0.01	0.02	0.03	0.02	0.05	0.02	0.06	0.01	0.02	0.01	0.01	0.04	0.03	0.03	0.01	0.00	0.01	0.00	0.01	0.01	0.02	0.05
Na	0.01	0.02	0.03	0.03	0.03	0.03	0.07	0.05	0.02	0.01	0.02	0.02	0.03	0.09	0.02	0.06	0.03	0.02	0.01	0.00	0.04	0.03	0.10	0.01
K	0.02	0.01	0.01	0.00	0.01	0.07	0.05	0.05	0.16	0.01	0.01	0.07	0.02	0.13	0.05	0.06	0.03	0.03	0.06	0.03	0.03	0.03	0.02	0.02
F	0.00	0.00	0.10	0.02	0.00	0.04	0.00	0.00	0.00	0.00	0.00	0.00	0.00	0.00	0.00	0.04	0.00	0.00	0.06	0.00	0.00	0.00	0.00	0.00
OH	16.00	16.00	15.90	15.98	16.00	15.96	16.00	16.00	16.00	16.00	16.00	16.00	16.00	16.00	16.00	15.96	16.00	16.00	15.94	16.00	16.00	16.00	16.00	16.00
Sum	35.96	35.95	35.97	36.04	36.10	35.92	35.91	35.75	35.62	35.92	35.85	35.85	36.19	35.79	35.80	36.16	35.90	35.90	36.00	36.01	36.09	35.86	36.02	35.88

Table SM 16: Representative iron oxide analyses and structural formula of microgranitic dikes.

Sample	**PY69B3**			**PY65G4**					
Analysis	**C8-1**	**C8-2**	**C8-3**	**C5-3**	**C5-5**	**C9-1**	**C10-1**	**C10-2**	**C12-7**
TiO_2	21.17	20.37	19.44	0.09	2.52	0.05	0.32	0.14	0.30
MnO	1.41	0.89	1.09	0.03	0.07	0.01	0.05	0.00	0.28
FeO	68.63	70.16	71.36	86.49	83.91	86.78	86.86	86.09	76.59
Total	91.53	91.92	92.14	87.33	87.31	87.91	88.04	86.81	86.88
TiO_2	21.17	20.37	19.44	0.09	2.52	0.05	0.32	0.14	0.30
MnO	1.41	0.89	1.09	0.03	0.07	0.01	0.05	0.00	0.28
FeO	47.32	47.14	46.14	-0.06	2.07	-0.06	0.24	-0.07	-0.32
Fe_2O_3	23.68	25.58	28.02	96.18	90.95	96.51	96.27	95.74	85.48
Total	93.60	94.22	94.76	96.64	95.69	97.06	97.27	96.11	89.55
Mol%									
FeO	0.68	0.67	0.66	0.00	0.03	0.00	0.00	0.00	0.00
Fe_2O_3	0.15	0.16	0.18	0.61	0.57	0.61	0.61	0.60	0.57
TiO_2	0.26	0.25	0.24	0.00	0.03	0.00	0.00	0.00	0.00
Sum	1.09	1.09	1.08	0.61	0.63	0.61	0.61	0.60	0.58
Norm 100%									
FeO	62.13	61.62	61.08	-0.06	4.71	-0.12	0.65	-0.15	-0.11
Fe_2O_3	13.60	14.90	16.31	99.88	90.29	100.01	98.71	99.86	99.47
TiO_2	24.27	23.48	22.60	0.18	5.00	0.11	0.65	0.29	0.64
Total	100	100	100	100	100	100	100	100	100

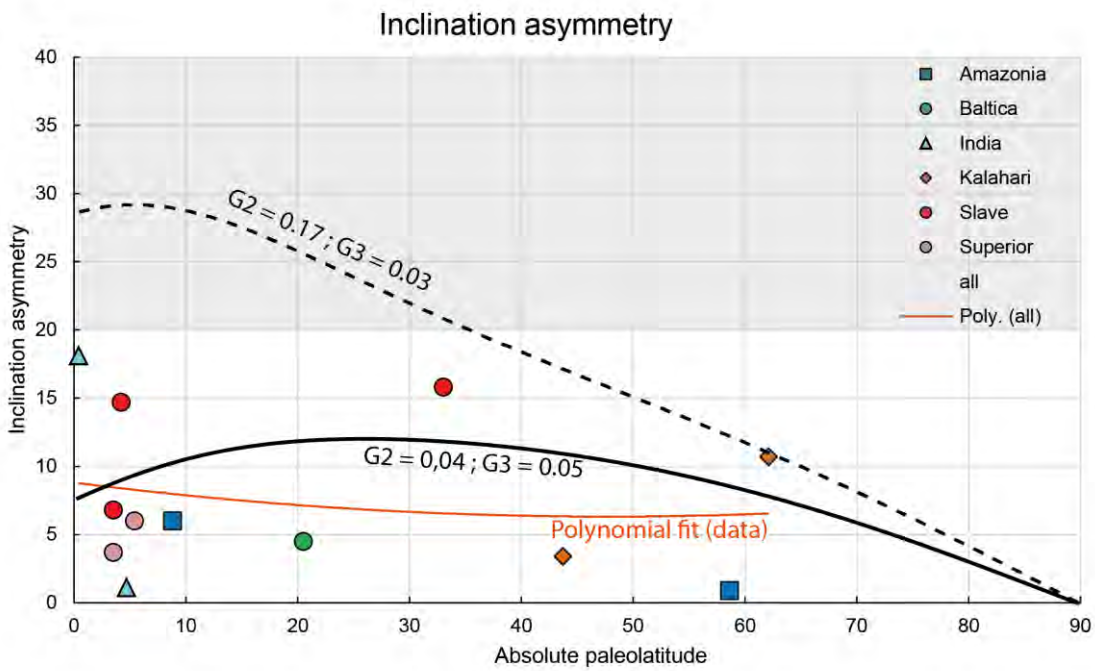

Figure SM1: Values of inclination asymmetries plotted as a function of absolute paleolatitude. Polynomial fit (order 2) is indicated but a small number of data is available. Solid black curve is a best fit using G2 = 0.04 and G3 = 0.05. Dashed grey curve is a best fit using G2 = 0.17 and G3 = 0.03.

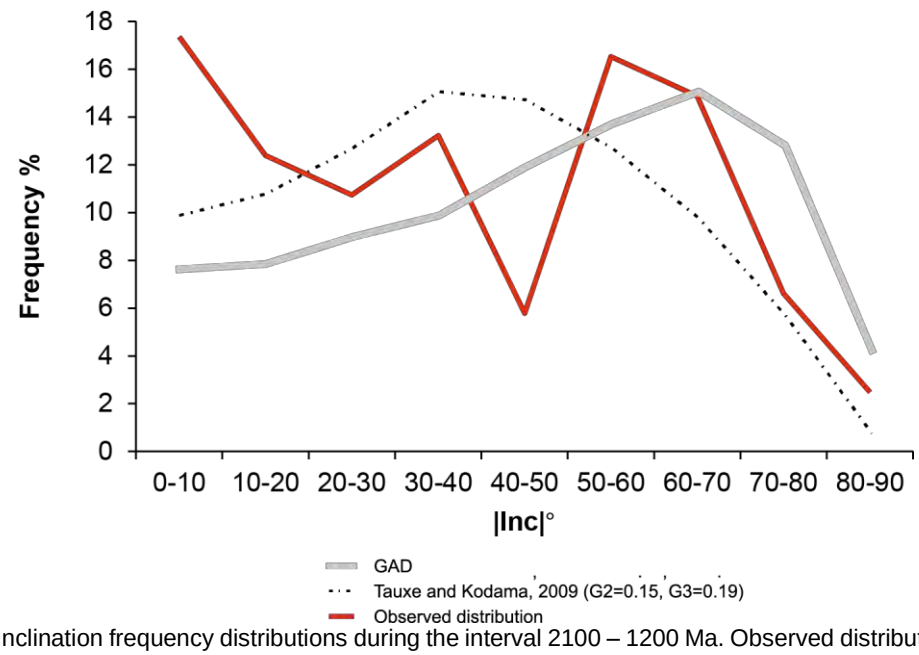

Figure SM2: Inclination frequency distributions during the interval 2100 – 1200 Ma. Observed distribution, GAD field and GAD + (G2 = 0.15, G3 = 0.19) of Tauxe and Kodama (2009) are shown.

Table SM 9: Paleomagnetic database between 2100 – 1200 Ma (code used are below the table).

Name	A_{95}	Plat (°N)	Plong (°E)	Age (Ma)	D ref	I ref	Pol	Q	Methods	Confidence	Paleo-age-references
AMAZONIA											
Mean GF1 (Approuague granite Mataroni)	11.2	1.8	292.5	2089	303.4	86.5	M	3	U-z	i-BCT	D'Agrella-Filho et al. (2011); (Théveniaut et al., 2006)
OYA Oyapok tonalite and meta-ultrabasite	9.9	-28	346	2036	124.5	57.1	R	5	U-z		Nomade et al. (2001)
ARMO, Armontabo River tonalite	10.1	-2.7	346.3	2030	91.7	61.1	M	4		i-BCT	Théveniaut et al. (2006)
Mean CA1 (Imataca-Encrucijada)	16.5	-42.9	21.9	2000	132.9	12.2	M	3			Bispo-Santos et al. (2014a)
ARO Guaniamo dikes AC (Comp II)	6	-42	0	1980	132	12.3	M	4	U-b		Onstott et al. (1984), Ibanez-meija (pers. Com)
Mean GF2 Coastal late monzogranite	5.8	-58.5	30.2	1970	148.5	1.7	M	3			D'Agrella-Filho et al. (2011)
Surumu volcanics	10.1	-27.4	54.8	1960	120.8	-39.2	N	5	U-z	i-BCT	Bispo-Santos et al. (2014a)
POLE SF1 – Uatumã –C	16	-24.7	319.7	1880	139.5	73.6	C	6	U-z	i-BCT	**This study**
POLE SF1 – Uatumã –N	16.6	-23.4	322.2	1880	134.7	73	N	6	U-z	i-BCT	**This study**
POLE SF1 – Uatumã –R	15.2	-25.4	317.9	1880	142.8	73.9	R	6	U-z	i-BCT	**This study**
POLE SF2 – Uatumã –C	9.7	-31.1	220.1	1855	121.3	21.4	C	6	U-z	BCT	**This study**
POLE SF2 – Uatumã –N	31.1	-27.9	217.2	1855	242.1	17.1	N	6	U-z	BCT	**This study**
POLE SF2 – Uatumã -R	15.1	-32.3	221.3	1855	237.4	23.1	R	6	U-z	BCT	**This study**
Avanavero sills mafic rocks	13	-48.4	27.9	1789	138.4	3.8	N	5	U-b, A-bi	BCT	Bispo-Santos et al. (2014b)
Mucajai complex (Rapakivi)	19.3	-44	179.2	1530	137.3	39.1	M	2	U-z, many ages		T. Veikkolainen et al. (2011)
Salto do Céu (*"Aguapei"*) -C	7.9	-56	278.5	1439	139.2	53.2	C	5	U-b	BCT	D'Agrella-Filho et al. (2016)
Salto do Céu (*"Aguapei"*) –N	7.4	-65.5	269.5	1439	192.6	40.8	N	5	U-b	BCT	D'Agrella-Filho et al. (2016)
Salto do Céu (*"Aguapei"*) -R	10.6	-52.2	280.7	1439	193.6	57.2	R	5	U-b	BCT	D'Agrella-Filho et al. (2016)
Rio Branco sills and baked sediments	6.5	-45.5	270	1430	205.8	59.2	N	4	U-z		D'Agrella-Filho et al. (2016)
Nova Guarita dykes -C	6.5	-47.9	245.9	1419	216.2	44	C	6	A-bi	BCT	Bispo-Santos et al. (2012)
Nova Guarita dykes -N	6	-58.1	243.6	1419	207.3	35.5	N	6	A-bi	BCT	Bispo-Santos et al. (2012)
Nova Guarita dykes -R	7.1	-47.1	244.5	1419	223.5	46.6	R	6	A-bi	BCT	Bispo-Santos et al. (2012)
Indiavai dykes	8	-57	249.7	1415	206.4	40.3	N	4	U-z		D'Agrella-Filho et al. (2012)
BALTICA (Karelia)											

Matozero sill MAT	12.3	-21	309	2150	248.8	-23.9	N	2	U-z		Fedotova et al. (1999)
Pudozhgora intrusion PGI	10	-64	329	1984	210.1	-61.6	N	3	U-z	APWP	Lubnina et al. (2016); Pasenko and Lubnina (2014)
Konchozero KON	10.4	-14	282	1974	275.7	-34.5	N	3	Sm-Nd (1930 Ma on APWP)	BCT	Pisarevsky and Sokolov (1999)
Unoi sill UNS	10	-54	292	1970	239.4	-65.1	N	3	U-b	APWP	Lubnina et al. (2016); Pasenko and Lubnina (2014)
Ludicovian dolerite dykes of Onega structure DDI	10	-59	297	1970	231.2	-66.3	N	3	U-b Unoi	BCT	Lubnina et al. (2016); Pasenko and Lubnina (2014)
Gabnev sill GBS	10	-40	268	1960	271.1	-65.4	N	3	? Younger APWP		Lubnina et al. (2016); Pasenko and Lubnina (2014)
Tsuomasvarri gabbro_norite intrusions TSU (D)	10	-20	285	1931	269.8	-40	N	3	U-z	APWP	Mertanen and Pesonen (1994)
Vittangi gabbro	4.9	42.6	227.9	1886 ± 14	343.5	29.5	N	2	U-z		Elming (1985); Skiöld (1988)
Kiuruvesi intrusions (mean)	10	43.1	235.2	1886 ± 5	338.1	32.1	N	3	U-z		Marttila (1981); Neuvonen et al. (1981)
Pohjanmaa-Ylivieska gabbro	10.9	38.6	239.8	1879 ± 5	333.5	26.4	N	3	U-z		Helovuori (1979); Pesonen and Stigzelius (1972)
Jalokoski gabbro	7.6	43.1	233.9	1871 ± 4	339.1	31.7	N	2	U-z		Mertanen and Pesonen (1992); Mertanen (unpublished, 2013)
Mean Baltica SVF1	5	41	233	~1881	339.3	28.2					Pesonen et al. (2003)
Svecofennian volcanics and intrusions	4.1	46	227	~1880	344.8	34.6	N	4			Elming (1994)
Keuruu diabase dyke swarm –C	5.5	45.4	230.9	1870 ± 9	341.8	34.5	C	6	U-z	BCT	Klein (2016); Klein et al. (2016)
Keuruu diabase dyke swarm –N	4	47.9	224.2	1870 ± 9	347.5	36.8	N	6	U-z	BCT	Klein (2016); Klein et al. (2016)
Keuruu diabase dyke swarm –R	7.2	32.8	285.7	1870 ± 9	295.7	41.3	R	6	U-z	BCT	Klein (2016); Klein et al. (2016)
Loftahammar gabbro	4.6	23	179	1859 ± 9	24.8	-5.1	N	3	U-z		Bergström et al. (2002); Poorter (1976)
Haukivesi lamprophyres	2.9	48	225	1839	347	37.1	N	4			Neuvonen et al. (1981)
Mean Fennoscandia 1	19.3	41.9	208.8	1790	357.9	25.9	M	5	U-bz		Bogdanova et al. (2013)
Mean Fennoscandia 2	13.3	34.8	209.6	1750	357.1	12.9	M	5	U-b		Bogdanova et al. (2013)
HG, Hoting gabbro –C	11	43	233	1786	339.8	31.3	C	5	U-z	BCT (p), i-BCT	Elming et al. (2009a)
HG, Hoting gabbro –N	10.9	43	233	1786	340.1	31.2	N	5	U-z	BCT (p), i-BCT	Elming et al. (2009b)

HG, Hoting gabbro –R	8.6	51.3	254.9	1786	327.6	48.3	R	5	U-z	BCT (p), i-BCT	Elming et al. (2009b)
Si, Smaland intrusive -C	6.7	46	183	1780	16.8	35	C	5	U-z	BCT, i-BCT	Pisarevsky and Bylund (2010)
Si, Smaland intrusive –N	6.5	45.5	179.5	1780	19.8	35.2	N	5	U-z	BCT, i-BCT	Pisarevsky and Bylund (2010)
Si, Smaland intrusive -R	7.6	41	212.9	1780	355.1	24.5	R	5	U-z	BCT, i-BCT	Pisarevsky and Bylund (2010)
Wiborg dykes rapakivi	9.4	30.2	175.4	1630	26.3	10.3	N	3	U-z	APWP	Neuvonen (1986)
AD, Aland dykes mean	2.8	23.7	191.4	1570	13.5	-7.5	C	6	U-z	BCT	Salminen et al. (2015)
AD-N, Aland dykes N polarity	6.5	34.6	185.5	1570	17	15.2	N	6	U-z	BCT	Salminen et al. (2015)
AD-R, Aland dykes R polarity	5	16.2	194.8	1570	11.1	-22.3	R	6	U-z	BCT	Salminen et al. (2015)
SKI, Satakunta dyke swarm –C	5.3	29	188	1565	15.8	3.7	C	6	U-bz	BCT	Salminen et al. (2014)
SKI, Satakunta dyke swarm –N	5.9	32.1	187	1565	16.6	10.2	N	5	U-bz	BCT	Salminen et al. (2014)
SKI, Satakunta dyke swarm –R	9.1	25.2	204	1565	2.4	-6.1	R	5	U-bz	BCT	Salminen et al. (2014)
LA, Lake Ladoga mafic rocks	6	15	177	1452	28.5	-19.3	R	4	U-b	BCT	Lubnina et al. (2010b)
PJ, Mean post-Jotnian intrusions	4	4	158	1265	52.4	-36.2	N	4		BCT	Elming and Mattsson (2001); Pesonen et al. (2003)
INDIA											
Dharwar dykes 2.37 Ga E-W -C	4	-15	242	2370	74.1	-80.6	C	6	U-b	BCT	Belica et al. (2014)
Dharwar dykes 2.37 Ga E-W –N	16.1	-14	226.7	2370	83.3	-72.2	N	6	U-b	BCT	Belica et al. (2014)
Dharwar dykes 2.37 Ga E-W –R	25.7	-13.7	243.6	2370	68.2	-81.1	R	6	U-b	BCT	Belica et al. (2014)
Dharwar dykes 2.21 Ga -C	11	-31	301	2210	246	-68.8	C	3	U-b	APWP	Belica et al. (2014)
Dharwar dykes 2.21 Ga –N	26.7	-23.6	307.4	2210	257.3	-64.6	N	3	U-b	APWP	Belica et al. (2014)
Dharwar dykes 2.21 Ga –R		-39.4	275.9	2210	212.5	-78.1	R	3	U-b	APWP	Belica et al. (2014)
Dharwar dyke 2.18 Ga NW	18	-68	265	2180	182.4	-61.6	N	3	U-bz	BCT	Belica et al. (2014)
Cuddapah dyke swarm (Dharwar)	4	-38	0	2082	231.3	-10.8	N	4	U-b	BCT	Kumar et al. (2015)

Bundelkhand NW- SE dykes –C	6.9	58.5	312.5	1979	335.6	0.7	C		U-z	BCT	Pradhan et al. (2012)
Bundelkhand NW- SE dykes -N	7.6	54	307.4	1979	334.4	-9.6	N	4	U-z	BCT	Pradhan et al. (2012)
Bundelkhand NW- SE dykes –R		60.3	312.9	1979	336.8	3.4	R	3	U-z	BCT	Pradhan et al. (2012)
Cuddapah Basin sediments	14.4	29.3	332.9	1880	303.4	-7.7	M	3			Prasad et al. (1987)
Bastar dolerite dykes -C (Group. 3)	15.7	29.3	331.7	1891	303.9	-9.6	C	5			French et al. (2008); Meert et al. (2011)
Bastar dolerite dykes –N	16.7	35.3	328.0	1891	310.7	-9.3	N	4			French et al. (2008); Meert et al. (2011)
Bastar dolerite dykes -R	41.5	20.7	337.1	1891	294	-8.2	R	4			French et al. (2008); Meert et al. (2011)
Dharwar 1.88 Ga dykes -C	7.7	35.9	331.1	1883	310	-4.4	C	4	U-b	BCT	Belica et al. (2014)
Dharwar 1.88 Ga dykes –N	6	36.8	333.0	1883	310.1	-0.9	N	4	U-b	BCT	Belica et al. (2014)
Dharwar 1.88 Ga dykes -R	26.6	31.7	323.5	1883	309.5	-19	R	4	U-b	BCT	Belica et al. (2014)
Mean around Cuddapah basin 1.88 Ga	6.4	50.5	331.4	1880	322.8	9.5	M	4			Radhakrishna et al. (2013a); Radhakrishna et al. (2013b)
Overall mean India 1.97-1.88 Ga direction	4.8	49.2	332.9	1979-1885	321.2	10.1	M	4	U-b		Radhakrishna et al. (2013a); Radhakrishna et al. (2013b)
Mean around Cuddapah basin (~1860 Ma)	2.5	69.6	286.7	1847	351	4.9	M	4	U-b		Radhakrishna et al. (2013a); Radhakrishna et al. (2013b)
Granulite region (South - Dhammapuri)	10.3	82.5	259.1	1855	0.1	25.5	M	5	A-phl		Radhakrishna et al. (2013a); Radhakrishna et al. (2013b)
Overall mean NNW-N shallow direction in India	2.9	73.7	282.6	1855-1847	353.8	11.4	M	4			Radhakrishna et al. (2013a); Radhakrishna et al. (2013b)
Lakhna Dykes -C India (Bastar craton)	14	41.3	132.8	1465	52.8	60.5	C	5	U-z	R	Pisarevsky et al. (2013)
Lakhna Dykes –N	15.4	44.6	50.1	1465	320.7	71.2	N	5	U-z	R	Pisarevsky et al. (2013)
Lakhna Dykes -R		12.7	98.7	1465	112	80	R	5	U-z	R	Pisarevsky et al. (2013)
Harohalli alkaline dyke (Dharwar craton)	15	24.9	78	1200	333.4	87.8	M	5	U-z		Pradhan et al. (2008)
KALAHARI											
BGM Basal Gamagara/Mapedi Fm.	8	2.2	81.9	2200/2000	72	50.6	M	6	Corr.	C, FT	Evans et al. (2002)

WUBS1 Waterberg unconf, Swaershoek Fm.	10.9	36.5	51.3	2054	21.2	44.6	M	5	Corr.	C, FT	de Kock et al. (2006); Dorland et al. (2006)
VRED Vredefort impactites	12	25.1	43.5	2023	18.8	58.6	R	4	U-z (shock zrn)	APWP, impact-rocks	Salminen et al. (2009)
WITS Witwatersrand shales "overprint" (*not used*)	8	19.1	45.6	1960	24.2	62.8	M	3	K-Ar	FT	Layer et al. (1988)
WUBS2 Waterberg unconf	9.8	-10.5	330.4	1930	272.9	53.7	M	6	Corr.	i-BCT, C	de Kock et al. (2006); Hanson et al. (2004)
HAR LIP Hartley mean	11.7	22.7	328.6	1920	304.5	30.9	N	4	U-b	"overprint in Gamarra)	Semami et al. (2016)
MASH Mashonaland sills (ZIMBABWE)	5	6.5	338.5	1886	295.7	53.1		4	U-b	BCT	Hanson et al. (2011); Söderlund et al. (2010)
PWD-Post Waterberg dolerites	8.9	15.6	17.1	1875	344.3	67.2	M	4	U-b	BCT	Hanson et al. (2004)
Sand River dykes	10.1	2.5	9.2	1876	322.8	73.1	M	4			Morgan (1985)
BHD Black Hills -C dyke swarm	5	9.4	352	1856	309.1	61.3	C	5	U-b	BCT	Lubnina et al. (2010a); Olsson et al. (2015)
BHD Black Hills –N	20.9	11.7	356.3	1856	315.5	62.4	N	4	U-b	BCT	Lubnina et al. (2010a); Olsson et al. (2015)
BHD Black Hills -R	22.3	9	359.9	1856	316.8	65.8	R	4	U-b	BCT	Lubnina et al. (2010a); Olsson et al. (2015)
Post-Bushveld mafic dykes -C	19.3	8.7	22	1854/1649	349.8	72.5	C	4	U-b/A-pl	BCT, R	Letts et al. (2005); Olsson et al. (2015)
Post-Bushveld mafic dykes –N	29.2	0.9	13	1854/1649	327.6	75.2	N	3	U-b/A-pl	BCT, R	Letts et al. (2005); Olsson et al. (2015)
Post-Bushveld mafic dykes -R	17	20.2	33	1854/1649	7.2	64.5	R	3	U-b/A-pl	BCT, R	Letts et al. (2005); Olsson et al. (2015)
Bathlaros kimberlite	8.9	30	8.2	1647	339.9	53.1	R	2	U-p		Donnelly et al. (2012); Hargraves (1989)
Van Dyk Mine dyke	7	12.4	13.9	~1600	338.1	68.7	R	2			Jones and McElhinny (1966)
P Premier Kimberlite	6	51.3	37.9	~1200	6.7	28.2	R	3			Hargraves and Onstott (1980)
LAURENTIA											
Slave											
Mal, Malley dykes	7	-51	310	2231	137.5	-56.8	N	5	U-b	> 2.19 Ga	Buchan et al. (2012)
Dog, Dogrib dykes	7	-31	315	2193	125.3	-36.2	R	5	U-b	BCT	Mitchell et al. (2014)
Ind, Indin dykes –C	7	36	284	2110	134.5	69	C	5	U-b	BCT (p)	Buchan et al. (2016)

Ind, Indin dykes –N	10.7	35.6	283.9	2110	134.8	68.8	N	5	U-b	BCT (p)	Buchan et al. (2016)
Ind, Indin dykes –R	6.5	37	285.3	2110	132.3	69.4	R	5	U-b	BCT (p)	Buchan et al. (2016)
LdG, Lac de Gras dykes	7	12	268	2020	160.9	51.4	R	5	U-b	BCT	Buchan et al. (2009)
Ghost dykes -C	6	2	254	1887	177.3	40.4	C	6	U-b	BCT	Buchan et al. (2016)
Ghost dykes -N	12.8	12	247.3	1887	184.9	52.4	N	6		BCT	Buchan et al. (2016)
Ghost dykes -R	5.5	-0.6	255.6	1887	175.7	36.6	R	6	U-b	BCT	Buchan et al. (2016)
Mean Seton/Akaitcho/Mara	4	-6	260	1885	171.3	27.9	M	6	Corr.		Mitchell et al. (2010)
Mean Kahochella/Peacock Hills	7	-12	285	1882	147.2	11.2	M	6	Corr.	Corr. (BCT)	Mitchell et al. (2010)
Douglas Peninsular	16	-17	245	1885-1870	186.3	7.8	M	4			Mitchell et al. (2010)
Takiyuak Fm.	8	-13	249	1885-1871	182.5	15.7	M	5			Mitchell et al. (2010)
Stark Fm –C	6.7	-11	199	1882-1870	231.2	4.2	C	5		C	Evans and Hoye (1981); Evans and Bingham (1976)
Stark Fm –N	7.6	-14.1	217.6	~1876	212.	7	N	5		C	Evans and Hoye (1981); Evans and Bingham (1976)
Stark Fm –R	6.6	-16.4	211.9	~1876	217.7	0.2	R	5		C	Evans and Hoye (1981); Evans and Bingham (1976)
Tochatwi Formation	15	-14	204	~1876	225.7	1.1	M	5			Evans and Bingham (1976)
Mean Pearson/Peninsular sills (PS)	6	-22	269	1870	163.8	-3.7	M	4	U-z		Mitchell et al. (2010)
Et-Then Fm –C	8	4	310	1840	118.5	27.6	C	6		i-BCT	Irving et al. (1972b)
Et-Then Fm –N	6.4	4.5	341.6	1840	88.3	8.3	N	6		i-BCT	Irving et al. (1972b)
Et-Then Fm –R	9.7	2.8	314.7	1840	114.4	23	R	6		i-BCT	Irving et al. (1972b)
Martin Fm.	9	-9	287	1818	144.6	16.1	M		U-b	FT	Evans and Bingham (1973); Morelli et al. (2009)
Superior											
Nip, Nipissing N1 sills	10	-17	272	2217	184.2	33	M	5	U-b	BCT	Buchan et al. (2000)
Sen, Senneterre dykes	6	-16	281	2216	175.1	34.4	M	6	U-b	S	Mitchell et al. (2014)

Bis, Biscotasing dykes W of KSZ	10	17	233	2170	238.4	59	N	4	U-b	D, X	Halls & Davis (2004)
BisE, Biscotasing dykes E of KZS	11	28	223	2167	257	62.2	N	5	U-bz	BCT (p)	Buchan *et al.* (1993), Buchan & Schwarz (1981)
MaN, Marathon N dykes (W of Ksz)	8	45	198	2125	292.5	60.5	N	5	U-b	D	Evans and Halls (2010)
MaR, Marathon R dykes (W of KSZ)	8	55	182	2105	311.4	59.5	R	4	U-b	BCT	Evans and Halls (2010)
Cau, Cauchon dykes (West of KSZ)	9	53	180	2091	310.5	57.5	R	5	U-bz	BCT	Halls and Heaman (2000)
FF, Fort Frances dykes (W of KSZ)	6	43	184	2076	299.5	52.3	R	4	U-bz	S	Halls (1986)
LEs, Lac Esprit dykes (E of KSZ)	7	62	169	2069	324.1	59.2	N	3	U-b	S, D	Buchan et al. (2007)
Min, Minto dykes	10	38	174	1998	302.4	41.8	M	5	U-b	BCT	Buchan *et al.* (1998)
Molson dykes B + C2	4	29	218	1884	262.4	60.5	M	5	U-b	BCT	Evans and Halls (2010)
Flaherty volcanics	7	0	244	1870	217.5	48.1	M	6	U-b	FT	Hamilton et al. (2009); Schmidt (1980)
Haig intrusives	6.1	1	247	1870	214.7	50.3	M	6	U-b	BCT, FT	Hamilton et al. (2009); Schmidt (1980)
Sokoman Fm. A –C	13.2	-28.6	247	1840-1829	205.4	5.5	C	4	U-z (Corr.)	FT	Williams and Schmidt (2004)
Sokoman Fm. A –N	19.6	-29.4	283.7	1840-1829	173.4	10.7	N	4	U-z (Corr.)	FT	Williams and Schmidt (2004)
Sokoman Fm. A –R	27	-22.8	304.6	1840-1829	153.6	16.7	R	4	U-z (Corr.)	FT	Williams and Schmidt (2004)
Sokoman Fm. B -C	6.4	-29.6	250.9	1840-1830	201.8	5.4	C	5	U-z (Corr.)	FT	Williams and Schmidt (2004)
Sokoman Fm. B –N	9.1	-31.1	286.4	1840-1830	171.2	7	N	5	U-z (Corr.)	FT	Williams and Schmidt (2004)
Sokoman Fm. B -R	10.7	-28.7	290.8	1840-1830	167.1	10.7	R	5	U-z (Corr.)	FT	Williams and Schmidt (2004)
APWP Laurentia (Slave+Superior)											
Cleav, Cleaver dikes (Wopmay)	6	19	277	1740	177.1	66.5	N	5	U-b	2*BCT	Irving et al. (2004)
MB, Melville Bugt dykes swarm	9	5	274	1630	181.2	54.5	M	4	U-b	i-BCT	Halls et al. (2011)
WCD, Western Channel diabase c	7	9	245	1592	216.7	53.7	R	4	U-b	S, D	Hamilton and Buchan (2010); Irving et al. (1972a)
StFr, St François Mtns	6	-13	219	1476	234.1	8.9	N	5	U-z	C, i-BCT, FT	Meert and Stuckey (2002)

MK, Michikamau intrusion c	5	-2	218	1460	239.7	26.5	M	5	U-z	BCT	Emslie et al. (1976)
Zig, Zig-zag Dal and intrusions	3	11	229	1382	235	49.6	M	3	U-b		Evans and Mitchell (2011)
Mac, Mackenzie mean	5	4	190	1267	267.7	11.8	N	5	U-b	BCT	Buchan and Halls (1990)

Code used: A_{95} is the semiangle of the cone of 95 % confidence about the pole, **Plat** and **Plong** are latitude and longitude of the paleomagnetic pole. $\mathbf{D_{ref}}$ and $\mathbf{I_{ref}}$ are declination and inclination for a reference locality (-2.1°N/298.4°E for Amazonian craton, 61.7°N/26.09°E for Baltica/Fennoscandia, 20.91°N/80.21°E for India, -23.15°N/27.5°E for Kalahari, 68.98°N/251.54°E for Slave, 54.95°N/276.16°E for Superior, and 60°N/275°E for Laurentia). **Pol** indicates the polarity of the paleopole, either normal (N) or reverse (R), and (C) combined. (M) indicates presence of mixed polarities (N and R not available). Q - Quality factors (1-7) of Van der Voo (1990a). **Age (Ma)** based on U-Pb baddeleyite, zircon and perovskite dating is listed as U-b, U-z and U-p, respectively. Age Ar-Ar based on biotite, plagioclase and phlogopite is listed A-bi, A-pl and A-phl. Age Sm-Nd, K-Ar are indicated. Corr. is indicated when the units are not dated but correlated with a coeval formation well-dated. “APWP” is indicated when the age is determined by correlation with the apparent polar wander path of the craton. **Confidence** is an indication that remanence is primary with presence of paleomagnetic field test (BCT = Baked Contact Test, i-BCT = inverse Baked Contact Test, BCT (p) = baked contact profile test, C = intraformational conglomerate test, FT = Fold Test, S = Secular variation test, X = regional consistency over a large geographical area, D = remanence direction correlation test, R = reversal test, APWP = correlation with APW path of the crato

Thèse de doctorat – Paul Yves Jean Antonio
DIRECTEUR/TRICE DE THESE : Prof. Anne Nédélec (GET) / Prof. Manoel D'Agrella-Filho (IAG-USP)
LIEU ET DATE DE SOUTENANCE : São Paulo, le jeudi 16 février 2017 (en cotutelle)

Paléomagnétisme et pétrogenèse des unités paléoprotérozoïques de l'événement Uatumã au nord du craton amazonien

Résumé

Un volumineux magmatisme anorogénique a recouvert une large partie du Craton Amazonien vers 1880 Ma : c'est l'évènement Uatumã. L'objectif de cette thèse est d'étudier le paléomagnétisme de ces roches afin de définir la place du Craton Amazonien au sein du premier supercontinent de l'histoire de la Terre, le Supercontinent Columbia. Deux régions ont été échantillonnées dans l'état du Pará (Brésil) : (1) la région de Tucumã, (2) la région de São Felix do Xingu. L'aimantation rémanente portée par ces roches a permis de déterminer deux nouveaux pôles paléomagnétiques primaires. Le pôle SF1 est obtenu pour des rhyolites et des andésites datées à ~1880 Ma. Le pôle SF2 est déterminé par l'aimantation rémanente d'un filon felsique daté à ~1855 Ma. Les pôles SF1 et SF2 sont très différents, malgré une différence d'âge de seulement ~25 Ma.

Des résultats paléomagnétiques similaires ont été obtenus pour des pôles de même âge dans d'autres cratons (Inde, Supérieur et Slave dans la Laurentia, Kalahari, Baltica, Sibérie). Ils peuvent être expliqués par un événement de Vraie Dérive Polaire (VDP, ou *TPW, True Polar Wander*). En effet, cette époque (~1880 Ma) est marquée par une forte activité du manteau (superpanaches), ce qui a provoqué des perturbations de densité modifiant le tenseur inertiel de gravité de la Terre. Ces événements peuvent être liés à une réorganisation globale du manteau à la suite d'une période de faible activité magmatique entre 2400 et 2200 Ma.

Mots clés : Craton amazonien, Paléomagnétisme, Columbia, Vraie dérive polaire (*VDP*), Uatumã.

Paleomagnetism and petrogenesis of Paleoproterozoic units from the Uatumã event in the northern Amazonian Craton

Abstract

A large anorogenic magmatism covered a large part of the Amazonian craton at *ca*. 1880 Ma: the so-called Uatumã event. The aim of this thesis is to study the paleomagnetism of these rocks to define the position of the Amazonian craton in the first Supercontinent of Earth's history, Supercontinent Columbia. Two areas were sampled in the state of Pará (Brazil): (1) the Tucumã area, (2) the São Felix do Xingu area. According to the remanent magnetization carried by these rocks we determined two new primary paleomagnetic poles. The SF1 pole is obtained for rhyolites and andesites well-dated (~1880 Ma). The SF2 pole is determined by the remanent magnetization of a felsic dike dated at ~1855 Ma. These two poles (SF1 and SF2) show a significant angular difference, despite a difference of ~25 Ma.

Similar paleomagnetic results for this period have been obtained in other cratons (India, Superior and Slave in Laurentia, Kalahari, Baltica, Siberia). They can be explained by a True Polar Wander event (TPW). Indeed, this period (~1880 Ma) is marked by a strong mantle activity as suggested by geological evidences (superswells), which caused density perturbations modifying the Earth's inertia tensor. These events may be related to a whole reorganization of the mantle convection following a period of magmatic shutdown between 2400 and 2200 Ma.

Keywords : Amazonian craton, Paleomagnetism, Columbia, True Polar Wander (*TPW*), Uatumã.

DISCIPLINE ADMINISTRATIVE : Sciences de la Terre et des Planètes Solides
LABORATOIRES : Géosciences Environnement Toulouse (GET), 14 avenue Edouard Belin, 31400 Toulouse (France) / Instituto de Astronomia, Geofísica e Ciências Atmosféricas (IAG-USP), Rua do Matão, 1226 - Cidade Universitária São Paulo-SP (Brésil)